

# Tumor microenvironment immunophenotypes and disease progression

**Edited by**

Ana Carolina Monteiro, Ana Paula Lepique, Martin Hernán Bonamino and Mercedes Beatriz Fuertes

**Published in**

Frontiers in Immunology



**FRONTIERS EBOOK COPYRIGHT STATEMENT**

The copyright in the text of individual articles in this ebook is the property of their respective authors or their respective institutions or funders. The copyright in graphics and images within each article may be subject to copyright of other parties. In both cases this is subject to a license granted to Frontiers.

The compilation of articles constituting this ebook is the property of Frontiers.

Each article within this ebook, and the ebook itself, are published under the most recent version of the Creative Commons CC-BY licence. The version current at the date of publication of this ebook is CC-BY 4.0. If the CC-BY licence is updated, the licence granted by Frontiers is automatically updated to the new version.

When exercising any right under the CC-BY licence, Frontiers must be attributed as the original publisher of the article or ebook, as applicable.

Authors have the responsibility of ensuring that any graphics or other materials which are the property of others may be included in the CC-BY licence, but this should be checked before relying on the CC-BY licence to reproduce those materials. Any copyright notices relating to those materials must be complied with.

Copyright and source acknowledgement notices may not be removed and must be displayed in any copy, derivative work or partial copy which includes the elements in question.

All copyright, and all rights therein, are protected by national and international copyright laws. The above represents a summary only. For further information please read Frontiers' Conditions for Website Use and Copyright Statement, and the applicable CC-BY licence.

ISSN 1664-8714  
ISBN 978-2-83251-620-1  
DOI 10.3389/978-2-83251-620-1

## About Frontiers

Frontiers is more than just an open access publisher of scholarly articles: it is a pioneering approach to the world of academia, radically improving the way scholarly research is managed. The grand vision of Frontiers is a world where all people have an equal opportunity to seek, share and generate knowledge. Frontiers provides immediate and permanent online open access to all its publications, but this alone is not enough to realize our grand goals.

## Frontiers journal series

The Frontiers journal series is a multi-tier and interdisciplinary set of open-access, online journals, promising a paradigm shift from the current review, selection and dissemination processes in academic publishing. All Frontiers journals are driven by researchers for researchers; therefore, they constitute a service to the scholarly community. At the same time, the *Frontiers journal series* operates on a revolutionary invention, the tiered publishing system, initially addressing specific communities of scholars, and gradually climbing up to broader public understanding, thus serving the interests of the lay society, too.

## Dedication to quality

Each Frontiers article is a landmark of the highest quality, thanks to genuinely collaborative interactions between authors and review editors, who include some of the world's best academicians. Research must be certified by peers before entering a stream of knowledge that may eventually reach the public - and shape society; therefore, Frontiers only applies the most rigorous and unbiased reviews. Frontiers revolutionizes research publishing by freely delivering the most outstanding research, evaluated with no bias from both the academic and social point of view. By applying the most advanced information technologies, Frontiers is catapulting scholarly publishing into a new generation.

## What are Frontiers Research Topics?

Frontiers Research Topics are very popular trademarks of the *Frontiers journals series*: they are collections of at least ten articles, all centered on a particular subject. With their unique mix of varied contributions from Original Research to Review Articles, Frontiers Research Topics unify the most influential researchers, the latest key findings and historical advances in a hot research area.

Find out more on how to host your own Frontiers Research Topic or contribute to one as an author by contacting the Frontiers editorial office: [frontiersin.org/about/contact](http://frontiersin.org/about/contact)

# Tumor microenvironment immunophenotypes and disease progression

## Topic editors

Ana Carolina Monteiro — Fluminense Federal University, Brazil

Ana Paula Lepique — University of São Paulo, Brazil

Martin Hernán Bonamino — National Cancer Institute (INCA), Brazil

Mercedes Beatriz Fuentes — CONICET Institute of Biology and Experimental Medicine (IBYME), Argentina

## Citation

Monteiro, A. C., Lepique, A. P., Bonamino, M. H., Fuentes, M. B., eds. (2023).

*Tumor microenvironment immunophenotypes and disease progression*.

Lausanne: Frontiers Media SA. doi: 10.3389/978-2-83251-620-1

# Table of contents

05 **Editorial: Tumor microenvironment immunophenotypes and disease progression**  
Ana Carolina Monteiro, Ana Paula Lepique, Martin Bonamino and Mercedes Beatriz Fuertes

08 **Desmoplastic Reaction, Immune Cell Response, and Prognosis in Colorectal Cancer**  
Naohiko Akimoto, Juha P. Väyrynen, Melissa Zhao, Tomotaka Ugai, Kenji Fujiyoshi, Jennifer Borowsky, Rong Zhong, Koichiro Haruki, Kota Arima, Mai Chan Lau, Junko Kishikawa, Tyler S. Twombly, Yasutoshi Takashima, Mingyang Song, Xuehong Zhang, Kana Wu, Andrew T. Chan, Jeffrey A. Meyerhardt, Marios Giannakis, Jonathan A. Nowak and Shuji Ogino

24 **Programmed Cell Death Tunes Tumor Immunity**  
Jing Liu, Minjing Hong, Yijia Li, Dan Chen, Yangzhe Wu and Yi Hu

39 **Tumor-Resident T Cells, Associated With Tertiary Lymphoid Structure Maturity, Improve Survival in Patients With Stage III Lung Adenocarcinoma**  
Hua Zhao, Hao Wang, Yu Zhao, Qian Sun and Xiubao Ren

51 **Neutrophil Extracellular Traps (NETs) Promote Non-Small Cell Lung Cancer Metastasis by Suppressing lncRNA MIR503HG to Activate the NF- $\kappa$ B/NLRP3 Inflammasome Pathway**  
Yong Wang, Fen Liu, Lin Chen, Chen Fang, Shuangyan Li, Shangkun Yuan, Xiaoying Qian, Yan Yin, Biao Yu, Biqi Fu, Xinwei Zhang and Yong Li

68 **Classification of colon adenocarcinoma based on immunological characterizations: Implications for prognosis and immunotherapy**  
Midie Xu, Jinjia Chang, Wenfeng Wang, Xin Wang, Xu Wang, Weiwei Weng, Cong Tan, Meng Zhang, Shujuan Ni, Lei Wang, Zhaohui Huang, Zhenzhong Deng, Wenhua Li, Dan Huang and Weiqi Sheng

87 **Oral squamous cell carcinoma (OSCC) tumors from heavy alcohol consumers are associated with higher levels of TLR9 and a particular immunophenotype: Impact on patient survival**  
Nicolás Bolesina, Gerardo Gatti, Silvia López de Blanc, Sabrina Dhooge, Darío Rocha, Elmer Fernandez, Ruth Ferreyra, Vanesa Palla, Verónica Grupe, Rosana Morelatto and Mariana Maccioni

100 **Metabolic-related gene pairs signature analysis identifies ABCA1 expression levels on tumor-associated macrophages as a prognostic biomarker in primary IDH<sup>WT</sup> glioblastoma**  
Shiqun Wang, Lu Li, Shuguang Zuo, Lingkai Kong, Jiwu Wei and Jie Dong

116 **A comprehensive investigation discovered the novel methyltransferase METTL24 as one presumably prognostic gene for kidney renal clear cell carcinoma potentially modulating tumor immune microenvironment**  
Zhongji Jiang, Wei Zhang, Zhipeng Zeng, Donge Tang, Chujiao Li, Wanxia Cai, Yumei Chen, Ya Li, Qiu Jin, Xinzhou Zhang, Lianghong Yin, Xueyan Liu, Yong Xu and Yong Dai

131 **EPSTI1 as an immune biomarker predicts the prognosis of patients with stage III colon cancer**  
Xitao Wang, Wei Cheng, Xingzhi Zeng, Xiaolin Dou, Zhongyi Zhou and Qian Pei

144 **Exploring the immunomodulatory role of virtual memory CD8<sup>+</sup> T cells: Role of IFN gamma in tumor growth control**  
Constanza Savid-Frontera, Maria Estefania Viano, Natalia S. Baez, Nicolas L. Lidon, Quentin Fontaine, Howard A. Young, Lene Vimeux, Emmanuel Donnadieu and Maria Cecilia Rodriguez-Galan

162 **Immune profiling identifies CD8<sup>+</sup> T-cell subset signatures as prognostic markers for recurrence in papillary thyroid cancer**  
Zhen Chen, Meng-Li Guo, Ya-Yi Li, Kai Yan, Liang Li, Fei Shen, Haixia Guan, Qing-Zhi Liu, Bo Xu and Zhe-Xiong Lian



## OPEN ACCESS

EDITED AND REVIEWED BY  
Jessica Dal Col,  
University of Salerno, Italy

## \*CORRESPONDENCE

Ana Carolina Monteiro  
✉ [anacarolinadossantosmonteiro@id.uff.br](mailto:anacarolinadossantosmonteiro@id.uff.br)  
Ana Paula Lepique  
✉ [alepique@icb.usp.br](mailto:alepique@icb.usp.br)  
Martin Bonamino  
✉ [mbonamino@inca.gov.br](mailto:mbonamino@inca.gov.br)  
Mercedes Beatriz Fuertes  
✉ [merfuer@gmail.com](mailto:merfuer@gmail.com)

## SPECIALTY SECTION

This article was submitted to  
Cancer Immunity  
and Immunotherapy,  
a section of the journal  
Frontiers in Immunology

RECEIVED 09 January 2023

ACCEPTED 17 January 2023

PUBLISHED 24 January 2023

## CITATION

Monteiro AC, Lepique AP, Bonamino M and  
Fuertes MB (2023) Editorial: Tumor  
microenvironment immunophenotypes  
and disease progression.  
*Front. Immunol.* 14:1141084.  
doi: 10.3389/fimmu.2023.1141084

## COPYRIGHT

© 2023 Monteiro, Lepique, Bonamino and  
Fuertes. This is an open-access article  
distributed under the terms of the [Creative  
Commons Attribution License \(CC BY\)](#). The  
use, distribution or reproduction in other  
forums is permitted, provided the original  
author(s) and the copyright owner(s) are  
credited and that the original publication in  
this journal is cited, in accordance with  
accepted academic practice. No use,  
distribution or reproduction is permitted  
which does not comply with these terms.

# Editorial: Tumor microenvironment immunophenotypes and disease progression

Ana Carolina Monteiro<sup>1,2\*</sup>, Ana Paula Lepique<sup>3\*</sup>,  
Martin Bonamino<sup>4,5\*</sup> and Mercedes Beatriz Fuertes<sup>6\*</sup>

<sup>1</sup>Osteo and tumor immunology laboratory (LOIT), Biology Institute (EGB), Fluminense Federal University (UFF), Rio de Janeiro, Brazil, <sup>2</sup>Laboratory on Thymus Research, Oswaldo Cruz Foundation, Rio de Janeiro, Brazil, <sup>3</sup>Instituto de Ciências Biomédicas, Universidade de São Paulo, Department of Immunology, São Paulo, Brazil, <sup>4</sup>Programa de Carcinogênese Molecular, National Cancer Institute (INCa), Rio de Janeiro, Brazil, <sup>5</sup>Vice-presidência de pesquisa e coleções biológicas, Oswaldo Cruz Foundation, Rio de Janeiro, Brazil, <sup>6</sup>Laboratorio de Fisiopatología de la Inmunidad Innata, Instituto de Biología y Medicina Experimental (IBYME), Consejo Nacional de Investigaciones Científicas y Técnicas (CONICET), Buenos Aires, Argentina

## KEYWORDS

tumor microenvironment (TME), immunophenotypes, tumor-infiltrating immune cells, biomarker, tumor immunity, disease progression

## Editorial on the Research Topic

### Tumor microenvironment immunophenotypes and disease progression

Tumor cells constantly interact with their microenvironment, which comprises a great diversity of immune cells and non-immune stromal cells, such as endothelial cells and fibroblasts. These interactions are considered critical regulators of tumor development, growth, invasion, and establishment of metastases. A variety of immune cells infiltrating the tumor microenvironment (TME) exists across different cancer types but also among patients with the same tumor disease and even in different tumor areas within the same patient. Indeed, their functional immunophenotypes, localization inside or outside the TME, molecular patterns, cytokine signatures, densities, and metabolic status have been implicated in the promotion or inhibition of cancer progression, recurrence, and successful response to immunotherapies. Therefore, studying the immunological phenotypes, “immune contexture”, or immunoscore of the TME is of paramount importance given the clinical impact of their composition and extent. For instance, a strong infiltration by CD8<sup>+</sup> cytotoxic T cells, Th1 CD4<sup>+</sup> T cells, type 1 like macrophages (M $\phi$ s) and neutrophils (N $\phi$ s), B cells and follicular helper T cells (T $F_h$ ) are generally associated with a favorable prognosis with long-term survival and prediction of response to treatment, while the presence of regulatory, Th2 and/or Th17 CD4<sup>+</sup> T cells, and type 2 like M $\phi$ s and N $\phi$ s infiltrating TME are widely considered negative prognostic markers.

Providing important insights, the past twenty years have witnessed an explosion of research into the biology and clinical applications of tumor immune contexture to restrict and impair tumorigenesis. Accordingly, this Research Topic was developed to update our current knowledge about the complexity and diversity of the immune contexture of TME and its influence in disease progression and response to therapy. Under this Research Topic, a

series of articles were published, providing meaningful insights toward this field. Briefly, this collection comprises ten original research articles, and one review of the current literature.

Three of the manuscripts focused on the study of colon cancers for identification of new biomarkers for prognosis. [Xu et al.](#) addressed the importance of colon adenocarcinoma classification based on immunophenotypes. These authors described seventeen prognostic-related immune characteristics (including IFNG signature, MDSC and T cell abundance) to cluster colon cancers in three distinct immune signatures (IS) with increasingly better prognostic and therapeutic responses. Briefly, IS1 is immune infiltrated but immunosuppressive, IS2 is immune “cold” and IS3 is immune “hot”. The authors believe that this immune-based classification could be employed as a tool for personalized colon cancer immunotherapy decision and/or tumor prognosis. [Wang et al.](#) explored the potential of TME *immunoscore* classification for stage-III colon cancer patients’ prognosis and therapeutics. They identified differentially expressed genes between the high and low TME immunoscore groups and characterized EPST11 as a novel immune prognostic biomarker for stage III colon cancer. EPST11 expression was positively associated with relapse-free survival and with M1-like M $\phi$ s and myeloid DCs infiltrating TME. [Akimoto et al.](#) showed that immature desmoplastic reaction and myxoid stroma were associated with lower frequency of memory CD8 $^{+}$  T cells and M1-like M $\phi$ s in the epithelial and stroma fractions of colorectal tumors, respectively. They described a relationship between immune and non-immune cells inside colorectal TME supporting the notion that these interactions can serve as prognostic markers.

Considering glioblastoma, [Wang et al.](#) developed a metabolic-related gene pair (MRGP) prognostic signature, that allows patient stratification into high- and low-risk groups, in terms of overall survival. The high-risk group showed a particular TME immunoscore, characterized by an increase in monocytes and fewer activated DCs, natural killer (NK) cells and gamma-delta ( $\gamma\delta$ ) T cells. MRGP analysis showed that ABCA1 expression increases on tumor-associated M $\phi$ s (TAMs) as tumor progresses, suggesting that cholesterol metabolism plays a vital role in the functional polarization of TAMs. Lovastatin treatment, both *in vitro* and *in vivo*, reduced ABCA1 expression in TAMs and promoted their polarization towards an inflammatory phenotype, which in turn controlled tumor progression. Therefore, they elected ABCA1 expressed on TAMs as a feasible prognostic biomarker for primary glioblastoma.

In the context of lung cancer, [Zhao et al.](#) investigated the clinical significance of tertiary lymphoid structure (TLS) maturity and its association with the spatial distribution of tumor-resident memory (T<sub>RM</sub>) T cell subsets, in advanced stage III lung adenocarcinoma (LUAD). The authors divided the patients in three groups, alongside TLS maturation state. The results showed that the proportion of CD4 $^{+}$ CD103 $^{+}$  and CD8 $^{+}$ CD103 $^{+}$  T<sub>RM</sub> T cells, preferentially located within TLS was significantly increased by TLS gradual maturation and disease-free survival. Taking together, these authors suggested that TLS maturation state and the frequency of T<sub>RM</sub> could be used as prognostic markers in stage III LUAD. In non-small cell lung cancer (NSCLC), [Wang et al.](#) showed that neutrophil extracellular traps (NETs) produced in the TME activate the NF- $\kappa$ B/NLRP3 pathway by

downregulating MIR503HG expression to promote epithelial to mesenchymal transition (EMT) and metastasis.

Regarding tumor infiltrating lymphocytes, [Chen et al.](#) investigated the controversial prognostic value of CD8 $^{+}$  T cells infiltrating papillary thyroid cancer (PTC). Flow cytometry analysis and multiplex immunohistochemistry of tissue samples from multinodular non-toxic goiter (MNG), — taken as normal thyroid tissue, versus PTC tumors showed that CD8 $^{+}$  T cells in cancer patients present a dysfunctional state. Importantly, compared data from immune cells status, during the process of MNG to PTC, showed that the CD8 $^{+}$  T cell immune contexture is altered after the occurrence of malignancy, moving from an activated anti-tumor status toward an inhibitory phenotype. [Savid-Frontera et al.](#) analyzed the role of virtual memory CD8 $^{+}$  T (T<sub>VM</sub>) cells, — a T cell subset with innate-like characteristics-, for anti-tumor immune response. They showed that systemic expression of both IL-12 and IL-18 in experimental models of melanoma and pancreatic ductal adenocarcinoma leads to an early accumulation of T<sub>VM</sub> cells in the TME, which contribute to control tumor growth.

[Liu et al.](#) published a review concerning the relationship between programmed cell death and the modulation of TME towards an immunosuppressive profile. [Bolesina et al.](#) reported a correlation between heavy alcohol consumption and a higher TLR9 expression on oral squamous cell carcinoma (OSCC). OSCC expressing TLR9 molecules showed a decrease in tumor infiltrating CD8 $^{+}$  T cells and a diminished overall survival. These authors suggest that the loop generated by alcohol consumption and a higher TLR9 expression might have an impact on the distribution of CD8 $^{+}$  T cells inside the tumor and patient survival. [Jiang et al.](#) showed that in patients with renal cell carcinoma the expression of methyltransferase METTL24 was lower in tumors than in adjacent normal tissue. METTL24 expression correlated with several immune parameters, many linked to NF- $\kappa$ B signaling and a low METTL24 expression correlated with poor prognosis.

Altogether, these articles highlight the progress in our understanding of how immunophenotypes infiltrating the TME regulate many facets of tumor development and progression, but also help underscore many unresolved and even controversial areas of tumor immunology research. We are grateful for the considerable efforts that the authors and reviewers have made to help us compile this collection for *Frontiers in Immunology*.

## Author contributions

ACM: Drafted the article; APL, MB and MF: provided critical inputs and corrected the manuscript. All authors contributed to the article and approved the submitted version.

## Funding

This work was supported by funds from Faperj (Foundation for Research Support of the State of Rio de Janeiro, ACM and MB); FOPESQ UFF (Programa de Fomento a Pesquisa da Universidade Federal Fluminense, ACM); CNPq (National Research Council, APL

and MB); FAPESP (São Paulo Estate Research Foundation, APL); CONICET (National Research Council of Argentina, MF) and ANPCYT (National Agency for Promotion of Science and Technology from Argentina, MF).

## Acknowledgments

We express our gratitude to all the authors who have contributed to this research topic and to the reviewers for their valuable work. We hope that the reader will find this Research Topic motivating and helpful. We invite you to read the following articles and immerse yourself in the interesting world of tumoral immunology.

## Conflict of interest

The authors declare that the research was conducted in the absence of any commercial or financial relationships that could be construed as a potential conflict of interest.

## Publisher's note

All claims expressed in this article are solely those of the authors and do not necessarily represent those of their affiliated organizations, or those of the publisher, the editors and the reviewers. Any product that may be evaluated in this article, or claim that may be made by its manufacturer, is not guaranteed or endorsed by the publisher.



# Desmoplastic Reaction, Immune Cell Response, and Prognosis in Colorectal Cancer

## OPEN ACCESS

### Edited by:

Ana Paula Lepique,  
University of São Paulo, Brazil

### Reviewed by:

Wilma Mesker,

Leiden University Medical Center,  
Netherlands  
Ines Nearchou,  
Indica Labs, United Kingdom

### \*Correspondence:

Shuji Ogino  
sogino@bwh.harvard.edu

<sup>†</sup>These authors have contributed  
equally to this work and share  
first authorship

<sup>‡</sup>These authors have contributed  
equally to this work and share  
last authorship

### Specialty section:

This article was submitted to  
Cancer Immunity and Immunotherapy,  
a section of the journal  
Frontiers in Immunology

**Received:** 20 December 2021

**Accepted:** 22 February 2022

**Published:** 22 March 2022

### Citation:

Akimoto N, Väyrynen JP, Zhao M, Ugai T, Fujiyoshi K, Borowsky J, Zhong R, Haruki K, Arima K, Lau MC, Kishikawa J, Twombly TS, Takashima Y, Song M, Zhang X, Wu K, Chan AT, Meyerhardt JA, Giannakis M, Nowak JA and Ogino S (2022) Desmoplastic Reaction, Immune Cell Response, and Prognosis in Colorectal Cancer. *Front. Immunol.* 13:840198. doi: 10.3389/fimmu.2022.840198

**Naohiko Akimoto**<sup>1,2†</sup>, **Juha P. Väyrynen**<sup>1,3,4†</sup>, **Melissa Zhao**<sup>1†</sup>, **Tomotaka Ugai**<sup>1,5†</sup>, **Kenji Fujiyoshi**<sup>1</sup>, **Jennifer Borowsky**<sup>1</sup>, **Rong Zhong**<sup>1</sup>, **Koichiro Haruki**<sup>1</sup>, **Kota Arima**<sup>1</sup>, **Mai Chan Lau**<sup>1</sup>, **Junko Kishikawa**<sup>1</sup>, **Tyler S. Twombly**<sup>1</sup>, **Yasutoshi Takashima**<sup>1</sup>, **Mingyang Song**<sup>6,7,8</sup>, **Xuehong Zhang**<sup>6,9</sup>, **Kana Wu**<sup>5,6,9</sup>, **Andrew T. Chan**<sup>7,8,9,10</sup>, **Jeffrey A. Meyerhardt**<sup>3‡</sup>, **Marios Giannakis**<sup>3,11,12‡</sup>, **Jonathan A. Nowak**<sup>1‡</sup> and **Shuji Ogino**<sup>1,5,11,13\*‡</sup>

<sup>1</sup> Program in Molecular Pathological Epidemiology, Department of Pathology, Brigham and Women's Hospital, Harvard Medical School, Boston, MA, United States, <sup>2</sup> Department of Gastroenterology, Nippon Medical School, Graduate School of Medicine, Tokyo, Japan, <sup>3</sup> Department of Medical Oncology, Dana-Farber Cancer Institute, Harvard Medical School, Boston, MA, United States, <sup>4</sup> Cancer and Translational Medicine Research Unit, Medical Research Center Oulu, Oulu University Hospital, and University of Oulu, Oulu, Finland, <sup>5</sup> Department of Epidemiology, Harvard T.H. Chan School of Public Health, Boston, MA, United States, <sup>6</sup> Department of Nutrition, Harvard T.H. Chan School of Public Health, Boston, MA, United States, <sup>7</sup> Clinical and Translational Epidemiology Unit, Massachusetts General Hospital, Harvard Medical School, Boston, MA, United States, <sup>8</sup> Division of Gastroenterology, Massachusetts General Hospital, Boston, MA, United States, <sup>9</sup> Channing Division of Network Medicine, Department of Medicine, Brigham and Women's Hospital, Harvard Medical School, Boston, MA, United States, <sup>10</sup> Department of Immunology and Infectious Diseases, Harvard T.H. Chan School of Public Health, Boston, MA, United States, <sup>11</sup> Broad Institute of MIT and Harvard, Cambridge, MA, United States, <sup>12</sup> Department of Medicine, Brigham and Women's Hospital, Harvard Medical School, Boston, MA, United States, <sup>13</sup> Cancer Immunology and Cancer Epidemiology Programs, Dana-Farber Harvard Cancer Center, Boston, MA, United States

**Background:** The relationships between tumor stromal features (such as desmoplastic reaction, myxoid stroma, and keloid-like collagen bundles) and immune cells in the colorectal carcinoma microenvironment have not yet been fully characterized.

**Methods:** In 908 tumors with available tissue among 4,465 incident colorectal adenocarcinoma cases in two prospective cohort studies, we examined desmoplastic reaction, myxoid stroma, and keloid-like collagen bundles. We conducted multiplex immunofluorescence for T cells [CD3, CD4, CD8, CD45RO (PTPRC), and FOXP3] and for macrophages [CD68, CD86, IRF5, MAF, and MRC1 (CD206)]. We used the inverse probability weighting method and the 4,465 incident cancer cases to adjust for selection bias.

**Results:** Immature desmoplastic reaction was associated with lower densities of intraepithelial CD3<sup>+</sup>CD8<sup>+</sup>CD45RO<sup>+</sup> cells [multivariable odds ratio (OR) for the highest (vs. lowest) density category, 0.43; 95% confidence interval (CI), 0.29–0.62;  $P_{\text{trend}} < 0.0001$ ] and stromal M1-like macrophages [the corresponding OR, 0.44; 95% CI, 0.28–0.70;  $P_{\text{trend}} = 0.0011$ ]. Similar relations were observed for myxoid stroma [intraepithelial CD3<sup>+</sup>CD8<sup>+</sup>CD45RO<sup>+</sup> cells ( $P_{\text{trend}} < 0.0001$ ) and stromal M1-like macrophages ( $P_{\text{trend}} = 0.0007$ )] and for keloid-like collagen bundles ( $P_{\text{trend}} < 0.0001$  for intraepithelial CD3<sup>+</sup>CD8<sup>+</sup>CD45RO<sup>+</sup> cells). In colorectal cancer-specific survival analyses,

multivariable-adjusted hazard ratios (with 95% confidence intervals) were 0.32 (0.23–0.44;  $P_{\text{trend}} < 0.0001$ ) for mature (vs. immature) desmoplastic reaction, 0.25 (0.16–0.39;  $P_{\text{trend}} < 0.0001$ ) for absent (vs. marked) myxoid stroma, and 0.12 (0.05–0.28;  $P_{\text{trend}} < 0.0001$ ) for absent (vs. marked) keloid-like collagen bundles.

**Conclusions:** Immature desmoplastic reaction and myxoid stroma were associated with lower densities of tumor intraepithelial memory cytotoxic T cells and stromal M1-like macrophages, likely reflecting interactions between tumor, immune, and stromal cells in the colorectal tumor microenvironment.

**Keywords:** cancer-associated fibroblast (CAF), clinical outcomes, host-tumor interaction, lymphocytic reaction, microsatellite instability, molecular pathological epidemiology (MPE), immune response, tumor immune microenvironment

## INTRODUCTION

Tumor–host interactions have been recognized as important determinants of cancer progression (1, 2). An antitumor immune response requires coordinated efforts of various cells including T cells and macrophages (1, 2). Evidence indicates that cancer development and progression are influenced by interactions between tumor, immune, and other stromal cells. However, the relationship between immune and other stromal cells in the tumor microenvironment remains to be further studied (3–5).

Desmoplastic reaction to tumor denotes the growth of fibrous connective tissue around tumor cells and has been recognized as a potential prognostic marker for colorectal cancer. It is usually classified into (1) an immature type that is characterized by myxoid stroma composed of basophilic, amorphous extracellular matrix; (2) an intermediate type, defined by hyalinized thick bundles of hypocellular keloid-like collagen; and (3) a mature type that demonstrates neither myxoid stroma nor keloid-like collagen (6–13).

Although a study has shown that the number of CD3<sup>+</sup> lymphocytes was lower in tumors with immature stroma (11), the relationship of desmoplastic reaction and its morphological components with more detailed immune cell types has not been adequately elucidated. Additionally, the three-tiered classification for desmoplastic reaction is based on a joint evaluation of myxoid stroma and keloid-like collagen, and the relative prognostic significance of each component remains unclear. While ample evidence supports the clinical efficacy of desmoplastic reaction in cases with pT3 and pT4 invasion, several studies, including patients who undergone surgical or endoscopic mucosal resection, have suggested an association of desmoplastic reaction in biopsy specimen with massive invasion into the submucosal layer in pT1 cases (14–17). Therefore, we have included all desmoplastic reaction cases regardless of pT stages.

**Abbreviations:** AJCC, American Joint Committee on Cancer; CI, confidence interval; CIMP, CpG island methylator phenotype; FFPE, formalin-fixed paraffin-embedded; HPFS, Health Professionals Follow-up Study; LINE-1, long interspersed nucleotide element-1; MSI, microsatellite instability; NHS, Nurses' Health Study; OR, odds ratio; PCR, polymerase chain reaction; SD, standard deviation; TNM, tumor, node and metastases.

In this study, we utilized a molecular pathological epidemiology database of 908 colorectal cancer cases among 4,465 cases that had occurred in two U.S.-wide prospective cohort studies. We measured T-cell and macrophage densities using two customized 7-plex immunofluorescence assays. We tested the hypothesis that densities of certain T-cell and macrophage subsets might be inversely associated with immature desmoplastic reaction. In addition, we assessed the prognostic role of desmoplastic reaction, myxoid stroma, and keloid-like collagen bundles as well as their statistical interactions with specific T-cell and macrophage subsets in survival analyses.

## MATERIAL AND METHODS

### Study Population

The study population base (Figure 1) consisted of a total of 173,229 participants of the Health Professionals Follow-up Study (HPFS) (18) and the Nurses' Health Study (NHS) (19). The participants had been followed over decades *via* biennial questionnaires up to 2014, and a fraction of them ( $N = 4,465$ ) developed colorectal carcinoma during the follow-up period. Deaths of colorectal cancer patients were ascertained through questionnaire return by next-of-kin and the use of the National Death Index, which also helped us find lethal unreported colorectal cancer cases. Medical record review conducted by a study physician could confirm all colorectal cancer cases and determine cause of death in case of lethal cancer. Formalin-fixed paraffin-embedded (FFPE) tumor tissue blocks were accessed and retrieved from the hospitals where participants had been treated with surgical resection. We utilized all of the 4,465 cases to adjust for selection bias due to tissue data availability (see *Statistical Analyses*). Among the 4,465 patients, histopathological features of desmoplastic reaction were successfully assessed in 935 cases. Among those, we analyzed T-cell and macrophage densities and desmoplastic reaction in colorectal cancer tissue in 908 patients. On the basis of the colorectal continuum model, both colon and rectal carcinomas were included (20, 21). The study population analyzed in this study overlapped with several of our previous studies (22–25), but differed by the number of patients, the tested hypotheses, and new data generated in this

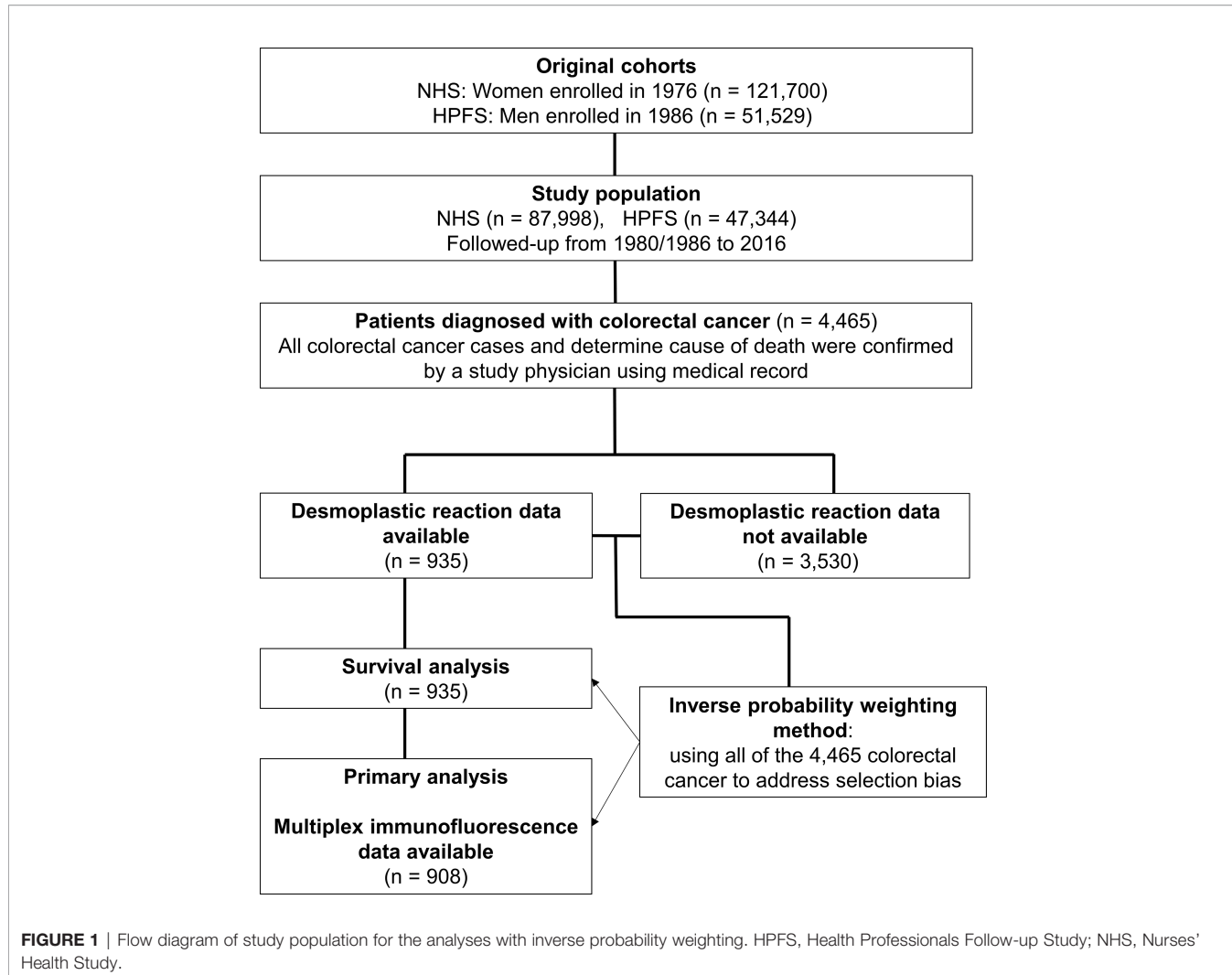


**FIGURE 1** | Flow diagram of study population for the analyses with inverse probability weighting. HPFS, Health Professionals Follow-up Study; NHS, Nurses' Health Study.

study. The study was approved by the institutional review boards of the Brigham and Women's Hospital and Harvard T.H. Chan School of Public Health (Boston, MA). All study participants provided informed consent. Participants with or without tumor tissue data exhibited no major clinical or demographic differences according to preceding preliminary studies (26–28).

## Immunohistochemistry and Tumor Morphology

Desmoplastic reaction was assessed using hematoxylin and eosin-stained tissue sections according to the three-tiered scale [mature (0), intermediate (1), and immature (2)] as described by Ueno et al. (5–11, 13, 29–31). In short, desmoplastic reaction was regarded as immature if myxoid changes were present in fibrotic stroma regardless of keloid-like collagen. Otherwise, it was classified into intermediate if stroma contained keloid-like collagen but no myxoid changes, or mature if stroma contained neither keloid-like collagen nor myxoid changes. In addition, myxoid stroma and keloid-like collagen bundles were separately assessed using four-tiered scales [absent (0), mild (1),

moderate (2), and marked (3)] (Figure 2). The myxoid stroma feature was classified as absent if stroma was composed of dense fibrotic tissue; mild if there was a mildly edematous and loose stromal appearance; moderate if there was loose, edematous, and pale-to-lightly basophilic stroma; or marked if there was prominently loose and pale-to-lightly basophilic stroma. The keloid-like collagen feature was classified into absent if there were no thick collagen bundles; mild if there were slightly thickened but not keloid-like collagen bundles; moderate if there were thick hyalinized bundles comprised of hypocellular eosinophilic hyalinized collagen; or marked if there were prominent and abundant keloid-like collagen bundles. These definitions were also transferred to a visual analog scale (Figure 2). These evaluations were conducted using a tumor slide containing the deepest level of invasion according to a previous study (32), and the final assessment was based on a single 10 $\times$  objective field at the invasive front with the most immature stroma. If two or more patterns were present in this field, the scoring was based on dominant characteristics, although immune cell populations were assessed in all fields regardless of

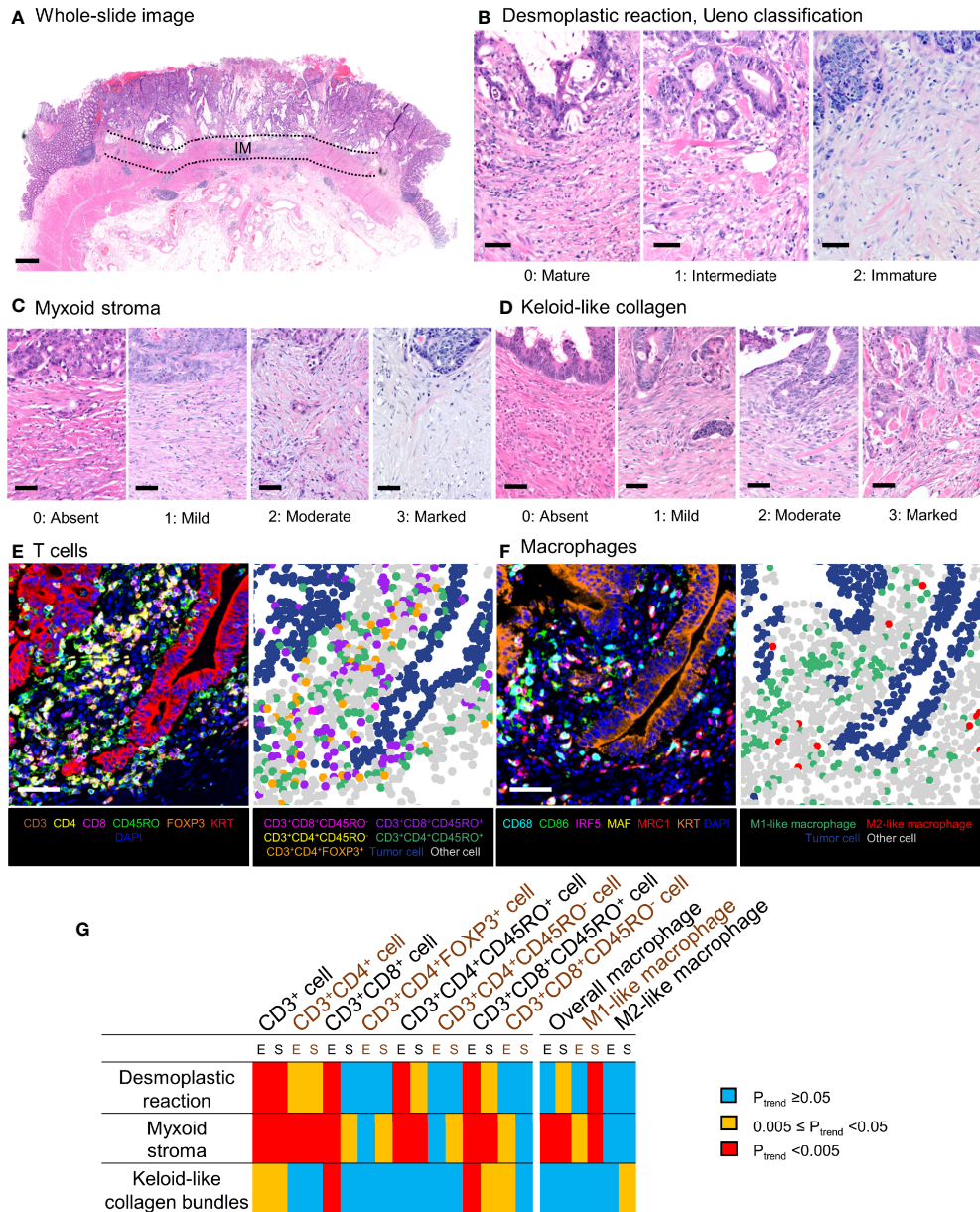


**FIGURE 2** | Evaluation of tumor stromal features and T-cell and macrophage infiltrates. Panels **(A–D)** demonstrate representative examples of the tumor stromal features using hematoxylin and eosin-stained sections. **(A)** The stroma was assessed according to the most immature stromal area at the invasive margin (IM) of the tumor. **(B)** Three-tiered Ueno classification of the desmoplastic reaction. **(C)** Four-tiered classification of myxoid stroma. **(D)** Four-tiered classification of keloid-like collagen. Scale bars indicate 1 mm **(A)** or 50  $\mu$ m **(B–D)**. **(E, F)** Examples of multiplex immunofluorescence images [**(E)** T cells, **(F)** macrophages]. The images, based on simultaneous measurement of the signal intensities of seven fluorophores, were used to identify individual tumor cells, immune cells, and other cells and further classify them using pathologist-supervised machine learning algorithms. Scale bars indicate 50  $\mu$ m **(E, F)**. **(G)** A matrix of  $P_{\text{trend}}$  values in multivariable logistic regression analyses to assess the associations of T-cell and macrophage densities in tumor intraepithelial or stromal regions with desmoplastic reaction and its components with inverse probability weighting. E, tumor intraepithelial region; IM, invasive margin; S, tumor stromal region.

the pattern of maturity. A single pathologist (JV) assessed all cases blinded to other data. A second pathologist (MZ) independently reviewed 135 cases, and the weighted kappa values between the two pathologists were 0.52 for desmoplastic reaction ( $P < 0.0001$ ), 0.57 for myxoid stroma ( $P < 0.0001$ ), and 0.40 for keloid-like collagen bundles ( $P < 0.0001$ ). A single pathologist (SO), blinded to

other data, categorized tumor differentiation into well to moderate vs. poor (>50% vs. ≤50% glandular area, respectively) and four components of lymphocytic reaction to tumors (tumor-infiltrating lymphocytes, intratumoral periglandular reaction, peritumoral lymphocytic reaction, and Crohn's-like lymphoid reaction) as negative/low (0) vs. intermediate (1+) vs. high (2+) (33).

## Analyses of T Cells and Macrophages in Tumor

Tissue microarrays were created using two to four tumor cores, selected to best represent overall tumor morphology (34, 35). The invasive margin or the areas utilized in the evaluation of desmoplastic reaction were not specifically sampled into the tissue microarrays. Two customized multiplex immunofluorescence assays were employed to determine patterns of expression of different T-cell markers [CD3, CD4, CD8, CD45RO (*PTPRC*), and FOXP3] as well as the epithelial cell marker KRT at the same time (panel 1). A second marker panel consisting of macrophage markers [CD68, CD86, IRF5, MAF, and MRC1 (*CD206*)], again together with KRT (panel 2), was also created, as we have previously published (22, 23, 36) using standardized protein nomenclature recommended by the expert panel (37). Tissue microarray core digital images were acquired with an automated multispectral imaging system (Vectra 3.0, Akoya Biosciences, Hopkinton, MA) at a magnification of  $\times 200$ . Supervised machine learning algorithms (inForm 2.4.1, Akoya Biosciences) were employed to analyze images using tissue segmentation (tumor epithelium, stroma, and other), cell segmentation (nuclear, cytoplasmic, and surface membrane compartments), and cell phenotyping algorithms built in the software (Figure 2). We investigated the coexpression patterns of CD3, CD4, CD8, CD45RO, and FOXP3 in each T cell and classified T-cell phenotypes as follows: CD3<sup>+</sup>CD8<sup>+</sup> cytotoxic T cells, CD3<sup>+</sup>CD4<sup>+</sup> helper T cells, CD3<sup>+</sup>CD4<sup>+</sup>FOXP3<sup>+</sup> regulatory T cells, CD3<sup>+</sup>CD4<sup>+</sup>CD45RO<sup>+</sup> memory T cells, and CD3<sup>+</sup>CD8<sup>+</sup>CD45RO<sup>+</sup> memory T cells. The inForm software used multinomial logistic regression in phenotype classification. For each cell [detected based on settings determined by study pathologists (JB for T-cell data; JV for macrophage data) such as size thresholds and DAPI intensity thresholds], inForm calculated hundreds of features, including morphological features (such as area and compactness) and texture features (such as Haralick features and spatial frequency measurements). Examples of different cell phenotypes (around 50 per phenotype) were manually annotated by the study pathologists. The software then used lasso regularization with cross-validation to select features and create models for the task. After the models showed satisfactory performance (based on visual examination by study pathologists in around 100 training images, including tumors with various morphologies), they were applied to all study images. The images were reviewed by study pathologists to confirm adequate performance of the classifiers and exclude unrepresentative images. Data were acquired at the single-cell level, and the presence of subsets of T cells and macrophages was quantified in the epithelial and stromal regions of the tumor, as we described earlier (22, 23, 36). Macrophages were characterized using an M1:M2 index of polarization defined by the levels of expression of two M1-polarization markers (CD86, IRF5) and two M2-polarization markers (MAF, MRC1) according to the formula  $(CD86 \times IRF5) / (MAF \times MRC1)$  (23). Thus, a higher M1:M2 value represents a greater degree of M1-polarization. For all macrophages identified in the tumor images, the 30% with the highest polarization indices were considered M1-like, whereas those with the lowest 30% were allocated to M2-like for the purpose of this analysis, as we have previously published (23). For each cell subset,

cases were classified into quartile categories (C1–C4) if there were  $\leq 25\%$  of cases with zero density. If there were  $> 25\%$  of cases with zero density for a specific cell type, these zero-density cases were grouped together (C1 category), and the remaining (nonzero) cases were divided into tertials (C2–C4). For a binary categorization, T-cell and macrophage densities were categorized as low vs. high based on the median value if the median was above zero; otherwise, as low (zero) vs. high (nonzero).

## Analyses of Tumor Molecular Characteristics

Genomic DNA was extracted from FFPE colorectal carcinoma tissue blocks. Ten microsatellite markers (D2S123, D5S346, D17S250, BAT25, BAT26, BAT40, D18S55, D18S56, D18S67, and D18S487) were assessed by PCR in order to determine the microsatellite instability (MSI) status, whereby the presence of  $\geq 30\%$  of these markers was taken to define MSI-high, as previously reported (20, 38). Eight CpG island methylator phenotype (CIMP)-specific promoters (*CACNA1G*, *CDKN2A*, *CRABP1*, *IGF2*, *MLH1*, *NEUROG1*, *RUNX3*, and *SOCS1*) were assessed using MethylLight assays on bisulfite-treated DNA, as described earlier (20, 38). CIMP-high status was assigned according to there being  $\geq 6$  of these 8 promoters that were methylated. Reciprocally, CIMP-low or negative was defined as having 0–5 methylated promoters, also as reported earlier (20). Methylation of long-interspersed nucleotide element-1 (LINE-1) was quantified by pyrosequencing of bisulfite-treated DNA, as previously described (20). PCR and pyrosequencing were carried out for *KRAS* (codons 12, 13, 61, and 146), *BRAF* (codon 600), and *PIK3CA* (exons 9 and 20) (20, 39).

## Statistical Analyses

The details of statistical analyses are described in **Supplementary Methods**. Briefly, all statistical analyses were performed using the SAS software (version 9.4, SAS Institute, Cary, NC). All P values were two-sided. We used the stringent two-sided  $\alpha$  level of 0.005, accounting for multiple comparisons (40). Our primary hypothesis testing was conducted to assess the association of T-cell and macrophage densities (four ordinal categories) in intraepithelial and stromal regions with desmoplastic reaction (three categories), myxoid stroma (four-tiered scale), and keloid-like collagen bundles (four-tiered scale) in the multivariable ordinal logistic regression models. All the other hypotheses were tested as secondary analyses. The American Joint Committee on Cancer TNM staging criteria were used to evaluate the disease stage. Chi-squared test was used to assess the relationship between clinicopathological features and desmoplastic reaction. To adjust for selection bias due to the availability of tumor tissue samples, we applied the inverse probability weighting (IPW) method in logistic regression, Cox regression, and Kaplan–Meier analyses, utilizing covariate data of 4,465 incident colorectal cancer cases (26–28, 41). To control for potential confounders, we used a multivariable ordinal logistic regression model that calculated odds ratios (ORs) for one category increase in desmoplastic reaction categories in relation to T-cell and macrophage densities.  $P_{\text{trend}}$  was calculated by the linear trend across the ordinal categories of desmoplastic reaction, myxoid stroma, and keloid-like collagen bundles while

adjusting for the same set of covariates. We also assessed a statistical interaction between T-cell/macrophage densities (four ordinal categories) and MSI status (high vs. non-high) for desmoplastic reaction (immature vs. intermediate vs. mature) using the Wald test for the cross-product term in multivariable logistic regression models. In the subgroup analysis of pT3 and pT4 cases, we assessed the association of T-cell and macrophage densities (four ordinal categories) in intraepithelial and stromal regions with desmoplastic reaction (three categories) in the multivariable ordinal logistic regression models.

In survival analyses, Kaplan–Meier method was used to estimate cumulative survival probabilities, and a linear trend in survival probability across ordinal categories of desmoplastic reaction, myxoid stroma, and keloid-like collagen bundles was determined using the log-rank test for trend. The inverse probability weighted multivariable Cox proportional hazard regression analyses were conducted for colorectal cancer-specific survival and overall survival according to desmoplastic reaction, myxoid stroma, and keloid-like collagen bundle grade. To control for potential confounders, we included the following covariates in the initial multivariable Cox regression model: age at diagnosis (continuous), sex (female vs. male), year of diagnosis (continuous), family history of colorectal cancer in any first-degree relative (present vs. absent), tumor location (proximal colon vs. distal colon vs. rectum), tumor differentiation (well-moderate vs. poor), American Joint Committee on Cancer (AJCC) disease stage (I-II vs. III-IV), MSI status (MSI-high vs. non-MSI-high), CIMP status (high vs. low/negative), LINE-1 methylation level (continuous), KRAS mutation (mutant vs. wild-type), BRAF mutation (mutant vs. wild-type), PIK3CA mutation (mutant vs. wild-type), tumor-infiltrating lymphocytes (negative/low vs. intermediate/high), intratumoral periglandular reaction (negative/low vs. intermediate/high), peritumoral lymphocytic reaction (negative/low vs. intermediate/high), Crohn's-like lymphoid reaction negative/low vs. intermediate/high), intraepithelial CD3<sup>+</sup>CD8<sup>+</sup>CD45RO<sup>+</sup> cell density (four ordinal categories), and stromal M1-like macrophage cell density (four ordinal categories). In addition, we assessed a statistical interaction between desmoplastic reaction/myxoid stroma/keloid-like collagen bundles (an ordinal variable) and T-cell/macrophage densities (a binary variable) for cancer-specific and overall survival using the Wald test for the cross-product term in multivariable-adjusted Cox regression models. In the subgroup analysis of AJCC disease stage I cases, we assessed colorectal cancer-specific survival and overall survival, according to the desmoplastic reaction, myxoid stroma, and keloid-like collagen bundle grade by using inverse probability weighted multivariable Cox proportional hazard regression models. A backward elimination was conducted with a threshold P of 0.05 to select variables for the final models in both logistic regression and Cox proportional hazard regression analyses.

## RESULTS

Among the 4,465 patients, histopathological features of desmoplastic reaction were successfully assessed in 935 cases.

Among those, we analyzed T-cell and macrophage densities and desmoplastic reaction in colorectal cancer tissue in 908 patients. Desmoplastic reaction at the invasive front was graded as mature, intermediate, and immature in 409 (45%), 230 (25%), and 269 (30%) cases, respectively. **Table 1, Supplementary Tables S1, and S2** summarize the clinical, pathological, and molecular characteristics. Immature desmoplastic reaction was associated with high pT, pN, and AJCC disease stage, poor tumor differentiation, lower intratumoral periglandular lymphocytic reaction, and lower peritumoral lymphocytic reaction (all  $P < 0.0001$ ).

In our primary hypothesis testing, we used both univariable and multivariable ordinal logistic regression analyses to assess the association of T-cell and macrophage densities in tumor intraepithelial and stromal regions with desmoplastic reaction, myxoid stroma, and keloid-like collagen bundles (**Tables 2, 3, Supplementary Tables S3, and S4**). In multivariable analyses, higher intraepithelial densities of CD3<sup>+</sup>CD4<sup>+</sup>CD45RO<sup>+</sup> cells, CD3<sup>+</sup>CD8<sup>+</sup>CD45RO<sup>+</sup> cells, CD3<sup>+</sup>CD8<sup>+</sup> cells, and CD3<sup>+</sup> cells were inversely associated with immature desmoplastic reaction and myxoid stroma (all  $P_{\text{trend}} < 0.001$ ). Multivariable odds ratios (ORs) for the highest (C4) (vs. lowest C1 category) intraepithelial CD3<sup>+</sup>CD8<sup>+</sup>CD45RO<sup>+</sup> cell density were 0.43 [95% confidence interval (CI) 0.29–0.62;  $P_{\text{trend}} < 0.0001$ ] for immature desmoplastic reaction, 0.33 (95% CI, 0.23–0.49;  $P_{\text{trend}} < 0.0001$ ) for myxoid stroma, and 0.44 (95% CI, 0.30–0.63;  $P_{\text{trend}} < 0.0001$ ) for keloid-like collagen bundles. In a subgroup of pT3 and pT4 cases ( $n = 605$ ), 233 cases were classified into immature, 172 intermediate, and 200 mature. In multivariable analyses, higher intraepithelial densities of CD3<sup>+</sup>CD8<sup>+</sup>CD45RO<sup>+</sup> cells were associated with immature desmoplastic reaction ( $P_{\text{trend}} = 0.0025$ ) in pT3 and pT4 cases (**Supplementary Table S5**).

Within the macrophage populations, higher tumor stromal M1-like macrophage densities were inversely associated with immature desmoplastic reaction [OR for the highest (vs. lowest) density category 0.44; 95% CI, 0.28–0.70;  $P_{\text{trend}} = 0.0011$ ] and myxoid stroma [OR for the highest (vs. lowest) density category 0.50; 95% CI, 0.34–0.74;  $P_{\text{trend}} = 0.0007$ ], while M2-like macrophage densities were not significantly associated with desmoplastic reaction, myxoid stroma, or keloid-like collagen bundles ( $P_{\text{trend}} > 0.03$ , with the  $\alpha$  level of 0.005). In the pT3 and pT4 case subgroup, higher overall tumor stromal macrophage densities were inversely associated with desmoplastic reaction ( $P_{\text{trend}} = 0.0036$ ), and higher tumor stromal M1-like macrophage densities showed a tendency toward an inverse association with immature desmoplastic reaction ( $P_{\text{trend}} = 0.0056$ ; with the  $\alpha$  level of 0.005; **Supplementary Table S6**).

The inverse associations of intraepithelial CD3<sup>+</sup>CD8<sup>+</sup>CD45RO<sup>+</sup> cell and stromal M1-like macrophage densities with immature desmoplastic reaction, myxoid stroma, and keloid-like collagen bundles did not significantly differ by tumor MSI status (all  $P_{\text{interaction}} > 0.3$ ; **Supplementary Table S7**).

In the survival analyses, we evaluated the prognostic significance of the desmoplastic reaction, myxoid stroma, and keloid-like collagen bundles, as well as their statistical interactions with T-cell or macrophage densities, using 935

**TABLE 1** | Clinical, pathological, and molecular characteristics of colorectal cancer cases according to desmoplastic reaction.

Characteristics <sup>a</sup>	Desmoplastic reaction			P value <sup>b</sup>
	Total No. (n = 908)	Mature (n = 409)	Intermediate (n = 230)	Immature (n = 269)
Sex				0.0060
Female (NHS)	496 (55%)	200 (49%)	133 (58%)	163 (61%)
Male (HPFS)	412 (45%)	209 (51%)	97 (42%)	106 (39%)
Mean age ± SD (years)	69.1 ± 8.8	70.0 ± 8.7	68.7 ± 9.3	68.0 ± 8.5
Year of diagnosis				0.014 0.23
1995 or before	290 (32%)	125 (31%)	74 (32%)	91 (34%)
1996–2000	298 (33%)	127 (32%)	73 (32%)	98 (36%)
2001–2010	320 (35%)	157 (38%)	83 (36%)	80 (30%)
Family history of colorectal cancer in a first-degree relative				0.38
Absent	709 (79%)	322 (79%)	186 (81%)	201 (76%)
Present	191 (21%)	85 (21%)	43 (19%)	63 (24%)
Tumor location				0.0017
Cecum	162 (18%)	63 (15%)	61 (27%)	38 (14%)
Ascending to transverse colon	296 (33%)	127 (31%)	64 (28%)	105 (39%)
Descending to sigmoid colon	267 (29%)	130 (32%)	63 (27%)	74 (28%)
Rectum	179 (20%)	88 (22%)	41 (18%)	50 (19%)
pT stage (depth of tumor invasion)				<0.0001
pT1 (submucosa)	65 (7.7%)	51 (13%)	13 (5.9%)	1 (0.4%)
pT2 (muscularis propria)	172 (20%)	128 (34%)	34 (15%)	10 (4.1%)
pT3 (subserosa)	560 (67%)	194 (51%)	157 (72%)	209 (86%)
pT4 (serosa or other organs)	45 (5.3%)	6 (1.6%)	15 (6.9%)	24 (10%)
pN stage				<0.0001
pN0	502 (61%)	301 (80%)	119 (57%)	82 (36%)
pN1	201 (25%)	51 (13%)	68 (32%)	82 (36%)
pN2	113 (14%)	26 (6.9%)	23 (11%)	64 (28%)
AJCC disease stage				<0.0001
I	188 (22%)	148 (40%)	32 (14%)	8 (3.2%)
II	281 (33%)	139 (37%)	83 (38%)	59 (23%)
III	248 (29%)	69 (19%)	75 (34%)	104 (41%)
IV	127 (15%)	16 (4.3%)	30 (14%)	81 (32%)
Tumor differentiation				0.0004
Well to moderate	825 (91%)	385 (94%)	210 (91%)	230 (85%)
Poor	82 (9.0%)	23 (6.0%)	20 (8.7%)	39 (15%)
MSI status				0.18
Non-MSI-high	733 (83%)	329 (83%)	179 (80%)	225 (86%)
MSI-high	150 (17%)	69 (17%)	45 (20%)	36 (14%)
CIMP status				0.67
Low/negative	691 (82%)	316 (83%)	172 (80%)	203 (82%)
High	154 (18%)	65 (17%)	43 (20%)	46 (18%)
Mean LINE-1 methylation level ± SD (%)	62.5 ± 9.6	62.9 ± 9.6	62.6 ± 9.4	61.9 ± 9.9
KRAS mutation				0.91
Wild-type	518 (59%)	234 (59%)	132 (60%)	152 (58%)
Mutant	363 (41%)	163 (41%)	89 (40%)	111 (42%)
BRAF mutation				0.12
Wild-type	756 (85%)	349 (87%)	192 (85%)	215 (81%)
Mutant	133 (15%)	51 (13%)	33 (15%)	49 (19%)
PIK3CA mutation				0.59
Wild-type	697 (84%)	313 (82%)	179 (84%)	205 (85%)
Mutant	137 (16%)	68 (18%)	33 (16%)	36 (15%)
Tumor-infiltrating lymphocytes				0.014
Negative/low	651 (73%)	280 (69%)	158 (69%)	213 (81%)
Intermediate	147 (16%)	75 (19%)	41 (18%)	31 (12%)
High	99 (11%)	49 (12%)	30 (13%)	20 (7.6%)
Intratumoral periglandular reaction				<0.0001
Negative/low	126 (14%)	34 (8.4%)	35 (15%)	57 (22%)
Intermediate	664 (74%)	311 (77%)	162 (71%)	191 (72%)
High	108 (12%)	59 (15%)	32 (14%)	17 (6.4%)

(Continued)

**TABLE 1** | Continued

Characteristics <sup>a</sup>	Desmoplastic reaction			P value <sup>b</sup>
	Total No. (n = 908)	Mature (n = 409)	Intermediate (n = 230)	
Peritumoral lymphocytic reaction				<0.0001
Negative/low	145 (16%)	42 (11%)	39 (17%)	64 (24%)
Intermediate	614 (69%)	287 (71%)	148 (65%)	179 (68%)
High	137 (15%)	73 (18%)	42 (18%)	22 (8.3%)
Crohn's-like lymphoid reaction				0.11
Negative/low	574 (74%)	252 (74%)	138 (70%)	184 (79%)
Intermediate	138 (18%)	58 (17%)	41 (21%)	39 (17%)
High	59 (7.7%)	32 (9.3%)	17 (8.7%)	10 (4.3%)

<sup>a</sup>Percentage indicates the proportion of patients with a specific clinical, pathological, or molecular characteristic among all patients or in the strata of desmoplastic reaction.

<sup>b</sup>To compare categorical data between the desmoplastic reaction classification, chi-squared test was performed. To compare continuous variables, an analysis of variance was performed.

AJCC, American Joint Committee on Cancer; CIMP, CpG island methylator phenotype; HPFS, Health Professionals Follow-up Study; LINE-1, long-interspersed nucleotide element-1; MSI, microsatellite instability; NHS, Nurses' Health Study; SD, standard deviation.

cases with available survival data. There were 663 all-cause deaths, including 300 colorectal cancer-specific deaths during the median follow-up time of 16.2 years (interquartile range, 12.8 to 20.2 years) for censored cases. Kaplan-Meier analysis showed that immature desmoplastic reaction, myxoid stroma, and keloid-like collagen bundles were associated with higher colorectal cancer-specific and overall mortality (all log-rank  $P < 0.001$ ) (Figure 3). Multivariable Cox regression models indicated that immature desmoplastic reaction, myxoid stroma, and keloid-like collagen bundles would be associated with worse prognosis. Due to the small numbers of deaths in some categories, we set patients with immature desmoplastic reaction, marked myxoid stroma, and marked keloid-like collagen bundles as references; multivariable-adjusted hazard ratios (HRs) were 0.32 (95% CI 0.23–0.44,  $P_{\text{trend}} < 0.0001$ ) for mature desmoplastic reaction, 0.25 (95% CI 0.16–0.39,  $P_{\text{trend}} < 0.0001$ ) for absent myxoid stroma, and 0.12 (95% CI 0.05–0.28,  $P_{\text{trend}} < 0.0001$ ) for absent keloid-like collagen bundles (Table 4 and Figure 4). In the subgroup analysis of AJCC disease stage I cases, multivariable Cox regression models indicated that only myxoid stroma would be associated with worse prognosis, although the number of events was extremely small. Multivariable-adjusted HRs were 0.02 (95% CI 0.002–0.25,  $P_{\text{trend}} = 0.0006$ ) for absent myxoid stroma (Supplementary Table S8). Given the associations of intraepithelial CD3<sup>+</sup>CD8<sup>+</sup>CD45RO<sup>+</sup> cell and stromal M1-like macrophage densities with desmoplastic reaction, myxoid stroma, and/or keloid-like collagen bundles, we evaluated the prognostic impact of desmoplastic reaction, myxoid stroma, and keloid-like collagen bundles in strata of intraepithelial CD3<sup>+</sup>CD8<sup>+</sup>CD45RO<sup>+</sup> cell and stromal M1-like macrophage densities. There were no statistically significant interactions between these immune cells and tumor stromal parameters in colorectal cancer-specific survival analyses ( $P_{\text{interaction}} > 0.02$ , with the  $\alpha$  level of 0.005) (Supplementary Tables S9 and S10). In the overall survival analyses, immature desmoplastic reaction and keloid-like collagen bundles appeared to have stronger survival association in tumors with low stromal M1-like macrophage densities (both  $P_{\text{interaction}} < 0.0005$ ) (Supplementary Table S10).

## DISCUSSION

Previous studies have supported the clinical and pathological impact of desmoplastic reaction in colorectal cancer (6–13). However, no studies have evaluated the detailed relationships between desmoplastic reaction and immune cells in the colorectal carcinoma microenvironment, although an association between immature stroma and lower density of CD3 has been suggested (11). Hence, we tested the hypothesis that specific T-cell and macrophage populations in the colorectal cancer microenvironment might be associated with immature desmoplastic reaction. The current study is the largest to evaluate the detailed immune cell populations, including T cells and macrophage, in relation to desmoplastic reaction and its components. We found an inverse association of intraepithelial CD3<sup>+</sup>CD8<sup>+</sup>CD45RO<sup>+</sup> memory cytotoxic T cells and stromal M1-like macrophages with immature desmoplastic reaction and its components (myxoid stroma and keloid-like collagen bundles). In the pT3 and pT4 case subgroup, a similar trend was observed as for the association between intraepithelial densities of CD3<sup>+</sup>CD8<sup>+</sup>CD45RO<sup>+</sup> and stromal M1-like macrophages and desmoplastic reaction in multivariable analyses. Additionally, immature desmoplastic reaction and its components would be associated with worse colorectal cancer-specific survival. Considering there were only limited events from AJCC disease stage I cases, we could not assess the prognostic impact of desmoplastic reaction and its components accurately, although myxoid stroma showed statistically significant association with worse prognosis.

The immune response to cancer antigens manifests as an accumulation of chemokine-induced immune cells (42). However, the tumor microenvironment may also harbor numerous immunosuppressive factors, and it is crucial to understand their interactions with the antitumorigenic immune cells (42). Cancer-associated fibroblasts play a crucial role in the development of desmoplastic reaction and shape the tumor immune microenvironment by the expression of immunoregulatory molecules such as TGFB1 (transforming growth factor-beta) (4, 5). Cancer-associated fibroblasts may directly and indirectly impact antitumor immune reaction through recruitment of protumorigenic inflammatory cells, such as M2-like macrophages (43).

**TABLE 2** | Multivariable logistic regression analysis to assess the associations of T cell densities with desmoplastic reaction with IPW.

	Multivariable OR (95% CI) <sup>a</sup>		
	Immature desmoplastic reaction	Myxoid stroma	Keloid-like collagen bundles
CD3 <sup>+</sup> cell density			
Tumor intraepithelial region			
C1 (lowest)	1 (referent)	1 (referent)	1 (referent)
C2 (second)	0.68 (0.46–1.00)	0.61 (0.42–0.90)	0.83 (0.56–1.24)
C3 (third)	0.63 (0.42–0.92)	0.55 (0.37–0.81)	0.70 (0.47–1.04)
C4 (highest)	0.49 (0.33–0.73)	0.39 (0.26–0.59)	0.60 (0.41–0.90)
P <sub>trend</sub> <sup>b</sup>	0.0005	<0.0001	0.0079
Tumor stromal region			
C1 (lowest)	1 (referent)	1 (referent)	1 (referent)
C2 (second)	0.77 (0.52–1.14)	0.76 (0.52–1.12)	0.73 (0.49–1.07)
C3 (third)	0.56 (0.38–0.81)	0.52 (0.35–0.77)	0.64 (0.43–0.94)
C4 (highest)	0.55 (0.38–0.80)	0.47 (0.32–0.69)	0.67 (0.46–0.98)
P <sub>trend</sub> <sup>b</sup>	0.0006	<0.0001	0.032
CD3 <sup>+</sup> CD4 <sup>+</sup> cell density			
Tumor intraepithelial region			
C1 (lowest)	1 (referent)	1 (referent)	1 (referent)
C2 (second)	0.68 (0.47–1.00)	0.63 (0.43–0.92)	0.70 (0.47–1.03)
C3 (third)	0.65 (0.45–0.95)	0.59 (0.41–0.85)	0.76 (0.52–1.13)
C4 (highest)	0.60 (0.41–0.88)	0.53 (0.36–0.78)	0.67 (0.47–0.96)
P <sub>trend</sub> <sup>b</sup>	0.0075	0.0011	0.047
Tumor stromal region			
C1 (lowest)	1 (referent)	1 (referent)	1 (referent)
C2 (second)	0.93 (0.63–1.37)	1.01 (0.69–1.47)	0.96 (0.65–1.43)
C3 (third)	0.79 (0.54–1.16)	0.76 (0.52–1.12)	0.96 (0.66–1.40)
C4 (highest)	0.64 (0.44–0.93)	0.55 (0.37–0.80)	0.75 (0.51–1.10)
P <sub>trend</sub> <sup>b</sup>	0.013	0.0007	0.16
CD3 <sup>+</sup> CD8 <sup>+</sup> cell density			
Tumor intraepithelial region			
C1 (lowest)	1 (referent)	1 (referent)	1 (referent)
C2 (second)	0.78 (0.53–1.15)	0.89 (0.60–1.30)	0.71 (0.48–1.03)
C3 (third)	0.60 (0.42–0.86)	0.67 (0.47–0.95)	0.55 (0.38–0.79)
C4 (highest)	0.50 (0.35–0.73)	0.42 (0.29–0.62)	0.48 (0.33–0.69)
P <sub>trend</sub> <sup>b</sup>	<0.0001	<0.0001	<0.0001
Tumor stromal region			
C1 (lowest)	1 (referent)	1 (referent)	1 (referent)
C2 (second)	1.08 (0.75–1.56)	1.10 (0.76–1.60)	1.07 (0.73–1.55)
C3 (third)	0.85 (0.59–1.22)	0.89 (0.62–1.27)	0.85 (0.58–1.24)
C4 (highest)	0.74 (0.51–1.07)	0.61 (0.41–0.89)	0.71 (0.50–1.03)
P <sub>trend</sub> <sup>b</sup>	0.075	0.012	0.056
CD3 <sup>+</sup> CD4 <sup>+</sup> FOXP3 <sup>+</sup> cell density			
Tumor intraepithelial region			
C1 (lowest)	1 (referent)	1 (referent)	1 (referent)
C2 (second)	1.11 (0.72–1.72)	0.78 (0.49–1.25)	0.93 (0.58–1.49)
C3 (third)	0.78 (0.50–1.21)	0.89 (0.59–1.35)	0.73 (0.47–1.15)
C4 (highest)	0.90 (0.58–1.39)	0.72 (0.47–1.12)	0.79 (0.53–1.18)
P <sub>trend</sub> <sup>b</sup>	0.41	0.12	0.12
Tumor stromal region			
C1 (lowest)	1 (referent)	1 (referent)	1 (referent)
C2 (second)	0.70 (0.47–1.04)	0.74 (0.51–1.08)	0.73 (0.49–1.08)
C3 (third)	0.86 (0.59–1.26)	0.75 (0.51–1.10)	1.06 (0.72–1.57)
C4 (highest)	0.83 (0.57–1.22)	0.69 (0.47–1.02)	0.77 (0.54–1.11)
P <sub>trend</sub> <sup>b</sup>	0.26	0.030	0.29
CD3 <sup>+</sup> CD4 <sup>+</sup> CD45RO <sup>+</sup> cell density			
Tumor intraepithelial region			
C1 (lowest)	1 (referent)	1 (referent)	1 (referent)
C2 (second)	0.69 (0.48–1.00)	0.69 (0.48–1.01)	0.76 (0.52–1.12)
C3 (third)	0.65 (0.45–0.94)	0.60 (0.42–0.86)	0.84 (0.57–1.23)
C4 (highest)	0.54 (0.37–0.77)	0.49 (0.34–0.72)	0.62 (0.43–0.89)
P <sub>trend</sub> <sup>b</sup>	0.0008	0.0001	0.020

(Continued)

**TABLE 2 |** Continued

	Multivariable OR (95% CI) <sup>a</sup>		
	Immature desmoplastic reaction	Myxoid stroma	Keloid-like collagen bundles
Tumor stromal region			
C1 (lowest)	1 (referent)	1 (referent)	1 (referent)
C2 (second)	1.09 (0.74–1.61)	1.14 (0.78–1.67)	0.99 (0.67–1.47)
C3 (third)	0.78 (0.53–1.14)	0.77 (0.52–1.13)	0.99 (0.68–1.46)
C4 (highest)	0.64 (0.44–0.92)	0.54 (0.36–0.79)	0.73 (0.50–1.06)
P <sub>trend</sub> <sup>b</sup>	0.0054	0.0003	0.12
CD3 <sup>+</sup> CD4 <sup>+</sup> CD45RO <sup>+</sup> cell density			
Tumor intraepithelial region			
C1 (lowest)	1 (referent)	1 (referent)	1 (referent)
C2 (second)	0.85 (0.57–1.26)	0.69 (0.46–1.03)	0.67 (0.44–1.04)
C3 (third)	0.99 (0.69–1.43)	0.82 (0.57–1.18)	0.98 (0.67–1.44)
C4 (highest)	0.96 (0.65–1.43)	0.80 (0.54–1.17)	0.93 (0.65–1.32)
P <sub>trend</sub> <sup>b</sup>	0.83	0.15	0.67
Tumor stromal region			
C1 (lowest)	1 (referent)	1 (referent)	1 (referent)
C2 (second)	0.71 (0.48–1.04)	0.90 (0.63–1.28)	0.73 (0.49–1.07)
C3 (third)	1.01 (0.70–1.47)	0.93 (0.63–1.36)	1.11 (0.75–1.62)
C4 (highest)	0.75 (0.52–1.08)	0.65 (0.45–0.94)	0.79 (0.56–1.11)
P <sub>trend</sub> <sup>b</sup>	0.27	0.042	0.42
CD3 <sup>+</sup> CD8 <sup>+</sup> CD45RO <sup>+</sup> cell density			
Tumor intraepithelial region			
C1 (lowest)	1 (referent)	1 (referent)	1 (referent)
C2 (second)	0.53 (0.36–0.76)	0.59 (0.41–0.86)	0.56 (0.39–0.81)
C3 (third)	0.55 (0.38–0.80)	0.56 (0.39–0.80)	0.53 (0.36–0.78)
C4 (highest)	0.43 (0.29–0.62)	0.33 (0.23–0.49)	0.44 (0.30–0.63)
P <sub>trend</sub> <sup>b</sup>	<0.0001	<0.0001	<0.0001
Tumor stromal region			
C1 (lowest)	1 (referent)	1 (referent)	1 (referent)
C2 (second)	1.16 (0.81–1.66)	1.22 (0.84–1.77)	1.23 (0.84–1.80)
C3 (third)	0.85 (0.59–1.24)	0.88 (0.60–1.28)	0.83 (0.57–1.21)
C4 (highest)	0.67 (0.46–0.98)	0.54 (0.37–0.78)	0.71 (0.50–1.02)
P <sub>trend</sub> <sup>b</sup>	0.033	0.0025	0.049
CD3 <sup>+</sup> CD8 <sup>+</sup> CD45RO <sup>+</sup> cell density			
Tumor intraepithelial region			
C1 (lowest)	1 (referent)	1 (referent)	1 (referent)
C2 (second)	1.12 (0.73–1.72)	1.14 (0.72–1.82)	0.97 (0.64–1.47)
C3 (third)	0.80 (0.52–1.22)	0.97 (0.66–1.43)	0.70 (0.47–1.04)
C4 (highest)	0.77 (0.51–1.16)	0.60 (0.39–0.92)	0.65 (0.43–0.97)
P <sub>trend</sub> <sup>b</sup>	0.15	0.056	0.014
Tumor stromal region			
C1 (lowest)	1 (referent)	1 (referent)	1 (referent)
C2 (second)	1.21 (0.82–1.79)	1.23 (0.84–1.82)	1.11 (0.75–1.65)
C3 (third)	0.88 (0.61–1.28)	0.85 (0.59–1.22)	0.93 (0.65–1.34)
C4 (highest)	1.12 (0.74–1.69)	0.92 (0.61–1.39)	0.84 (0.55–1.28)
P <sub>trend</sub> <sup>b</sup>	0.85	0.53	0.42

<sup>a</sup>The multivariable ordinal logistic regression model initially included age, sex, year of diagnosis, family history of colorectal cancer, tumor location, tumor grade, microsatellite instability, CpG island methylator phenotype, long-interspersed nucleotide element-1 methylation level, KRAS, BRAF, and PIK3CA mutations. A backward elimination with a threshold P of 0.05 was used to select variables for the final model.

<sup>b</sup>P<sub>trend</sub> was calculated by the linear trend across the ordinal categories of the T-cell densities (C1–C4, as an ordinal predictor variable) in an ordinal logistic regression model for desmoplastic reaction (three categories), myxoid stroma (four categories), or keloid-like collagen bundles (four categories) (as an ordinal outcome variable). CI, confidence interval; OR, odds ratio; IPW, inverse probability weighting.

Cytotoxic CD8<sup>+</sup> T cells are considered an important component of effective antitumor immune response. They may target cancer cells and infectious cells using PRF1 (perforin 1) from cytotoxic granules to penetrate the cell membrane and inject GZMB (granzyme B) to induce apoptosis (42). They also secrete interferon-gamma to induce macrophage phagocytic activity and to activate antigen-presenting cells. Furthermore, cytotoxic T cells express FASLG (Fas ligand, CD178), thereby inducing cancer cell apoptosis through its binding with FAS (Fas

cell surface death receptor, CD95) (42). In a previous study evaluating the same two U.S. nationwide colorectal cancer cohorts as the present study, we found that high tumor intraepithelial densities of CD3<sup>+</sup>CD8<sup>+</sup>CD45RO<sup>+</sup> memory cytotoxic T cells were inversely associated with tumor budding, suggesting that cytotoxic antitumor immunity suppresses tumor microinvasion (22). Our present study adds to these findings by revealing that the density of CD3<sup>+</sup>CD8<sup>+</sup>CD45RO<sup>+</sup> memory cytotoxic T cells is lower in tumors with immature stroma,

**TABLE 3** | Multivariable logistic regression analysis to assess the associations of macrophage densities with desmoplastic reaction with IPW.

	Multivariable OR (95% CI) <sup>a</sup>		
	Immature desmoplastic reaction <sup>b</sup>	Myxoid stroma	Keloid-like collagen bundles
<b>Overall macrophage density</b>			
<b>Tumor intraepithelial region</b>			
C1 (lowest)	1 (referent)	1 (referent)	1 (referent)
C2 (second)	0.81 (0.52–1.27)	0.65 (0.44–0.95)	0.84 (0.57–1.26)
C3 (third)	0.91 (0.57–1.45)	0.74 (0.50–1.10)	0.83 (0.55–1.26)
C4 (highest)	0.69 (0.43–1.11)	0.51 (0.35–0.76)	0.74 (0.50–1.10)
P <sub>trend</sub> <sup>c</sup>	0.20	0.0030	0.15
<b>Tumor stromal region</b>			
C1 (lowest)	1 (referent)	1 (referent)	1 (referent)
C2 (second)	0.73 (0.47–1.14)	0.83 (0.55–1.24)	0.98 (0.65–1.47)
C3 (third)	0.71 (0.45–1.11)	0.69 (0.47–1.03)	0.99 (0.66–1.48)
C4 (highest)	0.43 (0.27–0.69)	0.48 (0.32–0.71)	0.95 (0.64–1.41)
P <sub>trend</sub> <sup>c</sup>	0.0009	0.0002	0.82
<b>M1-like macrophage density</b>			
<b>Tumor intraepithelial region</b>			
C1 (lowest)	1 (referent)	1 (referent)	1 (referent)
C2 (second)	0.63 (0.39–1.00)	0.80 (0.55–1.18)	0.80 (0.53–1.19)
C3 (third)	0.97 (0.63–1.50)	0.85 (0.57–1.26)	0.89 (0.59–1.33)
C4 (highest)	0.64 (0.41–1.01)	0.64 (0.43–0.94)	0.66 (0.45–0.98)
P <sub>trend</sub> <sup>c</sup>	0.21	0.042	0.076
<b>Tumor stromal region</b>			
C1 (lowest)	1 (referent)	1 (referent)	1 (referent)
C2 (second)	0.66 (0.42–1.04)	0.73 (0.49–1.08)	0.83 (0.55–1.25)
C3 (third)	0.71 (0.46–1.11)	0.71 (0.48–1.05)	0.97 (0.65–1.44)
C4 (highest)	0.44 (0.28–0.70)	0.50 (0.34–0.74)	0.70 (0.47–1.03)
P <sub>trend</sub> <sup>c</sup>	0.0011	0.0007	0.14
<b>M2-like macrophage density</b>			
<b>Tumor intraepithelial region</b>			
C1 (lowest)	1 (referent)	1 (referent)	1 (referent)
C2 (second)	0.96 (0.61–1.51)	1.20 (0.81–1.78)	1.12 (0.74–1.69)
C3 (third)	0.94 (0.60–1.49)	0.93 (0.62–1.38)	1.02 (0.69–1.53)
C4 (highest)	0.83 (0.52–1.33)	0.82 (0.55–1.24)	1.00 (0.66–1.52)
P <sub>trend</sub> <sup>c</sup>	0.45	0.21	0.88
<b>Tumor stromal region</b>			
C1 (lowest)	1 (referent)	1 (referent)	1 (referent)
C2 (second)	1.09 (0.70–1.71)	1.05 (0.71–1.57)	1.20 (0.80–1.82)
C3 (third)	1.01 (0.64–1.60)	1.14 (0.77–1.68)	1.60 (1.09–2.37)
C4 (highest)	0.90 (0.57–1.44)	0.95 (0.65–1.39)	1.43 (0.96–2.12)
P <sub>trend</sub> <sup>c</sup>	0.60	0.90	0.032

<sup>a</sup>The multivariable ordinal logistic regression model initially included age, sex, year of diagnosis, family history of colorectal cancer, tumor location, tumor grade, microsatellite instability, CpG island methylator phenotype, long-interspersed nucleotide element-1 methylation level, KRAS, BRAF, and PIK3CA mutations. A backward elimination with a threshold P of 0.05 was used to select variables for the final model.

<sup>b</sup>To avoid violation of the proportional odds assumption, the binary categories were used for desmoplastic reaction (immature vs intermediate/mature).

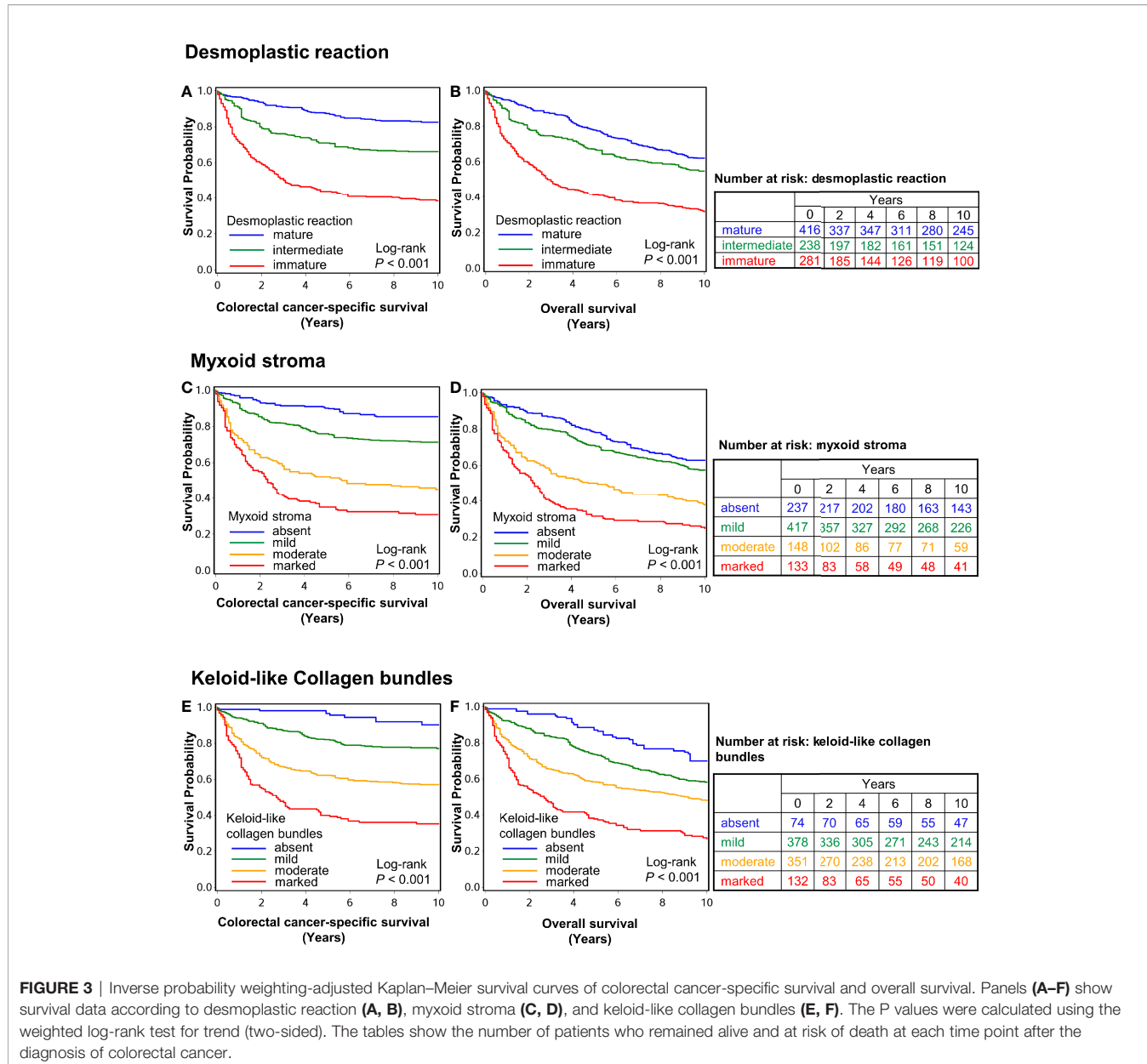
<sup>c</sup>P<sub>trend</sub> was calculated by the linear trend across the ordinal categories of the macrophage densities (C1–C4, as an ordinal predictor variable) in an ordinal logistic regression model for desmoplastic reaction (three categories), myxoid stroma (four categories), or keloid-like collagen bundles (four categories) (as an ordinal outcome variable).

CI, confidence interval; OR, odds ratio; IPW, inverse probability weighting.

which is another poor prognostic histologic feature. This finding is in line with a previous study that showed that the number of CD3<sup>+</sup> lymphocytes decreases according to loss of maturation of desmoplastic reaction (11), but the more exact subpopulations driving this association had previously been unclear. Our study was not able to assess the mechanisms underlying this association. However, these findings may reflect the inability of these antitumor effector cells to penetrate the immature desmoplastic stroma and attack tumor cells, or alternatively, immunosuppressive factors present in the immature stroma that inhibit the cytotoxic antitumor immunity.

Macrophages may play roles in both antitumor defense and tumor development. The concept of macrophage polarization

relates to the phenotypic state of macrophages at a given point in space and time (44). Macrophage polarization can be viewed as a spectrum from pro-inflammatory M1-like to anti-inflammatory M2-like populations, and there are no perfect markers for different polarization states (44). Under the stimulus of IFNG (interferon-gamma) and lipopolysaccharides, macrophages undergo M1 polarization and produce inflammatory cytokines such as TNF (tumor necrosis factor-alpha), thereby accelerating an inflammatory response (45), while M2-like macrophages produce anti-inflammatory cytokines, such as IL10 (interleukin-10) and TGFB1 (transforming growth factor-beta), inducing regulatory T cells and suppressing cytotoxic T-cell response (45). Our multiplex immunofluorescence assay



contained two markers for M1-polarization and two markers for M2-polarization, enabling more accurate characterization of the macrophage polarization state than single-marker approaches. We have found the inverse relationship of immature desmoplastic reaction with stromal M1-like macrophages but not with M2-like macrophages. These findings suggest that M1-like macrophages may suppress maturing of desmoplastic reaction, while it is also possible that immature desmoplastic reaction may influence macrophages and their polarization.

This study has several limitations. First, we assessed T-cell and macrophage densities using tissue microarrays, and such tissue sampling may not be representative of the overall tumor. The tissue microarrays contained two to four tumor tissue cores

from each tumor (34). We have confirmed that at least two tissue microarray cores can provide reasonably accurate immune cell density measurements when compared to more extensive sampling (unpublished data). Second, the data for desmoplastic reaction and its components were based on a pathologist's visual evaluation. However, we evaluated the interobserver agreement between the two pathologists, which resulted in at least moderate agreements for desmoplastic reaction, myxoid stroma, and keloid-like collagen bundles (weighted kappa 0.52, 0.57, and 0.40, respectively). This level of agreement is in line with a previous report (median weighted kappa 0.58) (46). Third, we cannot exclude the possibility of reverse causation. Nonetheless, reverse causation may not be the sole explanation to the observed interaction between desmoplastic reaction and immune cell

**TABLE 4 |** Desmoplastic reaction and its components and patient survival with inverse probability weighting (IPW).

	No. of cases	Colorectal cancer-specific survival <sup>a</sup>			Overall survival <sup>a</sup>		
		No. of events	Univariable HR (95% CI)*	Multivariable HR (95% CI) <sup>b</sup>	No. of events	Univariable HR (95% CI)*	Multivariable HR (95% CI) <sup>b</sup>
<b>Desmoplastic reaction</b>							
Immature	281	150	1 (referent)	1 (referent)	179	1 (referent)	1 (referent)
Intermediate	238	69	0.42 (0.31–0.57)	0.60 (0.45–0.80)	104	0.49 (0.38–0.64)	0.59 (0.45–0.78)
Mature	416	64	0.19 (0.14–0.26)	0.32 (0.23–0.44)	160	0.36 (0.29–0.46)	0.49 (0.38–0.63)
P <sub>trend</sub> <sup>c</sup>			<0.0001	<0.0001		<0.0001	<0.0001
<b>Myxoid stroma</b>							
C1 (marked)	133	79	1 (referent)	1 (referent)	91	1 (referent)	1 (referent)
C2 (moderate)	148	71	0.67 (0.48–0.93)	0.75 (0.54–1.04)	88	0.68 (0.49–0.93)	0.72 (0.52–1.00)
C3 (mild)	417	104	0.28 (0.21–0.38)	0.45 (0.33–0.62)	177	0.36 (0.27–0.47)	0.47 (0.35–0.52)
C4 (absent)	237	29	0.13 (0.08–0.20)	0.25 (0.16–0.39)	87	0.29 (0.21–0.40)	0.42 (0.30–0.59)
P <sub>trend</sub> <sup>c</sup>			<0.0001	<0.0001		<0.0001	<0.0001
<b>Keloid-like collagen bundles</b>							
C1 (marked)	132	73	1 (referent)	1 (referent)	90	1 (referent)	1 (referent)
C2 (moderate)	351	129	0.53 (0.40–0.72)	0.61 (0.46–0.81)	173	0.55 (0.41–0.72)	0.60 (0.45–0.79)
C3 (mild)	378	74	0.24 (0.17–0.33)	0.38 (0.27–0.54)	154	0.37 (0.28–0.48)	0.49 (0.37–0.65)
C4 (absent)	74	7	0.09 (0.04–0.19)	0.12 (0.05–0.28)	26	0.24 (0.15–0.38)	0.28 (0.18–0.45)
P <sub>trend</sub> <sup>c</sup>			<0.0001	<0.0001		<0.0001	<0.0001

<sup>a</sup>IPW was applied to reduce a bias due to the availability of tumor tissue after cancer diagnosis (see the Statistical Analysis subsection for details).

<sup>b</sup>The multivariable Cox regression model initially included sex, age, year of diagnosis, family history of colorectal cancer, tumor location, tumor grade, disease stage, microsatellite instability, CpG island methylator phenotype, long-interspersed nucleotide element-1 methylation level, KRAS, BRAF, and PIK3CA mutations, tumor-infiltrating lymphocytes, intratumoral periglandular reaction, peritumoral lymphocytic reaction, Crohn's-like lymphoid reaction, intraepithelial CD3<sup>+</sup>CD8<sup>+</sup>CD45RO<sup>+</sup> T cell density, and stroma M1-like macrophage density. A backward elimination with a threshold P of 0.05 was used to select variables for the final models.

<sup>c</sup>P<sub>trend</sub> value was calculated by the linear trend across the ordinal categories of the desmoplastic reaction, myxoid stroma, and keloid-like collagen bundles in the IPW-adjusted Cox regression model.

CI, confidence interval; HR, hazard ratio; IPW, inverse probability weighting.

densities. Fourth, most of the subjects in this research were non-Hispanic whites. Our findings should be evaluated in different populations. Fifth, detailed data on cancer treatments were not available in our study. However, we adjusted multivariable models for clinical, tumor characteristics, and demographic features as we utilized the MPE database. In addition, the treatment decision was not made on the basis of desmoplastic reaction features because the desmoplastic reaction data were generally not available for treating physicians. Sixth, stromal maturity measurements were the only tumor stroma parameters utilized in this study. The associations between immune cell infiltrates and other established, prognostically relevant stromal parameters such as the tumor-stroma ratio represent important topics for further investigation.

Our study has several strengths. First, the colorectal cancer cases in this study were collected from a large number of hospitals throughout the U.S., which facilitates the generalizability of our results. Our study is also one of the largest so far to evaluate the prognostic value of desmoplastic reaction and its components in colorectal cancer. Although desmoplastic reaction and its components were strongly associated with T-cell and macrophage densities, these stromal parameters showed a prognostic value independent of immune cells and potential confounders. Further studies are warranted to assess whether myxoid stroma and keloid-like collagen bundles could be reproducibly evaluated for prognostication of colorectal

cancer. Second, we utilize IPW methods in all survival analyses to specifically reduce the potential bias caused by the availability of tissue after colorectal cancer diagnosis (26–28, 41). Third, we utilized the comprehensive molecular pathological epidemiology dataset, which includes many potential confounding factors as well as detailed molecular data, which were utilized in the multivariable logistic regression model and Cox regression models (47–49). Fourth, we assessed immune cell densities by using multiplex immunofluorescence, which enabled simultaneous examination of multiple T-cell and macrophage markers and identification of specific T-cell and macrophage subsets that were not possible with conventional single-marker approaches.

Given the strong association between desmoplastic reaction and tumor-immune characteristics, it would be possible that our results may be useful for predicting the treatment effect of immunotherapy. Since our cohort lacks sufficient treatment data and is generally conducted before the use of immunotherapy for colorectal cancer, it is required to verify our hypothesis using a new cohort with sufficient treatment with an immune checkpoint inhibitor. If certain types of immune cells in tumor tissues, such as intraepithelial CD3<sup>+</sup>CD8<sup>+</sup>CD45RO<sup>+</sup> cells or stromal M1-like macrophages, could be used to predict the efficacy of certain immunotherapies, they may be attractive as an innovative biomarker using colonoscopy biopsies or surgically resected tissues prior to treatment. Further studies are warranted to

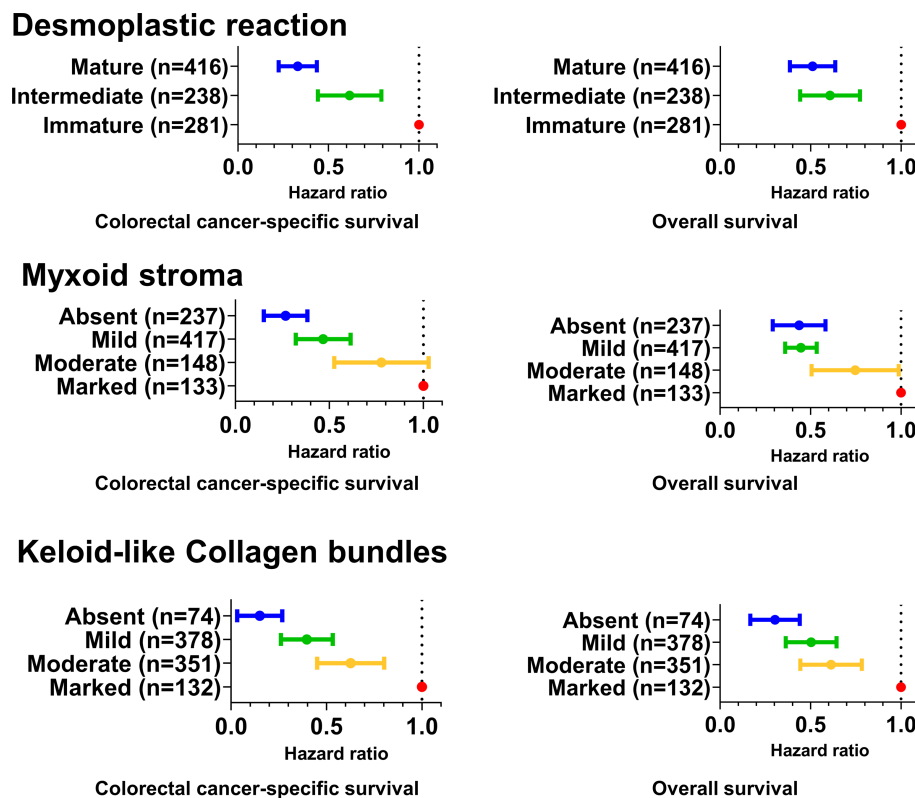


**FIGURE 4 |** Forrest plot of multivariable Cox hazards regression analyses for cancer-specific and overall survival. The dots and vertical bars indicate the hazard ratios and 95% confidential intervals, respectively. The multivariable Cox regression models initially included sex, age, year of diagnosis, family history of colorectal cancer, tumor location, tumor grade, disease stage, microsatellite instability, CpG island methylator phenotype, long-interspersed nucleotide element-1 methylation level, *KRAS*, *BRAF*, and *PIK3CA* mutations, tumor-infiltrating lymphocytes, intratumoral periglandular reaction, peritumoral lymphocytic reaction, Crohn's-like lymphoid reaction, intraepithelial CD3<sup>+</sup>CD8<sup>+</sup>CD45RO<sup>+</sup> T-cell density, and stromal M1-like macrophage density. A backward elimination with a threshold P of 0.05 was used to select variables for the final models.

investigate the efficacy of specific immune cell subtypes as new biomarkers. In addition, it would be worthwhile to develop a more reliable classification of the stroma by using digital image analysis.

In conclusion, we have shown that intraepithelial CD3<sup>+</sup>CD8<sup>+</sup>CD45RO<sup>+</sup> T cells and stromal M1-like macrophages are inversely associated with immature desmoplastic reaction and its components, supporting the role of those immune cells in the desmoplastic reaction maturity in the tumor immune microenvironment. Our study also suggests the potential role of the evaluation of the desmoplastic reaction and its components as prognostic markers.

## DATA AVAILABILITY STATEMENT

The original contributions presented in the study are included in the article/**Supplementary Material**. Further inquiries can be directed to <https://www.nurseshealthstudy.org/researchers/> and <https://sites.sph.harvard.edu/hpfs/for-collaborators/>.

## ETHICS STATEMENT

Informed consent was obtained from all study participants, and the study was approved by the institutional review boards of the Brigham and Women's Hospital and Harvard T.H. Chan School of Public Health (Boston, MA), and those of participating registries as required. The patients/participants provided their written informed consent to participate in this study.

## AUTHOR CONTRIBUTIONS

Study concept and design: NA, JV, and SO. Acquisition of tissue data: NA, JV, MZ, TU, KF, JB, RZ, KH, KA, ML, JK, TT, AC, JN, and SO. Statistical analysis: NA, TU, KF, and SO. Drafting of the manuscript: NA, JV, MZ, TU, and SO. Editing and critical revision for important intellectual contents: NA, JV, MZ, TU, KF, JB, RZ, KH, KA, ML, JK, TT, MS, XZ, KW, AC, JM, MG, JN, and SO. Obtained funding: MS, XZ, KW, AC, JM, MG, JN, and SO. All authors read and approved the final manuscript.

## FUNDING

This work was supported by the U.S. National Institutes of Health (NIH) grants (P01 CA87969; UM1 CA186107; P01 CA55075; UM1 CA167552; U01 CA167552; R35 CA253185 to AC; R35 CA197735 to SO; R01 CA151993 to SO; R01 CA248857 to SO); by Stand Up to Cancer Colorectal Cancer Dream Team Translational Research Grant (SU2C-AACR-DT22-17 to MG), administered by the American Association for Cancer Research, a scientific partner of SU2C; and by grants from the Project P Fund, The Friends of the Dana-Farber Cancer Institute, Bennett Family Fund, and the Entertainment Industry Foundation through National Colorectal Cancer Research Alliance and SU2C. XZ was supported by the American Cancer Society Research Scholar Grant (RSG NEC-130476). KF was supported by fellowship grants from the Uehara Memorial Foundation and Grant of The Clinical Research Promotion Foundation (2018). RZ was supported by a fellowship grant from Huazhong University of Science and Technology. KA and TU were supported by a grant from Overseas Research Fellowship (201860083 to KA; 201960541 to TU) from Japan Society for the Promotion of Science. KH was supported by fellowship grants from the Uehara Memorial Foundation and the Mitsukoshi Health and Welfare Foundation. AC is a Stuart and Suzanne Steele MGH Research Scholar. MG is supported

by an ASCO Conquer Cancer Foundation Career Development Award. The content is solely the responsibility of the authors and does not necessarily represent the official views of NIH. The funders had no role in study design, data collection and analysis, decision to publish, or preparation of the manuscript.

## ACKNOWLEDGMENTS

We would like to thank the participants and staff of the Nurses' Health Study and the Health Professionals Follow-up Study for their valuable contributions as well as the following state cancer registries for their help: AL, AZ, AR, CA, CO, CT, DE, FL, GA, ID, IL, IN, IA, KY, LA, ME, MD, MA, MI, NE, NH, NJ, NY, NC, ND, OH, OK, OR, PA, RI, SC, TN, TX, VA, WA, and WY. The authors assume full responsibility for analyses and interpretation of these data.

## SUPPLEMENTARY MATERIAL

The Supplementary Material for this article can be found online at: <https://www.frontiersin.org/articles/10.3389/fimmu.2022.840198/full#supplementary-material>

## REFERENCES

1. Binnewies M, Roberts EW, Kersten K, Chan V, Fearon DF, Merad M, et al. Understanding the Tumor Immune Microenvironment (TIME) for Effective Therapy. *Nat Med* (2018) 24:541–50. doi: 10.1038/s41591-018-0014-x
2. Yarchoan M, Johnson BA3rd, Lutz ER, Laheru DA, Jaffee EM. Targeting Neoantigens to Augment Antitumour Immunity. *Nat Rev Cancer* (2017) 17:209–22. doi: 10.1038/nrc.2016.154
3. Shibue T, Weinberg RA. EMT, CSCs, and Drug Resistance: The Mechanistic Link and Clinical Implications. *Nat Rev Clin Oncol* (2017) 14:611–29. doi: 10.1038/nrclinonc.2017.44
4. Koliaraki V, Pallangyo CK, Greten FR, Kollias G. Mesenchymal Cells in Colon Cancer. *Gastroenterology* (2017) 152:964–79. doi: 10.1053/j.gastro.2016.11.049
5. Mochizuki S, Ao T, Sugiura T, Yonemura K, Shiraishi T, Kajiwara Y, et al. Expression and Function of a Disintegrin and Metalloproteinases in Cancer-Associated Fibroblasts of Colorectal Cancer. *Digestion* (2020) 101:18–24. doi: 10.1159/000504087
6. Ueno H, Kanemitsu Y, Sekine S, Ishiguro M, Ito E, Hashiguchi Y, et al. A Multicenter Study of the Prognostic Value of Desmoplastic Reaction Categorization in Stage II Colorectal Cancer. *Am J Surg Pathol* (2019) 43:1015–22. doi: 10.1097/pas.00000000000001272
7. Ao T, Kajiwara Y, Yonemura K, Shinto E, Mochizuki S, Okamoto K, et al. Prognostic Significance of Histological Categorization of Desmoplastic Reaction in Colorectal Liver Metastases. *Virchows Arch* (2019) 475:341–8. doi: 10.1007/s00428-019-02580-2
8. Ueno H, Sekine S, Oshiro T, Kanemitsu Y, Hamaguchi T, Shida D, et al. Disentangling the Prognostic Heterogeneity of Stage III Colorectal Cancer Through Histologic Stromal Categorization. *Surgery* (2018) 163:777–83. doi: 10.1016/j.surg.2017.09.007
9. Ueno H, Kanemitsu Y, Sekine S, Ishiguro M, Ito E, Hashiguchi Y, et al. Desmoplastic Pattern at the Tumor Front Defines Poor-Prognosis Subtypes of Colorectal Cancer. *Am J Surg Pathol* (2017) 41:1506–12. doi: 10.1097/pas.0000000000000946
10. Ueno H, Shinto E, Shimazaki H, Kajiwara Y, Sueyama T, Yamamoto J, et al. Histologic Categorization of Desmoplastic Reaction: Its Relevance to the Colorectal Cancer Microenvironment and Prognosis. *Ann Surg Oncol* (2015) 22:1504–12. doi: 10.1245/s10434-014-4149-9
11. Ueno H, Jones AM, Wilkinson KH, Jass JR, Talbot IC. Histological Categorisation of Fibrotic Cancer Stroma in Advanced Rectal Cancer. *Gut* (2004) 53:581–6. doi: 10.1136/gut.2003.028365
12. Nearchou IP, Ueno H, Kajiwara Y, Lillard K, Mochizuki S, Takeuchi K, et al. Automated Detection and Classification of Desmoplastic Reaction at the Colorectal Tumour Front Using Deep Learning. *Cancers (Basel)* (2021) 13:1615. doi: 10.3390/cancers13071615
13. Ueno H, Ishiguro M, Nakatani E, Ishikawa T, Uetake H, Murotani K, et al. Prognostic Value of Desmoplastic Reaction Characterisation in Stage II Colon Cancer: Prospective Validation in a Phase 3 Study (SACURA Trial). *Br J Cancer* (2021) 124:1088–97. doi: 10.1038/s41416-020-01222-8
14. Hirose M, Fukui H, Igarashi Y, Fujimori Y, Katake Y, Sekikawa A, et al. Detection of Desmoplastic Reaction in Biopsy Specimens Is Useful for Predicting the Depth of Invasion of Early Colorectal Cancer: A Japanese Collaborative Study. *J Gastroenterol* (2010) 45:1212–8. doi: 10.1007/s00535-010-0288-3
15. Kimura R, Fujimori T, Ichikawa K, Ajioka Y, Ueno H, Ohkura Y, et al. Desmoplastic Reaction in Biopsy Specimens of Early Colorectal Cancer: A Japanese Prospective Multicenter Study. *Pathol Int* (2012) 62:525–31. doi: 10.1111/j.1440-1827.2012.02840.x
16. Ohno K, Fujimori T, Okamoto Y, Ichikawa K, Yamaguchi T, Imura J, et al. Diagnosis of Desmoplastic Reaction by Immunohistochemical Analysis, in Biopsy Specimens of Early Colorectal Carcinomas, Is Efficacious in Estimating the Depth of Invasion. *Int J Mol Sci* (2013) 14:13129–36. doi: 10.3390/ijms140713129
17. Okamoto Y, Fujimori T, Ohkura Y, Sugai T, Arai T, Watanabe G, et al. Histological Assessment of Intra- and Inter-Institutional Reliabilities in Detection of Desmoplastic Reaction in Biopsy Specimens of Early Colorectal Carcinomas. *Pathol Int* (2013) 63:539–45. doi: 10.1111/pin.12110
18. Nishihara R, Wu K, Lochhead P, Morikawa T, Liao X, Qian ZR, et al. Long-Term Colorectal-Cancer Incidence and Mortality After Lower Endoscopy. *N Engl J Med* (2013) 369:1095–105. doi: 10.1056/NEJMoa1301969

19. Mehta RS, Nishihara R, Cao Y, Song M, Mima K, Qian ZR, et al. Association of Dietary Patterns With Risk of Colorectal Cancer Subtypes Classified by Fusobacterium Nucleatum in Tumor Tissue. *JAMA Oncol* (2017) 3:921–7. doi: 10.1001/jamaoncol.2016.6374
20. Yamauchi M, Morikawa T, Kuchiba A, Immura Y, Qian ZR, Nishihara R, et al. Assessment of Colorectal Cancer Molecular Features Along Bowel Subsites Challenges the Conception of Distinct Dichotomy of Proximal Versus Distal Colorectum. *Gut* (2012) 61:847–54. doi: 10.1136/gutjnl-2011-300865
21. Yamauchi M, Lochhead P, Morikawa T, Huttenhower C, Chan AT, Giovannucci E, et al. Colorectal Cancer: A Tale of Two Sides or a Continuum? *Gut* (2012) 61:794–7. doi: 10.1136/gutjnl-2012-302014
22. Fujiyoshi K, Väyrynen JP, Borowsky J, Papke DJ Jr, Arima K, Haruki K, et al. Tumour Budding, Poorly Differentiated Clusters, and T-Cell Response in Colorectal Cancer. *EBioMedicine* (2020) 57:102860. doi: 10.1016/j.ebiom.2020.102860
23. Väyrynen JP, Haruki K, Lau MC, Väyrynen SA, Zhong R, Dias Costa A, et al. The Prognostic Role of Macrophage Polarization in the Colorectal Cancer Microenvironment. *Cancer Immunol Res* (2021) 9:8–19. doi: 10.1158/2326-6066.CIR-20-0527
24. Väyrynen JP, Lau MC, Haruki K, Väyrynen SA, Dias Costa A, Borowsky J, et al. Prognostic Significance of Immune Cell Populations Identified by Machine Learning in Colorectal Cancer Using Routine Hematoxylin and Eosin-Stained Sections. *Clin Cancer Res* (2020) 26:4326–38. doi: 10.1158/1078-0432.CCR-20-0071
25. Akimoto N, Zhao M, Ugai T, Zhong R, Lau MC, Fujiyoshi K, et al. Tumor Long Interspersed Nucleotide Element-1 (LINE-1) Hypomethylation in Relation to Age of Colorectal Cancer Diagnosis and Prognosis. *Cancers (Basel)* (2021) 13:2016. doi: 10.3390/cancers13092016
26. Liu L, Nevo D, Nishihara R, Cao Y, Song M, Twombly TS, et al. Utility of Inverse Probability Weighting in Molecular Pathological Epidemiology. *Eur J Epidemiol* (2018) 33:381–92. doi: 10.1007/s10654-017-0346-8
27. Hamada T, Cao Y, Qian ZR, Masugi Y, Nowak JA, Yang J, et al. Aspirin Use and Colorectal Cancer Survival According to Tumor CD274 (Programmed Cell Death 1 Ligand 1) Expression Status. *J Clin Oncol* (2017) 35:1836–44. doi: 10.1200/jco.2016.70.7547
28. Seaman SR, White IR. Review of Inverse Probability Weighting for Dealing With Missing Data. *Stat Methods Med Res* (2013) 22:278–95. doi: 10.1177/0962280210395740
29. Ao T, Kajiwara Y, Yonemura K, Shinto E, Mochizuki S, Okamoto K, et al. Morphological Consistency of Desmoplastic Reactions Between the Primary Colorectal Cancer Lesion and Associated Metastatic Lesions. *Virchows Arch* (2020) 477:47–55. doi: 10.1007/s00428-019-02742-2
30. Ueno H, Shinto E, Hashiguchi Y, Shimazaki H, Kajiwara Y, Sueyama T, et al. In Rectal Cancer, the Type of Desmoplastic Response After Preoperative Chemoradiotherapy Is Associated With Prognosis. *Virchows Arch* (2015) 466:655–63. doi: 10.1007/s00428-015-1756-1
31. Ueno H, Konishi T, Ishikawa Y, Shimazaki H, Ueno M, Aosasa S, et al. Histologic Categorization of Fibrotic Cancer Stroma in the Primary Tumor Is an Independent Prognostic Index in Resectable Colorectal Liver Metastasis. *Am J Surg Pathol* (2014) 38:1380–6. doi: 10.1097/pas.0000000000000232
32. Nearchou IP, Kajiwara Y, Mochizuki S, Harrison DJ, Caie PD, Ueno H. Novel Internationally Verified Method Reports Desmoplastic Reaction as the Most Significant Prognostic Feature For Disease-Specific Survival in Stage II Colorectal Cancer. *Am J Surg Pathol* (2019) 43:1239–48. doi: 10.1097/pas.0000000000001304
33. Haruki K, Kosumi K, Li P, Arima K, Väyrynen JP, Lau MC, et al. An Integrated Analysis of Lymphocytic Reaction, Tumour Molecular Characteristics and Patient Survival in Colorectal Cancer. *Br J Cancer* (2020) 122:1367–77. doi: 10.1038/s41416-020-0780-3
34. Noshio K, Baba Y, Tanaka N, Shima K, Hayashi M, Meyerhardt JA, et al. Tumour-Infiltrating T-Cell Subsets, Molecular Changes in Colorectal Cancer, and Prognosis: Cohort Study and Literature Review. *J Pathol* (2010) 222:350–66. doi: 10.1002/path.2774
35. Chan AT, Ogino S, Fuchs CS. Aspirin and the Risk of Colorectal Cancer in Relation to the Expression of COX-2. *N Engl J Med* (2007) 356:2131–42. doi: 10.1056/NEJMoa067208
36. Borowsky J, Haruki K, Lau MC, Dias Costa A, Väyrynen JP, Ugai T, et al. Association of Fusobacterium Nucleatum With Specific T-Cell Subsets in the Colorectal Carcinoma Microenvironment. *Clin Cancer Res* (2021) 27:2816–26. doi: 10.1158/1078-0432.CCR-20-4009
37. Fujiyoshi K, Bruford EA, Mroz P, Sims CL, O’Leary TJ, Lo AWI, et al. Opinion: Standardizing Gene Product Nomenclature-a Call to Action. *Proc Natl Acad Sci USA* (2021) 118:e2025207118. doi: 10.1073/pnas.2025207118
38. Ogino S, Noshio K, Kirkner GJ, Kawasaki T, Meyerhardt JA, Loda M, et al. CpG Island Methylator Phenotype, Microsatellite Instability, BRAF Mutation and Clinical Outcome in Colon Cancer. *Gut* (2009) 58:90–6. doi: 10.1136/gut.2008.155473
39. Liao X, Lochhead P, Nishihara R, Morikawa T, Kuchiba A, Yamauchi M, et al. Aspirin Use, Tumor PIK3CA Mutation, and Colorectal-Cancer Survival. *N Engl J Med* (2012) 367:1596–606. doi: 10.1056/NEJMoa1207756
40. Benjamin DJ, Berger JO, Johannesson M, Nosek BA, Wagenaars EJ, Berk R, et al. Redefine Statistical Significance. *Nat Hum Behav* (2018) 2:6–10. doi: 10.1038/s41562-017-0189-z
41. Xie J, Liu C. Adjusted Kaplan-Meier Estimator and Log-Rank Test With Inverse Probability of Treatment Weighting for Survival Data. *Stat Med* (2005) 24:3089–110. doi: 10.1002/sim.2174
42. Jhunjhunwala S, Hammer C, Delamarre L. Antigen Presentation in Cancer: Insights Into Tumour Immunogenicity and Immune Evasion. *Nat Rev Cancer* (2021) 21:298–312. doi: 10.1038/s41568-021-00339-z
43. Zhang J, Liu J. Tumor Stroma as Targets for Cancer Therapy. *Pharmacol Ther* (2013) 137:200–15. doi: 10.1016/j.pharmthera.2012.10.003
44. Murray PJ, Allen JE, Biswas SK, Fisher EA, Gilroy DW, Goerdt S, et al. Macrophage Activation and Polarization: Nomenclature and Experimental Guidelines. *Immunity* (2014) 41:14–20. doi: 10.1016/j.jimmuni.2014.06.008
45. Li X, Liu R, Su X, Pan Y, Han X, Shao C, et al. Harnessing Tumor-Associated Macrophages as Aids for Cancer Immunotherapy. *Mol Cancer* (2019) 18:177. doi: 10.1186/s12943-019-1102-3
46. Ueno H, Jones A, Jass JR, Talbot IC. Clinicopathological Significance of the ‘Keloid-Like’ Collagen and Myxoid Stroma in Advanced Rectal Cancer. *Histopathology* (2002) 40:327–34. doi: 10.1046/j.1365-2559.2002.01376.x
47. Ogino S, Nowak JA, Hamada T, Milner DA Jr, Nishihara R. Insights Into Pathogenic Interactions Among Environment, Host, and Tumor at the Crossroads of Molecular Pathology and Epidemiology. *Annu Rev Pathol* (2019) 14:83–103. doi: 10.1146/annurev-pathmechdis-012418-012818
48. Akimoto N, Ugai T, Zhong R, Hamada T, Fujiyoshi K, Giannakis M, et al. Rising Incidence of Early-Onset Colorectal Cancer - a Call to Action. *Nat Rev Clin Oncol* (2021) 18:230–43. doi: 10.1038/s41571-020-00445-1
49. Mima K, Kosumi K, Baba Y, Hamada T, Baba H, Ogino S. The Microbiome, Genetics, and Gastrointestinal Neoplasms: The Evolving Field of Molecular Pathological Epidemiology to Analyze the Tumor-Immune-Microbiome Interaction. *Hum Genet* (2021) 140:725–46. doi: 10.1007/s00439-020-02235-2

**Conflict of Interest:** JM has received institutional research funding from Boston Biomedical, has served as an advisor/consultant to COTA Healthcare, and served on a grant review panel for the National Comprehensive Cancer Network funded by Taiho Pharmaceutical. MG received research funding from Bristol-Myers Squibb, Merck, Servier, and Janssen. This study was not funded by any of these commercial entities. AC previously served as a consultant for Bayer Healthcare and Pfizer Inc. This study was not funded by Bayer Healthcare or Pfizer Inc.

The remaining authors declare that the research was conducted in the absence of any commercial or financial relationships that could be construed as a potential conflict of interest.

**Publisher’s Note:** All claims expressed in this article are solely those of the authors and do not necessarily represent those of their affiliated organizations, or those of the publisher, the editors and the reviewers. Any product that may be evaluated in this article, or claim that may be made by its manufacturer, is not guaranteed or endorsed by the publisher.

Copyright © 2022 Akimoto, Väyrynen, Zhao, Ugai, Fujiyoshi, Borowsky, Zhong, Haruki, Arima, Lau, Kishikawa, Twombly, Takashima, Song, Zhang, Wu, Chan, Meyerhardt, Giannakis, Nowak and Ogino. This is an open-access article distributed under the terms of the Creative Commons Attribution License (CC BY). The use, distribution or reproduction in other forums is permitted, provided the original author(s) and the copyright owner(s) are credited and that the original publication in this journal is cited, in accordance with accepted academic practice. No use, distribution or reproduction is permitted which does not comply with these terms.



# Programmed Cell Death Tunes Tumor Immunity

Jing Liu<sup>1,2</sup>, Minjing Hong<sup>1</sup>, Yijia Li<sup>1,2</sup>, Dan Chen<sup>1</sup>, Yangzhe Wu<sup>1\*</sup> and Yi Hu<sup>3\*</sup>

<sup>1</sup> Guangdong Provincial Key Laboratory of Tumour Interventional Diagnosis and Treatment, Zhuhai Institute of Translational Medicine, Zhuhai People's Hospital Affiliated with Jinan University, Jinan University, Zhuhai, China, <sup>2</sup> The Biomedical Translational Research Institute, Faculty of Medical Science, Jinan University, Guangzhou, China, <sup>3</sup> Microbiology and Immunology Department, School of Medicine, Faculty of Medical Science, Jinan University, Guangzhou, China

The demise of cells in various ways enables the body to clear unwanted cells. Studies over the years revealed distinctive molecular mechanisms and functional consequences of several key cell death pathways. Currently, the most intensively investigated programmed cell death (PCD) includes apoptosis, necroptosis, pyroptosis, ferroptosis, PANoptosis, and autophagy, which has been discovered to play crucial roles in modulating the immunosuppressive tumor microenvironment (TME) and determining clinical outcomes of the cancer therapeutic approaches. PCD can play dual roles, either pro-tumor or anti-tumor, partly depending on the intracellular contents released during the process. PCD also regulates the enrichment of effector or regulatory immune cells, thus participating in fine-tuning the anti-tumor immunity in the TME. In this review, we focused primarily on apoptosis, necroptosis, pyroptosis, ferroptosis, PANoptosis, and autophagy, discussed the released molecular messengers participating in regulating their intricate crosstalk with the immune response in the TME, and explored the immunological consequence of PCD and its implications in future cancer therapy developments.

## OPEN ACCESS

### Edited by:

Ana Paula Lepique,  
University of São Paulo, Brazil

### Reviewed by:

Thirumala-Devi Kanneganti,  
St. Jude Children's Research Hospital,  
United States  
Duanwu Zhang,  
Fudan University, China

### \*Correspondence:

Yi Hu  
yihu2020@jnu.edu.cn  
Yangzhe Wu  
tyzwu@jnu.edu.cn

### Specialty section:

This article was submitted to  
Cancer Immunity and Immunotherapy,  
a section of the journal  
Frontiers in Immunology

Received: 02 January 2022

Accepted: 28 February 2022

Published: 30 March 2022

### Citation:

Liu J, Hong M, Li Y, Chen D, Wu Y and Hu Y (2022) Programmed Cell Death Tunes Tumor Immunity. *Front. Immunol.* 13:847345.  
doi: 10.3389/fimmu.2022.847345

## INTRODUCTION

To maintain the physiological homeostasis in normal or stress-challenged (injury or infection, etc.) states, cells adopt different cell death pathways which generate distinctive morphological and functional outcomes (Table 1). In an adult, approximately 50~70 billion cells die each day to maintain a healthy turnover of cells (48). Programmed Cell Death (PCD) and non-PCD both are demonstrated to participate in this turnover process of the cells. However, PCD is orchestrated by precise molecular circuitry whereas non-PCD such as necrosis is characterized as a premature death caused by injury. We will limit our discussion on PCD and its communication with the immune milieu in the context of the tumor microenvironment (TME) in this review.

According to the ability to initiate further adaptive immune response or not, PCD can be further categorized as immunogenic and non-immunogenic (or tolerogenic) ones (44). Immunogenic PCD alerts the surrounding immune system of potential danger through the release of cellular components, mainly pro-inflammatory cytokines, or other damage-associated molecular patterns (DAMPs). These signals are recognized by the Pattern Recognition Receptors (PRRs) on innate immune cells, thus activating subsequent immune responses. On the other hand, non-immunogenic

**TABLE 1** | Summary of key features of PCD.

		Apo-ptosis	Pyro-ptosis	Ferro-ptosis	Necro-ptosis	PANo-ptosis	Auto-phagy	Ref.
Morphological features	Pore formation	X	✓	✓	✓	✓	X	(1–9)
	Membrane blebbing	✓	✓	X	X	TBD	X	(10–14)
	Mitochondria dysfunction	✓	✓	✓	✓	TBD	X	(15–25)
	DNA fragmentation	✓	✓	X	✓	TBD	X	(26–32)
Major regulatory components	Cell swelling	X	✓	✓	✓	TBD	X	(5, 33–35)
	Caspase cleavages	✓	✓	X	X	✓	X	(36–38)
	GSMD family activation	X	✓	X	X	✓	X	(27, 38–40)
	RIP/MLKL Signaling activation	X	X	X	✓	✓	X	(38, 41, 42)
Results	Autophagosome-lysosomal Pathway activation	X	X	X	X	X	✓	(43)
	Immunogenicity	X or ✓	✓	✓	✓	✓	X	(36, 44–46)
	Programmed Cell Death (PCD)	✓	✓	✓	✓	✓	✓	(7, 45, 47)

'X' means no; '✓' means yes. 'TBD' means 'to be defined'.

cell death such as apoptosis maintains the integrity of the cell membrane without leaking cellular contents, therefore leading to a "silent" clearance by phagocytic cells without initiating further inflammation (49).

Besides apoptosis, several other well-recognized PCD pathways, necroptosis (50, 51), pyroptosis (27, 36, 52), and ferroptosis (53–56), etc. have also been found to be tightly regulated and connected with the tumor immunity in TME. Interestingly, one pro-survival strategy to avoid extensive PCD adopted by cells is called autophagy. It's also worth mentioning that autophagy could convert into yet another type of PCD under certain physiological circumstances (57, 58). Therefore, a game between pro-survival and pro-death pathways shapes the heterogeneity and complexity of the tumor immunity in TMEs. Here, we will constrain our discussion on the following types of PCD, apoptosis, necroptosis, pyroptosis, PANoptosis, ferroptosis, and autophagy, respectively.

## APOPTOSIS

One of the earliest well-recognized non-immunogenic PCD is apoptosis (1, 59–65), which is elegantly orchestrated by the sequential cleavages of the aspartate-specific proteases [caspases (49, 65)]. This leads to cell membrane blebbing and the generation of apoptotic bodies, nucleus condensation, and cellular organelle/DNA fragmentation. These alterations eventually cause cell disintegration followed by the engulfment by phagocytic housekeepers from the innate immunity without releasing proinflammatory cellular contents to the extracellular environment. Although typical apoptosis is non-immunogenic, studies indicated that, under certain conditions such as caspase deficiency, apoptosis could indeed trigger adaptive anti-tumor or anti-viral immune responses by activating NF-κB signaling (66) and cGAS/STING pathway, respectively (67, 68). Moreover, radiotherapy or chemotherapy could induce immunogenic apoptosis as well.

In the TME, drugs or cytotoxic immune cells induced apoptosis has long been considered as the primary way of cancer cell clearance in TME. Unfortunately, drugs showing

potent anti-tumor potency *in vitro* mostly lost their cytotoxicity or quickly develop drug resistance in patients (69). Moreover, the immunosuppressive nature such as low pH, hypoxia, and ROS of the TME also mediates the exhaustion and apoptosis of cytotoxic immune cells at the same time, facilitating the growth of pro-tumoral immune cells such as Treg, M2 macrophage, and myeloid-derived suppressor cells (MDSC) (70–79). As a result, cancer cell apoptosis is commonly attenuated in the TME due to the loss of cytotoxic tumor immunity and/or apoptotic signals of cancer cells (77). Therefore, re-initiation of cancer cell-specific apoptosis in TME is one of the focuses of cancer study (80). For instance, Agonists such as APG350, AMP655 targeting TRAIL (tumor necrosis factor (TNF) related apoptosis-inducing ligand) receptor signaling could selectively induce cancer cell apoptosis in mice models but limited benefits was observed in cancer patients (81–86). It is also worth noticing that few studies evaluated the potential damage of chemotherapy or radiation to the immune cells. In fact, apoptosis of immune cells, such as cytotoxic T cells, can directly undermine the anti-tumor immunity in the TME (87, 88). Thus, careful assessments on different apoptosis-inducing strategies may pave a way for scientists to constrain or clear cancerous cells without compromising the anti-tumor immunity.

## NECROPTOSIS

Contrary to necrosis, necroptosis (89–91) belongs to PCD and can trigger inflammation in TME when apoptosis is prohibited (41, 51). Necroptosis differentiates itself from apoptosis in that its progression does not involve caspases activation. It is instead mediated by external signals that trigger activation of Receptor-Interacting Protein 1 (RIP1), RIP3, and Mixed-Lineage Kinase Domain-Like (MLKL) signaling cascade. MLKL pseudokinase is one of the main actors of necroptosis due to its ability to form membrane pores *via* polymerization and insertion into the plasma membrane. Notably, necroptosis involves the permeabilization of the lysosomal membrane followed by

mitochondrial damage and ultimately ends in necrosis-like death both morphologically and biochemically.

Necroptosis is finely tuned and plays various functions. For instance, in physiological states, necroptosis mediates the formation of the mammalian bone plate, generation of megakaryocytes (92), and maintaining epithelial hemostasis (93). Necroptosis has been found to have both pro- and anti-tumor roles in TME (94). On one hand, low expression of necroptosis regulators RIP(K)3 and MLKL correlated with poor prognosis in various types of solid tumors (95–97). Specifically, necroptotic cells have been shown to promote dendritic cell maturation (98) and determined cross-priming efficiency thus anti-tumor immunity of CD8+ T cells through RIPK1 and NF- $\kappa$ B signaling (99). In comparison, cells going through passive necrosis cannot effectively activate CD8+ T cells *in vivo* (99). Notably, RIP(K)3 deletion in mice impaired NKT cells' cytotoxicity against tumors (100). Thus, triggering well-targeted necroptosis of cancer cells whilst activating cytotoxic T cells becomes one of the novel strategies in cancer therapy. Moreover, vaccination with necroptotic cancer cells could stimulate the maturation of dendritic cells, cross-priming of CD8+ T cells, and IFN- $\gamma$  production, thereby enhancing anti-tumor immunity (101). On the other hand, inhibiting TCR restimulation-induced necroptosis in T cells could refresh the anti-tumor efficacy of T cells. Moreover, Endothelial cells necroptosis induced by tumor cells could in turn promote tumor metastasis (102). Similarly, necroptosis-induced signaling promotes macrophage-induced T cell suppression in pancreatic ductal adenocarcinoma (PDA) mice models (103). Recently, Jiao *et al.* demonstrated an elevated level of RIP(K)3-mediated MLKL phosphorylation in breast tumor necrotic area in late stages compared with early stages of breast cancer tumors. Meanwhile, lung metastasis was suppressed in MLKL deficient tumors, further correlating necroptosis with tumor metastasis (104). Thus, the “friend” or “foe” relationship between necroptosis and tumor immunity is highly context-dependent and needs to be carefully differentiated.

## PYROPTOSIS

Pyroptosis (33, 105), similar to necroptosis, is an immunogenic PCD that results in the perforation of plasma membrane followed by the release of pro-inflammatory cellular components. It was first discovered in macrophages upon pathogen infection (106, 107). Since caspase cleavages also orchestrate apoptosis processes, pyroptosis phenotype on macrophage has long been mistaken for apoptosis until the discovery of gasdermin family proteins. Pyroptosis could be initiated through both the pathogen-associated molecular patterns (PAMPs)/danger-associated molecular patterns (DAMPs) activated canonical caspase-1 inflammasome pathway (27, 33, 105) and lipopolysaccharide (LPS) activated non-canonical caspase-4/5/11 inflammasome pathway (108, 109). Activated caspases cleave GSDMD and release its N-terminal fragments, which then oligomerize on the cellular membrane, leading to pore formation. In the meantime,

caspase1 cleaves pro-IL-1 $\beta$ /IL-18 and releases the highly immunogenic IL-1 $\beta$ /IL-18 through the GSDMD pore (2, 27, 39, 110). In addition to the above pathways, recent studies indicated that caspase 3, which has long been considered the essential modulator of apoptosis, also regulates pyroptosis induction through GSDME cleavage (3, 111). This discovery further raises the possibility of caspase 3/GSDME signaling might act as a switch between apoptosis and pyroptosis, implying crosstalk of the two (112).

Pyroptosis also has both pro- and anti-tumor functions in regulating anti-tumor immunity in TMEs. Lower levels of caspase-1, IL-1 $\beta$ , and IL-18 were observed in hepatocellular carcinoma (HCC) tissues compared with adjacent normal ones (113), implying the role of pyroptosis in tumorigenicity. Being an immunogenic form of cell death, pyroptosis produces proinflammatory cytokines such as IL-1 $\beta$ , IL18 to facilitate the infiltration of immune cells to the immunosuppressive TME, demonstrating it can be utilized in anti-tumor therapy (114). It has been shown that Nlrp3 and caspase-1 deficient mice, lacking the ability to initiate effective pyroptosis, were more prone to chemical-induced colitis-associated colon cancer (CAC) than the wild type mice (115–117). Applying a bioorthogonal system, which helps investigate the pyroptotic processes in live animals, researchers found that the pyroptosis of less than 15% of cancer cells was enough to strengthen T cell response and eventually achieve the complete remission of solid tumor (118). Nanoparticles can be used as pyroptosis inducers as well, and thus potentiate antitumor immunity by enriching effector-memory T cells and inhibiting tumor growth and metastasis (119, 120). Cytotoxic immune cells such as natural killer cells and CD8+ T cells can also trigger cancer cell pyroptosis through lymphocyte-derived granzyme A (GZMA) or granzyme B (GZMB) but not caspases-mediated cleavage of the GSDM family proteins. The GZMA/GZMB triggered proteolytic cleavages subsequently activate the pyroptosis cascade, thus further recruiting more cytotoxic lymphocytes and amplifying the anti-tumor signals in TME (40, 121). Currently, there are attempts to utilize chemo- or radiotherapy to induce pyroptosis for cancer treatment (122). It should be mentioned here that apoptosis can convert into pyroptosis in the presence of TNF or chemotherapy treatment, in which GSDME cleavage by caspase plays a key role (3).

Alternatively, pyroptosis has also been implicated with cancer immune evasion in TME. Chronic inflammation induced by pro-inflammatory cytokines such as IL-1 $\beta$ , IL6, and IL-18, released *via* pyroptotic cell death, is considered to drive tumor progression and immune evasion (123, 124). Zhai *et al.* demonstrated the pro-tumoral aspect of NLRP1 inflammasomes, which promoted tumor growth by suppressing the apoptotic pathway (125). Furthermore, pyroptosis directly mediated immune cell death in cancer and other diseases. Although pyroptosis was initially discovered in macrophages (106) and neutrophils (126) as the host innate immune defense against pathogen invasion, pyroptosis of the adaptive immune cells (CD4+ T cells) was also observed in chronic HIV infected patients (127, 128). CARD8 inflammasome has been linked to T cell pyroptosis *via* the caspase-1-GSDMD axis (129). Notably,

GSDM family gene expressions have been observed in various B, T leukemia cell lines according to Cancer Cell Line Encyclopedia (CCLE) database (**Figure 1A**). These observations imply that pyroptosis is not limited to innate immunity, adaptive immune cells adopt pyroptosis as well. Thus, careful evaluation of both pros and cons of pyroptosis during the design of cancer treatment strategy will be helpful for better clinical outcomes.

## FERROPTOSIS

Ferroptosis (130), another emerging immunogenic PCD, is initiated by the excessive accumulation of intracellular reactive oxygen species (ROS) which oxidize polyunsaturated fatty acids (PUFAs) on the plasma membrane in an iron-dependent manner, leading to lipid peroxidation-induced cellular membrane destruction. Glutathione peroxidase 4 (GPX4) is

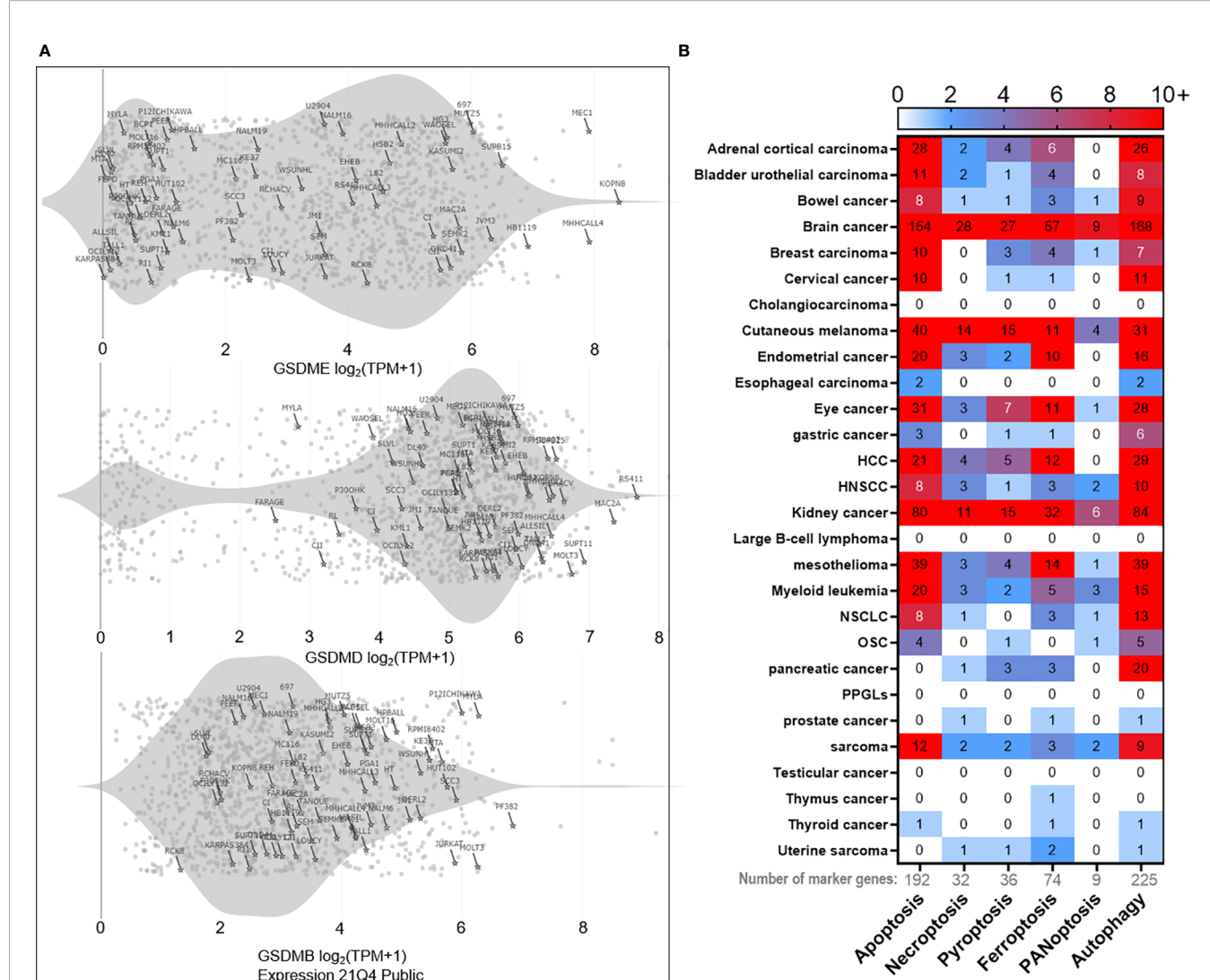


**FIGURE 1 |** Bioinformatics of PCD landscape. **(A)** PCD occurs in immune cells as well. For instance, expressions of the pyroptosis marker gene ‘gasdermin’ family (GSDME, GSDMD, GSDMB) can be detected in various T and B leukemia cell lines (marked with the cell line name and highlighted with stars) according to Cancer Cell Line Encyclopedia (CCLE) database. The rest of the points represent other types of cell lines deposited in the database. The gray shade represents the distribution density of T and B cell lines. **(B)** Based on PCD marker genes (192 for apoptosis, 32 for necroptosis, 36 for pyroptosis, 74 for ferroptosis, 9 for PANoptosis, and 225 for autophagy), we analyzed the correlation between each marker gene and the overall survival in pan-cancer. Only those genes with  $p < 0.01$  significance in correlation are used to plot the heatmap. The numeric mark in the heatmap means the number of marker genes that is significantly ( $p < 0.01$ ) correlated with the overall survival. The results reveal heterogeneous contributions of each PCD in the overall survival across cancers. In brief, brain cancer ranks first in overall survival correlation with apoptosis, necroptosis, pyroptosis, ferroptosis, and PANoptosis, followed by kidney cancer, cutaneous melanoma, mesothelioma, adrenal cortical cancer, and others. As for autophagy, it positively correlates with the overall survival in most cancers, with brain cancer being the most significantly correlated as well. Clinical data are acquired from the TCGA database. Marker gene lists of respective PCD are provided in the **Supplementary Excel File**. HNSCC, squamous cell carcinoma of the head and neck; HCC, hepatocellular carcinoma; NSCLC, non-small cell lung cancer; OSC, ovarian serous cystic adenocarcinoma; PPGLs, pheochromocytomas, and paragangliomas.

thus far the only enzyme known to prevent membrane lipid peroxidation. Ferroptosis occurs when the balance between the oxidation of the PUFAs and the detoxification of GPX4 is disrupted.

The induction of cancer cell ferroptosis in TME has been explored as a treatment alternative for cancers (131). Interestingly, recent discoveries indicated that cancer stem cells (CSCs) might be sensitive to ferroptosis due to their relatively strong dependency on the lipid intake pathways and higher intracellular iron levels compared with regular cancer cells (132, 133). Therefore, interference with GPX4 pathways seems to sensitize CSCs to ferroptosis (134–136). Furthermore, cytotoxic CD8<sup>+</sup> T cells could enhance tumor cell lipid peroxidation caused by ferroptosis, thus achieving higher efficacy of PD1 checkpoint blockade therapy (137). Ferroptosis has also been found to play a crucial role in regulating T cell immunity. Lack of glutathione peroxidase 4 (Gpx4) in CD8<sup>+</sup> and CD4<sup>+</sup> T cells, the major scavenger of phospholipid hydroperoxide, induces ferroptosis and loss of protection from infection (138, 139) and might facilitate cancer development. Moreover, it's shown that the overexpression of CD36, which is the fatty acid (AA) transporter on T cells, can lead to tumor-infiltrating CD8<sup>+</sup> T cell ferroptosis through excessive lipid peroxidation and eventually impaired anti-tumor immunity (140). As for regulatory T cell (Treg) in TME, it's well protected from ferroptosis by glutathione peroxidase 4 (Gpx4). Targeted ablation of Gpx4 in Treg inhibited tumor growth and potentiated anti-tumor immunity (141). Thus, the consequences of ferroptosis in the TME need to be carefully evaluated and interpreted (131, 142), which could be highly context-dependent for achieving a sound clinical outcome of anti-tumor therapy.

## PANOPTOSIS

From the above discussion, distinct and separate molecular pathways of apoptosis, pyroptosis, and necroptosis are described. Nonetheless, accumulating evidence indicated extensive cross-talk among these PCD pathways (36, 143–147). This led to the hypothesis that master regulators exist to orchestrate the interplay of different PCDs. Recently, the concept of PANoptosis PCD was established and shown to be able to incorporate and co-regulate apoptosis, pyroptosis, and necroptosis through the formation of PANoptosome as part of host innate immune defense (7, 47). PANoptosis could be triggered by the cooperative interactions of AIM2, pyrin, and ZBP1 that drives the formation of AIM2 PANoptosome. Specifically, the PANoptosome protein complex encompasses key signaling molecules of PCDs such as caspase-1, GSDMD, GSDME of pyroptosis, caspase-8, caspase-3, FADD of apoptosis, and RIPK3, MLKL of necroptosis. Therefore, the PANoptosome complex acts as a molecular scaffold to facilitate signal transduction and interplay among these PCDs, providing host protection against virus or bacterial infection (47). Meanwhile, excessive PANoptosis has been found to trigger cytokine release syndrome (CRS) (148) during SARS-CoV-2 infection (149). Lately, emerging studies highlighted the role of PANoptosis

in tumorigenesis and anti-tumor therapy. For instance, IFN $\gamma$ , together with TNF $\alpha$ , could induce PANoptosis in diverse cancer cell lines and reduced tumor size in an immunodeficient mice model (150). Moreover, blocking the interaction of ZBP1, (the key mediator in PANoptosis) with RIPK3 or deletion of key PANoptosis regulatory element IRF1 (Interferon regulatory factor 1) suppressed PANoptosis and promoted tumorigenesis in mice studies (151, 152). Therefore, harnessing the potent immunogenicity of PANoptosis might strengthen anti-tumor immunity in TME. It should be mentioned here that since PANoptosis is a newly established concept of PCD, further mechanistic exploration needs to be done at the single-cell level (single-cell multi-omics techniques etc.) to address the possibility that the observed "PANoptosis phenotype" is due to different cellular subclusters undergoing respective PCDs.

## AUTOPHAGY

Autophagy (153, 154) is a surviving mechanism adopted by eukaryotic cells under nutrient stress conditions. The autophagic pathway starts with the formation of an autophagosome, a double-membrane structure, which contains autophagic components such as ATG proteins and cellular organelles. Autophagosome then fuses with lysosome for degradation to provide an extra energy source. This pathway could help recycle cellular nutrients and organelles to prevent nutritional stress-induced premature cell death. Although autophagy is normally considered as a pro-survival strategy adopted by cells, it has also been proposed as a "suicide" mechanism committed by cells, including malignant cells, through self-digestion (155). Evidence indicated that excessive autophagy can lead to cell death (autophagy-dependent cell death, ADCD) (156, 157). ADCD should not be mistaken or obscured with the autophagy-associated or autophagy-mediated cell deaths, which coincides with or triggers apoptosis, respectively. ADCD, on the other hand, is defined as 'a form of regulated cell death that mechanistically depends on the autophagic machinery (or components thereof)' according to the Nomenclature Committee of Cell Death (45, 57, 58). ADCD has critical physiological role in suppressing the oncogenic transformation by eliminating pre-cancerous cells and is an integral component of the tumor-suppressive machinery (158). However, autophagy is also considered to play crucial role in establishing resistance to cancer therapies (159). Pharmacological inhibition of autophagy slowed pancreatic tumor growths (160, 161). Autophagy can cross-talk with other PCD (e.g. apoptosis), and actively regulate both cancer metastasis (162) and anti-tumor immunity (163, 164). Evidence indicated that autophagy regulated survival, and memory formation of cytotoxic T cells (165–167). Meanwhile, TME has long been known as a nutrient-depleted environment, study indicated that the autophagy of cancer cells rescued itself from T cell-mediated cytotoxicity by blocking cytokine-induced apoptosis (168). Inhibiting cancer cell autophagy could facilitate cancer cell clearance in the TME (169). Interestingly, naïve T cells in ovarian cancer patients could not effectively engage in autophagy under TME challenge, but go through apoptosis

instead, leading to poor anti-tumor immunity (170). Therefore, pharmacologic inhibition of overall autophagy in TME, regardless of which type of cells should be precisely targeted in the context of cancer therapy, might be problematic (171). Nevertheless, targeting autophagy might improve and/or synergize the efficacy of current cancer therapies.

## MOLECULAR MESSENGERS RELEASED BY PCD TUNE TUMOR IMMUNITY

The occurrence of PCD in the TME is accompanied by the release of intracellular components, including cytokines, small molecules, mtDNA (172), ncRNA (173, 174), and exosomes (175), etc. which are altogether involved in shaping the immune landscape of the TME. Subsequently, we focused on reviewing the effects of a few well-studied “end products” of immunogenic PCD on innate and adaptive immune cells in TME, mainly including cytokines (e.g. IL1) and small molecules (e.g. ATP).

### Family Cytokines

As pro-inflammatory cytokines, IL1 family cytokines such as IL1 $\beta$  and IL18 belong to the “end products” of pyroptosis and PANoptosis (27, 47, 52, 176). IL1 $\beta$  is one of the biomarkers for pyroptosis since it is produced from caspase 1 cleavage of pro-IL1 $\beta$  and subsequently secreted from GSDM pores. IL1 signaling cascade activates dendritic cells and macrophages, professional antigen-presenting cells (APCs), as well as regulates Th1/Th17 differentiation of CD4 $^{+}$  T cell and CD8 $^{+}$  T cell effector function (177). Moreover, IL1 signaling disruption in myeloid cells leads to colorectal cancer progression (117, 178). Notably, IL1 $\beta$  also plays beneficial roles in the initiation of anti-tumor immunity in TME (179, 180). Similar to IFN $\gamma$ , IL1 $\beta$  also plays both anti- and pro-tumoral roles in TME in a highly context-dependent manner. Accumulating evidence suggested the pro-tumoral role of IL1 $\beta$  across a wide range of cancer types (178, 181). This might be due to the increased level of IL1 cytokines, which leads to chronic inflammation and drives tumor development and progression *via* the stimulation of the epithelial-to-mesenchymal transition (182), the proliferation of cancer cells, and the enrichment of immunosuppressive cell populations in TME. In TME, the IL1 family creates a complex regulating network and orchestrates the local anti-tumor immunity (183). These dichotomous discoveries on the IL1 family emphasized comprehensive evaluations of the pro- and anti-tumor responses of therapies that focus on the induction of pyroptosis and PANoptosis will be necessary to clarify potential benefits and unexpected risks.

### HMGB1

As a type of DAMP molecule released by immunogenic PCD, high-mobility group box 1 (HMGB1) is a chromatin-associated protein first identified in 1973 (184). Since it tightly binds to chromatin, it could only be secreted from cells with destructed membrane structure (185). Once secreted to the extracellular milieu, HMGB1 could interact with various cellular receptors and form complexes with immune activators, regulating both the

innate and adaptive immune responses (186). For instance, through binding to the receptor of advanced glycation end products (RAGE) and Toll-like receptors (TLRs), HMGB1 could activate caspase 1 cleavage and induce macrophage pyroptosis (187). HMGB1 is a coactivator for NF- $\kappa$ B as well, regulating inflammatory gene expressions in mice macrophages *via* epigenetic chromatin remodulation (188). Similar to IL1 $\beta$ , HMGB1 is also involved in dendritic cell (DC) maturation, tumor antigen presentation (189), neutrophil polarization, and cytokine release in TME (190, 191). HMGB1 production positively correlates with tumor antigen-specific T cell response and thus could serve as a biomarker for patient prognosis (192, 193). HMGB1 signaling can directly trigger T (194, 195) and B lymphocytes (196) proliferation, and downregulate immunosuppressive CTLA4 and Foxp3 expression and IL-10 secretion in Tregs *via* the TLR pathway.

Nonetheless, HMGB1 plays immunosuppressive roles as well. For example, HMGB1 can facilitate the growth and differentiation of MDSCs to promote cancer progression in TME (197, 198). Evidence also indicated HMGB1, together with complement protein, could induce monocyte differentiation into anti-inflammatory macrophage M2, thus regulating immune homeostasis (199). Moreover, HMGB1 and its interaction with the RAGE receptor on tumor cells could also directly regulate tumor cell autophagy and result in HMGB1-mediated tumorigenesis (200). Furthermore, HMGB1 blockade inhibited tumor growth and could work synergistically with checkpoint immunotherapy (201). Interestingly, the expression level of HMGB1 gene is elevated in tumor specimens from TCGA database across almost all cancer types, but it does not significantly correlate with patient prognosis (<http://gepia.cancer-pku.cn/>). Therefore, the role of HMGB1 in TME needs to be further investigated.

### ATP and Its Intermediates

Adenosine triphosphate (ATP) has long been considered as the intracellular currency inside living cells, fueling numerous biological processes. Therefore, the concentration of intracellular ATP (iATP) is very high, ranging from 1-10 mM (202). In stark contrast, the concentration of extracellular ATP (eATP) under normal physiological condition is comparatively low (nM range). The physiological level of eATP does not induce an immune response (203). However, in the context of immunogenic PCD, ATP can leak from the “porous” cells into the extracellular milieu and serve as a type of “alarmins” or “find-me” and “eat-me” signals to attract phagocytes. Thus, elevated eATP level is highly pro-inflammatory (204). Notably, eATP can be further converted into the immunosuppressive metabolite adenosine by CD39 and CD73 ectonucleotidases on the cellular membrane. A main function of the extracellular adenosine is to create an immunosuppressive tumor environment by inducing tumor-infiltrating macrophage proliferation (205), regulatory immune cell, and MDSC activation (206-209) while repressing the anti-tumor function of cytotoxic T cells (210, 211). Therefore, PCD-induced release of eATP, together with adenosine, forms an intricate modulatory network of tumor immunity in TME.

## Other Immunogenic Molecules

Calreticulin, a calcium-binding chaperone protein, mainly resides in the endoplasmic reticulum (ER) but can translocate to the cellular membrane during immunogenic PCD. It can serve as a DAMP and “eat me” signal for antigen-presenting cells (APCs), thus is a proinflammatory element in TME. Genetic knockdown or antibody ablation of calreticulin attenuated the phagocytosis of cancer cells by APCs, resulting in the elimination of cancer cell immunogenicity (212). Interestingly, chemotherapy drugs can induce calreticulin exposure onto the cancer cell surface, leading to maturation of DC and activation of tumor-specific effector T cells (213).

Another ER chaperone is the heat shock protein (HSP) family, which exposes to the extracellular environment during immunogenic PCD. Like calreticulin, HSP was found to have an immunomodulatory role in the TME. For instance, recombinant rHsp70, combined with radiotherapy, can potentiate DC immunotherapy by inducing tumor-specific T cell response in mice models (214). Furthermore, several HSP protein cancer vaccines have been developed and are under clinical trials (215, 216). However, it's reported that HSP protein has both pro- and anti-inflammatory functions in TME, implying a sophisticated role of HSP proteins play in regulating tumor immunity.

Together, DAMPs released during immunogenic PCD not only can act as immunogens which lead to pro-inflammatory immune response but also might cause chronic inflammation or immune suppression, thus leading to tumor progression. Thus, it is necessary to comprehensively weigh both the pros and cons of the immune and systemic consequences of immunogenic PCD in tumor therapy designs.

## CLINICAL BENEFITS AND CONCERNs OF PCD

Currently, efforts have been made on designing chemo- or radiotherapies to induce immunogenic PCD in tumor cells. At least 19 clinical trials, mostly chemotherapies, have been completed or are underway in exploring the role of immunogenic PCD in cancer treatments (clinicaltrials.gov). Bleomycin (BLM) (217), Cyclophosphamide (CTX) (218), Shikonin (219), Anthracyclines (213), and Oxaliplatin (220) are examples of immunogenic PCD inducers being studied extensively. These chemo-drugs can stimulate DC maturation, subsequently affecting tumor antigen uptake and presentation of adaptive immune cells. In addition to chemotherapy, radiotherapy (221), phototherapy (222, 223), and targeted nano-drug delivery therapy (224, 225) can induce immunogenic PCD as well. Reports showed that combining a PCD-inducing regimen with immunotherapy could yield promising results (221, 226). However, chimeric antigen receptor T cell (CAR-T) therapy can trigger tumor cell pyroptosis-induced cytokine release syndrome (CRS), leading to mitigated benefits of the cell therapy (227). Moreover, PANoptosis, encompassing features of pyroptosis, has also been found to initiate CRS (148, 149), whether it also contributes to the CRS observed in CAR-T therapy awaits further investigation. Meanwhile, our previous

clinical studies demonstrated allogeneic V $\delta$ 2 $^{+}$   $\gamma$  $\delta$  T cells transfers do not cause CRS, and possess a high safety profile and clinical benefits in terminal cancer patients (228, 229). Therefore, how to utilize PCD to design safe and effective therapy protocol requires further investigation.

## FUTURE PROSPECTS

To vividly demonstrate the occurrence probability of respective PCD across cancer types, we profiled maker gene contributions of each PCD and generated a pan-cancer heatmap (Figure 1B). Interestingly, there are significant variations in terms of PCD occurrence in different cancer types, with brain cancer being the most PCD-prone one, prompting one to speculate cancer types might be a crucial factor in determining the response rate and efficacy of PCD-inducing treatments.

In summary, different types of PCD can be triggered by different or similar causes and lead to heterogeneous consequences in the TME, resulting in either immunogenic or non-immunogenic responses and eventually tumor regression or progression (Figure 2A). Importantly, we believe the TME is precisely regulated various types of PCD, including apoptosis, necroptosis, pyroptosis, ferroptosis, PANoptosis, autophagy, and others, as well as PCD-related cytokines, metabolites, and immunogenic molecules, which collaboratively participate in balancing the TME to enrich either anti-tumor effector immune cells (e.g. cytotoxic T cells, NK cells, V $\gamma$ 9V $\delta$ 2  $\gamma$  $\delta$  T cells, and M1 macrophages) or regulatory immune cells (e.g. Tregs, MDSCs, V $\gamma$ 9V $\delta$ 1  $\gamma$  $\delta$  T cells, and M2 macrophages), eventually lead to tumor regression or progress (Figure 2B). Though most of the current literatures focuses on exploring the role of cancer cell PCD plays in shaping the immune landscape of TME, recently, increasing evidence indicated that both immunogenic and non-immunogenic PCD of immune cells can compromise anti-tumor immunity. Specifically, Zou's group made an insightful discovery that apoptotic Tregs can exert significantly higher immunosuppressive function than live Tregs (230). Moreover, ferroptosis induced by T cell lipid peroxidation weakened T cell immunity to both virus infection and tumor (138, 231). Similarly, the pyroptosis of CD4 $^{+}$  T cells led to immunodeficiency in HIV (127, 128). Thus, it's imperative to further explore the immunological consequences of PCD of immune cells in the TME.

To better understand PCD in the TME, many scientific questions remain to be resolved. A few are listed below.

1. How do the heterogeneous cell populations in TME sense and respond to PCD signals respectively?
2. Do different types of PCD have crosstalk in the TME? What might be the immunological consequences of PCD crosstalk?
3. How do PCDs induce the depletion/deficiency of anti-tumor effector immune cells, while enriching the suppressive immune cells in TME, thus creating a “cold” tumor?
4. How can we strengthen the anti-tumor immunity of immunologic PCDs at the same time avoiding chronic inflammation?

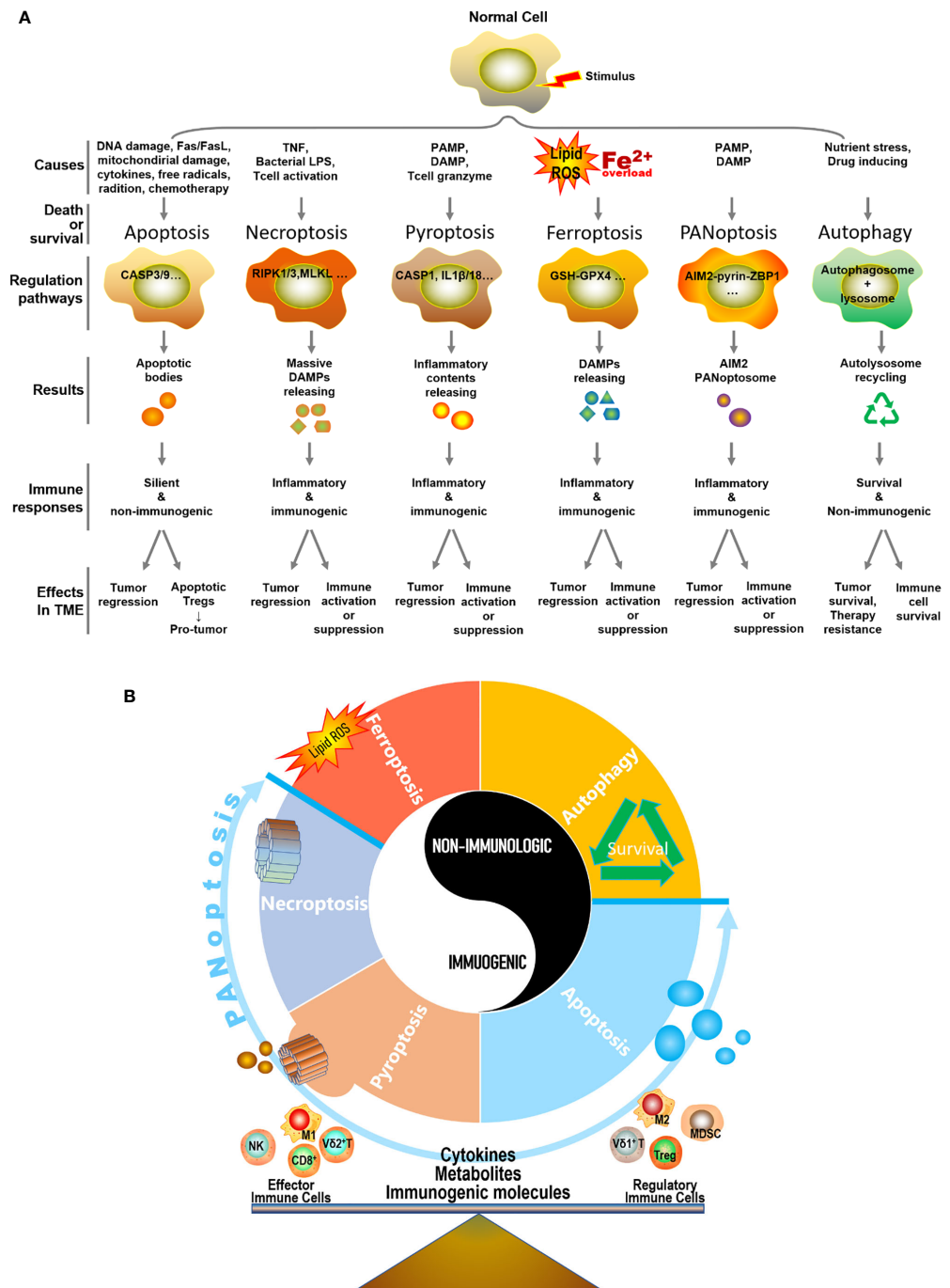


**FIGURE 2 |** Distinctive hallmarks and mechanisms of five types of PCDs and autophagy. **(A)** In the context of different types of extracellular stimulus and intracellular signaling, a normal cell may undergo a specific type of cell death or survival. This process is precisely regulated by a set of genes and signaling molecules. Necroptosis, pyroptosis, ferroptosis, and PANoptosis represent four typical ways of immunologic PCD in the TME, which releases various cytokines, metabolites, and immunogenic molecules, thus leading to either tumor regression accompanied by immune activation or tumor progress along with immune suppression. For non-immunologic apoptosis in the TME, it generally connects with tumor regression, however, immune cells in the TME are routinely apoptosis-activated as well and implicate with the depressed immune microenvironment. Particularly, apoptotic regulatory T cell (Treg) can serve as a strong pro-tumor player in the TME. As for autophagy (self-survival dominantly) in the TME, it is closely linked with cancer cell survival, tumor progress, and therapy resistance. Meanwhile, immune cells also adopt autophagy strategy to survive in the stressful condition of the TME, and to eventually perform either pro-tumor or anti-tumor function depending on circumstances. **(B)** Apoptosis, necroptosis, pyroptosis, ferroptosis, PANoptosis, and autophagy, as well as their respective produced cytokines, metabolites, and immunogenic molecules in the TME, collaboratively participate in balancing the TME to enrich either anti-tumor effector immune cells or regulatory immune cells, eventually lead to tumor regression or progression.

- How would PCD of tumor-infiltrating immune cells affect the therapeutic efficacy and patient prognosis in different cancers?

Currently, although certain “biomarkers” or “morphological characteristics” were identified to differentiate individual PCD, it is hard to exquisitely extinguish them apart from one another. Therefore, it’s still difficult to develop highly targeted pharmacological inhibitors for each PCD without causing unwanted “off-target” effects. However, multi-omics technologies at the single-cell level allow us to clarify the characteristics of individual cells in the TME. This might greatly benefit researchers to gain thorough understanding of the above questions, which then facilitate the design of optimal cancer treatment strategies.

## AUTHOR CONTRIBUTIONS

Work supervision and project design, YH and YW. Bioinformatics, YH and YW. Literature compiling and

summary, JL. Manuscript drafting, proof-reading, and revision: YH and YW. Discussion, MH, YL, and DC. All authors contributed to the article and approved the submitted version.

## FUNDING

YH is supported by the National Natural Science Foundation of China (82002787). YW is supported by the Startup Foundation of the Zhuhai People’s Hospital (YNXM20210305), the Natural Science Foundation of Guangdong Province (2020A1515010132), and partially by the Key Program of the National Natural Science Foundation of China (32030036).

## SUPPLEMENTARY MATERIAL

The Supplementary Material for this article can be found online at: <https://www.frontiersin.org/articles/10.3389/fimmu.2022.847345/full#supplementary-material>

## REFERENCES

- Kerr JF, Wyllie AH, Currie AR. Apoptosis: A Basic Biological Phenomenon With Wide-Ranging Implications in Tissue Kinetics. *Br J Cancer* (1972) 26 (4):239–57. doi: 10.1038/bjc.1972.33
- Orning P, Weng D, Starheim K, Ratner D, Best Z, Lee B, et al. Pathogen Blockade of TAK1 Triggers Caspase-8-Dependent Cleavage of Gasdermin D and Cell Death. *Science* (2018) 362(6418):1064–9. doi: 10.1126/science.aa2818
- Wang Y, Gao W, Shi X, Ding J, Liu W, He H, et al. Chemotherapy Drugs Induce Pyroptosis Through Caspase-3 Cleavage of a Gasdermin. *Nature* (2017) 547(7661):99–103. doi: 10.1038/nature22393
- Jorgensen I, Zhang Y, Krantz BA, Miao EA. Pyroptosis Triggers Pore-Induced Intracellular Traps (PITs) That Capture Bacteria and Lead to Their Clearance by Efferocytosis. *J Exp Med* (2016) 213(10):2113–28. doi: 10.1084/jem.20151613
- Riegman M, Sagie L, Galed C, Levin T, Steinberg N, Dixon SJ, et al. Ferroptosis Occurs Through an Osmotic Mechanism and Propagates Independently of Cell Rupture. *Nat Cell Biol* (2020) 22(9):1042–8. doi: 10.1038/s41556-020-0565-1
- Magtanong L, Ko PJ, Dixon SJ. Emerging Roles for Lipids in non-Apoptotic Cell Death. *Cell Death Differ* (2016) 23(7):1099–109. doi: 10.1038/cdd.2016.25
- Malireddi RKS, Kesavardhana S, Kanneganti TD. ZBP1 and TAK1: Master Regulators of NLRP3 Inflammasome/Pyroptosis, Apoptosis, and Necroptosis (PAN-Optosis). *Front Cell Infect Microbiol* (2019) 9:406. doi: 10.3389/fcimb.2019.00406
- Mizushima N, Komatsu M. Autophagy: Renovation of Cells and Tissues. *Cell* (2011) 147(4):728–41. doi: 10.1016/j.cell.2011.10.026
- Xia H, Green DR, Zou W. Autophagy in Tumour Immunity and Therapy. *Nat Rev Cancer* (2021) 21(5):281–97. doi: 10.1038/s41568-021-00344-2
- Zhang Y, Chen X, Gueydan C, Han J. Plasma Membrane Changes During Programmed Cell Deaths. *Cell Res* (2018) 28(1):9–21. doi: 10.1038/cr.2017.133
- Chen X, He WT, Hu L, Li J, Fang Y, Wang X, et al. Pyroptosis is Driven by non-Selective Gasdermin-D Pore and its Morphology is Different From MLKL Channel-Mediated Necroptosis. *Cell Res* (2016) 26(9):1007–20. doi: 10.1038/cr.2016.100
- Xie Y, Hou W, Song X, Yu Y, Huang J, Sun X, et al. Ferroptosis: Process and Function. *Cell Death Differ* (2016) 23(3):369–79. doi: 10.1038/cdd.2015.158
- Latunde-Dada GO. Ferroptosis: Role of Lipid Peroxidation, Iron and Ferritinophagy. *Biochim Biophys Acta Gen Subj* (2017) 1861(8):1893–900. doi: 10.1016/j.bbagen.2017.05.019
- Debnath J, Baehrecke EH, Kroemer G. Does Autophagy Contribute to Cell Death? *Autophagy* (2005) 1(2):66–74. doi: 10.4161/auto.1.2.1738
- Wang C, Youle RJ. The Role of Mitochondria in Apoptosis\*. *Annu Rev Genet* (2009) 43:95–118. doi: 10.1146/annurev-genet-102108-134850
- Li Q, Shi N, Cai C, Zhang M, He J, Tan Y, et al. The Role of Mitochondria in Pyroptosis. *Front Cell Dev Biol* (2020) 8:630771. doi: 10.3389/fcell.2020.630771
- Zhang YF, Zhou L, Mao HQ, Yang FH, Chen Z, Zhang L. Mitochondrial DNA Leakage Exacerbates Odontoblast Inflammation Through Gasdermin D-Mediated Pyroptosis. *Cell Death Discovery* (2021) 7(1):381. doi: 10.1038/s41420-021-00770-z
- Wang H, Liu C, Zhao Y, Gao G. Mitochondria Regulation in Ferroptosis. *Eur J Cell Biol* (2020) 99(1):151058. doi: 10.1016/j.ejcb.2019.151058
- Gao M, Yi J, Zhu J, Minikes AM, Monian P, Thompson CB, et al. Role of Mitochondria in Ferroptosis. *Mol Cell* (2019) 73(2):354–63.e3. doi: 10.1016/j.molcel.2018.10.042
- Gan B. Mitochondrial Regulation of Ferroptosis. *J Cell Biol* (2021) 220(9): e202105043. doi: 10.1083/jcb.202105043
- Wu C, Zhao W, Yu J, Li S, Lin L, Chen X. Induction of Ferroptosis and Mitochondrial Dysfunction by Oxidative Stress in PC12 Cells. *Sci Rep* (2018) 8(1):574. doi: 10.1038/s41598-017-18935-1
- Battaglia AM, Chirillo R, Aversa I, Sacco A, Costanzo F, Biamonte F. Ferroptosis and Cancer: Mitochondria Meet the “Iron Maiden” Cell Death. *Cells* (2020) 9(6):1505. doi: 10.3390/cells9061505
- Karch J, Kanisicak O, Brody MJ, Sargent MA, Michael DM, Molkentin JD. Necroptosis Interfaces With MOMP and the MPTP in Mediating Cell Death. *PloS One* (2015) 10(6):e0130520. doi: 10.1371/journal.pone.0130520
- Rambold AS, Lippincott-Schwartz J. Mechanisms of Mitochondria and Autophagy Crosstalk. *Cell Cycle* (2011) 10(23):4032–8. doi: 10.4161/cc.10.23.18384
- Lee J, Giordano S, Zhang J. Autophagy, Mitochondria and Oxidative Stress: Cross-Talk and Redox Signalling. *Biochem J* (2012) 441(2):523–40. doi: 10.1042/BJ20111451
- Matassov D, Kagan T, Leblanc J, Sikorska M, Zakeri Z. Measurement of Apoptosis by DNA Fragmentation. *Methods Mol Biol* (2004) 282:1–17. doi: 10.1385/1-59259-812-9:9001

27. Yu P, Zhang X, Liu N, Tang L, Peng C, Chen X. Pyroptosis: Mechanisms and Diseases. *Signal Transduct Target Ther* (2021) 6(1):128. doi: 10.1038/s41392-021-00507-5

28. Vande Walle L, Lamkanfi M. Pyroptosis. *Curr Biol* (2016) 26(13):R568–72. doi: 10.1016/j.cub.2016.02.019

29. Tang D, Chen X, Kang R, Kroemer G. Ferroptosis: Molecular Mechanisms and Health Implications. *Cell Res* (2021) 31(2):107–25. doi: 10.1038/s41422-020-00441-1

30. Shostak K, Jiang Z, Charlotteaux B, Mayer A, Habraken Y, Tharun L, et al. The X-Linked Trichothiodystrophy-Causing Gene RNF113A Links the Spliceosome to Cell Survival Upon DNA Damage. *Nat Commun* (2020) 11(1):1270. doi: 10.1038/s41467-020-15003-7

31. Challa S, Chan FK. Going Up in Flames: Necrotic Cell Injury and Inflammatory Diseases. *Cell Mol Life Sci* (2010) 67(19):3241–53. doi: 10.1007/s00018-010-0413-8

32. Hewitt G, Korolchuk VI. Repair, Reuse, Recycle: The Expanding Role of Autophagy in Genome Maintenance. *Trends Cell Biol* (2017) 27(5):340–51. doi: 10.1016/j.tcb.2016.11.011

33. Fink SL, Cookson BT. Apoptosis, Pyroptosis, and Necrosis: Mechanistic Description of Dead and Dying Eukaryotic Cells. *Infect Immun* (2005) 73(4):1907–16. doi: 10.1128/IAI.73.4.1907-1916.2005

34. Dhuriya YK, Sharma D. Necroptosis: A Regulated Inflammatory Mode of Cell Death. *J Neuroinflamm* (2018) 15(1):199. doi: 10.1186/s12974-018-1235-0

35. Jung S, Jeong H, Yu SW. Autophagy as a Decisive Process for Cell Death. *Exp Mol Med* (2020) 52(6):921–30. doi: 10.1038/s12276-020-0455-4

36. Bertheloot D, Latz E, Franklin BS. Necroptosis, Pyroptosis and Apoptosis: An Intricate Game of Cell Death. *Cell Mol Immunol* (2021) 18(5):1106–21. doi: 10.1038/s41423-020-00630-3

37. Legrand AJ, Konstantinou M, Goode EF, Meier P. The Diversification of Cell Death and Immunity: Memento Mori. *Mol Cell* (2019) 76(2):232–42. doi: 10.1016/j.molcel.2019.09.006

38. Wang Y, Kanneganti TD. From Pyroptosis, Apoptosis and Necroptosis to PANoptosis: A Mechanistic Compendium of Programmed Cell Death Pathways. *Comput Struct Biotechnol J* (2021) 19:4641–57. doi: 10.1016/j.csbj.2021.07.038

39. Shi J, Zhao Y, Wang K, Shi X, Wang Y, Huang H, et al. Cleavage of GSDMD by Inflammatory Caspases Determines Pyroptotic Cell Death. *Nature* (2015) 526(7575):660–5. doi: 10.1038/nature15514

40. Zhou Z, He H, Wang K, Shi X, Wang Y, Su Y, et al. Granzyme A From Cytotoxic Lymphocytes Cleaves GSDMB to Trigger Pyroptosis in Target Cells. *Science* (2020) 368(6494):eaaz7548. doi: 10.1126/science.aaz7548

41. Feoktistova M, Leverkus M. Programmed Necrosis and Necroptosis Signalling. *FEBS J* (2015) 282(1):19–31. doi: 10.1111/febs.13120

42. Giampietri C, Starace D, Petrungaro S, Filippini A, Ziparo E. Necroptosis: Molecular Signalling and Translational Implications. *Int J Cell Biol* (2014) 2014: p490275. doi: 10.1155/2014/490275

43. Zhou J, Tan SH, Nicolas V, Baudy C, Yang ND, Zhang J, et al. Activation of Lysosomal Function in the Course of Autophagy via Mtorc1 Suppression and Autophagosome-Lysosome Fusion. *Cell Res* (2013) 23(4):508–23. doi: 10.1038/cr.2013.11

44. Green DR, Ferguson T, Zitvogel L, Kroemer G. Immunogenic and Tolerogenic Cell Death. *Nat Rev Immunol* (2009) 9(5):535–63. doi: 10.1038/nri2545

45. Galluzzi L, Vitale I, Aaronson SA, Abrams JM, Adam D, Agostinis P, et al. Molecular Mechanisms of Cell Death: Recommendations of the Nomenclature Committee on Cell Death 2018. *Cell Death Differ* (2018) 25(3):486–541. doi: 10.1038/s41418-018-0102-y

46. Tang D, Kang R, Berghe TV, Vandebaelee P, Kroemer G. The Molecular Machinery of Regulated Cell Death. *Cell Res* (2019) 29(5):347–64. doi: 10.1038/s41422-019-0164-5

47. Lee S, Karki R, Wang Y, Nguyen LN, Kalathur RC, Kanneganti TD. AIM2 Forms a Complex With Pyrin and ZBP1 to Drive PANoptosis and Host Defence. *Nature* (2021) 597(7876):415–9. doi: 10.1038/s41586-021-03875-8

48. Reed JC. Drug Insight: Cancer Therapy Strategies Based on Restoration of Endogenous Cell Death Mechanisms. *Nat Clin Pract Oncol* (2006) 3(7):388–98. doi: 10.1038/ncponc0538

49. Taylor RC, Cullen SP, Martin SJ. Apoptosis: Controlled Demolition at the Cellular Level. *Nat Rev Mol Cell Biol* (2008) 9(3):231–41. doi: 10.1038/nrm2312

50. Galluzzi L, Kepp O, Chan FK, Kroemer G. Necroptosis: Mechanisms and Relevance to Disease. *Annu Rev Pathol* (2017) 12:103–30. doi: 10.1146/annurev-pathol-052016-100247

51. Pasparakis M, Vandebaelee P. Necroptosis and its Role in Inflammation. *Nature* (2015) 517(7534):311–20. doi: 10.1038/nature14191

52. Bergsbaken T, Fink SL, Cookson BT. Pyroptosis: Host Cell Death and Inflammation. *Nat Rev Microbiol* (2009) 7(2):99–109. doi: 10.1038/nrmicro2070

53. Zheng J, Conrad M. The Metabolic Underpinnings of Ferroptosis. *Cell Metab* (2020) 32(6):920–37. doi: 10.1016/j.cmet.2020.10.011

54. Stockwell BR, Friedmann Angel JP, Bayir H, Bush AI, Conrad M, Dixon SJ, et al. Ferroptosis: A Regulated Cell Death Nexus Linking Metabolism, Redox Biology, and Disease. *Cell* (2017) 171(2):273–85. doi: 10.1016/j.cell.2017.09.021

55. Chen X, Li J, Kang R, Klionsky DJ, Tang D. Ferroptosis: Machinery and Regulation. *Autophagy* (2021) 17(9):2054–81. doi: 10.1080/15548627.2020.1810918

56. Xu S, Min J, Wang F. Ferroptosis: An Emerging Player in Immune Cells. *Sci Bull* (2021) 66:2257–60. doi: 10.1016/j.scib.2021.02.026

57. Klionsky DJ, Abdelmohsen K, Abe A, Abedin MJ, Abeliovich H, Acevedo Arozena A, et al. Guidelines for the Use and Interpretation of Assays for Monitoring Autophagy (3rd Edition). *Autophagy* (2016) 12(1):1–222. doi: 10.1080/15548627.2015.1100356

58. Galluzzi L, Baehrecke EH, Ballabio A, Boya P, Bravo-San Pedro JM, Cecconi F, et al. Molecular Definitions of Autophagy and Related Processes. *EMBO J* (2017) 36(13):1811–36. doi: 10.1525/embj.201796697

59. Ellis HM, Horvitz HR. Genetic Control of Programmed Cell Death in the Nematode *C. elegans*. *Cell* (1986) 44(6):817–29. doi: 10.1016/0092-8674(86)90004-8

60. Boldin MP, Varfolomeev EE, Pancer Z, Mett IL, Camonis JH, Wallach D. A Novel Protein That Interacts With the Death Domain of Fas/APO1 Contains a Sequence Motif Related to the Death Domain. *J Biol Chem* (1995) 270(14):7795–8. doi: 10.1074/jbc.270.14.7795

61. Chinnaiyan AM, O'Rourke K, Tewari M, Dixit VM. FADD, a Novel Death Domain-Containing Protein, Interacts With the Death Domain of Fas and Initiates Apoptosis. *Cell* (1995) 81(4):505–12. doi: 10.1016/0092-8674(95)90071-3

62. Kischkel FC, Hellbardt S, Behrmann I, Germer M, Pawlita M, Krammer PH, et al. Cytotoxicity-Dependent APO-1 (Fas/CD95)-Associated Proteins Form a Death-Inducing Signaling Complex (DISC) With the Receptor. *EMBO J* (1995) 14(22):5579–88. doi: 10.1002/j.1460-2075.1995.tb00245.x

63. Boldin MP, Goncharov TM, Goltsev YV, Wallach D. Involvement of MACH, a Novel MORT1/FADD-Interacting Protease, in Fas/APO-1- and TNF Receptor-Induced Cell Death. *Cell* (1996) 85(6):803–15. doi: 10.1016/S0092-8674(00)81265-9

64. Muzio M, Chinnaiyan AM, Kischkel FC, O'Rourke K, Shevchenko A, Ni J, et al. FLICE, a Novel FADD-Homologous ICE/CED-3-Like Protease, is Recruited to the CD95 (Fas/APO-1) Death-Inducing Signaling Complex. *Cell* (1996) 85(6):817–27. doi: 10.1016/S0092-8674(00)81266-0

65. Zou H, Henzel WJ, Liu X, Lutschg A, Wang X. Apaf-1, a Human Protein Homologous to *C. elegans* CED-4, Participates in Cytochrome C-Dependent Activation of Caspase-3. *Cell* (1997) 90(3):405–13. doi: 10.1016/S0092-8674(00)80501-2

66. Giampazolias E, Zunino B, Dhayade S, Bock F, Cloix C, Cao K, et al. Mitochondrial Permeabilization Engages NF-κappaB-Dependent Anti-Tumour Activity Under Caspase Deficiency. *Nat Cell Biol* (2017) 19(9):1116–29. doi: 10.1038/ncb3596

67. Rongvaux A, Jackson R, Harman CC, Li T, West AP, de Zoete MR, et al. Apoptotic Caspases Prevent the Induction of Type I Interferons by Mitochondrial DNA. *Cell* (2014) 159(7):1563–77. doi: 10.1016/j.cell.2014.11.037

68. White MJ, McArthur K, Metcalf D, Lane RM, Cambier JC, Herold MJ, et al. Apoptotic Caspases Suppress mtDNA-Induced STING-Mediated Type I IFN Production. *Cell* (2014) 159(7):1549–62. doi: 10.1016/j.cell.2014.11.036

69. Yaacoub K, Pedeux R, Tarte K, Guillaudeux T. Role of the Tumor Microenvironment in Regulating Apoptosis and Cancer Progression. *Cancer Lett* (2016) 378(2):150–9. doi: 10.1016/j.canlet.2016.05.012

70. O'Donnell JS, Teng MWL, Smyth MJ. Cancer Immunoediting and Resistance to T Cell-Based Immunotherapy. *Nat Rev Clin Oncol* (2019) 16 (3):151–67. doi: 10.1038/s41571-018-0142-8

71. Leone RD, Powell JD. Metabolism of Immune Cells in Cancer. *Nat Rev Cancer* (2020) 20(9):516–31. doi: 10.1038/s41568-020-0273-y

72. Bunse L, Pusch S, Bunse T, Sahm F, Sanghvi K, Friedrich M, et al. Suppression of Antitumor T Cell Immunity by the Oncometabolite (R)-2-Hydroxyglutarate. *Nat Med* (2018) 24(8):1192–203. doi: 10.3410/f.733617626.793550723

73. Zhao E, Maj T, Kryczek I, Li W, Wu K, Zhao L, et al. Cancer Mediates Effector T Cell Dysfunction by Targeting microRNAs and EZH2 via Glycolysis Restriction. *Nat Immunol* (2016) 17(1):95–103. doi: 10.1038/ni.3313

74. Xiao Z, Dai Z, Locasale JW. Metabolic Landscape of the Tumor Microenvironment at Single Cell Resolution. *Nat Commun* (2019) 10 (1):3763. doi: 10.1038/s41467-019-11738-0

75. Li C, Jiang P, Wei S, Xu X, Wang J. Regulatory T Cells in Tumor Microenvironment: New Mechanisms, Potential Therapeutic Strategies and Future Prospects. *Mol Cancer* (2020) 19(1):116. doi: 10.1186/s12943-020-01234-1

76. Jiang Y, Li Y, Zhu B. T-Cell Exhaustion in the Tumor Microenvironment. *Cell Death Dis* (2015) 6:e1792. doi: 10.1038/cddis.2015.162

77. Hanahan D, Weinberg RA. Hallmarks of Cancer: The Next Generation. *Cell* (2011) 144(5):646–74. doi: 10.1016/j.cell.2011.02.013

78. Hanahan D. Hallmarks of Cancer: New Dimensions. *Cancer Discovery* (2022) 12(1):31–46. doi: 10.1158/2159-8290.CD-21-1059

79. Horton BL, Gajewski TF. Back From the Dead: TIL Apoptosis in Cancer Immune Evasion. *Br J Cancer* (2018) 118(3):309–11. doi: 10.1038/bjc.2017.483

80. Carneiro BA, El-Deiry WS. Targeting Apoptosis in Cancer Therapy. *Nat Rev Clin Oncol* (2020) 17(7):395–417. doi: 10.1038/s41571-020-0341-y

81. de Looff M, de Jong S, Kruyt FAE. Multiple Interactions Between Cancer Cells and the Tumor Microenvironment Modulate TRAIL Signaling: Implications for TRAIL Receptor Targeted Therapy. *Front Immunol* (2019) 10:1530. doi: 10.3389/fimmu.2019.01530

82. de Miguel D, Lemke J, Anel A, Walczak H, Martinez-Lostao L. Onto Better TRAILS for Cancer Treatment. *Cell Death Differ* (2016) 23(5):733–47. doi: 10.1038/cdd.2015.174

83. Legler K, Hauser C, Egberts JH, Willmms A, Heneweer C, Boretius S, et al. The Novel TRAIL-Receptor Agonist APG350 Exerts Superior Therapeutic Activity in Pancreatic Cancer Cells. *Cell Death Dis* (2018) 9(5):445. doi: 10.1038/s41419-018-0478-0

84. Fuchs CS, Fakih M, Schwartzberg L, Cohn AL, Yee L, Dreisbach L, et al. TRAIL Receptor Agonist Conatumumab With Modified FOLFOX6 Plus Bevacizumab for First-Line Treatment of Metastatic Colorectal Cancer: A Randomized Phase 1b/2 Trial. *Cancer* (2013) 119(24):4290–8. doi: 10.1002/cncr.28353

85. Paz-Ares L, Balint B, de Boer RH, van Meerbeeck JP, Wierzbicki R, De Souza P, et al. A Randomized Phase 2 Study of Paclitaxel and Carboplatin With or Without Conatumumab for First-Line Treatment of Advanced non-Small-Cell Lung Cancer. *J Thorac Oncol* (2013) 8(3):329–37. doi: 10.1097/JTO.0b013e31827ce54

86. Kindler HL, Richards DA, Garbo LE, Garon EB, Stephenson JJ Jr, Rocha-Lima CM, et al. A Randomized, Placebo-Controlled Phase 2 Study of Ganitumab (AMG 479) or Conatumumab (AMG 655) in Combination With Gemcitabine in Patients With Metastatic Pancreatic Cancer. *Ann Oncol* (2012) 23(11):2834–42. doi: 10.1093/annonc/mds142

87. Horton BL, Williams JB, Cabanov A, Spranger S, Gajewski TF. Intratumoral CD8(+) T-Cell Apoptosis Is a Major Component of T-Cell Dysfunction and Impedes Antitumor Immunity. *Cancer Immunol Res* (2018) 6(1):14–24. doi: 10.1158/2326-6066.CIR-17-0249

88. Jarosz-Biej M, Smolarczyk R, Cichon T, Kulach N. Tumor Microenvironment as A “Game Changer” in Cancer Radiotherapy. *Int J Mol Sci* (2019) 20 (13):3212. doi: 10.3390/ijms20133212

89. Degterev A, Huang Z, Boyce M, Li Y, Jagtap P, Mizushima N, et al. Chemical Inhibitor of Nonapoptotic Cell Death With Therapeutic Potential for Ischemic Brain Injury. *Nat Chem Biol* (2005) 1(2):112–9. doi: 10.1038/nchembio711

90. Degterev A, Hitomi J, Germscheid M, Ch'en IL, Korkina O, Teng X, et al. Identification of RIP1 Kinase as a Specific Cellular Target of Necrostatins. *Nat Chem Biol* (2008) 4(5):313–21. doi: 10.1038/nchembio.83

91. Galluzzi L, Kroemer G. Necroptosis: A Specialized Pathway of Programmed Necrosis. *Cell* (2008) 135(7):1161–3. doi: 10.1016/j.cell.2008.12.004

92. Moujalled D, Gangatirkar P, Kauppi M, Corbin J, Leboin M, Murphy JM, et al. The Necroptotic Cell Death Pathway Operates in Megakaryocytes, But Not in Platelet Synthesis. *Cell Death Dis* (2021) 12(1):133. doi: 10.1038/s41419-021-03418-z

93. Dannappel M, Vlantis K, Kumari S, Polykratis A, Kim C, Wachsmuth L, et al. RIPK1 Maintains Epithelial Homeostasis by Inhibiting Apoptosis and Necroptosis. *Nature* (2014) 513(7516):90–4. doi: 10.1038/nature13608

94. Qin X, Ma D, Tan YX, Wang HY, Cai Z. The Role of Necroptosis in Cancer: A Double-Edged Sword? *Biochim Biophys Acta Rev Cancer* (2019) 1871 (2):259–66. doi: 10.1016/j.bbcan.2019.01.006

95. Park JE, Lee JH, Lee SY, Hong MJ, Choi JE, Park S, et al. Expression of Key Regulatory Genes in Necroptosis and its Effect on the Prognosis in non-Small Cell Lung Cancer. *J Cancer* (2020) 11(18):5503–10. doi: 10.7150/jca.46172

96. Bozec D, Iuga AC, Roda G, Dahan S, Yeretssian G. Critical Function of the Necroptosis Adaptor RIPK3 in Protecting From Intestinal Tumorigenesis. *Oncotarget* (2016) 7(29):46384–400. doi: 10.1863/oncotarget.10135

97. He L, Peng K, Liu Y, Xiong J, Zhu FF. Low Expression of Mixed Lineage Kinase Domain-Like Protein is Associated With Poor Prognosis in Ovarian Cancer Patients. *Onco Targets Ther* (2013) 6:1539–43. doi: 10.2147/OTT.S52805

98. Schmidt SV, Seibert S, Walch-Ruckheim B, Vicinus B, Kamionka EM, Pahne-Zeppenfeld J, et al. RIPK3 Expression in Cervical Cancer Cells is Required for PolyIC-Induced Necroptosis, IL-1alpha Release, and Efficient Paracrine Dendritic Cell Activation. *Oncotarget* (2015) 6(11):8635–47. doi: 10.1863/oncotarget.3249

99. Yatim N, Jusforgues-Saklani H, Orozco S, Schulz O, Barreira da Silva R, Reis e Sousa C, et al. RIPK1 and NF-kappaB Signaling in Dying Cells Determines Cross-Priming of CD8(+) T Cells. *Science* (2015) 350(6258):328–34. doi: 10.1126/science.aad0395

100. Kang YJ, Bang BR, Han KH, Hong L, Shim EJ, Ma J, et al. Regulation of NKT Cell-Mediated Immune Responses to Tumours and Liver Inflammation by Mitochondrial PGAM5-Drp1 Signalling. *Nat Commun* (2015) 6:8371. doi: 10.1038/ncomms9371

101. Aaes TL, Kaczmarek A, Delvaeye T, De Craene B, De Koker S, Heyndrickx L, et al. Vaccination With Necroptotic Cancer Cells Induces Efficient Anti-Tumor Immunity. *Cell Rep* (2016) 15(2):274–87. doi: 10.1016/j.celrep.2016.03.037

102. Strilic B, Yang L, Albarran-Juarez J, Wachsmuth L, Han K, Muller UC, et al. Tumour-Cell-Induced Endothelial Cell Necroptosis via Death Receptor 6 Promotes Metastasis. *Nature* (2016) 536(7615):215–8. doi: 10.1038/nature19076

103. Seifert L, Werba G, Tiwari S, Giao Ly NN, Alothman S, Alqunaibit D, et al. The Necrosome Promotes Pancreatic Oncogenesis via CXCL1 and Mincle-Induced Immune Suppression. *Nature* (2016) 532(7598):245–9. doi: 10.1038/nature17403

104. Jiao D, Cai Z, Choksi S, Ma D, Choe M, Kwon HJ, et al. Necroptosis of Tumor Cells Leads to Tumor Necrosis and Promotes Tumor Metastasis. *Cell Res* (2018) 28(8):868–70. doi: 10.1038/s41422-018-0058-y

105. Cookson BT, Brennan MA. Pro-Inflammatory Programmed Cell Death. *Trends Microbiol* (2001) 9(3):113–4. doi: 10.1016/S0966-842X(00)01936-3

106. Zychlinsky A, Prevost MC, Sansonetti PJ. Shigella Flexneri Induces Apoptosis in Infected Macrophages. *Nature* (1992) 358(6382):167–9. doi: 10.1038/358167a0

107. Shi J, Gao W, Shao F. Pyroptosis: Gasdermin-Mediated Programmed Necrotic Cell Death. *Trends Biochem Sci* (2017) 42(4):245–54. doi: 10.1016/j.tibs.2016.10.004

108. Kayagaki N, Wong MT, Stowe IB, Ramani SR, Gonzalez LC, Akashi-Takamura S, et al. Noncanonical Inflammasome Activation by Intracellular LPS Independent of TLR4. *Science* (2013) 341(6151):1246–9. doi: 10.1126/science.1240248

109. Downs KP, Nguyen H, Dorfleutner A, Stehlik C. An Overview of the non-Canonical Inflammasome. *Mol Aspects Med* (2020) 76:100924. doi: 10.1016/j.mam.2020.100924

110. Kayagaki N, Stowe IB, Lee BL, O'Rourke K, Anderson K, Warming S, et al. Caspase-11 Cleaves Gasdermin D for non-Canonical Inflammasome Signalling. *Nature* (2015) 526(7575):666–71. doi: 10.1038/nature15541

111. Yu J, Li S, Qi J, Chen Z, Wu Y, Guo J, et al. Cleavage of GSDME by Caspase-3 Determines Lobaplatin-Induced Pyroptosis in Colon Cancer Cells. *Cell Death Dis* (2019) 10(3):193. doi: 10.1038/s41419-019-1441-4

112. Jiang M, Qi L, Li L, Li Y. The Caspase-3/GSDME Signal Pathway as a Switch Between Apoptosis and Pyroptosis in Cancer. *Cell Death Discovery* (2020) 6:112. doi: 10.1038/s41420-020-00349-0

113. Chu Q, Jiang Y, Zhang W, Xu C, Du W, Tuguzbaeva G, et al. Pyroptosis is Involved in the Pathogenesis of Human Hepatocellular Carcinoma. *Oncotarget* (2016) 7(51):84658–65. doi: 10.18632/oncotarget.12384

114. Tan Y, Chen Q, Li X, Zeng Z, Xiong W, Li G, et al. Pyroptosis: A New Paradigm of Cell Death for Fighting Against Cancer. *J Exp Clin Cancer Res* (2021) 40(1):153. doi: 10.1186/s13046-021-01959-x

115. Dupaul-Chicoine J, Yeretssian G, Doiron K, Bergstrom KS, McIntire CR, LeBlanc PM, et al. Control of Intestinal Homeostasis, Colitis, and Colitis-Associated Colorectal Cancer by the Inflammatory Caspases. *Immunity* (2010) 32(3):367–78. doi: 10.1016/j.jimmuni.2010.02.012

116. Hu B, Elinav E, Huber S, Booth CJ, Strowig T, Jin C, et al. Inflammation-Induced Tumorigenesis in the Colon Is Regulated by Caspase-1 and NLRCA4. *Proc Natl Acad Sci USA* (2010) 107(50):21635–40. doi: 10.1073/pnas.1016814108

117. Allen IC, TeKippe EM, Woodford RM, Uronis JM, Holl EK, Rogers AB, et al. The NLRP3 Inflammasome Functions as a Negative Regulator of Tumorigenesis During Colitis-Associated Cancer. *J Exp Med* (2010) 207(5):1045–56. doi: 10.1084/jem.20100050

118. Wang Q, Wang Y, Ding J, Wang C, Zhou X, Gao W, et al. A Bioorthogonal System Reveals Antitumour Immune Function of Pyroptosis. *Nature* (2020) 579(7799):421–6. doi: 10.1038/s41586-020-2079-1

119. Ding B, Sheng J, Zheng P, Li C, Li D, Cheng Z, et al. Biodegradable Upconversion Nanoparticles Induce Pyroptosis for Cancer Immunotherapy. *Nano Lett* (2021) 21(19):8281–9. doi: 10.1021/acs.nanolett.1c02790

120. Zhao P, Wang M, Chen M, Chen Z, Peng X, Zhou F, et al. Programming Cell Pyroptosis With Biomimetic Nanoparticles for Solid Tumor Immunotherapy. *Biomaterials* (2020) 254:120142. doi: 10.1016/j.biomaterials.2020.120142

121. Zhang Z, Zhang Y, Xia S, Kong Q, Li S, Liu X, et al. Gasdermin E Suppresses Tumour Growth by Activating Anti-Tumour Immunity. *Nature* (2020) 579(7799):415–20. doi: 10.1038/s41586-020-2071-9

122. Johnson DC, Taabazuing CY, Okondo MC, Chui AJ, Rao SD, Brown FC, et al. DPP8/DPP9 Inhibitor-Induced Pyroptosis for Treatment of Acute Myeloid Leukemia. *Nat Med* (2018) 24(8):1151–6. doi: 10.1038/s41591-018-0082-y

123. Coussens LM, Werb Z. Inflammation and Cancer. *Nature* (2002) 420(6917):860–7. doi: 10.1038/nature01322

124. Greten FR, Grivennikov SI. Inflammation and Cancer: Triggers, Mechanisms, and Consequences. *Immunity* (2019) 51(1):27–41. doi: 10.1016/j.jimmuni.2019.06.025

125. Zhai Z, Liu W, Kaur M, Luo Y, Domenico J, Samson JM, et al. NLRP1 Promotes Tumor Growth by Enhancing Inflammasome Activation and Suppressing Apoptosis in Metastatic Melanoma. *Oncogene* (2017) 36(27):3820–30. doi: 10.1038/onc.2017.26

126. Liu L, Sun B. Neutrophil Pyroptosis: New Perspectives on Sepsis. *Cell Mol Life Sci* (2019) 76(11):2031–42. doi: 10.1007/s00018-019-03060-1

127. Doitsh G, Galloway NL, Geng X, Yang Z, Monroe KM, Zepeda O, et al. Cell Death by Pyroptosis Drives CD4 T-Cell Depletion in HIV-1 Infection. *Nature* (2014) 505(7484):509–14. doi: 10.1038/nature12940

128. Zhang C, Song JW, Huang HH, Fan X, Huang L, Deng JN, et al. NLRP3 Inflammasome Induces CD4+ T Cell Loss in Chronically HIV-1-Infected Patients. *J Clin Invest* (2021) 131(6):e138861. doi: 10.1172/JCI138861

129. Linder A, Bauernfried S, Cheng Y, Albanese M, Jung C, Keppler OT, et al. CARD8 Inflammasome Activation Triggers Pyroptosis in Human T Cells. *EMBO J* (2020) 39(19):e105071. doi: 10.15252/embj.2020105071

130. Dixon SJ, Lemberg KM, Lamprecht MR, Skouta R, Zaitsev EM, Gleason CE, et al. Ferroptosis: An Iron-Dependent Form of Nonapoptotic Cell Death. *Cell* (2012) 149(5):1060–72. doi: 10.1016/j.cell.2012.03.042

131. Friedmann Angeli JP, Krysko DV, Conrad M. Ferroptosis at the Crossroads of Cancer-Acquired Drug Resistance and Immune Evasion. *Nat Rev Cancer* (2019) 19(7):405–14. doi: 10.1038/s41568-019-0149-1

132. Byström LM, Guzman ML, Rivella S. Iron and Reactive Oxygen Species: Friends or Foes of Cancer Cells? *Antioxid Redox Signal* (2014) 20(12):1917–24. doi: 10.1089/ars.2012.5014

133. Wu S, Li T, Liu W, Huang Y. Ferroptosis and Cancer: Complex Relationship and Potential Application of Exosomes. *Front Cell Dev Biol* (2021) 9:733751. doi: 10.3389/fcell.2021.733751

134. Recalcati S, Gammella E, Cairo G. Dysregulation of Iron Metabolism in Cancer Stem Cells. *Free Radic Biol Med* (2019) 133:216–20. doi: 10.1016/j.freeradbiomed.2018.07.015

135. Visweswaran M, Arfuso F, Warrier S, Dharmarajan A. Aberrant Lipid Metabolism as an Emerging Therapeutic Strategy to Target Cancer Stem Cells. *Stem Cells* (2020) 38(1):6–14. doi: 10.1002/stem.3101

136. Cosiáls E, El Hage R, Dos Santos L, Gong C, Mehrpour M, Hamai A. Ferroptosis: Cancer Stem Cells Rely on Iron Until “To Die for” it. *Cells* (2021) 10(11):2981. doi: 10.3390/cells10112981

137. Wang W, Green M, Choi JE, Gijon M, Kennedy PD, Johnson JK, et al. CD8(+) T Cells Regulate Tumour Ferroptosis During Cancer Immunotherapy. *Nature* (2019) 569(7755):270–4. doi: 10.1038/s41586-019-1170-y

138. Matsushita M, Freigang S, Schneider C, Conrad M, Bornkamm GW, Kopf M. T Cell Lipid Peroxidation Induces Ferroptosis and Prevents Immunity to Infection. *J Exp Med* (2015) 212(4):555–68. doi: 10.1084/jem.20140857

139. Yao Y, Chen Z, Zhang H, Chen C, Zeng M, Yunis J, et al. Selenium-GPx4 Axis Protects Follicular Helper T Cells From Ferroptosis. *Nat Immunol* (2021) 22(9):1127–39. doi: 10.1038/s41590-021-00996-0

140. Xu S, Chaudhary O, Rodriguez-Morales P, Sun X, Chen D, Zappasodi R, et al. Uptake of Oxidized Lipids by the Scavenger Receptor CD36 Promotes Lipid Peroxidation and Dysfunction in CD8(+) T Cells in Tumors. *Immunity* (2021) 54(7):1561–1577 e7. doi: 10.1016/j.jimmuni.2021.05.003

141. Xu C, Sun S, Johnson T, Qi R, Zhang S, Zhang J, et al. The Glutathione Peroxidase Gpx4 Prevents Lipid Peroxidation and Ferroptosis to Sustain Treg Cell Activation and Suppression of Antitumor Immunity. *Cell Rep* (2021) 35(11):109235. doi: 10.1016/j.celrep.2021.109235

142. Chen X, Kang R, Kroemer G, Tang D. Broadening Horizons: The Role of Ferroptosis in Cancer. *Nat Rev Clin Oncol* (2021) 18(5):280–96. doi: 10.1038/s41571-020-00462-0

143. Hou J, Zhao R, Xia W, Chang CW, You Y, Hsu JM, et al. PD-L1-Mediated Gasdermin C Expression Switches Apoptosis to Pyroptosis in Cancer Cells and Facilitates Tumour Necrosis. *Nat Cell Biol* (2020) 22(10):1264–75. doi: 10.1038/s41556-020-0575-z

144. Snyder AG, Oberst A. The Antisocial Network: Cross Talk Between Cell Death Programs in Host Defense. *Annu Rev Immunol* (2021) 39:77–101. doi: 10.1146/annurev-immunol-112019-072301

145. Doerflinger M, Deng Y, Whitney P, Salvamoser R, Engel S, Kueh AJ, et al. Flexible Usage and Interconnectivity of Diverse Cell Death Pathways Protect Against Intracellular Infection. *Immunity* (2020) 53(3):533–547 e7. doi: 10.1016/j.jimmuni.2020.07.004

146. Schwarzer R, Jiao H, Wachsmuth L, Tresch A, Pasparakis M. FADD and Caspase-8 Regulate Gut Homeostasis and Inflammation by Controlling MLKL- and GSDMD-Mediated Death of Intestinal Epithelial Cells. *Immunity* (2020) 52(6):978–993 e6. doi: 10.1016/j.jimmuni.2020.04.002

147. Taabazuing CY, Okondo MC, Bachovchin DA. Pyroptosis and Apoptosis Pathways Engage in Bidirectional Crosstalk in Monocytes and Macrophages. *Cell Chem Biol* (2017) 24(4):507–514 e4. doi: 10.1016/j.chembiol.2017.03.009

148. Karki R, Kanneganti TD. The ‘Cytokine Storm’: Molecular Mechanisms and Therapeutic Prospects. *Trends Immunol* (2021) 42(8):681–705. doi: 10.1016/j.it.2021.06.001

149. Karki R, Sharma BR, Tuladhar S, Williams EP, Zalduondo L, Samir P, et al. Synergism of TNF-Alpha and IFN-Gamma Triggers Inflammatory Cell Death, Tissue Damage, and Mortality in SARS-CoV-2 Infection and Cytokine Shock Syndromes. *Cell* (2021) 184(1):149–168 e17. doi: 10.1016/j.cell.2020.11.025

150. Malireddi RKS, Karki R, Sundaram B, Kancharana B, Lee S, Samir P, et al. Inflammatory Cell Death, PANoptosis, Mediated by Cytokines in Diverse Cancer Lineages Inhibits Tumor Growth. *Immunohorizons* (2021) 5(7):568–80. doi: 10.4049/immunohorizons.2100059

151. Karki R, Sundaram B, Sharma BR, Lee S, Malireddi RKS, Nguyen LN, et al. ADAR1 Restricts ZBP1-Mediated Immune Response and PANoptosis to

Promote Tumorigenesis. *Cell Rep* (2021) 37(3):109858. doi: 10.1016/j.celrep.2021.109858

152. Karki R, Sharma BR, Lee E, Banoth B, Malireddi RKS, Samir P, et al. Interferon Regulatory Factor 1 Regulates PANoptosis to Prevent Colorectal Cancer. *JCI Insight* (2020) 5(12):e136720. doi: 10.1172/jci.insight.136720

153. Noda T, Suzuki K, Ohsumi Y. Yeast Autophagosomes: De Novo Formation of a Membrane Structure. *Trends Cell Biol* (2002) 12(5):231–5. doi: 10.1016/S0962-8924(02)02278-X

154. Harnett MM, Pineda MA, Latre de Late P, Eason RJ, Besteiro S, Harnett W, et al. From Christian De Duve to Yoshinori Ohsumi: More to Autophagy Than Just Dining at Home. *BioMed J* (2017) 40(1):9–22. doi: 10.1016/j.bj.2016.12.004

155. Strasser A, Vaux DL. Cell Death in the Origin and Treatment of Cancer. *Mol Cell* (2020) 78(6):1045–54. doi: 10.1016/j.molcel.2020.05.014

156. Tsujimoto Y, Shimizu S. Another Way to Die: Autophagic Programmed Cell Death. *Cell Death Differ* (2005) 12 Suppl 2:1528–34. doi: 10.1038/sj.cdd.4401777

157. Denton D, Kumar S. Autophagy-Dependent Cell Death. *Cell Death Differ* (2019) 26(4):605–16. doi: 10.1038/s41418-018-0252-y

158. Nassour J, Radford R, Correia A, Fuste JM, Schoell B, Jauch A, et al. Autophagic Cell Death Restricts Chromosomal Instability During Replicative Crisis. *Nature* (2019) 565(7741):659–63. doi: 10.1038/s41586-019-0885-0

159. Amaravadi RK, Kimmelman AC, Debnath J. Targeting Autophagy in Cancer: Recent Advances and Future Directions. *Cancer Discovery* (2019) 9(9):1167–81. doi: 10.1158/2159-8290.CD-19-0292

160. Yang A, Kimmelman AC. Inhibition of Autophagy Attenuates Pancreatic Cancer Growth Independent of TP53/TRP53 Status. *Autophagy* (2014) 10(9):1683–4. doi: 10.4161/auto.29961

161. Yang S, Wang X, Contino G, Liesa M, Sahin E, Ying H, et al. Pancreatic Cancers Require Autophagy for Tumor Growth. *Genes Dev* (2011) 25(7):717–29. doi: 10.1101/gad.2016111

162. Su Z, Yang Z, Xu Y, Chen Y, Yu Q. Apoptosis, Autophagy, Necroptosis, and Cancer Metastasis. *Mol Cancer* (2015) 14:48. doi: 10.1186/s12943-015-0321-5

163. Maiuri MC, Zalckvar E, Kimchi A, Kroemer G. Self-Eating and Self-Killing: Crosstalk Between Autophagy and Apoptosis. *Nat Rev Mol Cell Biol* (2007) 8(9):741–52. doi: 10.1038/nrm2239

164. Mukhopadhyay S, Panda PK, Sinha N, Das DN, Bhutia SK. Autophagy and Apoptosis: Where do They Meet? *Apoptosis* (2014) 19(4):555–66. doi: 10.1007/s10495-014-0967-2

165. Dowling SD, Macian F. Autophagy and T Cell Metabolism. *Cancer Lett* (2018) 419:20–6. doi: 10.1016/j.canlet.2018.01.033

166. Puleston DJ, Zhang H, Powell TJ, Lipina E, Sims S, Panse I, et al. Autophagy is a Critical Regulator of Memory CD8(+) T Cell Formation. *Elife* (2014) 3:e03706. doi: 10.7554/elife.03706

167. Xu X, Araki K, Li S, Han JH, Ye L, Tan WG, et al. Autophagy is Essential for Effector CD8(+) T Cell Survival and Memory Formation. *Nat Immunol* (2014) 15(12):1152–61. doi: 10.1038/ni.3025

168. Young TM, Reyes C, Pasnikowski E, Castanaro C, Wong C, Decker CE, et al. Autophagy Protects Tumors From T Cell-Mediated Cytotoxicity via Inhibition of TNFalpha-Induced Apoptosis. *Sci Immunol* (2020) 5(54):eabb9561. doi: 10.1126/sciimmunol.abb9561

169. Pellegrini P, Strambi A, Zipoli C, Hagg-Olofsson M, Buoncervello M, Linder S, et al. Acidic Extracellular pH Neutralizes the Autophagy-Inhibiting Activity of Chloroquine: Implications for Cancer Therapies. *Autophagy* (2014) 10(4):562–71. doi: 10.4161/auto.27901

170. Xia H, Wang W, Crespo J, Kryczek I, Li W, Wei S, et al. Suppression of FIP200 and Autophagy by Tumor-Derived Lactate Promotes Naive T Cell Apoptosis and Affects Tumor Immunity. *Sci Immunol* (2017) 2(17):eaan4631. doi: 10.1126/sciimmunol.aan4631

171. Bryant KL, Stalnecker CA, Zeitouni D, Klomp JE, Peng S, Tikunov AP, et al. Combination of ERK and Autophagy Inhibition as a Treatment Approach for Pancreatic Cancer. *Nat Med* (2019) 25(4):628–40. doi: 10.1038/s41591-019-0368-8

172. Oresta B, Pozzi C, Braga D, Hurle R, Lazzeri M, Colombo P, et al. Mitochondrial Metabolic Reprogramming Controls the Induction of Immunogenic Cell Death and Efficacy of Chemotherapy in Bladder Cancer. *Sci Transl Med* (2021) 13(575):eaba6110. doi: 10.1126/scitranslmed.aba6110

173. He X, Qi Y, Zhang X, Liu X, Li X, Li S, et al. Current Landscape of Tumor-Derived Exosomal ncRNAs in Glioma Progression, Detection, and Drug Resistance. *Cell Death Dis* (2021) 12(12):1145. doi: 10.1038/s41419-021-04430-z

174. Villegas-Pineda JC, Lizarazo-Taborda MDR, Ramirez-de-Arellano A, Pereira-Suarez AL. Exosomal miRNAs and lncRNAs: The Modulator Keys of Cancer-Associated Fibroblasts in the Genesis and Progression of Malignant Neoplasms. *Front Cell Dev Biol* (2021) 9:717478. doi: 10.3389/fcell.2021.717478

175. Abu N, Rus Bakarurraini NAA. The Interweaving Relationship Between Extracellular Vesicles and T Cells in Cancer. *Cancer Lett* (2021) 12. doi: 10.3389/fimmu.2021.740548

176. Man SM, Karki R, Kanneganti TD. Molecular Mechanisms and Functions of Pyroptosis, Inflammatory Caspases and Inflammasomes in Infectious Diseases. *Immunol Rev* (2017) 277(1):61–75. doi: 10.1111/imr.12534

177. Ben-Sasson SZ, Hogg A, Hu-Li J, Wingfield P, Chen X, Crank M, et al. IL-1 Enhances Expansion, Effector Function, Tissue Localization, and Memory Response of Antigen-Specific CD8 T Cells. *J Exp Med* (2013) 210(3):491–502. doi: 10.1084/jem.20122006

178. Baker KJ, Houston A, Brint E. IL-1 Family Members in Cancer: Two Sides to Every Story. *Front Immunol* (2019) 10:1197. doi: 10.3389/fimmu.2019.01197

179. Haaberg OA, Lervik KB, Hammarstrom C, Donaldson IM, Haraldsen G, Bogen B, et al. Inflammation Driven by Tumour-Specific Th1 Cells Protects Against B-Cell Cancer. *Nat Commun* (2011) 2:240. doi: 10.1038/ncomms1239

180. Haaberg OA, Lervik KB, Yagita H, Bogen B, Corthay A. Interleukin-1 is Required for Cancer Eradication Mediated by Tumor-Specific Th1 Cells. *Oncogene* (2016) 35(1):e1039763. doi: 10.1080/2162402X.2015.1039763

181. Apte RN, Krelin Y, Song X, Dotan S, Recih E, Elkabets M, et al. Effects of Micro-Environment- and Malignant Cell-Derived Interleukin-1 in Carcinogenesis, Tumour Invasiveness and Tumour-Host Interactions. *Eur J Cancer* (2006) 42(6):751–9. doi: 10.1016/j.ejca.2006.01.010

182. Li R, Ong SL, Tran LM, Jing Z, Liu B, Park SJ, et al. Chronic IL-1beta-Induced Inflammation Regulates Epithelial-to-Mesenchymal Transition Memory Phenotypes via Epigenetic Modifications in non-Small Cell Lung Cancer. *Sci Rep* (2020) 10(1):377. doi: 10.1038/s41598-019-57285-y

183. Mantovani A, Dinarello CA, Molgora M, Garlanda C. Interleukin-1 and Related Cytokines in the Regulation of Inflammation and Immunity. *Immunity* (2019) 50(4):778–95. doi: 10.1016/j.jimmuni.2019.03.012

184. Goodwin GH, Sanders C, Johns EW. A New Group of Chromatin-Associated Proteins With a High Content of Acidic and Basic Amino Acids. *Eur J Biochem* (1973) 38(1):14–9. doi: 10.1111/j.1432-1033.1973.tb03026.x

185. Scaffidi P, Misteli T, Bianchi ME. Release of Chromatin Protein HMGB1 by Necrotic Cells Triggers Inflammation. *Nature* (2002) 418(6894):191–5. doi: 10.1038/nature00858

186. Kang R, Zhang Q, Zeh HJ, MT L, Tang D. HMGB1 in Cancer: Good, Bad, or Both? *Clin Cancer Res* (2013) 19(15):4046–57. doi: 10.1158/1078-0432.CCR-13-0495

187. Xu J, Jiang Y, Wang J, Shi X, Liu Q, Liu Z, et al. Macrophage Endocytosis of High-Mobility Group Box 1 Triggers Pyroptosis. *Cell Death Differ* (2014) 21(8):1229–39. doi: 10.1038/cdd.2014.40

188. Ma S, Ming Z, Gong AY, Wang Y, Chen X, Hu G, et al. A Long Noncoding RNA, lncRNA-Tnfaip3, Acts as a Coregulator of NF- $\kappa$ B to Modulate Inflammatory Gene Transcription in Mouse Macrophages. *FASEB J* (2017) 31(3):1215–25. doi: 10.1096/fj.201601056R

189. Gao Q, Li F, Wang S, Shen Z, Cheng S, Ping Y, et al. A Cycle Involving HMGB1, IFN-Gamma and Dendritic Cells Plays a Putative Role in Anti-Tumor Immunity. *Cell Immunol* (2019) 343:103850. doi: 10.1016/j.cellimm.2018.08.011

190. Wang Z, Yang C, Li L, Jin X, Zhang Z, Zheng H, et al. Tumor-Derived HMGB1 Induces CD62L(dim) Neutrophil Polarization and Promotes Lung Metastasis in Triple-Negative Breast Cancer. *Oncogenesis* (2020) 9(9):82. doi: 10.1038/s41389-020-00267-x

191. Zha C, Meng X, Li L, Mi S, Qian D, Li Z, et al. Neutrophil Extracellular Traps Mediate the Crosstalk Between Glioma Progression and the Tumor Microenvironment via the HMGB1/RAGE/IL-8 Axis. *Cancer Biol Med* (2020) 17(1):154–68. doi: 10.20892/j.issn.2095-3941.2019.0353

192. Suzuki Y, Mimura K, Yoshimoto Y, Watanabe M, Ohkubo Y, Izawa S, et al. Immunogenic Tumor Cell Death Induced by Chemoradiotherapy in Patients With Esophageal Squamous Cell Carcinoma. *Cancer Res* (2012) 72(16):3967–76. doi: 10.1158/0008-5472.CAN-12-0851

193. Huang CY, Chiang SF, Ke TW, Chen TW, Lan YC, You YS, et al. Cytosolic High-Mobility Group Box Protein 1 (HMGB1) and/or PD-1+ TILs in the Tumor Microenvironment may be Contributing Prognostic Biomarkers for Patients With Locally Advanced Rectal Cancer Who Have Undergone Neoadjuvant Chemoradiotherapy. *Cancer Immunol Immunother* (2018) 67(4):551–62. doi: 10.1007/s00262-017-2109-5

194. Sundberg E, Fasth AE, Palmblad K, Harris HE, Andersson U. High Mobility Group Box Chromosomal Protein 1 Acts as a Proliferation Signal for Activated T Lymphocytes. *Immunobiology* (2009) 214(4):303–9. doi: 10.1016/j.imbio.2008.09.006

195. Li G, Liang X, Lotze MT. HMGB1: The Central Cytokine for All Lymphoid Cells. *Front Immunol* (2013) 4:68. doi: 10.3389/fimmu.2013.00068

196. Avalos AM, Kiefer K, Tian J, Christensen S, Shlomchik M, Coyle AJ, et al. RAGE-Independent Autoreactive B Cell Activation in Response to Chromatin and HMGB1/DNA Immune Complexes. *Autoimmunity* (2010) 43(1):103–10. doi: 10.3109/08916930903384591

197. Parker KH, Sinha P, Horn LA, Clements VK, Yang H, Li J, et al. HMGB1 Enhances Immune Suppression by Facilitating the Differentiation and Suppressive Activity of Myeloid-Derived Suppressor Cells. *Cancer Res* (2014) 74(20):5723–33. doi: 10.1158/0008-5472.CAN-13-2347

198. Parker KH, Horn LA, Ostrand-Rosenberg S. High-Mobility Group Box Protein 1 Promotes the Survival of Myeloid-Derived Suppressor Cells by Inducing Autophagy. *J Leukoc Biol* (2016) 100(3):463–70. doi: 10.1189/jlb.3HI0715-305R

199. Son M, Porat A, He M, Suurmond J, Santiago-Schwarz F, Andersson U, et al. C1q and HMGB1 Reciprocally Regulate Human Macrophage Polarization. *Blood* (2016) 128(18):2218–28. doi: 10.1182/blood-2016-05-719757

200. Khambu B, Hong H, Liu S, Liu G, Chen X, Dong Z, et al. The HMGB1-RAGE Axis Modulates the Growth of Autophagy-Deficient Hepatic Tumors. *Cell Death Dis* (2020) 11(5):333. doi: 10.1038/s41419-020-2536-7

201. Hubert P, Roncarati P, Demoulin S, Pilard C, Ancion M, Reynders C, et al. Extracellular HMGB1 Blockade Inhibits Tumor Growth Through Profoundly Remodeling Immune Microenvironment and Enhances Checkpoint Inhibitor-Based Immunotherapy. *J Immunother Cancer* (2021) 9(3):e001966. doi: 10.1136/jitc-2020-001966

202. Huang H, Zhang X, Li S, Liu N, Lian W, McDowell E, et al. Physiological Levels of ATP Negatively Regulate Proteasome Function. *Cell Res* (2010) 20(12):1372–85. doi: 10.1038/cr.2010.123

203. Trabanielli S, Ocadilikova D, Gulinelli S, Curti A, Salvestrini V, Vieira RP, et al. Extracellular ATP Exerts Opposite Effects on Activated and Regulatory CD4+ T Cells via Purinergic P2 Receptor Activation. *J Immunol* (2012) 189(3):1303–10. doi: 10.4049/jimmunol.1103800

204. Cauwels A, Rogge E, Vandendriessche B, Shiva S, Brouckaert P. Extracellular ATP Drives Systemic Inflammation, Tissue Damage and Mortality. *Cell Death Dis* (2014) 5:e1102. doi: 10.1038/cddis.2014.70

205. Wang J, Wang Y, Chu Y, Li Z, Yu X, Huang Z, et al. Tumor-Derived Adenosine Promotes Macrophage Proliferation in Human Hepatocellular Carcinoma. *J Hepatol* (2021) 74(3):627–37. doi: 10.1016/j.jhep.2020.10.021

206. Ni C, Fang QQ, Chen WZ, Jiang JX, Jiang Z, Ye J, et al. Breast Cancer-Derived Exosomes Transmit lncRNA SNHG16 to Induce CD73 +gammadelta1 Treg Cells. *Signal Transduct Target Ther* (2020) 5(1):41. doi: 10.1038/s41392-020-0129-7

207. Ernst PB, Garrison JC, Thompson LF. Much Ado About Adenosine: Adenosine Synthesis and Function in Regulatory T Cell Biology. *J Immunol* (2010) 185(4):1993–8. doi: 10.4049/jimmunol.1000108

208. Neo SY, Yang Y, Record J, Ma R, Chen X, Chen Z, et al. CD73 Immune Checkpoint Defines Regulatory NK Cells Within the Tumor Microenvironment. *J Clin Invest* (2020) 130(3):1185–98. doi: 10.1172/JCI128895

209. Groth C, Hu X, Weber R, Fleming V, Altevogt P, Utikal J, et al. Immunosuppression Mediated by Myeloid-Derived Suppressor Cells (MDSCs) During Tumour Progression. *Br J Cancer* (2019) 120(1):16–25. doi: 10.1038/s41416-018-0333-1

210. Cekic C, Linden J. Adenosine A2A Receptors Intrinsically Regulate CD8+ T Cells in the Tumor Microenvironment. *Cancer Res* (2014) 74(24):7239–49. doi: 10.1158/0008-5472.CAN-13-3581

211. Young A, Ngiow SF, Barkauskas DS, Sult E, Hay C, Blake SJ, et al. Co-Inhibition of CD73 and A2AR Adenosine Signaling Improves Anti-Tumor Immune Responses. *Cancer Cell* (2016) 30(3):391–403. doi: 10.1016/j.ccr.2016.06.025

212. Obeid M, Tesniere A, Ghiringhelli F, Fimia GM, Apetoh L, Perfettini JL, et al. Calreticulin Exposure Dictates the Immunogenicity of Cancer Cell Death. *Nat Med* (2007) 13(1):54–61. doi: 10.1038/nm1523

213. Fucikova J, Kralikova P, Fialova A, Brtnicky T, Rob L, Bartunkova J, et al. Human Tumor Cells Killed by Anthracyclines Induce a Tumor-Specific Immune Response. *Cancer Res* (2011) 71(14):4821–33. doi: 10.1158/0008-5472.CAN-11-0950

214. Wang YS, Liu SJ, Huang SC, Chang CC, Huang YC, Fong WL, et al. Recombinant Heat Shock Protein 70 in Combination With Radiotherapy as a Source of Tumor Antigens to Improve Dendritic Cell Immunotherapy. *Front Oncol* (2012) 2:149. doi: 10.3389/fonc.2012.00149

215. Shimizu Y, Yoshikawa T, Kojima T, Shoda K, Nosaka K, Mizuno S, et al. Heat Shock Protein 105 Peptide Vaccine Could Induce Antitumor Immune Reactions in a Phase I Clinical Trial. *Cancer Sci* (2019) 110(10):3049–60. doi: 10.1111/cas.14165

216. Kelly M, McNeel D, Fisch P, Malkovsky M. Immunological Considerations Underlying Heat Shock Protein-Mediated Cancer Vaccine Strategies. *Immunol Lett* (2018) 193:1–10. doi: 10.1016/j.imlet.2017.11.001

217. Bugaut H, Bruchard M, Berger H, Derangere V, Odoul L, Euvrard R, et al. Bleomycin Exerts Ambivalent Antitumor Immune Effect by Triggering Both Immunogenic Cell Death and Proliferation of Regulatory T Cells. *PLoS One* (2013) 8(6):e65181. doi: 10.1371/journal.pone.0065181

218. Schiavoni G, Sistigu A, Valentini M, Mattei F, Sestili P, Spadaro F, et al. Cyclophosphamide Synergizes With Type I Interferons Through Systemic Dendritic Cell Reactivation and Induction of Immunogenic Tumor Apoptosis. *Cancer Res* (2011) 71(3):768–78. doi: 10.1158/0008-5472.CAN-10-2788

219. Chen HM, Wang PH, Chen SS, Wen CC, Chen YH, Yang WC, et al. Shikonin Induces Immunogenic Cell Death in Tumor Cells and Enhances Dendritic Cell-Based Cancer Vaccine. *Cancer Immunol Immunother* (2012) 61(11):1989–2002. doi: 10.1007/s00262-012-1258-9

220. Tesniere A, Schlemmer F, Boige V, Kepp O, Martins I, Ghiringhelli F, et al. Immunogenic Death of Colon Cancer Cells Treated With Oxaliplatin. *Oncogene* (2010) 29(4):482–91. doi: 10.1038/onc.2009.356

221. Hwang WL, Pike LRG, Royce TJ, Mahal BA, Loeffler JS. Safety of Combining Radiotherapy With Immune-Checkpoint Inhibition. *Nat Rev Clin Oncol* (2018) 15(8):477–94. doi: 10.1038/s41571-018-0046-7

222. Garg AD, Krysko DV, Verfaillie T, Kaczmarek A, Ferreira GB, Marysael T, et al. A Novel Pathway Combining Calreticulin Exposure and ATP Secretion in Immunogenic Cancer Cell Death. *EMBO J* (2012) 31(5):1062–79. doi: 10.1038/embj.2011.497

223. Galluzzi L, Kepp O, Kroemer G. Enlightening the Impact of Immunogenic Cell Death in Photodynamic Cancer Therapy. *EMBO J* (2012) 31(5):1055–7. doi: 10.1038/embj.2012.2

224. Huang J, Xiao Z, An Y, Han S, Wu W, Wang Y, et al. Nanodrug With Dual-Sensitivity to Tumor Microenvironment for Immuno-Sonodynamic Anti-Cancer Therapy. *Biomaterials* (2021) 269:120636. doi: 10.1016/j.biomaterials.2020.120636

225. Ding D, Zhong H, Liang R, Lan T, Zhu X, Huang S, et al. Multifunctional Nanodrug Mediates Synergistic Photodynamic Therapy and MDSCs-Targeting Immunotherapy of Colon Cancer. *Adv Sci (Weinh)* (2021) 8(14):e2100712. doi: 10.1002/advs.202100712

226. Srivastava S, Furlan SN, Jaeger-Ruckstuhl CA, Sarvothama M, Berger C, Smythe KS, et al. Immunogenic Chemotherapy Enhances Recruitment of CAR-T Cells to Lung Tumors and Improves Antitumor Efficacy When Combined With Checkpoint Blockade. *Cancer Cell* (2021) 39(2):193–208.e10. doi: 10.1016/j.ccr.2020.11.005

227. Liu Y, Fang Y, Chen X, Wang Z, Liang X, Zhang T, et al. Gasdermin E-Mediated Target Cell Pyroptosis by CAR T Cells Triggers Cytokine Release Syndrome. *Sci Immunol* (2020) 5(43):eaax7969. doi: 10.1126/sciimmunol.aax7969

228. Alnaggar M, Xu Y, Li J, He J, Chen J, Li M, et al. Allogeneic Vgamma9Vdelta2 T Cell as New Potential Immunotherapy Drug for Solid Tumor: A Case Study for Cholangiocarcinoma. *J Immunother Cancer* (2019) 7(1):36. doi: 10.1186/s40425-019-0501-8

229. Xu Y, Xiang Z, Alnaggar M, Kouakanou L, Li J, He J, et al. Allogeneic Vgamma9Vdelta2 T-Cell Immunotherapy Exhibits Promising Clinical Safety and Prolongs the Survival of Patients With Late-Stage Lung or Liver Cancer. *Cell Mol Immunol* (2021) 18(2):427–39. doi: 10.1038/s41423-020-0515-7

230. Maj T, Wang W, Crespo J, Zhang H, Wang W, Wei S, et al. Oxidative Stress Controls Regulatory T Cell Apoptosis and Suppressor Activity and PD-L1-Blockade Resistance in Tumor. *Nat Immunol* (2017) 18(12):1332–41. doi: 10.1038/ni.3868

231. Ma X, Xiao L, Liu L, Ye L, Su P, Bi E, et al. CD36-Mediated Ferroptosis Dampens Intratumoral CD8(+) T Cell Effector Function and Impairs Their Antitumor Ability. *Cell Metab* (2021) 33(5):1001–1012 e5. doi: 10.1016/j.cmet.2021.02.015

**Conflict of Interest:** The authors declare that the research was conducted in the absence of any commercial or financial relationships that could be construed as a potential conflict of interest.

**Publisher's Note:** All claims expressed in this article are solely those of the authors and do not necessarily represent those of their affiliated organizations, or those of the publisher, the editors and the reviewers. Any product that may be evaluated in this article, or claim that may be made by its manufacturer, is not guaranteed or endorsed by the publisher.

Copyright © 2022 Liu, Hong, Li, Chen, Wu and Hu. This is an open-access article distributed under the terms of the Creative Commons Attribution License (CC BY). The use, distribution or reproduction in other forums is permitted, provided the original author(s) and the copyright owner(s) are credited and that the original publication in this journal is cited, in accordance with accepted academic practice. No use, distribution or reproduction is permitted which does not comply with these terms.



# Tumor-Resident T Cells, Associated With Tertiary Lymphoid Structure Maturity, Improve Survival in Patients With Stage III Lung Adenocarcinoma

Hua Zhao<sup>1,2,3,4,5†</sup>, Hao Wang<sup>1,2,3,4,5†</sup>, Yu Zhao<sup>1,2,3,4,5</sup>, Qian Sun<sup>1,2,3,4,5\*</sup> and Xiubao Ren<sup>1,2,3,4,5,6\*</sup>

## OPEN ACCESS

### Edited by:

Mercedes Beatriz,  
CONICET Instituto de Biología y  
Medicina Experimental (IBYME),  
Argentina

### Reviewed by:

Shahram Salek-Ardakani,  
Pfizer, United States  
Arantzazu Alfranca,  
Hospital de la Princesa, Spain

### \*Correspondence:

Xiubao Ren  
renxiubao@tjmu.edu.cn  
Qian Sun  
sunqian923@126.com

<sup>†</sup>These authors have contributed  
equally to this work

### Specialty section:

This article was submitted to  
Cancer Immunity and Immunotherapy,  
a section of the journal  
Frontiers in Immunology

Received: 17 February 2022

Accepted: 21 April 2022

Published: 19 May 2022

### Citation:

Zhao H, Wang H, Zhao Y, Sun Q and Ren X (2022) Tumor-Resident T Cells, Associated With Tertiary Lymphoid Structure Maturity, Improve Survival in Patients With Stage III Lung Adenocarcinoma. *Front. Immunol.* 13:877689.  
doi: 10.3389/fimmu.2022.877689

<sup>1</sup> Department of Immunology, Tianjin Medical University Cancer Institute and Hospital, Tianjin, China, <sup>2</sup> National Clinical Research Center for Cancer, Tianjin, China, <sup>3</sup> Key Laboratory of Cancer Prevention and Therapy, Tianjin, China, <sup>4</sup> Tianjin's Clinical Research Center for Cancer, Tianjin, China, <sup>5</sup> Key Laboratory of Cancer Immunology and Biotherapy, Tianjin, China, <sup>6</sup> Department of Biotherapy, Tianjin Medical University Cancer Institute and Hospital, Tianjin, China

Tertiary lymphoid structure (TLS) and tumor-resident memory T cells ( $T_{RM}$ ) play crucial roles in the anti-tumor immune response, facilitating a good prognosis in patients with cancer. However, there have been no reports on the relationship between  $T_{RM}$  and TLS maturity. In this study, we detected  $T_{RM}$  and the maturity of TLS by immunofluorescence staining and analyzed the relationship between their distribution and proportion in patients with lung adenocarcinoma (LUAD). The proportion of  $T_{RM}$  within TLSs was significantly higher than that outside and was positively correlated with the survival of patients. In addition, the proportions of  $CD4^+CD103^+$   $T_{RM}$  and  $CD8^+CD103^+$   $T_{RM}$  were significantly increased with the gradually maturation of TLSs. We divided the patients into three levels (grade 1, grade 2, and grade 3) according to the presence of increasing maturation of TLSs. The proportion of  $CD103^+$   $T_{RM}$  in grade 3 patients was significantly higher than that in grade 1 and grade 2 patients, suggesting a close relationship between  $CD103^+$   $T_{RM}$  and TLS maturity. Furthermore, positive prognosis was associated with grade 3 patients that exhibited  $CD103^+$   $T_{RM}^{High}$  phenotype.

**Keywords:**  $T_{RM}$ , TLS, B cell, TIL, lung adenocarcinoma

## INTRODUCTION

Immunotherapy, e.g., treatment by immune checkpoint inhibitors (ICIs), has revolutionized therapeutic strategies for treating cancer, including non-small cell lung cancer (NSCLC) (1, 2). Previous studies on the mechanisms of ICIs have largely focused on tumor-infiltrating T cells (3). However, recently the findings of three independent studies have indicated that tertiary lymphoid structures (TLSs) and B cell signatures in the tumor site are key determinants of ICI therapeutic efficacy (4–6).

TLSs are ectopic immune cell aggregates that develop in peripheral tissues in response to a wide range of chronic inflammatory conditions, including tumors (7). The structure of TLSs includes B-cell- and T-cell-enriched areas; they have been reported to be the local site of initiation and

maintenance of humoral and cellular immune responses for anti-tumor immunity (8). The activity and function of TLSs differ according to their cellular composition and maturation status. Well-developed TLSs composed of mature dendritic cell (DC)/T cell clusters and CD20<sup>+</sup> B cell follicles are characterized by the presence of both a CD21<sup>+</sup> follicular-DC (FDC) network and Ki67<sup>+</sup> proliferating germinal center (GC)-B cells (9, 10). The density of mature TLS is associated with improved prognosis and is an effective predictive biomarker in cancer patients (11, 12). Researchers can synthesize tumor-specific antibodies, which are considered specific markers for prognosis (6). Moreover, B cells in TLSs can function as antigen-presenting cells and are associated with the induction of cytotoxic T cells (13). Therefore, these structures are major sources of tumor-infiltrating lymphocytes (TILs) and regulate the anti-tumor response (14).

Tissue-resident memory T (T<sub>RM</sub>) cells are tumor antigen-reactive TILs that produce a magnitude of cytotoxic mediators, such as granzyme B and perforin, as well as cytokines, such as interferon-gamma (IFN- $\gamma$ ) and tumor necrosis factor (TNF), in the tumor microenvironment (TME) (15, 16). T<sub>RM</sub> is a newly discovered subset of long-lived memory T cells that reside permanently in peripheral tissues without recirculation (17). In the tumor tissue, they mediate regional tumor surveillance and exhibit a protected anti-tumor function (15, 18). The permanence of T<sub>RM</sub> in NSCLC is mainly mediated by the expression of integrin  $\alpha$ E (CD103)  $\beta$ 7, which binds to E-cadherin in epithelial cells (19, 20). T<sub>RM</sub> is positively correlated with the survival of patients with cancer, including lung cancer (21, 22). The presence of intra-tumor CD8<sup>+</sup>CD103<sup>+</sup>T<sub>RM</sub> cells could predict a good clinical response in PD-1/PD-L1 blockade immunotherapy (23). CD8<sup>+</sup> T<sub>RM</sub> cells have been mainly located around TLSs—both are associated with a better prognosis in patients with gastric cancer (24). These results indicate that tumor-resident T cells may have a close relationship with TLSs. However, there have been no reports on the association of T<sub>RM</sub> subset distribution with TLS maturation and their relationship with the prognosis of patients.

Because patients with stage III NSCLC usually have quite heterogeneous prognoses, we selected patients with stage III lung adenocarcinoma (LUAD) for the current study. The aim of this study was to investigate the clinical significance of TLS maturation in patients with LUAD, its association with the spatial distribution of distinct T<sub>RM</sub> subsets in LUAD.

## MATERIALS AND METHODS

### Patients and Tumor Specimens

Forty-nine patients with stage III primary LUAD who underwent surgical resection at Tianjin Medical University Cancer Institute and Hospital between January 2015 and May 2016 were enrolled in this retrospective study. Pathological TNM staging was histologically diagnosed based on the 7th edition of the Union for International Cancer Control TNM classification. The inclusion criterion was complete clinical data, standardized

postoperative treatment and accurate pathological diagnosis. All patients underwent surgical resection of R0, and adjuvant therapy was mainly platinum-based chemotherapy, supplemented by radiotherapy or targeted therapy, when necessary. The exclusion criteria were those who had received anti-cancer treatment before surgery, had a second primary tumor, or were lacking follow-up. In this study, TLS positive tissues were selected for subsequent experiments which confirmed through hematoxylin and eosin (HE) staining slices. Formalin-fixed paraffin-embedded tumor tissues were collected from 49 patients for subsequent immunohistochemical staining and multiple immunofluorescence staining (Table 1). The study was approved by the Ethics Committee of the Tianjin Medical University Cancer Institute and Hospital. All patients signed relevant informed consent forms.

### Multiple Immunofluorescence Staining

Multiple immunofluorescence staining was performed using a PerkinElmer Opal 7-color Technology Kit (NEL81001KT). The tumor specimens in paraffin-embedded blocks were cut into 4- $\mu$ m-thick sections. The sections were deparaffinized in xylene and rehydrated in ethanol. Microwave repair was performed using EDTA buffer (PH=9.0) for 20 min. After cooling, the tissue was sealed with an antibody blocker at room temperature. The sections were then incubated overnight with primary antibody in a refrigerator at 4°C, and on the second day, the sections were co-incubated with poly-HRP-MS/Rb for 10 min at room temperature. Visualization was performed using Opal TSA (1:100). EDTA buffer was then heated by MWT to remove the AB-TSA complex. These steps were repeated for each round of the multiple staining. TSA-stained sections were washed with

**TABLE 1** | Baseline characteristics of patients (n=49).

Variable	Population, n (%)
Gender	
Male	24 (49%)
Female	25 (51%)
Age (years)	
<60	28 (57%)
≥60	21 (43%)
T stage	
T <sub>1</sub>	29 (59%)
T <sub>2</sub> +T <sub>3</sub> +T <sub>4</sub>	20 (41%)
N stage	
N <sub>1</sub> +N <sub>2</sub>	43 (88%)
N <sub>3</sub>	6 (12%)
TNM stage	
IIIA	39 (80%)
IIIB	10 (20%)
Micropapillary	
Positive	22 (45%)
Negative	27 (55%)
EGFR mutation	
Positive	15 (60%)
Negative	10 (40%)
Smoking	
Never	26 (53%)
Smoking	23 (47%)

MWT and counterstained with DAPI (1:100) for 10 min. Using this staining method, all samples were stained with the primary antibody for CD20 (1:600 dilution, clone L26, Abcam) visualized with Opal520 TSA, CD3 (1:400 dilution, clone SP162, Abcam) visualized with Opal540 TSA, CD103 (1:500 dilution, clone EPR4166(2), Abcam) visualized with Opal570 TSA, Bcl6 (1:200 dilution, clone LN22, Novus) visualized with Opal620 TSA, CD4 (1:1000 dilution, clone EPR6855, Abcam) visualized with Opal650 TSA, CD21(1:800 dilution, clone EP3093, Abcam) visualized with Opal690 TSA. Finally, the sections were covered with an anti-fluorescence attenuating tablet and cover glass.

## Multispectral Imaging and TLS Evaluation

Tumor sections were scanned using a PerkinElmer Mantra Quantitative Pathology Imaging System at 200 $\times$  magnification. Multispectral images were obtained using PerkinElmer inform Image Analysis software (version 2.4.0). Spectral libraries were built from the images of single-stained tissues with each antibody. The TLSs were then manually distinguished. We collected all TLSs of every tumor section and randomly collected three to five fields from areas outside the TLSs. A total of 958 fields were collected, including 807 TLSs and 151 outside fields of TLS.

The density of TLS was calculated as the number of TLSs per mm<sup>2</sup> of the tumor region in the sections. Immune subsets were determined by antibody expression, including CD4<sup>+</sup> T cells, CD8<sup>+</sup> T lymphocytes (CD3<sup>+</sup>CD4<sup>-</sup>), B cells (CD20<sup>+</sup>), FDC (CD21<sup>+</sup>), CD3<sup>+</sup> T<sub>RM</sub> (CD3<sup>+</sup>CD103<sup>+</sup>), CD4<sup>+</sup> T<sub>RM</sub> (CD4<sup>+</sup>CD103<sup>+</sup>), CD8<sup>+</sup> T<sub>RM</sub> (CD3<sup>+</sup>CD4<sup>-</sup>CD103<sup>+</sup>), and GC reaction (CD20<sup>+</sup>Bcl-6<sup>+</sup>) (25). The proportion of the immune subsets in each TLS (or field) was calculated as the percentage of this subpopulation to all nucleated cells in the TLS (or field). The proportion of the immune subsets in each patient was calculated by the average proportion in all fields (within the TLS and outside the TLS) across the entire section.

## Statistical Analysis

Disease-free survival (DFS) was defined as the time from the date of surgery to tumor recurrence. The surv\_cutpoint function in the survminer R package (version 4.1.2) was used to obtain the cutoff value of immune subsets proportion. Then the different immune subsets inside and outside TLS were divided into “high” and “low” groups. Kaplan-Meier curve was drawn with the survminer R package (4.1.2). The log-rank test in survival R package (4.1.2) was used to calculate the P value. Both the survminer and survival R package were downloaded from the public resource website: <https://cran.r-project.org/>. When comparing the prognostic differences of more than two of subgroups after combining TLS score and T<sub>RM</sub>, P value and HR ratio was calculated with log-rank test in GraphPad Prism software.

Chi-square (and Fisher's exact) test was used to evaluate the relationship between grade score, CD3<sup>+</sup> CD103<sup>+</sup> TRM and clinicopathological features. Wilcoxon rank test (paired nonparametric t test) was used to compare the difference of CD103<sup>+</sup>subsets inside and outside TLS. Kruskal-Wallis H test was used to compare the differences of immune subsets

proportion among different sub-group. All statistical analyses, except survival analyses, were performed with GraphPad Prism (version 9.1.0, US). P values of < 0.05 were considered statistically significant.

## RESULTS

### TLS in Patients With Stage III LUAD

According to the increasing prevalence of FDCs and the maturation of B cells, TLSs were classified into three maturity stages: 1) early TLS (E-TLS), characterized by dense lymphocytic aggregates without CD21 and Bcl-6 expression (**Figure 1A**); 2) primary follicle-like TLS (PFL-TLS), characterized by lymphocytic clusters with central network CD21 expression, but no GC reaction (Bcl-6<sup>-</sup>) (**Figure 1B**); and 3) secondary follicle-like TLS (SFL-TLS), characterized by lymphocytic clusters with GC reaction (CD20<sup>+</sup>Bcl-6<sup>+</sup>) (**Figure 1C**).

For the first time, we divided patients into three levels based on the maturity of TLSs: 1) grade 1: patients with TLSs characterized by only E-TLSs, and without PFL-TLSs and SFL-TLSs; 2) grade 2: patients with TLSs characterized by E-TLSs and at least one PFL-TLS, but no SFL-TLS; and 3) grade 3: patients with TLSs characterized by at least one SFL-TLS in the tumor tissue (**Table 2**).

### The Relationship Between TLS and Prognosis

We first evaluated the prognostic impact of the number and density of TLSs in patients. Kaplan-Meier analysis showed that patients with higher numbers of TLSs had a much better prognosis (median DFS 18.7 months vs. 7.4 months, P = 0.011, **Figure 2A**, left). A higher density of TLS was also positively associated with a good DFS (median 17.3 months vs. 12.4 months, P = 0.009, **Figure 2A**, right).

Furthermore, we analyzed the prognosis of patients with different grades. The results showed that the prognosis of grade 3 patients was significantly higher than that of those in grade 1 (median DFS 19.5 months vs. 4.3 months, P < 0.001, **Figure 2B**). The grade 2 patients also had a better DFS than those in grade 1 (median 12.6 months vs. 4.3 months, P = 0.039). The prognosis of grade 3 patients tended to be better than those in grade 2 (median DFS 19.5 months vs. 12.6 months, P = 0.059, **Figure 2B**). These results indicate that the maturity of TLS is crucial for the prognosis of patients.

### T<sub>RM</sub> High Within TLS Was Associated With Good Prognosis

By comparing the difference in the proportion of T<sub>RM</sub> inside and outside the TLS, we determined that all T<sub>RM</sub> subsets were mainly located in TLS, especially CD4<sup>+</sup> T<sub>RM</sub> (**Figures 3A, B**). The proportion of CD3<sup>+</sup> T<sub>RM</sub> in TLS (mean  $\pm$  SD: 1.34%  $\pm$  1.13%) was significantly higher than that outside (mean  $\pm$  SD: 0.71%  $\pm$  0.84%), P < 0.001. The proportion of CD4<sup>+</sup> T<sub>RM</sub> in TLS (mean  $\pm$  SD: 0.83%  $\pm$  0.75%) was significantly higher than that outside (mean  $\pm$  SD: 0.26%  $\pm$  0.33%), P < 0.001. The

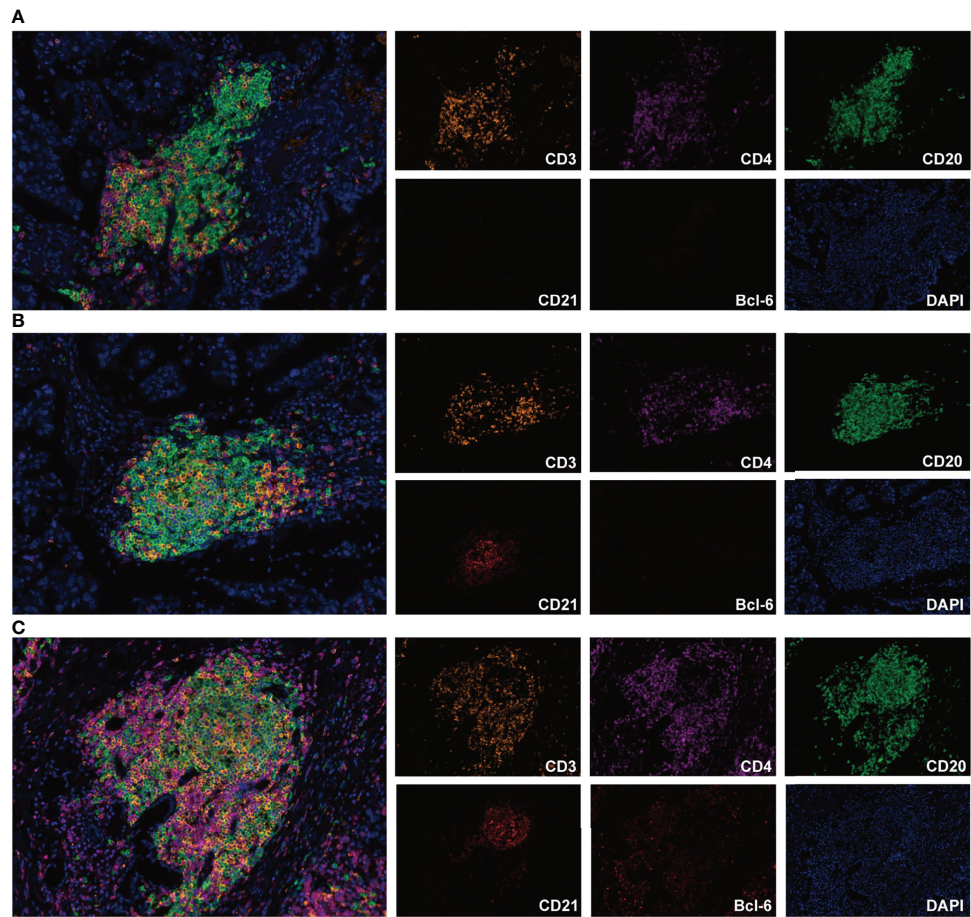


**FIGURE 1** | Representative images of TLS maturity (magnification,  $\times 200$ ). The slide was stained with CD3 (orange), CD4 (purple), CD20 (green), CD21 (brown), Bcl-6 (red), and DAPI (blue). **(A)**, E-TLS, both FDC and Bcl-6 markers were negative. **(B)**, PFL-TLS, FDC positive and Bcl-6 negative. **(C)**, SFL-TLS, both FDC and Bcl-6 markers were positive.

proportion of CD8<sup>+</sup> T<sub>RM</sub> in TLS (mean  $\pm$  SD: 0.78%  $\pm$  0.72%) was significantly higher than that outside (mean  $\pm$  SD: 0.55%  $\pm$  0.67%),  $P < 0.05$ .

Survival analysis showed that both CD3<sup>+</sup> T<sub>RM</sub> and CD8<sup>+</sup> T<sub>RM</sub> in TLS could predict longer survival (median DFS 17.3 months vs. 6.7 months, 17.5 months vs. 12.7 months,  $P < 0.05$ ; **Figure 3C**). Likewise, CD4<sup>+</sup> T<sub>RM</sub> within TLS tended to prolong DFS of patients although there was no significant difference between groups (median 15.2 months vs. 6.9 months,  $P = 0.078$ , **Figure 3C**). However, TRM outside the TLS had no effect on prognosis.

### The Relationship Between Patients Score, CD3<sup>+</sup>CD103<sup>+</sup> T<sub>RM</sub> Within TLS, and Various Clinical Parameters

The above findings suggested that T<sub>RM</sub> is mainly located within the TLS, and the T<sub>RM</sub> within the TLS can affect prognosis. Therefore, we next focused our research on T<sub>RM</sub> inside TLS. The relationships between patient score, CD3<sup>+</sup> T<sub>RM</sub> within TLS, and clinical features of patients including sex, age, TNM stage, micropapillary, EGFR mutation, and smoking are shown in **Table 3**. The results showed that patients with stage IIIA LUAD had more mature TLS than patients with IIIB LUAD ( $P = 0.041$ ). There were no significant

**TABLE 2** | Patients score criteria in this study.

Score	E-TLS	PFL-TLS	SFL-TLS
grade 1	+	-	-
grade 2	+	+	-
grade 3	+	+	+

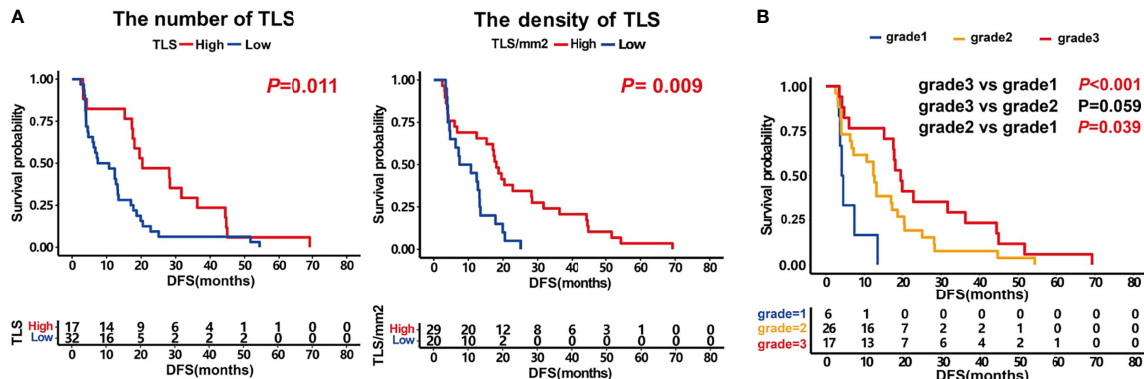


**FIGURE 2** | Prognostic impact of the number and density of TLS and patients' scores. **(A)** Kaplan-Meier survival curves showing DFS according to the number of TLS ( $P=0.011$ ) and the density of TLS ( $P=0.009$ ). **(B)** Kaplan-Meier survival curves showing DFS according to patients' scores.  $P$  values were calculated by the log-rank test.

associations between other clinical features and patient scores, as well as between CD3<sup>+</sup> T<sub>RM</sub> and TLS.

### Univariate Analysis of Clinical and Immune Characteristics Affecting DFS

Moreover, we analyzed the clinical and immune characteristics that affected the DFS of patients in this study. The results identified some univariate factors that could affect the DFS of patients, including the TLS number, TLS density, patient score, CD20<sup>+</sup> B cells in TLS, FDC in TLS, CD103<sup>+</sup> T<sub>RM</sub>, and CD8<sup>+</sup>CD103<sup>+</sup> T<sub>RM</sub> in TLS, average CD3<sup>+</sup> CD103<sup>+</sup> T<sub>RM</sub>, average CD4<sup>+</sup>CD103<sup>+</sup> T<sub>RM</sub>, and average CD8<sup>+</sup>CD103<sup>+</sup> T<sub>RM</sub> (Table 4).

### Patients With High Score Had More T<sub>RM</sub> in TLS

We analyzed the distribution of immune subsets in the TLS in different grades of patients. The results showed that the proportion of CD20<sup>+</sup> B cells in grade 3 patients was higher than that in grade 2 and grade 1 patients (mean  $\pm$  SD: 21.08%  $\pm$  6.72% vs. 15.59%  $\pm$  4.47%, 21.08%  $\pm$  6.72% vs. 11.41%  $\pm$  7.84%,  $P=0.037$ , and  $P=0.008$ , respectively; Figure 4A). The proportion of CD3<sup>+</sup> T<sub>RM</sub> in grade 3 patients was higher than that in grade 2 and grade 1 patients (mean  $\pm$  SD: 1.98%  $\pm$  1.23% vs. 1.10%  $\pm$  0.96%, 1.98%  $\pm$  1.23% vs. 0.57%  $\pm$  0.38%,  $P=0.027$ , and  $P=0.019$ , respectively; Figure 4A). Patients in grade 3 had higher CD4<sup>+</sup> T<sub>RM</sub> than patients in grade 1 (mean  $\pm$  SD: 1.33%  $\pm$  0.87% vs. 0.59%  $\pm$  0.53%,  $P=0.005$ ; Figure 4A). The proportion of CD8<sup>+</sup> T<sub>RM</sub> in grade 3 patients was higher than that in grade 1 (mean  $\pm$  SD: 1.06%  $\pm$  0.84% vs. 0.69%  $\pm$  0.63%,  $P=0.039$ , Figure 4A).

Next, we analyzed the proportion of T<sub>RM</sub> in all 807 TLSs, including E-TLSs, PFL-TLSs, and SFL-TLSs. The proportion of CD3<sup>+</sup> T<sub>RM</sub> in SFL-TLS was significantly higher than that of E-TLS and PFL-TLS (mean  $\pm$  SD: 3.60%  $\pm$  6.80% vs. 1.57%  $\pm$  2.71%, 3.60%  $\pm$  6.80% vs. 1.23%  $\pm$  1.62%,  $P<0.001$ ; Figure 4B), respectively. The proportion of CD4<sup>+</sup> T<sub>RM</sub> in SFL-TLS was significantly higher than that in E-TLS and PFL-TLS (mean  $\pm$  SD: 2.17%  $\pm$  2.19% vs. 0.98%  $\pm$  2.21%, 2.17%  $\pm$  2.19% vs. 0.67%  $\pm$  1.19%,  $P<0.001$ ; Figure 4B), respectively. The proportion of

CD8<sup>+</sup> T<sub>RM</sub> in SFL-TLS was significantly higher than that in E-TLS and PFL-TLS (mean  $\pm$  SD: 1.30%  $\pm$  1.78% vs. 0.98%  $\pm$  2.46%, 1.30%  $\pm$  1.78% vs. 0.81%  $\pm$  1.41%,  $P<0.001$ ; Figure 4B), respectively.

### Patients With a Combination of T<sub>RM</sub> and Grade 3 Predicted a Better Prognosis

Patients were stratified into four groups according to the proportion of CD103<sup>+</sup> T<sub>RM</sub> and patient scores. The prognosis of patients in the group of CD3CD103<sup>High</sup> and grade 3 was significantly higher than that of CD3CD103<sup>High</sup> and grade 1 + 2 (median DFS 19.7 months vs. 12.7 months,  $P=0.046$ ) and that of CD3CD103<sup>Low</sup> and grade 1 + 2 (median DFS 19.7 months vs. 7.2 months,  $P=0.003$ ), respectively (Figure 5A). Patients in the CD4CD103<sup>High</sup> and grade 3 groups had a significantly better prognosis than those in CD4CD103<sup>High</sup> and grade 1 + 2 (median DFS 19.5 months vs. 12.6 months,  $P=0.037$ ) and in CD4CD103<sup>Low</sup> and grade 1 + 2 (median DFS 19.5 months vs. 6.9 months,  $P=0.011$ ), respectively (Figure 5B). Similarly, the prognosis of patients in the group of CD8CD103<sup>High</sup> and grade 3 tended to be better than that of CD8CD103<sup>High</sup> and grade 1 + 2 (median DFS 19.7 months vs. 12.8 months,  $P=0.052$ ), and significantly higher than that of CD8CD103<sup>Low</sup> and grade 1 + 2 (median DFS 19.7 months vs. 7.3 months,  $P<0.001$ ; Figure 5C). However, there was no significant difference in prognosis between patients in the CD103<sup>High</sup> and grade 1 + 2 groups and the CD103<sup>Low</sup> and grade 1 + 2 groups, regardless of the CD3<sup>+</sup> T<sub>RM</sub>, CD4<sup>+</sup> T<sub>RM</sub>, or CD8<sup>+</sup> T<sub>RM</sub> subsets.

## DISCUSSION

In the present study, we evaluated the relationship among TLS maturity, clinical characteristics, and prognosis of patients with stage III LUAD. Although there is no standardized classification of TLS maturity, we used the classification method of TLS that Winder (26) had reported in colorectal carcinoma, and classified the TLSs into three mature stages, including E-TLSs, PFL-TLSs,

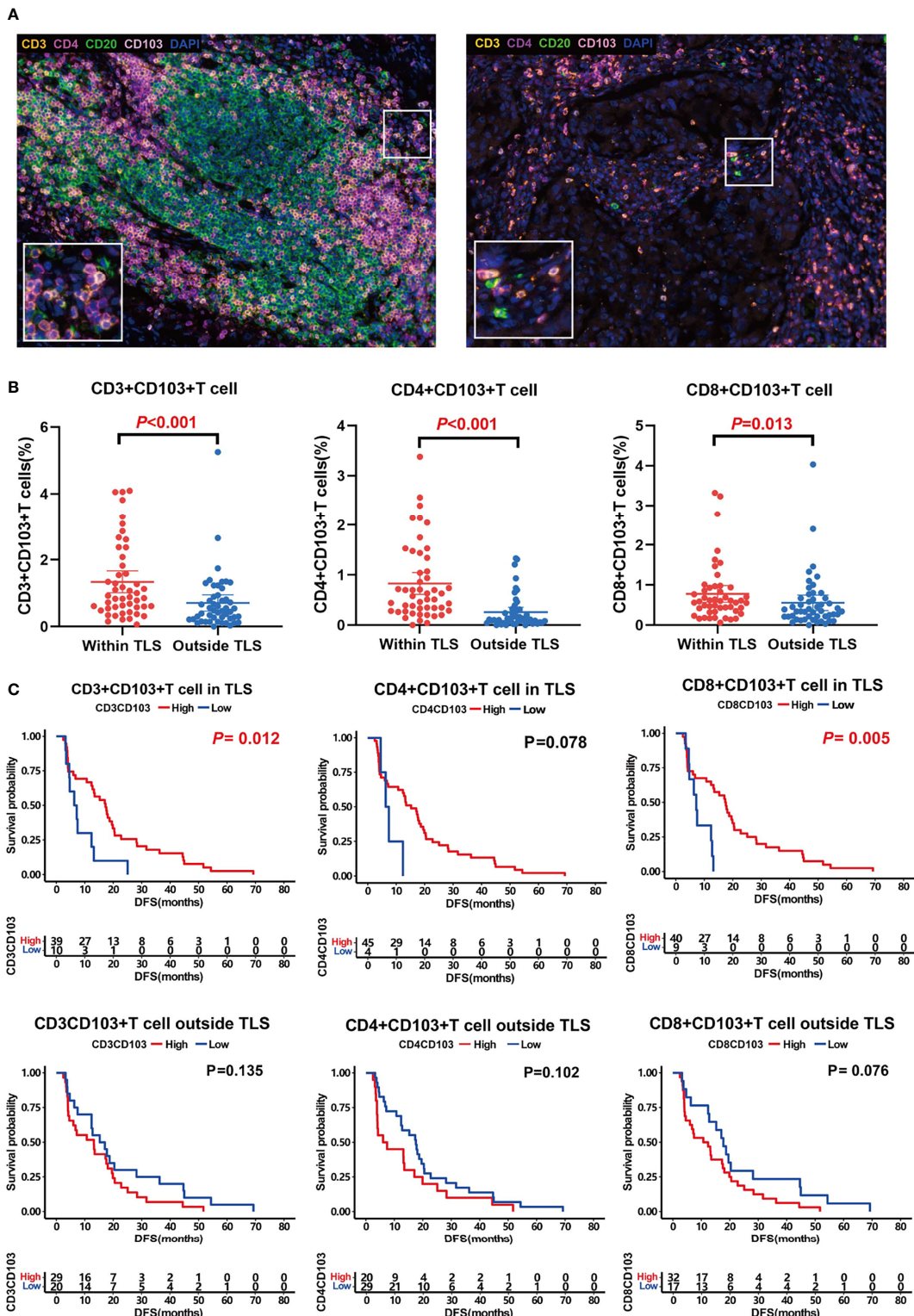


**FIGURE 3 |** T<sub>RM</sub> distribution and its association with prognosis. **(A)** Representative images of T<sub>RM</sub> inside (left) and outside (right) TLSs. **(B)** Comparison of CD3<sup>+</sup>CD103<sup>+</sup> T<sub>RM</sub> (left,  $P < 0.001$ ), CD4<sup>+</sup>CD103<sup>+</sup> T<sub>RM</sub> (middle,  $P < 0.001$ ), and CD8<sup>+</sup>CD103<sup>+</sup> T<sub>RM</sub> (right,  $P < 0.001$ ) distribution inside and outside TLSs. T<sub>RM</sub> were mainly located in TLS. **C**, Influence of T<sub>RM</sub> inside and outside of TLS on patient prognosis. T<sub>RM</sub> inside TLS predicted a better prognosis.

**TABLE 3** | The relationship between patients score, CD3<sup>+</sup>CD103<sup>+</sup>T<sub>RM</sub> within TLS and various clinical parameters in patients with stage III LUAD (n=49).

Variable	All cases (n)	Patients Score			Pvalue	CD3 <sup>+</sup> CD103 <sup>+</sup> T <sub>RM</sub> within TLS		Pvalue
		grade1,n (%)	grade2,n (%)	grade3,n (%)		Low,n (%)	High,n (%)	
Gender								
Male	24	1 (4%)	12 (50%)	11 (46%)	0.118	5 (21%)	19 (79%)	>0.999
Female	25	5 (20%)	14 (56%)	6 (24%)		5 (20%)	20 (80%)	
Age (years)								
<60	28	3 (11%)	16 (57%)	9 (32%)	0.797	6 (21%)	22 (79%)	>0.999
≥60	21	3 (14%)	10 (48%)	8 (38%)		4 (19%)	17 (81%)	
T stage								
T <sub>1</sub>	29	2 (7%)	18 (62%)	9 (31%)	0.221	7 (24%)	22 (76%)	0.496
T <sub>2</sub> +T <sub>3</sub> +T <sub>4</sub>	20	4 (20%)	8 (40%)	8 (40%)		3 (15%)	17 (85%)	
N stage								
N <sub>1</sub> +N <sub>2</sub>	43	5 (12%)	22 (51%)	16 (37%)	0.61	10 (23%)	33 (77%)	0.324
N <sub>3</sub>	6	1 (17%)	4 (66%)	1 (17%)		0	6 (100%)	
TNM stage								
IIIA	39	3 (8%)	22 (56%)	14 (36%)	0.041	9 (23%)	30 (77%)	0.663
IIIB	10	3 (30%)	4 (40%)	3 (30%)		1 (10%)	9 (90%)	
Micropapillary								
Positive	22	3 (14%)	11 (50%)	8 (36%)	0.925	4 (18%)	18 (82%)	>0.999
Negative	27	3 (11%)	15 (56%)	9 (33%)		6 (22%)	21 (78%)	
EGFR mutation								
Positive	15	1 (7%)	11 (73%)	3 (20%)	0.279	2 (13%)	13 (87%)	0.175
Negative	10	3 (30%)	5 (50%)	2 (20%)		4 (40%)	6 (60%)	
Smoking								
Never	26	3 (12%)	14 (54%)	9 (34%)	0.986	4 (15%)	22 (85%)	0.483
Smoking	23	3 (13%)	12 (52%)	8 (35%)		6 (26%)	17 (74%)	

**TABLE 4** | Univariate analysis of clinical and immune characteristics affecting DFS of patients in the study.

Variable	HR (95%CI)	P value
Gender (Female vs. Male)	0.830 (0.473,1.459)	0.496
Age (≥60 y vs. <60 y)	0.622 (0.354,1.091)	0.086
T stage (T2+T3+T4 vs. T1)	0.905 (0.515,1.593)	0.728
N stage (N3 vs. N1+N2)	1.011 (0.429,2.384)	0.979
TNM stage (IIIB vs. IIIA)	1.284 (0.585,2.819)	0.486
Micropapillary (Negative vs. Positive)	1.259 (0.719,2.205)	0.412
Smoking (Never vs. Smoking)	0.911 (0.520,1.597)	0.741
Numbers of TLS (≥26 vs. <26)	0.490 (0.280,0.857)	0.012
Density of TLS/mm <sup>2</sup> (≥0.074 vs. <0.074)	0.459 (0.239,0.844)	0.006
Grade scores (grade2 vs. grade1)	0.418 (0.123,1.421)	0.039
(grade3 vs. grade1)	0.226 (0.047,1.078)	<0.001
CD3 <sup>+</sup> T cell in TLS (≥19.17% vs. <19.17%)	1.326 (0.475,2.316)	0.316
CD4 <sup>+</sup> T cell in TLS (≥14.08% vs. <14.08%)	0.665 (0.366,1.208)	0.196
CD8 <sup>+</sup> T cell in TLS (≥18.81% vs. <18.81%)	1.483 (0.748,2.942)	0.202
CD20 <sup>+</sup> B cell in TLS (≥17.46% vs. <17.46%)	0.571 (0.325,1.001)	0.044
Bcl6 <sup>+</sup> B cell in TLS (≥0.05% vs. <0.05%)	0.564 (0.315,1.009)	0.070
CD21 <sup>+</sup> FDC in TLS (≥0.56% vs. <0.56%)	0.375 (0.312,1.067)	0.004
CD103 <sup>+</sup> cell in TLS (≥0.77% vs. <0.77%)	0.360 (0.097,1.338)	0.012
CD3 <sup>+</sup> CD103 <sup>+</sup> T <sub>RM</sub> in TLS (≥0.48% vs. <0.48%)	0.433 (0.171,1.103)	0.012
CD4 <sup>+</sup> CD103 <sup>+</sup> T <sub>RM</sub> in TLS (≥0.18% vs. <0.18%)	0.421 (0.093,1.888)	0.078
CD8 <sup>+</sup> CD103 <sup>+</sup> T <sub>RM</sub> in TLS (≥0.28% vs. <0.28%)	0.386 (0.137,1.084)	0.005
CD3 <sup>+</sup> T cell outside TLS (≥4.43% vs. <4.43%)	1.749 (0.939,3.258)	0.110
CD4 <sup>+</sup> T cell outside TLS (≥3.75% vs. <3.75%)	1.606 (0.888,2.904)	0.089
CD8 <sup>+</sup> T cell outside TLS (≥18.47% vs. <18.47%)	0.552 (0.286,1.072)	0.126
CD20 <sup>+</sup> B cell outside TLS (≥26.14% vs. <26.14%)	0.599 (0.293,1.225)	0.176
CD3 <sup>+</sup> CD103 <sup>+</sup> T <sub>RM</sub> outside TLS (≥0.37% vs. <0.37%)	1.514 (0.865,2.651)	0.135
CD4 <sup>+</sup> CD103 <sup>+</sup> T <sub>RM</sub> outside TLS (≥0.16% vs. <0.16%)	1.591 (0.865,2.926)	0.102
CD8 <sup>+</sup> CD103 <sup>+</sup> T <sub>RM</sub> outside TLS (≥0.25% vs. <0.25%)	1.654 (0.944,2.899)	0.076
CD3 <sup>+</sup> T cell (≥8.52% vs. <8.52%)	0.487 (0.180,1.317)	0.052
CD4 <sup>+</sup> T cell (≥12.67% vs. <12.67%)	0.637 (0.348,1.165)	0.160
CD8 <sup>+</sup> T cell (≥6.37% vs. <6.37%)	0.472 (0.148,1.510)	0.072
CD20 <sup>+</sup> B cell (≥19.04% vs. <19.04%)	0.555 (0.299,1.029)	0.092
Average CD3 <sup>+</sup> CD103 <sup>+</sup> T <sub>RM</sub> (≥0.54% vs. <0.54%)	0.384 (0.136,1.080)	0.004
Average CD4 <sup>+</sup> CD103 <sup>+</sup> T <sub>RM</sub> (≥0.26% vs. <0.26%)	0.490 (0.210,1.145)	0.026
Average CD8 <sup>+</sup> CD103 <sup>+</sup> T <sub>RM</sub> (≥0.48% vs. <0.48%)	0.549 (0.281,1.037)	0.037

HR, hazard ratio; CI, confidence interval.

and SFL-TLSs. For the first time, we divided patients into three levels based on the mature state of TLSs: 1) grade 1: only E-TLSs with no PFL-TLSs and SFL-TLSs; 2) grade 2: E-TLSs and PFL-TLSs in the tumor, and without SFL-TLS; and 3) grade 3: possess at least one SFL-TLS in the tumor tissue. The results showed that patients in grade 3 had the best DFS, followed by grade 2. The DFS of patients in grade 1 was the worst. This was consistent with the findings in colorectal cancer and lung squamous cell carcinoma that found that patients with GC reaction had a better prognosis (26, 27). This indicates that B cell maturity and humoral immunity play pivotal roles in the anti-tumor immune response.

In addition, we evaluated the distribution of CD4<sup>+</sup> T<sub>RM</sub> cells and CD8<sup>+</sup> T<sub>RM</sub> cells in the tumor tissue and found that the proportion of T<sub>RM</sub> within TLSs was significantly higher than that outside, especially CD4<sup>+</sup> T<sub>RM</sub>. The proportion of T<sub>RM</sub> within TLSs was positively correlated with the prognosis of patients, while there was no significant association between the proportion of T<sub>RM</sub> outside TLSs and prognosis. Furthermore, we compared the proportions of different immune subsets in LUAD patients of different grades. The proportions of CD20<sup>+</sup> B cells and CD3<sup>+</sup> T<sub>RM</sub> in grade 3 patients were significantly higher than those in grade 1

and grade 2, respectively. The proportions of CD4<sup>+</sup>CD103<sup>+</sup> T<sub>RM</sub> and CD8<sup>+</sup>CD103<sup>+</sup> T<sub>RM</sub> were significantly higher in grade 3 patients than in grade 1 patients (P<0.05). We then analyzed the proportion difference of T<sub>RM</sub> in different maturities of TLSs. The proportions of CD3<sup>+</sup> T<sub>RM</sub>, CD4<sup>+</sup> T<sub>RM</sub>, and CD8<sup>+</sup> T<sub>RM</sub> in SFL-TLSs were significantly higher than those in E-TLSs and PFL-TLSs, respectively (P<0.05). All these results indicate that there is a close relationship between T<sub>RM</sub> and TLS maturity.

In the subsequent prognosis analysis, the data showed that patients with both more mature TLSs and a higher proportion of CD103<sup>+</sup> T<sub>RM</sub> had a much better prognosis. CD3<sup>+</sup> T<sub>RM</sub>, CD4<sup>+</sup> T<sub>RM</sub>, and CD8<sup>+</sup> T<sub>RM</sub> showed similar results. The data further confirmed that CD103<sup>+</sup> T<sub>RM</sub> was closely related to the maturation of TLSs.

Although the exact mechanism by which T<sub>RM</sub> preferentially located into TLS had not been clarified, it was reported that CXCL13 was the key molecular determinant of TLS formation in the TME (27–30). Activated CD103<sup>+</sup>CTLs were involved in the migration of B cells to tumor via production of CXCL13. The high mutation load and CD8<sup>+</sup> T cell-rich tumors showed higher expression of CXCL13 and ITGAE (CD103) and that they presented with significantly higher numbers of B cells in a variety of tumors (30). A previous study on the distribution of CD8<sup>+</sup>CD103<sup>+</sup> T<sub>RM</sub> in gastric

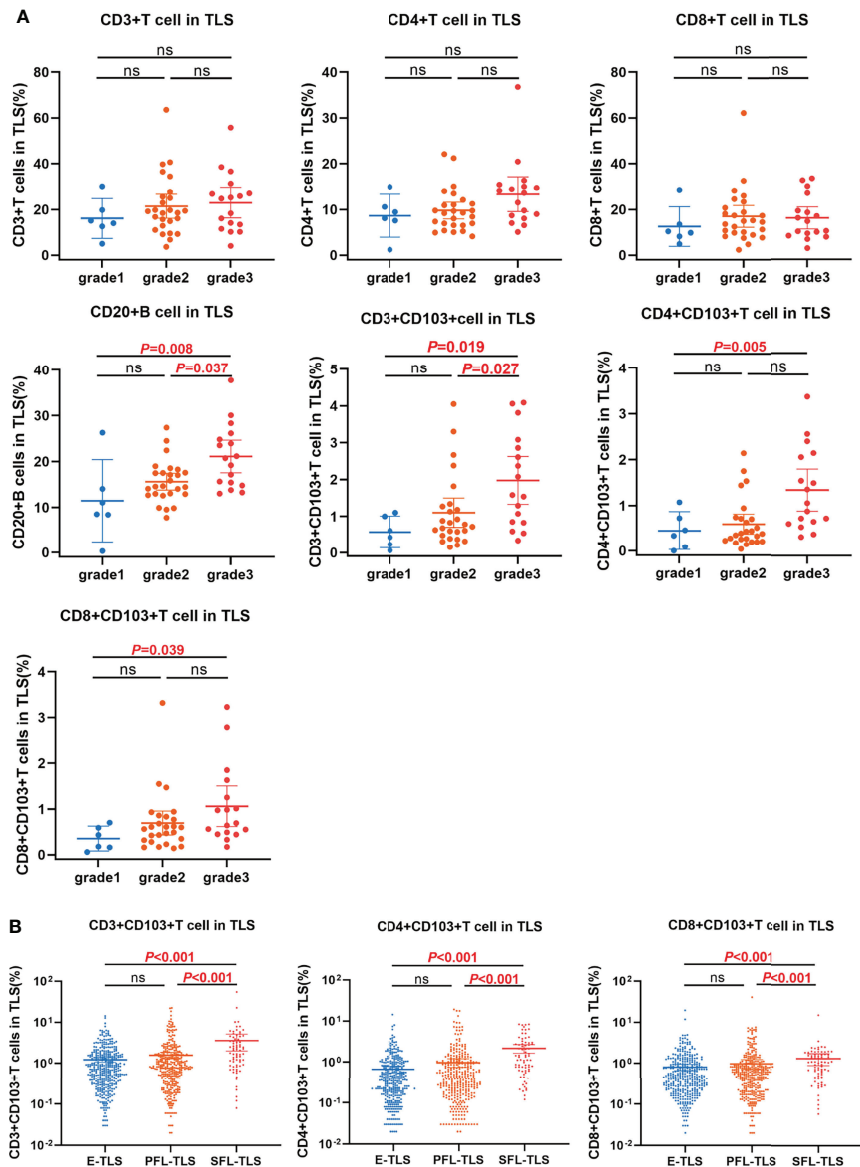


**FIGURE 4** | The relationship between T<sub>RM</sub> distribution and TLSs maturation. **(A)** The distributions of immune subsets within TLS in patients with different TLS scores. The proportion of CD20<sup>+</sup> B cell and CD3<sup>+</sup>CD103<sup>+</sup> T<sub>RM</sub> within TLS in grade 3 patients was significantly higher than that in grade 2 and grade 1 respectively. The proportion of CD4<sup>+</sup>CD103<sup>+</sup> T<sub>RM</sub> and CD8<sup>+</sup>CD103<sup>+</sup> T<sub>RM</sub> within TLS in grade 3 patients was significantly higher than that in grade 1. **(B)** The distribution of T<sub>RM</sub> in E-TLS, PFL-TLS, and SFL-TLS. The proportions of CD3<sup>+</sup>CD103<sup>+</sup> T<sub>RM</sub>, CD4<sup>+</sup>CD103<sup>+</sup> T<sub>RM</sub>, and CD8<sup>+</sup>CD103<sup>+</sup> T<sub>RM</sub> within SFL-TLS were significantly higher than those in E-TLS and PFL-TLS, respectively. ns, non-significant.

carcinoma reported similar results. CD103<sup>+</sup> T cells were located around TLSs, and patients with CD103<sup>High</sup> had more TLSs (24). Furthermore, patients who were CD103<sup>High</sup> and TLS<sup>Rich</sup> had a better prognosis than other groups (24). However, this study mainly focused on CD8<sup>+</sup> subsets and there was no analysis of the relationship between TLS maturity and CD103<sup>+</sup> T<sub>RM</sub>. Another study identified a new subset of CD4<sup>+</sup> Th-CXCL13 with tumor-resident gene characteristics in NPC (31). CD4<sup>+</sup> Th-CXCL13 recruits tumor-associated B cells and induces plasma cell differentiation and immunoglobulin production through

interleukin-21 (IL-21) secretion and CD84 interactions in TLSs. In a mouse model of influenza viral infection, Young Min Son et al. reported a population of lung-resident helper CD4<sup>+</sup> T cells (CD4<sup>+</sup> T<sub>RH</sub>) that developed after viral clearance. They found that the formation of CD4<sup>+</sup> T<sub>RH</sub> is dependent on transcription factors involved in the feather of follicular T cells and resident T cells, including BCL6 and Blh40. CD4<sup>+</sup> T<sub>RH</sub> could promote the development of protective B cells and CD8<sup>+</sup> T cell responses through IL-21 dependent mechanism (32). Moreover, B cells in

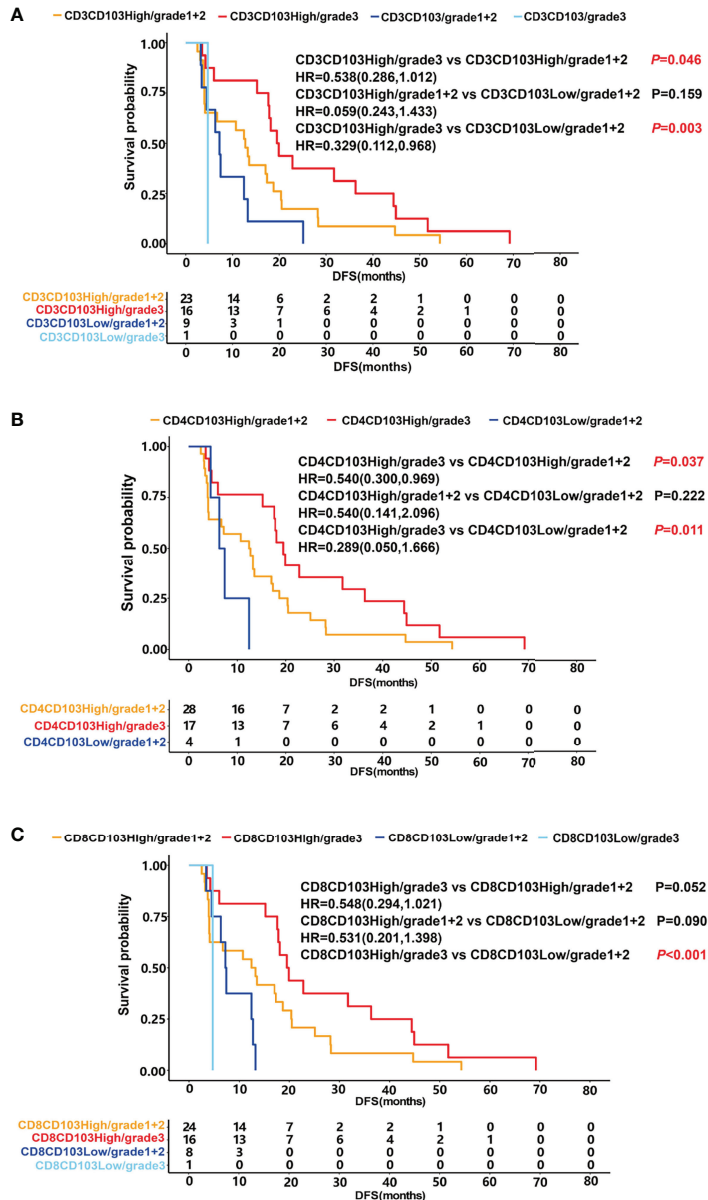


**FIGURE 5** | The relationship between T<sub>RM</sub>, patient score and prognosis. DFS was shown with Kaplan-Meier plots according to the combination of T<sub>RM</sub> and patient score. **(A)** DFS of patients in the group of CD3CD103<sup>High</sup> and grade 3 (median 19.7 months) was significantly higher than that of CD3CD103<sup>High</sup> and grade 1 + 2 (median 12.7 months) and that of CD3CD103<sup>Low</sup> and grade 1 + 2 (median 7.2 months), respectively,  $P<0.05$ . **(B)** DFS of patients in the group of CD4CD103<sup>High</sup> and grade 3 (median 19.5 months) was significantly higher than that of CD4CD103<sup>High</sup> and grade 1 + 2 (median 12.6 months) and that of CD4CD103<sup>Low</sup> and grade 1 + 2 (median 6.9 months), respectively,  $P<0.05$ . **(C)** DFS of patients in the group of CD8CD103<sup>High</sup> and grade 3 tended to be better than that of CD8CD103<sup>High</sup> and grade 1 + 2 (median 19.7 months vs. 12.8 months,  $P=0.052$ ), and significantly higher than that of CD8CD103<sup>Low</sup> and grade 1 + 2 (median DFS 19.7 months vs. 7.3 months,  $P<0.001$ ).

TLSs can function as antigen-presenting cells; they highly express the co-stimulatory molecules CD86 and CD80 and facilitate tumor antigen-specific T-cell responses, including CD8<sup>+</sup> TIL and CD4<sup>+</sup> TIL responses (33). Bradley et al. have demonstrated that B cells play important roles in memory CD4<sup>+</sup> T cell generation and differentiation because mice in a B cell knockout model did not develop memory CD4<sup>+</sup> T cells (34). These results indicated that there

might be synergy function between T<sub>RM</sub> and TLSs in the antitumor response.

In conclusion, our data highlight the proportion of T<sub>RM</sub> within TLSs was significantly increased with the maturation of TLSs. When we divided patients into three levels including grade 1, grade 2 and grade 3 according to the presence of different maturity of TLSs, the proportions of CD4<sup>+</sup>CD103<sup>+</sup>T<sub>RM</sub> and CD8<sup>+</sup>CD103<sup>+</sup>T<sub>RM</sub> in grade 3

of patients were significantly higher than grade 1 and grade 2. These results indicate a close relationship between CD103<sup>+</sup>T<sub>RM</sub> and TLS maturity. Furthermore, patients with a combination feature of grade 3 and CD103<sup>+</sup>T<sub>RM</sub><sup>High</sup> exhibited a good prognosis. The combination of TLS maturity and CD103<sup>+</sup>T<sub>RM</sub> proportion could be used as a biomarker to predict the prognosis of LUAD patients.

## DATA AVAILABILITY STATEMENT

The original contributions presented in the study are included in the article/**Supplementary Material**. Further inquiries can be directed to the corresponding authors.

## ETHICS STATEMENT

The studies involving human participants were reviewed and approved by Ethics Committee of the Tianjin Medical University Cancer Institute and Hospital. The patients/participants provided their written informed consent to participate in this study.

## AUTHOR CONTRIBUTIONS

HZ and XR designed the experiments. HW performed the experiments. HZ and HW performed the analyses and wrote

## REFERENCES

1. Hsu ML, Naidoo J. Principles of Immunotherapy in non-Small Cell Lung Cancer. *Thorac Surg Clin* (2020) 30(2):187–98. doi: 10.1016/j.thorsurg.2020.01.009
2. Suresh K, Naidoo J, Lin CT, Danoff S. Immune Checkpoint Immunotherapy for non-Small Cell Lung Cancer: Benefits and Pulmonary Toxicities. *Chest* (2018) 154(6):1416–23. doi: 10.1016/j.chest.2018.08.1048
3. Tumeh PC, Harview CL, Yearley JH, Shintaku IP, Taylor EJ, Robert L, et al. PD-1 Blockade Induces Responses by Inhibiting Adaptive Immune Resistance. *Nature* (2014) 515(7528):568–71. doi: 10.1038/nature13954
4. Helmink BA, Reddy SM, Gao J, Zhang S, Basar R, Thakur R, et al. B Cells and Tertiary Lymphoid Structures Promote Immunotherapy Response. *Nature* (2020) 577(7791):549–55. doi: 10.1038/s41586-019-1922-8
5. Cabrita R, Lauss M, Sanna A, Donia M, Skaarup Larsen M, Mitra S, et al. Tertiary Lymphoid Structures Improve Immunotherapy and Survival in Melanoma. *Nature* (2020) 577(7791):561–5. doi: 10.1038/s41586-019-1914-8
6. Petitprez F, de Reyniès A, Keung EZ, Chen TW, Sun CM, Calderaro J, et al. B Cells are Associated With Survival and Immunotherapy Response in Sarcoma. *Nature* (2020) 577(7791):556–60. doi: 10.1038/s41586-019-1906-8
7. Sautès-Fridman C, Petitprez F, Calderaro J, Fridman WH. Tertiary Lymphoid Structures in the Era of Cancer Immunotherapy. *Nat Rev Cancer* (2019) 19(6):307–25. doi: 10.1038/s41568-019-0144-6
8. Zhao H, Wang H, Zhou Q, Ren X. Insights Into Tertiary Lymphoid Structures in the Solid Tumor Microenvironment: Anti-Tumor Mechanism, Functional Regulation, and Immunotherapeutic Strategies. *Cancer Biol Med* (2021) 18(4):981–91. doi: 10.20892/j.issn.2095-3941.2021.0029
9. Dieu-Nosjean MC, Antoine M, Danel C, Heudes D, Wislez M, Poulot V, et al. Long-Term Survival for Patients With non-Small-Cell Lung Cancer With Intratumoral Lymphoid Structures. *J Clin Oncol* (2008) 26(27):4410–7. doi: 10.1200/JCO.2007.15.0284
10. Kroeger DR, Milne K, Nelson BH. Tumor-Infiltrating Plasma Cells are Associated With Tertiary Lymphoid Structures, Cytolytic T-Cell Responses, and Superior Prognosis in Ovarian Cancer. *Clin Cancer Res* (2016) 22(12):3005–15. doi: 10.1158/1078-0432.CCR-15-2762
11. Rodriguez AB, Engelhard VH. Insights Into Tumor-Associated Tertiary Lymphoid Structures: Novel Targets for Antitumor Immunity and Cancer Immunotherapy. *Cancer Immunol Res* (2020) 8(11):1338–45. doi: 10.1158/2326-6066.CIR-20-0432
12. Munoz-Erazo L, Rhodes JL, Marion VC, Kemp RA. Tertiary Lymphoid Structures in Cancer – Considerations for Patient Prognosis. *Cell Mol Immunol* (2020) 17(6):570–5. doi: 10.1038/s41423-020-0457-0
13. Yamakoshi Y, Tanaka H, Sakimura C, Deguchi S, Mori T, Tamura T, et al. Immunological Potential of Tertiary Lymphoid Structures Surrounding the Primary Tumor in Gastric Cancer. *Int J Oncol* (2020) 57(1):171–82. doi: 10.3892/ijo.2020.5042
14. Martinet L, Garrido I, Filleron T, Le Guellec SL, Bellard E, Fournie JJ, et al. Human Solid Tumors Contain High Endothelial Venules: Association With T- and B-Lymphocyte Infiltration and Favorable Prognosis in Breast Cancer. *Cancer Res* (2011) 71(17):5678–87. doi: 10.1158/0008-5472.CAN-11-0431
15. Djenidi F, Adam J, Goubar A, Durgeau A, Meurice G, de Montpréville V, et al. CD8+CD103+ Tumor-Infiltrating Lymphocytes are Tumor-Specific Tissue-Resident Memory T Cells and a Prognostic Factor for Survival in Lung Cancer Patients. *J Immunol* (2015) 194(7):3475–86. doi: 10.4049/jimmunol.1402711
16. Ganesan AP, Clarke J, Wood O, Garrido-Martin EM, Chee SJ, Mellows T, et al. Tissue-Resident Memory Features are Linked to the Magnitude of Cytotoxic T Cell Responses in Human Lung Cancer. *Nat Immunol* (2017) 18(8):940–50. doi: 10.1038/ni.3775
17. Schenkel JM, Masopust D. Tissue-Resident Memory T Cells. *Immunity* (2014) 41(6):886–97. doi: 10.1016/j.jimmuni.2014.12.007
18. Park SL, Gebhardt T, Mackay LK. Tissue-Resident Memory T Cells in Cancer Immunosurveillance. *Trends Immunol* (2019) 40(8):735–47. doi: 10.1016/j.it.2019.06.002
19. Oja AE, Piet B, van der Zwan D, Blaauwgeers H, Mensink M, de Kivit S, et al. Functional Heterogeneity of CD4+ Tumor-Infiltrating Lymphocytes With a

the manuscript. HW and YZ collected clinical data. QS and XR revised the manuscript. All authors have commented on and approved the manuscript. HZ and HW contributed equally to this work. All authors contributed to the article and approved the submitted version.

## FUNDING

The work in this study was supported by a grant from the National Natural Science Foundation of China (Grant No. U20A20375).

## ACKNOWLEDGMENTS

We sincerely appreciate the colleagues in the Department of Pathology for their help in the pathological diagnosis and tumor section preparation. The authors would like to thank all the patients for their consent to participate in this study.

## SUPPLEMENTARY MATERIAL

The Supplementary Material for this article can be found online at: <https://www.frontiersin.org/articles/10.3389/fimmu.2022.877689/full#supplementary-material>

Resident Memory Phenotype in NSCLC. *Front Immunol* (2018) 9:2654. doi: 10.3389/fimmu.2018.02654

20. Gaudreau PO, Negrao MV, Mitchell KG, Reuben A, Corsini EM, Li J, et al. Neoadjuvant Chemotherapy Increases Cytotoxic T Cell, Tissue Resident Memory T Cell, and B Cell Infiltration in Resectable NSCLC. *J Thorac Oncol* (2021) 16(1):127–39. doi: 10.1016/j.jtho.2020.09.027

21. Ida S, Takahashi H, Kawabata-Iwakawa R, Mito I, Tada H, Chikamatsu K. Tissue-Resident Memory T Cells Correlate With the Inflammatory Tumor Microenvironment and Improved Prognosis in Head and Neck Squamous Cell Carcinoma. *Oral Oncol* (2021) 122:105508. doi: 10.1016/j.oraloncology.2021.105508

22. Savas P, Virassamy B, Ye C, Salim A, Mintoff CP, Caramia F, et al. Single-Cell Profiling of Breast Cancer T Cells Reveals a Tissue-Resident Memory Subset Associated With Improved Prognosis. *Nat Med* (2018) 24(7):986–93. doi: 10.1038/s41591-018-0078-7

23. Banchereau R, Chitre AS, Scherl A, Wu TD, Patil NS, de Almeida P, et al. Intratumoral CD103+ CD8+ T Cells Predict Response to PD-L1 Blockade. *J Immunother Cancer* (2021) 9(4):e002231. doi: 10.1136/jitc-2020-002231

24. Mori T, Tanaka H, Suzuki S, Deguchi S, Yamakoshi Y, Yoshii M, et al. Tertiary Lymphoid Structures Show Infiltration of Effective Tumor-Resident T Cells in Gastric Cancer. *Cancer Sci* (2021) 112(5):1746–57. doi: 10.1111/cas.14888

25. Yamaguchi K, Ito M, Ohmura H, Hanamura F, Nakano M, Tsuhashi K, et al. Helper T Cell-Dominant Tertiary Lymphoid Structures Are Associated With Disease Relapse of Advanced Colorectal Cancer. *Oncoimmunology* (2020) 9(1):1724763. doi: 10.1080/2162402X.2020.1724763

26. Posch F, Silina K, Leibl S, Mündlein A, Moch H, Siebenhüner A, et al. Maturation of Tertiary Lymphoid Structures and Recurrence of Stage II and III Colorectal Cancer. *Oncoimmunology* (2018) 7(2):e1378844. doi: 10.1080/2162402X.2017.1378844

27. Siliņa K, Soltermann A, Attar FM, Casanova R, Uckley ZM, Thut H, et al. Germinal Centers Determine the Prognostic Relevance of Tertiary Lymphoid Structures and are Impaired by Corticosteroids in Lung Squamous Cell Carcinoma. *Cancer Res* (2018) 78(5):1308–20. doi: 10.1158/0008-5472.CAN-17-1987

28. Gräbner R, Lötzer K, Döpping S, Hildner M, Radke D, Beer M, et al. Lymphotoxin Beta Receptor Signaling Promotes Tertiary Lymphoid Organogenesis in the Aorta Adventitia of Aged ApoE-/- Mice. *J Exp Med* (2009) 206(1):233–48. doi: 10.1084/jem.20080752

29. Fleige H, Ravens S, Moschovakis GL, Böltner J, Willenzon S, Sutter G, et al. IL-17-Induced CXCL12 Recruits B Cells and Induces Follicle Formation in BALT in the Absence of Differentiated FDCs. *J Exp Med* (2014) 211(4):643–51. doi: 10.1084/jem.20131737

30. Winkel HH, Lubbers JM, Arnold R, Prins TM, van der Vlies P, de Lange K, et al. A Transcriptionally Distinct Cxcl13+ Cd103+ Cd8+ T-Cell Population Is Associated With B-Cell Recruitment and Neoantigen Load in Human Cancer. *Cancer Immunol Res* (2019) 7(5):784–96. doi: 10.1158/2326-6066.CIR-18-0517

31. Li JP, Wu CY, Chen MY, Liu SX, Yan SM, Kang YF, et al. PD-1+ CXCR5- CD4+ Th-CXCL13 Cell Subset Drives B Cells Into Tertiary Lymphoid Structures of Nasopharyngeal Carcinoma. *J Immunother Cancer* (2021) 9(7):e002101. doi: 10.1136/jitc-2020-002101

32. Son YM, Cheon IS, Wu Y, Li C, Wang Z, Gao X, et al. Tissue-Resident CD4+ T Helper Cells Assist the Development of Protective Respiratory B and CD8+ T Cell Memory Responses. *Sci Immunol* (2021) 6(55):eabb6852. doi: 10.1126/sciimmunol.abb6852

33. Behr DS, Peitsch WK, Hametner C, Lasitschka F, Houben R, Schönhaar K, et al. Prognostic Value of Immune Cell Infiltration, Tertiary Lymphoid Structures and PD-L1 Expression in Merkel Cell Carcinomas. *Int J Clin Exp Pathol* (2014) 7(11):7610–21.

34. Linton PJ, Harbertson J, Bradley LM. A Critical Role for B Cells in the Development of Memory CD4 Cells. *J Immunol* (2000) 165(10):5558–65. doi: 10.4049/jimmunol.165.10.5558

**Conflict of Interest:** The authors declare that the research was conducted in the absence of any commercial or financial relationships that could be construed as a potential conflict of interest.

**Publisher's Note:** All claims expressed in this article are solely those of the authors and do not necessarily represent those of their affiliated organizations, or those of the publisher, the editors and the reviewers. Any product that may be evaluated in this article, or claim that may be made by its manufacturer, is not guaranteed or endorsed by the publisher.

Copyright © 2022 Zhao, Wang, Zhao, Sun and Ren. This is an open-access article distributed under the terms of the Creative Commons Attribution License (CC BY). The use, distribution or reproduction in other forums is permitted, provided the original author(s) and the copyright owner(s) are credited and that the original publication in this journal is cited, in accordance with accepted academic practice. No use, distribution or reproduction is permitted which does not comply with these terms.



# Neutrophil Extracellular Traps (NETs) Promote Non-Small Cell Lung Cancer Metastasis by Suppressing lncRNA MIR503HG to Activate the NF- $\kappa$ B/NLRP3 Inflammasome Pathway

Yong Wang<sup>1,2</sup>, Fen Liu<sup>3</sup>, Lin Chen<sup>4</sup>, Chen Fang<sup>1,2</sup>, Shuangyan Li<sup>2,3</sup>, Shangkun Yuan<sup>1,2</sup>, Xiaoying Qian<sup>1,2</sup>, Yan Yin<sup>5</sup>, Biao Yu<sup>1</sup>, Biqi Fu<sup>6</sup>, Xinwei Zhang<sup>1,2</sup> and Yong Li<sup>1\*</sup>

<sup>1</sup> Department of Medical Oncology, The First Affiliated Hospital of Nanchang University, Nanchang, China, <sup>2</sup> Medical Innovation Center, The First Affiliated Hospital of Nanchang University, Nanchang, China, <sup>3</sup> Critical Care Medicine, The First Affiliated Hospital of Nanchang University, Nanchang, China, <sup>4</sup> Department of Internal Neurology, The Second Affiliated Hospital of Nanchang University, Nanchang, China, <sup>5</sup> Department of Pathology, The First Affiliated Hospital of Nanchang University, Nanchang, China, <sup>6</sup> Department of Rheumatology, The First Affiliated Hospital of Nanchang University, Nanchang, China

## OPEN ACCESS

### Edited by:

Martin Hernán Bonamino,  
National Cancer Institute (INCA), Brazil

### Reviewed by:

Qing Deng,  
Purdue University, United States  
Armando Rojas,  
Catholic University of the Maule, Chile

### \*Correspondence:

Yong Li  
liyongcsco@email.ncu.edu.cn

### Specialty section:

This article was submitted to  
Cancer Immunity and Immunotherapy,  
a section of the journal  
Frontiers in Immunology

Received: 01 February 2022

Accepted: 02 May 2022

Published: 30 May 2022

### Citation:

Wang Y, Liu F, Chen L, Fang C, Li S, Yuan S, Qian X, Yin Y, Yu B, Fu B, Zhang X and Li Y (2022) Neutrophil Extracellular Traps (NETs) Promote Non-Small Cell Lung Cancer Metastasis by Suppressing lncRNA MIR503HG to Activate the NF- $\kappa$ B/NLRP3 Inflammasome Pathway. *Front. Immunol.* 13:867516. doi: 10.3389/fimmu.2022.867516

Neutrophil extracellular traps (NETs) that are produced in the tumour microenvironment (TME) have been suggested to play an essential role in the dissemination of metastatic cancer under multiple infectious and inflammatory conditions. However, the functions of NETs in promoting non-small cell lung cancer (NSCLC) metastasis and the underlying mechanisms remain incompletely understood. Here, we found that NETs promoted NSCLC cell invasion and migration by inducing epithelial to mesenchymal transition (EMT). To explore how NETs contribute to NSCLC metastasis, microarrays were performed to identify substantial numbers of long noncoding RNAs (lncRNAs) and mRNAs that were differentially expressed in NSCLC cells after stimulation with NETs. Interestingly, we observed that the expression of lncRNA MIR503HG was downregulated after NETs stimulation, and ectopic MIR503HG expression reversed the metastasis-promoting effect of NETs *in vitro* and *in vivo*. Notably, bioinformatics analysis revealed that differentially expressed genes were involved in the NOD-like receptor and NF- $\kappa$ B signalling pathways that are associated with inflammation. NETs facilitated EMT and thereby contributed to NSCLC metastasis by activating the NF- $\kappa$ B/NOD-like receptor protein 3 (NLRP3) signalling pathway. Further studies revealed that MIR503HG inhibited NETs-triggered NSCLC cell metastasis in an NF- $\kappa$ B/NLRP3-dependent manner, as overexpression of NF- $\kappa$ B or NLRP3 impaired the suppressive effect of MIR503HG on NETs-induced cancer cell metastasis. Together, these results show that NETs activate the NF- $\kappa$ B/NLRP3 pathway by downregulating MIR503HG expression to promote EMT and NSCLC metastasis. Targeting the formation of NETs may be a novel therapeutic strategy for treating NSCLC metastasis.

**Keywords:** neutrophil extracellular traps (NETs), NOD-like receptor protein 3 (NLRP3), MIR503HG, epithelial to mesenchymal transition (EMT), non-small cell lung cancer (NSCLC)

## INTRODUCTION

Non-small cell lung cancer (NSCLC), a common malignant tumour, is the leading cause of cancer-related death worldwide (1). Despite the application of various innovative therapeutic strategies, such as targeted therapy and immunotherapy, to treat NSCLC, the 5-year survival rate of NSCLC patients remains unsatisfactory (2). Among the main reasons for this are high rates of recurrence and metastasis after comprehensive treatment, in particular, after surgical resection (3). Therefore, understanding the detailed molecular mechanism underlying NSCLC metastasis is imperative for improving the quality of treatment and prolonging survival time.

The tumour microenvironment (TME) is composed of various cellular components, such as inflammatory and immune cells, and noncellular components, including the extracellular matrix (ECM), and the TME plays a crucial role in the spread of metastatic cancer (4, 5). Neutrophils, which are the most abundant immune cells, play an essential role in inflammatory responses but are reported to function as tumour accomplices that contribute to the progression and metastasis of cancer (6–8). Neutrophil extracellular traps (NETs), extensive extracellular web-like structures produced and released by activated neutrophils, are composed of modified decondensed chromatin and granule proteins and play an especially crucial role in recognizing and removing pathogens during host defence (9–12). Over the years, NETs induced by inflammation, surgical stress, or cancer cells have been found to accelerate tumour progression by promoting metastasis or forming cancer-associated thrombosis, and these findings have revealed the cancer-promoting function of NETs (13–17). Studies have suggested that NETs facilitate the spread of metastatic tumour cells and their colonization of host tissues by catching circulating tumour cells (CTCs) and accelerating angiogenesis (18, 19). Neutrophil infiltration and NETs formation in lung cancer patient tissues have been described, suggesting that NETs may play an important role in tumour progression (20, 21). NETs have been revealed to play pathophysiological roles in NSCLC progression and metastasis in several studies (18, 22, 23). Despite these findings, little is known about the molecular mechanisms underlying the promotion of NSCLC metastasis by NETs.

Long noncoding RNAs (lncRNAs) are defined as a novel class of transcripts that are over 200 nucleotides in length and have limited or no protein-coding potential (24). In recent studies, multiple pathophysiological diseases processes have been closely related to the dysfunction or abnormal expression of lncRNAs (25, 26). LncRNAs are involved in various cellular processes and regulate multiple cancer-related factors, such as genome stability, cell cycle, growth and immortality, apoptosis, progression, metastasis, and angiogenesis (27). At present, it is not clear whether NETs affect the expression of lncRNAs in tumour cells and promote the metastasis of tumour cells by regulating lncRNA expression. In our previous study, microarrays were used to explore the differential expression profiles of lncRNAs and mRNAs in NSCLC cells after stimulation with NETs (28, 29). Substantial numbers of differentially expressed lncRNAs and mRNAs were identified in NSCLC cells with and without NETs

treatment. However, little is known about the role of NETs in NSCLC metastasis and the detailed mechanism by which NETs regulate the expression of specific lncRNAs.

Inflammation is closely related to cancer, and metastasis is complicated by inflammation (29). NOD-like receptor pyrin domain-containing 3 (NLRP3), the most well-characterized and well-studied inflammasome complex, is usually activated by a diverse range of ‘danger signals’, and substantial evidence suggests that the NLRP3 inflammasome exerts a significant effect on the pathogenesis, development, and progression of a variety of tumours, including lung cancer, breast cancer, colon cancer and hepatocellular carcinoma (30, 31). To date, numerous studies have shown that lncRNAs regulate various physiological and pathological processes by targeting the NLRP3 inflammasome (32). Recent studies have also suggested that NETs can promote the pathological process of multiple diseases, including diabetes, autoimmune disease, and inflammation-related disease, by activating the NLRP3 inflammasome (33–35). However, the role of the NLRP3 inflammasome in the effect of NETs on promoting NSCLC metastasis is largely unclear.

Using bioinformatics analysis, we found that the expression of lncRNA MIR503HG was significantly downregulated, whereas overexpression of MIR503HG reversed the metastasis-promoting effect of NETs. NETs activated the nuclear factor- $\kappa$ B (NF- $\kappa$ B) and NOD-like receptor signalling pathways and facilitated epithelial to mesenchymal transition (EMT), thereby contributing to NSCLC metastasis. Further study revealed that NETs promoted NSCLC metastasis by regulating lncRNA MIR503HG expression to facilitate NF- $\kappa$ B/NLRP3 signalling pathway activation, and lncRNA MIR503HG and NLRP3 may be new targets for the treatment of NSCLC.

## MATERIALS AND METHODS

### Population and Specimens

The cancer tissues and adjacent noncancerous lung tissues of 50 NSCLC patients were acquired from the pathological specimen repository of The First Affiliated Hospital of Nanchang University, China. Time to metastasis was calculated based on the date of initial treatment to the date of investigator-assessed radiographic organ or node metastasis. The data were censored at the last follow-up or when patients died without metastasis.

### Cell Culture and Animal Study

The human bronchial epithelial cell lines (BEAS-2B) and human NSCLC cell lines A549 and SK-MES-1 were obtained from the Type Culture Collection of the Chinese Academy of Sciences (Shanghai, China). Both cell lines were grown in high-glucose Dulbecco's modified Eagle's medium (DMEM, BI, Israel) supplemented with 10% foetal bovine serum (FBS, Gibco, Grand Island, USA) and 1% penicillin and streptomycin solution (Solarbio, China) at 37°C in a 5% CO<sub>2</sub> humidified atmosphere.

The Ethics Committee of the Medical Innovation Center of the First Affiliated Hospital of Nanchang University approved the animal experimental protocol. Eight-week-old female SD

rats, and four-week-old female BALB/c nude mice were purchased from Hunan SJA Laboratory Animal Co., Ltd. The mice were fed under specific pathogen-free (SPF) conditions in accordance with the regulations of the institution.

## Neutrophil Isolation

Neutrophils were isolated from the peripheral blood of healthy donors and SD rats with the peripheral blood neutrophil extraction kit (Solarbio, China). Isolated primary neutrophils were maintained in RPMI 1640 medium (BI, Israel) supplemented with 10% FBS. Giemsa staining and trypan blue viability assays were utilized to determine neutrophil purity (> 98%) and vitality (> 95%).

## Formation and Visualization of NETs

Neutrophils were plated and allowed to adhere in 6-well plates for 1 h before treatment with 100 nM phorbol-12-myristate-13-acetate (PMA, Sigma, USA) for 4 h at 37°C in 5% CO<sub>2</sub>; this treatment allowed NETosis to occur. Then, based on the protocol recommended by previous studies (36), NETs were harvested following a multistep centrifugation protocol. For quantification, equivalent numbers of neutrophils (1×10<sup>7</sup>/well) grown in 6-well plates were stimulated with PMA (100 nM) for 4 h to generate NETs. Then, the supernatants were slowly and gently extracted and washed twice to remove impurities without disrupting the NETs. The supernatants containing NETs were collected and centrifuged to purify the NETs, which were finally stored at -80°C for subsequent experiments.

Paraffin-embedded lung tissues from NSCLC patients were cut into 5-μm-thick sections for Immunofluorescence assays. The paraffin sections were deparaffinized and rehydrated. The sections were heated in Tris/EDTA buffer (pH 9.0) for antigen retrieval. Isolated neutrophils were seeded on coverslips in 24-well plates. Then, both cells and thin sections of lung tissues were fixed, permeabilized, blocked and stained with primary antibodies against citrullinated histone H3 (cit-H3) (1:250, Abcam, ab5103, UK), myeloperoxidase (MPO) (1:50, Abcam, ab90810, UK) or Ly6g (1:100, Abcam, ab25377, UK) overnight at 4 °C with shaking, followed by incubation with secondary antibodies conjugated to Alexa Fluor 488 (1:200, Elabscience, China) and Alexa Fluor 594 (1:200, Elabscience, China) for 1 h at 37°C. The nuclei were stained with 4',6-diamidino-2-phenylindole (DAPI, Boster Biological Technology, China) for 5 min. Neutrophil-produced NETs were imaged by fluorescence microscopy (Zeiss) or confocal laser scanning microscopy (Leica) to assess their components. The colocalization of NETs with cit-H3, MPO, Ly6g or DNA was observed. The quantification of NETs was analyzed using Image J software.

## Microarray Analysis

Twelve hours after NETs stimulation, cells were treated with TRIzol (Invitrogen, Carlsbad, USA) and then sent to OE Biotech Co., Ltd. (Shanghai, China) for transcriptome RNA microarray analysis. A |log<sub>2</sub> (fold change)| ≥ 2 and *P* < 0.01 were used as the thresholds to determine whether lncRNA expression was upregulated or downregulated. Volcano plots and heatmaps showing differential lncRNAs were generated with R soft and

related Bioconductor packages. The top 20 upregulated signalling pathways were identified by Kyoto Encyclopedia of Genes and Genomes (KEGG) analyses.

## In Vivo Tumour Metastasis Assay

MIR503HG-overexpressing and empty vector A549 cells were stimulated with NETs the day before the mouse metastasis model was established. These two kinds of A549 cells (2 × 10<sup>6</sup>/mouse) were injected into BALB/c nude mice through the tail vein. After 8 weeks, the mice were euthanized, and the lungs were collected and subjected to H&E and histological staining. Metastasis burden, number of metastasized tumours, volume, and maximum size were evaluated.

## Immunohistochemistry

Paraffin-embedded lung tissues from the above mouse model were cut into 5-μm-thick sections for immunohistochemical (IHC) analysis. Briefly, the paraffin sections were deparaffinized and rehydrated. The sections were heated in Tris/EDTA buffer (pH 9.0) for antigen retrieval and incubated in 3% hydrogen peroxide for 10 min at room temperature to block endogenous peroxidase activity. For IHC staining, the primary antibodies anti-N-cadherin (1:50, Abcam, ab76011, UK), anti-E-cadherin (1:200, Proteintech, 20874-1-AP, China), and anti-vimentin (1:200, Abcam, Ab92547, UK) were incubated with the tissue samples overnight at 4°C. Images of the IHC-stained slides were visualized and analysed at 100× and 400× magnification utilizing an ordinary optics microscope (Zeiss).

## Immunofluorescence Assays

A549 and SK-MES-1 cells were seeded on coverslips in 24-well plates overnight. After preprocessing, the cells were fixed with 4% paraformaldehyde (Solarbio, Beijing, China) for 20 min and permeabilized with 0.5% Triton X-100 (Solarbio, China) for 15 min at room temperature. After blocking with 5% goat serum for 1 h at room temperature, the cells were incubated with primary antibodies against NLRP3 (1:50, Proteintech, 19771-1-AP, China), Caspase1 (1:50, Proteintech, 22915-1-AP, China), and p50 (1:200, Cell Signaling Technologies, 13586, USA) overnight at 4°C with shaking. The cells were incubated with Alexa Fluor 488-conjugated secondary antibodies (1:200, Elabscience, China) for 1 h at 37 °C. The nuclei were stained with DAPI (Boster Biological Technology, China) for 5 min. The samples were visualized by fluorescence microscopy (Zeiss) or confocal laser scanning microscopy (Olympus).

## Reactive Oxygen Species Assay

ROS in A549 and SK-MES-1 cells were evaluated by using the ROS assay kit (Elabscience, China). Briefly, NSCLC cells after preprocessing were incubated with 10 μM 2,7-dichlorodihydrofluorescein diacetate (DCFH-DA) protected from light at 37°C for 30 min, and then followed by washing with PBS to remove excess fluorescence probe. The active cell nucleus was stained using Hoechst 33342. Fluorescence microscopy (Zeiss) was applied to test the fluorescence intensities in NSCLC cells.

## Enzyme-Linked Immunosorbent Assay

The human IL-1 $\beta$  and IL-18 ELISA kit (Boster Biological Technology, China) was performed to assess the level of IL-1 $\beta$  and IL-18 in NSCLC cells supernatant according to the manufacturer's instructions. Brief, the culture medium was collected after the removal of cell debris by centrifugation at a speed of 1000 $\times$ g for 10 min. The level of IL-1 $\beta$  and IL-18 in supernatants were analyzed by ELISA kit. Absorbance at 450 nm was detected with a microplate reader (ThermoScientific).

## Subcellular Fractionation

NE-PER Nuclear and Cytoplasmic Extraction Reagents (Thermo Fisher Scientific, 78833, USA) were used to determine the MIR503HG location in A549 and SK-MES-1 cells. According to the instructions of the kit, briefly, dry cells were collected in 1.5-mL microcentrifuge tubes (1-10 $\times$ 10<sup>6</sup> cells/tube) and washed with PBS, and ice-cold mixture that contained Cytoplasmic Extraction Reagent (CER I), CER II and Nuclear Extraction Reagent (NER) (200:11:100  $\mu$ L) was added. The tubes were vigorously vortexed at the highest setting and centrifuged at 16,000  $\times$ g for 5 min; then, the supernatant was transferred to a new tube. The above steps were repeated once more, and the extracts were obtained. All the steps were performed on ice, and then, the samples were purified using the FastPure<sup>®</sup> Cell/Tissue RNA Isolation Kit V2 (Vazyme, Nanjing, China) following the manufacturer's protocol to isolate the nuclear and cytoplasmic RNA. GAPDH (predominantly in the cytoplasm) and U6 (enriched in the nucleus) were used as controls.

## Transient Transfection

A549 and SK-MES-1 cells were seeded in dishes at an appropriate density and cultured in a 37°C incubator overnight. The cells were transfected with plasmids and siRNAs with Hieff Trans liposomal transfection reagent (Yeasen, Shanghai, China) according to the manufacturer's instructions. The cells were collected 24-48 h after transfection for Western blotting or qRT-PCR analysis.

The NLRP3 expression plasmid was purchased from Vigene Biosciences (Shandong, China). The p50-pcDNA3.1 plasmids were generated by inserting the full-length sequence of p50 cDNA, which was amplified by PCR, into the pcDNA3.1 vector, and then, the constructed p50-pcDNA3.1 plasmid was sent to Genewiz Biotechnology Co. Ltd. (Suzhou, China) for DNA sequencing. siRNAs targeting p50, MIR503HG and the negative controls were designed and synthesized by Gemar Pharmaceutical Technology Co. Ltd. (Shanghai, China). The sequences are as follows:

p50-siRNA-1: 5'-GCUAUAAUCCUGGACUCUUTT-3';

p50-siRNA-2: 5'-GCAAUCAUCCACCUUCAUUTT-3'.

MIR503HG-siRNA-1: 5'-CCUCUCCCACCAUUUCUU  
UTT-3';

MIR503HG-siRNA-2: 5'-GACAAGAACUAAAGUGGAA  
TT-3';

## Quantitative Real-Time Polymerase Chain Reaction

Total RNA was harvested using the FastPure<sup>®</sup> Cell/Tissue Total RNA Isolation Kit V2 (Vazyme, Nanjing, China) following the

manufacturer's protocol. Real-time quantitative polymerase chain reaction (RT-qPCR) analyses were conducted utilizing a SYBR Green Kit (TransGen Biotech, Beijing, China). The 20- $\mu$ L qRT-PCR mixture included 10  $\mu$ L of 2 $\times$  PCR master mix, 1  $\mu$ L of 10  $\mu$ M primers, 7  $\mu$ L of RNase-free water, and 2  $\mu$ L of the reverse-transcription template. The qRT-PCR amplification conditions were as follows: 95°C for 10 min, followed by 40 cycles at 95°C for 5 s and 60°C for 30 s. Human GAPDH was utilized as an internal control. The sequences of the PCR primers are provided in **Supplementary Table 1**.

## Western Blotting Analysis

Equal amounts of proteins were used for sodium dodecyl sulfate-polyacrylamide gel electrophoresis (SDS-PAGE). The proteins were transferred to a polyvinylidene fluoride membrane (PVDF, Merck Millipore, Darmstadt, Germany). The membranes were incubated with 5% buttermilk for 1 h at 25°C and then incubated with primary antibodies at 4°C overnight with gentle shaking. The primary antibodies included anti-N-cadherin (ab76011), anti-Vimentin (ab92547), anti-cit-H3 (ab5103), (1:1000, Abcam, UK), anti-NLRP3 (19771-1-AP), anti-E-cadherin (20874-1-AP), anti-Caspase1 (22915-1-AP), anti-GAPDH (60004-1-Ig) (1:1000, 1:5000, 1:1000, and 1:20000 Proteintech, China), anti-p50 (1:1000, Cell Signaling Technologies, 13586, USA), anti-p-p50 (sc-271908), anti-p65 (sc-8008), anti-p-p65 (sc-136548) (all at 1:500, Santa Cruz Biotechnology, USA), and anti-Histone H3 (1:1000, ImmunoWay Biotechnology, YT2163, USA). The next day, the membranes were incubated with horseradish peroxidase-conjugated secondary antibodies specific for rabbit or mouse primary antibodies (Proteintech, China) at a dilution of 1:2000 at 25°C for 1 h. The protein bands were detected utilizing ECL Detection Reagents (Proteintech, China).

## Transwell Invasion and Wound Healing Assay

For the cell invasion assay, the upper chamber of the Transwell 24-well plates (8  $\mu$ m pores, Corning, NY, USA) was coated with 5% Matrigel (Corning, NY, USA). A549 and SK-MES-1 cells (6 $\times$ 10<sup>4</sup>) suspended in 200  $\mu$ L of serum-free medium were plated in the upper chamber after treatment. The lower chambers were filled with 600  $\mu$ L of culture medium supplemented with 10% FBS. The NSCLC cells were permitted to invade through the Matrigel for 48 h, and the cells on the bottom side of the membrane were fixed using 4% paraformaldehyde, the cells on the upper surface were removed with cotton swabs, and then, the invaded cells were with crystal violet. The numbers of invaded cells were counted in five random fields under an optical microscope with ImageJ software.

For wound healing assays, treated cells were incubated in 6-well culture plates and grown to approximately 90% confluence. Scratches were manually established in the cell monolayers with a P200 pipette tip, which guaranteed that all wound widths were consistent. PBS was used to remove cell debris, and then, the scratched cells were cultured in medium supplemented with 1% serum that eliminated the effects of cell proliferation on migration. The wounds in three random fields were

photographed at 0 h and 36 h, and the wound widths were measured with ImageJ software.

## Statistical Analysis

The data are shown as the mean  $\pm$  standard deviation (SD). Statistical analysis was performed using Student's t test or one-way analysis of variance (ANOVA) to compare the means between two groups or multiple groups, respectively, followed by the nonparametric Wilcoxon rank sum test. The risk of NSCLC patient metastasis was determined with the Kaplan-Meier method. All the analyses were performed using GraphPad Prism 8.0.2 software (San Diego, CA, USA).  $P < 0.05$  was considered to be statistically significant.

## RESULTS

### The Release of NETs by Neutrophils Promotes the Metastasis of NSCLC *In Vitro*

To investigate whether released NETs are differentially expressed between healthy donors (HD) and NSCLC, we first isolated neutrophils from the blood of HD or NSCLC and observed the cell nuclear morphology by Giemsa staining to estimate neutrophil purity. Under the microscope, we observed the bulk multilobular nucleus of neutrophils (Figure 1A). Trypan blue dye exclusion assays revealed that the neutrophil viability was  $> 97\%$  (Figure 1B). We observed that neutrophils isolated from NSCLC patients spontaneously generated NETs, whereas neutrophils from HD produced fewer NETs by immunofluorescence. The capacity of NETs formation from NSCLC patients was higher than HD (Figure 1C). We further detected the formation of NETs in NSCLC clinical tissue specimens by immunofluorescence staining. We found that NETs were largely accumulated in the NSCLC tumor tissues, while fewer NETs were formed in normal lung tissues (Figure 1D). Activated neutrophils exhibited NETs formation under specific conditions. Freshly isolated neutrophils were evenly seeded in 6-well plates at  $1 \times 10^7$ /well and stimulated with 100 nM PMA for 4 h. After 4 h of PMA stimulation, light cloud-like substances appeared at the bottom of the 6-well plates. To further confirm whether these structures were NETs, several well-recognized NETs markers, including MPO and cit-H3, were measured by immunofluorescent staining. These markers were more highly expressed after PMA stimulation, and the structures were almost destroyed by treatment with DNase I (Figure 1E). In addition, we observed the colocalization of these protein markers with extracellular spider mesh-like DNA around neutrophils.

According to a previous study, the effect of NETs on tumours is not limited to their ability to physically capture cells (37). To explore the potential impact of NETs on the metastasis behaviour of NSCLC, NSCLC cells (A549 and SK-MES-1) were cocultured with PMA-induced NETs, DNase I, or NETs and DNase I together. The invasion assay results showed that NETs significantly promoted the number of invaded NSCLC cells, and these effects were abrogated by DNase I treatment, as the DNA

structures of the NETs were digested by DNase I (Figure 1F). Moreover, this phenomenon was also observed in wound healing assays; isolated NETs promoted the migration of A549 and SK-MES-1 cells (Figure 1G). To investigate the possibility that NETs might induce a switch from epithelial to mesenchymal properties, the expression of EMT marker proteins was evaluated. As shown in Figure 1H, NETs promoted the EMT process of NSCLC cells, which was characterized by decreased expression of epithelial markers, such as E-cadherin, and increased expression of mesenchymal markers, such as N-cadherin and vimentin. This effect was suppressed by the digestion of NETs with DNase I (Figure 1H). These data suggest that PMA-induced neutrophil NETs formation contributes to the metastatic potential of NSCLC cells.

### LncRNA MIR503HG Expression is Downregulated in NSCLC Cells Stimulated With NETs and is Associated With Poor Survival of NSCLC

To identify candidate lncRNAs that participate in the pro-metastasis effect of NETs, a transcriptome RNA microarray analysis of A549 cells treated with NETs was performed. We identified 99 differentially expressed lncRNAs (fold change  $\geq 4$  and  $P < 0.01$ ), of which 59 were upregulated and 40 were downregulated in the NETs-treated group compared to the untreated group (Figure 2A). According to bioinformatics analysis, the expression of lncRNA MIR503HG was downregulated in the NETs-stimulated A549 cell group (Figure 2B). We investigated the expression of MIR503HG in NETs-stimulated NSCLC cells (A549 and SK-MES-1 cells) by qRT-PCR. Consistently, the expression level of MIR503HG was dramatically lower ( $P < 0.01$ ) in both A549 and SK-MES-1 cells treated with NETs for 12 h than in the control cells (Figure 2C), which was consistent with the data generated from our microarray analysis.

To further examine the clinicopathological and prognostic implications of MIR503HG in patients with NSCLC, we next assessed tumour tissue data of NSCLC patients in The Cancer Genome Atlas (TCGA) and demonstrated decreased expression of MIR503HG in both lung adenocarcinoma (LUAD) and lung squamous cell carcinoma (LUSC) tissues compared to the corresponding adjacent normal lung tissues (Figure 2D). Then, we analysed the expression of MIR503HG in 50 pairs of NSCLC tissues and corresponding normal tissues from our cohort by qRT-PCR. Our results showed that the expression of MIR503HG was significantly downregulated ( $P < 0.01$ ) in NSCLC tissues compared to the corresponding adjacent normal tissues (Figure 2E). The Kaplan-Meier analysis revealed that NSCLC patients with a lower level of MIR503HG had a higher ( $P = 0.045$ ) risk of metastasis (Figure 2F). These data indicate that MIR503HG was expressed at low levels in NSCLC tissues or stimulated NETs and might act as a tumour suppressor.

To explore the underlying mechanism by which lncRNA MIR503HG functions in NSCLC, we subsequently explored the subcellular distribution of MIR503HG by subcellular fractionation and qRT-PCR analyses. The results of qRT-PCR, using GAPDH and U6 as controls, showed that MIR503HG was primarily located in the nucleus of A549 and SK-MES-1 cells (Figure 2G).

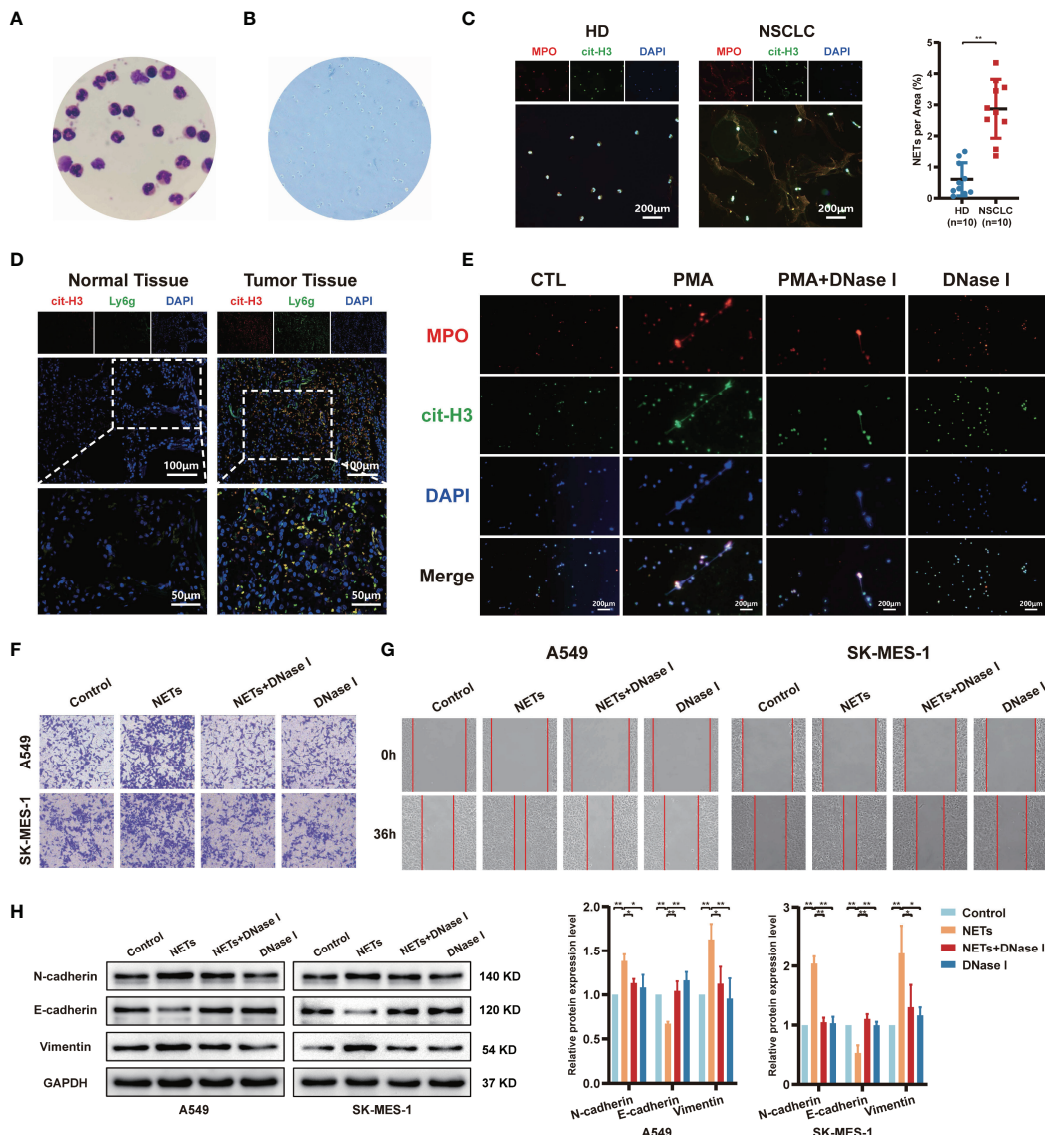


**FIGURE 1 |** The release of neutrophil extracellular traps (NETs) by neutrophils promotes migration and invasion of NSCLC. **(A)** The morphology of neutrophils isolated from healthy donors' blood was observed by Giemsa staining (magnification, 1000x). **(B)** The neutrophil viability was assessed by trypan blue dye exclusion assays (magnification, 100x). **(C)** Representative images and quantification of NETs formation of neutrophils from healthy donors (HD) and NSCLC patients. MPO (red), cit-H3 (green), and DAPI (blue), respectively (magnification, 50x; scale bar, 200μm). **(D)** Representative images of NETs formation in NSCLC patients' normal lung tissues and tumor tissues that were detected by con-focal microscopy. cit-H3 (red), Ly6g (green), and DAPI (blue), respectively (magnification, 200x; scale bar, 100μm and magnification, 400x; scale bar, 50μm). **(E)** Representative images of PMA-induced NETs formation of neutrophils from HD stained with MPO and cit-H3 were detected by immunofluorescence microscope; MPO (red), cit-H3 (green), and DAPI (blue), respectively (magnification, 50x; scale bar, 200μm). Transwell invasion **(F)** and wound healing assays **(G)** were performed to identify the effects of NETs on A549 and SK-MES-1 cells invasion (magnification, 100x) and migration (magnification, 50x). **(H)** Western blot analyzing the expressions levels of EMT markers protein (N-cadherin, E-cadherin, and Vimentin) in A549 and SK-MES-1 cells treated with NETs. (\*P < 0.05, \*\*P < 0.01).

## Overexpression of MIR503HG Substantially Reverses the Metastasis-Promoting Effect of NETs on NSCLC *In Vitro* and *In Vivo*

To fully understand the effect of MIR503HG on NETs metastasis promotion, we further detected the migration, invasion and EMT of NSCLC cells overexpressing MIR503HG. MIR503HG was

overexpressed in A549 and SK-MES-1 cells *via* a stable retroviral expression system, and its overexpression was validated by qRT-PCR (Figure 3A). We also examined the expression of MIR503HG in normal human bronchial epithelial cell lines (BEAS-2B), NSCLC cells and cells overexpressed. We found that MIR503HG is generally overexpressed in BEAS-2B compared to NSCLC cell lines

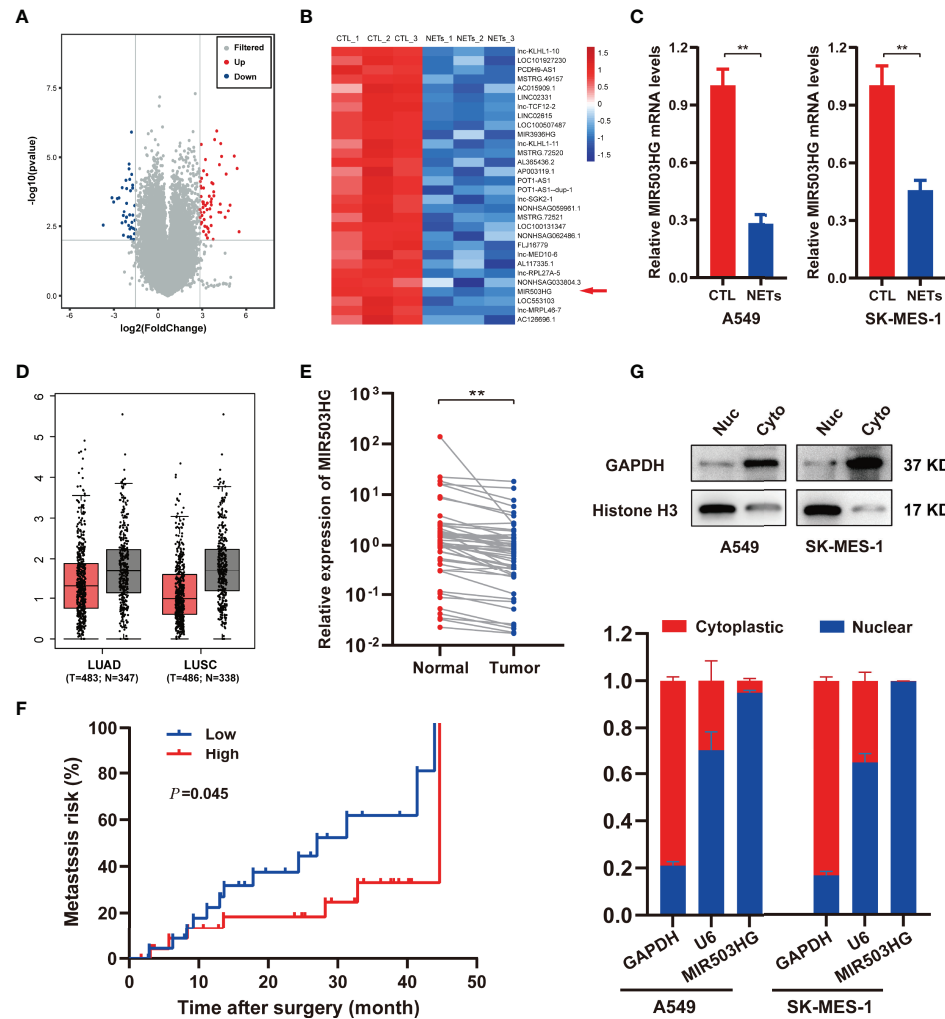


**FIGURE 2 |** MIR503HG is downregulated in NSCLC cells with NETs stimulation and is associated with poor survival of NSCLC. **(A)** Volcano plot illustrating the differentially expressed lncRNAs in A549 cells treated with or without NETs for 12 h ( $|\log_2$  fold change (FC)|  $> 2$ ,  $P$ -value  $< 0.01$ ). **(B)** Heat map showing the top 30 differentially down-regulated lncRNAs in A549 cells after treatment with NETs for 12 h. Red means up-regulated, blue means down-regulated, separately. **(C)** Relative expression of MIR503HG in A549 and SK-MES-1 cells with or without NETs stimulation. **(D)** MIR503HG is expressed at a lower level in both lung adenocarcinoma (LUAD) and lung squamous cell carcinoma (LUSC) tumor compared to corresponding adjacent normal lung tissues according to the TCGA database. **(E)** The expression of MIR503HG in 50 paired NSCLC tumors and normal tissues were quantified by qRT-PCR. **(F)** Kaplan-Meier analysis of metastasis risk of 50 NSCLC patients divided into two groups based on a middle cutoff of MIR503HG expression. **(G)** MIR503HG is mainly located in the nuclear of NSCLC cells. U6 snRNA (nuclear reserved) and GAPDH mRNAs (exposed to cytoplasm) were used as controls. Data are mean  $\pm$  SD (n=3). (\* $P$   $< 0.05$ ; \*\* $P$   $< 0.01$ ).

(Figure S1A). Wound healing assays showed that MIR503HG overexpression significantly impaired the NETs-induced migration abilities of NSCLC cells (Figure 3B). Similarly, Transwell assays revealed that MIR503HG overexpression inhibited the invasion abilities of cells treated with NETs (Figure 3C). Furthermore, the results showed that the expression of the EMT-related epithelial marker E-cadherin was increased but that of the mesenchymal markers N-cadherin and Vimentin was decreased in MIR503HG-overexpressing cells treated with NETs (Figure 3D). However, we did not observe significant changes for those markers in siRNA MIR503HG knockdown BEAS-2B cells (Figures S1B, C).

To explore the potential inhibitory effect of MIR503HG on NETs-induced NSCLC cell metastasis *in vivo*, MIR503HG-overexpressing NSCLC cells and the corresponding control NSCLC cells were treated with NETs one day before intravenous injection. Then, NETs-treated tumour cells were injected into mice *via* the tail vein, and the mice were sacrificed after 8 weeks (Figure 3E). The number of nodules on the surfaces of the lungs was counted (Figure 3F), and the presence of metastatic nodules inside the lung and the tumour size were also confirmed by H&E staining (Figure 3G). MIR503HG significantly reduced the NETs-induced lung metastasis of cancer cells. We quantified three features of tumours, namely,

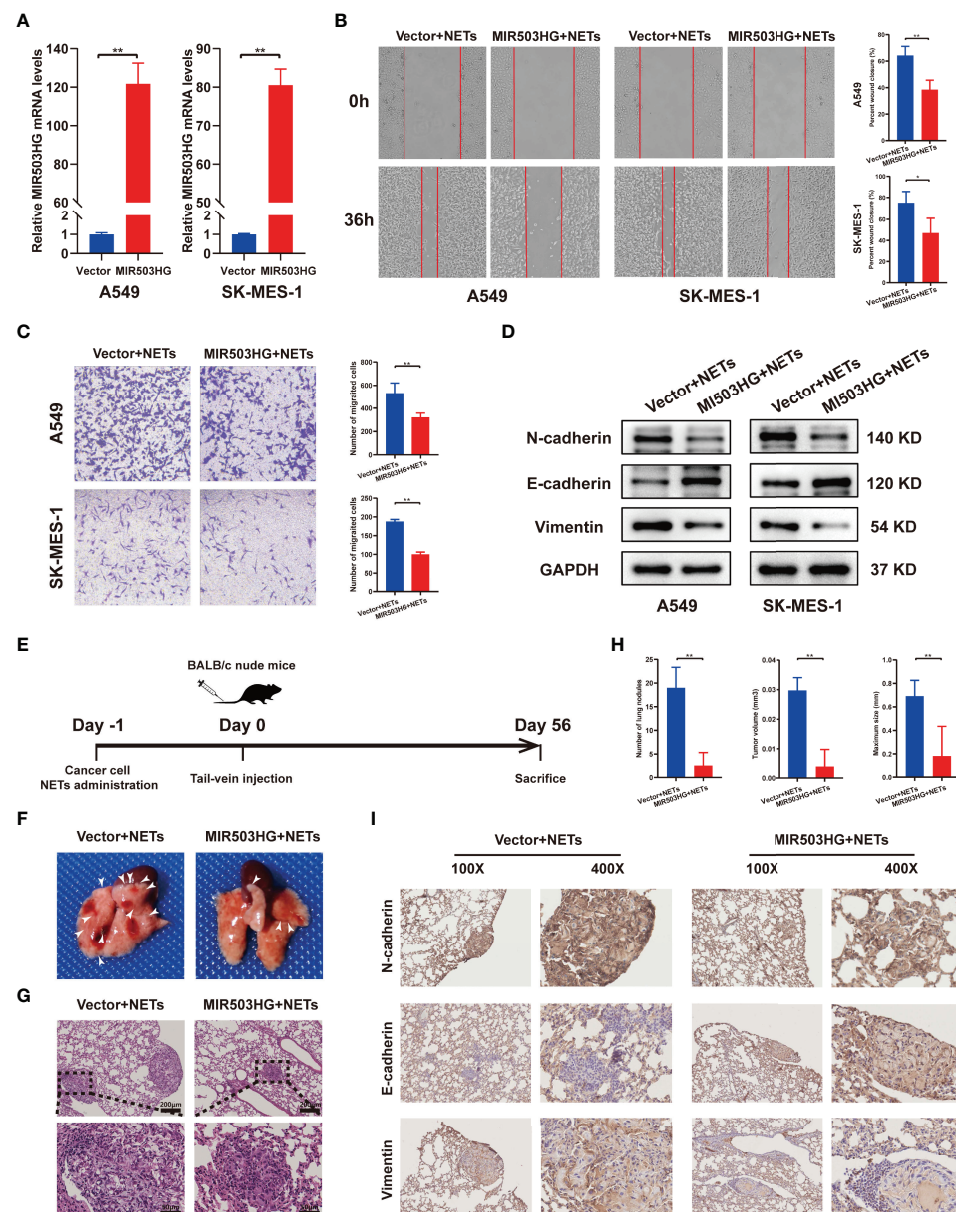


**FIGURE 3** | Overexpression of MIR503HG substantially reversed the metastasis-promoting effect of NETs on NSCLC *in vitro* and *in vivo*. **(A)** Expression of MIR503HG was successfully up-regulated in A549 and SK-MES-1 cells. **(B, C)** Wound healing (magnification, 50 $\times$ ) and invasion assays (magnification, 100 $\times$ ) of NSCLC cells that stable transfection of MIR503HG vector versus control vector both treat with NETs 12 h. **(D)** Western blot analysis of the expression of EMT (N-cadherin, E-cadherin, Vimentin) in control and MIR503HG overexpressing A549 and SK-MES-1 cells after NETs treated 12 h. **(E)** Schematic diagram showing the experimental design of the effect of MIR503HG on NETs-induced metastasis. Representative images of the gross lung **(F)** and H&E staining **(G)** of metastatic lung nodules in mice specimens. **(H)** Quantification of the number, volume, and maximum size of metastatic lung nodules. Data are mean  $\pm$  SD (n=5 nude mice in each group). (magnification, 100 $\times$ ; scale bar, 200  $\mu$ m, magnification, 200 $\times$ ; scale bar, 50  $\mu$ m). **(I)** Immunohistochemistry (IHC) detection of N-cadherin, E-cadherin, and Vimentin revealed EMT formation in the NETs-induced lung metastasis model (magnification, 100 $\times$  and 400 $\times$ ). (\*\*P < 0.01).

the number of nodules, tumour volume, and maximum size, to estimate the burden of lung metastasis. The results revealed that all these measures were significantly decreased compared with those in the control mice (**Figure 3H**). Furthermore, the results of IHC staining of tumour tissues suggested that the rate of E-

cadherin positivity was increased and N-cadherin and vimentin expression was decreased in the groups with stable MIR503HG expression (**Figure 3I**). All these results suggest that MIR503HG could reverse the facilitation of NSCLC metastasis by NETs both *in vitro* and *in vivo*.

## NETs Promote the Migration and Invasion of NSCLC by Activating the NLRP3 Inflammasome

NETs formation could induce the release of large amounts of cytokines, and inflammasomes are considered key mediators of this process in tumour cells. Nevertheless, inflammasomes have also been shown to suppress the antitumour immune response and play a vital role in tumour cell migration and invasion (38). KEGG pathway analyses of the differentially expressed genes suggested that NETs triggered responses associated with inflammation, including the NOD-like receptor signalling pathway and NF- $\kappa$ B signalling pathway (Figure 4A). qRT-PCR was performed to validate the RNA microarray data (Figure 4B; Figure S2A). The expression of a set of NLRP3 inflammasome-associated genes, including NLRP3, Caspase1, IL-1 $\beta$ , and IL-18, was upregulated in a time-dependent manner. NETs stimulation for 12 h induced the most significant increase in the expression levels of NLRP3, Caspase1, and IL-18 compared to the other groups, while IL-1 $\beta$  reached its highest expression levels after NETs stimulation for 24 h ( $P < 0.05$ ). We further validated the protein expression levels of NLRP3 and Caspase1 by Western blotting, and the results were consistent with the qRT-PCR results (Figure 4C). Immunofluorescence staining also supported the idea that NETs treatment could increase NLRP3 and Caspase1 expression in NSCLC cells (Figure S2B). Compared with the control group, the results of ELISA showed that the secretion level of IL-1 $\beta$  and IL-18 in the NSCLC cells supernatant of the NETs-treated group increased obviously (Figure S2C). Then, we used DCFH-DA to examine the effect of NETs on ROS levels in the intracellular. Intracellular ROS levels in both A549 and SK-MES-1 were significantly elevated after 12 h of NETs stimulation (Figure 4D). We next examined the role of NLRP3 inflammasomes by treating cells with the NLRP3 receptor-specific small molecule inhibitor MCC950 before NETs treatment. The results showed that MCC950 treatment before NETs treatment significantly decreased the mRNA expression levels of NLRP3 inflammasome-related genes (Figure 4E) and decreased the protein expression levels of NLRP3 and Caspase1 (Figure 4F). As expected, MCC950 reversed the protein expression levels of EMT-related markers after NETs treatment (Figure 4G). In the Transwell and wound healing assays, the number of invasive and migratory NETs-treated NSCLC cells was significantly decreased by treatment with MCC950 compared with the NSCLC cells treated with NETs alone (Figures 4H, I). Taken together, these results suggested that NLRP3 inflammasomes contribute to NETs-mediated metastasis promotion in NSCLC.

## NLRP3 Inflammasome Mediates the Effect of MIR503HG on the Inhibition of NETs-Triggered NSCLC Metastasis

Next, we investigated whether MIR503HG inhibited the NETs-triggered metastasis of NSCLC by affecting the NLRP3 inflammasome. We first examined the protein and mRNA expression levels of NLRP3 inflammasome components in MIR503HG-overexpressing A549 and SK-MES-1 cells treated

with NETs. Our Western blotting results revealed that the expression of NLRP3 and Caspase1 was significantly decreased ( $P < 0.05$ ) when MIR503HG was overexpressed in NETs-stimulated NSCLC cells (Figure 5A). Examination of NLRP3 and Caspase1 mRNA expression by qRT-PCR also confirmed these results (Figure 5B). The mRNA expression of lncRNA MIR503HG was negatively associated with NLRP3 expression in NETs-treated NSCLC cells (Figure 5C). A549 and SK-MES-1 cells were transfected with NLRP3-pENTER or empty vector, and the levels of NLRP3 were validated by Western blotting (Figure S3A). Then, we transfected NLRP3-pENTER into NSCLC cells stably overexpressing MIR503HG and treated these cells with NETs. NLRP3-pENTER transfection abolished the downregulation of the N-cadherin and vimentin protein levels and the upregulation of the E-cadherin level in the two cell lines overexpressing MIR503HG (Figure 5D). Transwell and wound healing assays also indicated that the overexpression of NLRP3 restored the NSCLC cell invasion and migration abilities that had been inhibited by MIR503HG overexpression (Figures 5E, F). These results indicated that MIR503HG might indirectly or directly regulate the expression of NLRP3 inflammasome components, and the NLRP3 inflammasome mediated the effect of MIR503HG on the inhibition of NETs-triggered NSCLC metastasis.

## NETs-Induced NLRP3 Inflammasome Activation Promotes NSCLC Progression and is Associated With the Activation of NF- $\kappa$ B

Activation of the NLRP3 inflammasome is associated with the NF- $\kappa$ B signalling pathway. The NF- $\kappa$ B pathway is one of the most important signalling pathways, and this pathway upregulates NLRP3 and pro-IL-1 protein expression (39). In addition, KEGG analysis revealed that the NF- $\kappa$ B signalling pathway ranked in the top 20 pathways in our NETs-stimulated A459 microarray data (Figure 4A). To further investigate whether NF- $\kappa$ B was involved in promoting the NETs-induced expression of NLRP3 inflammasome components, we first examined whether the NF- $\kappa$ B signalling pathway was activated in A549 and SK-MES-1 cells after NETs treatment. Our results showed that NETs treatment increased the phosphorylation of NF- $\kappa$ B (p-p50 and p-p65), and this effect was entirely abolished by DNase I treatment (Figure 6A). Furthermore, confocal microscopy showed that the translocation of p50 into the nucleus was increased by NETs and inhibited by DNase I (Figure 6B). This result indicated that NETs activated the NF- $\kappa$ B signalling pathway in NSCLC cells. To further verify the role of NF- $\kappa$ B in the NETs-induced expression of NLRP3 inflammasome-related proteins, we designed p50-siRNA to knockdown p50 expression in A549 and SK-MES-1 cells and validated the levels of p50 by Western blotting and qRT-PCR (Figures S3B, C). P50-siRNA significantly suppressed the expression of NLRP3 and Caspase1 in NETs-stimulated NSCLC cells, as shown by immunofluorescence (Figure 6C and Figure S3D). Similarly, Western blotting analysis showed that the expression of NLRP3 inflammasome-related proteins in NETs-stimulated NSCLC cells was decreased when the cells were transfected with p50-siRNA.

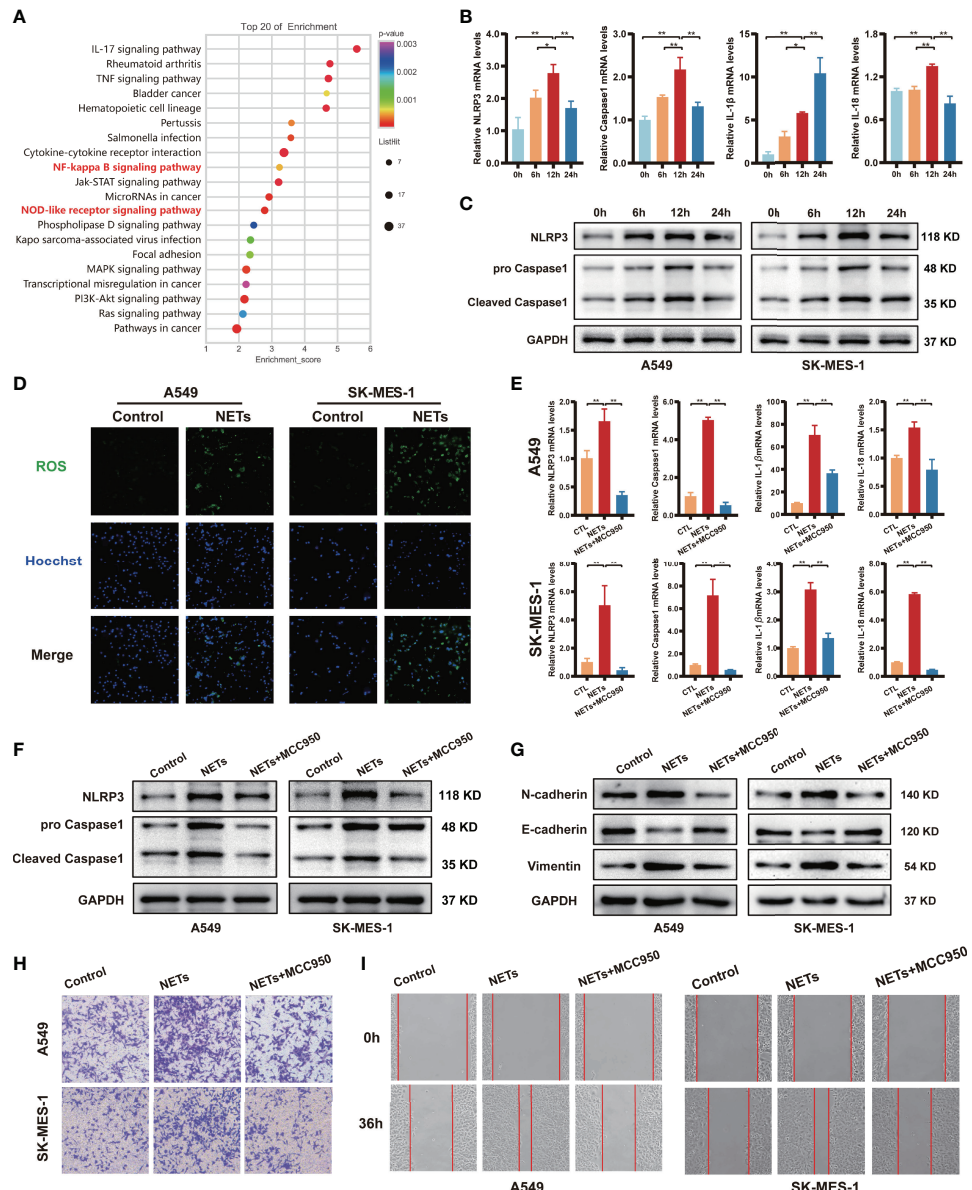


**FIGURE 4 |** NETs promote migration and invasion of NSCLC by activating the NLRP3 inflammasome. **(A)** Up-regulated NSCLC-related pathways in response to NETs stimulation revealed by KEGG enrichment. **(B)** The mRNA expression of NLRP3, Caspase1, IL-1 $\beta$  and IL-18 in A549 cells was analyzed by qRT-PCR after NETs stimulation at different times. **(C)** Western blotting was used to analyze the expression of NLRP3 and Caspase1 in A549 and SK-MES-1 cells after NETs stimulation for different periods. **(D)** Immunofluorescence was used to observe the expression of ROS in A549 and SK-MES-1 cells treated with NETs for 12 h (magnification, 100 $\times$ ). The expression of NLRP3, Caspase1, IL-1 $\beta$  and IL-18 were detected by qRT-PCR **(E)** and Western blot **(F)** in A549 and SK-MES-1 cells after treating with NETs and NLRP3 inflammasome inhibitor MCC950, respectively. **(G–I)** Estimate the effect of NETs on the level of N-cadherin, E-cadherin, and Vimentin (Western blot) **(G)** in A549 and SK-MES-1 cells and the capacity of invasion (transwell invasion assays; magnification, 100 $\times$ ) **(H)**, migration (wound healing assays; magnification, 50 $\times$ ) **(I)** when inhibiting the expression of the NLRP3 inflammasome by MCC950. (\* $P$  < 0.05, \*\* $P$  < 0.01).

compared to the negative control (Figure 6D). We further assessed the effect of NETs on the levels of EMT-related proteins and the metastatic ability of NSCLC cells after p50 expression was knocked down. Silencing p50 expression with p50-siRNA reversed the NETs-induced expression of EMT-related proteins (Figure 6E). Furthermore, the invasion and wound healing assay results showed

that the number of invaded and migrated NSCLC cells after NETs treatment was decreased by the downregulation of p50 expression (Figures 6F, G). These results confirmed that NETs triggered the expression of NLRP3 inflammasome components and enhanced the metastatic ability of NSCLC cells *via* activation of the NF- $\kappa$ B signalling pathway.

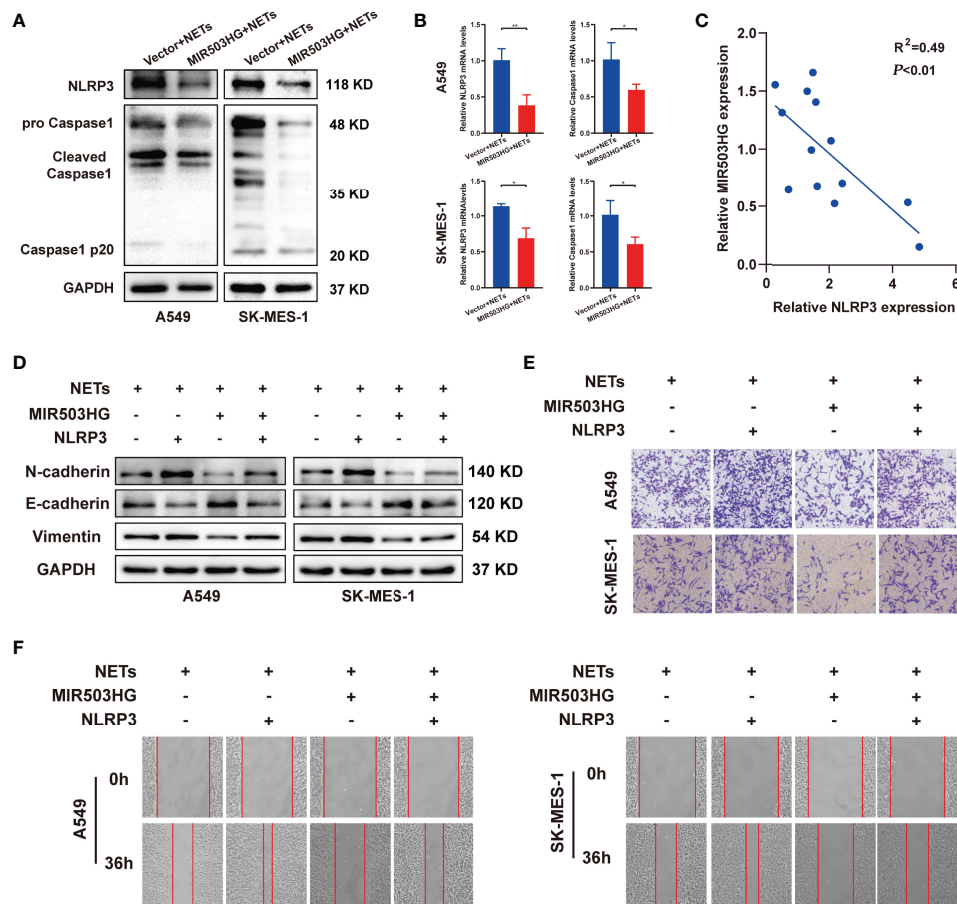


**FIGURE 5 |** NLRP3 inflammasome mediated the effect of MIR503HG to inhibit NETs-triggered metastasis of NSCLC. **(A, B)** The protein and mRNA expression of NLRP3 and Caspase1 in A549 and SK-MES-1 cells with MIR503HG overexpression were analyzed by Western blot **(A)** and qRT-PCR **(B)** after NETs were stimulated. **(C)** A negative relationship between MIR503HG and NLRP3 in NETs-induced NSCLC cells is presented by correlation analysis. **(D)** Overexpression of NLRP3 attenuated the effect of MIR503HG in inhibiting NETs-triggered EMT in NSCLC cells by Western blot. **(E, F)** Overexpression of NLRP3 effectively reverses the effect of MIR503HG in inhibiting NETs-triggered promotion of NSCLC cells metastasis using transwell assay (magnification, 100×) **(E)** and wound healing assays (magnification, 50×) **(F)**. (\* $P < 0.05$ , \*\* $P < 0.01$ ).

## MIR503HG Inhibits NETs-Triggered NSCLC Cell Metastasis and NLRP3 Inflammasome Activation in an NF- $\kappa$ B-Dependent Manner

The above results indicate that downregulation of MIR503HG expression could activate the NF- $\kappa$ B signalling pathway and induce the expression of NLRP3 inflammasome components, which in turn promotes tumour metastasis in NETs-treated NSCLC cells. We further explored the relationship between MIR503HG and the NF- $\kappa$ B/NLRP3 inflammasome *via* regulation of NF- $\kappa$ B expression. We treated MIR503HG-overexpressing A549 and SK-MES-1 cells with NETs and then measured the total and phosphorylated p50 and p65 protein levels by Western blotting. The results indicated that overexpression of MIR503HG decreased the NETs-induced phosphorylation of the NF- $\kappa$ B subunits p50 and p65 in the two NSCLC cell lines (**Figure 7A**). Then, these two NSCLC cell lines were transfected with p50-*pcDNA3.1* or empty vector, and the levels of p50 were validated by qRT-PCR and Western blotting

(**Figures 7B, C**). We further transfected p50-*pcDNA3.1* into NSCLC cells stably overexpressing MIR503HG after NETs treatment. Upregulation of p50 expression abolished the downregulated expression of NLRP3 inflammasome components in NSCLC cells stably overexpressing MIR503HG and treated with NETs (**Figure 7D**). Transwell and wound healing assays also indicated that overexpression of p50 restored the NSCLC cell invasion and migration abilities that had been inhibited by MIR503HG overexpression (**Figures 7E, F**). These data revealed that MIR503HG suppresses the NETs-induced expression of NLRP3 inflammasome components and promotion of metastasis by inhibiting NF- $\kappa$ B activation.

## DISCUSSION

NSCLC metastasis is a very complex multistep process that is closely related to the TME. Increasing evidence suggests that changes in

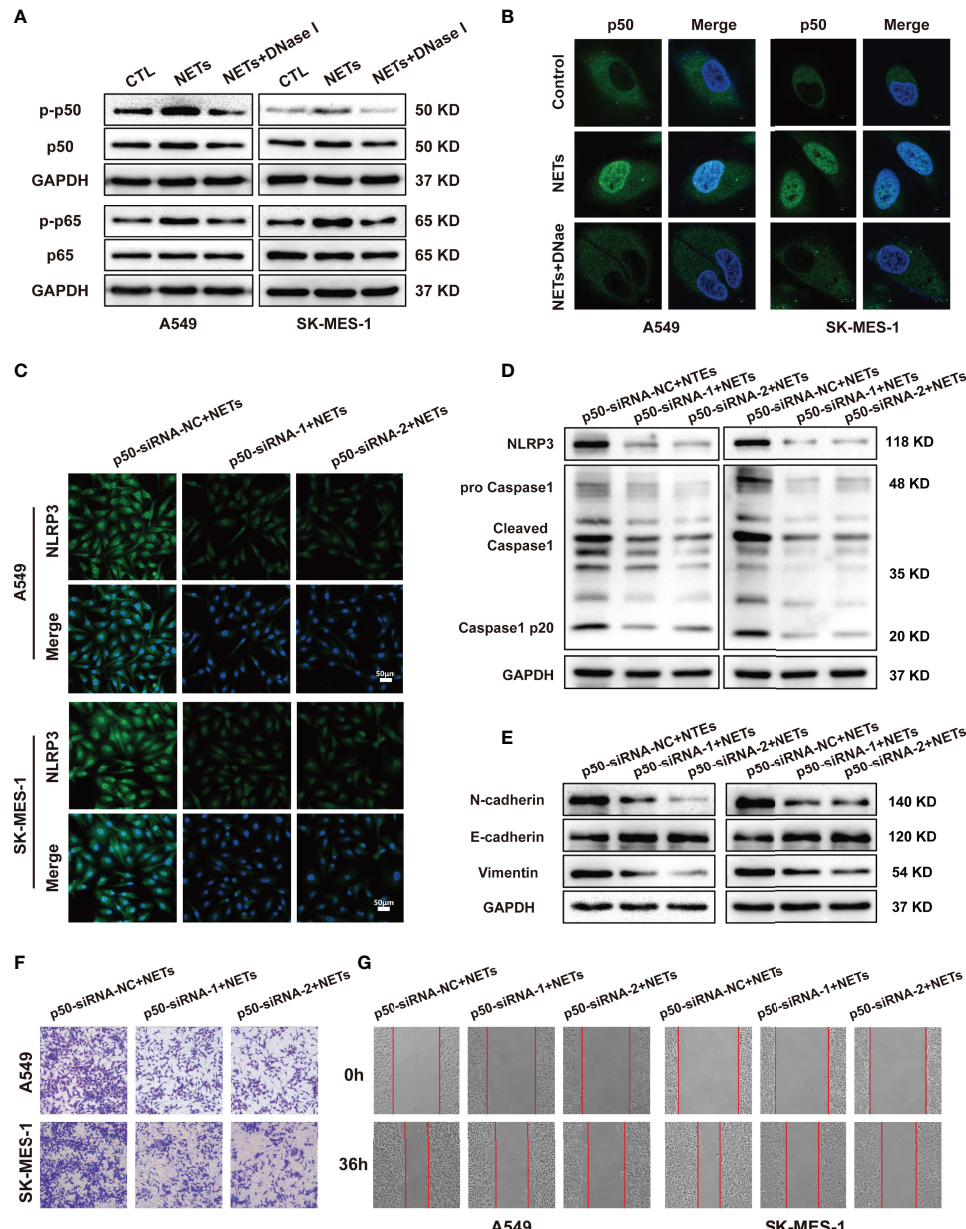
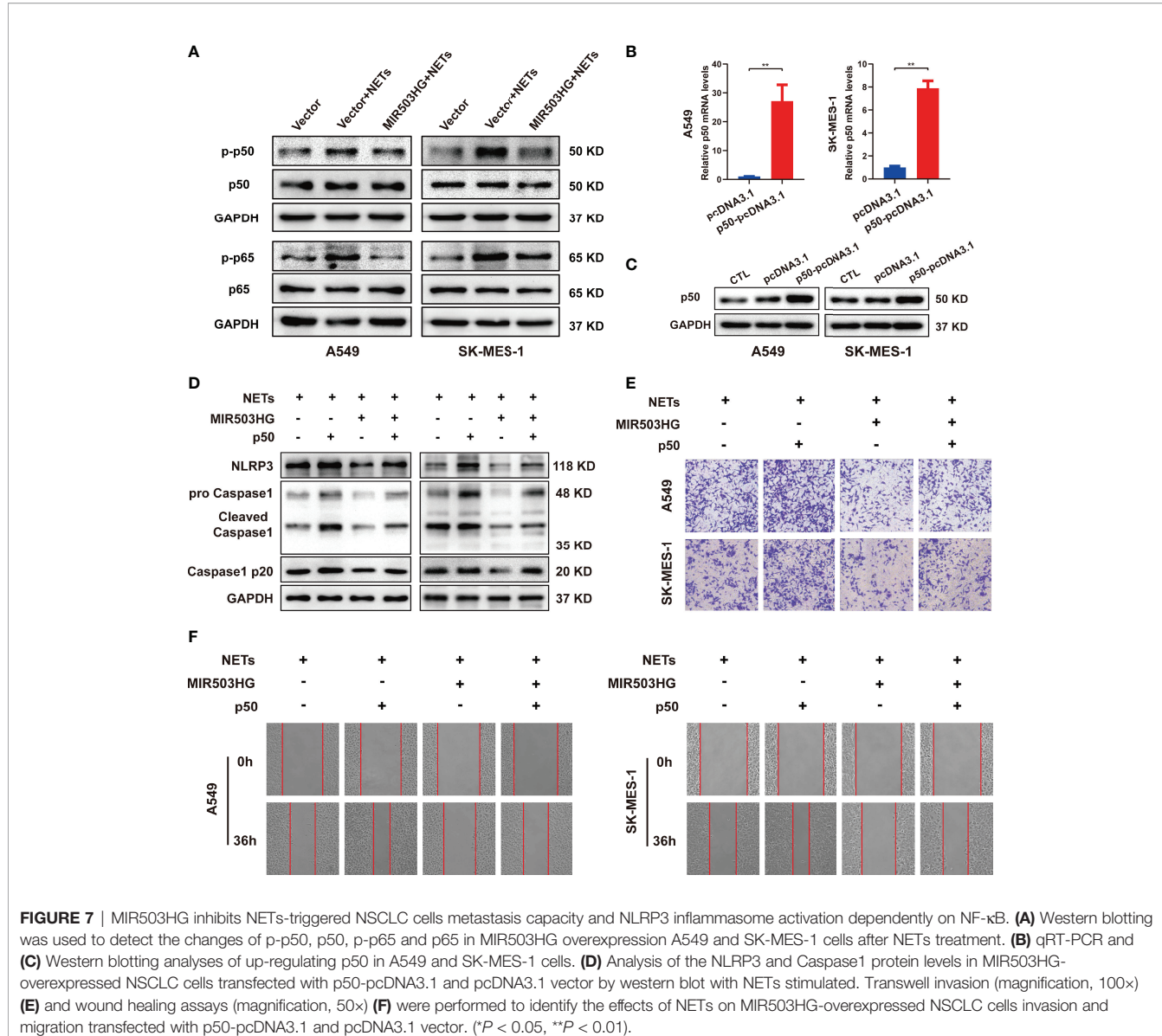


**FIGURE 6 |** NLRP3 inflammasome induced by NETs promotes NSCLC progression is associated with the activation of NF- $\kappa$ B. **(A)** The protein expression level of p-p50, p50, p-p65, p65 in NSCLC cells treated with NETs was detected by Western blotting. **(B)** Nuclear translocation of NF- $\kappa$ B in A549 and SK-MES-1 cells treated with NETs or combined with DNase I were detected by con-focal microscopy (magnification, 3000 $\times$ ; scale bar, 5  $\mu$ m). Immunofluorescence assays **(C)** and Western blot **(D)** were used to detect the effect of NETs on NLRP3 inflammasome in A549 and SK-MES-1 cells after p50 knockdown (magnification, 200 $\times$ ; scale bar, 50  $\mu$ m). **(E)** Downregulation of p50 attenuated the effect on promoting EMT of NETs in NSCLC cells by Western blot. **(F, G)** Downregulated p50 reverses NETs-induced promotion of NSCLC cells metastasis using transwell assay (magnification, 100 $\times$ ) **(E)** and wound healing assays (magnification, 50 $\times$ ) **(F)**.

inflammatory cells in the TME play an essential role in the metastasis of tumours (40). Neutrophils are the most abundant inflammatory cells and have been shown to be crucial in tumour progression (6). Tumour-associated neutrophils within the TME are associated with poor prognosis (41). NETs are produced by activated neutrophils and have been confirmed to promote the metastatic dissemination of tumour cells. However, the specific

mechanism by which NETs promote NSCLC metastasis remains to be further elucidated. In our present study, we demonstrated the role of neutrophil-secreted NETs in promoting the metastatic capacity of NSCLC by inducing EMT. Mechanistically, NETs induce EMT through the activation of the NF- $\kappa$ B/NLRP3 inflammasome pathway by downregulating lncRNA MIR503HG expression, ultimately mediating metastasis.



Accumulating evidence has revealed a relationship between NETs and tumour metastasis. Zha et al. suggested that NETs released by tumour-infiltrating neutrophils increase glioma cell proliferation and migration and regulate the microenvironment by modulating HMGB1/RAGE/IL-8 signalling (42). Recent studies have shown that NETs formation after surgical stress promotes liver and pancreatic cancer cell metastasis *via* the production of HMGB1 (14, 43). In our present study, we found that NETs induced by PMA enhanced the migration and invasion of A549 and SK-MES-1 cells, and these effects were abrogated by the NETs inhibitor DNase I. Previous studies have demonstrated that tumour progression and metastasis are associated with the EMT phenotype, which is characterized by the downregulated expression of the key epithelial marker E-cadherin. In contrast, the expression of mesenchymal markers,

such as N-cadherin and vimentin, is upregulated (44). Our data showed that E-cadherin expression was downregulated and N-cadherin and vimentin expression was increased by NETs treatment in these two NSCLC cell lines, suggesting that NETs promote NSCLC metastasis by affecting the EMT programme. Our findings are consistent with Zhu et al., who showed that the formation of NETs might be affected by the TME, and NETs-induced EMT is a pivotal event related to dissemination and metastasis in gastric cancer pathogenesis (45). These results indicated the crosstalk between NSCLC metastasis and NETs formation by regulating EMT.

Accumulating evidence has shown that lncRNAs play an essential role in the initiation, progression, and metastasis of various kinds of cancer, including NSCLC (46). At present, no study has reported whether NETs promote tumour progression

by affecting the lncRNA transcriptome. Our previous study used microarrays to identify many lncRNAs that are abnormally expressed in human NSCLC cells treated with NETs (28). Here, we revealed that MIR503HG expression is highly deregulated in NSCLC cells stimulated with NETs and that the downregulated expression of MIR503HG facilitated NSCLC cell metastasis *in vitro* and *in vivo*. Initially, MIR503HG was described as a hypoxia-related lncRNA in endothelial cells (47, 48). Several studies have explored the role of MIR503HG in cancer, revealing that MIR503HG inhibits the malignant development of cancer cells by inhibiting proliferation, invasion, and migration (49–51). For the first time, our study revealed that overexpression of MIR503HG substantially reversed the metastasis-promoting effect of NETs on NSCLC, which further suggested that MIR503HG plays a tumour suppressor role in cancers. EMT can be regulated by various factors in different ways, including by TNF- $\alpha$  and TGF- $\beta$  and through the dysregulation of lncRNA expression (52). Recently, a study reported that MIR503HG inhibits hepatocellular carcinoma cell line metastasis by regulating EMT (51). The present study suggested that MIR503HG reversed the NETs-induced EMT programme, which was consistent with a previous study (53). However, the underlying mechanisms by which NETs promote the EMT programme by affecting MIR503HG expression as well as how NETs enhance the metastatic ability of NSCLC cells remain unclear.

The effects of NETs on tumour metastasis include complex cascades and have been reported to be associated with multiple pathways, including the NF- $\kappa$ B (42, 54), STAT3 (14), MAPK (55), and TLR4/9 pathways (14, 56). NETs, which contain many proinflammatory molecules, have been described as a solid inflammatory stimulus and can stimulate host cells to produce abundant cytokines (57, 58). In light of RNA microarray data, we observed that the expression of a set of inflammatory-associated factors was upregulated in NSCLC cells treated with NETs, which suggested that an aggressive inflammatory response was induced. Through KEGG analysis, the NOD-like receptor and NF- $\kappa$ B signalling pathways were identified as inflammatory-associated events in NETs-triggered metastasis. The NLRP3 inflammasome is a crucial inflammatory factor in the response to pathogens and innate immune stimuli, such as tumorigenesis and development (59). Recent studies have demonstrated that excessive activation of the NLRP3 inflammasome enhances the invasion and metastasis of multiple tumours, including melanoma, hepatocellular carcinoma and pancreatic cancer (59–63). Activation of the NLRP3 inflammasome leads to the release of the proinflammatory cytokines IL-1 $\beta$  and IL-18, which may contribute to cancer development (64). In this study, we reveal a new role for NETs released by neutrophils in the activation and regulation of the inflammasome during the progression of NSCLC. To our knowledge, this is the first time that NETs have been identified as an effective activator of the inflammasome system to promote the malignant development of NSCLC. The current study observed that NLRP3 inflammasomes were activated in NSCLC cells in response to NETs treatment. In

contrast, inhibiting the NLRP3 inflammasome led to impaired metastatic cell potential and reversed the EMT programme following increased E-cadherin expression coupled with decreased N-cadherin and vimentin expression. Consistent with our study, Wang et al. also demonstrated that activation of the NLRP3 inflammasome increased the proliferation and migration of NSCLC A549 cells (38). These findings suggest a potential role for NLRP3 activation by NETs in promoting NSCLC. This finding indicates that NLRP3 could be an excellent target for preventing NETs-enhanced metastasis.

Two-signals model of NLRP3 inflammasome activation has been proposed in macrophages (65). The first signal is priming, which is provided by microbial or endogenous molecules that activates NF- $\kappa$ B signalling to promote the expression of NLRP3 and pro-IL-1 $\beta$ , which is a prerequisite for the second signal. The second signal is activation, which is triggered by a variety of stimulation such as ATP, pore-forming toxins and particulate matter that induce events such as K $^{+}$  efflux, generation of ROS and others to initiate NLRP3 inflammasome assembly. Activation of NF- $\kappa$ B was shown to be an intermediate link between NETs and NLRP3 inflammasome activation in NETs-stimulated NSCLC cells. Several reports have revealed that NF- $\kappa$ B mediates the inflammatory response of tumour cells after exposure to NETs, and NETs can activate the NF- $\kappa$ B signalling pathway (42, 54, 66). Growing evidence suggests that NF- $\kappa$ B, a critical transcription factor, is an upstream regulator of NLRP3 and affects the expression of NLRP3 inflammasome components (32, 67–69). Lin et al. revealed that the Platr4 protein interferes with the binding of the NF- $\kappa$ B/Rx $\alpha$  complex to  $\kappa$ B sites, which in turn prevents the transcriptional activation of NLRP3 by NF- $\kappa$ B (69). When NF- $\kappa$ B was blocked, we further found that NETs failed to induce the expression of NLRP3 inflammasome components and enhance the metastatic capacity of NSCLC cells. These findings revealed that the NF- $\kappa$ B/NLRP3 signalling pathway plays a crucial role in NETs-triggered metastasis potential.

Increasing studies have revealed that the particular subcellular localization of lncRNAs usually affects their function; for instance, nuclear lncRNAs can regulate transcription by influencing the activity of transcription factors (70). Yi et al. showed that Gm4419 can directly interact with the p50 subunit of NF- $\kappa$ B and activate the NF- $\kappa$ B pathway (68). Our study revealed that MIR503HG was primarily located in the nucleus. MIR503HG might play a similar role to nuclear lncRNAs in regulating cellular transcription, so we further explored whether the transcription factor NF- $\kappa$ B was regulated by MIR503HG. We found that overexpression of MIR503HG could inhibit NETs-induced NF- $\kappa$ B phosphorylation and NLRP3 inflammasome activation and then suppress the migration and invasion of NSCLC cells, and upregulation of NF- $\kappa$ B expression reversed this effect. MIR503HG might interact with NF- $\kappa$ B to form a nuclear lncRNA-protein complex, which might regulate the downstream NLRP3. These results suggested that MIR503HG inhibited NETs-induced activation of the NF- $\kappa$ B/NLRP3 signalling pathway.

In conclusion, in this study, we demonstrated that NETs promoted NSCLC cell migration and invasion *via* the EMT process. MIR503HG expression was downregulated in NSCLC patient tissues and NETs-treated NSCLC cells. MIR503HG inhibited the NETs-triggered, inflammation-associated metastatic potential of NSCLC cell by inhibiting the activation of the NF- $\kappa$ B/NLRP3 pathway. Our research provides a new mechanism by which NETs function in NSCLC metastasis and identifies novel effective therapeutic targets to treat NSCLC metastasis.

## DATA AVAILABILITY STATEMENT

The original contributions presented in the study are included in the article/**Supplementary Material**. Further inquiries can be directed to the corresponding author.

## ETHICS STATEMENT

The studies involving human participants were reviewed and approved by The Ethics Committee of Medical innovation center of the First Affiliated Hospital of Nanchang University. The patients/participants provided their written informed consent to participate in this study.

## AUTHOR CONTRIBUTIONS

YW carried out most experiments, analyzed the data and drafted the main manuscript. YW, XYQ, SKY and XWZ participated in the animal experiments. YY conducted the assessment of histopathological changes. SYL and BQF participated in the immunofluorescence and con-focal microscopy experiments. CF and LC drew up part of the manuscript. BY participated in the part of the PCR, WB and ELISA experiments. YL and FL contributed to the study's design, supervision, data analysis and guided writing. All authors read and approved the final version of the manuscript.

## REFERENCES

1. Siegel RL, Miller KD, Jemal A. Cancer Statistics, 2020. *CA Cancer J Clin* (2020) 70(1):7–30. doi: 10.3322/caac.21590
2. Chen VW, Ruiz BA, Hsieh MC, Wu XC, Ries LA, Lewis DR. Analysis of Stage and Clinical/Prognostic Factors for Lung Cancer From SEER Registries: AJCC Staging and Collaborative Stage Data Collection System. *Cancer* (2014) 120 Suppl 23:3781–92. doi: 10.1002/cncr.29045
3. Ekeke CN, Mitchell C, Schuchert M, Dhupar R, Luketich JD, Okusanya OT. Early Distant Recurrence in Patients With Resected Stage I Lung Cancer: A Case Series of "Blast Metastasis". *Clin Lung Cancer* (2021) 22(1):e132–5. doi: 10.1016/j.cllc.2020.09.002
4. Zhuang X, Zhang H, Hu G. Cancer and Microenvironment Plasticity: Double-Edged Swords in Metastasis. *Trends Pharmacol Sci* (2019) 40 (6):419–29. doi: 10.1016/j.tips.2019.04.005
5. Quail DF, Joyce JA. Microenvironmental Regulation of Tumor Progression and Metastasis. *Nat Med* (2013) 19(11):1423–37. doi: 10.1038/nm.3394
6. Tütting T, de Visser KE. CANCER. How Neutrophils Promote Metastasis. *Science* (2016) 352(6282):145–6. doi: 10.1126/science.aaf7300
7. Coffelt SB, Kersten K, Doornbehal CW, Weiden J, Vrijland K, Hau CS, et al. IL-17-Producing  $\gamma\delta$  T Cells and Neutrophils Conspire to Promote Breast Cancer Metastasis. *Nature* (2015) 522(7556):345–8. doi: 10.1038/nature14282
8. Coffelt SB, Wellenstein MD, de Visser KE. Neutrophils in Cancer: Neutral No More. *Nat Rev Cancer* (2016) 16(7):431–46. doi: 10.1038/nrc.2016.52
9. Brinkmann V, Reichard U, Goosmann C, Fauler B, Uhlemann Y, Weiss DS, et al. Neutrophil Extracellular Traps Kill Bacteria. *Science* (2004) 303 (5663):1532–5. doi: 10.1126/science.1092385
10. Fuchs TA, Abed U, Goosmann C, Hurwitz R, Schulze I, Wahn V, et al. Novel Cell Death Program Leads to Neutrophil Extracellular Traps. *J Cell Biol* (2007) 176(2):231–41. doi: 10.1083/jcb.200606027

## FUNDING

This study was supported by the grants from National Natural Science Foundation of China (No.81560379, 81460292, 81660315), Surface project of the Natural Science Foundation of Jiangxi Province (No.20181BAB205046, No.20202BAB216031), The Graduate Student Innovation Special Fund Project of Jiangxi Province (No. YC2021-B039).

## ACKNOWLEDGMENTS

The authors wish to express gratitude to Dr. Huang YD for the technical mentorship and assistance.

## SUPPLEMENTARY MATERIAL

The Supplementary Material for this article can be found online at: <https://www.frontiersin.org/articles/10.3389/fimmu.2022.867516/full#supplementary-material>

**Supplementary Figure 1 | (A)** The expression of MIR503HG mRNA levels in BEAS-2B, up-regulating MIR503HG in A549 and SK-MES-1 cells were analyzed by qRT-PCR. **(B)** qRT-PCR was used to analyze MIR503HG knockdown efficiency in BEAS-2B cells. **(C)** Western blot analyzing the expressions levels of EMT markers protein in BEAS-2B cells after MIR503HG knockdown. (\* $P$  < 0.05, \*\* $P$  < 0.01, ns, not significant).

**Supplementary Figure 2 | (A)** The mRNA expression of NLRP3, Caspase1, IL-1 $\beta$  and IL-18 in SK-MES-1 cells were analyzed by qRT-PCR after NETs stimulation at different times. **(B)** Immunofluorescence was used to observe the expression of NLRP3 and Caspase1 in A549 and SK-MES-1 cells treated with NETs for 12 h (magnification, 200 $\times$ ; scale bar, 50  $\mu$ m). **(C)** The expression of IL-1 $\beta$  and IL-18 in the supernatant of A549 and SK-MES-1 treated with NETs 12 h was assessed by ELISA. (\*\* $P$  < 0.01, ns, not significant).

**Supplementary Figure 3 | (A)** Western blotting was used to analyze NLRP3 overexpression transfection efficiency in A549 and SK-MES-1 cells. Western blotting **(B)** and qRT-PCR **(C)** were used to analyze p50 knockdown efficiency in A549 and SK-MES-1 cells. **(D)** Immunofluorescence assays were used to detect the effect of NETs on NLRP3 inflammasome in A549 and SK-MES-1 cells after p50 knockdown (magnification, 200 $\times$ ; scale bar, 50  $\mu$ m). (\*\* $P$  < 0.01).

**Supplementary Table 1** | The primers sequences for qRT-PCR analyses.

11. Papayannopoulos V. Neutrophil Extracellular Traps in Immunity and Disease. *Nat Rev Immunol* (2018) 18(2):134–47. doi: 10.1038/nri.2017.105
12. Nicolás-Ávila JA, Adrover JM, Hidalgo A. Neutrophils in Homeostasis, Immunity, and Cancer. *Immunity* (2017) 46(1):15–28. doi: 10.1016/j.jimmuni.2016.12.012
13. Albrengues J, Shields MA, Ng D, Park CG, Ambrico A, Poindexter ME, et al. Neutrophil Extracellular Traps Produced During Inflammation Awaken Dormant Cancer Cells in Mice. *Science* (2018) 361(6409):eaao4227. doi: 10.1126/science.aao4227
14. Tohme S, Yazdani HO, Al-Khafaji AB, Chidi AP, Loughran P, Mowen K, et al. Neutrophil Extracellular Traps Promote the Development and Progression of Liver Metastases After Surgical Stress. *Cancer Res* (2016) 76(6):1367–80. doi: 10.1158/0008-5472.CAN-15-1591
15. Yang L, Liu Q, Zhang X, Liu X, Zhou B, Chen J, et al. DNA of Neutrophil Extracellular Traps Promotes Cancer Metastasis via CCDC25. *Nature* (2020) 583(7814):133–8. doi: 10.1038/s41586-020-2394-6
16. Teijeira Á, Garasa S, Gato M, Alfaro C, Migueliz I, Cirella A, et al. CXCR1 and CXCR2 Chemokine Receptor Agonists Produced by Tumors Induce Neutrophil Extracellular Traps That Interfere With Immune Cytotoxicity. *Immunity* (2020) 52(5):856–871.e8. doi: 10.1016/j.jimmuni.2020.03.001
17. Demers M, Wagner DD. Neutrophil Extracellular Traps: A New Link to Cancer-Associated Thrombosis and Potential Implications for Tumor Progression. *Oncoimmunology* (2013) 2(2):e22946. doi: 10.4161/onci.22946
18. Cools-Lartigue J, Spicer J, McDonald B, Gowing S, Chow S, Giannias B, et al. Neutrophil Extracellular Traps Sequester Circulating Tumor Cells and Promote Metastasis. *J Clin Invest* (2013) 123(8):3446–58. doi: 10.1172/JCI67484
19. Aldabbous L, Abdul-Salam V, McKinnon T, Duluc L, Pepke-Zaba J, Southwood M, et al. Neutrophil Extracellular Traps Promote Angiogenesis: Evidence From Vascular Pathology in Pulmonary Hypertension. *Arterioscler Thromb Vasc Biol* (2016) 36(10):2078–87. doi: 10.1161/ATVBAHA.116.307634
20. Stankovic B, Bjorhovde H, Skarshaug R, Aamodt H, Frafjord A, Müller E, et al. Immune Cell Composition in Human Non-Small Cell Lung Cancer. *Front Immunol* (2018) 9:3101. doi: 10.3389/fimmu.2018.03101
21. Oklu R, Sheth RA, Wong K, Jahromi AH, Albadawi H. Neutrophil Extracellular Traps are Increased in Cancer Patients But Does Not Associate With Venous Thrombosis. *Cardiovasc Diagn Ther* (2017) 7(Suppl 3):S140–9. doi: 10.21037/cdt.2017.08.01
22. Lee J, Lee D, Lawler S, Kim Y. Role of Neutrophil Extracellular Traps in Regulation of Lung Cancer Invasion and Metastasis: Structural Insights From a Computational Model. *PLoS Comput Biol* (2021) 17(2):e1008257. doi: 10.1371/journal.pcbi.1008257
23. Rayes RF, Mouhanna JG, Nicolau I, Bourdeau F, Giannias B, Rousseau S, et al. Primary Tumors Induce Neutrophil Extracellular Traps With Targetable Metastasis Promoting Effects. *JCI Insight* (2019) 5(16):e128008. doi: 10.1172/jci.insight.128008
24. Kopp F, Mendell JT. Functional Classification and Experimental Dissection of Long Noncoding RNAs. *Cell* (2018) 172(3):393–407. doi: 10.1016/j.cell.2018.01.011
25. Khan S, Masood M, Gaur H, Ahmad S, Syed MA. Long non-Coding RNA: An Immune Cells Perspective. *Life Sci* (2021) 271:119152. doi: 10.1016/j.lfs.2021.119152
26. Acha-Sagredo A, Uko B, Pantazi P, Bediaga NG, Moschandrea C, Rainbow L, et al. Long non-Coding RNA Dysregulation is a Frequent Event in non-Small Cell Lung Carcinoma Pathogenesis. *Br J Cancer* (2020) 122(7):1050–8. doi: 10.1038/s41416-020-0742-9
27. Schmitt AM, Chang HY. Long Noncoding RNAs in Cancer Pathways. *Cancer Cell* (2016) 29(4):452–63. doi: 10.1016/j.ccr.2016.03.010
28. Fang C, Liu F, Wang Y, Yuan S, Chen R, Qiu X, et al. A Innovative Prognostic Symbol Based on Neutrophil Extracellular Traps (NETs)-Related lncRNA Signature in non-Small-Cell Lung Cancer. *Aging (Albany NY)* (2021) 13(13):17864–79. doi: 10.18632/aging.203289
29. Zitvogel L, Kepp O, Galluzzi L, Kroemer G. Inflammasomes in Carcinogenesis and Anticancer Immune Responses. *Nat Immunol* (2012) 13(4):343–51. doi: 10.1038/ni.2224
30. Missiroli S, Perrone M, Boncompagni C, Borghi C, Campagnaro A, Marchetti F, et al. Targeting the NLRP3 Inflammasome as a New Therapeutic Option for Overcoming Cancer. *Cancers (Basel)* (2021) 13(10):2297. doi: 10.3390/cancers13102297
31. Wang Z, Zhang S, Xiao Y, Zhang W, Wu S, Qin T, et al. NLRP3 Inflammasome and Inflammatory Diseases. *Oxid Med Cell Longev* (2020) 2020:4063562. doi: 10.1155/2020/4063562
32. Ma M, Pei Y, Wang X, Feng J, Zhang Y, Gao MQ. LncRNA XIST Mediates Bovine Mammary Epithelial Cell Inflammatory Response via NF- $\kappa$ B/NLRP3 Inflammasome Pathway. *Cell Prolif* (2019) 52(1):e12525. doi: 10.1111/cpr.12525
33. Kahlenberg JM, Carmona-Rivera C, Smith CK, Kaplan MJ. Neutrophil Extracellular Trap-Associated Protein Activation of the NLRP3 Inflammasome is Enhanced in Lupus Macrophages. *J Immunol* (2013) 190(3):1217–26. doi: 10.4049/jimmunol.1202388
34. Hu Q, Shi H, Zeng T, Liu H, Su Y, Cheng X, et al. Increased Neutrophil Extracellular Traps Activate NLRP3 and Inflammatory Macrophages in Adult-Onset Still's Disease. *Arthritis Res Ther* (2019) 21(1):9. doi: 10.1186/s13075-018-1800-z
35. Huang W, Jiao J, Liu J, Huang M, Hu Y, Ran W, et al. MFG-E8 Accelerates Wound Healing in Diabetes by Regulating "NLRP3 Inflammasome-Neutrophil Extracellular Traps" Axis. *Cell Death Discovery* (2020) 6(1):84. doi: 10.1038/s41420-020-00318-7
36. Najmeh S, Cools-Lartigue J, Giannias B, Spicer J, Ferri LE. Simplified Human Neutrophil Extracellular Traps (NETs) Isolation and Handling. *J Vis Exp* (2015) (98):52687. doi: 10.3791/52687
37. Masucci MT, Minopoli M, Del Vecchio S, Carriero MV. The Emerging Role of Neutrophil Extracellular Traps (NETs) in Tumor Progression and Metastasis. *Front Immunol* (2020) 11:1749. doi: 10.3389/fimmu.2020.01749
38. Wang Y, Kong H, Zeng X, Liu W, Wang Z, Yan X, et al. Activation of NLRP3 Inflammasome Enhances the Proliferation and Migration of A549 Lung Cancer Cells. *Oncol Rep* (2016) 35(4):2053–64. doi: 10.3892/or.2016.4569
39. Liu D, Yang P, Gao M, Yu T, Shi Y, Zhang M, et al. NLRP3 Activation Induced by Neutrophil Extracellular Traps Sustains Inflammatory Response in the Diabetic Wound. *Clin Sci (Lond)* (2019) 133(4):565–82. doi: 10.1042/CS20180600
40. Lambert AW, Patabiraman DR, Weinberg RA. Emerging Biological Principles of Metastasis. *Cell* (2017) 168(4):670–91. doi: 10.1016/j.cell.2016.11.037
41. Gregory AD, Houghton AM. Tumor-Associated Neutrophils: New Targets for Cancer Therapy. *Cancer Res* (2011) 71(7):2411–6. doi: 10.1158/0008-5472.CAN-10-2583
42. Zha C, Meng X, Li L, Mi S, Qian D, Li Z, et al. Neutrophil Extracellular Traps Mediate the Crosstalk Between Glioma Progression and the Tumor Microenvironment via the HMGB1/RAGE/IL-8 Axis. *Cancer Biol Med* (2020) 17(1):154–68. doi: 10.20892/j.issn.2095-3941.2019.0353
43. Kajioka H, Kagawa S, Ito A, Yoshimoto M, Sakamoto S, Kikuchi S, et al. Targeting Neutrophil Extracellular Traps With Thrombomodulin Prevents Pancreatic Cancer Metastasis. *Cancer Lett* (2021) 497:1–13. doi: 10.1016/j.canlet.2020.10.015
44. Kalluri R, Weinberg RA. The Basics of Epithelial-Mesenchymal Transition. *J Clin Invest* (2009) 119(6):1420–8. doi: 10.1172/JCI39104
45. Zhu T, Zou X, Yang C, Li L, Wang B, Li R, et al. Neutrophil Extracellular Traps Promote Gastric Cancer Metastasis by Inducing Epithelial-Mesenchymal Transition. *Int J Mol Med* (2021) 48(1):127. doi: 10.3892/ijmm.2021.4960
46. Luo DB, Lv HB, Sun XH, Wang Y, Chu JH, Salai AL. LncRNA TRERNA1 Promotes Malignant Progression of NSCLC Through Targeting Foxl1. *Eur Rev Med Pharmacol Sci* (2020) 24(3):1233–42. doi: 10.26355/eurrev\_202002\_20176
47. Fiedler J, Breckwoldt K, Remmeli CW, Hartmann D, Dittrich M, Pfanne A, et al. Development of Long Noncoding RNA-Based Strategies to Modulate Tissue Vascularization. *J Am Coll Cardiol* (2015) 66(18):2005–15. doi: 10.1016/j.jacc.2015.07.081
48. Cao X, Fan QL. LncRNA MIR503HG Promotes High-Glucose-Induced Proximal Tubular Cell Apoptosis by Targeting miR-503-5p/Bcl-2 Pathway. *Diabetes Metab Syndr Obes* (2020) 13:4507–17. doi: 10.2147/DMSO.S277869
49. Muys BR, Lorenzi JC, ZaNETste DL, de Barros Lima e Bueno R, de Araújo LF, Dinarte-Santos AR, et al. Placenta-Enriched LncRNAs MIR503HG and LINC00629 Decrease Migration and Invasion Potential of JEG-3 Cell Line. *PLoS One* (2016) 11(3):e0151560. doi: 10.1371/journal.pone.0151560

50. Wang SM, Pang J, Zhang KJ, Zhou ZY, Chen FY. lncRNA MIR503HG Inhibits Cell Proliferation and Promotes Apoptosis in TNBC Cells *via* the miR-224-5p/HOXA9 Axis. *Mol Ther Oncolytics* (2021) 21:62–73. doi: 10.1016/j.mto.2021.03.009

51. Song S, Qiu X. lncRNA Mir503hg Inhibits Epithelial-Mesenchymal Transition and Angiogenesis in Hepatocellular Carcinoma by Enhancing PDCD4 *via* Regulation of miR-15b. *Dig Liver Dis* (2021) 53(1):107–16. doi: 10.1016/j.dld.2020.09.008

52. Lamouille S, Xu J, Deryck R. Molecular Mechanisms of Epithelial-Mesenchymal Transition. *Nat Rev Mol Cell Biol* (2014) 15(3):178–96. doi: 10.1038/nrm3758

53. Lin H, Wang J, Wang T, Wu J, Wang P, Huo X, et al. The lncRNA MIR503HG/miR-224-5p/TUSC3 Signaling Cascade Suppresses Gastric Cancer Development *via* Modulating ATF6 Branch of Unfolded Protein Response. *Front Oncol* (2021) 11:708501. doi: 10.3389/fonc.2021.708501

54. Yang L, Liu L, Zhang R, Hong J, Wang Y, Wang J, et al. IL-8 Mediates a Positive Loop Connecting Increased Neutrophil Extracellular Traps (NETs) and Colorectal Cancer Liver Metastasis. *J Cancer* (2020) 11(15):4384–96. doi: 10.7150/jca.44215

55. Zhou J, Yang Y, Gan T, Li Y, Hu F, Hao N, et al. Lung Cancer Cells Release High Mobility Group Box 1 and Promote the Formation of Neutrophil Extracellular Traps. *Oncol Lett* (2019) 18(1):181–8. doi: 10.3892/ol.2019.10290

56. Yang LY, Luo Q, Lu L, Zhu WW, Sun HT, Wei R, et al. Increased Neutrophil Extracellular Traps Promote Metastasis Potential of Hepatocellular Carcinoma *via* Provoking Tumorous Inflammatory Response. *J Hematol Oncol* (2020) 13(1):3. doi: 10.1186/s13045-019-0836-0

57. Warnatsch A, Ioannou M, Wang Q, Papayannopoulos V. Inflammation. Neutrophil Extracellular Traps License Macrophages for Cytokine Production in Atherosclerosis. *Science* (2015) 349(6245):316–20. doi: 10.1126/science.aaa8064

58. Tall AR, Westerterp M. Inflammasomes, Neutrophil Extracellular Traps, and Cholesterol. *J Lipid Res* (2019) 60(4):721–7. doi: 10.1194/jlr.S091280

59. Moossavi M, Parsamanesh N, Bahrami A, Atkin SL, Sahebkar A. Role of the NLRP3 Inflammasome in Cancer. *Mol Cancer* (2018) 17(1):158. doi: 10.1186/s12943-018-0900-3

60. Hu H, Wang Y, Ding X, He Y, Lu Z, Wu P, et al. Long non-Coding RNA XLOC\_000647 Suppresses Progression of Pancreatic Cancer and Decreases Epithelial-Mesenchymal Transition-Induced Cell Invasion by Down-Regulating Nlrp3. *Mol Cancer* (2018) 17(1):18. doi: 10.1186/s12943-018-0761-9

61. Ahmad I, Muneer KM, Tamimi IA, Chang ME, Ata MO, Yusuf N. Thymoquinone Suppresses Metastasis of Melanoma Cells by Inhibition of NLRP3 Inflammasome. *Toxicol Appl Pharmacol* (2013) 270(1):70–6. doi: 10.1016/j.taap.2013.03.027

62. Fan SH, Wang YY, Lu J, Zheng YL, Wu DM, Li MQ, et al. Luteoloside Suppresses Proliferation and Metastasis of Hepatocellular Carcinoma Cells by Inhibition of NLRP3 Inflammasome. *PLoS One* (2014) 9(2):e89961. doi: 10.1371/journal.pone.0089961

63. Karki R, Man SM, Kanneganti TD. Inflammasomes and Cancer. *Cancer Immunol Res* (2017) 5(2):94–9. doi: 10.1158/2326-6066.CIR-16-0269

64. Baker KJ, Houston A, Brint E. IL-1 Family Members in Cancer; Two Sides to Every Story. *Front Immunol* (2019) 10:1197. doi: 10.3389/fimmu.2019.01197

65. He Y, Hara H, Núñez G. Mechanism and Regulation of NLRP3 Inflammasome Activation. *Trends Biochem Sci* (2016) 41:1012–21. doi: 10.1016/j.tibs.2016.09.002

66. Zhu B, Zhang X, Sun S, Fu Y, Xie L, Ai P. NF- $\kappa$ b and Neutrophil Extracellular Traps Cooperate to Promote Breast Cancer Progression and Metastasis. *Exp Cell Res* (2021) 405(2):112707. doi: 10.1016/j.yexcr.2021.112707

67. Zou J, Yang Y, Yang Y, Liu X. Polydatin Suppresses Proliferation and Metastasis of non-Small Cell Lung Cancer Cells by Inhibiting NLRP3 Inflammasome Activation *via* NF- $\kappa$ b Pathway. *BioMed Pharmacother* (2018) 108:130–6. doi: 10.1016/j.bioph.2018.09.051

68. Yi H, Peng R, Zhang LY, Sun Y, Peng HM, Liu HD, et al. LincRNA-Gm4419 Knockdown Ameliorates NF- $\kappa$ b/NLRP3 Inflammasome-Mediated Inflammation in Diabetic Nephropathy. *Cell Death Dis* (2017) 8(2):e2583. doi: 10.1038/cddis.2016.451

69. Lin Y, Wang S, Gao L, Zhou Z, Yang Z, Lin J, et al. Oscillating lncRNA Platr4 Regulates NLRP3 Inflammasome to Ameliorate Nonalcoholic Steatohepatitis in Mice. *Theranostics* (2021) 11(1):426–44. doi: 10.7150/thno.50281

70. Chen LL. Linking Long Noncoding RNA Localization and Function. *Trends Biochem Sci* (2016) 41(9):761–72. doi: 10.1016/j.tibs.2016.07.003

**Conflict of Interest:** The authors declare that the research was conducted in the absence of any commercial or financial relationships that could be construed as a potential conflict of interest.

**Publisher's Note:** All claims expressed in this article are solely those of the authors and do not necessarily represent those of their affiliated organizations, or those of the publisher, the editors and the reviewers. Any product that may be evaluated in this article, or claim that may be made by its manufacturer, is not guaranteed or endorsed by the publisher.

Copyright © 2022 Wang, Liu, Chen, Fang, Li, Yuan, Qian, Yin, Yu, Fu, Zhang and Li. This is an open-access article distributed under the terms of the Creative Commons Attribution License (CC BY). The use, distribution or reproduction in other forums is permitted, provided the original author(s) and the copyright owner(s) are credited and that the original publication in this journal is cited, in accordance with accepted academic practice. No use, distribution or reproduction is permitted which does not comply with these terms.



## OPEN ACCESS

## EDITED BY

Ana Paula Lepique,  
University of São Paulo, Brazil

## REVIEWED BY

Luciana Rodrigues Carvalho Barros,  
University of São Paulo, Brazil  
Fuxiang Zhou,  
Wuhan University, China

## \*CORRESPONDENCE

WeiQi Sheng  
shengweiqi2006@163.com  
Dan Huang  
diane Huang fdcc@gmail.com  
Wenhua Li  
whliiris@hotmail.com  
Zhenzhong Deng  
dengzhenzhong@xinhuaumed.com.cn

<sup>†</sup>These authors have contributed  
equally to this work

## SPECIALTY SECTION

This article was submitted to  
Cancer Immunity  
and Immunotherapy,  
a section of the journal  
Frontiers in Immunology

RECEIVED 02 May 2022

ACCEPTED 28 June 2022

PUBLISHED 27 July 2022

## CITATION

Xu M, Chang J, Wang W, Wang X, Wang X, Weng W, Tan C, Zhang M, Ni S, Wang L, Huang Z, Deng Z, Li W, Huang D and Sheng W (2022) Classification of colon adenocarcinoma based on immunological characterizations: Implications for prognosis and immunotherapy. *Front. Immunol.* 13:934083. doi: 10.3389/fimmu.2022.934083

## COPYRIGHT

© 2022 Xu, Chang, Wang, Wang, Wang, Weng, Tan, Zhang, Ni, Wang, Huang, Deng, Li, Huang and Sheng. This is an open-access article distributed under the terms of the [Creative Commons Attribution License \(CC BY\)](#). The use, distribution or reproduction in other forums is permitted, provided the original author(s) and the copyright owner(s) are credited and that the original publication in this journal is cited, in accordance with accepted academic practice. No use, distribution or reproduction is permitted which does not comply with these terms.

# Classification of colon adenocarcinoma based on immunological characterizations: Implications for prognosis and immunotherapy

Midie Xu<sup>1,2,3†</sup>, Jinjia Chang<sup>2,4†</sup>, Wenfeng Wang<sup>5†</sup>, Xin Wang<sup>1,2,3</sup>, Xu Wang<sup>1,2,3</sup>, Weiwei Weng<sup>1,2,3</sup>, Cong Tan<sup>1,2,3</sup>, Meng Zhang<sup>1,2,3</sup>, Shujuan Ni<sup>1,2,3</sup>, Lei Wang<sup>1,2,3</sup>, ZhaoHui Huang<sup>6</sup>, Zhenzhong Deng<sup>7\*</sup>, Wenhua Li<sup>2,4\*</sup>, Dan Huang<sup>1,2,3\*</sup> and WeiQi Sheng<sup>1,2,3\*</sup>

<sup>1</sup>Department of Pathology, Fudan University Shanghai Cancer Center, Shanghai, China

<sup>2</sup>Department of Oncology, Shanghai Medical college, Fudan University, Shanghai, China, <sup>3</sup>Institute of Pathology, Fudan University, Shanghai, China, <sup>4</sup>Department of Medical Oncology, Fudan University Shanghai Cancer Center, Shanghai, China, <sup>5</sup>Shanghai Urological Cancer Institute, Cancer Institute, Fudan University Shanghai Cancer Center, Fudan University, Shanghai, China, <sup>6</sup>Wuxi Cancer Institute, Affiliated Hospital of Jiangnan University, Wuxi, China, <sup>7</sup>Department of Oncology, Xinhua Hospital, School of Medicine, Shanghai Jiaotong University, Shanghai, China

Accurate immune molecular typing is pivotal for screening out patients with colon adenocarcinoma (COAD) who may benefit from immunotherapy and whose tumor microenvironment (TME) was needed for reprogramming to beneficial immune-mediated responses. However, little is known about the immune characteristic of COAD. Here, by calculating the enrichment score of immune characteristics in three online COAD datasets (TCGA-COAD, GSE39582, and GSE17538), we identified 17 prognostic-related immune characteristics that overlapped in at least two datasets. We determined that COADs could be stratified into three immune subtypes (IS1–IS3), based on consensus clustering of these 17 immune characteristics. Each of the three ISs was associated with distinct clinicopathological characteristics, genetic aberrations, tumor-infiltrating immune cell composition, immunophenotyping (immune “hot” and immune “cold”), and cytokine profiles, as well as different clinical outcomes and immunotherapy/therapeutic response. Patients with the IS1 tumor had high immune infiltration but immunosuppressive phenotype, IS3 tumor is an immune “hot” phenotype, whereas those with the IS2 tumor had an immune “cold” phenotype. We further verified the distinct immune phenotype of IS1 and IS3 by an in-house COAD cohort. We propose that the immune subtyping can be utilized to identify COAD patients who will be affected by the tumor immune microenvironment. Furthermore, the ISs may provide a guide for personalized cancer immunotherapy and for tumor prognosis.

## KEYWORDS

colon adenocarcinoma, immune characteristics, prognosis, therapy response, immune subtype analysis

## Introduction

Colon adenocarcinoma (COAD) is a common malignant tumor (1, 2). According to the latest data released by the World Health Organization's International Agency for Research on Cancer (IARC) in 2020, COAD was the third most commonly diagnosed cancer and the second leading cause of cancer death worldwide (3). Most patients with COADs are diagnosed with resectable tumors and are treated with excisional surgery plus adjuvant therapy, if necessary. For patients with advanced colorectal cancer, target therapy combined with chemotherapy (containing oxaliplatin or irinotecan) is the primary treatment strategy. However, the current first-line chemotherapy regimens often cause severe side effects, such as gastrointestinal reactions, immune system damage, and even bone marrow suppression (4). There is therefore an urgent need to develop effective treatment regimens with fewer side effects.

Due to the rapid advancements and the remarkable survival benefits in patients with a variety of tumors, tumor immunotherapy, including treatment with or the use of monoclonal antibodies, immune checkpoint inhibitors, cytokine therapy, tumor vaccines, and adoptive cell therapy, is now considered to be the fifth pillar of antitumor therapy after surgery, chemotherapy, radiation, and targeted therapy (5, 6). Based on the degree of immune infiltration of the tumor, tumors can be divided into categories of highly infiltrating “hot tumors”, “variable tumors” with rejection and immunosuppression, and non-infiltrating “cold tumors” (7). Manipulation of immune regulatory pathways has been demonstrated as effective in different subsets of tumors, especially in paradigmatic immune-sensitive/“hot” tumors, such as melanoma (8) and non-small cell lung cancer (9). This is because these tumors harbor high levels of tumor mutational burden (TMB) (10–13), CD8 lymphocyte infiltration (14, 15), and programmed death-ligand 1 (PD-L1) expression. Scientists have also tried various approaches to increase immune-mediated responses, such as messenger RNA (mRNA) vaccines to reprogram the tumor microenvironment (TME) and switch “cold” tumors to “hot” tumors (16). At present, immunotherapy has become a research hotspot in the field of COAD treatment. Immune checkpoint inhibitors (ICIs), such as nivolumab and pembrolizumab, were approved by the FDA for patients with unresectable high microsatellite instability (MSI-H) or deficient DNA mismatch repair (dMMR) COAD. Despite numerous attempts, immunotherapy for the treatment of COADs has presented challenges, however (17–19).

Immunotherapy for COAD is not as effective as for immune “hot” tumors because most COADs harbor a low tumor mutation burden and lack of immune cell infiltration. Approximately 80%–85% of COAD patients are considered “cold” tumors, with microsatellite stable (MSS) or low microsatellite instability (MSI-L) (called MSS/MSI-L colorectal cancer), indicating a lack of response to immune checkpoint inhibitors (ICIs) (18–20). COADs can be divided into hypermutated and non-hypermutated types at the genomic level (21). In general, the more mutations the tumor harbors, the higher the immunogenicity detected in the TME. Therefore, the non-hypermutated types harbor fewer immune cells in the TME and have lower immunotherapy efficacy (22). In addition, according to the consensus molecular subtype (CMS) system, only 14% of the COAD population is characterized by hypermutation, microsatellite instability (MSI), and highly activated immune system (23) and is therefore sensitive to ICIs. According to driver mutations, TCGA pan-cancer study stratifies COAD into four subtypes: chromosomal instability (CIN), genetically stable (GS), hypermutated-insertion deletion mutation (HM-indel), and hypermutated-single-nucleotide variant predominant (HM-SNV), which also defined cancers into six immune subtypes (C1–C6) (24). For effective treatment strategies, accurate immune molecular typing is needed to screen out patients with COAD who may benefit from immunotherapy and whose TME require reprogramming to increase immune-mediated responses.

In this study, we conducted a multi-cohort retrospective study and classified COAD into three distinct immune subtypes (ISs), based on consensus clustering of immune characteristics. We demonstrated the stability and reproducibility of this classification in three independent datasets. Each of the three ISs was associated with distinct molecular and cellular features, clinical outcomes, and therapeutic response. The identification of ISs may facilitate the optimal selection of COAD patients sensitive to immunotherapy.

## Materials and methods

### Patients and datasets

We collected the medical data of 1,267 patients with COAD from two online databases: *The Cancer Genome Atlas* (TCGA)

database and Gene Expression Omnibus (GEO) database (including three datasets: GSE39582, GSE17538, and GSE72970). For TCGA cohort ( $n = 437$ ), the RNA-seq data, somatic mutation, and corresponding clinical information of cases with follow-up information were obtained using the GDC-client tool (<https://portal.gdc.cancer.gov/>). The microarray gene expression profiles and patients' clinical data of datasets GSE39582 ( $n = 519$ ), GSE17538 ( $n = 187$ ), and GSE72970 ( $n = 124$ ) were downloaded from the GEO database (<https://www.ncbi.nlm.nih.gov/geo/>). Furthermore, we downloaded the gene expression profile of patients from the GSE72970 dataset, in which samples were obtained before treatment with different chemotherapy regimens (5-FU-based FOLFIRI/FOLFOX or anti-CLDN1 monoclonal antibody treatment), and calculated the therapeutic response of each IS. Gene IDs were converted into official gene symbols according to the Genome Reference Consortium Human Build 38 (GRCh38) assembly. Only genes with Transcripts Per Kilobase Million (TPM; calculated in relation to exon reads) greater than 0 in more than 50% of the samples were included for analysis. Patient informed consent existed in both the public databases, and this study was conducted in accordance with the Helsinki Declaration.

A series of tissue microarray (TMA) slides, which includes 223 patients with COAD that was stored in the tissue bank of Fudan University Shanghai Cancer Center (FUSCC), were used for immunohistochemistry (IHC) analysis. IHC analysis on these samples was approved by the Research Ethics Committee of FUSCC, and all patients provided informed consent.

## Discovery and validation of the COAD immune subtypes

We calculated the enrichment score of immune characteristics in TCGA-COAD (Supplementary Table 1), GSE39582 (Supplementary Table 2), and GSE17538 (Supplementary Table 3) datasets using the IOBR TME-associated package in R software. The prognostic significance of the enrichment score was analyzed by performing univariate Cox regression analysis. Each of the immune characteristics related to disease-free survival (DFS) overlapped in at least two datasets we selected for further analysis (Supplementary Tables 4–6). We applied consensus clustering (25) to identify clusters of patients in robust immune subtypes (IS). Five hundred bootstraps with 80% item resampling were calculated based on the partition around medoids (PAM) classifier and Euclidean distance, the evaluated K-selected clustering was set between 2 and 10, and the optimal classification was determined by calculating a consistency matrix and a consistency cumulative distribution function. The ISs in the GSE39582 and GSE17538 datasets were then validated as follows: the in-group proportion (IGP) (26) and Pearson correlation among centroids of gene

module scores were used to quantitatively measure the consistency and reproducibility of the acquired IS in the GSE39582 and GSE17538 cohorts. The study design and workflow are outlined in Figure 1. We analyzed the difference between the present ISs and other previous proposed COAD classification using a one-way ANOVA and the ssGSEA method.

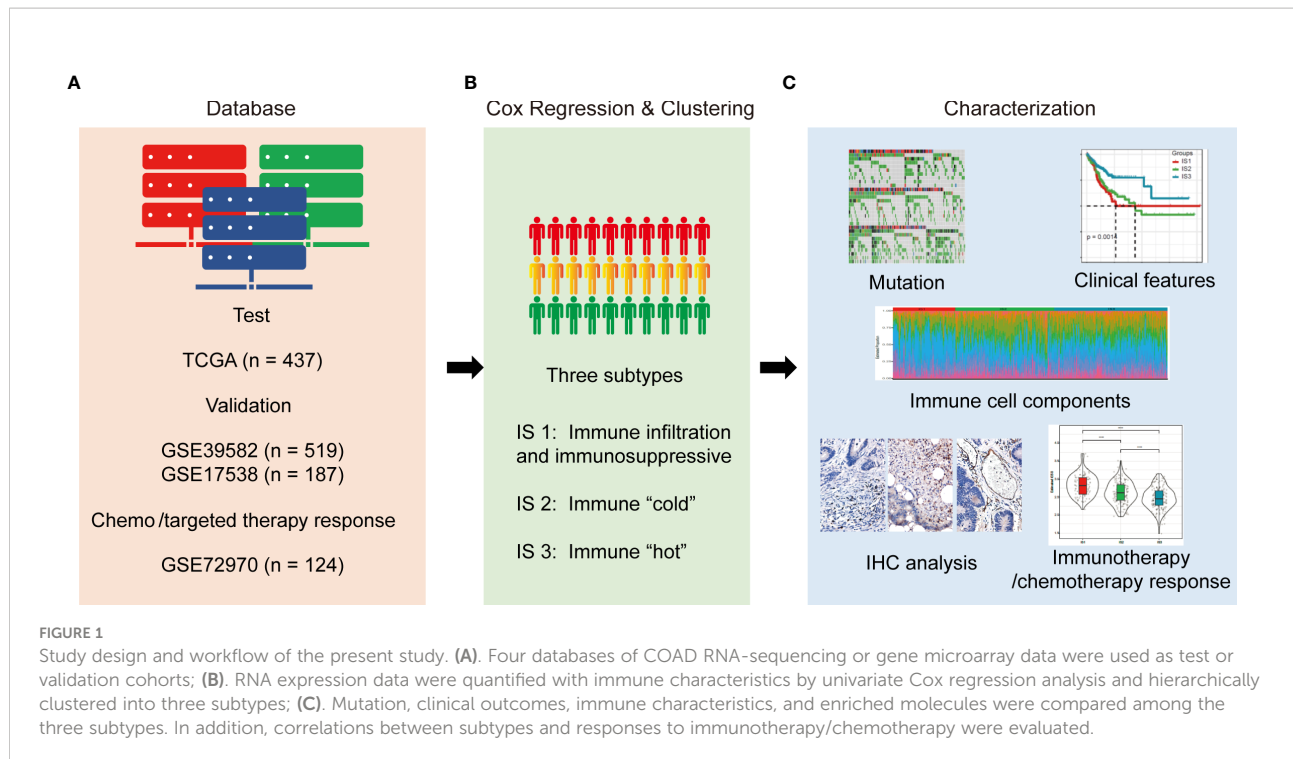
## Evaluation of clinicopathological, molecular, and cellular characteristics associated with the IS

The disease-free survival (DFS) period of each COAD patient was calculated using the Kaplan–Meier method with the log-rank test and univariable Cox regression. Samples with survival time less than 30 days were excluded from the analysis. We downloaded the mutation data from TCGA-COAD dataset and calculated the TMB of each patient, then analyzed the distribution of TMB in each IS. Relationships between ISs and clinicopathological features, including age, sex, and histological type, were analyzed by non-parametric (Fisher's exact) assessments, as appropriate.

## Evaluation of characteristics between molecular subtypes

We first calculated the gene expression of chemokines and chemokine receptors among the three ISs in TCGA-COAD cohort. Next, we obtained 47 immune checkpoint-related genes from the previous study (27) and analyzed their expression profiles among the three ISs. The innate immune cyclic GMP-AMP synthase (cGAS)/stimulator of interferon genes (STING) pathway has recently emerged as a nodal player in cancer immunity and is currently being explored as a potential therapeutic target (28). We compared the expression changes of four key genes in the innate immune cGAS/STING signal pathway, CGAS (encoding cGAS protein), TMEM173 (encoding STING protein), and tank-bound kinase 1 (TBK1) and IFN regulator 3 (IRF3) (both are downstream effectors), among ISs using one-way ANOVAs and the ssGSEA method. We extracted Th1/IFN- $\gamma$  gene signatures (27) and calculated the IFN- $\gamma$  level of each patient among ISs by ssGSEA. Furthermore, we evaluated the intratumoral immune cytolytic activity (CYT) of each patient in TCGA-COAD cohort by calculating the average value of GZMA and PRF1 expression levels. Lastly, we obtained the angiogenesis-related gene set from the previous study (29) and evaluated the angiogenesis score of each patient.

In order to analyze the distribution of immune cell components in each IS, we determined the scores of 22 immune cells in each patient in TCGA-COAD, using the CIBERSORT database (30). In order to analyze the



distribution of immune cell characteristics, especially T-cell components in each IS, we determined the enrichment score of 28 immune cells in each patient in TCGA-COAD cohort, by analyzing 28 immune cell marker genes using the ssGSEA method. The abundances of tumor-infiltration immune cells (B cells, plasma cells, T cells, NK cells, monocytes, mast cells, macrophages, eosinophils, neutrophils, and dendritic cell) were estimated from gene expression data, using the CIBERSORT database (<https://cibersort.stanford.edu/>) (30). The “Estimation of STromal and Immune cells in MAlignant Tumours using Expression data (ESTIMATE)” algorithm was applied to calculate the ImmuneScore and StromalScore, which represent the level of infiltrating immune cells and the presence of stromal cells in tumor tissues (31). The ESTIMATEScore is the sum of the ImmuneScore and StromalScore and refers to the purity of tumor tissues; the score specifies tumor cellularity in the TME. The T-cell dysfunction scores, T-cell rejection scores, and potential clinical efficacy of immune checkpoint inhibitors in each IS were evaluated using Tumor Immune Dysfunction and Exclusion (TIDE) software (<http://tide.dfci.harvard.edu/>) (32). Moreover, a high TIDE score is positively correlated with immune escape, and patients with a high TIDE score are less likely to benefit from ICIs (32). Therefore, we investigated the possibility of immune escape of each IS by calculating the TIDE score for TCGA-COAD cohort. Tumor-associated inflammation characteristics can promote tumor growth and progression by promoting angiogenesis and metastasis, subverting antitumor immune response, and changing the sensitivity of tumor cells to chemotherapeutic drugs (33–35). In order to analyze the

distribution of inflammation characteristics in each IS, we determined the expression level of inflammation-related genes in each patient in TCGA-COAD cohort, using the ssGSEA method. We then analyzed the differences in the enrichment scores of the seven inflammation-related metagenes (*HCK*, *IgG*, *LCK*, *MHC-I*, *MHC-II*, *Interferon*, *STAT1*) among the ISs.

## Prediction of IS response to immunotherapy or chemotherapy

The R package “pRRophetic” was used to estimate the chemotherapeutic response of cisplatin and 5-fluorouracil in TCGA-COAD cohort (36). Gastrointestinal cancer cell lines and the “cgp2016” dataset were applied when implementing the “pRRopheticPredict” function. This methodology fitted the ridge regression model based on the drug sensitivity of the cell line and baseline of gene expression, thus predicting the chemotherapeutic response by using patients’ baseline gene expression data. Drug sensitivity was measured by the concentration required for 50% cellular growth inhibition (IC50). Based on genomic expression profiles and therapeutic and prognostic data in TCGA-COAD dataset, the potential response of each IS to traditional chemotherapy drugs cisplatin and 5-FU were predicted by the unsupervised subclass mapping (SubMap) method (37). In short, the IS of each sample was determined by analyzing their genomic expression profile, then the therapeutic and prognostic data of each sample were mapped (unsupervised subclass) to the IS, to predict the potential response of each IS to chemotherapy drugs.

## Analysis of the immune-related gene co-expression module

We clustered the 437 patients in TCGA-COAD cohort based on the expression of all genes with median absolute deviation (MAD)  $>50\%$ , and the weighted gene correlation network analysis (WGCNA) co-expression algorithm was used to detect co-expressed gene modules using the R package WGCNA (38) (Supplementary Figure S3A). To ensure that the co-expression network can be a scale-free network, the co-expression modules were screened by setting a soft threshold power  $\beta$  as 10 (Supplementary Figures S3B, C). Among the gene co-expression modules obtained from cluster analysis and module fusion, gray modules represent gene sets that could not be merged. The topology overlap matrix (TOM) was then constructed from the adjacency matrix to avoid the influence of noise and spurious associations. Based on TOM, average-linkage hierarchical clustering using the dynamic shear tree method was conducted to define co-expression modules. The minimum gene size of each module was set to 60. To explore the relationship among modules, the feature vector values (eigengenes) of each module were calculated in turn, and modules with highly correlated eigengenes were merged into a new module through cluster analysis with the threshold as follows: height = 0.25, DeepSplit = 4, and minModuleSize = 60.

## Identification of hub genes by protein–protein interaction analysis

Since protein–protein interaction (PPI) analysis can help identify hub genes with core functions, PPIs among genes in the identified key modules were further explored. The Search Tool for the Retrieval of Interacting Genes (STRING) is a well-known database containing comprehensive PPI information (version 11.0, <https://string-db.org/>). The PPI network among these genes was thus mapped to the STRING assembly and then visualized by the Cytoscape software.

## Immunohistochemical staining

The expressions of angiogenesis marker-CD31, cytolytic activity marker-interferon-gamma (IFN- $\gamma$ ), and granzyme B (GZMB) of these CRC patients were also determined by IHC staining. IHC staining was performed as described previously (39). The primary antibodies are listed as follows: Anti-Interferon gamma antibody (Abcam, ab218426, 1:100), Granzyme B Monoclonal Antibody (Abcam, ab255598, 1:100), and CD31 (Gene Tech, M082304).

## Statistical analysis

All statistical analyses were performed using R 3.6.0 (<https://mirrors.tuna.tsinghua.edu.cn/CRAN/>) with default software parameters. A  $P$  value  $<0.05$  was considered statistically significant. The biological function of genes in each immune gene co-expression module was annotated in Gene Ontology using the R package clusterProfiler. The Pearson correlation coefficient was used for correlation analysis. Univariate Cox regression analysis was performed to determine the immune-related gene co-expression modules with prognostic significance. A one-way ANOVA was applied for assessing the association between IS and the immune-related molecular and cellular characteristics using the ssGSEA method (24).

## Results

### Identification of potential immune subtypes of COAD

We identified 14 disease-free survival (DFS)-related characteristics in TCGA-COAD cohort (Supplementary Table 4), 36 prognostic characteristics in the GSE39582 cohort (Supplementary Table 5), and 17 prognostic characteristics in the GSE17538 cohort (Supplementary Table 6), respectively. Specific immune characteristics varied among the three cohorts, with little overlapping characteristics (Figure 2A). From the DFS-related immune characteristics, 17 characteristics that were overlapped in at least two cohorts were included for subsequent analysis ( $P < 0.05$ , Figure 2B). By applying consensus clustering of 437 COAD samples using the enrichment score of these 17 DFS-related immune characteristics, we identified three molecular immune subtypes (ISs), IS1–IS3, in TCGA-COAD cohort (Figures 2C–E). Of these identified ISs, IS3 was associated with the longest DFS and IS1 with the shortest (Figure 2F). The ISs obtained from the datasets GSE39582 and GSE17538 displayed similar survival patterns (Figures 2G, H). There were significant differences in the distribution of patients' clinicopathological characteristics, including T stage, N stage, M stage, and TNM stage among the three ISs in TCGA-COAD (Figure 2I) and GSE39582 cohorts (Supplementary Figure S1B), whereas there was no significant difference in the distribution of age and gender among the three ISs in both two datasets (Supplementary Figures S1A, B). In the GSE17538 cohort, there were significant differences in the distribution of patients' TNM stage, histological grade, and gender among the three ISs (Supplementary Figure S1C). However, the same IS was differently distributed in these three cohorts, indicating the tumor heterogeneity. We further analyzed the distribution of four consensus molecular subtypes (CMS) (23) in these three ISs: IS1 consisted mostly of the CMS4 subtype, IS2 consisted mostly of the CMS2 subtype, and IS3 was more congruent

with the CMS1 subtypes; CMS3 was mostly distributed in IS2 and IS3 (Figure 2). When comparing the MMR status among each IS using TCGA COAD dataset, patients with the MSS status mostly fell into IS1, while IS2 and IS3 had the highest percentage of patients with MSI-L and MSI-H, respectively (Figure 2K). When analyzing the distribution of four TCGA pan-cancer mutation classification subtypes (CIN, GS, HM-indel, and HM-SNV) in these three ISs, IS1 and IS2 consisted mostly of the CIN subtype, while IS3 was more congruent with the HM-indel and HM-SNV subtypes (Figure 2L). We further compared the results of ISs with the six previous immune subtypes (C1~C6), which was also defined by TCGA pan-cancer study, and discovered that the identified IS1 and IS2 subtypes are most similar to C1 subtypes, whereas the C6 subtype is mainly distributed within IS1. Moreover, in comparison to IS1 and IS2, the percent of C2 subtypes was highest in IS3 (Figure 2M).

## The relationship between IS, tumor mutation burden, and common gene mutations in TCGA-COAD dataset

The TMB was significantly higher in IS3 than in IS1 or IS2, whereas no significant difference was observed between IS1 and IS2 (Supplementary Figure S2A). Additionally, there were 12,744 genes with mutation frequency  $>3$  in at least one of all three ISs (Supplementary Table 7), and 5,414 genes showed a significantly different mutation frequency among the three ISs ( $P < 0.05$ , chi-square test; Supplementary Table 8). The number of gene mutations in IS1 and IS2 subtypes was significantly lower than that of IS3, whereas no significant difference was observed between IS1 and IS2 (Supplementary Figure S2B). Additionally, among the 10 mutation characteristics with the highest mutation frequency in each subtype, the proportion of adenomatous polyposis coli (APC) mutations in IS2 was significantly greater than for IS1 and IS3; the proportion of TP53 mutations in IS1 was significantly higher than for IS2 and IS3; while the proportion of KRAS mutations in IS1 was significantly lower than in IS2 and IS3 (Supplementary Figure S2C). The frequency of the DNA polymerase  $\epsilon$  (POLE) mutation showed no significant difference between the IS1 and IS2 subtypes but was significantly higher in the IS3 subtype (Supplementary Table 8).

## Distribution of immune-related molecular characteristics among IS by using TCGA-COAD dataset

The gene expression of chemokines and chemokine receptors among these three ISs showed that the expression of most (30/41) chemokines, such as CCL4, CCL5, CXCL9, and CXCL10, in IS2 was significantly lowest among all three IS

(Figure 3A). CXCR6 and the other most chemokine receptors (17/18) were significantly lower in IS2 compared to the other two ISs (Figure 3B). The expression of 41 (87.2%) of the immune checkpoint-related genes was significantly lower in IS2 than in IS1 and IS3, including LAG3, ICOS, CTLA-4, HAVCR2 (TIM3), PDCD1, and CD274 (PD-L1) (Figure 3C). For the four genes in the innate immune cGAS/STING signal pathway, CGAS was significantly higher in IS3 than in IS1 and IS2, whereas the expression of TMEM173 and TBK1 was significantly lower in IS2 than in IS1 and IS3, and there was no significant difference in IRF3 expression level among the three ISs (Figures 3D–G). The expression level of IFN- $\gamma$  was lowest in IS2, while it was the highest in IS3 (Figure 3H). IS2 had the lowest intra-tumoral immune cytolytic activity (CYT) level, and IS3 the highest (Figure 3I). The angiogenesis level of IS1 was significantly higher than that of IS2 and IS3 (Figure 3J). The data from the pathological archive showed that in the 223 patients with CRC we enrolled for IHC, 12 cases were dMMR (MSI-H) and the other 211 cases were pMMR (MSS) (Table 1). The expressions of CD31, IFN- $\gamma$ , and GZMB in 12 randomly selected pMMR cases were compared with these 12 dMMR samples by IHC, which indicated that IFN- $\gamma$  and GZMB were expressed robustly in patients with a dMMR status, while the angiogenesis marker CD31 expressed more strongly in patients with pMMR status (Figures 3K, L).

## Immune characteristics of ISs by using TCGA-COAD dataset

The distribution of most immune cell components differed among the three ISs (Figures 4A, B). For example, monocytes in IS1 were significantly higher than those in IS2 and IS3, CD8 $^{+}$  T cells in IS1 were significantly lower than in IS2 and IS3, while CD4 $^{+}$  naïve T cells, plasma cells, and macrophages M1 in IS3 were significantly higher than in IS1 and IS2 (Figures 4A, B). The relative proportion of stromal cells in all ISs showed that IS1 had the highest relative proportion of stromal cells in TME, while IS2 had the lowest relative proportion of immune cells (Figures 4C, D).

## Distribution of immune cell and inflammation characteristics among ISs

In TCGA-COAD cohort, the enrichment scores of most immune cell components in IS1 and IS3 were significantly higher than in IS2, such as activated CD8 $^{+}$  and CD4 $^{+}$  T cells, effector memory CD8 $^{+}$  and CD4 $^{+}$  T cells, macrophages, and MDSCs (Figures 5A, B). Overall, the enrichment scores of most of immune cells in IS1 and IS3 were significantly higher than in

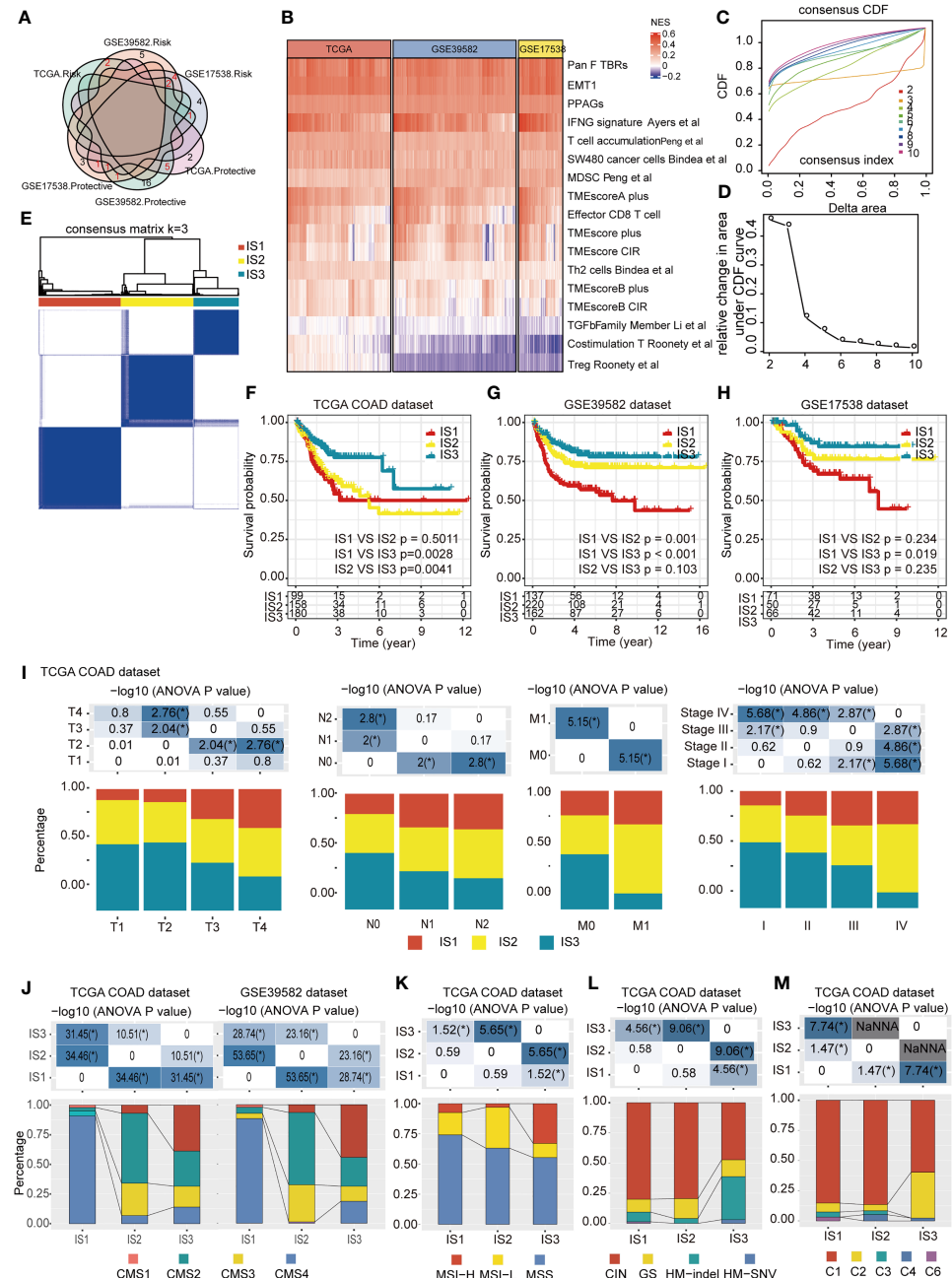


FIGURE 2

Identification of potential immune subtypes of COAD. **(A)** Overlapping prognostic immune characteristics among TCGA-COAD, GSE39582, and GSE17538 cohorts; the lines correspond to different gene sets in each dataset; red numbers represent the intersection genes of different datasets. **(B)** The distribution of 17 immune characteristics among three cohorts; **(C, D)**. Cumulative distribution function (CDF) curve (C) and (D) delta area showed the stability of different cluster numbers in the consensus clustering result by using the enrichment score of the 17 immune characteristics. The consensus CDF diagram allows us to determine at what number of clusters,  $k$ , the CDF reaches an approximate maximum; thus, consensus and cluster confidence are at a maximum at this  $k$  (Please See Xue et al. PMID: 19351533). In this manuscript, we set the  $k$  value = 3. **(E)** Sample clustering heat map of the 437 samples in TCGA-COAD cohort. **(F–H)** Kaplan–Meier curves with log-rank test showing DFS of ISS in TCGA-COAD **(F)**, GSE39582 **(G)** and GSE17538 **(H)** cohorts. **(I)** Distribution of IS1-IS3 among the indicated clinicopathological characteristics in TCGA-COAD cohort. **(J)** Distribution of IS1-IS3 among CMS classification in TCGA-COAD and GSE39582 cohort. **(K)** Distribution of IS1-IS3 among patients with different microsatellite instability (MSI) statuses; IS2 and IS3 had the highest percent of patients with MSI-L and MSI-H subtypes, respectively. **(L)** Distribution of IS1-IS3 among TCGA mutation classification; IS1 and IS2 are mainly composed of the CIN subtype, while IS3 showed more relevance with the HM-indel and HM-SNV subtype. **(M)** Distribution of IS1–IS3 among TCGA immune subtypes; the IS1 and IS2 subtypes are mainly inclined to C1 subtypes, and the C6 subtype is mainly distributed within IS1, while the percent of C2 subtypes in IS3 was higher than that in IS1 and IS2. \*  $P < 0.01$ , \*\*  $P < 0.001$ , \*\*\*  $P < 0.0001$ , and \*\*\*\*  $P < 0.00001$ .

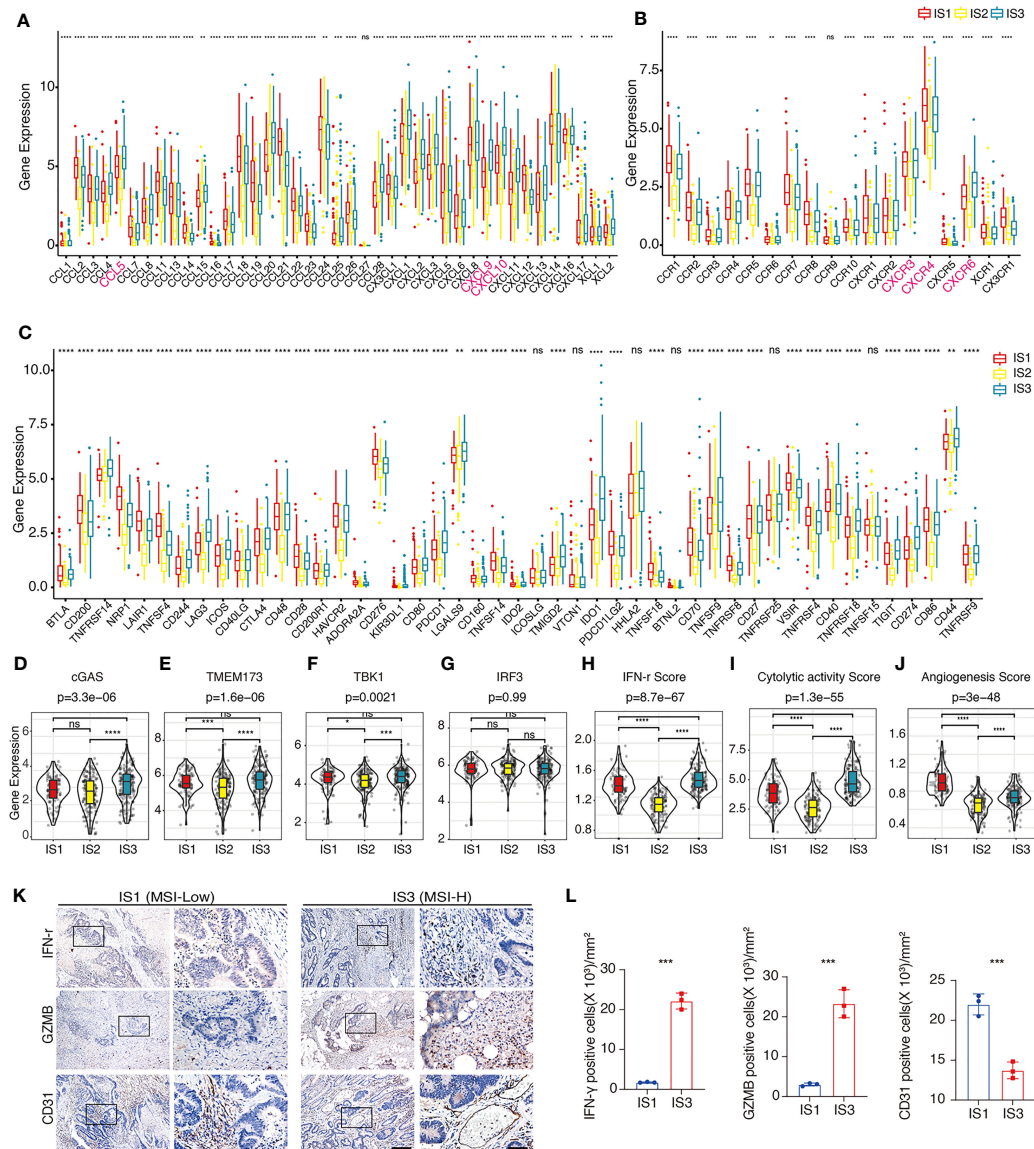


FIGURE 3

Distribution of immune-related molecular characteristics among ISs in TCGA-COAD and FUSCC cohorts (A, B). Differential expression of chemokines (A) or chemokine receptors (B) among the COAD immune subtypes in TCGA-COAD cohort. *CCL4*, *CCL5*, *CXCL9*, *CXCL10*, *CXCR3*, *CXCR4*, and *CXCR6* are highlighted in pink. The top and bottom of the box are the upper quartile (Q3) and the lower quartile (Q1) of the data, respectively. The solid line in the box represents the median. The whiskers represent the maximum and minimum values of this group of data. The Kruskal–Wallis test was used to assess for significant differences. ns not significant, \*P < 0.01, \*\*P < 0.001, \*\*\*P < 0.0001, and \*\*\*\*P < 0.00001. (C). Differential expression of immune checkpoint-related genes among the COAD immune subtypes in TCGA-COAD cohort. The top and bottom of the box are the upper quartile (Q3) and the lower quartile (Q1) of the data, respectively. The solid line in the box represents the median. The whiskers represent the maximum and minimum values of this group of data. The Kruskal–Wallis test was used to assess for significant differences. ns not significant, \*P < 0.01, \*\*P < 0.001, \*\*\*P < 0.0001, and \*\*\*\*P < 0.00001. (D–G). Differential expression of *cGAS* (D), *TMEM173* (E), *TBK1* (F), and *IRF3* (G) among the COAD immune subtypes in TCGA-COAD cohort. We used the Kruskal–Wallis test and Wilcoxon test to compare the significance among the three groups and pairwise comparison between groups, respectively. The solid black line in the box represents the median, and the black box in the violin plot represents the quartile range. The black vertical line running through the violin chart represents the interval from the minimum value to the maximum value, respectively. ns not significant, \*P < 0.01, \*\*P < 0.001, \*\*\*P < 0.0001, and \*\*\*\*P < 0.00001. (H–J). The estimated IFN-γ level (H), CYT level (I), and angiogenesis level (J) among the COAD immune subtypes in TCGA-COAD cohort. We used Kruskal–Wallis test and Wilcoxon test to compare the significance among the three groups and pairwise comparison between groups, respectively. The solid black line in the box represents the median, and the inner black box in the violin plot represents the quartile range. The black vertical line running through the violin chart represents the interval from the minimum value to the maximum value, respectively. ns not significant, \*P < 0.01, \*\*P < 0.001, \*\*\*P < 0.0001, and \*\*\*\*P < 0.00001. (K). Representative IHC result of IFN-γ, GZMB, and CD31 in dMMR and pMMR subtypes in the FUSCC cohort. The box area is magnified in the right panel. Scale bars: 100 μm (left panel) and 20 μm (right panel). (L). Scatter plots show the difference of IFN-γ, GZMB, and CD31 in dMMR and pMMR subtypes in the FUSCC cohort. Unpaired t-test. Data are shown as mean ± SD. \*\*\*P < 0.0001.

IS2. The expression level of inflammation-related genes, which can be categorized into seven inflammation-related metagenes (MHC-I, MHC-II, HCK, LCK, interferon, STAT1, and IgG), showed that the majority of genes in MHC-II (HLA-DP, HLA-DQ, CD74), HCK (HCK, MA4A4A, CD163, C1QA, C1QB), LCK (LCK, CD2, CD3, GZMA, GZMK), MHC-I (HLA-A/B/C), interferon (IFIT1, IFIT3, IFI44), and STAT1 metagenes were highly expressed in IS1 (Figure 5C). With the exception of IgG, the enrichment scores of all the other six metagenes in IS1 and IS3 were significantly higher than that in IS2 (Figure 5D).

## The predicted IS response to immunotherapy and chemotherapy

The TIDE score was calculated to predict the possibility of immune escape of each IS using TCGA-COAD cohort, which showed that IS1 had the highest TIDE score (Figure 6A) and the highest predicted T-cell dysfunction score (Figure 6B). In addition, the proportion of predicted immunotherapy responses in IS1 was significantly lower than that of IS2 and IS3 (Figure 6C). These data suggest that the IS1 subtype is less likely to benefit from the anti-PD-L1 therapy. Besides, by analyzing the gene expression profile of TCGA-COAD cohort, the IS3 subtypes are predicted to be more sensitive to cisplatin than other ISs (Figure 6D), while IS1 is more sensitive to 5-FU (Figure 6E). Moreover, the gene expression profile and therapeutic response of patients from the GSE72970 dataset showed that, in patients who underwent 5-FU-based chemotherapy, the ratio of partial response (PR) cases in IS2 and IS3 was significantly higher than that in IS1, and the ratio of complete response (CR) cases in IS3 was significantly higher than that in IS1 and IS2 (Figure 6F).

## Function and prognosis analysis of co-expression gene modules among ISs

By clustering the 437 cases in TCGA-COAD cohort, a total of 22 gene co-expression modules were obtained after cluster analysis and module fusion (Figure 7A; Supplementary Figures S3A–C, Supplementary Table 9). Gene numbers in each module are shown in Figure 7B. The distribution of these 22 modules in each clinicopathological feature and IS was further evaluated, which showed that the brown module was positively correlated with IS1 (Figures 7C, D), while it was negatively correlated with IS2 (Figure 7C); the darkolivegreen module was negatively correlated with IS2 (Figure 7C) and positively correlated with IS3 (Figures 7C, E). Functional enrichment analysis showed that the brown

module was related to leukocyte activation regulation, leukocyte migration, and extracellular matrix or structure organization (Figure 7F). The darkolivegreen module was related to immune-related pathways, such as the cellular response to IFN- $\gamma$ , response to type I interferon (IFN), and IFN signaling pathway (Figure 7G).

Correlation analysis showed that 25 genes from the brown module (Supplementary Table 10) while no gene from the darkolivegreen module (Supplementary Table 11) were significantly correlated with brown module ( $r > 0.85$ ) and DFS ( $P < 0.05$ ). From these 25 genes, 12 hub genes (*AEBP1*, *CLEC14A*, *COL5A1*, *COL6A2*, *ITGA4*, *PDGFRB*, *EFEMP2*, *MMRN2*, *MRC2*, *THY1*, and *TNS1*) were obtained by constructing a PPI network, and the other genes with no interaction were excluded (Figure 7H). Univariate and multivariate Cox regression analyses results showed that the collated hub genes can predict the DFS of patients in TCGA-COAD cohort (Figure 7I). Thus, these 12 genes were selected as the final module feature gene. These hub genes can act as biomarkers for screening of the high-risk COAD population in IS1 and IS2.

## Discussion

COAD remains one of the most common malignancies worldwide, whereas the efficacy of current systemic treatment options is still limited (2, 4). At the time of admission, approximately 20%–25% of COAD patients are diagnosed with metastatic disease (40), and 25% develop locally recurrent or metastatic disease within 5 years. The 5-year survival of patients with metastatic COAD is only 15% (41). It is thus critical to investigate novel therapeutic targets so as to apply new treatments with improved clinical efficacy, whereas new immunotherapy techniques are not effective for all cancer patients. Accurate immune molecular typing is pivotal for screening out patients with COAD who may benefit from immunotherapy and whose TME requires reprogramming to increase immune-mediated responses. In the current study, we presented a comprehensive characterization of the immunological profile of COADs. Using TCGA-COAD dataset, we found that COADs can be stratified into three ISs, based on consensus clustering of immune characteristics. This IS stratification was confirmed using the GSE39582 and GSE17538 datasets as validation cohorts. These results indicate that the three molecular subtypes, based on immune characteristic enrichment scores, were reproducible in different COAD cohorts. Each of the three ISs was associated with distinct clinicopathological characteristics, genetic aberrations, tumor-infiltrating immune cell composition, immunophenotyping (immune “hot” and immune “cold”) (42), cytokine profiles, and different clinical outcomes and immunotherapy/therapeutic response. Our study suggests that identification of IS may facilitate the optimal selection of COAD patients responsive to adequate therapeutic strategies.

TABLE 1 Clinicopathological features of colorectal cancer patients.

Characteristics	n	%
Age (years)	233	
<60	106	45.49%
≥60	117	50.21%
Gender		
Male	129	55.36%
Female	94	40.34%
Primary cancer site		
Colon,	124	53.22%
Rectum	96	41.20%
Unspecified	3	1.29%
Tumor size		
<5cm	138	59.23%
≥5cm	85	36.48%
Tumor differentiation		
Well	1	0.43%
Moderate	165	70.82%
Poor	50	21.46%
Unspecified	7	3.00%
Vascular invasion		
Positive	38	16.31%
Negative	185	79.40%
Perineural invasion		
Positive	48	20.60%
Negative	175	75.11%
Staging at diagnosis		
Stage II	193	82.83%
Stage III	30	12.88%
Primary tumor size		
pT2	3	1.29%
pT3	80	34.33%
pT4	140	60.09%
Involvement of lymph node		
pN0	193	82.83%
pN1	20	8.58%
pN2	10	4.29%
MMR status		
dMMR	12	5.15%
pMMR	211	90.56%

The innate immune cyclic GMP-AMP synthase (cGAS)/stimulator of interferon genes (STING) pathway has recently emerged as a nodal player in cancer immunity and is currently being explored as a potential therapeutic target (28). Our data showed that CGAS was significantly highest in IS3, suggesting that the cGAS/STING signal pathway is more active in IS3. IS3 also had the highest IFN- $\gamma$  level, which can be produced by CD8 $^{+}$  T cells and inducing the overexpression of the *PD-L1/PD-L2* gene (43, 44). In addition, IS3 showed significantly higher CD4 $^{+}$  T-cell, CD8 $^{+}$  T-cell, and macrophage M1 percentages among the three

ISs. These findings suggest that the immune characteristics displayed by IS3 present a classic immune “hot” phenotype, which is sensitive to immunotherapy (42), and the variation in COAD prognosis may be related to the distribution of these cell types. The tumor microenvironment (TME) of IS1 showed composite immune signatures reflecting a high immune cell component, including macrophages, activated B cells, activated CD8 $^{+}$  T cells, effector memory CD8 $^{+}$  T cells, immature B cells, and MDSCs, indicating that IS1 acts as a high immune infiltration (immune “hot”) (7) phenotype. However, IS1 conferred the

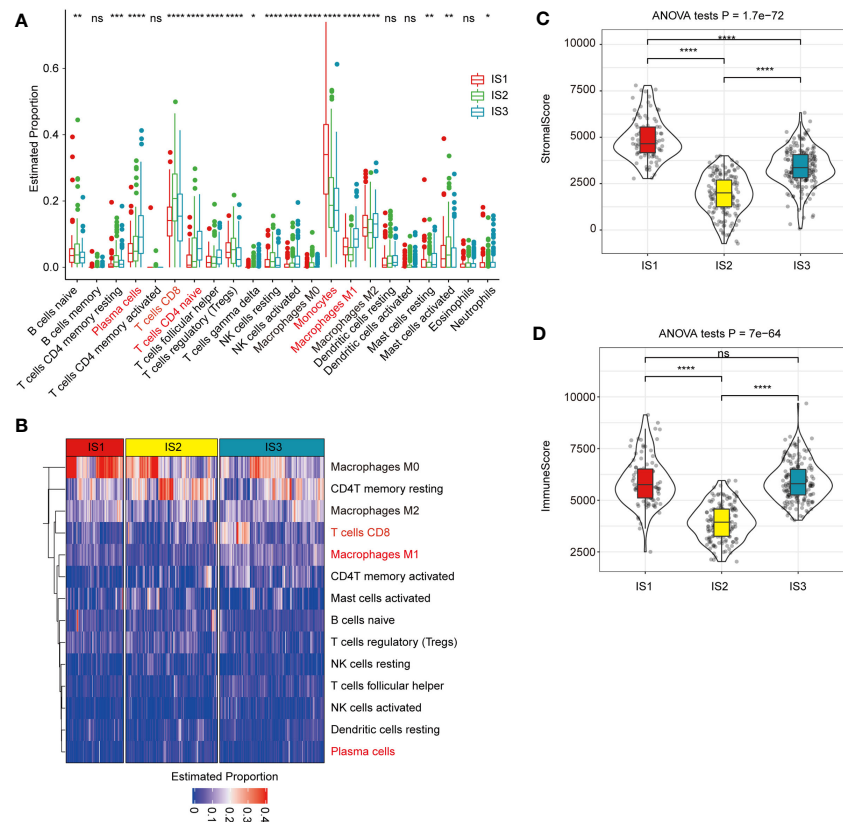


FIGURE 4

Association between immune subtypes and COAD-related tumor biomarkers in TCGA-COAD dataset (A). The estimated proportion of immune cell infiltration among immune subtypes. CD8 T cell is highlighted in pink. The top and bottom of the box are the upper quartile (Q3) and the lower quartile (Q1) of the data, respectively. The solid black line in the box represents the median. The whiskers represent the maximum and minimum values of this group of data. The Kruskal–Wallis test was used to assess for significant differences. ns, not significant,  $*P < 0.01$ ,  $**P < 0.001$ ,  $***P < 0.0001$ , and  $****P < 0.00001$ . (B) Heat map for the estimated proportions of immune cells in the samples among immune subtypes. CD8+ T cell is highlighted in pink and significantly higher in IS3 subtypes. (C, D) The proportions of StromalScore (C) or ImmuneScore (D) among immune subtypes in TCGA-COAD cohorts. IS1 has the highest relative proportion of stromal cells in TME, while IS2 has the lowest relative proportion of immune cells. We used the Kruskal–Wallis test and Wilcoxon test to compare the significance among the three groups and pairwise comparison between groups, respectively. The solid black line in the box represents the median, and the inner black box in the violin plot represents the quartile range. The black vertical line running through the violin chart represents the interval from the minimum value to the maximum value, respectively. ns, not significant,  $*P < 0.01$ ,  $**P < 0.001$ ,  $***P < 0.0001$ , and  $****P < 0.00001$ .

poorest DFS. Stromal cells have been reported as key contributors to an immunosuppressive TME and hinder antitumor immunity (45, 46). IS1 had the highest angiogenesis level and proportion of stromal cells, which both suggests a more invasive and metastatic potential of tumors (47) and is therefore linked with a poor prognosis. It has been reported that the tumor immune dysfunction and exclusion (TIDE) score positively predicts the possibility of immune escape, with a high TIDE score positively correlated with immune escape and a lower chance of patients benefiting from ICIs (32). IS1 had the highest TIDE score and predicted T-cell dysfunction scores in TME, as well as the highest tumor immune dysfunction and exclusion score, which was more similar to immune escape. Thus, IS1 may also be an “immunosuppressive” phenotype. In comparison, the majority of cases in IS2 were MSS/MSI-L, which showed the lowest relative

proportion of immune cells, which was potentially due to the low checkpoint-related gene expression levels. It has been reported that a high *CCL4/CCL5/CXCL9/CXCL10* expression is strongly associated with CD8<sup>+</sup> T-cell infiltration and T-cell activation (48–51). Moreover, CXCL9, CXCL10, and CXCL11/CXCR3 axis play a central role in immune activation (52, 53). CXCR6, which was reported to be exclusively expressed on intratumoral CD8<sup>+</sup> T cells in colon cancer, positions cytotoxic T cells to receive critical survival signals in the tumor microenvironment (54, 55). Our data showed that the expression levels of all these genes were significantly lower in the IS2 subtype among the three ISs, which suggest that IS2 has the lowest minimal immune activation; it tends to be an immune “cold” phenotype. In patients within this subtype, a combination of therapies aimed at converting the “cold” tumor to a “hot” tumor, with another

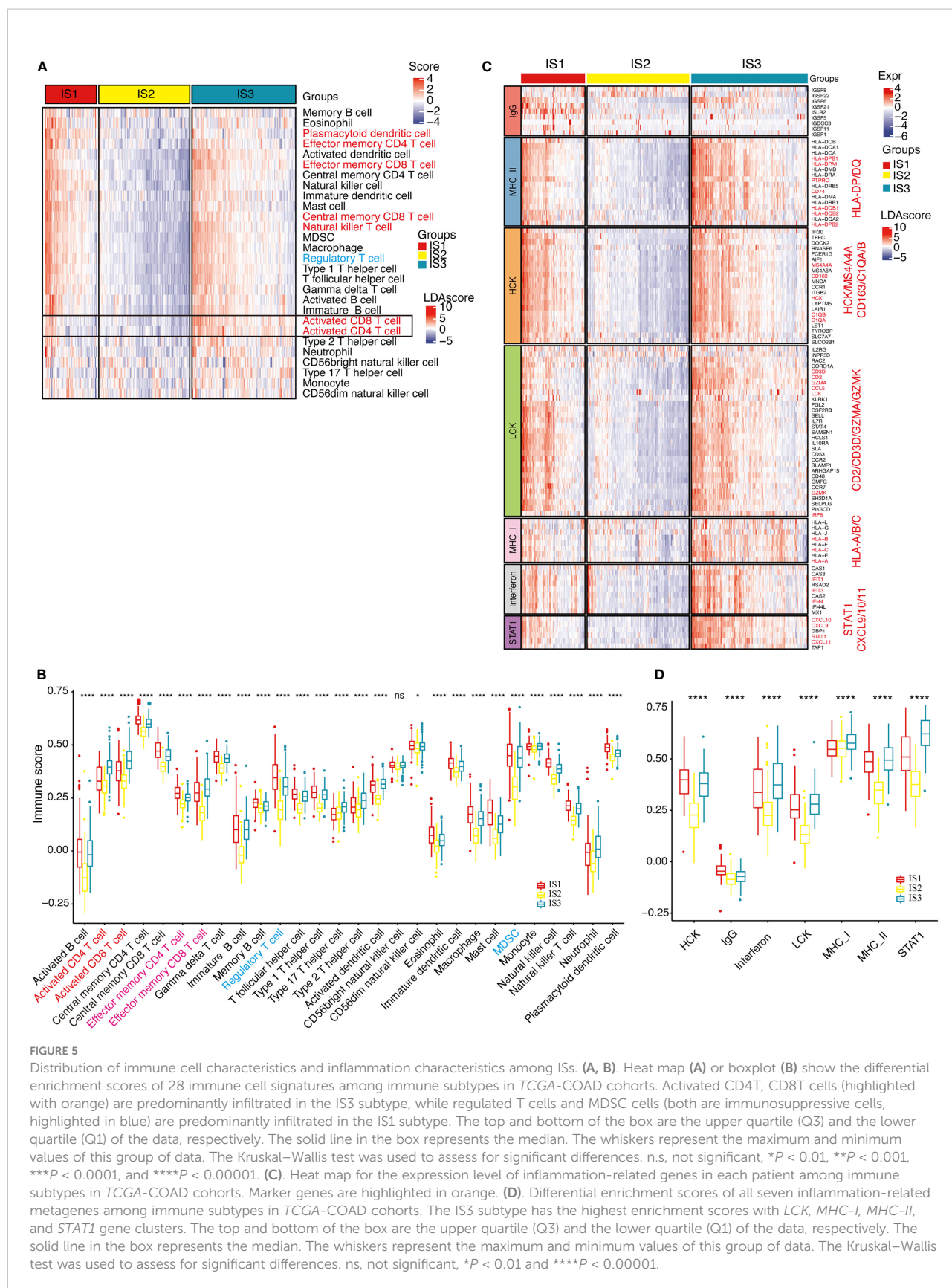
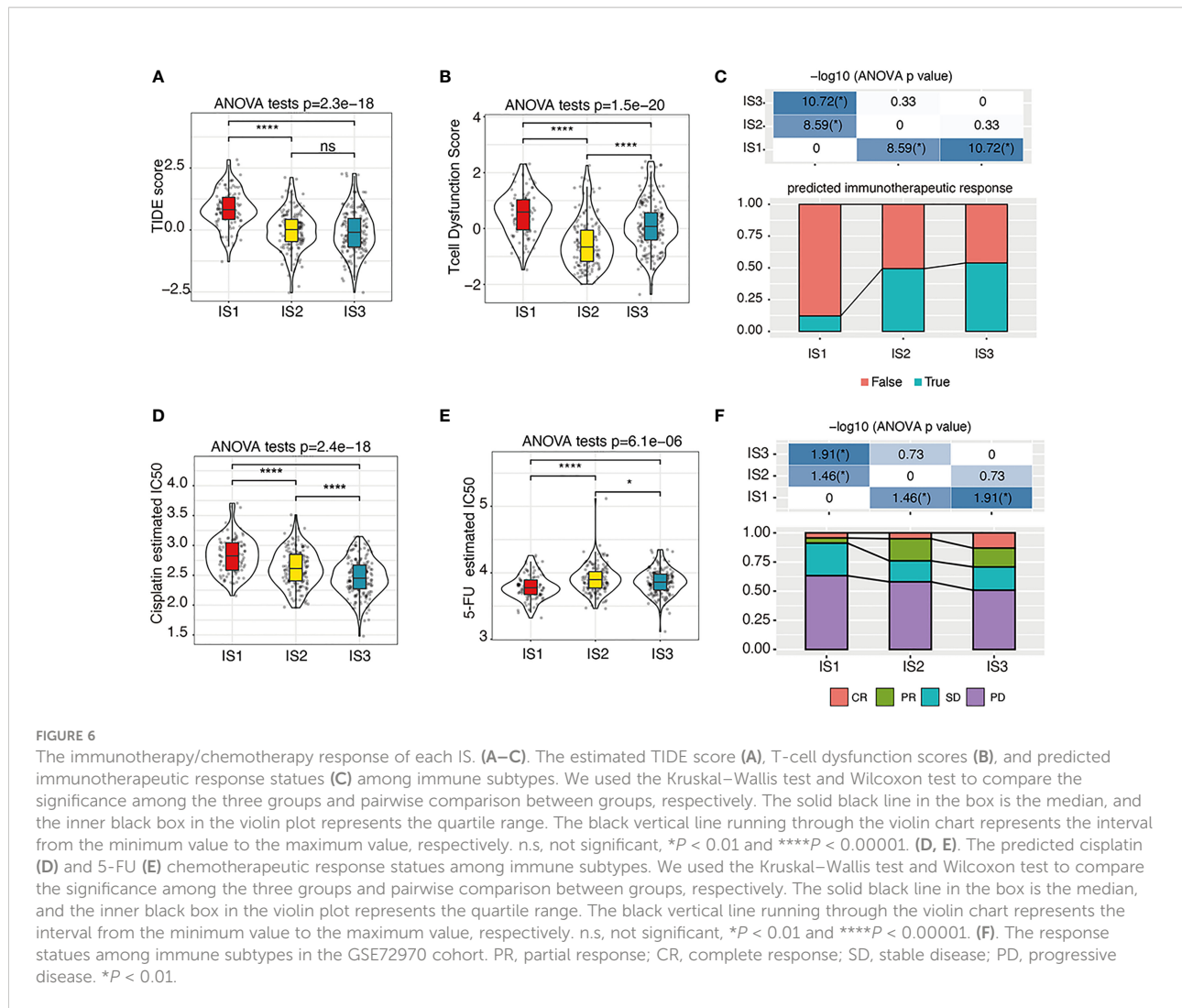


FIGURE 5

**FIGURE 3**  
 Distribution of immune cell characteristics and inflammation characteristics among ISs. **(A, B)**. Heat map (**A**) or boxplot (**B**) show the differential enrichment scores of 28 immune cell signatures among immune subtypes in TCGA-COAD cohorts. Activated CD4T, CD8T cells (highlighted with orange) are predominantly infiltrated in the IS3 subtype, while regulated T cells and MDSC cells (both are immunosuppressive cells, highlighted in blue) are predominantly infiltrated in the IS1 subtype. The top and bottom of the box are the upper quartile (Q3) and the lower quartile (Q1) of the data, respectively. The solid line in the box represents the median. The whiskers represent the maximum and minimum values of this group of data. The Kruskal–Wallis test was used to assess for significant differences. n.s. not significant,  $*P < 0.01$ ,  $**P < 0.001$ ,  $***P < 0.0001$ , and  $****P < 0.00001$ . **(C)**. Heat map for the expression level of inflammation-related genes in each patient among immune subtypes in TCGA-COAD cohorts. Marker genes are highlighted in orange. **(D)**. Differential enrichment scores of all seven inflammation-related metagenes among immune subtypes in TCGA-COAD cohorts. The IS3 subtype has the highest enrichment scores with *LCK*, *MHC-I*, *MHC-II*, and *STAT1* gene clusters. The top and bottom of the box are the upper quartile (Q3) and the lower quartile (Q1) of the data, respectively. The solid line in the box represents the median. The whiskers represent the maximum and minimum values of this group of data. The Kruskal–Wallis test was used to assess for significant differences. ns, not significant,  $*P < 0.01$  and  $****P < 0.00001$ .



immunotherapy or chemotherapy, might modulate both the host immune response and the TME toward a state more conducive to successful therapy. Moreover, in addition to harboring the highest adenomatous polyposis coli (APC) mutations and low *KRAS* and *TP53* mutations, IS2 have the most gene mutations. This suggests that, although the IS2 tumor may derive primarily from APC mutation, the pathogenesis of tumors in this subtype may be much more complex than the other ISs. Further functional and mechanistic studies of the mutated genes may identify the pathogenesis and therapeutic targets.

We further analyzed the distribution of four consensus molecular subtypes (CMS) (23) in these three ISs: IS1 consisted mostly of the CMS4 subtype, IS2 consisted mostly of the CMS2 subtype, and IS3 was more congruent with the CMS1 subtypes; CMS3 was mostly distributed in IS2 and IS3. The CMS4 subtype was characterized by a high stromal infiltration, TGF- $\beta$  activation, and angiogenesis (23), and all these are also prominent features of IS1. Similarly, the IS3 subtype with better prognosis has a larger proportion of CMS1, both subtypes are

characterized by high immune infiltration, and MSI-H CRC is mainly a feature in CMS1 (23) and IS3 subtypes. Moreover, CMS2 and CMS3 CRCs with intermediate prognosis are mainly distributed in the IS2 type, which also had intermediate prognosis. Nevertheless, it should be pointed out that the CMS cannot clearly predict the prognosis of COAD. In addition, CMS shows a relatively indistinct characterization on the tumor immune microenvironment of COAD. For CMS2–4 CRCs with relatively lower immune infiltration than CMS1, COAD ISs help to show distinct prognosis and more detailed immune characteristics. When compared with the previously defined pan-cancer immune-subtypes based on the data compiled by TCGA (24), IS1 and IS2 were most similar to the C1 (wound healing) subtype, which had a poorer prognosis than the other five subtypes in TCGA-COAD dataset. The C6 subtype, with an immunologically suppressed feature and poorest prognosis in all six subtypes in TCGA-COAD dataset, displays the highest TGF- $\beta$  signature and a high CD4 $^{+}$  T-cell infiltrate and is mainly distributed in IS1. The C2 subtypes enriched in many immune-

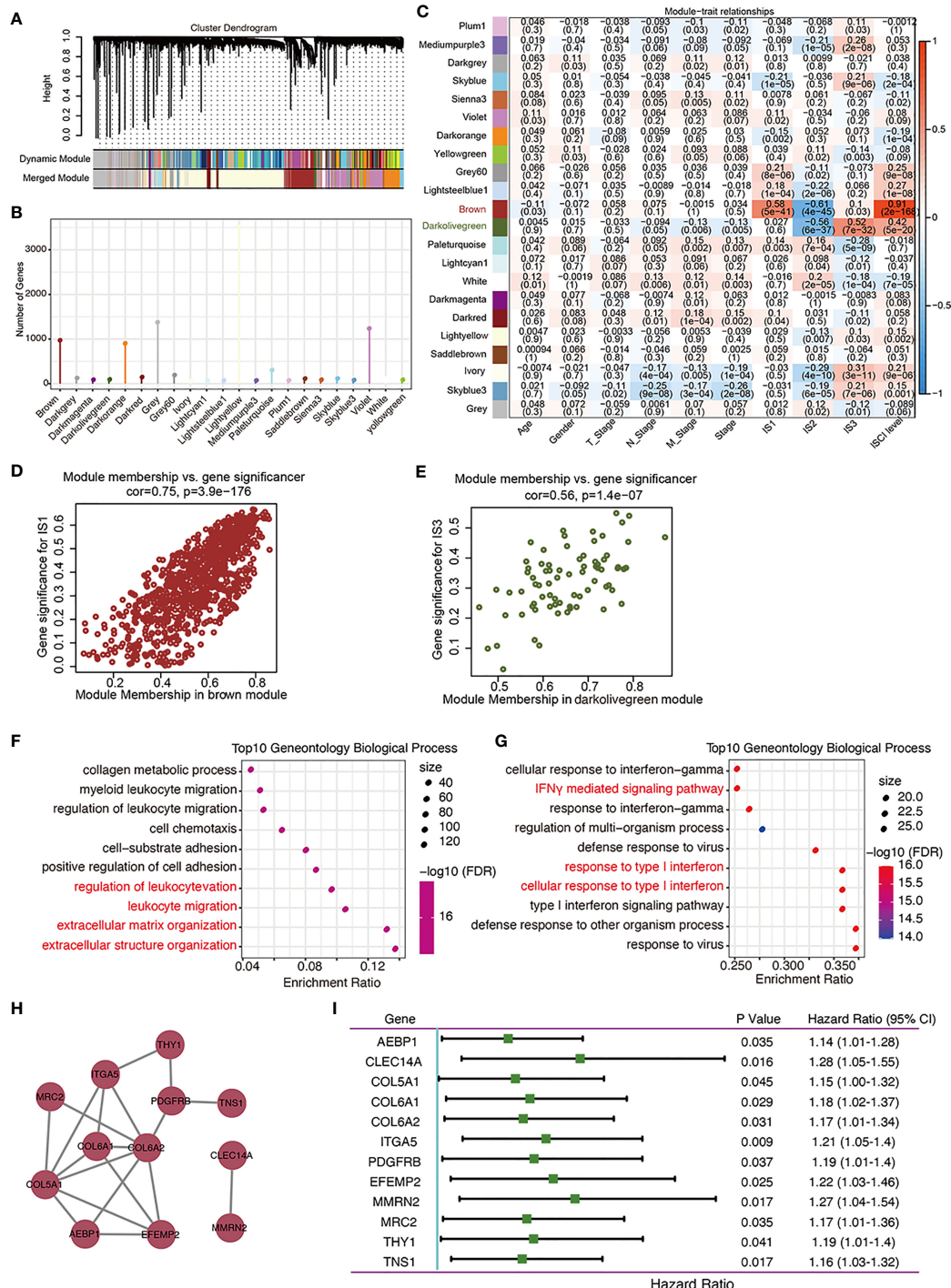


**FIGURE 7**  
 Identification of immune gene co-expression modules of COAD. **(A)** Dendrogram of all differentially expressed genes clustered based on a dissimilarity measure. **(B)** Gene numbers in each module. **(C–E)** Evaluation of the distribution of these 22 modules in each clinicopathological feature and immune subtype **(C)**. The brown module was positively correlated with IS1 **(D)** and negatively correlated with IS2, while the darkolivegreen module was negatively correlated with IS2 and positively correlated with IS3 **(E)**. **(F, G)** Dot plot showing top 10 gene ontology biological processes in the brown **(F)** and darkolivegreen **(G)** module. **(H)** Protein–protein interaction network of 12 DFS-related hub genes: AEBP1, CLEC14A, COL5A1, COL6A2, ITGA4, PDGFRB, EFEMP2, MMRN2, MRC2, THY1, and TNS1. **(I)** Forest plot of the univariate Cox regression analyses for the prognosis value of the indicated 12 genes in TCGA-COAD cohort.

evading related genes and with a high CD8<sup>+</sup> T-cell infiltrate was mainly distributed in IS3. These results indicate that the three COAD ISs were mapping to different TCGA pan-cancer categories with a similar immune microenvironment. The comparison analysis with other well-established clustering methods demonstrated the reliability of the proposed IS classification. In addition, our data suggest that different and higher-resolution ISs may be useful for better identifying potential recipients of targeted immunotherapies. Our results, therefore, may provide a useful and additional complement in the classification of TME.

Multiple immune checkpoint inhibitors (ICIs) were approved by the FDA for the treatment of patients with unresectable MSI-H or dMMR COAD. From the perspective of TME, MSI-H CRC is mainly of immune-inflamed type, while MSI-L CRC is insensitive and unlikely to benefit from immunotherapy, and MSS CRC mostly belongs to the immune-privileged type and immune-desert type (56). Several studies have shown that the expressions of cytotoxic cells, CD8+, Th1, Th2, follicular helper T cells, and T-cell markers in MSI-H CRC were significantly higher than those in MSS patients (20). Our results suggest, however, that patients presenting with COAD in different ISs would benefit from IS-specific treatment strategies using ICIs. In TCGA-COAD dataset, most of the MSS patients fell into IS1, while IS3 had the highest percentage of patients with MSI-H. Consistently, by identifying the MMR status and determining the expressions of IFN- $\gamma$ , GZMB, and CD31 in 223 samples in our FUSCC cohort, we confirmed that patients with a dMMR status had lower IFN- $\gamma$  and GZMB expressions than patients with a pMMR status. Our IHC results to some extent verified the molecular characteristics of IS1 and IS3.

Moreover, IS1 had the highest TIDE score and the highest predicted T-cell dysfunction score, suggesting that although IS1 is an immune “hot” phenotype, patients may be less likely to benefit from ICIs due to T-cell dysfunction and tumor immune escape. IS1 was predicted to have the highest angiogenesis level. Consistently, our IHC results also showed that the CD31 immunostaining intensity in pMMR cases was higher than that in dMMR cases. Thus, a combination of anti-angiogenic therapeutic drugs with ICIs might have a synergistic antitumor effect for the IS1 type. Being inspired by the “REGONIVO/EPOC1603” trial (57), a phase Ib trial of anti-angiogenic inhibitors (regorafenib) plus ICIs (nivolumab) for gastric and colorectal cancer, several clinical trials have been established to assess the therapeutic efficacy of a combination of VEGFR/VEGF inhibitors and ICIs in solid tumors, which we believe could benefit patients with IS1 COAD (58). For IS2, the absence of immune cell infiltration consequently represents a non-inflamed TME and so therapeutic strategies that induce immune infiltration may be useful to reinvigorate the immune system in these patients, such as demethylating agents (59), chemo/radiotherapy-inducing immunogenic cell death (60), and tumor vaccines (61). It has been demonstrated that the

application of the seasonal influenza vaccine into a tumor facilitates the shift toward a “hot” tumor (16). There is therefore a possibility that this method could be included in the treatment of colorectal cancer, which is highly instructive for the algorithms of treatment for patients with IS2 “cold” tumors. Regarding the 12 prognostic hub genes, given that they belong to the brown module that was negatively correlated with IS2, these genes are the potential targets of a colorectal cancer mRNA vaccine and could be beneficial for patients with IS2. The rich immune cell infiltration of IS3 represents an extremely inflamed TME, making this colorectal cancer subtype most suitable for ICIs (7).

The 12 prognostic hub genes are the major immune genes related to the disease progression risk of IS1 and IS2-COAD, which may serve as potential prognostic and therapeutic markers. Among them, PDGFRB-related multitargeted receptor tyrosine kinase inhibitor regorafenib (BAY 73-4506) has been FDA approved for the treatment of metastatic COAD that has progressed after all standard therapies (62). PDGFRB<sup>+</sup> cancer-associated fibroblasts (CAFs) are an important component of stromal cells in the tumor microenvironment. Previous studies have found that in breast cancer, PDGFRB+CAFs recruit CD4<sup>+</sup>CD25<sup>+</sup>FOXP3<sup>+</sup> Treg cells, and the recruited Treg cells inhibit the activation and proliferation of CD8<sup>+</sup>T cells in the TME, thereby inducing local immunosuppression (63). In addition, as a pivotal functional molecule in PDGF-BB-PDGFRB signaling, PFGFRB is implicated in the promotion of pericyte-fibroblast transition, which is a propellant for tumor growth and metastasis (64). Similarly, COL5A1, COL6A1, COL6A2, ITGA5, TNS1, and THY1 are markers of CAF activation (65–69). As we present, IS1 has the most abundant stromal content; therefore, stromal cells may play a very important role in this immune “hot” but immunosuppressive phenotype. CLEC14A was also a novel anti-angiogenic target for VEGF-dependent angiogenesis and tumor angiogenesis (70). CLEC14A is highly expressed in IS1 subtypes, which is consistent with our angiogenesis-related analysis results (IS1 has the highest angiogenesis score) and IHC staining results (CD31 has a higher expression in MSS subtypes of COAD). Blood vessel endothelial cells have long been known to modulate inflammation by regulating immune cell trafficking, migration, and activation (71), and the IS1 subtype is rich in immune cell infiltration. The possible reason is that specific subtypes of endothelial cells participate in immune cell recruitment or direct interaction with immune cells in tissue-specific immunity, which was collectively referred to as “immunomodulatory ECs” (71). Both AEBP1 (72) and EFEMP2 (73) have been functionally implicated in malignant tumor behavior and were potential gene therapy targets. The expression level of EFEMP2 is correlated with M0 macrophages infiltrating the TME (74), and our data yielded the same results (the proportion of macrophage M0 and macrophage M2 was significantly higher in IS1 than that in IS2). Considering that IS1 is an immune “hot” but immunosuppressive phenotype, the infiltrated macrophage M0 may be more inclined to polarize to

M2 status (switches into the anti-inflammatory M2 phenotype) under the stimulation of various cytokines (such as IL4 and IL-10).

Although further clinical evaluation is required, the potential of these tumor antigens to be successful targets for COADs has been consolidated in these previous reports.

This study provides the conceptual framework of IS for a better understanding of the tumor-specific immune microenvironment of COAD. Stratification of the patients according to the IS system can be used for identifying patients that may respond well to targeted therapies and for designing adequate therapeutic strategies to improve the efficacy of immunotherapy.

## Conclusion

We identified three ISs of COAD that represent distinct clinicopathological, cellular, and molecular characteristics and constructed a robust stable classification method for determining the IS. Immune subtyping could be used to identify COAD patients sensitive to immunotherapy and might guide a personalized approach to cancer immunotherapy.

## Data availability statement

Publicly available datasets were analyzed in this study. This data can be found here: We applied 4 COAD datasets from two online databases: The Cancer Genome Atlas (TCGA, <https://portal.gdc.cancer.gov/>) database, and Gene Expression Omnibus (GEO) database (including three datasets: GSE39582, GSE17538 and GSE72970; [http://www.ncbi.nlm.nih.gov/geo/](https://www.ncbi.nlm.nih.gov/geo/)). We had uploaded all the working sheets as additional files in the submission system.

## Ethics statement

The studies involving human participants were reviewed and approved by Fudan University Shanghai Cancer Center. The patients/participants provided their written informed consent to participate in this study.

## Author contributions

MX, JC, and WnW conceived the study, performed the literature search and bioinformatics analysis, and prepared the figures. XiW, XuW, WiW, CT, MZ, SN, ZD, and LW helped with data collection, analysis, and interpretation. MX, ZH, JC, WW, ZD, and DH wrote and revised the manuscript. MX, JC, and WnW contributed equally to this work. WL, ZD, DH, and WS share the senior authorship of this study. The authors read and approved the final manuscript.

## Funding

This work was supported by the National Natural Science Foundation of China (81972249, 82172702, 81902430), Shanghai Clinical Science and Technology Innovation Project of Municipal Hospital (SHDC12020102), Clinical Research Project of Shanghai Shenkang Hospital Development Center (SHDC2020CR4068), Natural Science Foundation of Shanghai (21ZR1414900, 22ZR1413000), Artificial Intelligence Medical Hospital Cooperation Project of Xuhui District (2021-017), Shanghai Science and Technology Development Fund (19MC1911000), Shanghai Municipal Key Clinical Specialty (shslczdk01301), Clinical Research Project of Shanghai Municipal Health Committee (20194Y0348), Shanghai “Rising Stars of Medical Talents” Youth Development Program Youth Medical Talents – Specialist Program (SHWSRS(2020)\_087), and the Interdisciplinary Program of Shanghai Jiao Tong University (YG2019QNA40).

## Acknowledgements

We would like to thank TCGA (<http://cancergenome.nih.gov>) and the GEO database (<https://www.ncbi.nlm.nih.gov/geo/>) for data collection. We would like to thank Gao Qin and Wang Zhaoxi from Xinhua Harvard International Healthcare Innovation Collaboration Initiatives for manuscript discussion and review.

## Conflict of interest

The authors declare that the research was conducted in the absence of any commercial or financial relationships that could be construed as a potential conflict of interest.

## Publisher's note

All claims expressed in this article are solely those of the authors and do not necessarily represent those of their affiliated organizations, or those of the publisher, the editors and the reviewers. Any product that may be evaluated in this article, or claim that may be made by its manufacturer, is not guaranteed or endorsed by the publisher.

## Supplementary material

The Supplementary Material for this article can be found online at: <https://www.frontiersin.org/articles/10.3389/fimmu.2022.934083/full#supplementary-material>.

## References

1. Siegel RL, Miller KD, Fuchs HE, Jemal A. Cancer statistics, 2021. *CA Cancer J Clin* (2021) 71(1):7–33. doi: 10.3322/caac.21654
2. Siegel RL, Miller KD, Goding Sauer A, Fedewa SA, Butterly LF, Anderson JC, et al. Colorectal cancer statistics, 2020. *CA Cancer J Clin* (2020) 70(3):145–64. doi: 10.3322/caac.21601
3. Sung H, Ferlay J, Siegel RL, Laversanne M, Soerjomataram I, Jemal A, et al. Global cancer statistics 2020: GLOBOCAN estimates of incidence and mortality worldwide for 36 cancers in 185 countries. *CA Cancer J Clin* (2021) 71(3):209–49. doi: 10.3322/caac.21660
4. Dekker E, Tanis PJ, Vleugels JLA, Kasi PM, Wallace MB. Colorectal cancer. *Lancet* (2019) 394(10207):1467–80. doi: 10.1016/s0140-6736(19)32319-0
5. Weiden J, Tel J, Fidgor CG. Synthetic immune niches for cancer immunotherapy. *Nat Rev Immunol* (2018) 18(3):212–9. doi: 10.1038/nri.2017.89
6. Mittra A, Takebe N, Florou V, Chen AP, Naqash AR. The emerging landscape of immune checkpoint inhibitor based clinical trials in adults with advanced rare tumors. *Hum Vaccin Immunother.* (2021) 17(7):1935–9. doi: 10.1080/21645515.2020.1854604
7. Galon J, Bruni D. Approaches to treat immune hot, altered and cold tumours with combination immunotherapies. *Nat Rev Drug Discovery* (2019) 18(3):197–218. doi: 10.1038/s41573-018-0007-y
8. Sade-Feldman M, Yizhak K, Bjørgaard SL, Ray JP, de Boer CG, Jenkins RW, et al. Defining T cell states associated with response to checkpoint immunotherapy in melanoma. *Cell* (2018) 175(4):998–1013.e20. doi: 10.1016/j.cell.2018.10.038
9. Perets R, Bar J, Rasco DW, Ahn MJ, Yoh K, Kim DW, et al. Safety and efficacy of quavonlimab, a novel anti-CTLA-4 antibody (MK-1308), in combination with pembrolizumab in first-line advanced non-small-cell lung cancer. *Annals of oncology: official journal of the European society for medical oncology.* (2021) 32(3):395–403. doi: 10.1016/j.annonc.2020.11.020
10. Cao D, Xu H, Xu X, Guo T, Ge W. High tumor mutation burden predicts better efficacy of immunotherapy: a pooled analysis of 103078 cancer patients. *Oncimmunology* (2019) 8(9):e1629258. doi: 10.1080/2162402X.2019.1629258
11. Chan TA, Yarchoan M, Jaffee E, Swanton C, Quezada SA, Stenzinger A, et al. Development of tumor mutation burden as an immunotherapy biomarker: utility for the oncology clinic. *Ann Oncol Off J Eur Soc Med Oncol* (2019) 30(1):44–56. doi: 10.1093/annonc/mdy495
12. Goodman AM, Kato S, Bazhenova L, Patel SP, Frampton GM, Miller V, et al. Tumor mutational burden as an independent predictor of response to immunotherapy in diverse cancers. *Mol Cancer Ther* (2017) 16(11):2598–608. doi: 10.1158/1535-7163.MCT-17-0386
13. Goodman AM, Sokol ES, Frampton GM, Lippman SM, Kurzrock R. Microsatellite-stable tumors with high mutational burden benefit from immunotherapy. *Cancer Immunol Res* (2019) 7(10):1570–3. doi: 10.1158/2326-6066.CIR-19-0149
14. Wang W, Green M, Choi JE, Gijon M, Kennedy PD, Johnson JK, et al. CD8 (+) T cells regulate tumour ferroptosis during cancer immunotherapy. *Nature* (2019) 569(7755):270–4. doi: 10.1038/s41586-019-1170-y
15. Golstein P, Griffiths GM. An early history of T cell-mediated cytotoxicity. *Nat Rev Immunol* (2018) 18(8):527–35. doi: 10.1038/s41577-018-0009-3
16. Newman JH, Chesson CB, Herzog NL, Bommareddy PK, Aspromonte SM, Pepe R, et al. Intratumoral injection of the seasonal flu shot converts immunologically cold tumors to hot and serves as an immunotherapy for cancer. *Proc Natl Acad Sci U S A* (2020) 117(2):1119–28. doi: 10.1073/pnas.1904022116
17. Chung KY, Gore I, Fong L, Venook A, Beck SB, Dorazio P, et al. Phase II study of the anti-cytotoxic T-lymphocyte-associated antigen 4 monoclonal antibody, tremelimumab, in patients with refractory metastatic colorectal cancer. *J Clin Oncol* (2010) 28(21):3485–90. doi: 10.1200/JCO.2010.28.3994
18. Le DT, Uram JN, Wang H, Bartlett BR, Kemberling H, Eyring AD, et al. PD-1 blockade in tumors with mismatch-repair deficiency. *N Engl J Med* (2015) 372(26):2509–20. doi: 10.1056/NEJMoa1500596
19. Chen DS, Mellman I. Elements of cancer immunity and the cancer-immune set point. *Nature* (2017) 541(7637):321–30. doi: 10.1038/nature21349
20. Lizardo DY, Kuang C, Hao S, Yu J, Huang Y, Zhang L. Immunotherapy efficacy on mismatch repair-deficient colorectal cancer: From bench to bedside. *Biochim Biophys Acta Rev Cancer* (2020) 1874(2):188447. doi: 10.1016/j.bbcan.2020.188447
21. Cancer Genome Atlas N. Comprehensive molecular characterization of human colon and rectal cancer. *Nature* (2012) 487(7407):330–7. doi: 10.1038/nature11252
22. Guo TA, Wu YC, Tan C, Jin YT, Sheng WQ, Cai SJ, et al. Clinicopathologic features and prognostic value of KRAS, NRAS and BRAF mutations and DNA mismatch repair status: A single-center retrospective study of 1,834 Chinese patients with stage I–IV colorectal cancer. *Int J Cancer* (2019) 145(6):1625–34. doi: 10.1002/ijc.32489
23. Guinney J, Dienstmann R, Wang X, de Reyniès A, Schlicker A, Soneson C, et al. The consensus molecular subtypes of colorectal cancer. *Nat Med* (2015) 21(11):1350–6. doi: 10.1038/nm.3967
24. Thorsson V, Gibbs DL, Brown SD, Wolf D, Bortone DS, Ou Yang T-H, et al. The immune landscape of cancer. *Immunity* (2018) 48(4):812–830.e14. doi: 10.1016/j.immuni.2018.03.023
25. Wilkerson MD, Hayes DN. ConsensusClusterPlus: a class discovery tool with confidence assessments and item tracking. *Bioinf (Oxford England)* (2010) 26(12):1572–3. doi: 10.1093/bioinformatics/btq170
26. Kapp AV, Tibshirani R. Are clusters found in one dataset present in another dataset? *Biostatistics (Oxford England)* (2007) 8(1):9–31. doi: 10.1093/biostatistics/kxj029
27. Danilova L, Ho WJ, Zhu Q, Vithayathil T, De Jesus-Acosta A, Azad NS, et al. Programmed cell death ligand-1 (PD-L1) and CD8 expression profiling identify an immunologic subtype of pancreatic ductal adenocarcinomas with favorable survival. *Cancer Immunol Res* (2019) 7(6):886–95. doi: 10.1158/2326-6066.CIR-18-0822
28. Wang Y, Luo J, Alu A, Han X, Wei Y, Wei X. cGAS-STING pathway in cancer biotherapy. *Mol Cancer* (2020) 19(1):136. doi: 10.1186/s12943-020-01247-w
29. Masiero M, Simoes FC, Han HD, Snell C, Peterkin T, Bridges E, et al. A core human primary tumor angiogenesis signature identifies the endothelial orphan receptor ELTD1 as a key regulator of angiogenesis. *Cancer Cell* (2013) 24(2):229–41. doi: 10.1016/j.ccr.2013.06.004
30. Newman AM, Liu CL, Green MR, Gentles AJ, Feng W, Xu Y, et al. Robust enumeration of cell subsets from tissue expression profiles. *Nat Methods* (2015) 12(5):453–7. doi: 10.1038/nmeth.3337
31. Yoshihara K, Shahmoradgoli M, Martinez E, Vegesna R, Kim H, Torres-Garcia W, et al. Inferring tumour purity and stromal and immune cell admixture from expression data. *Nat Commun* (2013) 4:2612. doi: 10.1038/ncomms3612
32. Jiang P, Gu S, Pan D, Fu J, Sahu A, Hu X, et al. Signatures of T cell dysfunction and exclusion predict cancer immunotherapy response. *Nat Med* (2018) 24(10):1550–8. doi: 10.1038/s41591-018-0136-1
33. Greten FR, Grivennikov SI. Inflammation and cancer: Triggers, mechanisms, and consequences. *Immunity* (2019) 51(1):27–41. doi: 10.1016/j.immuni.2019.06.025
34. Grivennikov SI, Greten FR, Karin M. Immunity, inflammation, and cancer. *Cell* (2010) 140(6):883–99. doi: 10.1016/j.cell.2010.01.025
35. Zhao H, Wu L, Yan G, Chen Y, Zhou M, Wu Y, et al. Inflammation and tumor progression: signaling pathways and targeted intervention. *Signal Transduct Target Ther* (2021) 6(1):263. doi: 10.1038/s41392-021-00658-5
36. Geeleher P, Cox N, Huang RS. pRRophetic: an r package for prediction of clinical chemotherapeutic response from tumor gene expression levels. *PLoS One* (2014) 9(9):e107468. doi: 10.1371/journal.pone.0107468
37. Hoshida Y, Brunet JP, Tamayo P, Golub TR, Mesirov JP. Subclass mapping: identifying common subtypes in independent disease data sets. *PLoS One* (2007) 2(11):e1195. doi: 10.1371/journal.pone.00001195
38. Langfelder P, Horvath S. WGCNA: an r package for weighted correlation network analysis. *BMC Bioinf* (2008) 9:559. doi: 10.1186/1471-2105-9-559
39. Ni S, Ren F, Xu M, Tan C, Weng W, Huang Z, et al. CTHRC1 overexpression predicts poor survival and enhances epithelial-mesenchymal transition in colorectal cancer. *Cancer Med* (2018) 7(11):5643–54. doi: 10.1002/cam4.1807
40. Yu IS, Cheung WY. Metastatic colorectal cancer in the era of personalized medicine: A more tailored approach to systemic therapy. *Can J Gastroenterol Hepatol* (2018) 2018:9450754. doi: 10.1155/2018/9450754
41. Miller KD, Nogueira L, Mariotto AB, Rowland JH, Yabroff KR, Alfano CM, et al. Cancer treatment and survivorship statistics, 2019. *CA Cancer J Clin* (2019) 69(5):363–85. doi: 10.3322/caac.21565
42. Ochoa de Olza M, Navarro Rodrigo B, Zimmermann S, Coukos G. Turning up the heat on non-immunoreactive tumours: opportunities for clinical development. *Lancet Oncol* (2020) 21(9):e419–30. doi: 10.1016/s1470-2045(20)30234-5
43. Lee SM, Park HY, Suh YS, Yoon EH, Kim J, Jang WH, et al. Inhibition of acute lethal pulmonary inflammation by the IDO-AhR pathway. *Proc Natl Acad Sci U S A* (2017) 114(29):E5881–90. doi: 10.1073/pnas.1615280114
44. Garcia-Diaz A, Shin DS, Moreno BH, Saco J, Escuin-Ordinas H, Rodriguez GA, et al. Interferon receptor signaling pathways regulating PD-L1 and PD-L2 expression. *Cell Rep* (2017) 19(6):1189–201. doi: 10.1016/j.celrep.2017.04.031

45. Bussard KM, Mutkus L, Stumpf K, Gomez-Manzano C, Marini FC. Tumor-associated stromal cells as key contributors to the tumor microenvironment. *Breast Cancer Res* (2016) 18(1):84. doi: 10.1186/s13058-016-0740-2

46. Turley SJ, Cremasco V, Astarita JL. Immunological hallmarks of stromal cells in the tumour microenvironment. *Nat Rev Immunol* (2015) 15(11):669–82. doi: 10.1038/nri3902

47. Chen X, Song E. Turning foes to friends: targeting cancer-associated fibroblasts. *Nat Rev Drug Discovery* (2019) 18(2):99–115. doi: 10.1038/s41573-018-0004-1

48. Romero JM, Grunwald B, Jang GH, Bavi PP, Jhaveri A, Masoomian M, et al. A four-chemokine signature is associated with a T-cell-Inflamed phenotype in primary and metastatic pancreatic cancer. *Clin Cancer Res* (2020) 26(8):1997–2010. doi: 10.1158/1078-0432.CCR-19-2803

49. Kwak M, Erdag G, Leick KM, Bekiranov S, Engelhard VH, Slingluff CL. Associations of immune cell homing gene signatures and infiltrates of lymphocyte subsets in human melanomas: discordance with CD163(+) myeloid cell infiltrates. *J Transl Med* (2021) 19(1):371. doi: 10.1186/s12967-021-03044-5

50. Garris CS, Luke JJ. Dendritic cells, the T-cell-inflamed tumor microenvironment, and immunotherapy treatment response. *Clin Cancer Res* (2020) 26(15):3901–7. doi: 10.1158/1078-0432.CCR-19-1321

51. Dangaj D, Bruand M, Grimm AJ, Ronet C, Barras D, Duttagupta PA, et al. Cooperation between constitutive and inducible chemokines enables T cell engraftment and immune attack in solid tumors. *Cancer Cell* (2019) 35(6):885–900.e10. doi: 10.1016/j.ccr.2019.05.004

52. Tokunaga R, Zhang W, Naseem M, Puccini A, Berger MD, Soni S, et al. CXCL9, CXCL10, CXCL11/CXCR3 axis for immune activation – a target for novel cancer therapy. *Cancer Treat Rev* (2018) 63:40–7. doi: 10.1016/j.ctrv.2017.11.007

53. Hong M, Puaux AL, Huang C, Loumagne L, Tow C, Mackay C, et al. Chemotherapy induces intratumoral expression of chemokines in cutaneous melanoma, favoring T-cell infiltration and tumor control. *Cancer Res* (2011) 71(22):6997–7009. doi: 10.1158/0008-5472.CAN-11-1466

54. Wang B, Wang Y, Sun X, Deng G, Huang W, Wu X, et al. CXCR6 is required for antitumor efficacy of intratumoral CD8(+) T cell. *J Immunother Cancer* (2021) 9(8):e003100. doi: 10.1136/jitc-2021-003100

55. Di Pilato M, Kfuri-Rubens R, Pruessmann JN, Ozga AJ, Messemaek M, Cadilha BL, et al. CXCR6 positions cytotoxic T cells to receive critical survival signals in the tumor microenvironment. *Cell* (2021) 184(17):4512–30.e22. doi: 10.1016/j.cell.2021.07.015

56. Bai J, Chen H, Bai X. Relationship between microsatellite status and immune microenvironment of colorectal cancer and its application to diagnosis and treatment. *J Clin Lab Anal* (2021) 35(6):e23810. doi: 10.1002/jcla.23810

57. Fukuoka S, Hara H, Takahashi N, Kojima T, Kawazoe A, Asayama M, et al. Regorafenib plus nivolumab in patients with advanced gastric or colorectal cancer: An open-label, dose-escalation, and dose-expansion phase ib trial (REGONIVO, EPOC1603). *J Clin Oncol* (2020) 38(18):2053–61. doi: 10.1200/jco.19.03296

58. Lee WS, Yang H, Chon HJ, Kim C. Combination of anti-angiogenic therapy and immune checkpoint blockade normalizes vascular-immune crosstalk to potentiate cancer immunity. *Exp Mol Med* (2020) 52(9):1475–85. doi: 10.1038/s12276-020-00500-y

59. Peng D, Kryczek I, Nagarsheth N, Zhao L, Wei S, Wang W, et al. Epigenetic silencing of TH1-type chemokines shapes tumour immunity and immunotherapy. *Nature* (2015) 527(7577):249–53. doi: 10.1038/nature15520

60. Golden EB, Apetoh L. Radiotherapy and immunogenic cell death. *Semin Radiat Oncol* (2015) 25(1):11–7. doi: 10.1016/j.semradonc.2014.07.005

61. Sahin U, Derhovanessian E, Miller M, Kloke BP, Simon P, Lower M, et al. Personalized RNA mutanome vaccines mobilize poly-specific therapeutic immunity against cancer. *Nature* (2017) 547(7662):222–6. doi: 10.1038/nature23003

62. Garcia-Alfonso P, Munoz Martin AJ, Ortega Moran L, Soto Alsar J, Torres Perez-Soler G, Blanco Codesido M, et al. Oral drugs in the treatment of metastatic colorectal cancer. *Ther Adv Med Oncol* (2021) 13:17588359211009001. doi: 10.1177/17588359211009001

63. Costa A, Kieffer Y, Scholer-Dahirel A, Pelon F, Bourachot B, Cardon M, et al. Fibroblast heterogeneity and immunosuppressive environment in human breast cancer. *Cancer Cell* (2018) 33(3):463–79.e10. doi: 10.1016/j.ccr.2018.01.011

64. Hosaka K, Yang Y, Seki T, Fischer C, Dubey O, Fredlund E, et al. Pericyte-fibroblast transition promotes tumor growth and metastasis. *Proc Natl Acad Sci U S A* (2016) 113(38):E5618–27. doi: 10.1073/pnas.1608384113

65. Deng CC, Hu YF, Zhu DH, Cheng Q, Gu JJ, Feng QL, et al. Single-cell RNA-seq reveals fibroblast heterogeneity and increased mesenchymal fibroblasts in human fibrotic skin diseases. *Nat Commun* (2021) 12(1):3709. doi: 10.1038/s41467-021-24110-y

66. Guerrero-Juarez CF, Dedhia PH, Jin S, Ruiz-Vega R, Ma D, Liu Y, et al. Single-cell analysis reveals fibroblast heterogeneity and myeloid-derived adipocyte progenitors in murine skin wounds. *Nat Commun* (2019) 10(1):650. doi: 10.1038/s41467-018-08247-x

67. Muhl L, Genové G, Leptidis S, Liu J, He L, Moccia G, et al. Single-cell analysis uncovers fibroblast heterogeneity and criteria for fibroblast and mural cell identification and discrimination. *Nat Commun* (2020) 11(1):3953. doi: 10.1038/s41467-020-17740-1

68. Sebastian A, Hum NR, Martin KA, Gilmore SF, Peran I, Byers SW, et al. Single-cell transcriptomic analysis of tumor-derived fibroblasts and normal tissue-resident fibroblasts reveals fibroblast heterogeneity in breast cancer. *Cancers (Basel)* (2020) 12(5):1307. doi: 10.3390/cancers12051307

69. Liu JW, Yu F, Tan YF, Huo JP, Liu Z, Wang XJ, et al. Profiling of tumor microenvironment components identifies five stroma-related genes with prognostic implications in colorectal cancer. *Cancer Biother Radiopharm* (2020). Oct 21 doi: 10.1089/cbr.2020.4118

70. Kim TK, Park CS, Jang J, Kim MR, Na HJ, Lee K, et al. Inhibition of VEGF-dependent angiogenesis and tumor angiogenesis by an optimized antibody targeting CLEC14a. *Mol Oncol* (2018) 12(3):356–72. doi: 10.1002/1878-0261.12169

71. Amersfoort J, Eelen G, Carmeliet P. Immunomodulation by endothelial cells – partnering up with the immune system? *Nat Rev Immunol* (2022), 1–13. Mar 14 doi: 10.1038/s41577-022-00694-4

72. Xing Y, Zhang Z, Chi F, Zhou Y, Ren S, Zhao Z, et al. AEBP1, a prognostic indicator, promotes colon adenocarcinoma cell growth and metastasis through the NF-κappaB pathway. *Mol Carcinog* (2019) 58(10):1795–808. doi: 10.1002/mc.23066

73. Zhao J, Xu J, Zhao J, Zhang R. EFEMP2 promotes colon cancer cell invasion and growth through the ERK1/2 signaling pathway. *Int J Clin Exp Pathol* (2019) 12(3):851–6. doi: 10.1038/s41577-022-00694-4

74. Huang L, Wang Z, Chang Y, Wang K, Kang X, Huang R, et al. EFEMP2 indicates assembly of M0 macrophage and more malignant phenotypes of glioma. *Aging (Albany NY)* (2020) 12(9):8397–412. doi: 10.18632/aging.103147

## Glossary

---

APC	adenomatous polyposis coli
APCs:	antigen presenting cells
cGAS	cyclic GMP-AMP synthase
CMS	consensus molecular subtype
COAD	colon adenocarcinoma
ISs	immune subtypes
CYT	immune cytolytic activity
DAVID	Database for Annotation Visualization and Integrated Discovery
DFS	disease-free survival
ESTIMATE	Estimation of Stromal and Immune cells in Malignant Tumours using Expression data
FFPE	formalin fixed paraffin-embedded
FUSCC	Fudan University Shanghai Cancer Center
GRCh38	Genome Reference Consortium Human Build 38
IFN	type I interferon
MAD	median absolute deviation
MCFAUC	comprehensive forecast area under the curve
MSS	microsatellite stable
MSI-L	low microsatellite instability
IARC	International Agency for Research on Cancer
ICIs	immune checkpoint inhibitors
IGP	in-group proportion
IHC	immunohistochemistry
IRF3	IFN regulator 3
pMMR	proficient mismatched repair
PD-L1	programmed death-ligand 1
ROC	receiver operating characteristic
SubMap	subclass mapping
STING	stimulator of interferon genes
TBK1	tank-bound kinase 1
TCGA	The Cancer Genome Atlas
GEO	Gene Expression Omnibus
TMA	tissue microarray
TMB	tumor mutation burden
TME	tumor microenvironment
TIDE	tumor immune dysfunction and exclusion
TOM	topology overlap matrix
TPM	Transcripts Per Kilobase of exon model per Million mapped reads
PAM	partition around medoids
WGCNA	weighted gene correlation network analysis
PR	partial response
CR	complete response
HCK	HCK proto-oncogene Src family tyrosine kinase
LCK	LCK Proto-Oncogene Src Family Tyrosine Kinase
	Lymphocyte Cell Specific Protein-Tyrosine Kinase

---



## OPEN ACCESS

## EDITED BY

Mercedes Beatriz Fuertes,  
CONICET Instituto de Biología y  
Medicina Experimental (IBYME),  
Argentina

## REVIEWED BY

Alison Mary Rich,  
University of Otago, New Zealand  
Jessica Dal Col,  
University of Salerno, Italy

## \*CORRESPONDENCE

Mariana Maccioni  
mariana.maccioni@unc.edu.ar  
Rosana Andrea Morelatto  
rosana.morelatto@unc.edu.ar

<sup>†</sup>These authors have contributed  
equally to this work and share  
first authorship

<sup>‡</sup>These authors have contributed  
equally to this work and share  
last authorship

## SPECIALTY SECTION

This article was submitted to  
Cancer Immunity  
and Immunotherapy,  
a section of the journal  
Frontiers in Immunology

RECEIVED 11 May 2022

ACCEPTED 15 July 2022

PUBLISHED 05 August 2022

## CITATION

Bolesina N, Gatti G, López de Blanc S,  
Dhooge S, Rocha D, Fernandez E,  
Ferreyra R, Palla V, Grupe V,  
Morelatto R and Maccioni M (2022)  
Oral squamous cell carcinoma (OSCC)  
tumors from heavy alcohol consumers  
are associated with higher levels of  
TLR9 and a particular  
immunophenotype: impact  
on patient survival.  
*Front. Immunol.* 13:941667.  
doi: 10.3389/fimmu.2022.941667

# Oral squamous cell carcinoma (OSCC) tumors from heavy alcohol consumers are associated with higher levels of TLR9 and a particular immunophenotype: Impact on patient survival

Nicolás Bolesina<sup>1†</sup>, Gerardo Gatti<sup>2†</sup>, Silvia López de Blanc<sup>1</sup>,  
Sabrina Dhooge<sup>2</sup>, Dario Rocha<sup>3</sup>, Elmer Fernandez<sup>3</sup>,  
Ruth Ferreyra<sup>1</sup>, Vanesa Palla<sup>2</sup>, Verónica Grupe<sup>2</sup>,  
Rosana Morelatto<sup>1\*‡</sup> and Mariana Maccioni<sup>4\*\*</sup>

<sup>1</sup>Departamento de Patología Oral, Cátedra de Estomatología, Facultad de Odontología, Universidad Nacional de Córdoba, Córdoba, Argentina, <sup>2</sup>Fundación para el Progreso de la Medicina. Laboratorio de Investigación en Cáncer, Córdoba, Argentina, <sup>3</sup>Centro de Investigación y Desarrollo en Inmunología y Enfermedades Infecciosas, CIDIE-CONICET, Universidad Católica de Córdoba; Facultad de Ciencias Exactas, Físicas y Naturales, Universidad Nacional de Córdoba, Córdoba, Argentina, <sup>4</sup>Centro de Investigaciones en Bioquímica Clínica e Inmunología, CIBICI-CONICET, Departamento de Bioquímica Clínica, Facultad de Ciencias Químicas, Universidad Nacional de Córdoba, Córdoba, Argentina

Oral squamous cell carcinoma (OSCC) is one of the most frequent types of oral cancer in developing countries and its burden correlates with exposure to tobacco and excessive alcohol consumption. Toll like receptors (TLRs) are major sensors of inflammatory stimuli, from both microbial and sterile causes and as such, they have been related to tumor progression and metastasis. Here, we evaluated the expression of TLR2, 4 and 9 as well as CD3+, CD8+ and Granzyme B+ cell infiltration by immunohistochemistry in oral samples of 30 patients with OSCC, classified according to their consumption of alcohol. Our findings indicate that there is a significant association between heavy alcohol consumption and tumors with higher expression levels of TLR9. Moreover, patients with TLR9high tumors, as well as those who indicated high consumption of alcohol exhibited a diminished overall survival. TCGA data analysis indicated that TLR9high tumors express a significant increase in some genes related with the oral cavity itself, inflammation and tumor promotion. Our analysis of tumor infiltrating leukocytes demonstrated that the major differences perceived in heavy alcohol consumers was the location of CD8+ T cells infiltrating the tumor, which showed lower numbers intratumorally. Our data suggest the existence of a pathogenic loop that involves alcohol

consumption, high TLR9 expression and the immunophenotype, which might have a profound impact on the progression of the disease.

**KEYWORDS**

oral squamous cell carcinoma, immunophenotype, alcohol consumption, CD8+T cell infiltration, TLR9

## Introduction

Head and neck cancer was identified as the seventh most common cancer worldwide in 2018, with 890,000 new cases and 450,000 deaths being reported (1). Oral squamous cell carcinoma (OSCC) is the most prevalent subgroup of head and neck cancer and includes the lips, the tongue, the gums, the buccal mucosa, the floor of the mouth, the hard palate, and the alveolar ridge. It represents a major cause of morbidity and mortality worldwide, especially in Southern Asia and the Pacific islands (2). It arises as a consequence of multifactorial risk factors that include tobacco and alcohol, chronic inflammation, ultraviolet radiation (for lip cancer), human papilloma virus (HPV) or *Candida* infections, immunosuppression, genetic predisposition, and diet. However, tobacco smoking and alcohol consumption are considered as the main causal factors (3, 4). OSCC is still a leading cause of cancer death among men in many places and despite several advancements in therapeutic approaches, the 5-year survival rate is around 50% (1).

Toll-like receptors are an evolutionary conserved family of transmembrane receptors, key players in the initiation of the immune response. They are present almost in any cell type and tissue in the body, although they are preferentially expressed on antigen presenting cells. Twelve members of the TLR family have been identified in mammals so far (5, 6) and it is well established that, besides interacting with microbial molecular structures to trigger the inflammatory response, they also recognize self-molecules that are released, secreted or exposed by cells that are suffering stress or damage. These self-molecules are called “danger associated molecular patterns” or “DAMPs”. Thus, they are at the crossroad between immunity and inflammation, being important components of immunotherapeutic strategies designed to awaken the immune response against tumor antigens, but also mediating chronic inflammatory processes involved in carcinogenesis and promotion of the neoplastic lesion (7).

Up to  $10^{10}$  bacteria reside in the oral cavity, which in physiologic conditions presents a relatively small number of resident immune cells, including neutrophils, lymphocytes, and monocytes/macrophages (5). As in other mucosal sites, the expression of TLRs in oral epithelial cells seems to be tightly controlled as a way of maintaining tissue homeostasis in a site full of commensal microflora. Most TLRs are expressed in the

oral epithelial cells, at mRNA and protein levels, but their levels are modified and their location can change from basal to superficial layers when invading pathogens are detected (8–10). Except for TLR7 and TLR8, which do not increase their protein levels in inflammatory conditions, TLR1, TLR3, TLR4, TLR5, and TLR9 expression depends on the state of the tissue (inflamed vs. non-inflamed) (5, 11).

The expression of TLRs has been thoroughly investigated in most types of cancer and oral cancer is not an exception. In general, the levels of the most studied TLRs (TLR9, TLR4, TLR2) are enhanced in OSCC tissues compared to healthy controls and in most cases they have been associated with invasion and metastasis (11). Usually, most studies have relied on measurements of mRNA levels, immunohistochemistry and correlation analysis with clinical data such as tumor size and presence or not of metastasis and invasion. However, there are few studies trying to associate their enhanced expression with the presence of carcinogenic stimuli. In this study we have analyzed the expression levels of TLR9, TLR4 and TLR2 in OSCC samples by immunohistochemistry and found that patients with excessive alcohol consumption exhibit a higher frequency of TLR9<sup>high</sup> tumors. Also, these patients have a reduced survival. We have characterized the differences of immune infiltrate in tumors from heavy and low alcohol consumers and distinct TLR9 expression levels (TLR9<sup>high</sup> and <sup>low</sup>). We also evaluated the differentially expressed genes by interrogating TCGA data. Genes like ADAM6 (a member of the family of A disintegrin and metalloproteases) and TNFRSF13B (member of the superfamily of TNF receptors), which contribute to the inflammatory process and have been involved in cell migration and metastasis, are significantly elevated in TLR9<sup>high</sup> tumors. Our data suggest the existence of a pathogenic loop that involves alcohol consumption, high TLR9 expression, and the immunophenotype, which could have a profound impact on the progression of the disease.

## Material and methods

### Study population and tissue source

This is a retrospective, observational and analytical study that included 30 biopsy samples from patients with a pathological diagnosis of OSCC as a primary tumor, with

complete clinical history and HPV determination as shown in **Table 1**. All the patients attended at the Stomatology Service of the Faculty of Dentistry of the National University of Córdoba, Argentina. Patients who had consumed anti-inflammatory drugs or had been treated with chemo and/or radiotherapy were excluded. Written informed consent was obtained from all subjects and all studies were conducted in accordance with Good Clinical Practice guidelines and the Declaration of Helsinki. The protocol was approved by the Academic Committee for Health Research of the Facultad de Odontología. Universidad Nacional de Córdoba, (UNC) (Project 31, 06/25/2015).

Tumors were staged according to the UICC-TNM classification of malignant tumors (12). Stages I and II were defined as initial and stages III and IV as advanced. Also, tumor differentiation was defined as well or moderate/poorly according to the World Health Organization (13).

Cumulative tobacco use was evaluated following the criteria established by Biondi et al., 1998 (14). A subject who smoked more than 200,000 cigarettes during his lifespan was considered a high consumer. In the same way, alcohol consumption was registered taking into account the type and quantity of alcoholic beverages consumed. One unit of alcohol per day (one drink) was considered as regular alcohol consumption, according to Pentenero et al., 2011 (15). The consumption of at least one alcohol unit per day (1 unit=8–10g of ethanol=1 glass of wine=1/4l of beer=1 measure of liqueur) was considered alcohol exposure.

**TABLE 1** Patient characteristics.

Patient characteristics	n (%)
Age (years)	
>60	18 (60)
<60	12 (40)
Gender	
Female	15 (50)
Male	15 (50)
Tumor differentiation	
Well	11 (39)
Moderate/poorly	18 (61)
Cancer stage	
I/II (initial)	19 (68)
III/IV (advanced)	9 (32)
Smoking habit	
High	15 (50)
Low	15 (50)
Alcohol consumption	
High	9 (30)
Low	21 (70)
HPV	
Yes	12 (41)
No	17 (59)

Patients consuming more than 60g of alcohol/day were considered heavy alcohol consumers, according to the Ministry of Health of Spain (16) and the National Institute of Alcohol Abuse and Alcoholism of the U.S (17).

Other clinical aspects such as HPV determination were evaluated following protocols established. Briefly, DNA-HPV was detected *via* PCR using Bioneer AccuPrep genomic DNA Extraction kit, and consensus primers MY09 and MY11.

## Immunohistochemistry

All collected tissue samples were fixed in formalin, embedded in paraffin and cut at 4 $\mu$ m and then standard IHC staining was performed.

For detection of the TLR receptors, the following antibodies were used: anti-TLR2 (H-175, rabbit polyclonal antibody against amino acids 180 to 354 of TLR2 of human origin, Santa Cruz Biotechnology); anti-TLR4 (H-80, rabbit polyclonal antibody against amino acids 242-321 of TLR4 of human origin, Santa Cruz Biotechnology) and anti-TLR9 (H-100, rabbit polyclonal IgG antibody against TLR9 of human origin, Santa Cruz Biotechnology).

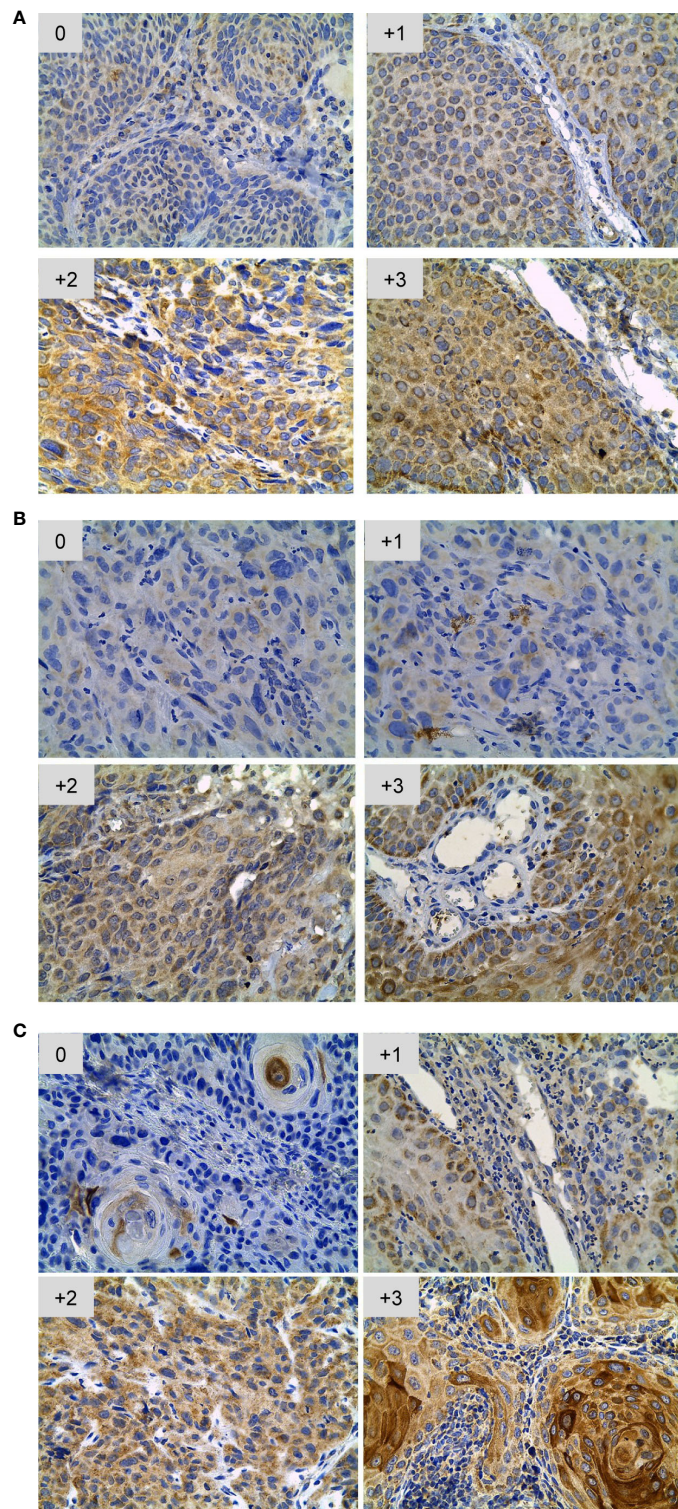
TLR staining patterns were evaluated and scored based on intensity and percentage of positive cells as previously described (18, 19). The score is designated as 0 when no tumor cells stain, 1+ when 10–20% of cells stain (weak), 2+ when 20–50% of cells stain (moderate), and 3+ when > 50% of cells stain (strong). The immunohistochemistry scoring was performed by two observers that were blinded and the degree of agreement was good (Kappa statistics: 0.8). Tumors were then classified as TLR low (< 2 score) or TLR high ( $\geq$  2 score). **Figure 1** shows representative images of each staining pattern for TLR2, TLR4 and TLR9.

CD3+, CD4+, CD8+ and Granzyme B+ cells were visualized at 40x of magnification and quantified using the Image J software. The results show the average number obtained after counting infiltrating cells in 3 fields per patient.

To study the location of CD3+, CD4+ and CD8+ T cell infiltration, we analyzed the number of cells/fields at the invasive margin or at the center of the tumor (intratumoral). Therefore, 3 fields per sample were visualized at 20x magnification and a scoring system was established as follows: 0 when no cells were present, 1+ when 10–20% of cells were present, 2+ when 20–50% of cells were present, and 3+ when > 50% of cells were present. Each sample received two scores corresponding to the location of the cells: one score for the invasive margin and another one for the center (intratumoral).

## TCGA data analysis and MIXTURE

The results reported here are partially based on data generated by The Cancer Genome Atlas (TCGA: <https://www.ncbi.nlm.nih.gov/geo/query/acc.cgi?acc=GSE12100>).

**FIGURE 1**

Scoring system for immunohistochemical staining of TLR2 (A), TLR4 (B) and TLR9 (C) in OSCC. Each panel shows representative pictures of the increasing scores (from 0 to +3) according to the different expression levels of TLR expression. The intensity of the staining is designated as 0 when no tumor cells are stained; 1+ when 10- 20% of cells are stained (weak), 2+ when 20- 50% of cells are stained (moderate), and 3+ when >50% of cells are stained (strong). Micrographs were obtained at 40x.

([cancer.gov/tcga](https://cancer.gov/tcga)). MIXTURE, a v-support vector regression-based noise constrained recursive feature selection algorithm based on validated immune cell molecular signatures (20), was used to estimate tumor immune infiltration from expression data. TLR9 expression was categorized as high or low according to the median TLR9 expression value.

## Statistical analysis

Data handling, analysis, and graphic representation (all shown as mean  $\pm$  SEM) were performed using Prism 8.0.2 (GraphPad Software) and R studio (<https://www.rstudio.com/products/rstudio/download/>). For the comparison between two groups, a difference of proportions Z-test was performed. A  $p < 0.05$  was considered statistically significant. Survival analyses were performed in R with Kaplan-Meier estimator and log-rank test. The comparisons for the abundance of TLR9, TLR4 and TLR2 between the different stages were performed with the Student T test. The comparisons for the abundance of CD8+ T cells, CD3+ T cells and Granzyme B+ cells between TLR9<sup>high</sup> and TLR9<sup>low</sup> groups, was performed with the Mann-Whitney test. In the MIXTURE analysis, the Wilcoxon test was used.

## Results

### Patients with OSCC tumors expressing elevated levels of TLR9, but not of TLR2 or TLR4, exhibit a reduced 10-years overall survival

There exists abundant data regarding the expression of different TLRs in the oral cavity, both in physiological and in pathological conditions; however, it is not clear yet if the up-regulation observed in inflammatory settings such as OSCC has a prognostic meaning. We measured TLR9, 2 and 4 expressions in our tumor samples and classified our cohort of patients as showing high ( $\geq 2$ ) or low ( $< 2$ ) score expression levels of TLR9 ( $n=22$ ), TLR2 ( $n=28$ ) and TLR4 ( $n=29$ ) (Figures 1, 2A). Of note, the staining was observed mainly in tumor cells and not in infiltrating immune leukocytes. We then analyzed the epidemiological data collected in Table 1 to calculate the 10-year survival rates in our cohort according to these three TLRs expression levels. Interestingly, patients whose tumors showed an enhanced expression of TLR9, but not of TLR4 or TLR2, showed a significant decrease in their overall survival (Figure 2A). It could be argued that the pattern of survival observed could be driven by the stages of the disease and not by the TLR9 expression. However as can be seen in Figure 2B, there are non-significant differences between the expression levels of TLR9, 4 and 2 in tumors of different stages indicating that, in our

cohort, other factors besides the conventional disease staging drives the overall survival.

We next interrogated the TCGA database to see which genes that were differentially expressed between TLR9<sup>high</sup> and TLR9<sup>low</sup> OSCC samples could explain the marked reduction in the overall survival observed in patients with TLR9<sup>high</sup> tumors. Figure 2C shows the myriad of genes whose expression increases significantly (red dots) in TLR9<sup>high</sup> vs TLR9<sup>low</sup> tumors. Among those genes, we focused on KCNA2, TNFRSF13B and ADAM6, which exhibit a 11x, 7x and 3.5x fold increase respectively, since they were among the 9 differential expressed genes with  $p$  values  $<0.00001$  that have a clearer biological role in cancer.

### A significant proportion of OSCC tumors from heavy alcohol consumers express high levels of TLR9

In neurodegenerative or liver diseases, the molecular and cellular mechanisms that link alcohol and the disruption of the organ homeostasis have been thoroughly investigated (21, 22). Indeed, in these studies, innate immune receptors play a protagonist role. In contrast, whereas tobacco and alcohol consumption are very well-known carcinogens in oral cancer and the altered presence of TLRs has been extensively documented, their association has been scarcely analyzed.

To see if the expression levels of TLR9, 4 or 2 was somehow related to alcohol consumption, we divided our cohort ( $n=28$ ) according to their alcohol consumption ( $60\text{g/day} >$  or  $< 60\text{g/day}$ ) and analyzed the frequency of tumors expressing high or low levels of TLR9, 4 and 2 in each group (Figure 3A). A similar approach was done splitting the cohort according to the levels of tobacco intake in each group (Figure 3B). We found that heavy alcohol consumers show a significantly elevated proportion of tumors expressing higher scores of TLR9 staining, but not of TLR4 or 2, compared to those patients consuming less alcohol (Figure 3A). Indeed, 88% of the patients that drank more than 60g alcohol/day and were cataloged as heavy alcohol consumers exhibit tumor samples that showed an enhanced expression of TLR9. In contrast, only 50% of the lower alcohol consumers exhibited samples with high TLR9 expression (Figure 3A). When we looked at tobacco consumers, there was not a significant distribution of TLR9<sup>high</sup> expressing tumors in a particular subgroup of patients. However, we could observe a trend in associating patients with higher tobacco intake with samples with an enhanced TLR9 expression (Figure 3B). Interestingly, both heavy alcohol and tobacco consumers showed a significant reduction in their 10-year overall survival (Figure 3C).

In conclusion, these findings indicate that there is an uneven distribution of TLR9<sup>high</sup> tumor samples, with a significant association between heavy alcohol consumption and tumors with higher expression levels of TLR9.

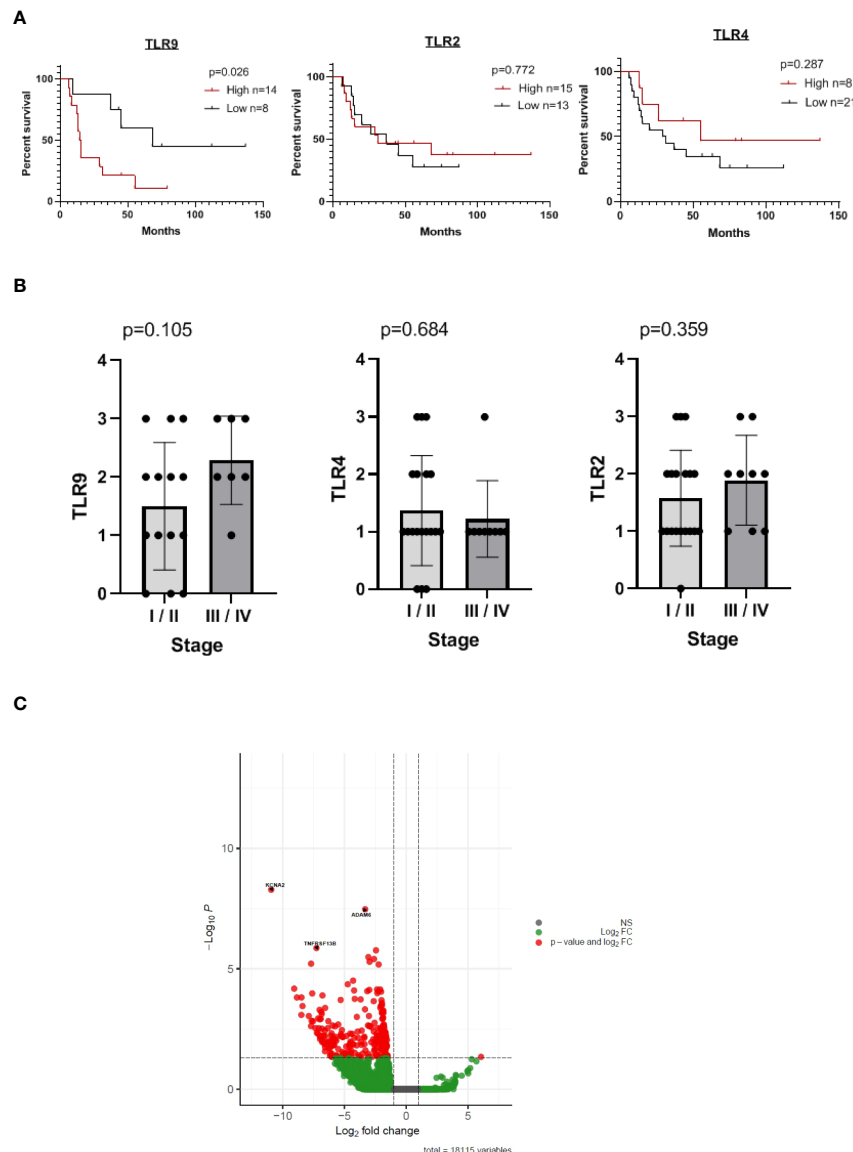


FIGURE 2

Patients with OSCC tumors expressing elevated levels of TLR9, but not of TLR2 or TLR4, exhibit a reduced 10-years overall survival. **(A)** Kaplan-Meier plots of overall survival of patients from the cohort under study. Patients were categorized as high or low TLR9, TLR4 and TLR2 as detailed in M&M. **(B)** Patients were categorized according to UICC- TNM criteria. Stages I and II were considered "initial" whereas stages III and IV were considered "advanced". **(C)** Volcano plot showing the differential expressed genes in samples analyzed from the TCGA and categorized as TLR9<sup>low</sup> and <sup>high</sup> according to their median expression value. The plot shows genes that have a significantly up-regulated expression in TLR9<sup>high</sup> samples (red dots) based on both biological difference (absolute  $\log_2$ ; estimated fold change) and statistical difference ( $-\log_{10}$ ;  $p$  value). Negative log fold changes indicate that the expression is higher in the TLR9<sup>high</sup> samples.

## Heavy alcohol consumers exhibit a significant reduction in intratumoral CD8+ T cells, whereas the total number of CD3+ T cells, CD8+ T cells and Granzyme B+ is not altered

We then quantified the total number of CD3+, CD8+ and Granzyme B+ cells and analyzed their spatial distribution

(invasive margin vs intratumoral) by conventional IHC (**Figure 4**). CD4+ T cells were also analyzed but non-statistically significant differences were found among the groups (data not shown). As can be seen in **Figure 5A**, the total number of cells in these populations is not modified between tumors showing distinct scores of TLR9. Similar results were obtained when we analyzed the infiltration of immune cells in tumor samples of our cohort categorized

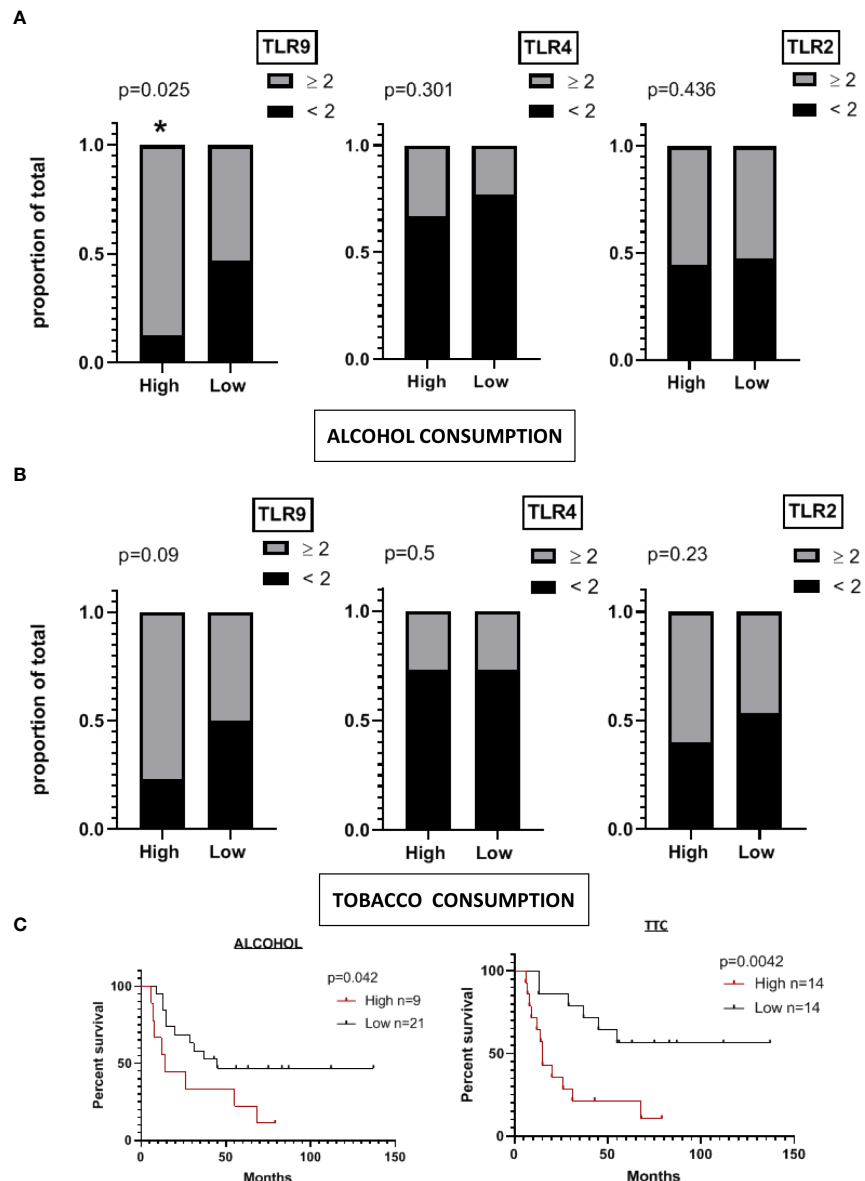


FIGURE 3

A significant proportion of OSCC tumors from heavy alcohol consumers express higher levels of TLR9. (A) Frequency of samples expressing scores  $\geq 2$  or  $< 2$  of TLR9, TLR4 and TLR2 among patients categorized as heavy (n=9; high) or low alcohol consumers (n=21) (alcohol consumption  $>$  or  $< 60$  g/day). (B) Patients were categorized as high or low tobacco consumers. More than 200.000 cigarettes during his lifetime was considered to be a high consumer. A difference of proportions Z-test was performed to calculate the statistical significance. (C) Kaplan-Meier plots of overall survival of patients categorized as high or low alcohol or tobacco (TTC) consumers. \*  $p < 0.05$  was considered statistically significant.

according to their alcohol consumption levels (Figure 5B). However, whereas the numbers and location of CD3+ T cells do not vary significantly between patients with different levels of alcohol consumption, the location of CD8+ T cells is modified in tumor samples from heavy alcohol consumers. Indeed, they seem to develop tumors that not only express higher levels of TLR9, but also exhibit a reduced number of intratumoral CD8+

T cells (Figure 5C). This is clearly demonstrated in Figure 6 that shows that in our study cohort: a) most heavy alcohol consumers display TLR9<sup>high</sup> tumors (as shown previously in Figure 3); b) those TLR9<sup>high</sup> tumors that belonged to heavy alcohol consumers presented significantly fewer CD8+ T cells in the tumor center compared to those TLR9<sup>high</sup> tumors from low alcohol consumers and c) tumors from low alcohol consumers

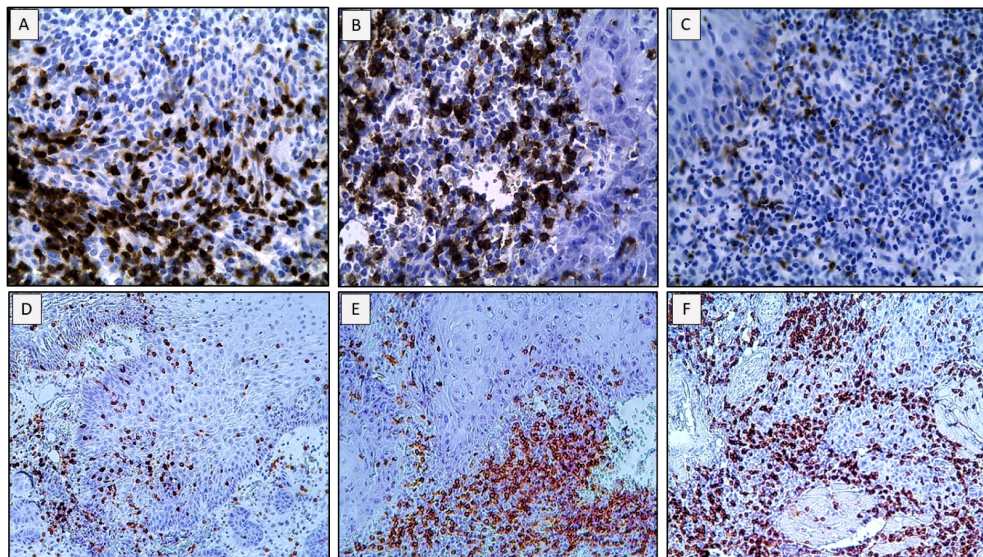


FIGURE 4

Representative pictures of immunohistochemistry images used to quantify CD3+, CD8+ and Granzyme B+ cells and to analyze their local distribution inside the tumor samples. (A) CD3+ cells; (B) CD8+ cells; (C) Granzyme B+ cells. Micrographs were obtained at 40x. (D) CD8+ cells located intratumorally in the center of the tumor or (E) CD8+ cells located mainly at the invasive margin; (F) in both the invasive margin and in the center of the tumor. Micrographs were obtained at 20x.

develop tumors with CD8+T cells that are distributed homogeneously between the invasive margins and in the center of the tumor, independently of TLR9 expression.

To corroborate our results analyzing data from larger cohorts, we used TCGA data to see if a particular gene signature could explain the distribution of CD8+T cells in heavy alcohol consumers with TLR9<sup>high</sup> tumors, but we could not identify a precise set of genes (data not shown).

Thus, we used TCGA data combined with MIXTURE, an immune tumor microenvironment estimation method based on gene expression data (n=200 samples). In this case, the algorithm categorizes the data into those patients who drink alcohol or not (yes or no), without specifying neither levels of consumption nor location of the infiltrating cells. Interestingly, using this algorithm, non-significant differences between these two groups of patients were seen regarding the numbers of tumor infiltrating leukocytes in initial stage tumors (Figure 7A). A slight increase in CD8+ T cells was observed as tumor stages progressed, which is accompanied with minor augment of activated CD4+ T cell numbers. However, the most remarkable change in the immune infiltration detected by MIXTURE is the elevated number of activated NK cells in advanced stage tumors from non-alcohol consumers (Figure 7B), an aspect that deserves further investigation.

In sum, our analysis of tumor infiltrating leukocytes in tumor samples of patients with different consumption habits indicate that the major differences perceived in patients with heavy alcohol intake are that their tumors express higher levels

of TLR9, with decreased numbers of CD8+ cells inside the tumor center and lower numbers of activated NK cells. Remarkably, both populations, CD8+ and NK cells represent the tumor killing cells par excellence.

## Discussion

The role of TLRs in cancer have been thoroughly investigated along the last decade and evidence indicate that these receptors can act as double-edged swords, promoting chronic inflammation, tumor cell migration and invasion, but also being required for an immunogenic cell death and the success of many types of therapies (6). In this work, we have analyzed tumor samples from a cohort that included 30 patients from Argentina and investigated possible connections among the expression levels of TLR9, 4 and 2, the consumption habits of the patients and CD8+T cell infiltration by IHC, regardless of their HPV status. As a support of our findings, we relied on MIXTURE, an algorithm that can predict the type of immune infiltration in a particular tumor type by collecting gene expression data from the TCGA (20).

Surprisingly, although TLR9 expression in OSCC is very well studied, there is scarce data regarding its prognostic value (23). Indeed, it is well known that TLR9 expression is enhanced in OSCC compared to normal tissue and it has significantly been associated with tumor size, clinical stage and proliferative status. Moreover, *in vitro* stimulation of oral cell lines with a TLR9

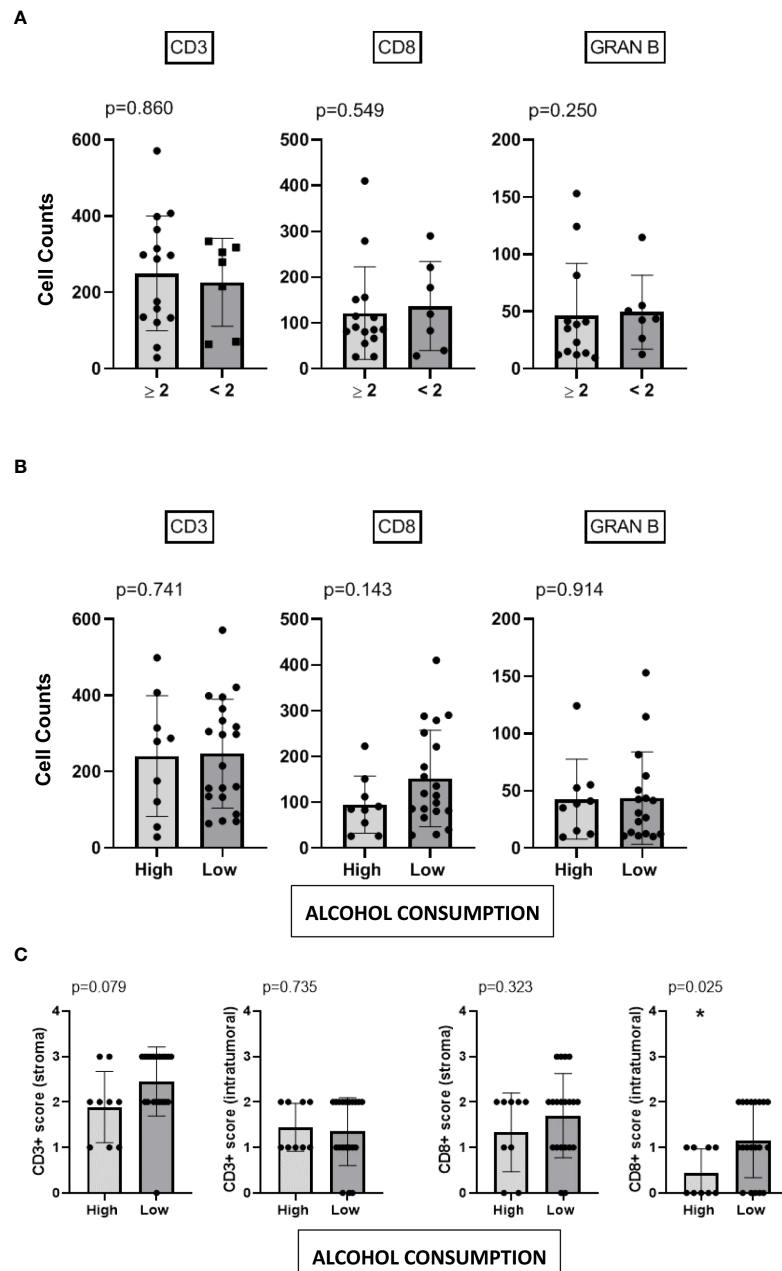


FIGURE 5

Heavy alcohol consumers exhibit a significant reduction of CD8+ T cells in the tumor center, whereas the total number of CD3+ T cells, CD8+ cells and Granzyme B+ is not altered. Total cell counts of CD3+, CD8+ and Granzyme B (GRANB+) cells (average count from 3 fields visualized at 40x) in patients categorized as  $\geq 2$  or  $< 2$  of TLR9 (A) and high (heavy) or low alcohol consumers (B). Location of CD3+ and CD8+ cells (at the invasive margin or in the center of the tumor) in the tumor samples expressed according to the scoring system detailed in M&M in patients categorized as high (heavy) or low alcohol consumers (C). \* $p < 0.05$  was considered statistically significant.

agonist, up-regulates the secretion of molecules involved in cancer cell invasion (8, 23–26). However, in spite of the existence of many reports supporting a putative correlation of TLR9 expression with worsening clinical parameters, its impact

on the survival is confusing due to small sample sizes and other inherent methodological limitations (27). Our first compelling finding is the fact that, in our cohort, patients presenting TLR9<sup>high</sup> tumors, have a reduced overall survival compared to

those who present TLR9<sup>low</sup> samples. Non-significant differences in the survival rates of the patients were observed when the expression of TLR4 or TLR2 was studied.

In an attempt to understand the impact of TLR9 expression levels on OSCC prognosis, we interrogated the TCGA database. It is important to note that data collected from the TCGA comes from the bulk lysate and as such involves tumor stroma, immune cells, and tumor cells. However, it could provide a hint regarding which molecular processes could be involved in TLR9<sup>high</sup> tumors. Interestingly, many genes showed an up-regulated expression in TLR9<sup>high</sup> vs TLR9<sup>low</sup> tumors, but we could not detect genes presenting a significant down regulation of their expression. Some of them, like KCNA2 (a voltage-gated K<sup>+</sup>channel, present at the fungiform papillae in the tongue and acts as the receptor to polyunsaturated fatty acid chemoreception), reflect specific features of the oral cavity (28, 29). Others, such as TNFRSF13B (member of the superfamily of TNF receptors) and ADAM6 (a member of the family of A disintegrin and metalloproteases) and contribute to a huge variety of biological processes such as cell growth, cell differentiation and metabolism and can participate in tumor promotion (30, 31).

ADAM6, for example is a member of the family of A disintegrin and metalloproteases, which are proteases involved in “ectodomain shedding” of diverse growth factors, cytokines, receptors and adhesion molecules (31–34). ADAM family of metalloproteases play a decisive role in regulating cell phenotype via their effects on cell adhesion, migration, proteolysis and signaling, and consequently, affecting the progression of the tumor. Another up-regulated gene is TNFRSF13B (TACI), which belongs to the superfamily of TNF receptors (TNF(R)

SF) and contributes to a huge variety of biological processes such as cell growth, cell differentiation and metabolism. Whereas its role in B cell biology is very well known, it has recently been revealed other functions in solid tumor pathogenesis, such as in breast cancer (30). In sum, the fact that these genes are up-regulated are in accordance with our findings demonstrating a shorter survival in patients bearing TLR9<sup>high</sup> tumors.

Another important result from our work is the significant association observed between heavy alcohol consumers and TLR9<sup>high</sup> tumors. Indeed, alcohol consumption has been indicated as a risk factor for a number of cancers and its main metabolite, acetaldehyde, was declared a carcinogen by the International Agency for Research on Cancer (IARC) in 1999 and has been confirmed as a Group 1 carcinogen to humans in 2009 (35). Besides its genotoxic role, alcohol strongly disrupts the organ homeostasis. In general, alcohol is capable of: a) changing the microbiome composition, selecting microbes that are capable of high-rate acetaldehyde metabolism or are more tolerant to acetaldehyde; b) directly inducing tissue damage and consequently, increasing the release of DAMPs such as self-DNA; c) generating reactive oxygen species and lipid-originated metabolites and; d) promoting the recruitment of immune cells and thus, chronic inflammation. In all these processes, innate immune receptors have been involved. Regarding TLR9 expression and alcohol, much of what is currently known comes from experiments done in *TLR9KO* mice models of alcohol-induced liver injury, but information is still controversial. There are reports indicating that TLR9 signaling in hepatocytes counteract alcohol-induced hepatotoxicity but worsens the proinflammatory response (36, 37), while other

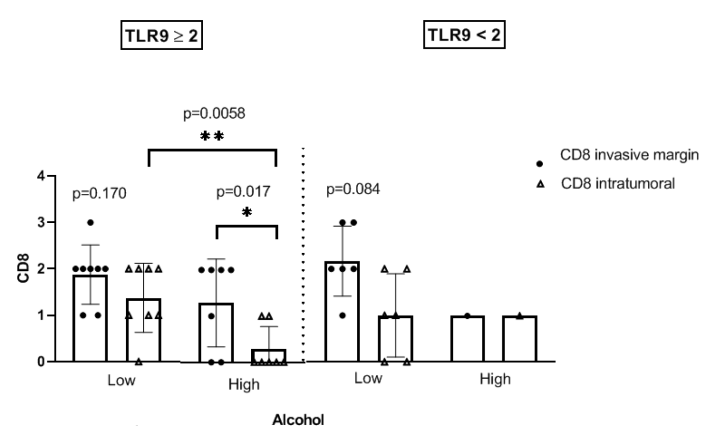


**FIGURE 6**  
TLR9<sup>high</sup> tumors that belonged to heavy alcohol consumers presented significantly fewer CD8+ T cells in the center of the tumor compared to those TLR9<sup>high</sup> tumors from low alcohol consumers. Location and scores of CD8+ cells in TLR9<sup>high</sup> and <sup>low</sup> samples from patients who were cataloged as high (heavy) or low alcohol consumers. Student T test was performed. \*p < 0.05; \*\*p < 0.001 were considered statistically significant.

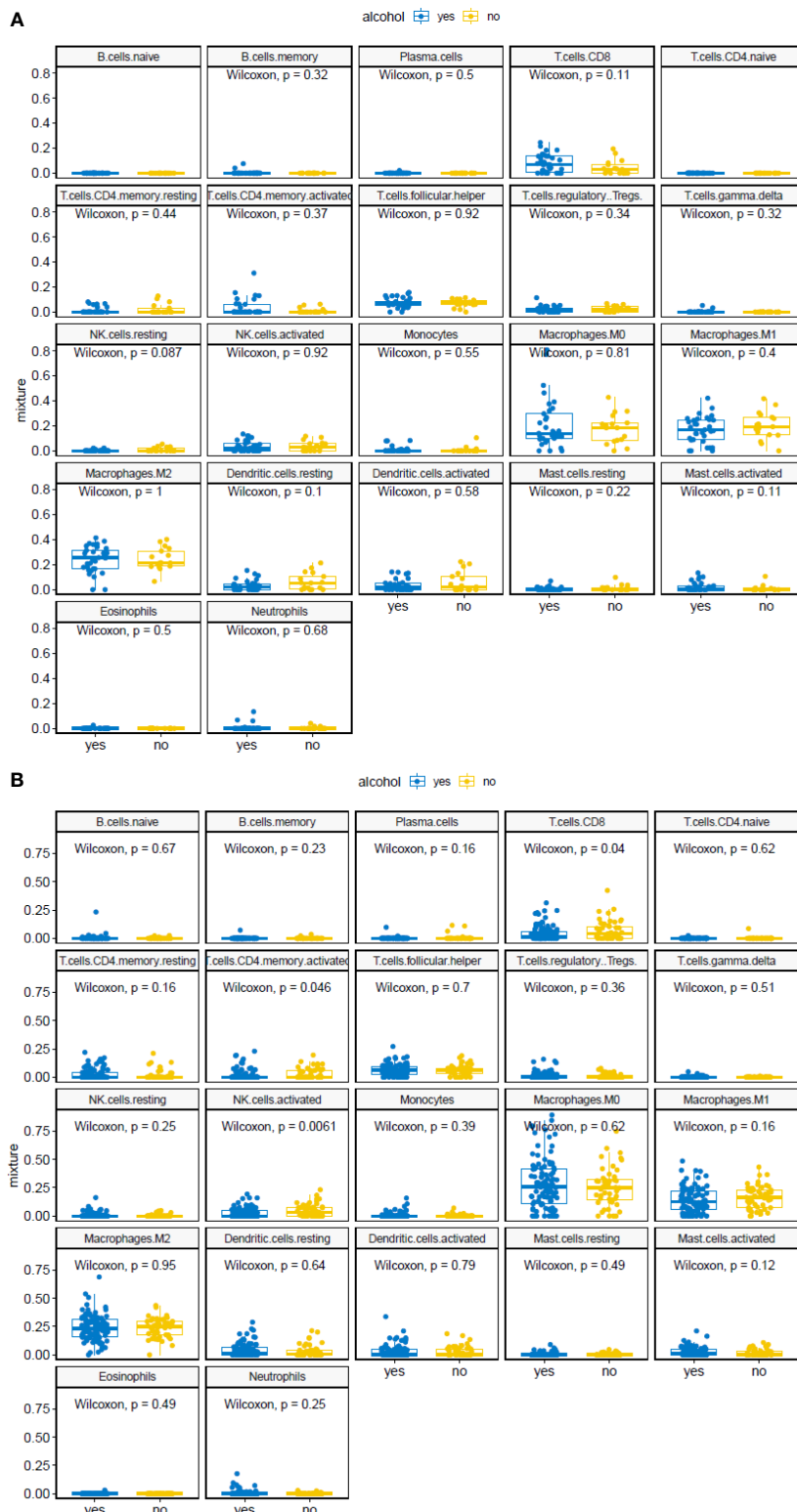


FIGURE 7

MIXTURE analysis of OSCC patients with or without alcohol consumption. Relative abundance of tumor infiltrating leukocytes in OSCC from patients with or without alcohol consumption, classified according to their tumor stages. Stages I-II (A) or III-IV (B). Wilcoxon signed-rank test was performed.

authors indicate just the opposite (38). Therefore, it is still not clear how alcohol consumption is related to TLR9 expression and its signaling, but they both affect the outcome of the patient.

An intriguing aspect of our results is the selective location that CD8+ cells display in TLR9<sup>high</sup> tumors from heavy alcohol consumers. Interestingly, this group of patients selectively show less CD8+ cells inside the tumor center (intratumoral), although no significant differences in the total numbers of infiltrating CD8+ cells was observed. The fact that TLR9<sup>high</sup> tumors from low alcohol consumers do not present this selective CD8+ cell location (Figure 6), suggests that a conjunction of factors could be taking place in heavy alcohol consumer patients with TLR9<sup>high</sup> samples. It can be hypothesized that the expression of certain chemokines is modified in TLR9<sup>high</sup> tumors from heavy alcohol consumers that could be impeding the recruitment of these cells intratumorally. Another possibility would be that the activation state of these CD8+ cells were inefficient or that excessive alcohol consumption reinforces TLR9 signaling and all the protumorigenic effects involved in this pathway.

On the other hand, in our study population, there was only one patient with heavy consumption of alcohol and a TLR9<sup>low</sup> tumor (12% of our cohort). Thus, a larger number of samples would be needed to see if this particular distribution of CD8+ cells is independent of TLR9 expression and only linked to alcohol consumption.

In any case, our results open up new avenues to investigate the possible interaction between consumption habits and immune characteristics of oral cancer and provide new evidence to consider TLR9 as a therapeutic target in OSCC.

## Data availability statement

The original contributions presented in the study are included in the article/supplementary material. Further inquiries can be directed to the corresponding authors.

## Ethics statement

The studies involving human participants were reviewed and approved by Academic Committee for Health Research of the Faculty of Dentistry – National University of Cordoba UNC (Project 31, 06/25/2015). The patients/participants provided their written informed consent to participate in this study.

## References

- Bray F, Ferlay J, Soerjomataram I, Siegel RL, Torre LA, Jemal A. Global cancer statistics 2018: GLOBOCAN estimates of incidence and mortality worldwide for 36 cancers in 185 countries. *CA Cancer J Clin* (2018) 68:394–424. doi: 10.3322/caac.21492
- Irani S. New insights into oral cancer–risk factors and prevention: A review of literature. *Int J Prev Med* (2020) 11:202. doi: 10.4103/ijpvm.IJPVM\_403\_18
- Chai AWY, Lim KP, Cheong SC. Translational genomics and recent advances in oral squamous cell carcinoma. *Semin Cancer Biol* (2020) 61:71–83. doi: 10.1016/j.semcan.2019.09.011
- Cillo AR, Kürten CHL, Tabib T, Qi Z, Onkar S, Wang T, et al. Immune landscape of viral- and carcinogen-driven head and neck cancer. *Immunity* (2020) 52:183–199.e9. doi: 10.1016/j.immuni.2019.11.014

## Author contributions

NB and GG contributed equally to the work by collecting the samples and performing the IHC analysis and infiltration characterization. SLB and RM were in charge of collecting the sample as and clinical characterization of the cohort. DR and EF performed the bioinformatic interrogation of the TCGA and MIXTURE analysis. SD did the statistical analysis of the data. RF, VP, and VG participated as pathologists and assessed tumor sample features. MM contributed to the conception and design of the study and wrote the manuscript. All authors contributed to manuscript revision, read, and approved the submitted version.

## Funding

This work was supported by grants from Instituto Nacional del Cáncer (INC-MSAL, II Convocatoria, 2016 and VI Convocatoria, 2020), Fondo Tecnológico Córdoba-MINCYT Cba and Fundación para el Progreso de la Medicina. Programa SECYT-UNC 30920190100043CB. FONCyT-PICT 2018-1789. Proyectos Institucionales de IDTyA de interés regional 2020 de SeCyT-UNC con fondos de SPU. Res. SeCyT-UNC 322/20.

## Acknowledgments

We thank Vanesa Losi and Fernanda Ponce for their technical assistance in immunohistochemistry assays.

## Conflict of interest

The authors declare that the research was conducted in the absence of any commercial or financial relationships that could be construed as a potential conflict of interest.

## Publisher's note

All claims expressed in this article are solely those of the authors and do not necessarily represent those of their affiliated organizations, or those of the publisher, the editors and the reviewers. Any product that may be evaluated in this article, or claim that may be made by its manufacturer, is not guaranteed or endorsed by the publisher.

5. McClure R, Massari P. TLR-dependent human mucosal epithelial cell responses to microbial pathogens. *Front Immunol* (2014) 5:386. doi: 10.3389/fimmu.2014.00386

6. Urban-Wojciuk Z, Khan MM, Oyler BL, Fähraeus R, Marek-Trzonkowska N, Nita-Lazar A, et al. The role of TLRs in anti-cancer immunity and tumor rejection. *Front Immunol* (2019) 10:2388. doi: 10.3389/fimmu.2019.02388

7. Sharma U, Singh P, Bandil K, Patle R, Kumar A, Neyaz K, et al. Genetic variations of TLRs and their association with HPV/EBV, co-infection along with nicotine exposure in the development of premalignant/malignant lesions of the oral cavity in Indian population. *Cancer Epidemiol* (2019) 61:38–49. doi: 10.1016/j.canep.2019.05.003

8. Beklen A, Hukkanen M, Richardson R, Konttinen YT. Immunohistochemical localization of toll-like receptors 1–10 in periodontitis. *Oral Microbiol Immunol* (2008) 23:425–31. doi: 10.1111/j.1399-302X.2008.00448.x

9. Uehara A, Fujimoto Y, Fukase K, Takada H. Various human epithelial cells express functional toll-like receptors, NOD1 and NOD2 to produce anti-microbial peptides, but not proinflammatory cytokines. *Mol Immunol* (2007) 44:3100–11. doi: 10.1016/j.molimm.2007.02.007

10. Chattopadhyay I, Verma M, Panda M. Role of oral microbiome signatures in diagnosis and prognosis of oral cancer. *Technol Cancer Res Treat* (2019) 18:153303381986735. doi: 10.1177/153303381986735

11. Pisani LP, Estadella D, Ribeiro DA. The role of toll like receptors (TLRs) in oral carcinogenesis. *Anticancer Res* (2017) 37:5389–94. doi: 10.21873/anticanres.11965

12. Brierley JD, Gospodarowicz MK, Wittekind C. *TNM classification of malignant tumours*, New Jersey: John Wiley & Sons; (2017). 272 p. Available at: <https://www.wiley.com/en-gb/TNM+Classification+of+Malignant+Tumours%2C+8th+Edition-p-9781119263579>.

13. E-N AK, C JKC, G JR, T T, S PJ. *WHO classification of head and neck tumours*. Available at: <https://publications.iarc.fr/Book-And-Report-Series/Who-Classification-Of-Tumours/WHO-Classification-Of-Head-And-Neck-Tumours-2017>.

14. Biondi K, Belloni S, Velasco M, Robledo G, Gallardo M, Femopase F. International association in dental research, Argentine division, annual meeting. La cumbre, Cordoba, argentina. October 23–25, 1997. abstracts. *J Dent Res* (1998) 77:1101–363. doi: 10.1111/00220345980770050201

15. Pentenero M, Navone R, Motta F, Marino R, Gassino L, Broccoletti R, et al. Clinical features of microinvasive stage I oral carcinoma. *Oral Dis* (2011) 17:298–303. doi: 10.1111/j.1601-0825.2010.01740.x

16. González JÁlvarez. *Límites de consumo de bajo riesgo de alcohol. actualización del riesgo relacionado con los niveles de consumo de alcohol, el patrón de consumo y el tipo de bebida. parte 1. Actualización de los límites de consumo de bajo riesgo de alcohol* (2020). Available at: [https://www.sanidad.gob.es/profesionales/saludPublica/prevPromocion/Prevencion/alcohol/docs/Límites\\_Consumo\\_Bajo\\_Riesgo\\_Alcohol\\_Actualizacion.pdf](https://www.sanidad.gob.es/profesionales/saludPublica/prevPromocion/Prevencion/alcohol/docs/Límites_Consumo_Bajo_Riesgo_Alcohol_Actualizacion.pdf).

17. *Drinking levels defined*. National Institute on Alcohol Abuse and Alcoholism (NIAAA). Available at: <https://www.niaaa.nih.gov/alcohol-health/overview-alcohol-consumption/moderate-binge-drinking>.

18. Gatti G, Betts C, Rocha D, Nicola M, Grupe V, Ditada C, et al. High IRF8 expression correlates with CD8 T cell infiltration and is a predictive biomarker of therapy response in ER-negative breast cancer. *Breast Cancer Res* (2021) 23:40. doi: 10.1186/s13058-021-01418-7

19. Gatti G, Quintar AA, Andreani V, Nicola JP, Maldonado CA, Masini-Repiso AM, et al. Expression of toll-like receptor 4 in the prostate gland and its association with the severity of prostate cancer. *Prostate* (2009) 69:1387–97. doi: 10.1002/pros.20984

20. Fernández EA, Mahmoud YD, Veigas F, Rocha D, Miranda M, Merlo J, et al. Unveiling the immune infiltrate modulation in cancer and response to immunotherapy by MIXTURE—an enhanced deconvolution method. *Briefings Bioinf* (2021) 22:bbaa317. doi: 10.1093/bib/bbaa317

21. Crews FT, Walter TJ, Coleman LG, Vetreto RP. Toll-like receptor signaling and stages of addiction. *Psychopharmacology* (2017) 234:1483–98. doi: 10.1007/s00213-017-4560-6

22. Petrasek J, Iracheta-Vellve A, Saha B, Satishchandran A, Kody K, Fitzgerald KA, et al. Metabolic danger signals, uric acid and ATP, mediate inflammatory cross-talk between hepatocytes and immune cells in alcoholic liver disease. *J Leukocyte Biol* (2015) 98:249–56. doi: 10.1189/jlb.3AB1214-590R

23. Kauppila JH, Korvala J, Siirilä K, Manni M, Mäkinen LK, Hagström J, et al. Toll-like receptor 9 mediates invasion and predicts prognosis in squamous cell carcinoma of the mobile tongue. *J Oral Pathol Med* (2015) 44:571–7. doi: 10.1111/jop.12272

24. Min R, Siyi L, Wenjun Y, Shengwen L, Ow A, Lizheng W, et al. Toll-like receptor-9 agonists increase cyclin D1 expression partly through activation of activator protein-1 in human oral squamous cell carcinoma cells. *Cancer Sci* (2012) 103:1938–45. doi: 10.1111/j.1349-7006.2012.02394.x

25. Kotrashetti VS, Nayak R, Bhat K, Hosmani J, Somannavar P. Immunohistochemical expression of TLR4 and TLR9 in various grades of oral epithelial dysplasia and squamous cell carcinoma, and their roles in tumor progression: a pilot study. *Biotech Histochem* (2013) 88:311–22. doi: 10.3109/10520295.2013.785592

26. Ruan M, Thorn K, Liu S, Li S, Yang W, Zhang C, et al. The secretion of IL-6 by CpG-ODN-treated cancer cells promotes T-cell immune responses partly through the TLR-9/AP-1 pathway in oral squamous cell carcinoma. *Int J Oncol* (2014) 44:2103–10. doi: 10.3892/ijo.2014.2356

27. Hasnat S, Hujanen R, Nwaru BI, Salo T, Salem A. The prognostic value of toll-like receptors in head and neck squamous cell carcinoma: A systematic review and meta-analysis. *Int J Mol Sci* (2020) 21:7255. doi: 10.3390/ijms21197255

28. Gilbertson TA, Fontenot DT, Liu L, Zhang H, Monroe WT. Fatty acid modulation of k+ channels in taste receptor cells: gustatory cues for dietary fat. *Am J Physiol-Cell Physiol* (1997) 272:C1203–10. doi: 10.1152/ajpcell.1997.272.4.C1203

29. Costanzo A, Liu D, Nowson C, Duesing K, Archer N, Bowe S, et al. A low-fat diet up-regulates expression of fatty acid taste receptor gene FFAR4 in fungiform papillae in humans: a co-twin randomised controlled trial. *Br J Nutr* (2019) 122:1212–20. doi: 10.1017/S0007114519002368

30. Kampa M, Notas G, Stathopoulos EN, Tsapis A, Castanás E. The TNFSF members APRIL and BAFF and their receptors TACI, BCMA, and BAFFR in oncology, with a special focus in breast cancer. *Front Oncol* (2020) 10:827. doi: 10.3389/fonc.2020.00827

31. Schumacher N, Rose-John S, Schmidt-Arras D. ADAM-mediated signalling pathways in gastrointestinal cancer formation. *IJMS* (2020) 21:5133. doi: 10.3390/ijms21145133

32. Kataoka H. EGFR ligands and their signaling scissors, ADAMs, as new molecular targets for anticancer treatments. *J Dermatol Sci* (2009) 56:148–53. doi: 10.1016/j.jdermsci.2009.10.002

33. Edwards D, Handsley M, Pennington C. The ADAM metalloproteinases. *Mol Aspects Med* (2008) 29:258–89. doi: 10.1016/j.mam.2008.08.001

34. Buranaphathana W, Wu S, Makeudom A, Sastraruji T, Supanchart C, Krisanaprakornkit S. Involvement of the a disintegrin and metalloproteinase 9 in oral cancer cell invasion. *Eur J Oral Sci* (2021) 129:e12775. doi: 10.1111/eos.12775

35. IARC Working Group on the Evaluation of Carcinogenic Risks to Humans. Personal habits and indoor combustions. Volume 100 E. A review of human carcinogens. *IARC Monogr Eval Carcinog Risks Hum* (2012) 100:1–538.

36. Gaonkar PP, Patankar SR, Tripathi N, Sridharan G. Oral bacterial flora and oral cancer: The possible link? *J Oral Maxillofac Pathol* (2018) 22:234–8. doi: 10.4103/jomfp.JOMFP\_89\_16

37. Hao L, Zhong W, Sun X, Zhou Z. TLR9 signaling protects alcohol-induced hepatic oxidative stress but worsens liver inflammation in mice. *Front Pharmacol* (2021) 12:709002. doi: 10.3389/fphar.2021.709002

38. Roh YS, Zhang B, Loomba R, Seki E. TLR2 and TLR9 contribute to alcohol-mediated liver injury through induction of CXCL1 and neutrophil infiltration. *Am J Physiology-Gastrointestinal Liver Physiol* (2015) 309:G30–41. doi: 10.1152/ajpgi.00031.2015

## COPYRIGHT

© 2022 Bolesina, Gatti, López de Blanc, Dhooge, Rocha, Fernandez, Ferreyra, Palla, Grupe, Morelatto and Maccioni. This is an open-access article distributed under the terms of the [Creative Commons Attribution License \(CC BY\)](https://creativecommons.org/licenses/by/4.0/). The use, distribution or reproduction in other forums is permitted, provided the original author(s) and the copyright owner(s) are credited and that the original publication in this journal is cited, in accordance with accepted academic practice. No use, distribution or reproduction is permitted which does not comply with these terms.



## OPEN ACCESS

## EDITED BY

Mercedes Beatriz Fuertes,  
CONICET Instituto de Biología y  
Medicina Experimental (IBYME),  
Argentina

## REVIEWED BY

Jason M. Miska,  
Northwestern University, United States  
Zeyu Wang,  
University of Edinburgh,  
United Kingdom

## \*CORRESPONDENCE

Jie Dong  
dongjie@nju.edu.cn  
Jiwu Wei  
wjw@nju.edu.cn

<sup>†</sup>These authors have contributed  
equally to this work and share  
the first authorship

## SPECIALTY SECTION

This article was submitted to  
Cancer Immunity  
and Immunotherapy,  
a section of the journal  
Frontiers in Immunology

RECEIVED 03 February 2022  
ACCEPTED 14 September 2022  
PUBLISHED 30 September 2022

## CITATION

Wang S, Li L, Zuo S, Kong L, Wei J and  
Dong J (2022) Metabolic-related gene  
pairs signature analysis identifies  
ABCA1 expression levels on tumor-  
associated macrophages as a  
prognostic biomarker in primary  
IDH<sup>WT</sup> glioblastoma.  
*Front. Immunol.* 13:869061.  
doi: 10.3389/fimmu.2022.869061

## COPYRIGHT

© 2022 Wang, Li, Zuo, Kong, Wei and  
Dong. This is an open-access article  
distributed under the terms of the  
[Creative Commons Attribution License  
\(CC BY\)](#). The use, distribution or  
reproduction in other forums is  
permitted, provided the original  
author(s) and the copyright owner(s)  
are credited and that the original  
publication in this journal is cited, in  
accordance with accepted academic  
practice. No use, distribution or  
reproduction is permitted which does  
not comply with these terms.

# Metabolic-related gene pairs signature analysis identifies ABCA1 expression levels on tumor-associated macrophages as a prognostic biomarker in primary IDH<sup>WT</sup> glioblastoma

Shiqun Wang<sup>1,2†</sup>, Lu Li<sup>3†</sup>, Shuguang Zuo<sup>4†</sup>, Lingkai Kong<sup>1</sup>,  
Jiwu Wei<sup>1\*</sup> and Jie Dong<sup>1\*</sup>

<sup>1</sup>Jiangsu Key Laboratory of Molecular Medicine, Medical School of Nanjing University, Nanjing, Jiangsu, China, <sup>2</sup>The Cancer Hospital of the University of Chinese Academy of Sciences (Zhejiang Cancer Hospital), Institute of Basic Medicine and Cancer (IBMC), Chinese Academy of Sciences, Hangzhou, Zhejiang, China, <sup>3</sup>Department of Nephrology, Affiliated Children's Hospital of Zhejiang University, Hangzhou, Zhejiang, China, <sup>4</sup>Liuzhou Key Laboratory of Molecular Diagnosis, Guangxi Key Laboratory of Molecular Diagnosis and Application, Affiliated Liutie Central Hospital of Guangxi Medical University, Liuzhou, Guangxi, China

**Background:** Although isocitrate dehydrogenase (IDH) mutation serves as a prognostic signature for routine clinical management of glioma, nearly 90% of glioblastomas (GBM) patients have a wild-type IDH genotype (IDH<sup>WT</sup>) and lack reliable signatures to identify distinct entities.

**Methods:** To develop a robust prognostic signature for IDH<sup>WT</sup> GBM patients, we retrospectively analyzed 4 public datasets of 377 primary frozen tumor tissue transcriptome profiling and clinical follow-up data. Samples were divided into a training dataset (204 samples) and a validation (173 samples) dataset. A prognostic signature consisting of 21 metabolism-related gene pairs (MRGPs) was developed based on the relative ranking of single-sample gene expression levels. GSEA and immune subtype analyses were performed to reveal differences in biological processes between MRGP risk groups. The single-cell RNA-seq dataset was used to examine the expression distribution of each MRG constituting the signature in tumor tissue subsets. Finally, the association of MRGs with tumor progression was biologically validated in orthotopic GBM models.

**Results:** The metabolic signature remained an independent prognostic factor (hazard ratio, 5.71 [3.542–9.218],  $P < 0.001$ ) for stratifying patients into high- and low-risk levels in terms of overall survival across subgroups with MGMTp methylation statuses, expression subtypes, and chemo/ratio therapies. Immune-related biological processes were significantly different between MRGP risk groups. Compared with the low-risk group, the high-risk group

was significantly enriched in humoral immune responses and phagocytosis processes, and had more monocyte infiltration and less activated DC, NK, and  $\gamma\delta$  T cell infiltration. scRNA-seq dataset analysis identified that the expression levels of 5 MRGs (ABCA1, HMOX1, MTHFD2, PIM1, and PTPRE) in TAMs increased with metabolic risk. With tumor progression, the expression level of ABCA1 in TAMs was positively correlated with the population of TAMs in tumor tissue. Downregulation of ABCA1 levels can promote TAM polarization towards an inflammatory phenotype and control tumor growth.

**Conclusions:** The metabolic signature is expected to be used in the individualized management of primary IDH<sup>WT</sup> GBM patients.

#### KEYWORDS

primary glioblastoma, wild-type isocitrate dehydrogenase, metabolic-related gene pairs, prognosis, tumor-associated macrophages, ABCA1

## Highlights

1. The metabolic signature can individually assess the prognosis of primary IDH<sup>WT</sup> GBM patients.
2. Immune and metabolic processes were integrated into the molecular profiling descriptions of different GBM entities.

## Introduction

Since the WHO Classification of Central Nervous System tumors was revised in 2016, the diagnosis of glioma has developed into a new paradigm integrating molecular and histological features (1, 2). The mutation status of isocitrate dehydrogenase (IDH) is the primary biomarker for classifying distinct glioma entities. More than 90% of glioblastoma (GBM, WHO IV) patients have a wild-type IDH genotype (IDH<sup>WT</sup>), however, they currently lack robust prognostic biomarkers to further determine whether they benefit from chemoradiation (3). Therefore, the identification of prognostic factors in IDH<sup>WT</sup> GBM patients is needed.

Despite ongoing efforts to define the prognostic molecular features of these patients (4–7), no biomarkers have been incorporated into routine clinical practice to date. Limitations are attributed to the lack of effective validation and overfitting of small discovery datasets; or the difficulty of multiple datasets merging to effectively eliminate batch effects from different techniques, laboratories, and samples (8). However, the

elimination of batch effects is crucial for the robustness of the prognostic signature. Recently, a few studies have proposed new methods based on the relative ranking of gene expression levels to eliminate the biological variability of merging multiple datasets (9, 10).

Metabolic reprogramming is considered an emerging hallmark of cancer (11). Alterations in metabolism-related genes, such as IDH1 mutation, O<sup>6</sup>-methylguanine-DNA methyltransferase gene (MGMT) promoter methylation, or epidermal growth factor receptor (EGFR) amplification, are frequent in glioma patients and are closely related to prognosis (12–15). However, the prognostic performance of metabolic features in IDH<sup>WT</sup> GBMs has not been adequately described. Therefore, extracting tumor hallmarks helps to outline the molecular features of patients and minimize data redundancy for pairwise ranking of full-size gene sets.

In this study, we integrated gene expression profiles of tumor tissue samples from multiple IDH<sup>WT</sup> GBM datasets, and constructed and validated an individualized prognostic signature based on their metabolism-related genes.

## Materials and methods

### In silico study and public datasets

In this study, we retrospectively analyzed the gene expression profiles of tumor tissue samples from four public glioblastoma (GBM) datasets, including one microarray dataset from the Chinese Glioma Genome Atlas (CGGA), two RNA-seq datasets from CGGA, and one RNA-seq dataset from The

Cancer Genome Atlas (TCGA, **Table S1**). Only patients who met the following criteria were included: a) histologically confirmed grade IV glioma according to the WHO classification; b) fresh frozen tissue sample; c) no history of neoadjuvant therapy or other preoperative treatment; d) availability of isocitrate dehydrogenase (IDH) mutation status; and e) availability of data on overall survival, clinical annotation, genetics, and treatment information (16–18). Patients in CGGA\_301 that overlapped with CGGA\_325 and CGGA\_693 (n = 24) were removed. Overall, a total of 377 patients were selected and divided into a training dataset (n = 204) and a validation dataset (n = 173). Further clinical characteristics of patients in each dataset are shown in **Table S2**. Details about the preprocessing of gene expression profiles and sample

preparation used to obtain these datasets can be found in the **Supplemental Methods** or previous studies (19–21). The overall design of this study is shown in **Figure 1A**. The diagnostic accuracy study was based on the STARD guidelines and approved by the Institutional Review Committee of Nanjing University.

## Development of a prognostic signature based on single-sample MRGPs

To eliminate batch effects from different biological samples, we performed a pairing operation on 802 common metabolism-

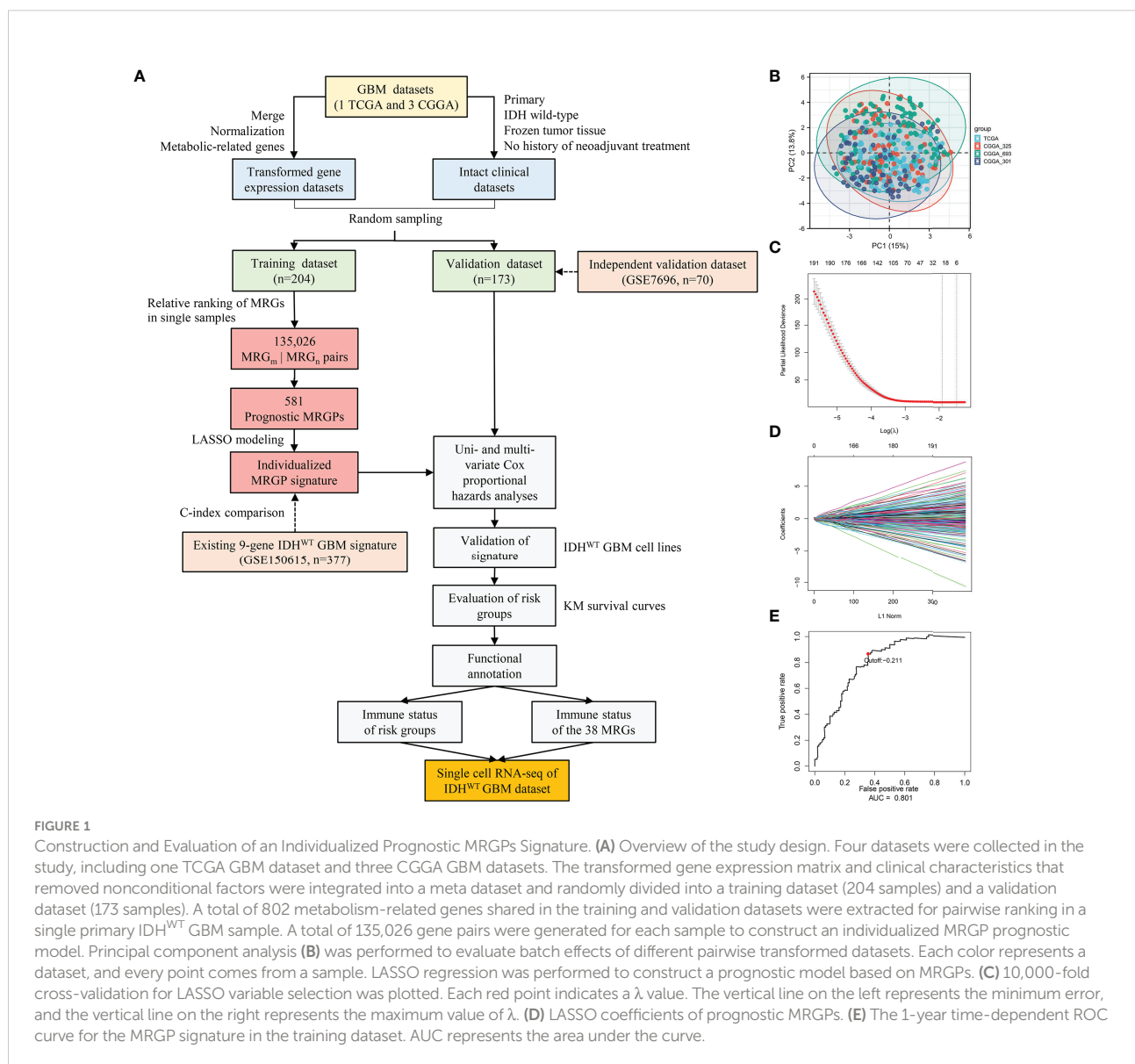


**FIGURE 1**

Construction and Evaluation of an Individualized Prognostic MRGPs Signature. **(A)** Overview of the study design. Four datasets were collected in the study, including one TCGA GBM dataset and three CGGA GBM datasets. The transformed gene expression matrix and clinical characteristics that removed nonconditional factors were integrated into a meta dataset and randomly divided into a training dataset (204 samples) and a validation dataset (173 samples). A total of 802 metabolism-related genes shared in the training and validation datasets were extracted for pairwise ranking in a single primary IDH<sup>WT</sup> GBM sample. A total of 135,026 gene pairs were generated for each sample to construct an individualized MRGP prognostic model. Principal component analysis **(B)** was performed to evaluate batch effects of different pairwise transformed datasets. Each color represents a dataset, and every point comes from a sample. LASSO regression was performed to construct a prognostic model based on MRGPs. **(C)** 10,000-fold cross-validation for LASSO variable selection was plotted. Each red point indicates a  $\lambda$  value. The vertical line on the left represents the minimum error, and the vertical line on the right represents the maximum value of  $\lambda$ . **(D)** LASSO coefficients of prognostic MRGPs. **(E)** The 1-year time-dependent ROC curve for the MRGP signature in the training dataset. AUC represents the area under the curve.

related genes (MRGs) for each sample. A new matrix of 135,026 MRG pairs (MRGPs) for 377 samples was generated. Details can be found in the [Supplemental Methods](#) or previous studies (9, 10). Principal component analysis (PCA) was further used to evaluate the platform or biological variability across different datasets.

In the training dataset, prognostic MRGPs were identified by using univariate Cox regression analysis to evaluate the association between each MRGP and patients' overall survival ( $P < 0.001$ ). A total of 581 prognostic MRGPs were selected to build a prognostic model by using the Lasso Cox proportional hazards regression model with 10-fold cross-validation (glmnet package, version: 3.0-2) (22). Robustness assessment of the metabolic signature against 1,000 randomizations of the training dataset can be found in the [Supplemental Methods](#). A prognostic model including 21 MRGPs was constructed and used to calculate the risk score for each patient. Details of the 21 MRGPs can be obtained in [Table S4](#). The formula of the risk score is as follows:

$$\text{Risk score} = \sum_{i=1}^n \text{Coefficient}_i \times \text{Value}_i$$

Finally, we defined the optimum cut-off value for stratifying high- or low-risk groups by using a 1-year time-dependent receiver operating characteristic (ROC) curve (survival ROC package, version: 1.0.3).

## Evaluation and validation of the single-sample MRGPs signature

To determine whether the metabolic signature can be used as an independent prognostic factor in the management of IDH<sup>WT</sup> GBM, we performed uni- and multivariate Cox proportional hazards analyses on patients in the training and validation datasets ([Table S5](#)). Age, gender, MGMTp methylation status, and risk were coded as continuous variables (e.g., female was coded as 0, male as coded as 1; MGMTp methylation was coded as 0, MGMTp unmethylation was coded as 1).

Furthermore, we evaluated the prognostic accuracy of our MRGPs signature and one existing 9-gene IDH<sup>WT</sup> GBM signature in a continuous form by using the concordance index (C-index). Details about the C-index comparison can be found in the [Supplemental Methods](#). Kaplan–Meier curve analysis was used to validate the overall survival stratification of our MRGPs signature and 9-gene signature in the training and validation datasets.

In the training and validation datasets, we utilized a Pearson correlation heatmap (pheatmap, version: 1.0.12) to explore the expression correlation of 38 MRGs that make up the prognostic signature. Considering that the main population of tumor tissues was tumor cells, we performed real-time PCR to identify the

expression profile of 38 MRGs of two human IDH<sup>WT</sup> GBM cell lines (U87-MG and U251-MG) and three human control cell lines (HeLa S3, HEK293, and HA1800) and to mimic risk decisions based on the metabolic risk score. Details about cell lines, RNA isolation, PCR, and identification of IDH1 mutations can be found in the [Supplemental Methods](#).

## Functional annotation and enrichment analyses

To reveal the biological significance of the MRGPs signature, we conducted Gene Ontology (GO) functional annotation analysis of its component MRGs with the Database for Annotation, Visualization and Integrated Discovery (DAVID) Bioinformatics Resources database (<https://david.ncifcrf.gov/>). Significant GO biological processes ( $P < 0.05$ ) were detected ([Table S6](#)). In addition, the meta dataset was divided into high- and low-risk groups according to MRGPs, and gene set enrichment analysis (GSEA) was performed on these groups (fgsea package, version: 1.12.0; C5.bp.v7.1; 10,000 permutations). Significantly enriched biological processes ( $P$  value  $< 0.05$ ) were examined.

## Tumor purity and immune infiltration analyses

Tumor purity possesses important clinical implications in glioma classification (23). Estimation of STromal and Immune cells in MAlignant Tumor tissues using Expression data (ESTIMATE) analysis was performed to estimate differences in tumor purity between MRGP risk groups in the meta dataset (estimate package, version: 1.0.13). The ESTIMATE score was considered to be negatively correlated with tumor purity. Pearson correlation analysis was used to determine the correlation between tumor purity and the expression levels of 38 MRGs in risk groups in the meta dataset.

We further explored the immune infiltration status of the metabolic high- and low-risk groups by using xCell (<https://xcell.ucsf.edu/>) and Cell-type Identification by Estimating Relative Subsets of RNA Transcripts (CIBERSORT package, version: 1.03). Specifically, the normalized gene expression matrix in the meta dataset was divided into high- and low-risk groups based on the MRGPs signature. The relative abundances of immune cells between MRGP risk groups were identified (matrix at 1,000 permutations). The profile of immune infiltration of different risk groups was displayed by the radar chart (fmsb package, version: 0.7.1). Pearson correlation analysis was used to determine the correlation between the relative abundances of immune cells and the expression levels of 38 MRGs in risk groups in the meta dataset.

## Expression distribution of the 38 MRGs in the single-cell RNA-seq dataset

A single-cell RNA-seq dataset for IDH<sup>WT</sup> GBM (GEO: GSE131928) was downloaded from the Single Cell Portal (<https://singlecell.broadinstitute.org/>). Data processing as previously described (24). Briefly, use with arguments “-q -phred33-quals -n 1 -e 99999999 -l 25 -I 1 -X 2000 -a -m 15 -S -p 6”. Expression values were calculated by RSEM v1.2.3 in paired-end mode, using the parameter “-estimate-rspd -paired end -sam -p 6”, from which TPM values for each gene were extracted. For cells annotations treated with 10X, we used CellRanger with default parameters. The dataset included 24131 cell sequencing data points from 28 tumor samples (24). Scaled mean expression data (robust z score) were used to identify the expression levels of 38 MRGs in 28 samples. Furthermore, the risk level of each single-cell sequencing sample was defined by our MRGP model (Figure S8). Four main cell populations were found in all single cells, including macrophages, malignancies, oligodendrocytes, and T cells. t-distributed stochastic neighbor embedding (tSNE) was performed to plot the expression distribution of all 38 MRGs in the four populations. A heatmap was generated to show changes in the expression levels of 38 MRGs from low risk to high risk in the four populations.

## MRGPs risk coefficient connection and protein–protein interaction network

The Search Tool for the Retrieval of Interacting Genes/Proteins (STRING, <https://www.string-db.org/>) database was used to identify the direct interaction network between 38 proteins. To reveal the inherent association of the metabolic signature, we used Cytoscape (version 3.7.2) to draw a network diagram for these MRGs.

## Cell lines

The human glioblastoma (GBM) cell lines (U87-MG and U251-MG), the human cervical carcinoma cell line (HeLa S3), the human embryonic kidney cells 293 (HEK293), and human normal astrocyte cell line (HA1800) were purchased from ATCC, tested for mycoplasma contamination, and authenticated by short tandem repeat (STR) analysis. The murine GBM cell line GL261 was purchased from the China Center for Type Culture Collection. TAMs were isolated by anti-mouse F4/80 MicroBeads UltraPure (Miltenyi Biotec, 130-110-443) from GL261 tumors. Bone marrow-derived macrophages (BMDMs) were obtained by *in vitro* M-CSF differentiation of C57 mouse bone marrow cells. All GBM cells were cultured in DMEM/F12 medium (D8437, Sigma); HeLa S3, HEK293, and

HA1800 cells were cultured in DMEM containing 4.5 g/L glucose (Cat No. 11965-092, Gibco) supplemented with 10% fetal bovine serum (Cat No. 10099-141, Gibco), 100 U/mL penicillin, and 100 µg/mL streptomycin (Cat No. 15140-122, Gibco). All cells were maintained at 37°C in a humidified incubator with 5% CO<sub>2</sub>.

## Animal studies

Animal care and handling procedures were carried out following the NIH Guide for the Care and Use of Laboratory Animals and were approved by the Institutional Review Board of Nanjing University. For the intracranial GBM model, 6- to 8-week-old male C57BL/6 mice and NOD-Prkdcscid Il2rgnull (NCG) mice were purchased from Nanjing University Model Animal Institute. As described in a previous study, the mice were anesthetized, and dissociated GBM cells were implanted into 2.0 mm depth to the skull 1.0 mm anterior and 2.0 mm lateral to bregma by using a stereotactic apparatus (25). GL261<sup>IDH-WT</sup> cells (2 x 10<sup>5</sup> cells/2 µl PBS) were intracranially inoculated into the caudate nucleus of C57BL/6 mice. U87-MG<sup>IDH-WT</sup> cells (5 x 10<sup>5</sup> cells/4 µl PBS) were injected into NCG mice. The survival and neurological symptoms of the mice were monitored every other day. To assess the mRNA expression levels of the 5 MRGs of TAMs during tumor progression, orthotopic GL261<sup>IDH-WT</sup>-bearing mice were sacrificed on days 7, 14, and 21, and tumor tissues were collected for magnetic bead sorting of TAMs. The isolated TAMs were further extracted for total RNA and the expression of these genes was performed by qPCR. To assess the expression levels of ABCA1 on TAMs during tumor progression, orthotopic GL261<sup>IDH-WT</sup>- or U87-MG<sup>IDH-WT</sup>-bearing mice were sacrificed on days 7, 14, and 21, and tumor tissues were collected for FCM analysis. To assess the association between cholesterol metabolism and ABCA1 expression levels in macrophages, differentiated BMDMs were ex vivo treated with vehicle, 1 µg/ml and 10 µg/ml cholesterol (Sigma, C4951) for 24 hours for FCM analysis; orthotopic GL261<sup>IDH-WT</sup>-bearing mice were sacrificed on days 17 to isolate TAMs, and these sorted TAMs were ex vivo treated with vehicle (DMSO), 2 µM and 5 µM lovastatin (Sigma, 75330-75-5) for 24 hours for FCM analysis. To assess the therapeutic activity of modulating ABCA1 expression, GL261<sup>IDH-WT-Luc</sup> cells (2 x 10<sup>5</sup> cells/2 µl PBS) were intracranially inoculated into the caudate nucleus of C57BL/6 mice. On day 7 after tumor inoculation, mice were given oral gavage with vehicle (0.5% methylcellulose, 2% Tween-80 in water) or 10 mg/kg lovastatin (NJDULY, A0157) daily for 14 days. At the end of dosing, tumor growth was examined by an *In Vivo* Imaging System (IVIS, LB 983 NC100). To assess TAMs polarization following modulation of ABCA1 expression, FCM analysis of TAMs inflammatory factor expression was performed in lovastatin-treated GL261<sup>IDH-WT-Luc</sup> tumors for 14 days as previously described.

## Flow cytometry

For *in vivo* macrophage analysis, tumor tissue was collected at set time points after tumor cell engraftment, digested, and filtered through a 70  $\mu\text{m}$  strainer. Dissociated cells were further incubated with the following antibodies: anti-mouse CD16/CD32 (Multi Sciences, clone 2.4G2, Cat No. AM016-100), IgG2a,  $\kappa$  isotype ctrl (Biolegend, clone MOPC-173, Cat No. 400233), anti-mouse ABCA1 (BIO-RAD, clone 5A1-1422, Cat No. MCA2681), anti-mouse F4/80 (Biolegend, clone BM8, Cat No. 123110), anti-mouse\human CD11b CM1/70, Cat No. 101229, anti-mouse CD86 (Biolegend, clone GL-1, Cat No. 105005), anti-mouse CD206 (Biolegend, clone C068C2, Cat No. 141715), anti-mouse TNF- $\alpha$  (Biolegend, clone MP6-XT22, Cat No. 506303), anti-mouse IFN- $\gamma$  (Biolegend, clone XMG1.2, Cat No. 506303), anti-mouse Arginase 1 (Abbexa, Polyclonal, Cat No. abx319179), and anti-mouse CD45 (Biolegend, clone 30-F11, Cat No. 103112). Intracellular staining was done using Fixation/Permeabilization kit (BD, 554722). Samples were subjected to FCM by using BD FACS Calibur, BD Aria I, and Beckman CytoFLEX. Data were analyzed with FlowJo (vX.0.7).

## Statistical analysis

Statistical analyses were performed by using R software (version: 3.6.3; <https://www.r-project.org/>) or GraphPad Prism (v. 8.0.1). Continuous variables were compared by using Student's t test, the Mann-Whitney test, or the Wilcoxon rank-sum test. Cumulative survival analyses were performed using the Kaplan-Meier method, and the survival differences were analyzed using the log-rank test (survival package, version: 3.1-12). In the univariate and multivariate analyses, the Wald test was used to assess the association of the MRGP and clinicopathologic factors with overall survival. Pearson correlation tests were performed to assess the correlation of MRGs with tumor purity or immune cell abundances (corrplot package, version: 0.84).

## Results

### Development and definition of MRGPs signature based on single IDH<sup>WT</sup> GBM samples

In this retrospective study, a total of 377 IDH<sup>WT</sup> GBM patients (236 female, 141 male) were selected from the TCGA and CGGA databases according to the criteria shown in Figure 1A. Patients were further randomly assigned to the training dataset ( $n = 204$ ) and validation dataset ( $n = 173$ ). No significant differences in clinical characteristics between the training and validation datasets were observed (Table S2).

Among the 3,679 MRGs we obtained in the KEGG database, a total of 802 MRGs shared with all datasets were identified, and 135,026 MRGPs were further constructed for each sample. Details about the elimination of platform bias and biological variability can be found in the *Supplementary Methods*. The PCA plot (Figure 1B) indicated that four datasets had no significant clustering after normalization and pairing.

In the training dataset, we evaluated and obtained 581 MRGPs related to overall survival (OS). Then, on the basis of these prognostic MRGPs, we performed Lasso Cox proportional hazard regression to construct a prognostic signature consisting of 21 MRGPs (Figures 1C, D). The 21 MRGPs signature was composed of 38 unique MRGs. The coefficient values of 13 MRGPs out of 21 MRGPs (62%) were  $> 0.05$  or  $< -0.05$ , indicating higher prognostic power (Table S4). We further assessed the robustness of the MRGPs signature, and its frequency was significantly higher than the frequency obtained by 1000 randomizations ( $P < 0.001$ , *Supplemental Results*). The optimum cut-off value for MRGPs risk stratification was identified to be -0.211 by using a 1-year time-dependent ROC curve analysis (area under the curve [AUC] = 0.801; Figure 1E).

### Validation of the MRGPs signature as an independent prognostic factor

Next, we conducted a comprehensive evaluation of the prognostic power of the MRGPs signature. The MRGP signature significantly stratified patients into high- and low-risk groups in terms of OS in the training and validation datasets (Figures 2A, B), their four original datasets [TCGA (Figure 2C), CGGA\_693 (Figure 2D), CGGA\_325 (Figure 2E), and CGGA\_301 (Figure 2F)], and an external independent validation dataset [GSE7696 (Figure S1)]. We also found that the survival of high-risk patients with upper quartile risk scores was worse than that of low-risk patients with lower quartiles in the training dataset ( $P < 0.001$ , Figure S2). Univariate Cox proportional hazards analysis demonstrated that the metabolic signature was a high-risk factor in the prognosis of patients (hazard ratio [HR] ranged from 5.921 [95% CI, 3.703-9.470;  $P < 0.001$ ] to 6.676 [95% CI, 4.526-9.849;  $P < 0.001$ ]; Table S5). After adjusting for clinical factors such as age, gender, and MGMTp methylation status, we further determined that the metabolic signature was an independent prognostic factor in multivariate analysis. The HR ranged from 5.714 [95% CI, 3.542-9.218;  $P < 0.001$ ] to 6.698 [95% CI, 4.478-10.018;  $P < 0.001$ ]; Table S5). Here, although the covariate of MGMTp methylation status in multivariate analysis was not statistically significant ( $P = 0.533$  [training];  $P = 0.681$  [validation]), the prognostic accuracy of the MRGPs signature in the validation dataset was improved for MGMTp nonmethylated patients (C-index = 0.801 [0.751] - [0.852]) compared with MGMTp methylated patients (C-index = 0.648 [0.564] - [0.733]; Figure S3). Furthermore, we also

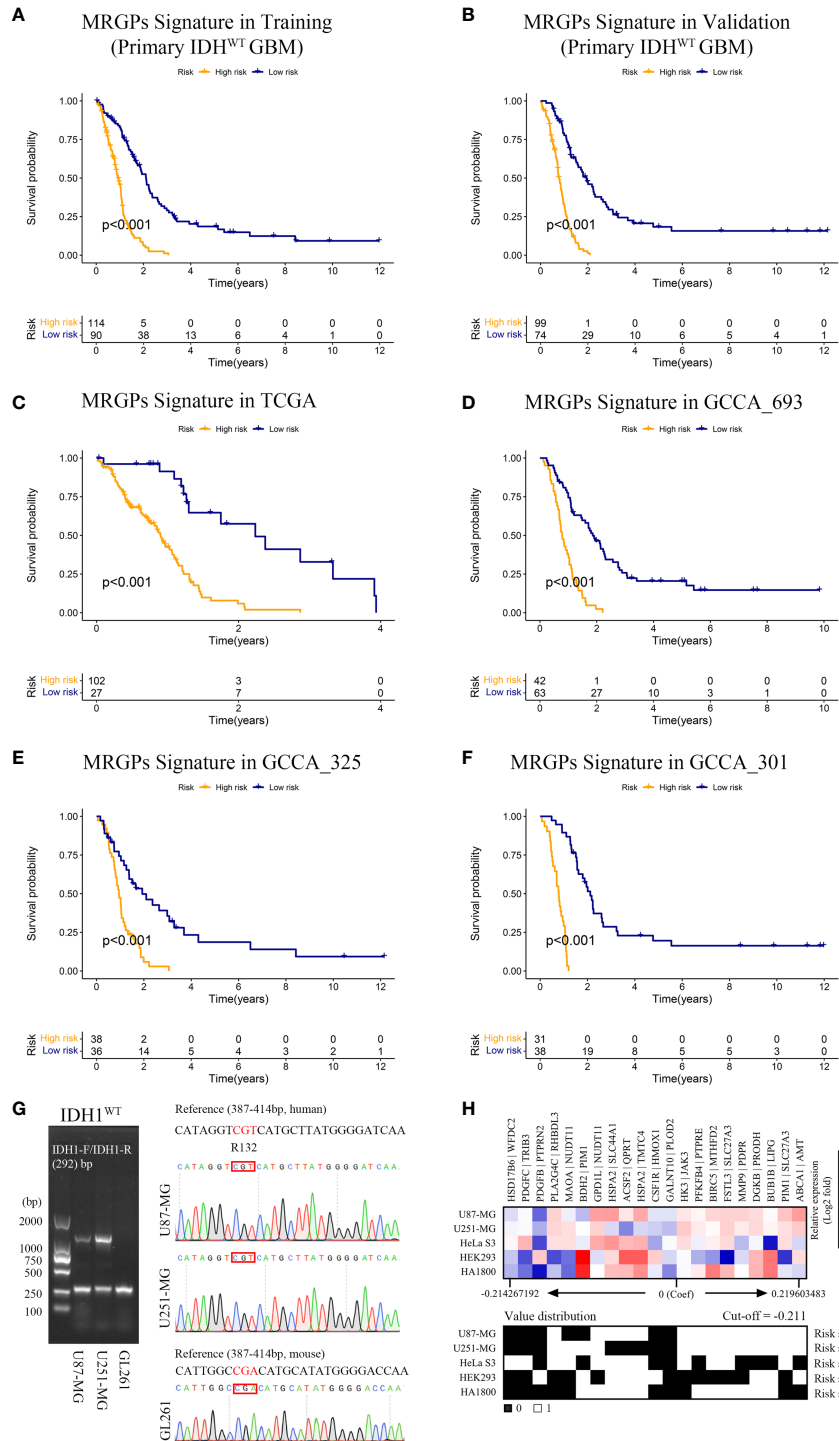


FIGURE 2

MRGPs Signature Stratifies the Overall Survival of IDH<sup>WT</sup> GBM With Different MRGP Risks. Kaplan-Meier curves of overall survival in IDH<sup>WT</sup> GBM patients in the MRGP risk groups. The overall survival of patients in the training (A) and validation (B) datasets was stratified by the MRGP risk score. The overall survival of IDH<sup>WT</sup> GBM in TCGA (C), CGCA\_693 (D), CGCA\_325 (E), and CGCA\_301 (F) datasets was stratified into high- and low-risk groups based on MRGP risk score ( $P$  values are all  $< 0.001$ , log-rank test). (G) Identification of IDH1 gene status in human GBM cells. No mutations were observed at the R132 site in the U87-MG and U251-MG cell lines. (H) Validation of the predictive efficacy of the MRGPI for human GBM cell lines. RT-PCR assays were performed to identify the expression levels of 38 MRGs relative to GAPDH in GBM cell lines and the control cell lines (HeLa S3, HEK293, and HA1800). The relative expression data between MRGs were used to calculate the risk level of cell lines *in vitro*. The cut-off value is equal to -0.211. GBM cell risk scores were all greater than the cut-off value (U87-MG = 0.284, U251-MG = 0.204), indicating high risk.

evaluated the survival stratification efficacy of the MRGPs signature in classical, mesenchymal, neural, and proneural GBM subtypes in the training and validation datasets (Figure S4). In addition to the neurotype subtype ( $P = 0.041$  [training];  $P = 0.865$  [validation]; C-index range from 0.500 to 0.650), our signature achieved significant survival stratification efficiency and accuracy for the other three subtypes ( $P \leq 0.032$  in training and validation datasets; C-index range from 0.699 to 0.793).

Furthermore, we compared our MRGP signature with one recently developed 9-gene  $IDH^{WT}$  GBM biomarker in continuous form, the C-index, in the training and validation datasets (Figure S5). Our signature achieved superior performance to that of the 9-gene signature on both the training and validation datasets (mean C-index 0.73 vs. 0.57).

Given that malignant tumor cells account for the main population of the sequenced tumor tissue samples and the high expression correlation between 38 unique MRGs composed of the MRGPs signature (Figure S6), we tried to mimic and validate the reliability and specificity of the prognostic model at the *in vitro* cell line level (Figures 2G, H). Compared with the control cell lines (HeLa S3, HEK293, and HA1800), our signature showed consistent risk prediction results in two  $IDH^{WT}$  GBM cell lines (risk score = 0.284 [U87-MG]; risk score = 0.204 [U251-MG]).

Finally, we evaluated the survival stratification efficacy of the signature on patients with postoperative chemotherapy (temozolomide) and/or radiotherapy regimens in the integrated meta dataset (Figure 3). The prognostic accuracy of the MRGPs signature for patients with radiotherapy and chemotherapy was superior to that of single treatment (C-index: 0.767 [chem + radio] vs. 0.738 [chem only] or 0.679 [radio only]). In summary, our MRGP signature could soundly predict the prognosis of patients with  $IDH^{WT}$  GBM.

## Functional annotation of the MRGPs signature

We conducted a GO annotation analysis on the 38 MRGs composed of the signature in DAVID (Table S6). Most biological processes were focused on phosphorylation (red underline) and lipid metabolic processes (blue underline). Interestingly, immune-related process macrophage differentiation was also enriched (green underline). Thus, we further performed GSEA on MRGPs risk groups in a meta dataset to explore potential biological differences (Figure 4A). We found that the top 20 GO biological process terms ( $P < 0.05$ ) included not only phosphorylation but also various immune-related processes, such as humoral immune response and phagocytosis processes, which was enriched in the high-risk group.

## Differentiation of immune infiltrating subgroups between different risk groups based on the MRGPs signature

Given that our metabolic signature was closely related to multiple immune processes, we tried to further discover the association between risk groups or the corresponding 38 MRGs and patient immune status. No significant difference in tumor purity between risk groups was observed (Figures 4B, C). There was only a low negative correlation between the expression levels of the 6 MRGs and tumor purity in high-risk patients (Figure 4D). We found a significant difference in the percentage of necrosis between the risk groups in the bottom sections of the TCGA dataset (Figure S7). The average level of necrosis in the high-risk group was ~2-fold that of the low-risk group (9.9% vs. 5.5%,  $P < 0.05$ ), suggesting a change in immune status.

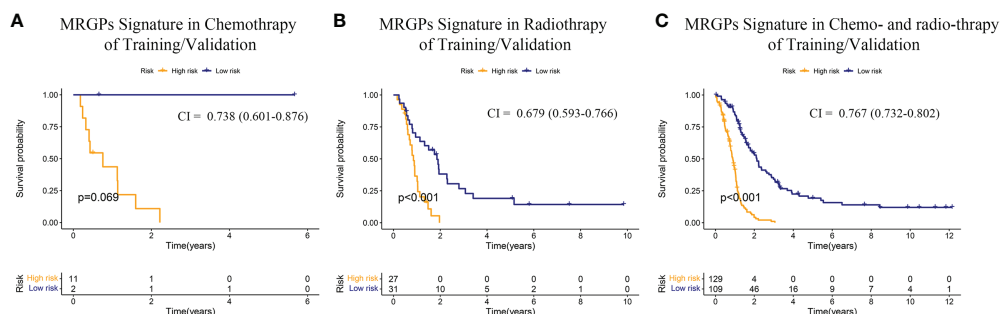


FIGURE 3

Kaplan-Meier Overall Survival Curve Analysis of the Responses of  $IDH^{WT}$  GBM With Different MRGP Risks to Chemotherapy/Radiotherapy. Patients from the training and validation datasets were integrated into a meta-dataset. Patients receiving chemotherapy only (A), radiotherapy only (B), and radiotherapy combined with chemotherapy (C) were further divided into high- and low-risk groups based on the MRGP score. Kaplan-Meier overall survival curves were generated to show the risk stratification of the prognostic model. CI indicates the C-index, which was used to evaluate the accuracy of the prognostic model. The performance of the MRGP model in the combination therapy group (CI = 0.767,  $P < 0.001$ ) was superior to that in the single therapy groups (Chem, CI = 0.738,  $P = 0.069$ ; Radio, CI = 0.679,  $P < 0.001$ ).

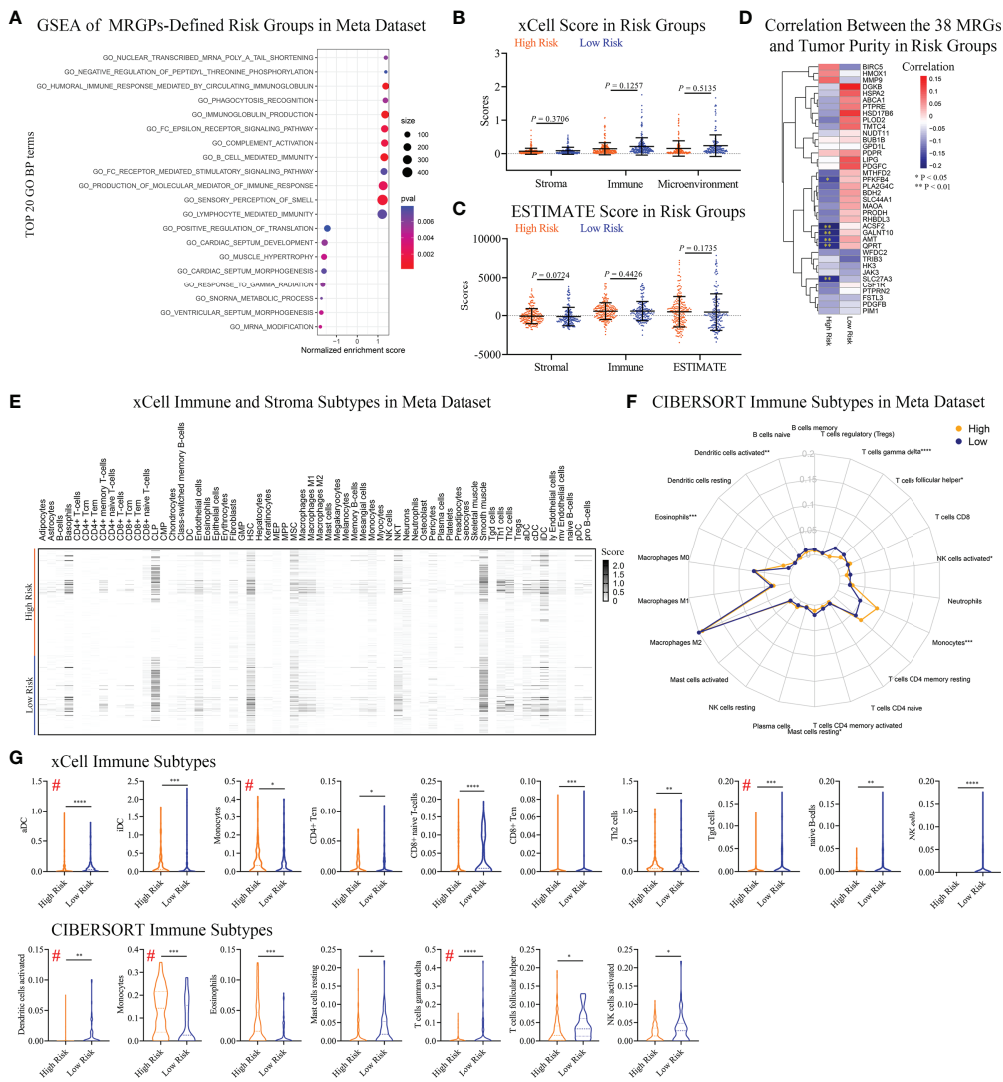


FIGURE 4

Differences in Immune Infiltration Profiles Between Risk Groups Defined by Metabolic Signature. (A) GSEA of MRGP risk groups in the meta dataset ( $P < 0.05$ ). The top 20 GO biological processes are shown. Multiple GO biological processes related to immunology, including immunoglobulin-mediated responses, were enriched in high-risk patients. (B, C) xCELL (B) and ESTIMATE (C) analyses of tumor purity between MRGP risk groups in the meta dataset. No significant differences between risk groups were observed (Mann-Whitney test). (D) Pearson correlation heatmaps of the expression of 38 MRGs and tumor purity in the risk groups of the meta-dataset. Value  $> 0$  indicates that gene expression is positively correlated with tumor purity, indicating less immune infiltration. \* $P < 0.05$ ; \*\* $P < 0.01$ . (E) xCell heatmap of the abundance of 64 immune and stroma cells in IDH<sup>WT</sup> GBM patients within risk groups in the meta dataset. (F) CIBERSORT analysis of the abundance of 22 immune cells in IDH<sup>WT</sup> GBM patients within risk groups in the meta dataset. (G) Immune cell subtypes significantly different between risk groups. Data is related to (E, F). # indicates the same immune subtype in xCell and CIBERSORT analyses. The difference between risk groups was calculated by the Mann-Whitney test (\* $P < 0.05$ , \*\* $P < 0.01$ , \*\*\* $P < 0.001$ , \*\*\*\* $P < 0.0001$ ).

To reveal immune status between risk groups defined by MRGPs, we performed xCELL and CIBERSORT subtypes analyses. The results indicated that the MRGPs signature can profile the abundance of immune cell infiltration in patients with different risks (Figures 4E, F) and showed that MRGP-defined high-risk patients had more monocytes and less activated DC and T cell gamma delta ( $\gamma\delta$  T cell)

infiltration in the TME (Figure 4G). For example, in CIBERSORT analysis (Figure 4G lower panel), high-risk patients had higher monocyte abundance than low-risk patients (14.4% vs. 7.5% immune cells,  $P < 0.001$ ). Studies have shown that the cell density of glioma-infiltrating microglia/macrophages (GAMs) is related to the degree of malignancy of gliomas and gradually increases with

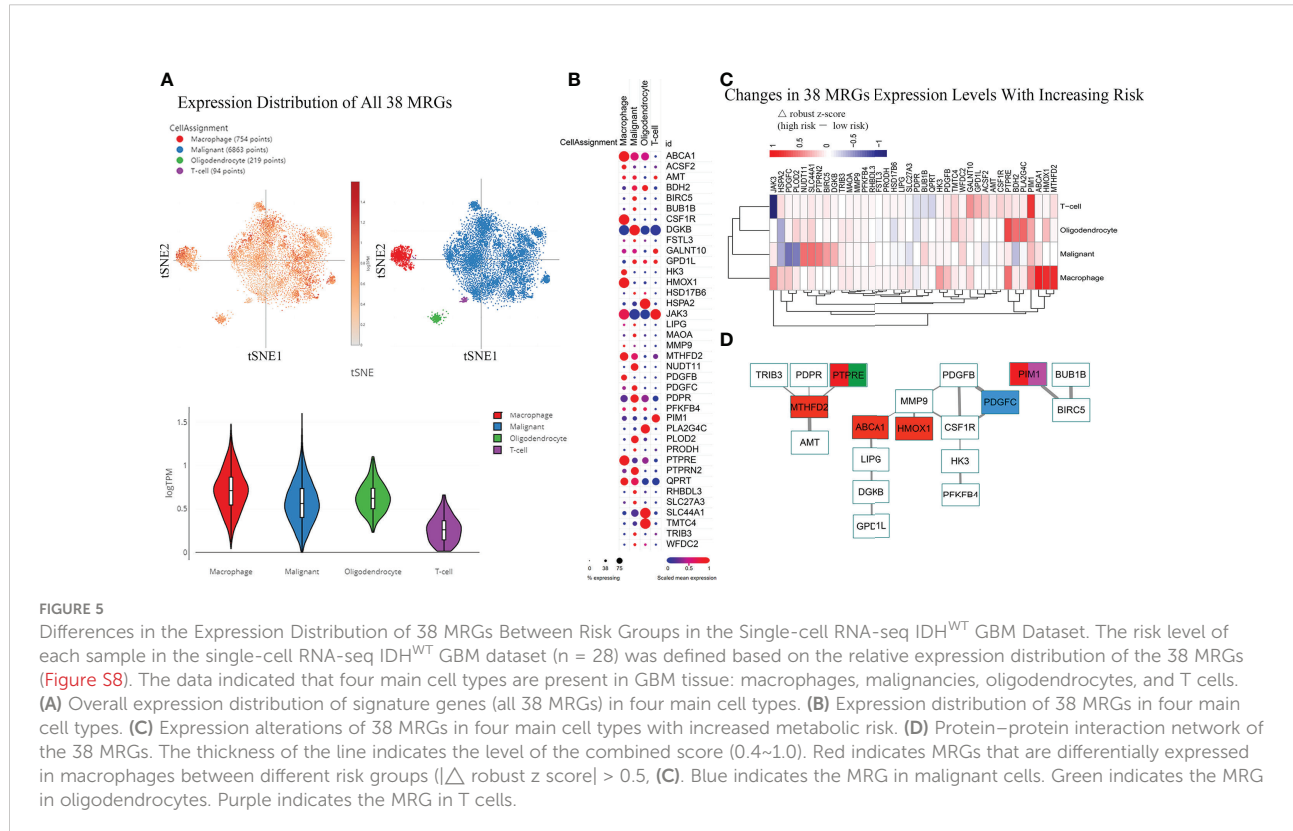
progression (26, 27). Interestingly, our study indicated that although the macrophage family dominated the population of infiltrating immune cells, there was no difference in abundance between the two groups (Figures 4E–G).

To reveal the association of MRGPs signature with immune subtypes, we performed Pearson correlation analysis on 38 MRGs and 22 immune cells (Figure S8). The heatmap indicated that the expression level of MRGs had a significant correlation with the abundance of immune cells. We found that the MRGPs signature can also characterize the molecular profile of immune cells with no significant differences in abundance in different risk groups. For example, in low-risk patients, M2 macrophage (31.4% vs. 31.7%) abundance was positively correlated with the expression levels of PLA2G4C, GALNT10, BDH2, AMT, SLC44A1, HSPA2, and FSTL3 (coefficient  $> 0.3$ ), while in the high-risk group, there was no obvious correlation.

## Expression distribution of the 38 MRGs in the single-cell RNA-seq dataset

Above, we determined the association between infiltrating immune cells and the molecular profile of the MRGPs signature

in different risk groups. However, their expression distribution in tumor tissues is not yet clear. Thus, we tried to retrieve the expression distribution of 38 MRGs in the IDH<sup>WT</sup> GBM single-cell sequencing dataset and to calculate the risk score for each sample according to the risk cut-off (Figure S9). Twenty samples (71.4%) were defined as high risk. Four main cell populations in tumor bulks were identified, including macrophages, malignant cells, oligodendrocytes, and T cells. The main population of tumor-infiltrating immune cells shown in scRNA-seq data was consistent with our immune subtype analysis, in which the main populations of immune infiltrating cells in patients with IDH<sup>WT</sup> GBM were monocytes/macrophages and T-cell families (Figure 4F). More expression distribution for all 38 MRGs was identified in macrophages, malignant cells, and oligodendrocytes and less in T cells (Figure 5A). The distribution of each MRG is shown in Figure 5B. Furthermore, according to the risk grouping, the expression changes of 38 MRGs were identified (Figure 5C). In macrophages, 5 MRGs (ABCA1, HMOX1, MTHFD2, PIM1, and PTPRE) were identified as having significant expression differences between the risk groups. The 4 MRGs (NUDT11, PDGFC, PLOD2, and SLC44A1) in malignant cells. The 3 MRGs (BDH2, PLA2G4C, and PTPRE) in oligodendrocytes. The 2 MRGs (JAK3 and PIM1) in T cells.



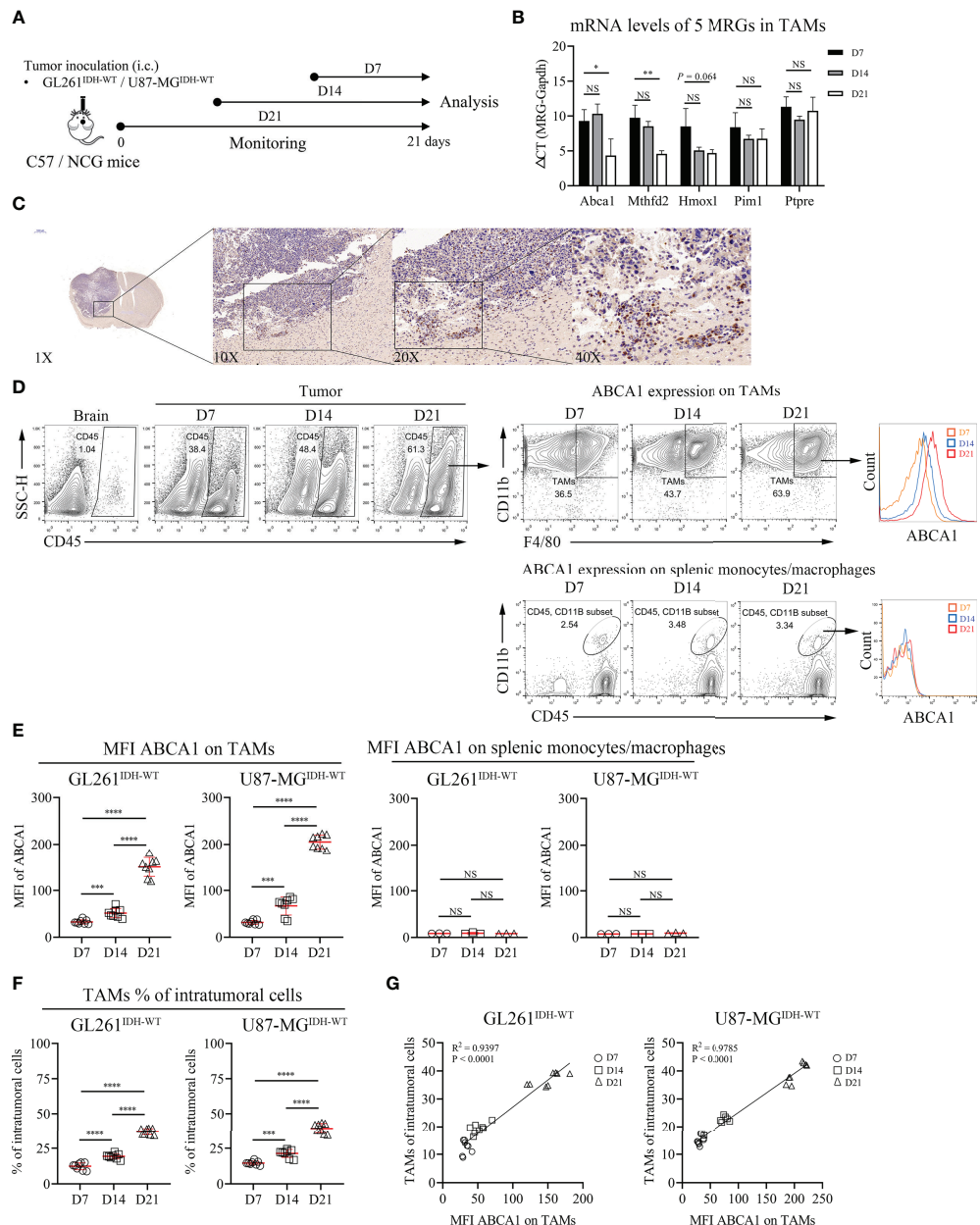


FIGURE 6

The Expression Level of ABCA1 in TAMs Positively Correlated with the Population of TAMs with IDH<sup>WT</sup> GBM Tumor Progression. (A) Experimental setup to study the links between MRGs expression in macrophage and tumor progression. (B) Quantitative analysis of mRNA expression levels of 5 MRGs in TAMs with tumor progression. C57 mice were intracranially inoculated with GL261 cells. On day 7, day 14 and day 21, mice were sacrificed and collected tumor tissues. TAMs were isolated from tumors by anti-F4/80 microbeads and subjected to qPCR to detect mRNA expression (n = 3). (C) Immunohistochemical analysis of the expression levels of ABCA1 in mouse tumor and normal brain tissue. (D, E) Representative flow cytometry plots (D) and quantitative analysis (E) of TAMs and peripherally splenic monocytes/macrophage ABCA1 expression levels with tumor progression. Orthotopic tumors were collected on days 7, 14 and 21 after tumor inoculation. n = 8. f-g: Quantitative analysis of TAM populations (F) and pearson correlation analysis of TAM populations and TAM ABCA1 expression levels (G). Data is related to (D, E). The difference between risk groups was calculated by the Mann-Whitney test (NS, no statistical significance, \*P < 0.05, \*\*P < 0.01, \*\*\*P < 0.001, \*\*\*\*P < 0.0001).

The PPI network of the 38 MRGs demonstrated that 19 MRGs constituted 3 potential interactive modules (Figure 5D). The 19 MRGs included 5 differentially expressed MRGs from macrophages (red color), 1 MRG from malignant cells (blue color), 1 MRG from

oligodendrocytes (green color), and 1 MRGs from T cells (purple color). The in-silico study suggests that MRGPs-based survival risk stratification is closely related to changes in the abundance and/or molecular features of the monocyte/macrophage family.

## Biological validation of the correlation between tumor-associated macrophage ABCA1 expression and IDH<sup>WT</sup> GBM progression

There is abundant clinical and experimental evidence that strongly links increased numbers of TAMs with poor prognosis (28). However, metabolism in TAMs and GBM tumorigenesis or prognosis remain poorly understood. Thus, we performed further biological validation to determine whether the 5 MRGs identified in TAMs were associated with the development of IDH<sup>WT</sup> GBMs (Figure 6A). We found that the mRNA expression levels of ABCA1 and MTHFD2 genes in TAMs increased significantly with tumor progression (Figure 6B). Given that ABCA1 is among the gene pairs with the highest risk factor compared to MTHFD2 (Table S4; MRGP-01 = 0.2196 vs. MRGP-07 = 0.0248), we further explored the potential biological associations between ABCA1 and TAMs. In IHC of brain tissue from GL261 tumor-bearing mice, we identified that the expression level of ABCA1 in tumor tissue was higher than that in normal brain tissue (Figure 6C). Furthermore, in the distribution analysis of ABCA1 expression on tumor cells and tumor-infiltrating immune cells, we found that the expression level of ABCA1 in TAMs was significantly higher than that in TILs and monocytes (Figure S10). And in two IDH<sup>WT</sup> GBM models, we found that both the expression level of ABCA1 on TAMs and the intratumoral population of TAMs increased with tumors progression (Figures 6D–F) and showed a high positive correlation between them (Figure 6G). These results demonstrate that the expression level of ABCA1 on TAMs was a risk factor for IDH<sup>WT</sup> GBMs.

Annotation analysis of MRGs indicated that ABCA1 was related to lipid metabolism- related processes (Table S6). ABCA1 uses cholesterol as its substrate to mediate cholesterol efflux in the cellular lipid removal pathway (29). Thus, we further investigated whether modulating cellular cholesterol levels significantly alters ABCA1 expression in macrophages and whether reducing ABCA1 expression levels in TAMs affects tumor progression. *In vitro* cholesterol loading assay showed that modulating cholesterol levels in macrophages can significantly affect their ABCA1 levels (Figure 7A). Lovastatin treatment *in vitro* and *in vivo* reduced ABCA1 levels in TAMs (Figures 7B, D–F) and shifted TAMs functional specialization from an inhibitory to a pro-inflammatory phenotype (Figures 7C, G–J). Finally, to determine whether ABCA1 can be an effective target for the treatment of IDH<sup>WT</sup> GBMs, we performed a lovastatin treatment experiment in the orthotopic GL261<sup>IDH1-WT-Luc</sup> model and showed that this modulation of immune metabolism can significantly control tumor progression (Figures 7K–M). These results confirm the reliability of our constructed metabolic signature and indicate a crucial role for

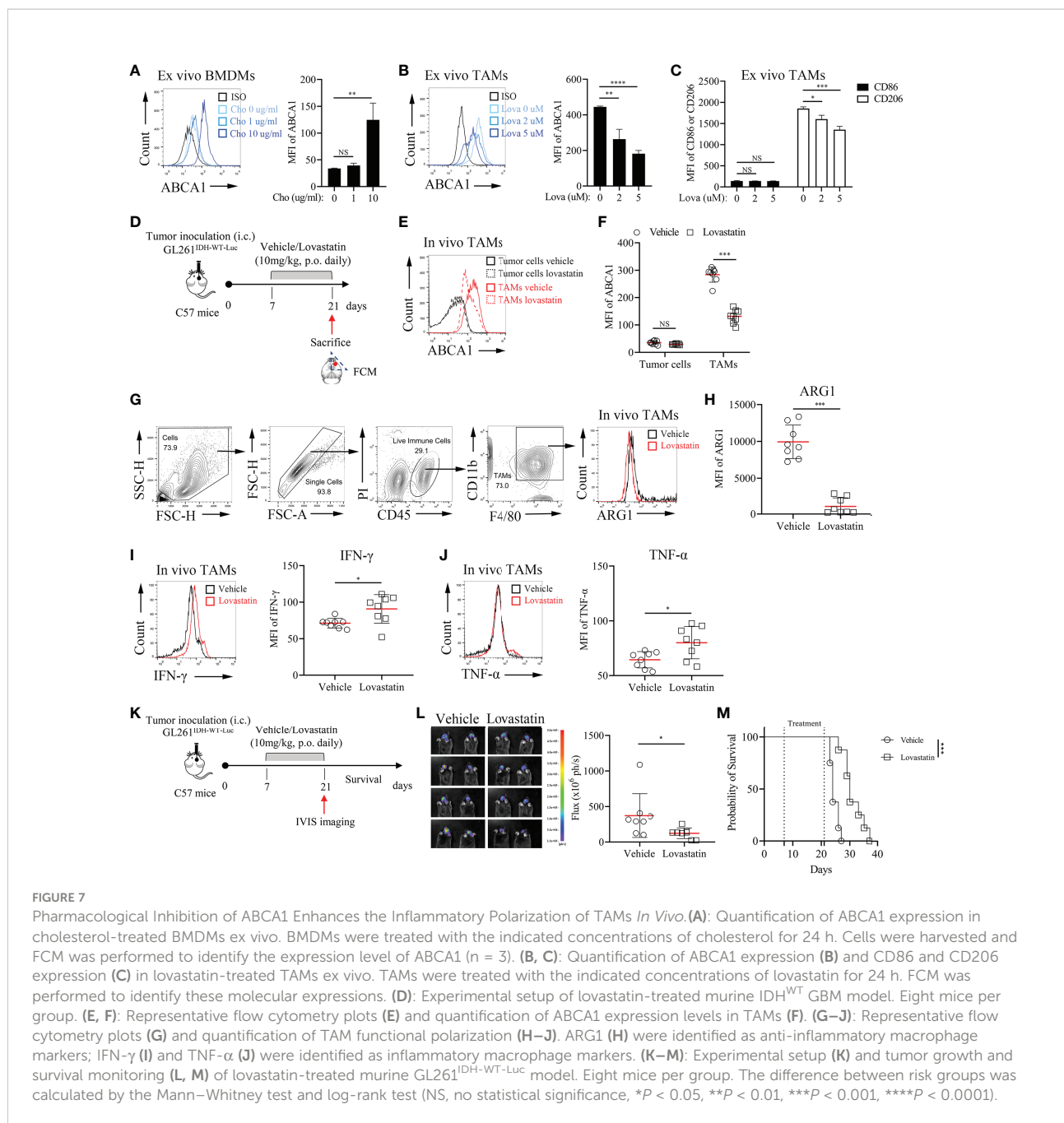
macrophage lipid-related metabolism in maintaining malignant progression.

## Discussion

Patients with IDH<sup>WT</sup> GBM are at high risk of recurrence, even with postoperative chemoradiotherapy. Intratumoral heterogeneity allows patients to respond differently to the same intervention (24, 30). Therefore, reliable prognostic biomarkers are urgently needed to identify patients who may benefit from additional therapy and who may be at risk of recurrence. Significant research on prognostic molecular signatures has led to breakthroughs in the estimation of survival in GBM patients (4, 31–34), but their accuracy in the IDH<sup>WT</sup> subgroup remains limited. In this study, we developed an individualized prognostic signature of primary IDH<sup>WT</sup> GBM based on 21 MRGPs, and validated its prognostic value in multiple independent datasets. Our metabolic signature can further stratify patients into distinct survival risk subgroups, when considering other clinical variables (e.g., clinical care, MGMTp methylation status, and expression subtypes). In the combination index comparison, our metabolic signature exhibited superior accuracy compared with another 9-gene IDH<sup>WT</sup> GBM signature (31).

To identify reliable prognostic biomarkers for IDH<sup>WT</sup> GBMs, we integrated gene expression profiles from four datasets and employed a relative ranking method that is based on gene expression levels and specifically designed to robustly eliminate technical and sampling biases (9, 35). As such, our metabolic signature can individually assess the prognosis of IDH<sup>WT</sup> GBM and may be easily translated into the clinic.

Discovery of novel biomarkers associated with metabolic reprogramming in GBM tumors might have important implications for identifying potential molecular targets and developing precision medicine (36–38). He et al. discovered that glycolysis, gluconeogenesis and oxidative phosphorylation processes differ significantly among GBM patients with different prognoses (15). Patients with wild-type or mutant IDH GBMs have distinct clinical features and survival differences. Under hypoxic conditions, the IDH gene is highly activated and mediates reductive glutamine to lipogenesis to maintain cell proliferation under hypoxia (39, 40). Because the gene expression profiles used in the study were derived from IDH<sup>WT</sup> GBM tumor tissue samples, we did not observe significant differences in glucose metabolism in the risk groups defined by MRGPs. Similarly, most genes contained in the metabolic signature were related to redox, phosphorylation, and lipid metabolism. Increasing evidence indicates that metabolic rewiring in the tumor microenvironment may be responsible for changes in immune cell fate and function (41–44). Sören et al. (45) discovered that blood-derived TAMs but



not microglia show altered metabolism and preferentially express immunosuppressive cytokines, which are associated with significantly poorer prognosis in glioma patients. In the present study, our signature also identified significant immune-related processes, such as phagocytosis regulation. Consistently, the abundance of monocytes in tumor tissue and the expression of some MRGs changed significantly with increasing risk levels. In the analysis of IDH<sup>WT</sup> GBM single-cell RNA-seq data, we further determined that macrophage-related MRGs have closer molecular interactions with other MRGs than other cells, and

identified 5 MRGs (ABCA1, MTHFD2, HMOX1, PIM1, and PTPRE) that were significantly changed in TAMs upon switching from low to high risk. Therefore, our study also provides a molecular profile integrating diverse biological processes to characterize the possible prognostic status of IDH<sup>WT</sup> GBM patients.

The heterogeneity of TAMs has long been recognized as plasticity in response to different tumor microenvironments (46); however, the underlying mechanisms remain unclear. A recent study suggested that lipid accumulation and metabolism

are required for TAM differentiation and activation (47). Our study identified that as tumors progressed, the expression of ABCA1 in TAMs was significantly increased, indicating that cholesterol metabolism plays a vital role in the functional polarization of TAMs. This finding is consistent with that of Goossens et al, who showed that ovarian cancer cells promote membrane cholesterol efflux in TAMs by upregulating ABCA1/G1 expression (48). Our and other studies have shown that cholesterol deletion can repolarize TAMs, promoting M2-to-M1 phenotypic conversion by downregulating ABCA1 expression (49). These results further confirm the reliability of our metabolic signature and may provide potential targets for IDH<sup>WT</sup> GBM therapy.

Notably, although our findings indicate that the expression level of ABCA1 on TAMs can serve as a robust biomarker to assess the prognostic outcomes of GBMs, this study does have some limitations. In addition to ABCA1, other MRGs whose expression in TAMs increases significantly with increasing risk, alone or in combination, may also be more important in IDH<sup>WT</sup> GBM development and progression. However, it is very challenging to characterize the protein expression levels of all prognostic MRGs in TAMs and to determine the weight of each MRG in prognostic stratification. Therefore, in this study, we selected only the highest-risk MRG ABCA1 for a biological proof-of-concept.

In summary, our MRGPs signature is a promising prognostic biomarker for individualized management of primary IDH<sup>WT</sup> GBMs. Diverse biological processes involving metabolism and immunity in this study were integrated to outline a more complete molecular profile of the tumor.

## Data availability statement

The datasets presented in this study can be found in online repositories. The names of the repository/repositories and accession number(s) can be found in the article/[Supplementary Material](#). The original data supporting the conclusions of this paper will be provided by the authors without undue retention.

## Ethics statement

The animal study was reviewed and approved by the Institutional Review Board of Nanjing University.

## References

1. Louis DN, Perry A, Reifenberger G, von Deimling A, Figarella-Branger D, Cavenee WK, et al. The 2016 world health organization classification of tumors of the central nervous system: A summary. *Acta Neuropathol* (2016) 131(6):803–20. doi: 10.1007/s00401-016-1545-1

## Author contributions

All authors conceived and designed the study. SW, LL, and SZ contributed to collecting and analyzing the data. SW and LK performed the biological experiments. All authors participated in the writing of the manuscript. JW and JD conducted the critical revision of the manuscript. JW and JD provided financial support. All authors contributed to the article and approved the submitted version.

## Funding

This study was supported by the National Natural Science Foundation of China (82273261, 81773255 and 81472820).

## Acknowledgments

The authors thank all lab members and collaborators, especially Dr. Gang Meng, who contributed to this study. We also apologize to other researchers who contributed to this field but whose studies we did not discuss or cite due to limited space.

## Conflict of interest

The authors declare that the research was conducted in the absence of any commercial or financial relationships that could be construed as a potential conflict of interest.

## Publisher's note

All claims expressed in this article are solely those of the authors and do not necessarily represent those of their affiliated organizations, or those of the publisher, the editors and the reviewers. Any product that may be evaluated in this article, or claim that may be made by its manufacturer, is not guaranteed or endorsed by the publisher.

## Supplementary material

The Supplementary Material for this article can be found online at: <https://www.frontiersin.org/articles/10.3389/fimmu.2022.869061/full#supplementary-material>

2. Reifenberger G, Wirsching HG, Knobbe-Thomsen CB, Weller M. Advances in the molecular genetics of gliomas - implications for classification and therapy. *Nat Rev Clin Oncol* (2017) 14(7):434–52. doi: 10.1038/nrclinonc.2016.204

3. Stupp R, Mason WP, van den Bent MJ, Weller M, Fisher B, Taphoorn MJ, et al. Radiotherapy plus concomitant and adjuvant temozolomide for glioblastoma. *N Engl J Med* (2005) 352(10):987–96. doi: 10.1056/NEJMoa043330

4. Simon M, Hosen I, Gousias K, Rachakonda S, Heidenreich B, Gessi M, et al. TERT promoter mutations: A novel independent prognostic factor in primary glioblastomas. *Neuro Oncol* (2015) 17(1):45–52. doi: 10.1093/neuonc/nou158

5. Cheng Q, Huang C, Cao H, Lin J, Gong X, Li J, et al. A novel prognostic signature of transcription factors for the prediction in patients with GBM. *Front Genet* (2019) 10:906. doi: 10.3389/fgene.2019.00906

6. Wang Z, Gao L, Guo X, Feng C, Lian W, Deng K, et al. Development and validation of a nomogram with an autophagy-related gene signature for predicting survival in patients with glioblastoma. *Aging (Albany NY)* (2019) 11(24):12246–69. doi: 10.1863/aging.102566

7. Santangelo A, Rossato M, Lombardi G, Benfatto S, Lavezzari D, De Salvo GL, et al. A molecular signature associated with prolonged survival in glioblastoma patients treated with regorafenib. *Neuro Oncol* (2021) 23(2):264–76. doi: 10.1093/neuonc/noaa156

8. Leek JT, Sharpf RB, Bravo HC, Simcha D, Langmead B, Johnson WE, et al. Tackling the widespread and critical impact of batch effects in high-throughput data. *Nat Rev Genet* (2010) 11(10):733–9. doi: 10.1038/nrg2825

9. Heinaniemi M, Nykter M, Kramer R, Wienecke-Baldaccino A, Sinkkonen L, Zhou JX, et al. Gene-pair expression signatures reveal lineage control. *Nat Methods* (2013) 10(6):577–83. doi: 10.1038/nmeth.2445

10. Li B, Cui Y, Diehn M, Li R. Development and validation of an individualized immune prognostic signature in early-stage nonsquamous non-small cell lung cancer. *JAMA Oncol* (2017) 3(11):1529–37. doi: 10.1001/jamaoncol.2017.1609

11. Bi J, Chowdhry S, Wu S, Zhang W, Masui K, Mischel PS. Altered cellular metabolism in gliomas - an emerging landscape of actionable co-dependency targets. *Nat Rev Cancer* (2020) 20(1):57–70. doi: 10.1038/s41568-019-0226-5

12. Beiko J, Suki D, Hess KR, Fox BD, Cheung V, Cabral M, et al. IDH1 mutant malignant astrocytomas are more amenable to surgical resection and have a survival benefit associated with maximal surgical resection. *Neuro Oncol* (2014) 16(1):81–91. doi: 10.1093/neuonc/not159

13. Hegi ME, Diserens AC, Gorlia T, Hamou MF, de Tribolet N, Weller M, et al. MGMT gene silencing and benefit from temozolomide in glioblastoma. *N Engl J Med* (2005) 352(10):997–1003. doi: 10.1056/NEJMoa043331

14. Cominelli M, Grisanti S, Mazzoleni S, Branca C, Buttolo L, Furlan D, et al. EGFR amplified and overexpressing glioblastomas and association with better response to adjuvant metronomic temozolomide. *J Natl Cancer Inst* (2015) 107(5):1–13. doi: 10.1093/jnci/djv041

15. He Z, Wang C, Xue H, Zhao R, Li G. Identification of a metabolism-related risk signature associated with clinical prognosis in glioblastoma using integrated bioinformatic analysis. *Front Oncol* (2020) 10:1631. doi: 10.3389/fonc.2020.01631

16. Hu X, Martinez-Ledesma E, Zheng S, Kim H, Barthel F, Jiang T, et al. Multigene signature for predicting prognosis of patients with 1p19q co-deletion glioma. *Neuro Oncol* (2017) 19(6):786–95. doi: 10.1093/neuonc/now285

17. Zhao Z, Zhang KN, Wang Q, Li G, Zeng F, Zhang Y, et al. Chinese Glioma genome atlas (CGGA): A comprehensive resource with functional genomic data from Chinese glioma patients. *Genomics Proteomics Bioinf* (2021) 19(1):1–12. doi: 10.1016/j.gpb.2020.10.005

18. Wang Y, Qian T, You G, Peng X, Chen C, You Y, et al. Localizing seizure-susceptible brain regions associated with low-grade gliomas using voxel-based lesion-symptom mapping. *Neuro Oncol* (2015) 17(2):282–8. doi: 10.1093/neuonc/nou130

19. Freije WA, Castro-Vargas FE, Fang Z, Horvath S, Cloughesy T, Liau LM, et al. Gene expression profiling of gliomas strongly predicts survival. *Cancer Res* (2004) 64(18):6503–10. doi: 10.1158/0008-5472.CAN-04-0452

20. Kawaguchi A, Yajima N, Tsuchiya N, Homma J, Sano M, Natsumeda M, et al. Gene expression signature-based prognostic risk score in patients with glioblastoma. *Cancer Sci* (2013) 104(9):1205–10. doi: 10.1111/cas.12214

21. McIntyre A, Harris AL. Metabolic and hypoxic adaptation to anti-angiogenic therapy: A target for induced essentiality. *EMBO Mol Med* (2015) 7(4):368–79. doi: 10.15252/emmm.201404271

22. Simon N, Friedman J, Hastie T, Tibshirani R. Regularization paths for cox's proportional hazards model via coordinate descent. *J Stat Softw* (2011) 39(5):1–13. doi: 10.18637/jss.v039.i05

23. Zhang C, Cheng W, Ren X, Wang Z, Liu X, Li G, et al. Tumor purity as an underlying key factor in glioma. *Clin Cancer Res an Off J Am Assoc Cancer Res* (2017) 23(20):6279–91. doi: 10.1158/1078-0432.CCR-16-2598

24. Neftel C, Laffy J, Filbin MG, Hara T, Shore ME, Rahme GJ, et al. An integrative model of cellular states, plasticity, and genetics for glioblastoma. *Cell* (2019) 178(4):835–49.e21. doi: 10.1016/j.cell.2019.06.024

25. Kober C, Weibel S, Rohn S, Kirscher L, Szalay AA. Intratumoral INF- $\gamma$  triggers an antiviral state in GL261 tumor cells: A major hurdle to overcome for oncolytic vaccinia virus therapy of cancer. *Mol Ther oncolysis* (2015) 2:15009. doi: 10.1038/mto.2015.9

26. Hussain SF, Yang D, Suki D, Aldape K, Grimm E, Heimberger AB. The role of human glioma-infiltrating microglia/macrophages in mediating antitumor immune responses. *Neuro Oncol* (2006) 8(3):261–79. doi: 10.1215/15228517-2006-008

27. Yi L, Xiao H, Xu M, Ye X, Hu J, Li F, et al. Glioma-initiating cells: A predominant role in microglia/macrophages tropism to glioma. *J Neuroimmunol* (2011) 232(1–2):75–82. doi: 10.1016/j.jneuroim.2010.10.011

28. Komohara Y, Fujiwara Y, Ohnishi K, Takeya M. Tumor-associated macrophages: Potential therapeutic targets for anti-cancer therapy. *Adv Drug Delivery Rev* (2016) 99(Pt B):180–5. doi: 10.1016/j.addr.2015.11.009

29. Vaidya M, Jentsch JA, Peters S, Keul P, Weske S, Gräler MH, et al. Regulation of ABCA1-mediated cholesterol efflux by sphingosine-1-phosphate signaling in macrophages. *J Lipid Res* (2019) 60(3):506–15. doi: 10.1194/jlr.M088443

30. Patel AP, Tirosh I, Trombetta JJ, Shalek AK, Gillespie SM, Wakimoto H, et al. Single-cell RNA-seq highlights intratumoral heterogeneity in primary glioblastoma. *Science* (2014) 344(6190):1396–401. doi: 10.1126/science.1254257

31. Johnson RM, Phillips HS, Bais C, Brennan CW, Cloughesy TF, Daemen A, et al. Development of a gene expression-based prognostic signature for IDH wild-type glioblastoma. *Neuro Oncol* (2020) 22(12):1742–56. doi: 10.1093/neuonc/noaa157

32. Jovčevska I, Zottel A, Šamec N, Mlakar J, Sorokin M, Nikitin D, et al. High FREM2 gene and protein expression are associated with favorable prognosis of IDH-WT glioblastomas. *Cancers (Basel)* (2019) 11(8):1–18. doi: 10.3390/cancers11081060

33. Liu H, Sun Y, Zhang Q, Jin W, Gordon RE, Zhang Y, et al. Pro-inflammatory and proliferative microglia drive progression of glioblastoma. *Cell Rep* (2021) 36(11):109718. doi: 10.1016/j.celrep.2021.109718

34. Arita H, Yamasaki K, Matsushita Y, Nakamura T, Shimokawa A, Takami H, et al. A combination of TERT promoter mutation and MGMT methylation status predicts clinically relevant subgroups of newly diagnosed glioblastomas. *Acta Neuropathol Commun* (2016) 4(1):79. doi: 10.1186/s40478-016-0351-2

35. Tan AC, Naiman DQ, Xu L, Winslow RL, Geman D. Simple decision rules for classifying human cancers from gene expression profiles. *Bioinformatics* (2005) 21(20):3896–904. doi: 10.1093/bioinformatics/bti631

36. Prabhu AH, Kant S, Kesarwani P, Ahmed K, Forsyth P, Nakano I, et al. Integrative cross-platform analyses identify enhanced heterotropy as a metabolic hallmark in glioblastoma. *Neuro Oncol* (2019) 21(3):337–47. doi: 10.1093/neuonc/noy185

37. Kesarwani P, Prabhu A, Kant S, Chinnaiyan P. Metabolic remodeling contributes towards an immune-suppressive phenotype in glioblastoma. *Cancer Immunol Immunother* (2019) 68(7):1107–20. doi: 10.1007/s00262-019-02347-3

38. Aldape K, Zadeh G, Mansouri S, Reifenberger G, von Deimling A. Glioblastoma: pathology, molecular mechanisms and markers. *Acta Neuropathol* (2015) 129(6):829–48. doi: 10.1007/s00401-015-1432-1

39. Metallo CM, Gameiro PA, Bell EL, Mattaini KR, Yang J, Hiller K, et al. Reductive glutamine metabolism by IDH1 mediates lipogenesis under hypoxia. *Nature* (2011) 481(7381):380–4. doi: 10.1038/nature10602

40. Wise DR, Ward PS, Shay JE, Cross JR, Gruber JJ, Sachdeva UM, et al. Hypoxia promotes isocitrate dehydrogenase-dependent carboxylation of alpha-ketoglutarate to citrate to support cell growth and viability. *Proc Natl Acad Sci United States America* (2011) 108(49):19611–6. doi: 10.1073/pnas.111773108

41. Ma X, Bi E, Lu Y, Su P, Huang C, Liu L, et al. Cholesterol induces CD8(+) T cell exhaustion in the tumor microenvironment. *Cell Metab* (2019) 30(1):143–55.e5. doi: 10.1016/j.cmet.2019.04.002

42. Colegio OR, Chu NQ, Szabo AL, Chu T, Rhebergen AM, Jairam V, et al. Functional polarization of tumour-associated macrophages by tumour-derived lactic acid. *Nature* (2014) 513(7519):559–63. doi: 10.1038/nature13490

43. Vitale I, Manic G, Coussens LM, Kroemer G, Galluzzi L. Macrophages and metabolism in the tumor microenvironment. *Cell Metab* (2019) 30(1):36–50. doi: 10.1016/j.cmet.2019.06.001

44. Lim SA, Wei J, Nguyen TM, Shi H, Su W, Palacios G, et al. Lipid signalling enforces functional specialization of treg cells in tumours. *Nature* (2021) 591(7849):306–11. doi: 10.1038/s41586-021-03235-6

45. Muller S, Kohanbash G, Liu SJ, Alvarado B, Carrera D, Bhaduri A, et al. Single-cell profiling of human gliomas reveals macrophage ontogeny as a basis for regional differences in macrophage activation in the tumor microenvironment. *Genome Biol* (2017) 18(1):234. doi: 10.1186/s13059-017-1362-4

46. Gordon S, Plüddemann A, Martinez Estrada F. Macrophage heterogeneity in tissues: Phenotypic diversity and functions. *Immunol Rev* (2014) 262(1):36–55. doi: 10.1111/imr.12223

47. Su P, Wang Q, Bi E, Ma X, Liu L, Yang M, et al. Enhanced lipid accumulation and metabolism are required for the differentiation and activation of tumor-associated macrophages. *Cancer Res* (2020) 80(7):1438–50. doi: 10.1158/0008-5472.CAN-19-2994

48. Goossens P, Rodriguez-Vita J, Etzerodt A, Masse M, Rastoin O, Gouirand V, et al. Membrane cholesterol efflux drives tumor-associated macrophage reprogramming and tumor progression. *Cell Metab* (2019) 29(6):1376–89.e4. doi: 10.1016/j.cmet.2019.02.016

49. Jin H, He Y, Zhao P, Hu Y, Tao J, Chen J, et al. Targeting lipid metabolism to overcome EMT-associated drug resistance via integrin  $\beta$ 3/FAK pathway and tumor-associated macrophage repolarization using legumain-activatable delivery. *Theranostics* (2019) 9(1):265–78. doi: 10.7150/thno.27246



## OPEN ACCESS

## EDITED BY

Ana Paula Lepique,  
University of São Paulo, Brazil

## REVIEWED BY

Zongsheng He,  
Daping Hospital, China  
Changliang Shan,  
Nankai University, China  
Nan Liu,  
Shenzhen University, China

## \*CORRESPONDENCE

Yong Xu  
xuyong\_2000@tom.com  
Yong Dai  
daiyong22@aliyun.com;  
dai.yong@szhospital.com

<sup>†</sup>These authors have contributed  
equally to this work

## SPECIALTY SECTION

This article was submitted to  
Cancer Immunology  
and Immunotherapy,  
a section of the journal  
Frontiers in Immunology

RECEIVED 22 April 2022

ACCEPTED 28 September 2022

PUBLISHED 14 October 2022

## CITATION

Jiang Z, Zhang W, Zeng Z, Tang D, Li C, Cai W, Chen Y, Li Y, Jin Q, Zhang X, Yin L, Liu X, Xu Y and Dai Y (2022) A comprehensive investigation discovered the novel methyltransferase METTL24 as one presumably prognostic gene for kidney renal clear cell carcinoma potentially modulating tumor immune microenvironment. *Front. Immunol.* 13:926461. doi: 10.3389/fimmu.2022.926461

## COPYRIGHT

© 2022 Jiang, Zhang, Zeng, Tang, Li, Cai, Chen, Li, Jin, Zhang, Yin, Liu, Xu and Dai. This is an open-access article distributed under the terms of the Creative Commons Attribution License (CC BY). The use, distribution or reproduction in other forums is permitted, provided the original author(s) and the copyright owner(s) are credited and that the original publication in this journal is cited, in accordance with accepted academic practice. No use, distribution or reproduction is permitted which does not comply with these terms.

# A comprehensive investigation discovered the novel methyltransferase METTL24 as one presumably prognostic gene for kidney renal clear cell carcinoma potentially modulating tumor immune microenvironment

Zhongji Jiang<sup>1,2†</sup>, Wei Zhang<sup>1†</sup>, Zhipeng Zeng<sup>1</sup>, Donge Tang<sup>1</sup>, Chujiao Li<sup>1</sup>, Wanxia Cai<sup>1</sup>, Yumei Chen<sup>1</sup>, Ya Li<sup>3</sup>, Qiu Jin<sup>3</sup>, Xinzhou Zhang<sup>3</sup>, Lianghong Yin<sup>4</sup>, Xueyan Liu<sup>5</sup>, Yong Xu<sup>2\*</sup> and Yong Dai<sup>1\*</sup>

<sup>1</sup>Clinical Medical Research Center, The Second Clinical Medical College of Jinan University, Shenzhen People's Hospital, Shenzhen, China, <sup>2</sup>Department of Laboratory Medicine, Shenzhen Institute of Translational Medicine, The First Affiliated Hospital of Shenzhen University, Shenzhen Second People's Hospital, Shenzhen, China, <sup>3</sup>Key Renal Laboratory of Shenzhen, Department of Nephrology, Shenzhen People's Hospital, The Second Clinical Medical College of Jinan University, Shenzhen, China, <sup>4</sup>Department of Nephrology, Institute of Nephrology and Blood Purification, The First Affiliated Hospital of Jinan University, Jinan University, Guangzhou, China, <sup>5</sup>Department of Intensive Care Unit, Shenzhen Key Laboratory of Prevention and Treatment of Severe Infections, The Second Clinical Medical College of Jinan University (Shenzhen People's Hospital), Shenzhen, China

**Background:** Recently, an increasing number of studies have uncovered the aberrant expression of methyltransferase-like family (METTL) plays an important role in tumorigenesis, such as METTL3 (an m6A writer). In our recent work, we discovered METTL24 expression was highly associated with the hazard ratio (HR) of kidney renal clear cell carcinoma (KIRC) compared to other tumors, implying a special function of METTL24 in KIRC carcinogenesis. Until now, the functions and mechanisms of METTL24 in KIRC have remained mostly unknown.

**Methods:** The mRNA expression of METTL24 in KIRC was analyzed using the TIMER 2.0, GEPIA, and UALCAN databases. The immunohistochemical assay was performed to validate METTL24 expression in our self-built Chinese cohort ( $n_{\text{tumor}} = 88$ ,  $n_{\text{normal}} = 85$ ). The gene set enrichment analysis (GSEA) was used to investigate the biological processes in which METTL24 might be engaged. The Spearman analysis was used to evaluate the expression correlations between METTL24 and a range of immunological variables, and the effects of METTL24 on the infiltration levels of multiple immune cells were explored using

TCGA data. The upstream transcription factors of METTL24 were screened through a multi-omics analysis.

**Results:** METTL24 expression in KIRC tissues was significantly decreased compared to normal adjacent kidney tissues, which was associated with the lower survival rate of KIRC patients. METTL24 potentially participated in the immune-relevant biological processes such as cytokine binding, NF- $\kappa$ B binding, MHC protein complex, and interleukin-12 action. Besides, METTL24 expression was linked to a number of immune checkpoints, cytokines, chemokines, and chemokine receptors, and also correlated with the infiltration levels of 10 types of immune cells in KIRC. Meanwhile, METTL24 expression differently affected the overall survival rates (OS) of KIRC patients with high or low levels of immune infiltration. Finally, CTCF and EP300 were discovered to be the probable transcription factors of METTL24 in KIRC.

**Conclusion:** This study revealed that METTL24 might serve as a prognostic marker in KIRC and as one immune-relevant target for clinical treatment.

#### KEYWORDS

METTL24, methyltransferase, immune microenvironment, prognostic biomarker, kidney cancer

## Introduction

After prostate and bladder cancer, kidney cancer is the third most frequent urological malignancy, with 431,288 new cases and 179,368 deaths reported by the Global Cancer Observatory in 2020 (1). Kidney renal clear cell carcinoma (KIRC) is the most frequent subtype of kidney cancer, accounting for over 70% of all cases each year (2). Due to the lack of typical manifestations and screening indicators, KIRC is usually diagnosed at an advanced stage, which makes therapy challenging and increases the risk of recurrence (3). Patients with metastatic KIRC have a 5-year survival rate of only 10% (4).

Anti-tumor therapy has been incredibly challenging for a long time since the focus on tumor treatment has been limited to the tumor itself. The tumor microenvironment (TME), consisting of immune cells, endothelial cells, fibroblasts, and various biological molecules, is critical for carcinogenesis and therapeutic responses (5–7). Immune checkpoint blockade (ICB) therapy has achieved success in multiple cancers (8), but the evidence for its effectiveness in kidney cancer is inconclusive, and only some patients may benefit from it (9, 10). Therefore, more research into potential treatment targets for kidney cancer is required.

Methyltransferase-like (METTL) genes encode proteins with seven  $\beta$ -chain with S-adenosylmethionine binding domains that typically act as methyltransferases, writing methylations on DNAs, RNAs, or proteins (11–13). Recent studies have demonstrated that the aberrant expression of METTL family

genes, such as METTL3 (one m6A writer), plays a key role in tumorigenesis (11, 14). In our previous study, we found that the METTL family was more closely associated with the risk of kidney cancer than other malignancies (Wei Zhang, et al), indicating that these proteins might be crucial for the initiation and progression of kidney cancer. Also, we identified METTL24 as one protecting factor for renal cancer (Supplementary Figure S1). There are currently few reports about METTL24, and only one article has proclaimed that METTL24 expression is likely connected with the prognosis of rectal cancer patients (15). METTL24's role and mechanisms in tumorigenesis are still barely known.

In this study, we analyzed METTL24 expression in KIRC tissues and normal adjacent tissues using the data sets from the Cancer Genome Atlas (TCGA) and Genotype-Tissue Expression (GTEx) databases ( $n_{\text{tumor}} = 523$ ,  $n_{\text{normal}} = 72$ ) and evaluated its prognostic value for KIRC patients. Next, we clarified the potential biological processes and pathways that METTL24 was involved in. Subsequently, we explored the role of METTL24 in the immune microenvironment, including analyzing the correlation between METTL24 expression and the infiltration ratios of immune cells and investigating the expression correlation between METTL24 and several immune families. We also looked at the impact of METTL24 on the survival rates of KIRC patients with high or low immune infiltration. Ultimately, we explored the potential transcription factors of METTL24 in KIRC.

## Methods

### Patients

The Shanghai Outdo Biotech Company contributed 90 tumorous samples and paired normal nearby samples from KIRC patients. Patient exclusion criteria: Older than 85 years old or younger than 18 years old, with severe organ failure, as well as a history of chemotherapy or radiotherapy. All participants gave their informed consent, and the Ethics Committee of Shanghai Outdo Biotech Company approved this study (No.YB-M-05-02), which followed the World Medical Association's Code of Ethics.

### Immunohistochemistry assay

The tissue sections were incubated at 63°C for 60 minutes before being immersed in xylene for 15 minutes. Then, the soaking step was repeated once more. The chips were dewaxed twice in 100% ethanol for 7 minutes, then in 90%, 80%, and 70% ethanol for 5 minutes each on LEICAST5020 fully automated stainlers (Leica, Biosystems), with antigen retrieval using the Automatic DAKO PT-Link. After that, the chips were placed in distilled water at room temperature to allow natural cooling for 10 minutes. The chip was then washed three times with the PBS solution, each time for 5 minutes. Following that, the chip was incubated at 4°C for 12 hours with METTL24 antibody incubation solution (Invitrogen, PA557952, 1:1000). The rewarming process was carried out at room temperature for 45 minutes. The chip was then washed three times with the PBS solution, each time for 5 minutes. A biotin blocking kit was used to saturate the endogenous biotin (Maixin, BLK-0002), and the chip was then incubated at 37°C for one hour with the secondary antibody incubation solution (Boster, SA1055). The chip was cleaned three times with PBS solution for 5 minutes each time before being colored with diaminobenzidine (DABs). After that, the chip was stained with hematoxylin for 1 minute, submerged in 0.25% hydrochloric acid alcohol for around 10 seconds, then washed for 5 minutes with running water. The chip was dehydrated and sealed after being cleaned with running water for 10 minutes. The stained chip was scanned with the Aperio Scanner (LEICA, Aperio XT), and two pathologists evaluated the staining intensity and proportion of stained cells. Under low magnification, the staining intensity was graded as follows: The score of light yellow was 1, brownish yellow was 2, and tan was 3. In terms of the proportion, three different staining intensity fields were chosen to measure their positive rate, and then the average value was calculated. Finally, the staining score was calculated by multiplying the staining intensity and proportion.

### Tumor immune estimation resource online database 2.0 (TIMER 2.0)

TIMER 2.0 (16) is a comprehensive database that displays the amount of various immune cells within cancer as computed using the immune deconvolution approach and provides gene expression in tumorous tissues vs normal neighboring tissues. The “Exploration-Gene DE” module of TIMER 2.0 was used to assess METTL24 expression in more than 30 tumors and nearby normal tissues, and the link between METTL24 expression and immune cell infiltration ratios was also explored using the TIMER 2.0 database.

### Kaplan-Meier plotter

Kaplan-Meier plotter (17) is a database collecting the published microarray and RNA-sequencing data sets from GEO, European Genome-Phenome Archive (EGA), and TCGA databases, with an emphasis on the discovery and verification of survival relevant genes across all malignancies. In our research, the “kidney cancer RNA-seq” module was utilized to assess the effect of METTL24 mRNA expression on the overall survival rate (OS) of KIRC patients. In Figure 4A, according to the best cut-off value, the patients were divided into METTL24-high-expression and METTL24-low-expression groups; in Figure 4B, “median value” was used to divide patients into two groups. Using the Kaplan-Meier plotter, the effect of METTL24 expression on the OS of patients with high or low levels of immune infiltration was also investigated.

### Human transcription factor targets (hTFtarget)

The hTFtarget database (18) is a transcription factor database that includes a significant number of human chromatin immunoprecipitation (ChIP) sequencing data sets (7,190 experimental samples) and 659 identified transcription factors. The hTFtarget database was used to find the seven possible upstream transcription factors of METTL24 in kidney tissue.

### Linkedomics

Linkedomics (19) is a comprehensive database that combines the multi-omics data sets from the Clinical Proteomic Tumor Analysis Consortium (CPTAC) and TCGA databases. The METTL24 co-expressed genes in KIRC tissues were retrieved from the Linkedomics database, and gene set

enrichment analysis (GSEA) of METTL24 was performed using the Linkedomics' module "LinkInterpreter".

## Gene expression profiling interactive analysis (GEPIA)

GEPIA (20) is an online database containing data sets of 9736 tumor samples and 8587 normal samples from TCGA and The Genotype-Tissue Expression (GTEx) projects. Here, METTL24 expression between tumorous tissues of KIRC, kidney chromophobe (KICH), and kidney renal papillary cell carcinoma (KIRP) and normal surrounding tissues was analyzed using the "Expression DIY" module of GEPIA. The Spearman method was used for the expression correlation between AR, CTCF, EP300, and METTL24.

## UALCAN

UALCAN (21) is an interactive network database that gathers multi-platform-based data sets from other publicly available databases like TCGA, MET500, and CPTCA, and lets users to analyze them. In this study, the UALCAN database was utilized to study METTL24 expression in different patient groups. Meanwhile, the UALCAN database was used to look into protein expression and phosphoprotein levels (AR, CTCF, and EP300).

## SangerBox

SangerBox is an integrated bioinformatic analysis tool that can perform a wide range of bioinformatic studies and visualizations. SangerBox was used to compare METTL24 expression in tumor tissues from 27 cancers to normal tissues in this study.

## Assistant for clinical bioinformatics (ACLBI)

ACLBI is a web-based interactive application that allows users to analyze data from TCGA, the Cancer Cell Line Encyclopedia (CCLE), and the International Cancer Genome Consortium (ICGC) databases. ACLBI was utilized in this study to execute univariate and multivariate Cox regression analysis to identify the risk factors and independent prognostic genes in KIRC. Also, the nomogram was drawn based on the results of multivariate Cox regression analysis, which provides a graphical representation of multiple factors that might be used to assess the risk of recurrence. The ACLBI was also used to study the impact of METTL24 expression on OS and progression-free survival rate (PFS). Furthermore, the correlation of METTL24

mRNA expression and immune-relevant scores and immune cell infiltration levels were calculated using the algorithms including MCPOUNTER, QUANTISEQ, and TIMER in ACLBI.

## Statistical analyses

The log-rank method was utilized to determine the significance of METTL24 expression on patient survival. Fisher's exact test was used to analyze the significance of enrichment results. And the Spearman method was used for the correlation analysis. A p-value of less than 0.05 was regarded as significant. \*\*\*p < 0.001, \*\*p < 0.01, and \*p < 0.05.

## Results

### METTL24 is decreasingly expressed in tumor tissues versus normal tissues in most cancers

We initially looked at the expression of METTL24 in various cancers to see if it had a role in carcinogenesis. We discovered that METTL24 was considerably lower expressed in tumor tissues compared to normal tissues in 15 types of tumors as analyzed using data sets from TCGA (Figure 1A). Besides, we revealed that METTL24 was decreasingly expressed in cancer tissues of 17 tumors compared to normal tissues using data sets from TCGA and GTEx (Figure 1B). As we were focusing on kidney cancer, we confirmed METTL24 expression in KICH, KIRC, KIPR tissues and normal neighboring kidney tissues using the GEPIA database (Figure 1C).

### The validation of METTL24 expression based on a self-built Chinese cohort

As mentioned above, METTL24 was significantly downregulated in three renal cancer subtypes, and since KIRC accounts for more than 70% of renal malignancies (2), this study selected KIRC as a representative model of renal cancer for follow-up studies. To verify METTL24 expression in KIRC, we used IHC to detect METTL24 protein expression in 88 cancer samples and 85 para-cancer samples (Table 1). The result indicated that the protein level of METTL24 in KIRC tissues was appreciably lower than normal adjacent tissues (p<0.0001) (Figure 2A). Figure 2B depicts METTL24 protein expression in KIRC tissue and para-cancer, whereas Figures 2C, D depict exemplary microscopic illustrations of clear cell papillary renal cell carcinoma (CCPRCC) and KIRC with sarcomatoid variation, respectively. These findings showed that METTL24 expression was lower in tumorous tissues compared to normal surrounding tissues in Chinese KIRC patients, which was in line with the above computer-analyzing-based results.

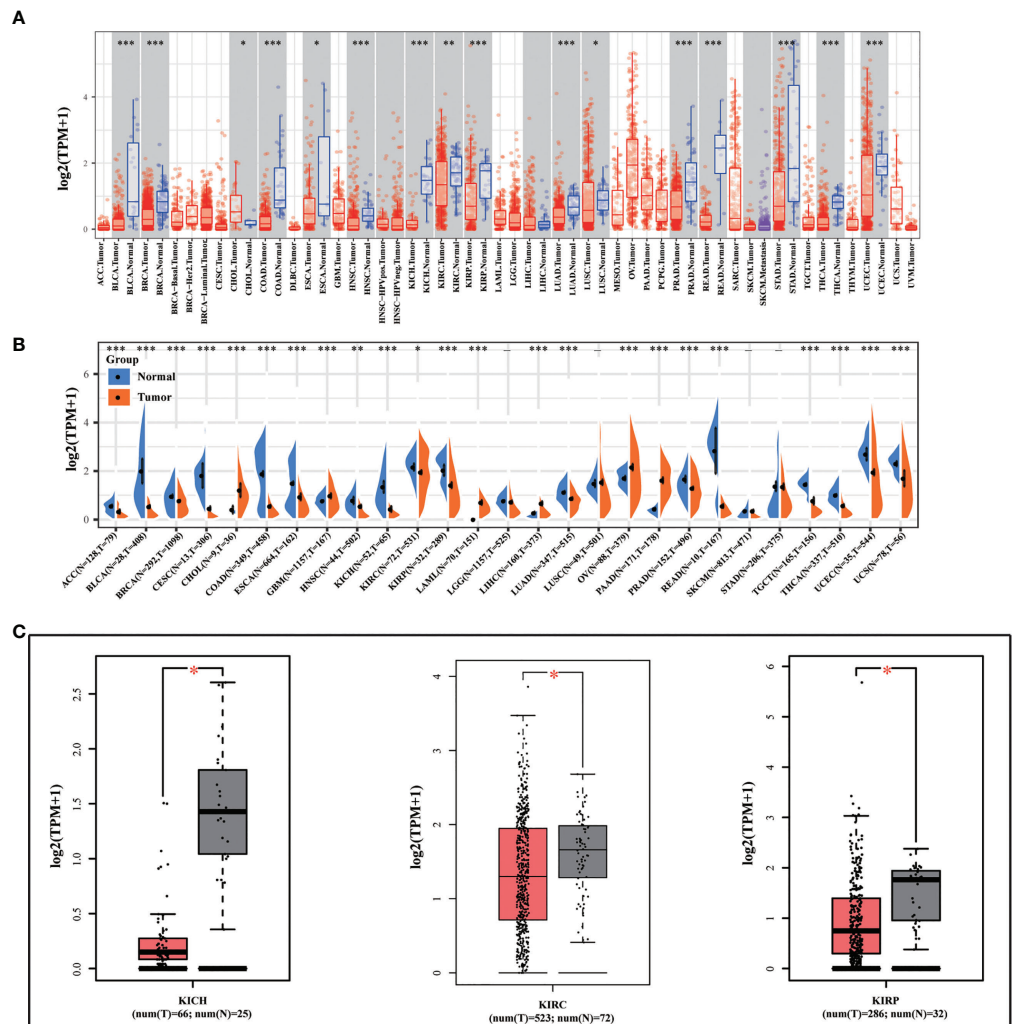


FIGURE 1

METTL24 was increasingly expressed in KIRC tissues versus normal kidney tissues. **(A)** METTL24 expression in various cancers and normal tissues as analyzed using the TIMER database. **(B)** METTL24 expression in various cancers and normal tissues as analyzed using the data sets from TCGA and GTEx. **(C)** METTL24 expression in KIHC, KIRC, and KIRP tissues and adjacent normal tissues as analyzed using the GEPIA database. \*\*\*p < 0.001, \*\*p < 0.01 and \*p < 0.05.

TABLE 1 The characteristics of 90 kidney cancer patients of self-built Chinese cohort.

	Type	Patients
Age	≤65	60 (66.7%)
	>65	30 (33.3%)
Sex	Female	59 (65.6%)
	Male	31 (34.4%)
Subtypes	Kidney clear cell renal cell carcinoma (KIRC)	87 (96.7%)
	KIRC with partial papillary renal cell carcinoma	2 (2.2%)
	KIRC with partial sarcomatoid variant	1 (1.1%)
Staging	1	55 (61.1%)
	2	24 (26.7%)

(Continued)

TABLE 1 Continued

	Type	Patients
T-stage	3	6 (6.7%)
	4	2 (2.2%)
	–	3 (3.3%)
N-stage	T1	58 (64.4%)
	T2	25 (27.8%)
	T3	7 (7.8%)
	–	0 (0.0%)
M-stage	N0	85 (94.5%)
	N1	2 (2.2%)
	N2	0 (0.0%)
	N3	0 (0.0%)
	–	3 (3.3%)
	M0	88 (97.8%)
M1	M1	2 (2.2%)
	–	0 (0.0%)

“–”: The staging and T-stage of patients with distal or lymphatic metastases was not identified.

## METTL24 expression in different KIRC groups

We evaluated METTL24 expression in different clinical subgroups using data sets from the UALCAN database to see if there was a link between METTL24 expression and other KIRC clinical characteristics. In male KIRC patients, METTL24 expression was downregulated in tumorous tissues compared to normal surrounding tissues, but not in females (Figure 3A). When it came to age, METTL24 expression dropped drastically in KIRC tissues compared to normal tissues in patients of various ages (21-40 years, 61-80 years), but there was no difference between the age groups (Figure 3B). In terms of tumor stage, METTL24 expression revealed a substantial downregulation trend as tumor grade increased, with grade 4 having the lowest expression (Figure 3C). In addition, as tumor stages progressed, the level of METTL24 in KIRC tissues fell considerably (Figure 3D). In terms of tumor subtypes, METTL24 expression was significantly lower in CCB tumorous tissues than in normal tissues (Figure 3E), but it was much greater in CCA carcinogenic tissues than in normal samples. Furthermore, as the N stage increased, METTL24 expression showed a strong downregulation trend (Figure 3F). The results regarding grade, stage, and N stage elucidated that METTL24 was potentially related to the advancement of KIRC.

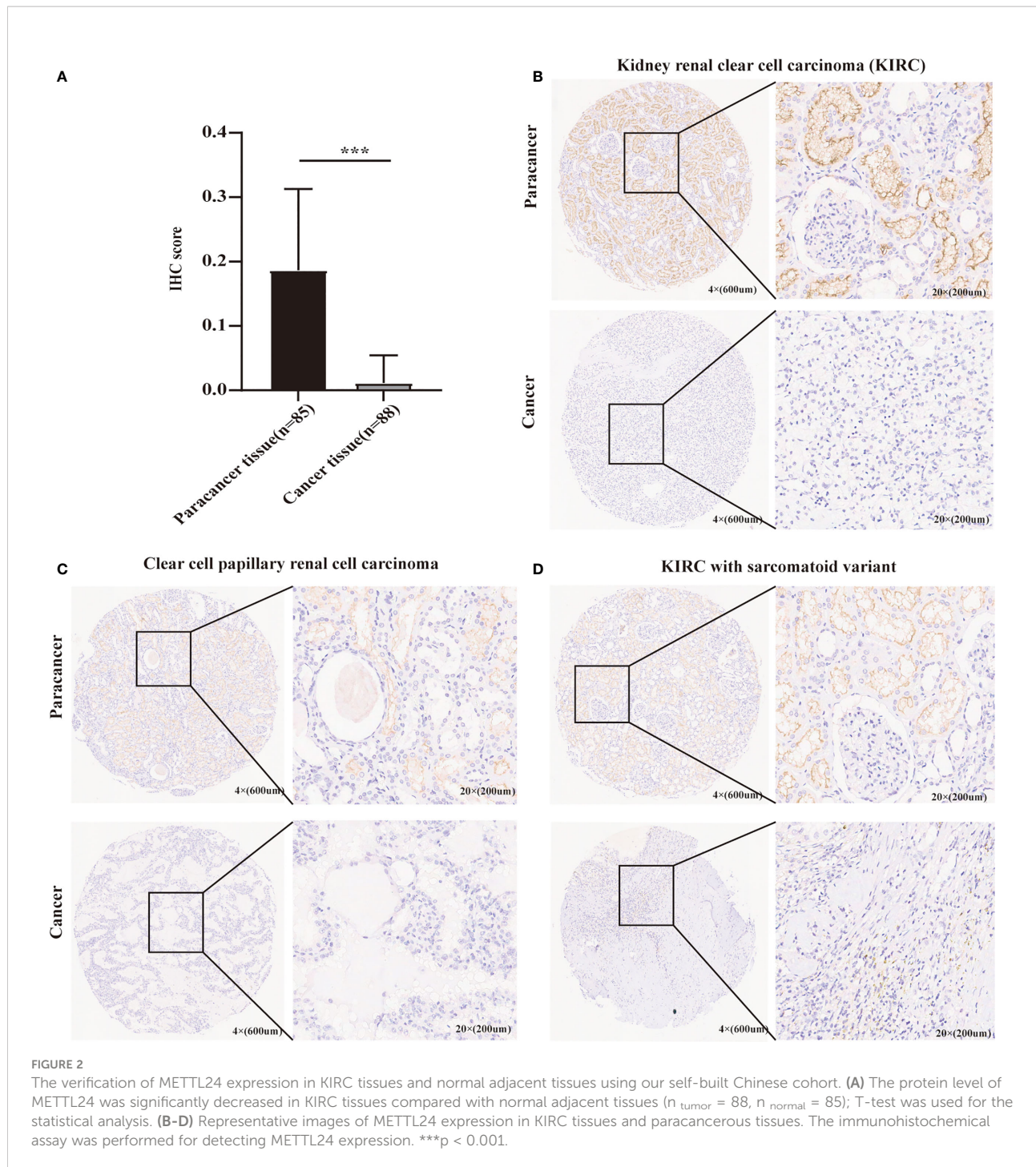
## METTL24 as an independent prognostic gene for KIRC

To preliminarily explore the function of METTL24 in KIRC, we plotted the survival curve of METTL24 using TCGA data

sets. As a result, reduced METTL24 expression in KIRC was linked to a shorter OS, PFS and DSS, but not RFS or DFS (Figures 4A–C, Supplementary Figures S2). Following that, we conducted the univariate Cox regression analysis using OS data, which revealed that low METTL24 expression was a risk factor for KIRC ( $HR= 0.59$ , 95% confidence interval (CI) = 0.50-0.70,  $p <0.0001$ ) (Figure 4D). Furthermore, METTL24 was discovered as an independent predictive predictor for KIRC in a multivariate Cox regression analysis based on the OS (Figure 4E). Similarly, we used disease-specific survival (DSS) and PFS to conduct univariate and multivariate Cox regression analysis and came to similar conclusions (Supplementary Figures S3). Moreover, we created a nomogram that included METTL24 expression and TNM stages to predict the OS, DSS, and PFS of KIRC patients. The forecast model's anticipated values were highly compatible with the actual 1-, 3-, and 5-year OS, DSS, and PFS, according to the findings. The OS, DSS, and PFS nomograms had concordance indexes of 0.778, 0.85, and 0.842, respectively (Figures 4D–G, Supplementary Figures S3). As a result, this nomogram may aid clinicians in identifying high-risk and low-risk patients and providing tailored treatment.

## METTL24 may play a role in KIRC's immune microenvironment modulation

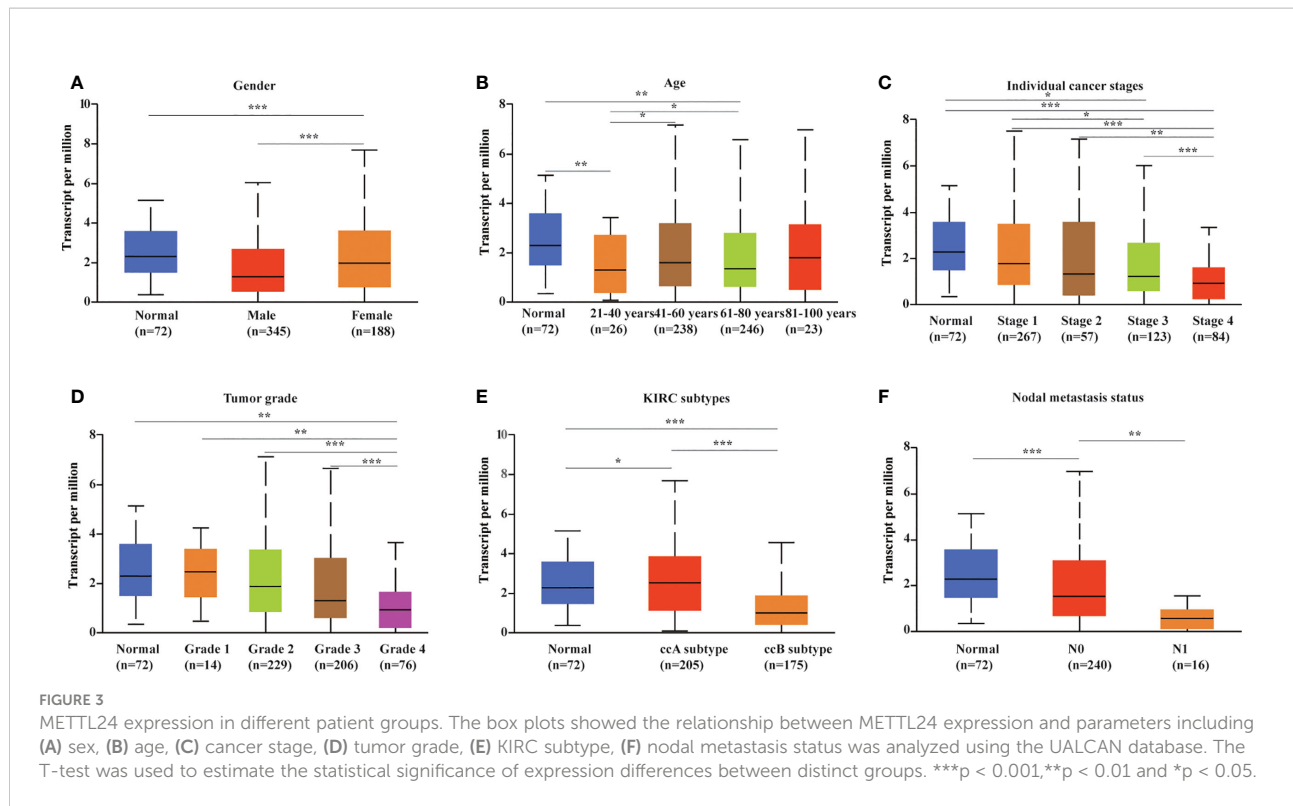
We retrieved 1,3977 co-expressed mRNAs of METTL24 in KIRC patients from the Linkedomics database to investigate the mechanism of METTL24 in KIRC (Supplementary Table S1). Figures 5A,B showed the 50 METT24 genes that were most positively and adversely associated. Then, using an enrichment analysis of these co-expressed genes, we looked into the



biological processes that METTL24 might be involved in. As a consequence, METTL24 was presumably connected with a range of immunological functions, including cytokine binding, NF-kappa B binding, MHC protein complex, and interleukin-12 activity (Figures 5C–F), suggesting METTL24 might have a role in the control of immune milieu of KIRC.

We then looked at the relationship between the expression of METTL24 and numerous immune genes in KIRC to confirm the

immunological functions of METTL24. As demonstrated in Figure 6A, METTL24 and the traditional immunological checkpoints CD274, HAVCR2, PDCD1LG2, SIGLEC15, and TIGIT have a significant positive expression connection. METTL24 was also discovered to be commonly co-expressed with a variety of cytokines, including CD276, CD28, CD40, CD40LG, CD48, CD80, CD86, CXCL12, CXCR4, ENTPD1, HHLA2, ICOS, ICOSLG, IL2RA, IL6R, MICB, NT5E, PVR,



RAET1E, TNFRSF14, TNFRSF4 (Figure 6B). CCL13, CCL14, CCL15, CCL16, CCL2, CCL22, CCL23, CCL24, CCL28, CCL4 CCL8, CX3CL1, CXCL10, CXCL11, CXCL12, CXCL14, CXCL16, CXCL9, CCL1, CCL25, CXCL1, CXCL13, and CXCL15 were also substantially linked with METTL24 expression. METTL24 expression was also tied to the expression of a number of chemokine receptors, including CCR1, CCR10, CCR2, CCR3, CCR4, CCR5, CCR6, CCR7, CCR8, CX3CR1, CXCR1, CXCR2, CXCR4, CXCR5, CXCR6, CXCR9, and CXCR3 (Figures 6C, D). Notably, the expression of METTL24 was positively connected with the majority of immune genes, with only a few immune genes being adversely correlated. The foregoing finding also suggested that METTL24 might play a function in immunological modulation in KIRC patients.

Following that, we used various algorithms, such as MCP COUNTER, QUANTISEQ, and TIMER, to investigate the relationship between METTL24 expression and the infiltration ratios of various immune cells (Figures 6E–G). As a result, the infiltration levels of 10 types of immune cells in KIRC, including CD4+ T cells, CD8+ T cells, neutrophils, natural killer (NK) cells, myeloid dendritic cells, macrophages, and B cells, were correlated with METTL24 expression. CD4+ T cells, CD8+ T cells, neutrophils, natural killer (NK) cells, and myeloid dendritic cells were all positively linked with METTL24 expression among these immune cells. Infiltrating CD4+ T cells and CD8+ T cells within malignancies are known to limit tumor activity, whereas Tregs are more

likely to promote tumor growth (22, 23). Our findings revealed that METTL24 was more likely to be a tumor suppressor gene in KIRC tumorigenesis, and the findings suggested that METTL24's effects on CD4+ and CD8+ T cell infiltration might be involved in its functions in tumors.

The effects of METTL24 expression on the OS of KIRC patients with high or low immune cell infiltration were next explored using data sets from the Kaplan-Meier Plotter database to see if it altered the progression of KIRC *via* controlling the immune microenvironment. The results revealed a difference in METTL24 expression between patients with high immune infiltration and those with low immune infiltration (Figure 7, Supplementary Figure S4). For example, METTL24 expression had no influence on the OS of patients with enriched B cells ( $p = 0.0011$ ), but had a substantial effect on patients with depleted B cells ( $p = 2.3e-08$ ). Similar results were seen in basophils and NKT cells. As a result of the previous findings, it appears that METTL24 regulates carcinogenesis by influencing the immune system.

### Multi-omics-based analyses identified CTCF and EP300 as the potential transcription factors of METTL24 in KIRC

Gene expression is known to be influenced in part by transcription factors. To better understand the reasons for

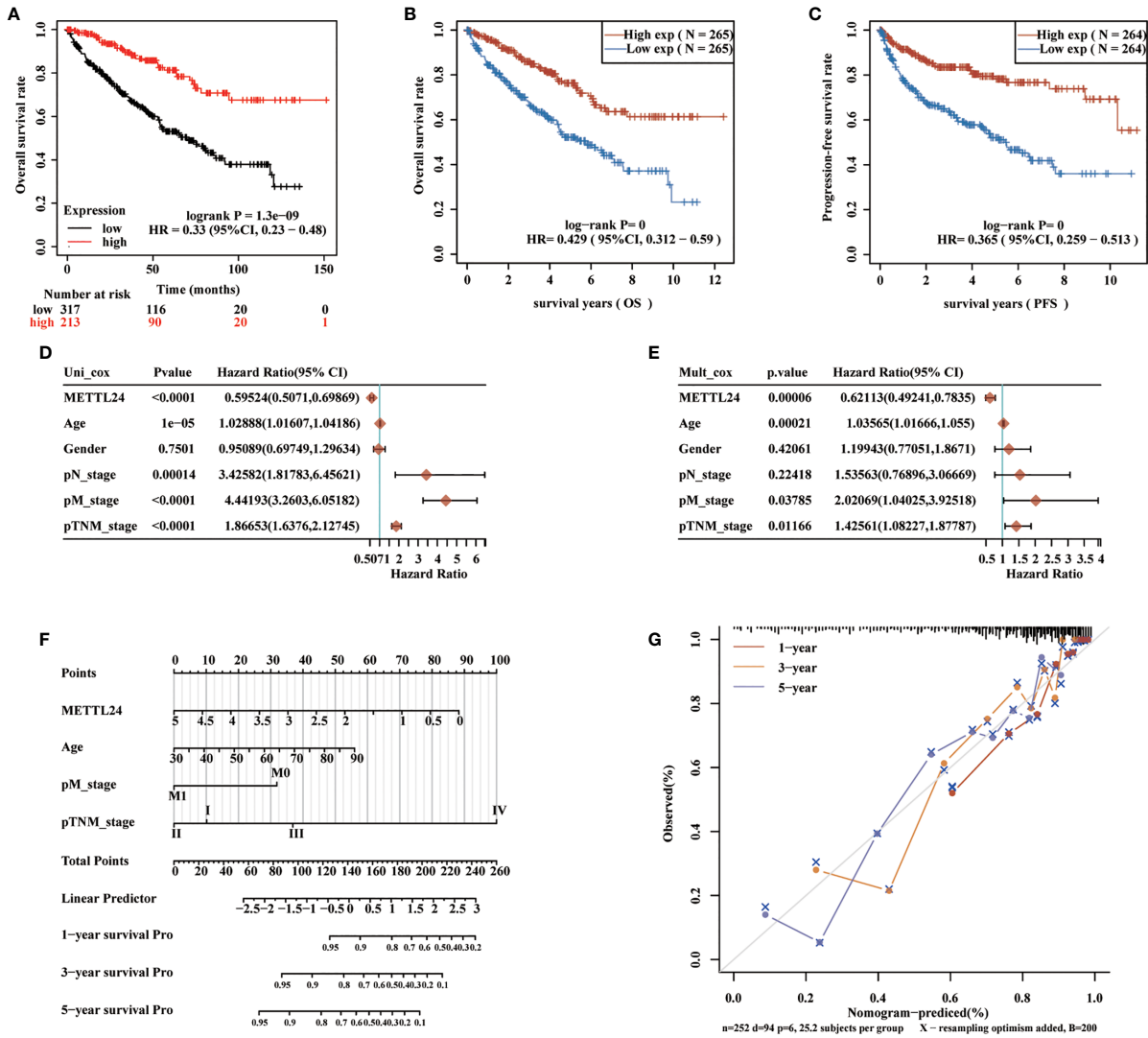
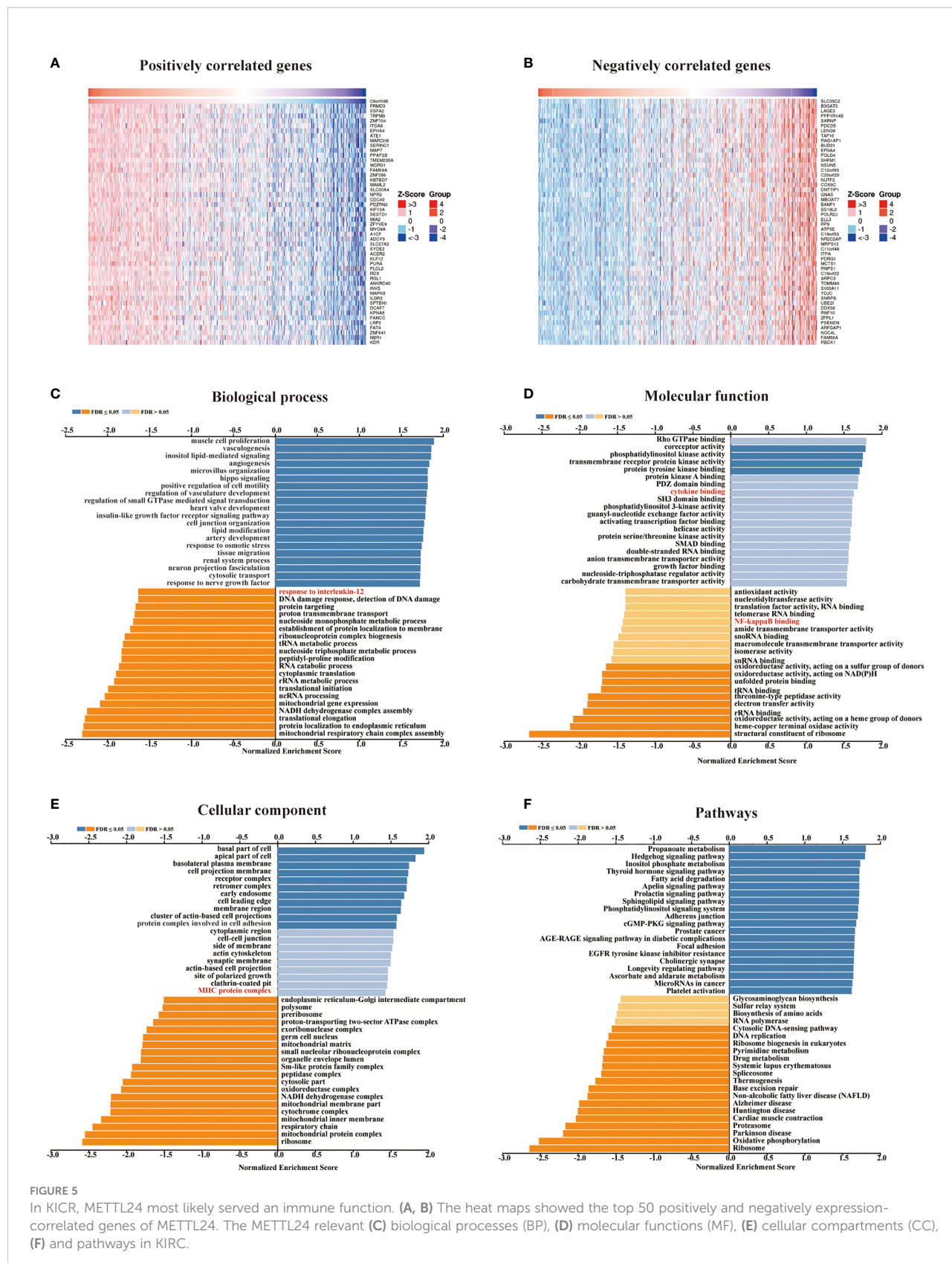


FIGURE 4

METTL24 as one potential prognostic gene for KIRC. (A, B) The Kaplan-Meier curve showed the impacts of METTL24 expression on the OS (C) and PFS of KIRC patients. (D) The forest image showed METTL24 as a potential risk factor for KIRC as analyzed using the univariate Cox regression. (E) The forest image showed METTL24 as one potential prognostic factor for KIRC as analyzed using the multivariate Cox regression. (F) A predictive nomogram based on the METTL24 risk score and other clinicopathological variables predicted the 1-, 3-, and 5-year survival rates of KIRC patients. (G) The Calibration curves indicated the agreement between anticipated and actual survival rates after 1, 3, and 5 years.

METTL24's downregulation in KIRC, we performed a multi-omics investigation to look for putative METTL24 upstream transcription factors. To begin, we used the hTFtarget database identifying seven probable transcription factors of METTL24 found in kidney tissue by ChIP sequencing, including AR, BRD2, CTCF, EP300, MYC, SPI1, and ZNF76. Then, the co-expression relationship between METTL24 and these genes was investigated, and we discovered that AR, CTCF, and EP300 were all positively linked with METTL24 (Supplementary Table S2). Furthermore, Spearman correlation analysis revealed that AR, CTCF, and EP300 gene expression were

substantially linked with METTL24 expression, with correlation coefficients of 0.52, 0.56, and 0.60, respectively (Figures 8A–C). The protein expression and phosphorylation levels of AR, CTCF, and EP300 in KIRC tissues were next studied, and it was observed that the protein contents of EP300 and CTCF were significantly up-regulated in KIRC tissues compared to normal kidney tissues, as were the phosphorylation levels of AR at Ser96 and EP300 at Thr1698 (Figures 8D–G). Since METTL24 potentially regulated the immune microenvironment, we hypothesized that transcription factors upstream of METTL24 should also be



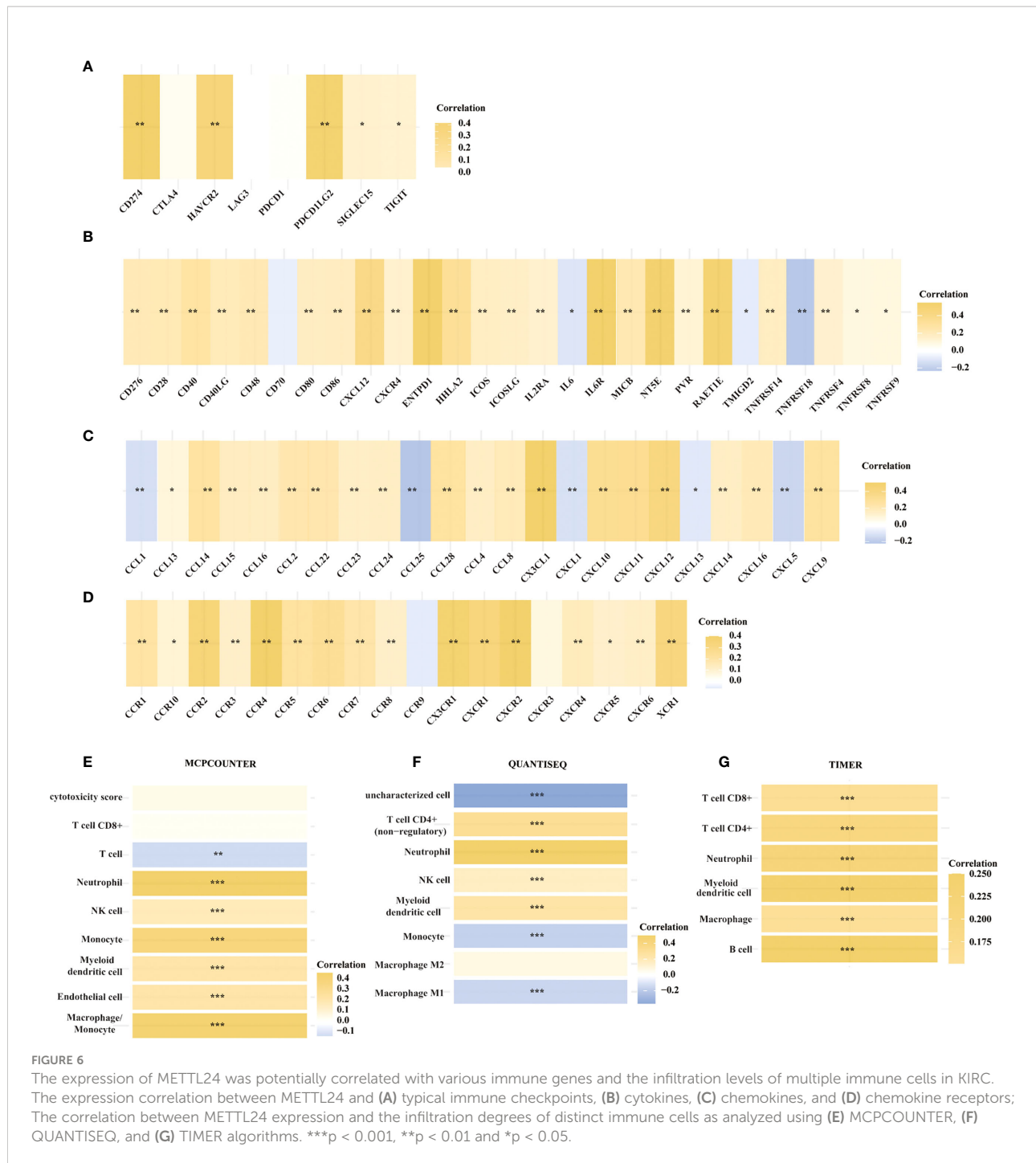


FIGURE 6

The expression of METTL24 was potentially correlated with various immune genes and the infiltration levels of multiple immune cells in KIRC. The expression correlation between METTL24 and (A) typical immune checkpoints, (B) cytokines, (C) chemokines, and (D) chemokine receptors; The correlation between METTL24 expression and the infiltration degrees of distinct immune cells as analyzed using (E) MCPOUNTER, (F) QUANTISEQ, and (G) TIMER algorithms. \*\*\*p < 0.001, \*\*p < 0.01 and \*p < 0.05.

involved in immune regulation. Therefore, we investigated the correlation between CTCF and EP300 expression and the infiltration ratios of various immune cells in KIRC using distinct algorithms. The result showed that the expression of CTCF and EP300 were significantly correlated with the infiltration levels of multiple immune cells, and METTL24's trend was also present in the link between CTCF and EP300 and the majority of immune cells (Figures 8H–J). This result

suggested that CTCF and EP300 might also play a role in immunomodulation of KIRC tumorigenesis as METTL24.

## Discussion

KIRC is the most frequent kind of kidney cancer, accounting for more than 70% of all occurrences (24). In the clinic,

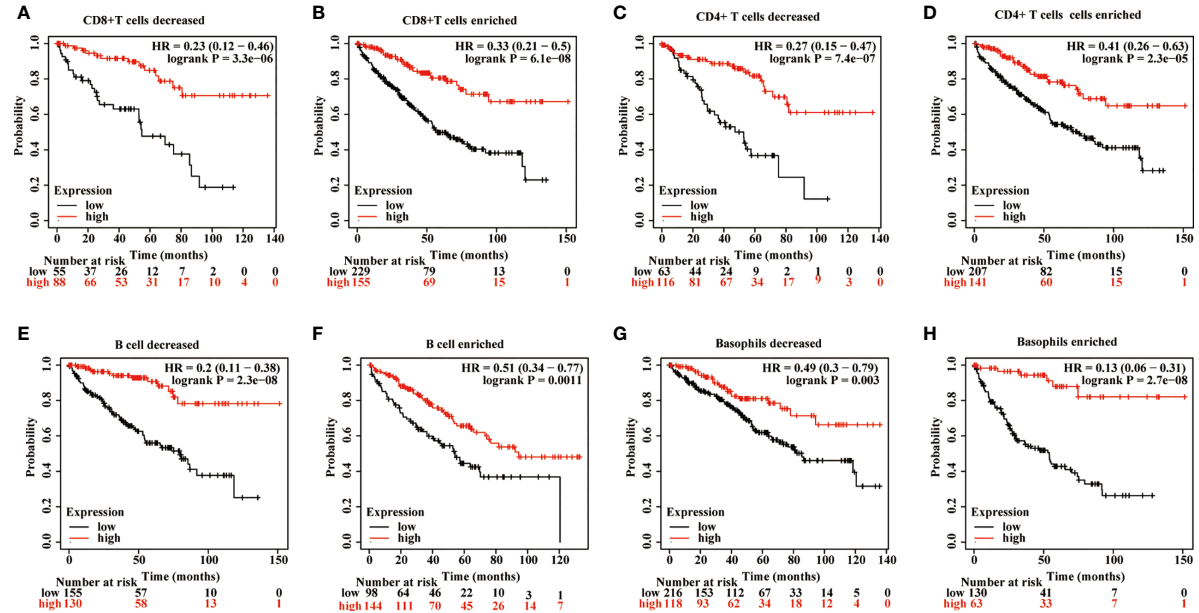


FIGURE 7

The influence of METTL24 expression on the OS of KIRC patients with high or low infiltration degrees of immune cells. The impact of METTL24 expression on the OS of KIRC patients with enriched or decreased infiltration ratios of (A, B) CD8+ T cells, (C, D) CD4+ memory T cells, (E, F) B cells, (G, H) basophils. The survival analysis was performed on Kaplan-Meier plotter database.

approximately 15% of KIRC patients have metastatic tumors at the time of diagnosis, and only a few patients benefit from targeted therapy, cytokine therapy, and ICB (25–27). Prognostic biomarkers will aid in the identification of high-risk and low-risk individuals in order to develop a tailored treatment plan. There have been no clinically employed molecular prognostic biomarkers till recently. This study revealed that METTL24 expression was significantly decreased in KIRC tissues compared to normal adjacent tissues and identified METTL24 as one potential independent prognostic biomarker for KIRC. As a result, METTL24 might be employed as a prognostic factor in renal carcinoma clinical diagnosis and treatment.

The immune microenvironment, which consists of tumor cells, immune cells, endothelial cells, cytokines, and other factors, has a significant impact on tumor initiation and progression (28, 29). Because renal carcinoma is not inherently susceptible to radiotherapy or chemotherapy; Cytokines, such as interleukin and interferon, were mostly utilized for treatment in the 1990s, but the objective response rate is only 5% to 27%, and the median PFS is only 3–5 months (30–32). Although the median survival of kidney cancer patients has increased significantly as a result of ICB treatment, most advanced renal carcinoma patients still do not benefit from the treatment in the long run (33, 34). In this study, we elucidated that METTL24 expression correlated with the infiltration levels of various

immune cells, and the expression of immune checkpoints, cytokines, chemokines, and chemokine receptors in KIRC, suggesting that METTL24 might be used as an immune target combined with the typical targets in KIRC.

In eukaryotic organisms, the METTL family usually encodes functional proteins that operate as methyltransferases. Previous research has identified METTL3 and METTL14 are m6A methylation writers on mRNAs, which regulate the growth and metastasis of renal cancer, colorectal cancer, pancreatic cancer, and other cancers (11, 14, 35, 36). Despite this, there are few publications on the role of METTL24 in carcinogenesis. According to Guoying's research, elevated METTL24 expression is associated with a worse prognosis in individuals with rectal cancer (HR = 2.1) (15). In our study, we discovered that the expression of METTL24 and numerous immune genes were highly correlated (Figure 6). Meanwhile, we found that METTL24 was potentially associated with NF-κB pathway, according to the GSEA analysis (Figure 5D). As is well-known, NF-κB signaling pathway is one of indispensable pathways for immune microenvironment regulation (37–39). For example, NF-κB pathway has been reported to maintain the activity of tumor-associated macrophages in tumor progression. Therefore, we speculated that the correlation between METTL24 and the immune genes might be mediated by NF-κB pathway. We discovered that METTL24 expression affects the survival rate of KIRC patients

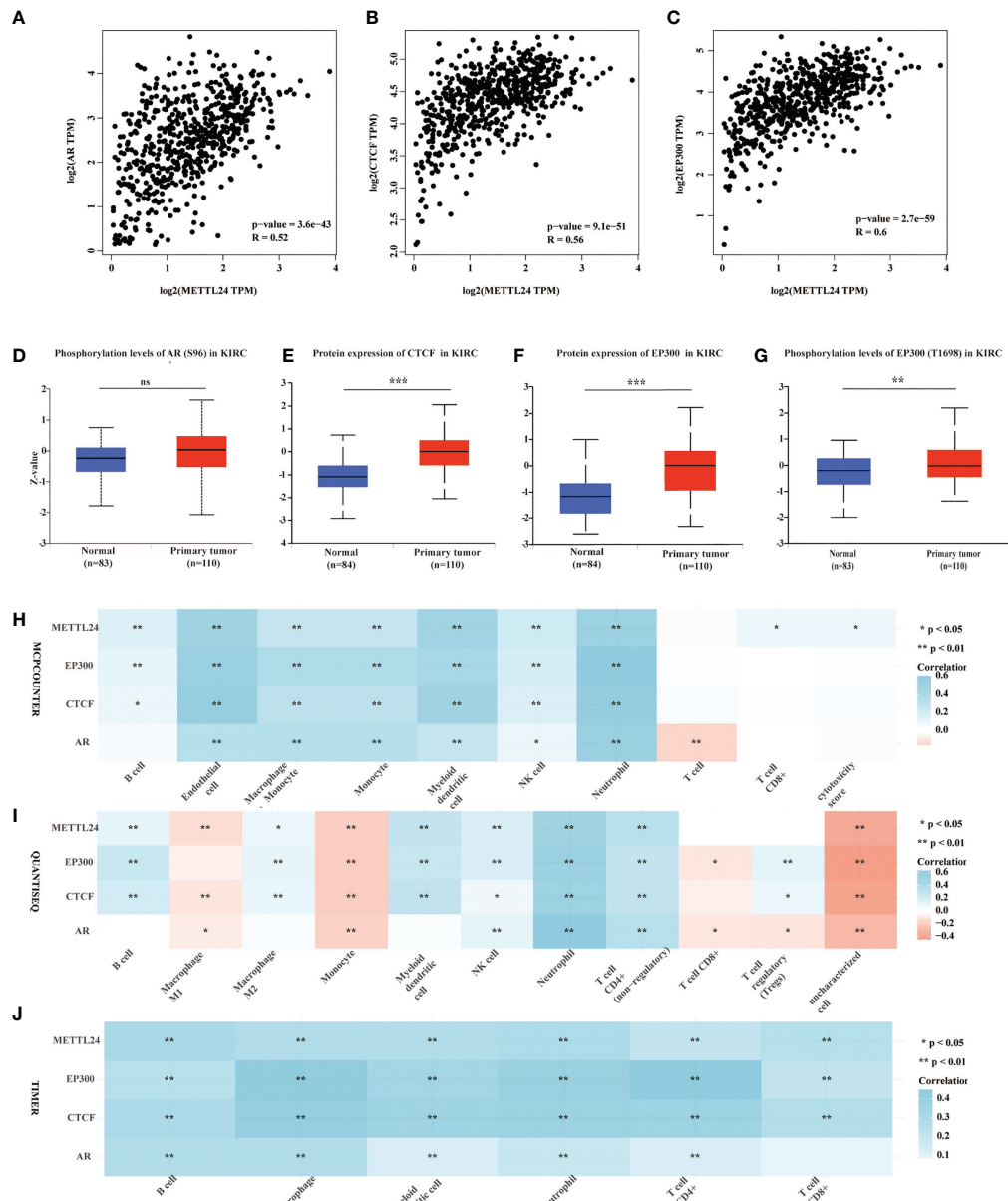


FIGURE 8

Protein levels and phosphorylation content of EP300, CTCF and AR, the possible METTL24 transcription factors, were altered in KIRC tissues compared to normal kidney tissues. The Spearman correlation between METTL24 expression and (A) AR, (B) CTCF, and (C) EP300 expression in KIRC. The phosphorylation levels of (D) AR and (E) EP300 in KIRC and normal kidney tissues. The protein expression levels of (F) CTCF and (G) EP300 in KIRC versus normal kidney tissues. The correlation between METTL24, EP300, CTCF, AR expression and the infiltration degrees of distinct immune cells in KIRC as analyzed using (H) MCPOUNTER, (I) QUANTISEQ, and (J) TIMER algorithms. \*\*\* $p < 0.001$ , \*\* $p < 0.01$  and \* $p < 0.05$ ; ns, not significant.

and that it might play a function in controlling the immune microenvironment in this study. The immunomodulatory role of METTL24 has been discovered for the first time, to our knowledge.

In conclusion, this work found lower levels of METTL24 expression in KIRC tissues compared to normal tissues,

discovered METTL24's prognostic relevance in KIRC, and established METTL24's possible activities in the immune microenvironment. As a result, METTL24 might be used as a prognostic marker in KIRC as well as an immune target in the clinic.

## Data availability statement

The original contributions presented in the study are included in the article/[Supplementary Material](#). Further inquiries can be directed to the corresponding authors.

## Ethics statement

The studies involving human participants were reviewed and approved by the Ethics Committee of Shanghai Xinchao Biotechnology Co., Ltd (NO. YB-M-05-02). Written informed consent for participation was not required for this study in accordance with the national legislation and the institutional requirements.

## Author contributions

Study concept and design: WZ, ZJ, YX, and YD. Experiment and data acquisition: WZ, ZZ, DT, CL, WC, and YC. Analysis and interpretation of data: ZJ, WZ, YL, and QJ. Statistical analysis: ZJ and WZ. Drafting of the manuscript: ZJ, WZ, and CL. Funding: WZ, LY, and YD. Study supervision: XZ, XL, YX, and YD. All authors contributed to the article and approved the submitted version.

## Funding

This study was supported by the National Natural Science Foundation of China (Grant No. 82003172), Shenzhen Fund for Guangdong Provincial High-level Clinical Key Specialties

## References

1. Sung H, Ferlay J, Siegel RL, Laversanne M, Soerjomataram I, Jemal A, et al. Global cancer statistics 2020: GLOBOCAN estimates of incidence and mortality worldwide for 36 cancers in 185 countries. *CA: Cancer J Clin* (2021) 71:209–49. doi: 10.3322/caac.21660
2. Gansler T, Fedewa S, Amin MB, Lin CC, Jemal A. Trends in reporting histological subtyping of renal cell carcinoma: association with cancer center type. *Hum Pathol* (2018) 74:99–108. doi: 10.1016/j.humpath.2018.01.010
3. Scelo G, Larose TL. Epidemiology and risk factors for kidney cancer. *J Clin Oncol* (2018) 36:JCO2018791905. doi: 10.1200/JCO.2018.79.1905
4. Turajlic S, Swanton C, Boshoff C. Kidney cancer: The next decade. *J Exp Med* (2018) 215:2477–9. doi: 10.1084/jem.20181617
5. Bruni D, Angell HK, Galon J. The immune contexture and immunoscore in cancer prognosis and therapeutic efficacy. *Nat Rev Cancer* (2020) 20:662–80. doi: 10.1038/s41568-020-0285-7
6. Zhou G, Boor PPC, Bruno MJ, Sprengers D, Kwekkeboom J. Immune suppressive checkpoint interactions in the tumour microenvironment of primary liver cancers. *Br J Cancer* (2022) 126:10–23. doi: 10.1038/s41416-021-01453-3
7. Rotte A, Jin JY, Lemaire V. Mechanistic overview of immune checkpoints to support the rational design of their combinations in cancer immunotherapy. *Ann Oncol* (2018) 29:71–83. doi: 10.1093/annonc/mdx686
8. McDermott DF, Lee JL, Bjarnason GA, Larkin JMG, Gafanov RA, Kochenderfer MD, et al. Open-label, single-arm phase II study of pembrolizumab monotherapy as first-line therapy in patients with advanced clear cell renal cell carcinoma. *J Clin Oncol* (2021) 39:1020–8. doi: 10.1200/JCO.20.02363
9. Desai J, Deva S, Lee JS, Lin CC, Yen CJ, Chao Y, et al. Phase IA/IB study of single-agent tisilizumab, an investigational anti-PD-1 antibody, in solid tumors. *J Immunother Cancer* (2020) 8:e000453. doi: 10.1136/jitc-2019-000453
10. Xu W, Atkins MB, McDermott DF. Checkpoint inhibitor immunotherapy in kidney cancer. *Nat Rev Urol* (2020) 17:137–50. doi: 10.1038/s41585-020-0282-3
11. Li T, Hu PS, Zuo Z, Lin JF, Li X, Wu QN, et al. METTL3 facilitates tumor progression via an m(6)A-IGF2BP2-dependent mechanism in colorectal carcinoma. *Mol Cancer* (2019) 18:112. doi: 10.1186/s12943-019-1038-7
12. Chen Z, Zhu W, Zhu S, Sun K, Liao J, Liu H, et al. METTL1 promotes hepatocarcinogenesis via m(7) G tRNA modification-dependent translation control. *Clin Transl Med* (2021) 11:e661. doi: 10.1002/ctm2.661
13. Wong JM, Eirin-Lopez JM. Evolution of methyltransferase like (METTL) proteins in metazoa: A complex gene family involved in epitranscriptomic

(No. SZGSP001), the Postdoctoral Science Foundation of China (No. 2020M673065) and Guangzhou Development Zone entrepreneurship leading talent project (No: 2017-L153).

## Acknowledgments

Thanks to Shanghai Outdo Biotech Company for donating commercial tissue chip.

## Conflict of interest

The authors declare that the research was conducted in the absence of any commercial or financial relationships that could be construed as a potential conflict of interest.

## Publisher's note

All claims expressed in this article are solely those of the authors and do not necessarily represent those of their affiliated organizations, or those of the publisher, the editors and the reviewers. Any product that may be evaluated in this article, or claim that may be made by its manufacturer, is not guaranteed or endorsed by the publisher.

## Supplementary material

The Supplementary Material for this article can be found online at: <https://www.frontiersin.org/articles/10.3389/fimmu.2022.926461/full#supplementary-material>

regulation and other epigenetic processes. *Mol Biol Evol* (2021) 38:5309–27. doi: 10.1093/molbev/msab267

- Li X, Tang J, Huang W, Wang F, Li P, Qin C, et al. The M6A methyltransferase METTL3: acting as a tumor suppressor in renal cell carcinoma. *Oncotarget* (2017) 8:96103–16. doi: 10.18632/oncotarget.21726
- Cai G, Sun M, Li X, Zhu J. Construction and characterization of rectal cancer-related lncRNA-mRNA ceRNA network reveals prognostic biomarkers in rectal cancer. *IET Syst Biol* (2021) 15:192–204. doi: 10.1049/syb2.12035
- Li T, Fu J, Zeng Z, Cohen D, Li J, Chen Q, et al. TIMER2.0 for analysis of tumor-infiltrating immune cells. *Nucleic Acids Res* (2020) 48:W509–w514. doi: 10.1093/nar/gkaa407
- Győrffy B. Survival analysis across the entire transcriptome identifies biomarkers with the highest prognostic power in breast cancer. *Comput Struct Biotechnol J* (2021) 19:4101–9. doi: 10.1016/j.csbj.2021.07.014
- Zhang Q, Liu W, Zhang HM, Xie GY, Miao YR, Xia M, et al. hTFtarget: A comprehensive database for regulations of human transcription factors and their targets. *Genomics Proteomics Bioinf* (2020) 18:120–8. doi: 10.1016/j.gpb.2019.09.006
- Vasaikar SV, Straub P, Wang J, Zhang B. LinkedOmics: analyzing multi-omics data within and across 32 cancer types. *Nucleic Acids Res* (2018) 46:D956–d963. doi: 10.1093/nar/gkx1090
- Tang Z, Kang B, Li C, Chen T, Zhang Z. GEPIA2: an enhanced web server for large-scale expression profiling and interactive analysis. *Nucleic Acids Res* (2019) 47:W556–w560. doi: 10.1093/nar/gkz430
- Chandrashekhar DS, Bashel B, Balasubramanya SAH, Creighton CJ, Ponce-Rodriguez I, Chakravarthi B, et al. UALCAN: A portal for facilitating tumor subgroup gene expression and survival analyses. *Neoplasia (New York N.Y.)* (2017) 19:649–58. doi: 10.1016/j.neo.2017.05.002
- Binnewies M, Mujal AM, Pollack JL, Combes AJ, Hardison EA, Barry KC, et al. Unleashing type-2 dendritic cells to drive protective antitumor CD4(+) T cell immunity. *Cell* (2019) 177:556–571.e16. doi: 10.1016/j.cell.2019.02.005
- Tanaka A, Sakaguchi S. Regulatory T cells in cancer immunotherapy. *Cell Res* (2017) 27:109–18. doi: 10.1038/cr.2016.151
- Siegel RL, Miller KD, Jemal A. Cancer statistics, 2019. *CA: Cancer J Clin* (2019) 69:7–34. doi: 10.3322/caac.21551
- Anker J, Miller J, Taylor N, Kyprianou N, Tsao CK. From bench to bedside: How the tumor microenvironment is impacting the future of immunotherapy for renal cell carcinoma. *Cells* (2021) 10:3231. doi: 10.3390/cells10113231
- Barata PC, Rini BI. Treatment of renal cell carcinoma: Current status and future directions. *CA: Cancer J Clin* (2017) 67:507–24. doi: 10.3322/caac.21411
- Chehراzi-Raffle A, Meza L, Alcantara M, Dizman N, Bergerot P, Salgia N, et al. Circulating cytokines associated with clinical response to systemic therapy in metastatic renal cell carcinoma. *J Immunother Cancer* (2021) 9:e002009. doi: 10.1136/jitc-2020-002009
- Binnewies M, Roberts EW, Kersten K, Chan V, Fearon DF, Merad M, et al. Understanding the tumor immune microenvironment (TIME) for effective therapy. *Nat Med* (2018) 24:541–50. doi: 10.1038/s41591-018-0014-x
- Singer K, Cheng WC, Kreutz M, Ho PC, Siska PJ. Immunometabolism in cancer at a glance. *Dis Models Mech* (2018) 11:dmm034272. doi: 10.1242/dmm.034272
- Fyfe G, Fisher RI, Rosenberg SA, Sznol M, Parkinson DR, Louie AC. Results of treatment of 255 patients with metastatic renal cell carcinoma who received high-dose recombinant interleukin-2 therapy. *J Clin Oncol* (1995) 13:688–96. doi: 10.1200/JCO.1995.13.3.688
- Fishman M, Dutcher JP, Clark JI, Alva A, Miletello GP, Curti B, et al. Overall survival by clinical risk category for high dose interleukin-2 (HD IL-2) treated patients with metastatic renal cell cancer (mRCC): data from the PROCLAIM(SM) registry. *J Immunother Cancer* (2019) 7:84. doi: 10.1186/s40425-019-0567-3
- Escudier B, Pluzanska A, Koralewski P, Ravaud A, Bracarda S, Szczylak C, et al. Bevacizumab plus interferon alfa-2a for treatment of metastatic renal cell carcinoma: a randomised, double-blind phase III trial. *Lancet* (2007) 370:2103–11. doi: 10.1016/S0140-6736(07)61904-7
- Braun DA, Bakouny Z, Hirsch L, Flippot R, Van Allen EM, Wu CJ, et al. Beyond conventional immune-checkpoint inhibition - novel immunotherapies for renal cell carcinoma. *Nat Rev Clin Oncol* (2021) 18:199–214. doi: 10.1038/s41571-020-00455-z
- Díaz-Montero CM, Rini BI, Fink JH. The immunology of renal cell carcinoma. *Nat Rev Nephrol* (2020) 16:721–35. doi: 10.1038/s41581-020-0316-3
- Chen X, Xu M, Xu X, Zeng K, Liu X, Pan B, et al. METTL14-mediated N6-methyladenosine modification of SOX4 mRNA inhibits tumor metastasis in colorectal cancer. *Mol Cancer* (2020) 19:106. doi: 10.1186/s12943-020-01220-7
- Wang M, Liu J, Zhao Y, He R, Xu X, Guo X, et al. Upregulation of METTL14 mediates the elevation of PERP mRNA N(6) adenosine methylation promoting the growth and metastasis of pancreatic cancer. *Mol Cancer* (2020) 19:130. doi: 10.1186/s12943-020-01249-8
- Adelaja A, Taylor B, Sheu KM, Liu Y, Luecke S, Hoffmann A. Six distinct NF $\kappa$ B signaling codons convey discrete information to distinguish stimuli and enable appropriate macrophage responses. *Immunity* (2021) 54:916–30.e7. doi: 10.1016/j.jimmuni.2021.04.011
- Li C, Xue VW, Wang QM, Lian GY, Huang XR, Lee TL, et al. The Mincle/Syk/NF- $\kappa$ B signaling circuit is essential for maintaining the protumoral activities of tumor-associated macrophages. *Cancer Immunol Res* (2020) 8:1004–17. doi: 10.1158/2326-6066.CIR-19-0782
- Zhang J, Wu T, Simon J, Takada M, Saito R, Fan C, et al. VHL substrate transcription factor ZHX2 as an oncogenic driver in clear cell renal cell carcinoma. *Sci (New York N.Y.)* (2018) 361:290–5. doi: 10.1126/science.aap841



## OPEN ACCESS

## EDITED BY

Mercedes Beatriz Fuertes,  
CONICET Instituto de Biología y  
Medicina Experimental (IBYME),  
Argentina

## REVIEWED BY

Julien Faget,  
El Colegio de la Frontera Sur, Mexico  
Xiao Li,  
Nanjing Medical University, China

## \*CORRESPONDENCE

Qian Pei  
peiqian1221@csu.edu.cn

## SPECIALTY SECTION

This article was submitted to  
Cancer Immunity  
and Immunotherapy,  
a section of the journal  
Frontiers in Immunology

RECEIVED 06 July 2022

ACCEPTED 29 September 2022

PUBLISHED 18 October 2022

## CITATION

Wang X, Cheng W, Zeng X, Dou X,  
Zhou Z and Pei Q (2022) EPSTI1 as an  
immune biomarker predicts the  
prognosis of patients with stage III  
colon cancer.  
*Front. Immunol.* 13:987394.  
doi: 10.3389/fimmu.2022.987394

## COPYRIGHT

© 2022 Wang, Cheng, Zeng, Dou, Zhou  
and Pei. This is an open-access article  
distributed under the terms of the  
[Creative Commons Attribution License  
\(CC BY\)](#). The use, distribution or  
reproduction in other forums is  
permitted, provided the original  
author(s) and the copyright owner(s)  
are credited and that the original  
publication in this journal is cited, in  
accordance with accepted academic  
practice. No use, distribution or  
reproduction is permitted which does  
not comply with these terms.

# EPSTI1 as an immune biomarker predicts the prognosis of patients with stage III colon cancer

Xitao Wang<sup>1,2,3</sup>, Wei Cheng<sup>1</sup>, Xingzhi Zeng<sup>5</sup>, Xiaolin Dou<sup>4</sup>,  
Zhongyi Zhou<sup>4</sup> and Qian Pei<sup>2,3,4\*</sup>

<sup>1</sup>Department of Hepatobiliary Surgery, Hunan Provincial People's Hospital, The First Affiliated Hospital of Hunan Normal University, Changsha, China, <sup>2</sup>Key Laboratory of Molecular Radiation Oncology Hunan Province, Changsha, China, <sup>3</sup>National Clinical Research Center for Geriatric Disorders, Xiangya Hospital, Central South University, Changsha, China, <sup>4</sup>Department of General Surgery, Xiangya Hospital, Central South University, Changsha, China, <sup>5</sup>Department of General Surgery, The First Affiliated Hospital of Shaoyang University, Shaoyang, China

**Objective:** The poor prognosis and heterogeneity of stage III colon cancer (CC) suggest the need for more prognostic biomarkers. The tumor microenvironment (TME) plays a crucial role in tumor progression. We aimed to explore novel immune infiltration-associated molecules that serve as potential prognostic and therapeutic targets.

**Methods:** TME immune scores were calculated using "TMEscore" algorithm. Differentially expressed genes between the high and low TME immune score groups were identified and further investigated through a protein-protein interaction network and the Molecular Complex Detection algorithm. Cox regression, meta-analysis and immunohistochemistry were applied to identify genes significantly correlated with relapse-free survival (RFS). We estimated immune infiltration using three different algorithms (TIMER 2.0, CIBERSORTx, and TIDE). Single-cell sequencing data were processed by Seurat software.

**Results:** Poor RFS was observed in the low TME immune score groups (log-rank  $P < 0.05$ ). EPSTI1 was demonstrated to be significantly correlated with RFS ( $P < 0.05$ ) in stage III CC. Meta-analysis comprising 547 patients revealed that EPSTI1 was a protective factor (HR = 0.79, 95% CI, 0.65–0.96;  $P < 0.05$ ). More immune infiltrates were observed in the high EPSTI1 group, especially M1 macrophage and myeloid dendritic cell infiltration ( $P < 0.05$ ).

**Conclusion:** The TME immune score is positively associated with better survival outcomes. EPSTI1 could serve as a novel immune prognostic biomarker for stage III CC.

## KEYWORDS

colon cancer, immune infiltration, single-cell sequencing, EPSTI1, prognostic marker

## Introduction

Colorectal cancer is the third most common malignant disease and the second leading cause of cancer death in the world, with approximately 1.93 million new cases and 930,600 related deaths in 2020 (1). Tumor-node-metastasis (TNM) staging remains the key determinant of colorectal cancer prognosis and therapy. In patients with localized colon cancer (CC), the 5-year overall survival (OS) is 99% and 70% for stage I and II CC, respectively, versus only 45–65% for stage III patients (2). However, an increasing number of reports have demonstrated the wide variability of survival outcomes in stage III CC according to T and N sub-stages (3), possibly reflecting tumor heterogeneity. Prognostic assessment in stage III CC could be refined by using validated biomarkers beyond the TNM classification system.

The molecular features and prognostic value of the tumor immune microenvironment have been extensively reported in various cancer types (4, 5). The colon harbors a large number of diverse immune cells to maintain gut homeostasis. In CC, however, these cells lose their tight and well-organized modulation (6). It was found that *in-situ* immune cell infiltration in CC is associated with favorable survival (7, 8) and that reduced immune cytotoxicity and lack of T-cell infiltration in CC predict adverse outcomes (9, 10), suggesting that the tumor microenvironment (TME) might be a promising source of novel diagnostic and prognostic biomarkers.

Immunohistochemistry (IHC) and fluorescence-activated cell sorting (FACS) have long been the primary methods for assessing tumor-infiltrating immune populations. Due to the limited number of immune markers that can be measured simultaneously, these two conventional methods are incapable of demonstrating a comprehensive landscape of diverse immune cell infiltrates and do not provide sufficient resolution to discriminate closely related immune cell clusters. Recent studies have revealed that the number of various infiltrating immune cell types in a specimen can be inferred from gene expression patterns specific or abundant to a particular cell type (11, 12). Remarkably, based on accumulating transcriptomic data, several computational algorithms have been established to evaluate large-scale immune landscapes (13, 14, 15).

Based on the transcriptome data, we categorized stage III CC patients from two independent cohorts into high and low TME immune score groups. Consistent with previous studies, better survival was observed in patients with higher TME immune scores. Additional results from various public datasets confirmed that EPSTI1 was differentially expressed between the high and low TME immune score groups and that its expression was significantly associated with relapse-free survival (RFS) in patients with stage III CC. To our knowledge, few investigations have explored EPSTI1's role in the tumor immunity of stage III CC. In this study, we revealed that more immune infiltrates, especially M1 macrophages and myeloid

dendritic cells (mDCs), were found in tumors with higher EPSTI1 expression. The association between EPSTI1 and the above two immune cell types was further validated by single-cell RNA sequencing analysis, suggesting that EPSTI1, as an immune biomarker, could predict the RFS in stage III CC.

## Materials and methods

### Data source

We systematically searched publicly available colon cancer datasets. Studies with no survival or TNM staging information were removed from further assessment. Five cohorts with bulk sequencing (TCGA-COAD, GSE39582, GSE37892, GSE17538, GSE14333) and one single-cell sequencing dataset (GSE178341) were enrolled. The RNA sequencing and clinical data of GSE39582, GSE37892, GSE17538, GSE14333 and GSE178341 were downloaded from the medics Gene Expression Omnibus (GEO, <https://www.ncbi.nlm.nih.gov/geo/>). Gene expression data and corresponding clinical information from The Cancer Genome Atlas (TCGA) colon cancer project were downloaded from the UCSC Xena browser (<https://xenabrowser.net/datapages/>).

Mutation data of the TCGA-COAD cohort were downloaded from the National Cancer Institute Genomic Data Commons (<https://gdc.cancer.gov/about-data/publications/mc3-2017>). Only TNM stage III CC patients in each dataset were included in this study. The above datasets were utilized in compliance with the ethical requirements of the GEO and TCGA projects. The study was conducted in accordance with the Declaration of Helsinki.

### Identification and verification of genes related to the TME immune score and RFS

We performed TME immune scoring for stage III CC patients in the GSE39582 and TCGA-COAD cohorts using R package “TMEscore”. The cut-off value of the TME immune score was selected by X-tile software (version 3.6.1, <https://medicine.yale.edu/lab/rimm/research/software/>). Based on the cut-off values, patients in both cohorts were divided into high and low TME immune score groups. We compared the difference in relapse-free survival (RFS) between the two groups using the Kaplan-Meier method. The receiver operating characteristic (ROC) curves were then plotted to assess the predictive power of the TME immune score for RFS. Genes with  $|\log_2 \text{Fold Change}| > 1$  and adjusted  $P$  value  $< 0.05$  were defined as differentially expressed genes (DEGs). The intersection of the DEGs from the GSE39582 and TCGA-COAD datasets was entered into the STRING database (<https://cn.string-db.org/>) to construct the

protein-protein interaction (PPI) network. The network was then imported into Cytoscape software (version 3.9.0, <https://cytoscape.org/>), and key gene modules were identified using the Molecular Complex Detection (MCODE) algorithm. Functional and pathway enrichment analysis of key gene modules were performed in the Metascape database (<https://metascape.org/gp/index.html#/main/step1>).

We then used univariate Cox regression analysis to identify genes significantly associated with RFS in the above key gene modules. The association between each gene and RFS was further assessed by meta-analysis combining the datasets GSE39582 (n = 206), TCGA-COAD (n = 128), GSE14333 (n = 81), GSE17538 (n = 75) and GSE37892 (n = 57). If robust heterogeneity was not observed ( $I^2 < 40\%$ ,  $P > 0.05$ ), the fixed-effects model was chosen to pool HRs from different cohorts. Otherwise, the random-effects model was selected.

## Gene mutation analysis

In the TCGA-COAD dataset, 113 patients with stage III CC had complete somatic mutation data. In contrast, only TP53, KRAS, BRAF and mismatch repair mutations were available in the GSE39582 dataset. We compared the mutations and the tumor mutation burden (TMB) between the high and low EPSTI1 groups in the TCGA-COAD cohort. We also analyzed the mutation status of TP53, KRAS, and BRAF and microsatellite stability in both groups.

## Inference of TME immune cell infiltration

To quantify the degree of immune cell infiltration in each stage III CC sample, we applied three widely accepted algorithms for evaluation: TIMER 2.0 (<http://timer.cistrome.org/>), TIDE (<http://tide.dfci.harvard.edu/>) and CIBERSORTx (<https://cibersortx.stanford.edu>). According to the algorithm instructions, we uploaded the prepared gene expression matrix into the web tool to obtain infiltration scores. Only the immune cell types detected in more than 50% of the samples were included in further analysis. In the CIBERSORTx estimation procedure, we ran the web tool with LM22 gene signatures and 1000 permutations.

## Single-cell RNA sequencing data analysis

We performed scRNA-seq analysis using the R package “Seurat” (version 4.1.0). Cells with less than 200 genes and more than 50% mitochondrial counts were excluded from the analysis. The expression matrix was then normalized using the “SCTransform” function, and the top 3000 highly variable genes were subjected to principal component analysis (PCA). We

constructed the shared nearest neighbor (SNN) graph and the uniform manifold approximation and projection (UMAP) embedding with the top 20 principal components. The identification of main cell types was consistent with the original literature. Based on the M1/M2 macrophage and pDC/mDC gene signatures summarized in the literature (see Table S3), we further subclustered the macrophages and DCs using the R package CellID (16). The proportion of cells in each subpopulation was then calculated. The expression of M1 versus M2 up- and down-regulated genes (17), and plasmacytoid cell type DC (pDC) versus mDC up- and down-regulated genes (18) were scored using the “AddModuleScore” function. The same function was also used to compute the activity scores of immune-related signaling pathways from the Broad Institute’s Hallmark collection.

## Statistical analysis

Patient groups or cell groups were compared using Welch’s t-test if the continuous variables were normally distributed; otherwise, the Mann-Whitney U test was applied. Categorical variables were compared using the chi-square test. We plotted survival curves using the Kaplan-Meier method and used the log-rank test to compare survival differences. The predictive validity of the model was quantified by the area under the ROC curve (AUC). For correlation analysis, we calculated Pearson or Spearman correlation coefficients as indicated. A  $P$  value  $< 0.05$  was considered significant. All statistical analyses were performed using R software (version 4.1.0).

## Results

### TME immune score predicts the RFS of stage III CC patients

To investigate the relationship between the tumor immune microenvironment and RFS in stage III CC patients, we applied the TMEscore model to perform immune scoring in the GSE39582 (n = 206) and TCGA-COAD (n = 128) cohorts. The cut-off value of the TME immune score in each cohort was determined by X-tile software, and the patients were then divided into high- and low-immune score groups (Table S1). According to the cut-off value, 103 patients in the GSE38582 cohort were assigned to the high immune score group, and the remaining 103 patients were assigned to the low immune score group. In the TCGA-COAD cohort, the numbers were 82 and 46, respectively. The high and low TME score groups had different distribution features on the PCA dimensionality reduction map, reflecting the difference in the expression of immune-related genes between the two groups (Figures 1 A, D). In both cohorts, the Kaplan-Meier survival curves showed that

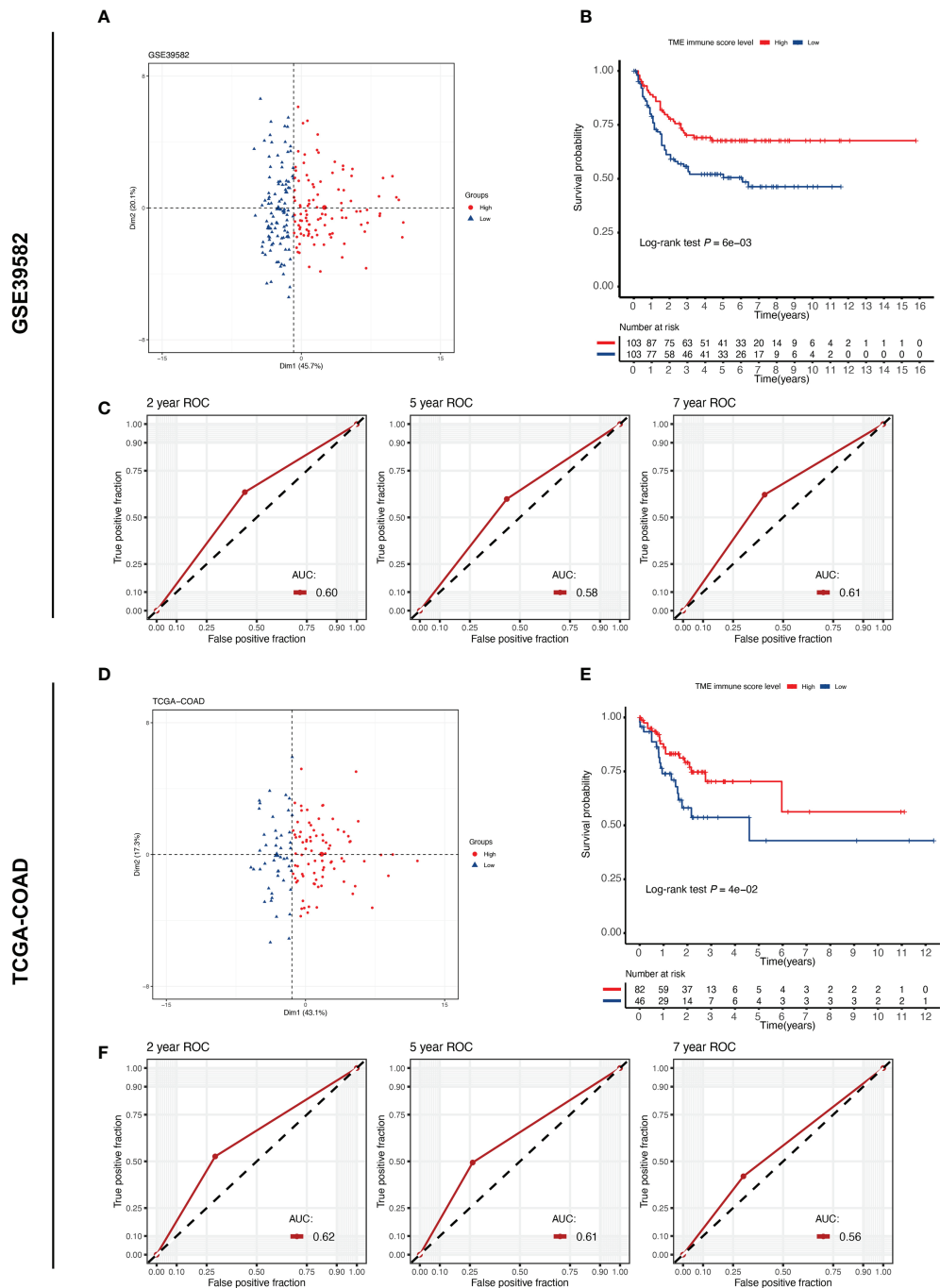


## FIGURE 1

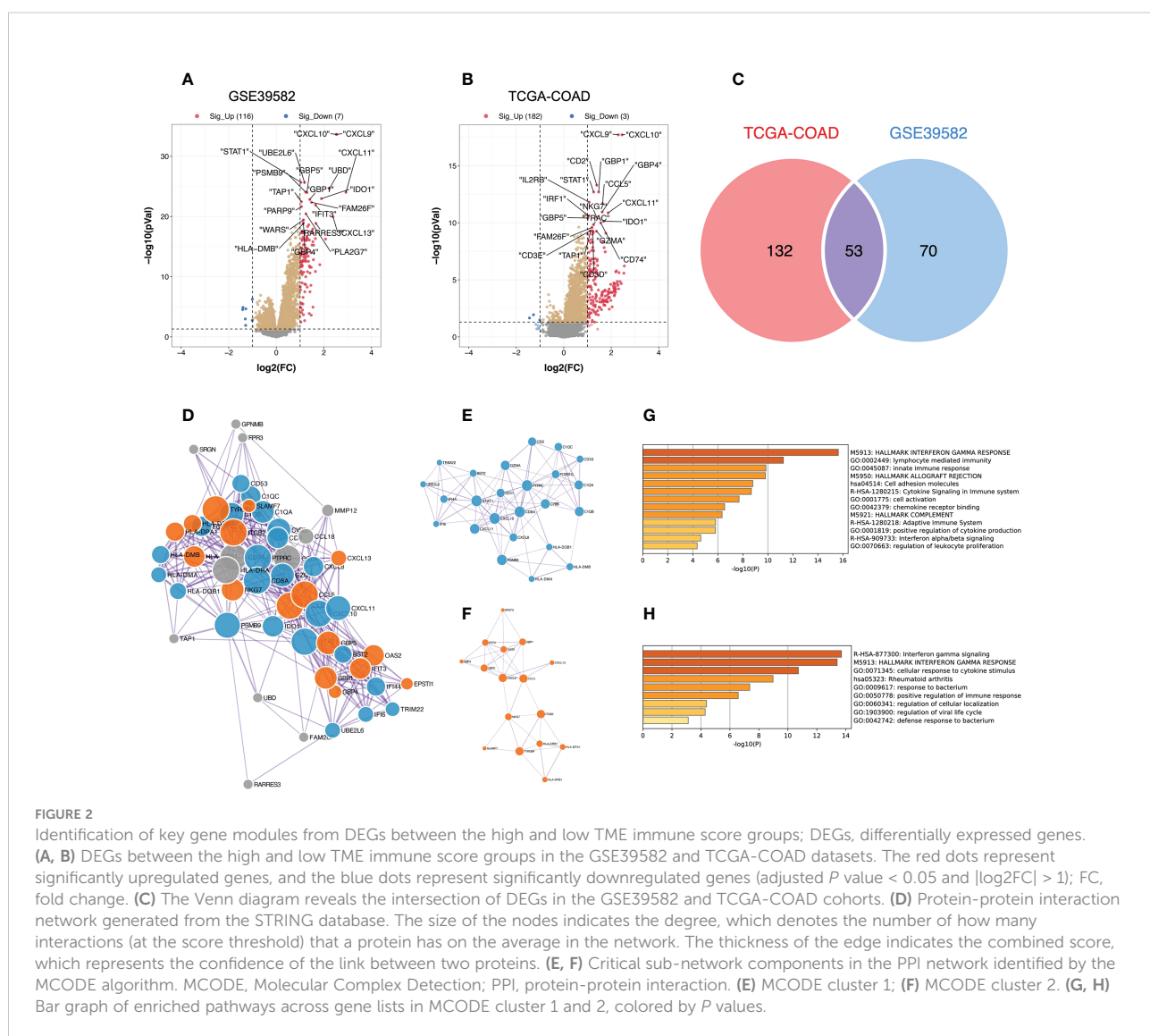
TME immune score correlates with the prognosis of patients with stage III CC. TME, tumor microenvironment. **(A, D)** PCA plot reveals different expression patterns of TME immune score-related genes in different groups of stage III CC patients from the GSE39582 and TCGA-COAD cohorts. **(B, E)** Kaplan–Meier curves of relapse-free survival according to TME immune score levels in the GSE39582 and TCGA-COAD cohorts. Stage III CC patients with high TME immune scores have a better prognosis (log-rank test  $P < 0.05$ ) in both datasets. **(C, F)** The time-dependent ROC curves measuring the predictive power of the TME immune score on 2-, 5-, and 7-year RFS in the GSE39582 and TCGA-COAD datasets. RFS, relapse-free survival.

RFS was significantly worse in the low-immune score group (Figures 1 B, E; log-rank  $P = 0.006$  in GSE39582, log-rank  $P = 0.04$  in TCGA-COAD). To measure the predictive performance of the TMEscore model, we calculated the time-dependent AUC values for both cohorts at 2, 5 and 7 years. The AUCs at these time points were 0.60, 0.58 and 0.61 in the GSE39582 cohort, while they were 0.62, 0.61 and 0.56 in the TCGA-COAD cohort (Figures 1C, F). These results suggest that the TME immune score can predict RFS in patients with stage III CC.

## Identification of key gene modules associated with TME immune score

We then analyzed the DEGs between the different TME immune scoring groups in the GSE39582 and TCGA-

COAD datasets. Compared to the low TME immune score group, patients in the high TME immune score group had 116 genes that were significantly upregulated and 7 genes that were significantly downregulated in GSE39582 (Figures 2A, Table S2), while 182 genes were upregulated and 3 genes were downregulated in the high immune score group in TCGA-COAD (Figure 2B). We then intersected the DEGs from the two cohorts to obtain 53 common genes (Figure 2C). By entering these genes into the STRING database, we constructed a protein-protein interaction network (Figure 2D). The minimum required interaction score was set as medium confidence (0.400). The PPI network was then imported into Cytoscape software, and two key gene modules were identified by the MCODE algorithm: MCODE cluster 1 contained 24 genes (Figure 2E), while MCODE cluster 2 contained 16 genes (Figure 2F). The enrichment analysis suggests that these genes are mainly related to human



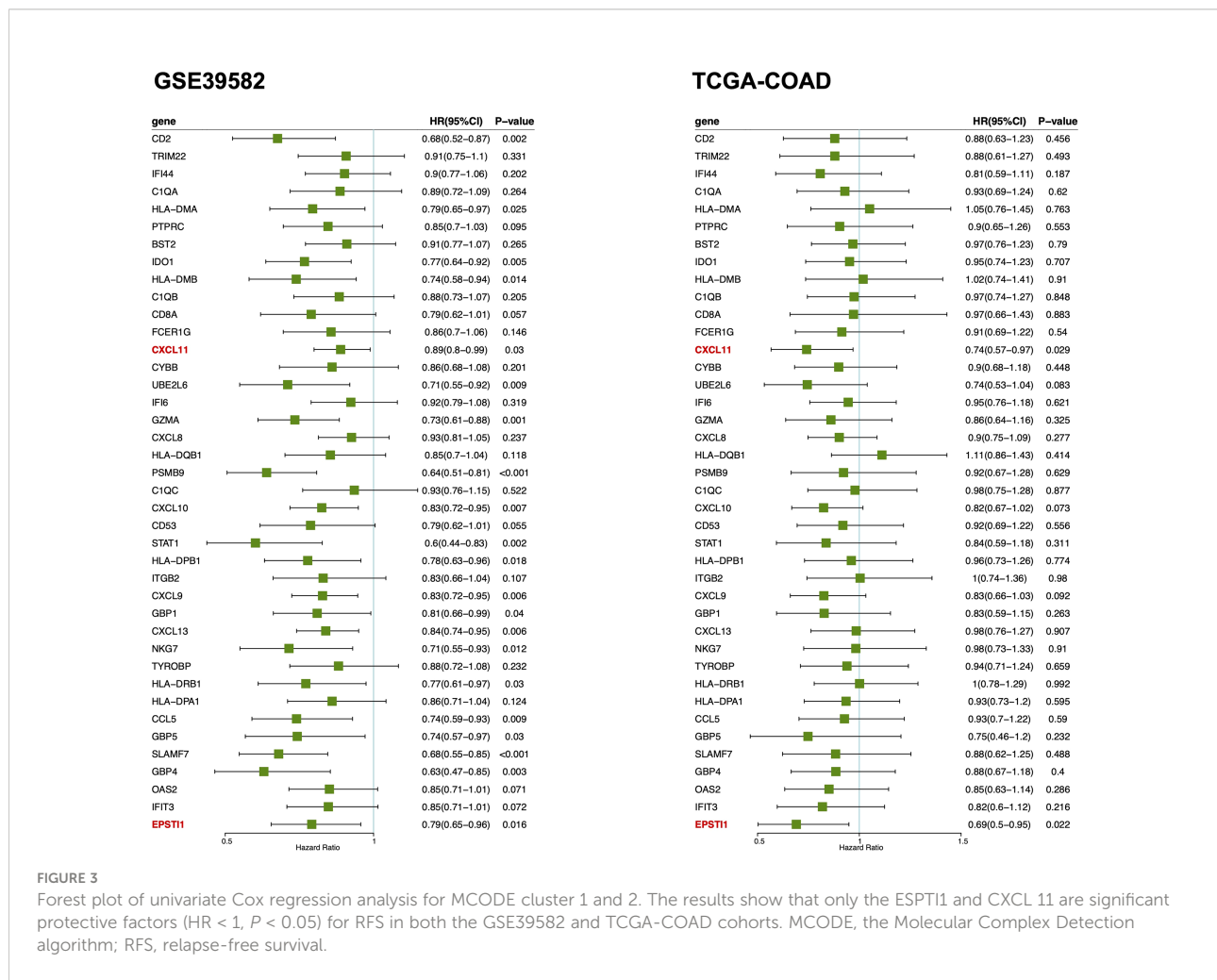
immune function, particularly the interferon gamma signaling pathway (Figure 2G, H).

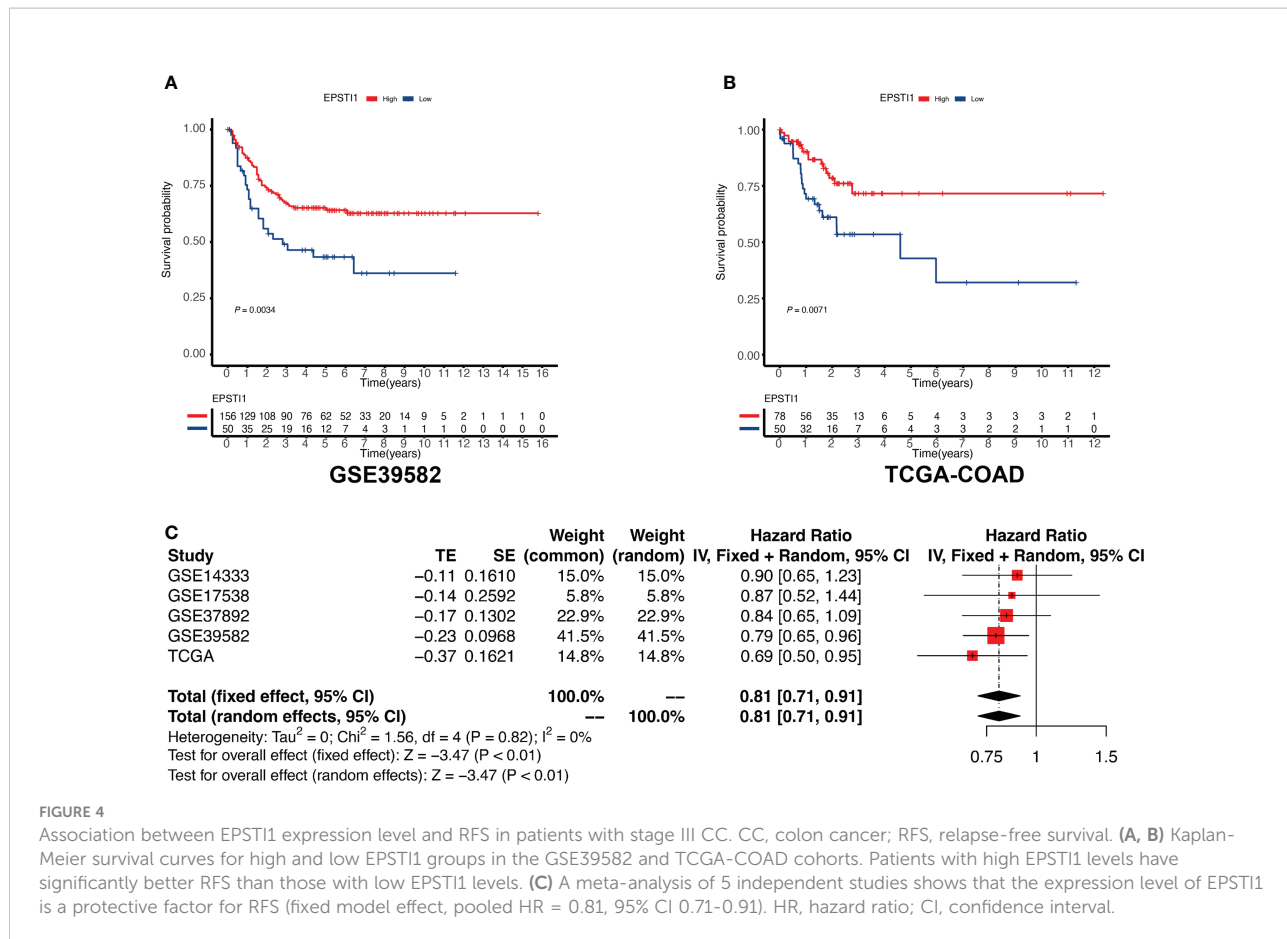
## Genes associated with TME immune scores and RFS

Survival analysis was performed *via* univariate Cox regression to identify a subset of genes closely related to RFS in the MCODE clusters. The results revealed that only EPSTI1 and CXCL11 were significantly associated with RFS in both the GSE39582 and TCGA-COD cohorts (Figure 3). In GSE39582, the hazard ratios (HRs) for EPSTI1 and CXCL11 were 0.79 (95% CI, 0.65-0.96;  $P < 0.05$ ) and 0.89 (95% CI, 0.80-0.99;  $P < 0.05$ ), respectively. In TCGA-COAD, the HRs for the two genes were 0.69 (95% CI, 0.50-0.95;  $P < 0.05$ ) and 0.74 (95% CI, 0.57-0.97;  $P < 0.05$ ), respectively. Using X-tile software, we determined the cut-off values for EPSTI1 and CXCL11 expression levels, respectively, and divided patients in the GSE39582 and TCGA-COAD cohorts into groups with high and low

expression levels of the corresponding genes. Kaplan-Meier survival curves showed that the high EPSTI1 group had prolonged RFS (Figure 4A, B;  $P < 0.05$ ), and the high CXCL11 group also had a better prognosis (Supplementary Figure 1A, B;  $P < 0.05$ ). To further confirm the relationship between these two genes and RFS in patients with stage III CC, 547 patients from five datasets, GSE39582 ( $n = 206$ ), TCGA-COAD ( $n = 128$ ), GSE14333 ( $n = 81$ ), GSE17538 ( $n = 75$ ) and GSE37892 ( $n = 57$ ), were subjected to meta-analysis. No significant heterogeneity was observed among these datasets ( $I^2 < 40\%$ ,  $P > 0.05$ ), and thus, the fixed effects model was selected for the meta-analysis. The pooled HRs of EPSTI1 and CXCL11 were 0.81 (95% CI, 0.71-0.91) and 0.92 (95% CI, 0.86-0.98), respectively (Figure 4C; Supplementary Figure 1C). These results suggest that high levels of EPSTI1 and CXCL11 expression in stage III CC are significantly associated with prolonged RFS.

To date, a wide range of studies have explored the role of CXCL11 in antitumor immunity in diverse tumors, including CC (19, 20). However, the role of EPSTI1 in antitumor immunity in CC has not yet been reported. Therefore, in the





following analysis, we focused on the association of EPSTI1 with the immune microenvironment of CC and its impact on RFS.

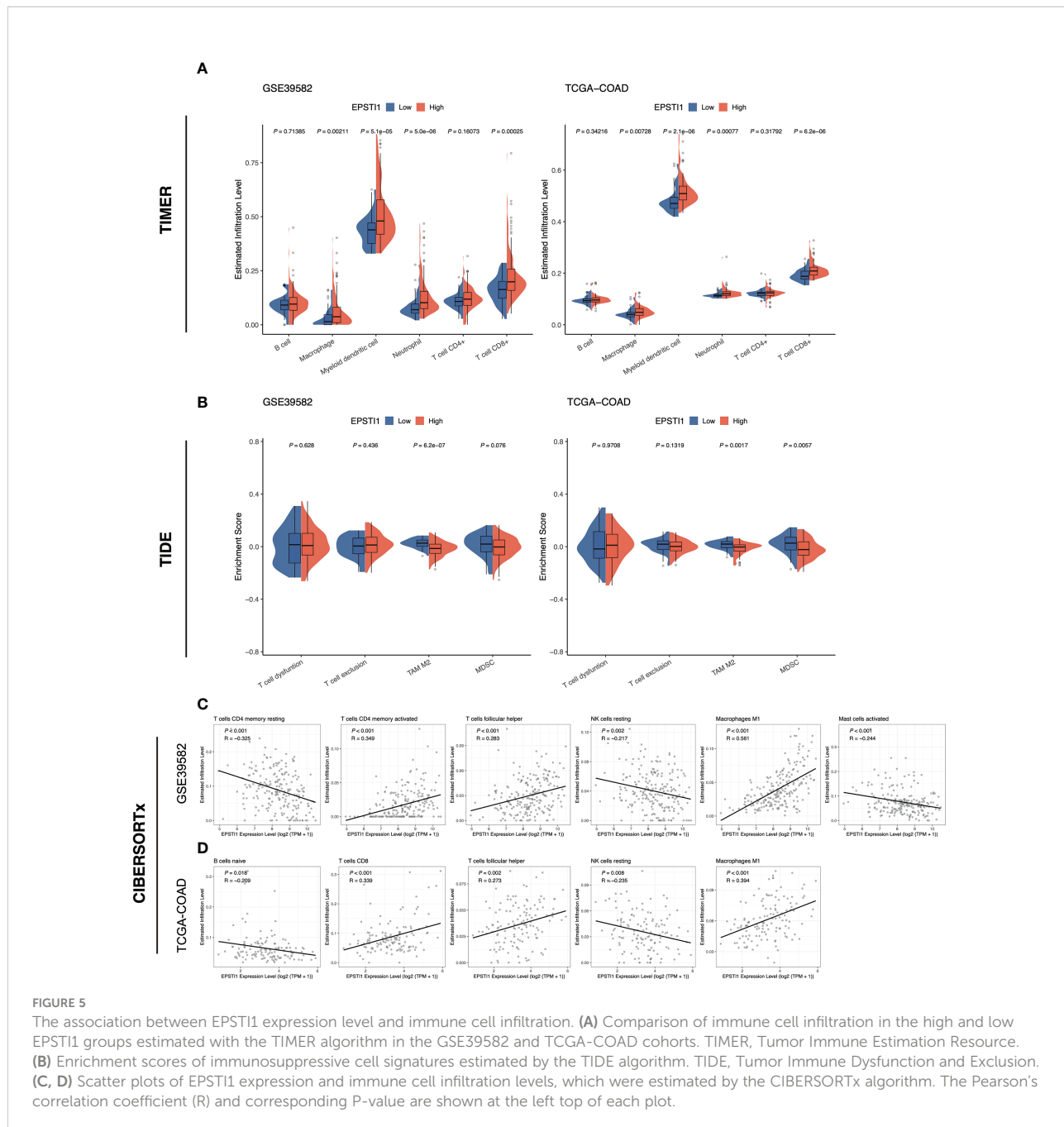
### Mutations in the high and low EPSTI1 groups

The top 20 mutated genes in the high and low EPSTI1 groups from the TCGA-COAD are illustrated in Supplementary Figure 2A. Although the mean TMB was greater in the high EPSTI1 group, there was no significant difference between the two groups (Supplementary Figure 2B;  $P > 0.05$ ). The mutation rate of TP53 exceeded 50% in both groups, but no significant difference was observed (Supplementary Figures 2C, D). The proportions of patients with BRAF mutation or microsatellite instability were also not significantly different between the two groups (Supplementary Figures 2C, D). In the GSE39582 cohort, the KRAS mutation rate in the high EPSTI1 group was 37%, which was significantly lower than the 61% rate in the low EPSTI group (Supplementary Figure 2D). Although the KRAS mutation rate in the high EPSTI1 group was still smaller than that in the low EPSTI group in the TCGA-COAD cohort (33%

vs. 41%), the difference was not statistically significant (Supplementary Figure 2C).

### Association between EPSTI1 and immune infiltrates

In this study, we evaluated immune infiltration in tumor tissue based on bulk RNA-seq data using three different approaches, including TIMER 2.0, TIDE and CIBERSORTx. TIMER 2.0 analysis demonstrated that macrophages, myeloid dendritic cells, neutrophils and CD8 T cells were more abundantly infiltrated in the high EPSTI1 group (Figure 5A;  $P < 0.05$ ). TIDE found significantly lower infiltration abundance of M2 tumor-associated macrophages (TAM) in the high EPSTI1 group in both cohorts when assessing immunosuppressive cells (Figure 5B;  $P < 0.05$ ). For MDSCs, the infiltration abundance was significantly lower in the high EPSTI1 group in the TCGA-COAD cohort (Figure 5B;  $P < 0.05$ ). In the GSE39582 cohort, the difference was only marginally significant (Figure 5B;  $P = 0.076$ ), although the high EPSTI1 group still had a smaller infiltration abundance than the low EPSTI1 group. The CIBERSORTx algorithm calculates the infiltration status of 22



types of immune cells. In this study, we excluded a cell type if its infiltrative abundance was calculated to be zero in more than 50% of the samples. Pearson correlation analysis revealed that in the GSE39582 cohort, EPSTI1 expression was positively correlated with the infiltration of memory activated CD4 T cells, follicular helper T cells, and M1 macrophages (Figure 5C;  $R > 0.2$ ,  $P < 0.05$ ), and negatively correlated with the infiltration of resting memory CD4 T cells, resting NK cells and activated mast cells (Figure 5C;

$R < -0.2$ ,  $P < 0.05$ ). In the TCGA-COAD cohort, EPSTI1 expression was positively correlated with the infiltration of CD8 T cells, follicular helper T cells and M1 macrophages (Figure 5D;  $R > 0.2$ ,  $P < 0.05$ ), and negatively correlated with the infiltration of naive B cells and resting NK cells (Figure 5D;  $R < -0.2$ ,  $P < 0.05$ ). Notably, M1 macrophages displayed a strong correlation with EPSTI1 expression in both cohorts ( $R = 0.561$  in GSE39582;  $R = 0.394$  in TCGA-COAD).

## Expression of EPSTI1 at the single-cell level

In the bulk RNA-seq datasets above, EPSTI1 was closely associated with immune infiltrates. To further investigate the relationship between EPSTI1 and tumor immune cells, we analyzed 32 stage III CC patients from the single-cell dataset GSE178341. According to the quality control criteria in the original literature, we obtained 114,928 cells from CC tissues. Cell types were identified with reference to the original paper. From the EPSTI1 dimplot and dotplot (Figure 6A), we found that EPSTI1 was predominantly expressed in immune cells, both in terms of EPSTI1 expression levels and the proportion of EPSTI1-positive cells. Further sorting of immune cells revealed that macrophages and DCs were the main cell clusters expressing EPSTI1 (Figure 6B), similar to the immune infiltration analysis of the bulk RNA-seq datasets above.

Several studies have indicated that M1 macrophages exert tumor-preventing activities, whereas M2 macrophages are associated with immunosuppression (21, 22, 23). At the single-cell level, the ratio of EPSTI1<sup>+</sup> macrophages was significantly correlated with that of M1 macrophages ( $R = 0.405$ ,  $P = 0.022$ ; Figure 6C, Supplementary Figure 3A), which was consistent with the CIBERSORTx analysis of bulk sequencing described previously. Moreover, EPSTI1<sup>+</sup> macrophages scored significantly lower on the M2 but significantly higher on the M1 signature modules (Figures 6D, E;  $P < 0.05$ ). In the scoring of cell signaling pathway activity, EPSTI1<sup>+</sup> macrophages had a higher mean score for immune-related signaling pathways (Figure 6F), showing a different function pattern from EPSTI1<sup>-</sup> macrophages.

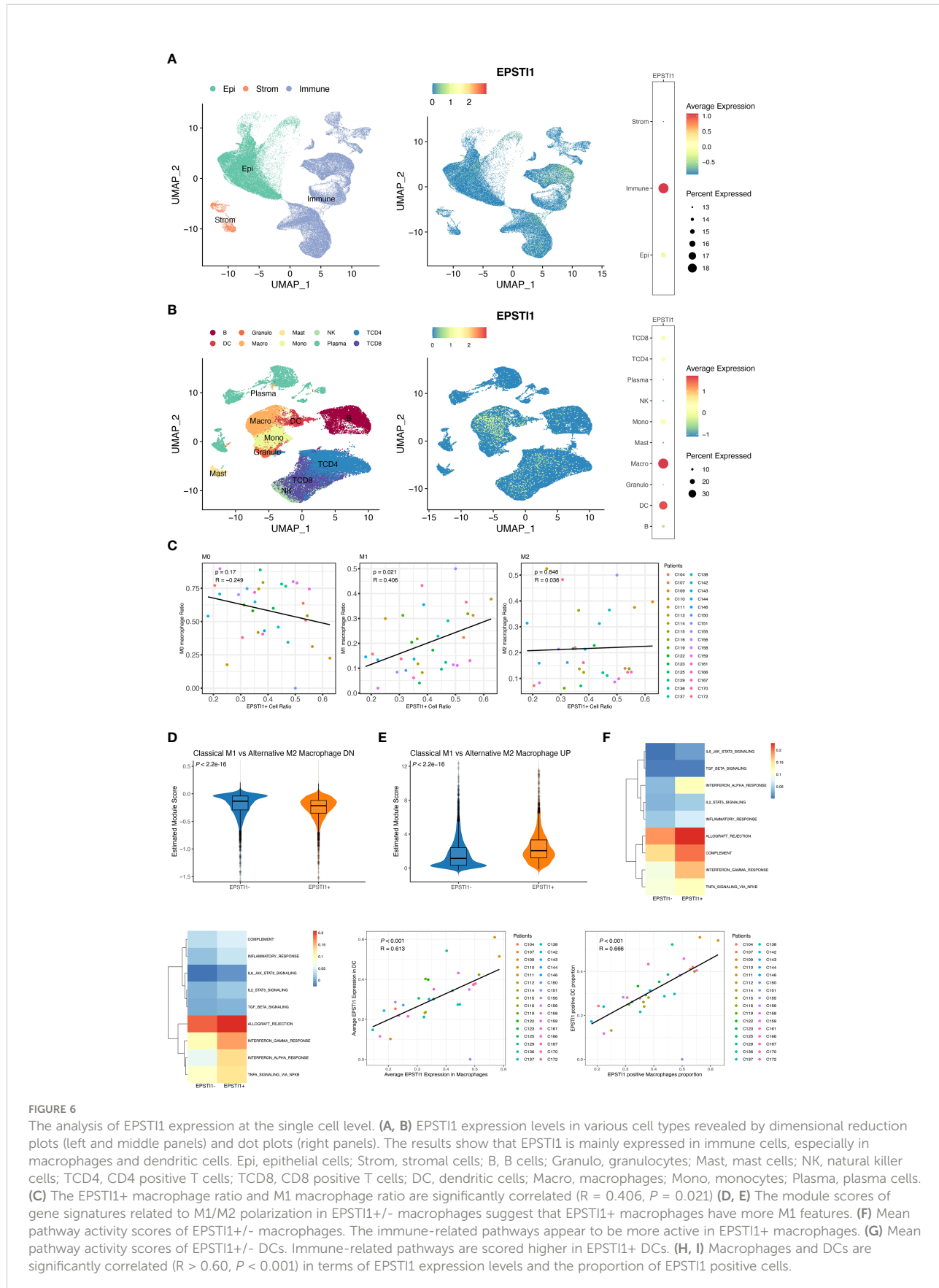
DCs were another major cell cluster that expressed EPSTI1 in our study. By origin, DCs can be classified into mDCs, which are derived from common myeloid progenitors (CMPs) that also produce macrophages, and pDCs, which are derived from common lymphocyte progenitors (CLPs) that also produce B cells, T cells and NK cells. Although the proportion of EPSTI1<sup>+</sup> DCs was positively correlated with that of mDCs without statistical significance ( $R = 0.302$ ,  $P = 0.093$ ; Supplementary Figure 3B, C), EPSTI1<sup>+</sup> DCs had significantly lower pDC but higher mDC feature scores (Supplementary Figures 3D, E;  $P < 0.05$ ). Similar to EPSTI1<sup>+</sup> macrophages, the mean scores of immune-related signaling pathways were higher in EPSTI1<sup>+</sup> DCs (Figure 6G). The association between DCs and macrophages in EPSTI1 expression was also inspected by Pearson correlation analysis. In the 32 patients with stage III CC in GSE178341, macrophages and DCs were significantly correlated ( $R > 0.6$ ,  $P < 0.05$ ), both in terms of the average level of EPSTI1 expression and the proportion of EPSTI1<sup>+</sup> cells (Figures 6H, I).

## Discussion

The immunocyte infiltration has received extensive attention for its important role in both tumor prognosis and therapy (24, 25). In our study, patients with a high TME immune score, which reflects immunocyte infiltration, experienced better RFS. The result was consistent with previous reports using Immunoscore calculated by assessing CD3 and CD8 immunohistochemical staining both in the tumor center and invasive margin (26). To explore more potential molecules associated with both immunocyte infiltration and prognosis, we compared the DEGs between the high and low TME immune score groups and screened out EPSTI1 and CXCL11. However, CXCL11 has been included in the TME immune score algorithm and widely investigated in various cancers, including colon cancer (20, 27). EPSTI1, initially identified as an induced gene in a three-dimensional tumor environment assay (28), was reported to promote epithelial-mesenchymal transition (EMT) and tumor metastasis in breast cancer (29, 30, 31). Its significance in colon cancer, especially its participation in the immune response, has not been well explored.

To further confirm the prognostic significance of EPSTI1 in stage III CC, we explored the relationship between RFS and EPSTI1 expression in a meta-analysis including more than 500 patients in 5 datasets at the mRNA level. The results indicated that high expression of EPSTI1 was significantly associated with better RFS. Analysis of the single-cell dataset further showed that the average expression of EPSTI1 was highest in immune cells.

The types and functions of infiltrative immune cells are various and complex. Analysis results from both bulk tissue and single-cell RNA sequencing revealed that the expression of EPSTI1 was significantly high in macrophages and DCs, especially classically activated M1 macrophages, playing roles in antitumor immunity (32, 33, 34). In our analysis of pathway activity assessment for macrophages and DCs, EPSTI1 was found to be associated with several immune-related pathways, such as interferon- $\gamma$  (IFN $\gamma$ ) response, interleukin-6 (IL6)-Jak-Stat3 signaling and tumor necrosis factor- $\alpha$  (TNF- $\alpha$ ) signaling activated by nuclear factor  $\kappa$ B (NF $\kappa$ B). M1 phenotypes of macrophages are usually polarized *via* IFN $\gamma$ , and subsequently release numerous cytokines (such as TNF- $\alpha$  and IL-6) and reactive oxygen/nitrogen species to realize the tumoricidal activity (35). An NF $\kappa$ B-dependent and IFN $\gamma$ -regulated gene network in mDCs promotes antigen presentation from dying tumor cells and the subsequent recruitment and activation of cytotoxic T cells (36). In Kim YH et al.'s research, EPSTI1 was found to be highly expressed in macrophages exposed to IFN $\gamma$  and lipopolysaccharide (LPS) and to modulate M1 polarization *via* the Stat1 and p65 pathways (37). Therefore, we speculate that EPSTI1 in the stage III CC exerts antitumor immunity and inhibits tumor progression by promoting macrophage and mDC infiltration, accelerating the M1 polarization of macrophages,



enhancing the antigen presentation ability of M1 macrophages and DCs and reinforcing subsequent tumor killing.

Apart from chemotherapy, radiotherapy and targeted therapy, immunotherapy has been emerging as another pillar for tumor treatment (38, 39). Although immune checkpoint blockers (ICBs), which primarily target cytotoxic T lymphocytes, are widely used in current clinical practice (40, 41), TAMs and DCs have also been favored and explored in recent decades. A variety of therapeutic strategies targeting TAMs and DCs are being tested in basic researches and clinical trials (42, 43, 44), for example, inhibiting mononuclear macrophage recruitment, TAM depletion and inhibition of activation, reprogramming TAMs and DC-based cancer vaccines. Correspondingly, a variety of relevant molecules are being targeted, for instance, blockade of CD47 to enhance the phagocytic abilities of antigen-presenting cells, inhibition of phosphoinositide 3-kinase  $\gamma$  (PI3K $\gamma$ ) to interrupt M2 polarization, and Toll-like receptor (TLR) agonists to induce M1 polarization. Considering the potential significance in macrophages and DCs, EPSTI1 deserves more in-depth research and might be another target for cancer immunotherapy.

In conclusion, the TME immune score is positively associated with better survival outcomes. EPSTI1 could serve as a novel immune prognostic biomarker for stage III CC.

## Data availability statement

The original contributions presented in the study are included in the article/[Supplementary Material](#). Further inquiries can be directed to the corresponding authors.

## Ethics statement

The studies involving human participants were reviewed and approved by The Institutional Review Board of Xiangya Hospital. The patients/participants provided their written informed consent to participate in this study.

## Author contributions

Conception and design: XW, ZZ, QP. Data acquisition: XW, QP. Data analysis/interpretation: XW, WC, XZ, XD, QP. Writing of original draft: XW, WC, ZZ, QP. All authors contributed to the article and approved the submitted version.

## Funding

This work was supported by China Postdoctoral Science Foundation: 2020M670103ZX; and the Construction of

Innovative Ability of National Clinical Research Center for Geriatric Disorders (no. 2019SK2335).

## Conflict of interest

The authors declare that the research was conducted in the absence of any commercial or financial relationships that could be construed as a potential conflict of interest.

## Publisher's note

All claims expressed in this article are solely those of the authors and do not necessarily represent those of their affiliated organizations, or those of the publisher, the editors and the reviewers. Any product that may be evaluated in this article, or claim that may be made by its manufacturer, is not guaranteed or endorsed by the publisher.

## Supplementary material

The Supplementary Material for this article can be found online at: <https://www.frontiersin.org/articles/10.3389/fimmu.2022.987394/full#supplementary-material>

### SUPPLEMENTARY FIGURE 1

Identification of RFS-related genes in MCODE cluster 1 and 2. (A) Forest plot of univariate Cox regression analysis for MCODE cluster 1 and 2. The results show that only the EPSTI1 and CXCL11 are protective factors (HR < 1,  $P < 0.05$ ) for RFS in both the GSE39582 and TCGA-COAD cohorts. MCODE, the Molecular Complex Detection algorithm; RFS, relapse-free survival. (B, C) Kaplan-Meier survival curves for high and low CXCL11 groups in the GSE39582 and TCGA-COAD cohorts. Patients with high CXCL11 levels have significantly better RFS than those with low CXCL11 levels. (D) A meta-analysis of 5 independent studies shows that the expression level of CXCL11 is a protective factor for RFS (fixed model effect, pooled HR = 0.92, 95% CI 0.86–0.98). HR, hazard ratio; CI, confidence interval.

### SUPPLEMENTARY FIGURE 2

Analyses of somatic mutation profiles in stage III CC patients. (A) Oncoplot of detailed mutation information of top 20 genes in low and high EPSTI1 groups of the TCGA-COAD cohort. Genes are ordered by their mutation frequency. (B) Comparison of tumor mutation burden between low and high EPSTI1 groups in the TCGA-COAD cohort. (C, D) Stacked bar plot shows the distribution of mutation spectra for low and high EPSTI1 groups in the TCGA-COAD and GSE39582 cohorts.

### SUPPLEMENTARY FIGURE 3

Supplementary analysis of EPSTI1 expression at the single-cell level. (A, B) Subclusters of macrophages and DCs identified by the R package CellID. (C) The proportion of EPSTI1+ cells is positively correlated with that of mDCs without statistical significance ( $R = 0.302, P = 0.093$ ). (D, E) The module scores of gene signatures related to plasmacytoid/myeloid DC. The results show that EPSTI1+ DCs have more myeloid features.

## References

1. Sung H, Ferlay J, Siegel RL, Laversanne M, Soerjomataram I, Jemal A, et al. Global cancer statistics 2020: GLOBOCAN estimates of incidence and mortality worldwide for 36 cancers in 185 countries. *CA: A Cancer J Clin* (2021) 71(3):209–49. doi: 10.3322/caac.21660
2. Brierley JD, Gospodarowicz MK, Wittekind C. TNM classification of malignant tumours. *John Wiley Sons*; (2017) 272:73–6.
3. Grothey A, Sobrero AF, Shields AF, Yoshino T, Paul J, Taieb J, et al. Duration of adjuvant chemotherapy for stage III colon cancer. *N Engl J Med* (2018) 378(13):1177–88. doi: 10.1056/NEJMoa1713709
4. Understanding the tumor immune microenvironment (TIME) for effective therapy | nature medicine. Available at: <https://www.nature.com/articles/s41591-018-0014-x?sf187653081=1>.
5. McGranahan N, Swanton C. Cancer evolution constrained by the immune microenvironment. *Cell* (2017) 170(5):825–7. doi: 10.1016/j.cell.2017.08.012
6. Bian S, Hou Y, Zhou X, Li X, Yong J, Wang Y, et al. Single-cell multiomics sequencing and analyses of human colorectal cancer. *Science* (2018) 362(6418):1060–3. doi: 10.1126/science.aa03791
7. Koelzer VH, Dawson H, Andersson E, Karamitopoulou E, Masucci GV, Lugli A, et al. Active immunosurveillance in the tumor microenvironment of colorectal cancer is associated with low frequency tumor budding and improved outcome. *Transl Res* (2015) 166(2):207–17. doi: 10.1016/j.trsl.2015.02.008
8. Pagès F, Mlecnik B, Marliot F, Bindea G, Ou FS, Bifulco C, et al. International validation of the consensus immunoscore for the classification of colon cancer: a prognostic and accuracy study. *Lancet* (2018) 391(10135):2128–39. doi: 10.1016/S0140-6736(18)30789-X
9. Mlecnik B, Bindea G, Kirilovsky A, Angell HK, Obenauf AC, Tosolini M, et al. The tumor microenvironment and immunoscore are critical determinants of dissemination to distant metastasis. *Sci Transl Med* (2016) 8(327):327ra26. doi: 10.1126/scitranslmed.aad6352
10. Galon J, Costes A, Sanchez-Cabo F, Kirilovsky A, Mlecnik B, Lagorce-Pagès C, et al. Type, density, and location of immune cells within human colorectal tumors predict clinical outcome. *Science* (2006) 313(5795):1960–4. doi: 10.1126/science.1129139
11. Aran D, Hu Z, Butte AJ. xCell: digitally portraying the tissue cellular heterogeneity landscape. *Genome Biol* (2017) 18(1):220. doi: 10.1186/s13059-017-1349-1
12. Sun J, Zhang Z, Bao S, Yan C, Hou P, Wu N, et al. Identification of tumor immune infiltration-associated lncRNAs for improving prognosis and immunotherapy response of patients with non-small cell lung cancer. *J Immunother Cancer* (2020) 8(1):e000110. doi: 10.1136/jitc-2019-000110
13. Li T, Fu J, Zeng Z, Cohen D, Li J, Chen Q, et al. TIMER2.0 for analysis of tumor-infiltrating immune cells. *Nucleic Acids Res* (2020) 48(W1):W509–14. doi: 10.1093/nar/gkaa407
14. Newman AM, Steen CB, Liu CL, Gentles AJ, Chaudhuri AA, Scherer F, et al. Determining cell type abundance and expression from bulk tissues with digital cytometry. *Nat Biotechnol* (2019) 37(7):773–82. doi: 10.1038/s41587-019-0114-2
15. Zeng D, Li M, Zhou R, Zhang J, Sun H, Shi M, et al. Tumor microenvironment characterization in gastric cancer identifies prognostic and immunotherapeutically relevant gene signatures. *Cancer Immunol Res* (2019) 7(5):737–50. doi: 10.1158/2326-6066.CIR-18-0436
16. Cortal A, Martignetti L, Six E, Rausell A. Gene signature extraction and cell identity recognition at the single-cell level with cell-ID. *Nat Biotechnol* (2021) 39(9):1095–102. doi: 10.1038/s41587-021-00896-6
17. Solinas G, Schiarella S, Liguori M, Fabbri M, Pesce S, Zammataro L, et al. Tumor-conditioned macrophages secrete migration-stimulating factor: a new marker for M2-polarization, influencing tumor cell motility. *J Immunol* (2010) 185(1):642–52. doi: 10.4049/jimmunol.1000413
18. Nakaya HI, Wrammert J, Lee EK, Racioppi L, Marie-Kunze S, Haining WN, et al. Systems biology of vaccination for seasonal influenza in humans. *Nat Immunol* (2011) 12(8):786–95. doi: 10.1038/ni.2067
19. Tokunaga R, Zhang W, Naseem M, Puccini A, Berger MD, Soni S, et al. CXCL9, CXCL10, CXCL11/CXCR3 axis for immune activation – a target for novel cancer therapy. *Cancer Treat Rev* (2018) 63:40–7. doi: 10.1016/j.ctrv.2017.11.007
20. Cao Y, Jiao N, Sun T, Ma Y, Zhang X, Chen H, et al. CXCL11 correlates with antitumor immunity and an improved prognosis in colon cancer. *Front Cell Dev Biol* (2021) 9:646252. doi: 10.3389/fcell.2021.646252
21. Edin S, Wikberg ML, Oldenborg PA, Palmqvist R. Macrophages. *Oncol Immunol* (2013) 2(2):e23038. doi: 10.4161/onci.23038
22. Xia Y, Rao L, Yao H, Wang Z, Ning P, Chen X. Engineering macrophages for cancer immunotherapy and drug delivery. *Advanced Materials* (2020) 32(40):2002054. doi: 10.1002/adma.202002054
23. Cheng Y, Zhu Y, Xu J, Yang M, Chen P, Xu W, et al. PKN2 in colon cancer cells inhibits M2 phenotype polarization of tumor-associated macrophages via regulating DUSP6-Erk1/2 pathway. *Mol Cancer* (2018) 17(1):13. doi: 10.1186/s12943-017-0747-z
24. Roma-Rodrigues C, Mendes R, Baptista PV, Fernandes AR. Targeting tumor microenvironment for cancer therapy. *Int J Mol Sci* (2019) 20(4):E840. doi: 10.3390/ijms20040840
25. Lei X, Lei Y, Li JK, Du WX, Li RG, Yang J, et al. Immune cells within the tumor microenvironment: Biological functions and roles in cancer immunotherapy. *Cancer Lett* (2020) 470:126–33. doi: 10.1016/j.canlet.2019.11.009
26. Mlecnik B, Bifulco C, Bindea G, Marliot F, Lugli A, Lee JJ, et al. Multicenter international society for immunotherapy of cancer study of the consensus immunoscore for the prediction of survival and response to chemotherapy in stage III colon cancer. *J Clin Oncol* (2020) 38(31):3638–51. doi: 10.1200/JCO.19.03205
27. Liu M, Fu X, Jiang L, Ma J, Zheng X, Wang S, et al. Colon cancer cells secreted CXCL11 via RBP-jκ to facilitate tumor-associated macrophage-induced cancer metastasis. *J Cell Mol Med* (2021) 25(22):10575–90. doi: 10.1111/jcmm.16989
28. Nielsen HL, Rønnow-Jessen L, Villadsen R, Petersen OW. Identification of EPSTI1, a novel gene induced by epithelial-stromal interaction in human breast cancer. *Genomics* (2002) 79(5):703–10. doi: 10.1006/geno.2002.6755
29. Chen B, Wei W, Huang X, Xie X, Kong Y, Dai D, et al. circEPSTI1 as a prognostic marker and mediator of triple-negative breast cancer progression. *Theranostics* (2018) 8(14):4003–15. doi: 10.7150/thno.24106
30. Tan YY, Xu XY, Wang JF, Zhang CW, Zhang SC. MiR-654-5p attenuates breast cancer progression by targeting EPSTI1. *Am J Cancer Res* (2016) 6(2):522–32.
31. Li T, Lu H, Shen C, Lahiri SK, Wason MS, Mukherjee D, et al. Identification of epithelial stromal interaction 1 as a novel effector downstream of krüppel-like factor 8 in breast cancer invasion and metastasis. *Oncogene* (2014) 33(39):4746–55. doi: 10.1038/onc.2013.415
32. Lee YS, Song SJ, Hong HK, Oh BY, Lee WY, Cho YB. The FBW7-MCL-1 axis is key in M1 and M2 macrophage-related colon cancer cell progression: validating the immunotherapeutic value of targeting PI3Kγ. *Exp Mol Med* (2020) 52(5):815–31. doi: 10.1038/s12276-020-0436-7
33. Wanderley CW, Colón DF, Luiz JPM, Oliveira FF, Viacava PR, Leite CA, et al. Paclitaxel reduces tumor growth by reprogramming tumor-associated macrophages to an M1 profile in a TLR4-dependent manner. *Cancer Res* (2018) 78(20):5891–900. doi: 10.1158/0008-5472.CAN-17-3480
34. Eom YW, Akter R, Li W, Lee S, Hwang S, Kim J, et al. M1 macrophages promote TRAIL expression in adipose tissue-derived stem cells, which suppresses colitis-associated colon cancer by increasing apoptosis of CD133+ cancer stem cells and decreasing M2 macrophage population. *Int J Mol Sci* (2020) 21(11):E3887. doi: 10.3390/ijms21113887
35. Martinez FO, Helming L, Gordon S. Alternative activation of macrophages: an immunologic functional perspective. *Annu Rev Immunol* (2009) 27:451–83. doi: 10.1146/annurev.immunol.021908.132532
36. Ghislard G, Cheema AS, Baudoin E, Verthuy C, Ballester PJ, Crozat K, et al. NF-κB-dependent IRF1 activation programs cDC1 dendritic cells to drive antitumor immunity. *Sci Immunol* (2021) 6(61):eabg3570. doi: 10.1126/sciimmunol.abg3570
37. Kim YH, Lee JR, Hahn MJ. Regulation of inflammatory gene expression in macrophages by epithelial-stromal interaction 1 (Epstii). *Biochem Biophys Res Commun* (2018) 496(2):778–83. doi: 10.1016/j.bbrc.2017.12.014
38. Ganesh K. Optimizing immunotherapy for colorectal cancer. *Nat Rev Gastroenterol Hepatol* (2022) 19(2):93–4. doi: 10.1038/s41575-021-00569-4
39. Pointer KB, Pirooda SP, Weichselbaum RR. Radiotherapy and immunotherapy: open questions and future strategies. *Trends Cancer* (2022) 8(1):9–20. doi: 10.1016/j.trecan.2021.10.003
40. Morad G, Helmink BA, Sharma P, Wargo JA. Hallmarks of response, resistance, and toxicity to immune checkpoint blockade. *Cell* (2021) 184(21):5309–37. doi: 10.1016/j.cell.2021.09.020
41. Gaikwad S, Agrawal MY, Kaushik I, Ramachandran S, Srivastava SK. Immune checkpoint proteins: Signaling mechanisms and molecular interactions in cancer immunotherapy. *Semin Cancer Biol* (2022) S1044-579X(22)00070-0. doi: 10.1016/j.semancer.2022.03.014
42. Wang S, Yang Y, Ma P, Huang H, Tang Q, Miao H, et al. Landscape and perspectives of macrophage-targeted cancer therapy in clinical trials. *Mol Ther Oncolytics* (2022) 24:799–813. doi: 10.1016/j.omto.2022.02.019

43. Ghorbaninezhad F, Asadzadeh Z, Masoumi J, Mokhtarzadeh A, Kazemi T, Aghebati-Maleki L, et al. Dendritic cell-based cancer immunotherapy in the era of immune checkpoint inhibitors: From bench to bedside. *Life Sci* (2022) 297:120466. doi: 10.1016/j.lfs.2022.120466

44. Guan YH, Wang N, Deng ZW, Chen XG, Liu Y. Exploiting autophagy-regulative nanomaterials for activation of dendritic cells enables reinforced cancer immunotherapy. *Biomaterials* (2022) 282:121434. doi: 10.1016/j.biomaterials.2022.121434



## OPEN ACCESS

## EDITED BY

Mercedes Beatriz Fuertes,  
CONICET Instituto de Biología y  
Medicina Experimental (IBYME),  
Argentina

## REVIEWED BY

Ondrej Stepanek,  
Institute of Molecular Genetics (ASCR),  
Czechia

Jing Hong Wang,  
University of Pittsburgh Medical  
Center, United States

## \*CORRESPONDENCE

Maria Cecilia Rodriguez-Galan  
maria.rodriguez.galan@unc.edu.ar

## SPECIALTY SECTION

This article was submitted to  
Cancer Immunity  
and Immunotherapy,  
a section of the journal  
Frontiers in Immunology

RECEIVED 16 June 2022

ACCEPTED 23 September 2022

PUBLISHED 18 October 2022

## CITATION

Savid-Frontera C, Viano ME, Baez NS,  
Lidon NL, Fontaine Q, Young HA,  
Vimeux L, Donnadieu E and  
Rodriguez-Galan MC (2022) Exploring  
the immunomodulatory role of virtual  
memory CD8<sup>+</sup> T cells: Role of IFN  
gamma in tumor growth control.  
*Front. Immunol.* 13:971001.  
doi: 10.3389/fimmu.2022.971001

## COPYRIGHT

© 2022 Savid-Frontera, Viano, Baez,  
Lidon, Fontaine, Young, Vimeux,  
Donnadieu and Rodriguez-Galan. This is  
an open-access article distributed under  
the terms of the [Creative Commons  
Attribution License \(CC BY\)](#). The use,  
distribution or reproduction in other  
forums is permitted, provided the  
original author(s) and the copyright  
owner(s) are credited and that the  
original publication in this journal is  
cited, in accordance with accepted  
academic practice. No use,  
distribution or reproduction is  
permitted which does not comply with  
these terms.

# Exploring the immunomodulatory role of virtual memory CD8<sup>+</sup> T cells: Role of IFN gamma in tumor growth control

Constanza Savid-Frontera<sup>1</sup>, Maria Estefania Viano<sup>1</sup>,  
Natalia S. Baez<sup>1</sup>, Nicolas L. Lidon<sup>1</sup>, Quentin Fontaine<sup>1</sup>,  
Howard A. Young<sup>2</sup>, Lene Vimeux<sup>3</sup>, Emmanuel Donnadieu<sup>3</sup>  
and Maria Cecilia Rodriguez-Galan<sup>1\*</sup>

<sup>1</sup>Inmunología CIBICI-CONICET Facultad de Ciencias Químicas, Universidad Nacional de Córdoba, Córdoba, Argentina, <sup>2</sup>Cancer Innovation Laboratory, Center for Cancer Research, National Cancer Institute, Frederick, MD, United States, <sup>3</sup>Université Paris Cité, CNRS, INSERM, Equipe Labelisée Ligue Contre le Cancer, Institut Cochin, F-75014 Paris, France

Virtual memory CD8<sup>+</sup> T cells (T<sub>VM</sub>) have been described as cells with a memory-like phenotype but without previous antigen (Ag) exposure. T<sub>VM</sub> cells have the ability to respond better to innate stimuli rather than by TCR engagement, producing large amounts of interferon gamma (IFN $\gamma$ ) after stimulation with interleukin (IL)-12 plus IL-18. As a result of the phenotypic similarity, T<sub>VM</sub> cells have been erroneously included in the central memory T cell subset for many years. However, they can now be discriminated via the CD49d receptor, which is up-regulated only on conventional memory T cells (T<sub>MEM</sub>) and effector T cells (T<sub>EFF</sub>) after specific cognate Ag recognition by a TCR. In this work we show that systemic expression of IL-12 plus IL-18 induced an alteration in the normal T<sub>VM</sub> vs T<sub>MEM</sub>/T<sub>EFF</sub> distribution in secondary lymphoid organs and a preferential enrichment of T<sub>VM</sub> cells in the melanoma (B16) and the pancreatic ductal adenocarcinoma (KPC) tumor models. Using our KPC bearing OT-I mouse model, we observed a significant increase in CD8<sup>+</sup> T cell infiltrating the tumor islets after IL-12+IL-18 stimulation with a lower average speed when compared to those from control mice. This finding indicates a stronger interaction of T cells with tumor cells after cytokine stimulation. These results correlate with a significant reduction in tumor size in both tumor models in IL-12+IL-18-treated OT-I mice compared to control OT-I mice. Interestingly, the absence of IFN $\gamma$  completely abolished the high antitumor capacity induced by IL-12+IL-18 expression, indicating an important role for these cytokines in early tumor growth control. Thus, our studies provide significant new information that indicates an important role of T<sub>VM</sub> cells in the immune response against cancer.

## KEYWORDS

virtual memory CD8<sup>+</sup> T cells, cancer, IL-12, IL-18, IFN $\gamma$

## 1 Introduction

The ability of CD8<sup>+</sup> T cells to respond to cytokines in a bystander T cell receptor (TCR)-independent way has been studied for a long time. The work of Slifka et al. examined the effects of more than 1800 cytokine combinations on virus-specific CD8<sup>+</sup> T-cell activation, demonstrating that certain cytokine combinations could synergize to induce antigen-independent IFN $\gamma$  production, CD69 up-regulation and in some cases exhibit differential regulatory functions (1).

Interestingly, a recent review by Maier et al. has summarized data demonstrating that recognition of cancer cells is mainly restricted to a small subset of antigen (Ag)-specific tumor infiltrating leukocytes (TILs). In fact, many TILs are “cancer ignorant” and have been defined as “bystander T cells”, that recognize non-cancer peptides, including viral antigens (2). Although the most recent evidence has pointed to bystander T cells as being the majority of infiltrating T cells in tumors, there is still a lack of consensus regarding the activation status of these cells and if their presence in tumors plays a role in anti-cancer immunity.

Within the bystander T cell subset, virtual memory T cells are a population of CD8<sup>+</sup> T cells that, despite their antigen inexperience, exhibit many hallmarks compatible with conventional Ag-specific memory T cells. By consensus, the lineage markers for T<sub>VM</sub> cells are: CD8<sup>+</sup> CD44<sup>hi</sup> CD122<sup>hi</sup> CD49d<sup>lo</sup>. The most recent marker is integrin alpha 4 (CD49d) as it is highly expressed in T cells after a strong signal through the TCR, *via* the cognate Ag-TCR-MHC-I interaction. As a result, CD49d is highly expressed by T<sub>MEM</sub>/T<sub>EFF</sub> but not by T<sub>VM</sub> cells, thus becoming an essential marker that discriminates between these 2 populations of CD8<sup>+</sup> memory T cells (3–5). Also, a transcription factor, eomesodermin (Eomes), is highly expressed by T<sub>VM</sub> cells and is associated with their functional capacity (6, 7).

During their thymic maturation these “memory-like” cells can be differentiated into two populations: T<sub>VM</sub> and T<sub>IM</sub> (innate memory) by the expression of different markers, including CD5<sup>hi</sup> in T<sub>VM</sub> and interleukin (IL)-4R<sup>hi</sup> and CD49d<sup>hi</sup> in T<sub>IM</sub> cells. However, when they reach secondary lymphoid organs (SLO), T<sub>IM</sub> cells downregulate CD49d, and as such, CD5 and IL-4R expression is not sufficient to discriminate between both cell types (8). As a result, they became indistinguishable from each other and compose a heterogeneous group of memory-like cells designated as T<sub>VM</sub> cells (3, 8, 9).

In spite of never having contacted their specific Ags, T<sub>VM</sub> cells are capable of developing a powerful cytotoxic response in a TCR-independent manner, mainly through mechanisms that may involve interaction through the receptor NKG2D (10, 11). Also, their lytic capacity is mediated by production of large amounts of the interferon gamma (IFNg), especially after IL-12 and IL-18 stimulation (3, 12–14) and by granzymes release (15,

16). Even though these cells have been described as being important in controlling infectious diseases through innate bystander mechanisms, the role of T<sub>VM</sub> cells in cancer has not been widely studied.

Interleukin-12 and IL-18 are inflammatory cytokines mainly produced by activated macrophages and dendritic cells at the initiation of an immune response (17). It has been reported that IL-12 and IL-18 are capable of activating virtual memory CD8<sup>+</sup> T cells leading to rapid production of IFN $\gamma$ , resulting in crucial pathogen control during certain viral and bacterial infectious processes (10, 18–21). Moreover, we have previously described the role of T<sub>IM</sub> cells during a murine model of parasitic infection with *Trypanosoma cruzi* (13).

Infiltration of CD8<sup>+</sup> T cells into tumors is associated with a better prognosis for response in cancer patients (22, 23). Moreover, it has been long assumed that CD8<sup>+</sup> T cells present in tumors are conventional memory CD8<sup>+</sup> T specific for tumor antigens. In this context, the role of T<sub>VM</sub> cells present in tumors and their Ag-independent antitumor mechanisms has not been thoroughly investigated.

The few reports that have addressed the role of T<sub>VM</sub> cells (or cells compatible with T<sub>VM</sub> phenotype, not identified by the current consensus lineage markers) mainly focus on the antitumor mechanism mediated by the receptor NKG2D (10, 11). However, the presence and activity of T<sub>VM</sub> vs T<sub>MEM</sub> cells in tumor growth control has not been thoroughly studied, especially with regard to the role of effector mechanisms. This is quite important, especially with respect to tumors that do not express the ligands for NKG2D. In this context, IFN $\gamma$  is a cytokine highly produced by T<sub>VM</sub> cells, able to promote a potent antitumor activity especially through anti-angiogenic mechanisms (24). Importantly, we have recently demonstrated that after IL-12 systemic expression, a significant reduction is observed in the number of blood vessels present in B16 and EL-4 tumors (25). This data is quite relevant to the biology of these tumors as they do not express NKG2D ligands (26) and their growth seems to rely upon neovascularization (24).

Based on this evidence, we decided to focus on the role of IFN $\gamma$  in murine cancer models utilizing cell lines that lack NKG2D ligands, in order to avoid interference with this potential cytotoxic mechanism (26). Previously, our group demonstrated that systemic expression of IL-12+IL-18 was capable of inducing a strong antitumor effect against 2 different tumor cell lines *in vivo* (B16, melanoma and 3LL, lung carcinoma). However this occurred at the expense of toxic side effects resulting in only 50% survival over a period of 50 days post-treatment (27). Because toxicity was associated with IL-12 but not to IL-18 (27, 28), we used lower doses of IL-12 cDNA to minimize the side effects. Utilizing this lower dose, we demonstrated that survival reached 100% and the antitumor effect was still present (25). Interestingly, IL-12 systemic expression does not affect the total number of CD8<sup>+</sup> T cells

but induces an increase in the percentage of  $\text{IFN}\gamma^+ \text{CD8}^+$  infiltrating B16 and EL-4 tumors (25). As we have reported, a rapid and strong antitumor effect early after IL-12+IL-18 expression (27), we speculated that  $\text{T}_{\text{VM}}$  ( $\text{CD8}^+ \text{CD44}^{\text{hi}} \text{CD122}^{\text{hi}} \text{CD49d}^{\text{lo}}$ ) along with tumor Ag-specific  $\text{CD8}^+$  effector T cells ( $\text{T}_{\text{EFF}}$ ) and  $\text{T}_{\text{MEM}}$  ( $\text{CD8}^+ \text{CD44}^{\text{hi}} \text{CD122}^{\text{hi}} \text{CD49d}^{\text{hi}}$ ) could be playing a role in tumor growth control in an Ag-independent manner.

In the present work we have evaluated the balance between these populations in SLO and tumors, both in steady-state conditions and after systemic stimulation with IL-12+IL-18. We observed that the number and the phenotypic characteristics of these T cells experienced changes from a normal state to inflammatory T helper 1 conditions following cytokine expression. Moreover, systemic expression of IL-12+IL-18 leads to a prevalence of  $\text{T}_{\text{VM}}$  cells expressing  $\text{IFN}\gamma$  in tumors and defines these cells as an essential factor for tumor growth control in the early stages of disease.

## 2 Material and methods

### 2.1 Mice

Female and male WT C57BL/6, IL4KO (C57BL/6J-IL4tm1Nnt), IFNARKO (Ifnar1tm1Ag), IFN $\gamma$ KO (B6.129S7-Ifngtm1Ts/J), and OT-I (RAG-sufficient, B6 background) used in this study were 6–7-weeks-old and were maintained under specific pathogen-free conditions. Animal care was provided in accordance with the procedures outlined in the Guide for the Care and Use of Laboratory Animals (NIH-Publication No. 86-23, 1985). The experimental protocols were approved by the Institutional Animal Care and Use Committee of Centro de Investigaciones en Bioquímica Clínica e Inmunología (CIBICI), Consejo Nacional de Investigaciones Científicas y Técnicas (CONICET). Our animal facility has obtained NIH animal welfare assurance (assurance no. A5802-01, Office of Laboratory Animal Welfare, NIH, Bethesda, MD, USA).

### 2.2 Cell lines

B16-F10 melanoma cells were obtained from the American Type Culture Collection (ATCC). KPC pancreatic ductal adenocarcinoma cells were previously used at Dr. Donnadieu's laboratory (INSERM U1016, Institut Cochin, Paris, France). Both cell lines were free of Mycoplasma infection (tested by PCR every 12 months). B16-F10 melanoma cells were cultured in DMEM and KPC in DMEM/F12, both containing 10% Fetal Bovine Serum (FBS), 100 U/ml penicillin, 2mM L-Glutamine, 100  $\mu\text{g}/\text{ml}$  streptomycin at 37°C, 5%  $\text{CO}_2$ .

### 2.3 Hydrodynamic cDNA injections

The hydrodynamic gene transfer procedure was described previously by our group (13, 25, 27–30). The designated amount of each DNA was suspended in 1.6 mL of sterile 0.9% sodium chloride solution. Animals were injected in the tail vein with the cDNAs in less than 8 s and separated in two groups, control: 15  $\mu\text{g}$  of ORF empty vector cDNA and IL-12+IL-18: 1  $\mu\text{g}$  of IL-12 cDNA (pscIL-12, p40-p35 fusion gene) plus 10  $\mu\text{g}$  of IL-18 cDNA (pDEF pro-IL-18). All the expression plasmids utilize the human elongation 1- $\alpha$  promoter to drive transcription.

### 2.4 *In vivo* tumor models

WT, OT-I, IL4KO, IFNARKO and IFN $\gamma$ KO mice were shaved and injected subcutaneously (s.c.) in the left flank with  $1 \times 10^6$  B16-F10 cells or  $10 \times 10^6$  KPC cells in 100  $\mu\text{l}$  of a sterile 0.9% sodium chloride solution. After 7–10 days, when solid tumors were visible (4–5 mm diameter), mice were hydrodynamically injected (HI) with the designated cDNAs (Day 0). At the specified time points, tumor growth was monitored with a caliper and tumor volume was calculated as:

$$\text{Tumorvolume: } \frac{(d^2) \times D}{2}$$

in which “ $d$ ” corresponds to the lower diameter of the tumor, and “ $D$ ” to the longest one. At day 7 post-hydrodynamic injection, animals were euthanized and tumors were removed and weighed using an analytical scale.

### 2.5 Tissue processing

At day 7 post-HI, spleens, tumor-draining lymph nodes (dLN) and tumors were harvested and mechanically disrupted with a disposable mesh (Filtrabags). Cell suspensions were collected and stained for flow cytometry analysis. B16-tumors were harvested, weighed, cut into small pieces, mechanically disrupted, and resuspended at 1g of tumor/7mL of Phosphate Buffered Saline (PBS) + 10% FBS for flow cytometry analysis. KPC tumors were harvested, weighed, cut into small pieces, mechanically and enzymatically (with DNase and Liberase) disrupted, and counted. Five million cells were stained for flow cytometry analysis. Splenocyte suspensions were depleted of red cells by treatment with ACK lysis buffer before staining.

### 2.6 Flow cytometry

Phenotypic analysis of cells from spleens, dLN and B16-F10 tumors, was performed by flow cytometry *ex vivo* on day 7 post-

HI. Samples were first washed with PBS and stained with Zombie Acqua Fixable Viability Kit (Biolegend) 15 minutes at room temperature for exclusion of dead cells. Expression of different surface markers was assessed by staining with appropriate combinations of the following monoclonal antibodies (mAbs) for 30 min at 4°C: CD4 (RM4-5, Biolegend), CD8 (53-6.7, Biolegend), CD44 (IM7, eBioscience), CD45 (30-F11, Biolegend), CD49d (R1-2, Biolegend), CD122 (TM-β1, Biolegend), NK1.1 (PK136, Biolegend) and TCRb (H57-597, Biolegend) or its respective isotype matched antibody. Cells were washed twice with PBS and acquired on a BD LSR Fortessa X-20 cytometer (BD Biosciences).

To detect intranuclear Eomes expression, cells were stained for surface markers, washed, and fixed with IC Fixation Buffer (eBioscience) for 90 minutes at 4°C. Cells were washed with Permeabilization Buffer (eBioscience) and incubated for 30 minutes with the same buffer. Cells were centrifuged and incubated with the Eomes PE anti-mouse Ab (Dan11mag, eBioscience), or isotype-matched antibody for 45 min at 4°C and then acquired in a BD LSR Fortessa X-20.

For Ovalbumin (OVA)-specific CD8<sup>+</sup> T cell detection, cells were L/D stained, washed and then stained using H-2K(b) chicken ova amino acids 257–264 SIINFEKL APC-labeled Tetramer (ProImmune or NIH Tetramer Core Facility) for 30 min, followed by washing steps and surface staining. Cells were acquired in a BD LSR Fortessa X-20. Analysis was performed using FlowJo VX software (Tree Star, Inc.).

## 2.7 Tumor slice imaging

For studying CD8<sup>+</sup> infiltrating T cells in KPC tumors, tumors from control and 12+18-treated OT-I mice were harvested and placed in a PLP solution (containing PFA 1%, Lysine, Sodium Periodate (NaIO4) in PBS) for 2 hours at RT, washed with PBS and embedded in 5% low-gelling-temperature agarose (type VII-A, Sigma-Aldrich) prepared in PBS.

Real-time imaging experiments were performed with KPC tumor specimens obtained 2–4 h after tumor resection from control or 12+18-treated OT-I mice at day 7 post-HI. Tumor slices were prepared as previously described (31, 32). In brief, samples were embedded in 5% low-gelling-temperature agarose (type VII-A, Sigma-Aldrich) prepared in PBS. In both cases, 200 μm slices were cut with a vibratome (VT 1000S, Leica) in a bath of ice-cold PBS. Slices were transferred to 0.4-μm organotypic culture inserts (Millicell, Millipore) in 35-mm Petri dishes containing 1 ml phenol red free RPMI 1640 in an incubator at 37°C and 5% CO<sub>2</sub>. Live vibratome sections were stained for 15 min at 37°C with the following antibodies: PerCP-eFluor710-conjugated anti-CD8 (53-6.7, eBiosciences), BV421-conjugated anti-EpCAM (G8.8, BD Horizon) and eFluor660-conjugated

anti-gp38 (8.1.1, eBioscience) and washed thereafter. All antibodies were diluted in phenol red free RPMI and used at a concentration of 10 μg/ml. To concentrate the antibodies on the tissue, a stainless-steel ring was placed in the agarose surrounding the slice.

Tumor slices were imaged with a DM500B upright microscope equipped with a SP5 confocal head (Leica) and a 37°C thermostat controlled chamber. For dynamic imaging, tumor slices were secured with a stain-less steel slice anchor (Warner Instruments) and perfused at a rate of 1 ml/min with a solution of phenol red free RPMI and then, bubbled with 95% O<sub>2</sub> and 5% CO<sub>2</sub>. Ten minutes later, images from a first microscopic field were acquired with a 25× water immersion objective (Olympus, 20×/0.95 NA). For four-dimensional analysis of cell migration, stacks of 6–10 sections (z step = 5–7 μm) were acquired every 30 s for 20–40 min, at depths up to 80 μm. Regions were selected for imaging when tumor parenchyma, stroma and T cells were simultaneously present in the same microscopic field. For most of the tumors included in the study, between 2 and 4 microscopic fields were selected for time-lapse experiments.

## 2.8 Image data analysis

Image analysis was performed at the Cochin Imaging Facility (Institut Cochin, Paris). A 3D image analysis was performed on x, y, and z planes using Imaris 7.4 (Bitplane AG). First, superficial planes from top of the slice to 15 μm in depth were removed to exclude T cells located near the cut surface. Cellular speed means were calculated using Imaris. Tracks >10% of the total recording time were included in the analysis. To reveal the relationship between CD8<sup>+</sup> T cell motility and the tumor structure (tumor islets and stroma), confocal time-lapse images of T cells were superimposed onto the corresponding gp38 and EpCAM images. CD8<sup>+</sup> T cells localized in the stroma were distinguished from those infiltrated in tumor cell nests by looking at individual planes along the z axis. Videos and images were made by compressing the z information into a single image using Imaris. When a drift in the x, y dimension was noticed, it was corrected using the “Correct 3D Drift” plug-in in Image J. For the automated detection of resident CD8<sup>+</sup> T cells in different tumor areas (stroma or tumor islets), we used the Image J software. First, fluorescent images threshold was obtained and converted to binary images. Angles between the cell trajectory vectors, which are the connecting lines between starting points and end points of each track, and tumor-stroma boundaries were calculated using Image J software. Only the cells positioned within a maximum distance of 100 μm from the tumor-stroma interfaces were included in further analysis.

## 2.9 Statistical analysis

Statistical analyses were performed using GraphPad Prism version 7.0 (GraphPad Software). Data was analyzed by means of a Student unpaired *t* test (comparison of 2 experimental groups), One-way analyses of variance (ANOVA) test (for comparing more than 2 experimental groups) or Two-way ANOVA test (composition of more than 2 variables). Results are expressed as means  $\pm$  SEM and were considered statistically significant when  $p < 0.05$ .

## 3 Results

### 3.1 Antitumor effect of systemic IL-12+IL-18 expression

In order to induce systemic expression of the cytokines IL-12 and IL-18, we have used hydrodynamic injection as a tool. By rapidly injecting naked cDNA encoding these cytokines i.v., mostly hepatocytes uptake the cDNA and systemically and transiently produce the protein of interest. This methodology was first described by Liu et al. (33) and has been used in our laboratory in several publications (13, 25, 27–30).

Previous work from our group has shown that systemic expression of IL-12 and IL-18 is capable of inducing the expression of IL-15 in the thymus (13). When we evaluated if a similar induction was happening in the periphery, we observed that the procedure was capable of inducing the expression of IL-15 RNA in LNs, spleen and liver, the main sites of  $T_{VM}$  cell residence (34) (Supplementary Figure 1). Thus, we created an *in*

*vivo* environment where 3 cytokines, important for maintenance/development and functional activities of  $T_{VM}$  cells, were simultaneously present. Moreover, the systemic amounts of IL-12 and IL-18 we induced by hydrodynamic injections were previously assessed by our laboratory and were completely tolerated by the mice and similar to what is described for certain pathological scenarios like infectious diseases (25, 27, 35–37).

As seen in Figure 1, we first determined the antitumor effect of systemic expression of IL-12 + IL-18 at the tolerated doses (see M&M section). We observed significant growth control of B16 tumors evaluated by tumor volume *in vivo* up to 7 days post-treatment (Figures 1A, B) as well as by tumor weight at day 7 post treatment, compared to control mice (Figure 1C).

### 3.2 Effects of systemic IL-12+IL-18 expression on CD8<sup>+</sup> T cells in SLO and tumors

#### 3.2.1 Alterations in SLO

Taking into account that the tumor growth control was observed in a rapid time period (7 days) due to systemic cytokine stimulation, we wondered if  $T_{VM}$ ,  $T_{EFF}$  and early  $T_{MEM}$  cells (or pre-existing  $T_{MEM}$  cells) could be playing a role in the antitumor immune response. We focused our attention on the contribution of these cell types because they rapidly respond to IL-12, IL-18 and IL-15 stimulation as previously reported (34). While it is possible that NK cells could be also contributing, in this experimental system, NK cells are almost undetectable as we have previously reported (25, 27).

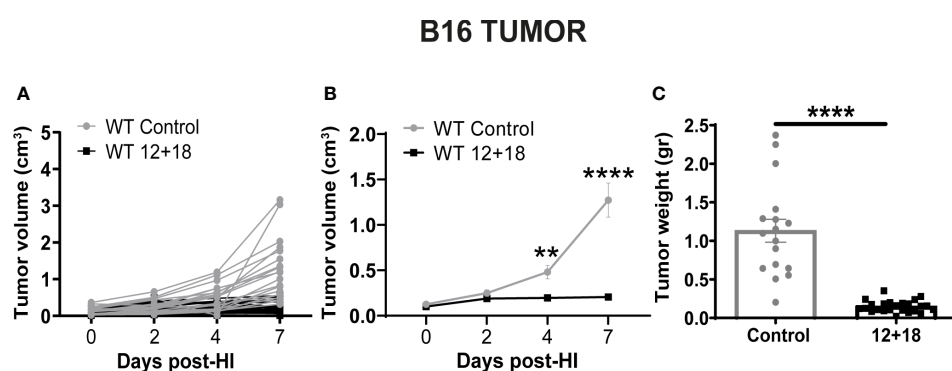


FIGURE 1

Effects of the systemic co-expression of IL-12 plus IL-18 on tumor growth. B16-bearing C57BL/6 WT mice were hydrodynamically injected (HI) with IL-12 plus IL-18 cDNA (12 + 18) or empty cDNA as the control. At the indicated time points post-HI tumor size was measured using a caliper. After 7 days post-HI mice were euthanized, and tumors were harvested and weighed using an analytical scale. (A, B) Tumor growth represented as tumor volume (in  $\text{cm}^3$ ) at specified days post-HI is shown (A) for each mouse individually or (B) as an average (mean  $\pm$  SEM) for each group. (C) Tumor weight in grams is represented as mean  $\pm$  SEM for each experimental group. Statistical analysis was performed using a two-way ANOVA with Sidak's multiple comparison test on (B) or a Student *t* test in (C). Values of \*\* $p < 0.01$ , and \*\*\*\* $p < 0.0001$  were considered significant.

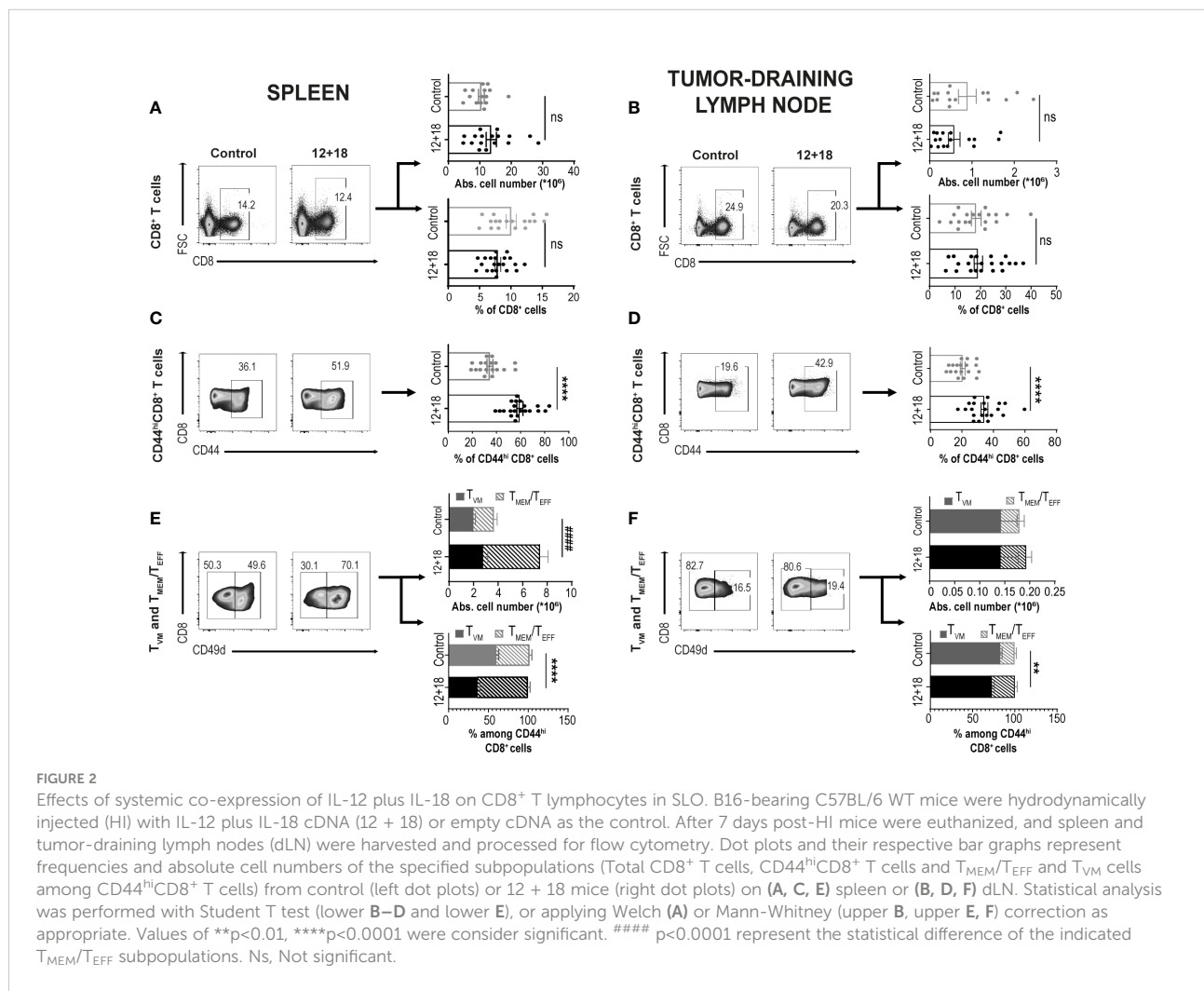
Next, we performed a comparative analysis of the frequency and phenotype of the CD8<sup>+</sup> T cells in a distant (spleen) and a close (draining lymph nodes, dLNs) SLO to the tumor site in the absence (control) or presence of systemic IL-12+IL-18 (12 + 18). See strategy gates in [Supplementary Figure 2](#).

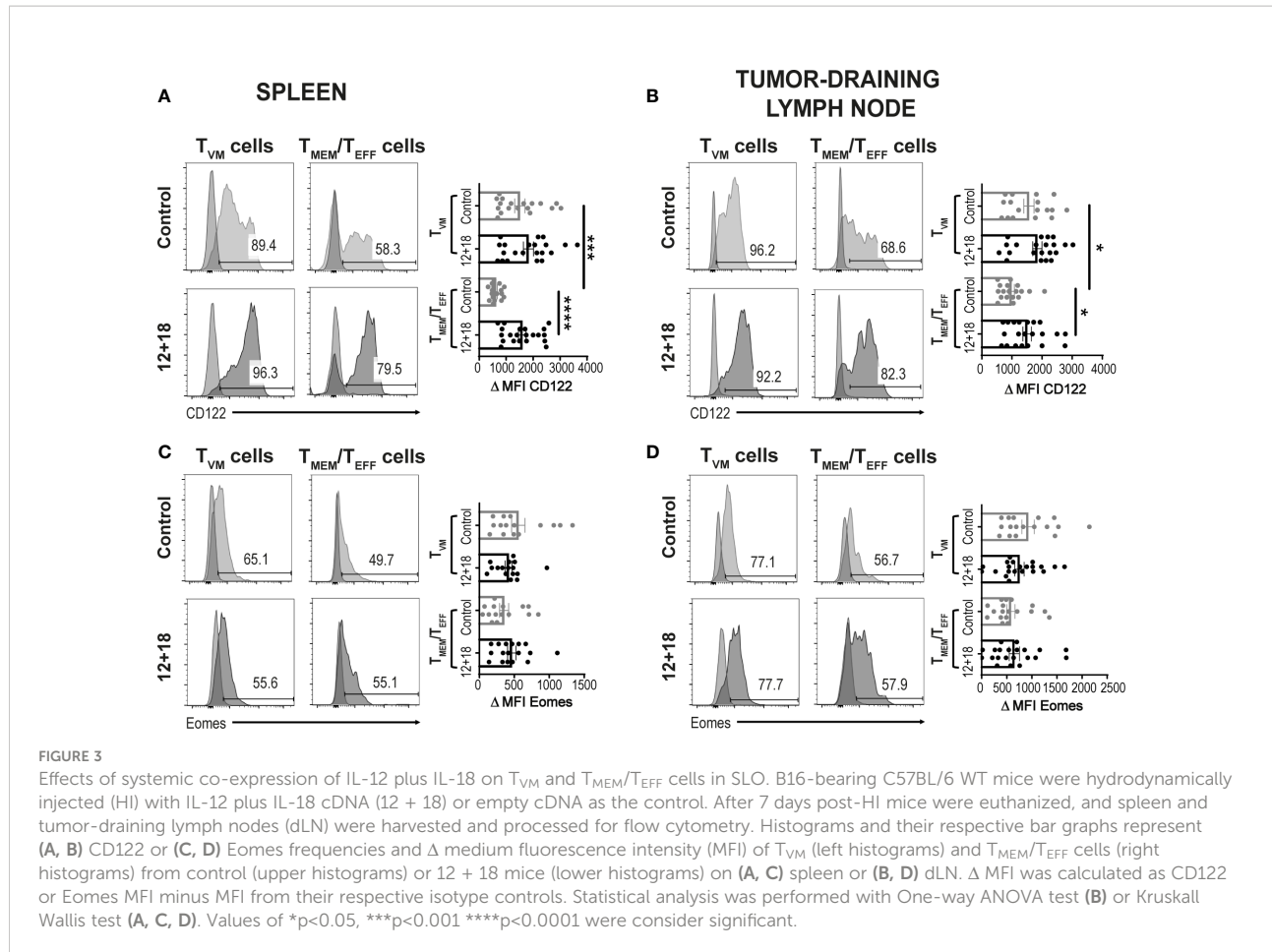
As shown in [Figure 2](#), both the percentage and the absolute cell number of total CD8<sup>+</sup> T cells in the spleen ([Figure 2A](#)) and dLNs ([Figure 2B](#)) did not change when comparing control and 12+18-treated mice. However, the treatment induced a significant increase in the proportion of CD8<sup>+</sup>CD44<sup>hi</sup> T cells in both examined SLO ([Figures 2C, D](#)). Of note, it is important to mention that CD44 expression is a consensus marker for memory and activated T cells and it is highly expressed by both T<sub>VM</sub> and T<sub>MEM/TEFF</sub> cells ([8, 34](#)).

As previously reported, CD49d is the integrin subunit alpha 4 and is up-regulated after a strong signal through the TCR in T cells driven by a cognate antigen. This important marker allows one to distinguish T<sub>VM</sub> cells from conventional effector memory T cells ([3–5](#)). Based on this receptor expression, we found that in the spleen of control mice, there are similar percentages of T<sub>VM</sub>

vs T<sub>MEM/TEFF</sub> cells but after exposure to systemic IL-12+IL-18, T<sub>MEM/TEFF</sub> cells expanded almost 3 times while the number of T<sub>VM</sub> cells remained almost unchanged ([Figure 2E](#)). A similar pattern was observed in dLNs. Of note, T<sub>VM</sub> are highly enriched in this tissue, representing approximately 80% of total CD8<sup>+</sup>CD44<sup>hi</sup> cells in steady-state conditions (control mice) ([Figure 2F](#)). Overall, we observed that IL-12+IL-18 systemic expression preferentially favors the expansion of T<sub>MEM/TEFF</sub> over T<sub>VM</sub> cells in SLO.

Next, we evaluated if systemic IL-12+IL-18 treatment was able to alter the expression of the different consensus markers of T<sub>VM</sub> and T<sub>MEM/TEFF</sub> cells. Evaluation of CD122 expression demonstrated that this marker is already highly expressed on T<sub>VM</sub> cells in the spleen ([Figure 3A](#)) and dLNs ([Figure 3B](#)) under steady-state conditions compared to conventional memory/effector CD8<sup>+</sup> T cells, as previously reported ([8, 34](#)). However, after systemic expression of IL-12+IL-18, only T<sub>MEM/TEFF</sub> cells up-regulate this marker to levels similar to that observed in T<sub>VM</sub> cells. When we evaluated Eomes expression, we observed that both cell subsets expressed high levels of this transcription factor





and expression levels were not altered by the *in vivo* treatment with the cytokines, both in the spleen and dLNs (Figures 3C, 3D, respectively).

### 3.2.2 Alterations in tumors

After evaluation of these parameters in SLO, we focused next on determining the frequency and phenotype of  $T_{VM}$  and  $T_{MEM}/T_{EFF}$  cells infiltrating B16 tumors. We observed that the treatment did not alter the percentage of total CD45<sup>+</sup> infiltrating leukocyte (TILs) (Figure 4A). However, the frequency of CD8<sup>+</sup> T cells within TILs is significantly increased in mice that received IL-12+IL-18 *in vivo* (Figure 4B). We observed that most CD8<sup>+</sup> T cells express high levels of CD44<sup>hi</sup>, and this percentage is even higher after IL-12+IL-18 treatment (Figure 4C). After the treatment with the cytokines, we expected to see an enrichment of  $T_{MEM}/T_{EFF}$  cells similar to data obtained in SLO. However, in the tumor site, the frequency of  $T_{VM}$  cells increased from about 25% in control mice to more than 60% in 12 + 18-treated mice (Figure 4D). When we evaluated CD122 and Eomes expression in these cells, we obtained similar results to SLO, but in this case CD122 expression increased in both  $T_{VM}$  and  $T_{MEM}/T_{EFF}$  cells after IL-12+IL-18 systemic expression (Figure 4E) while Eomes levels remained high and unaffected (Figure 4F).

### 3.3 Systemic IL-12 and IL-18 expression impacts the number and phenotype of $T_{VM}$ and $T_{MEM}/T_{EFF}$ cells but not the antitumor capacity in IL-4KO and IFNAR KO mice

Previously, we have shown that expression of systemic IL-12 and IL-18 is able to induce IL-15 expression in sites where memory T cells usually reside. Moreover, we demonstrated how the frequency and phenotype of both  $T_{VM}$  and  $T_{MEM}/T_{EFF}$  cells are affected both in SLO and tumors in a bystander mechanism after non-antigenic *in vivo* stimulation. Other than the mentioned cytokines, it has been reported that IL-4 and type I IFNs play a crucial role during development/maintenance and functional stages of  $T_{VM}$  cells in steady-state conditions (38, 39). However, their role after systemic Th1 inflammatory situations has not been completely addressed. To evaluate the impact of IL-4 and type I interferons, we examined the frequency and phenotype of  $T_{VM}$  and  $T_{MEM}/T_{EFF}$  cells in SLO and the antitumor ability of systemic IL-12 and IL-18 expression in mice deficient in IL-4 or type I IFNs receptor (IFNAR). As shown in Supplementary Figure 3, we observed that the total CD8<sup>+</sup> absolute T cell number were not affected after 12 + 18 treatment either in IL-

4KO nor in IFNAR KO mice both in spleen (Supplementary Figure 3A) and dLNs (Supplementary Figure 3B).

As previously determined for WT mice, systemic expression of IL-12+IL-18 also increased the percentages of CD8<sup>+</sup>CD44<sup>hi</sup> T cells in IL-4 KO. Surprisingly, in IFNAR KO mice, this increase is observed in spleen (Supplementary Figure 3C) but not in dLNs (Supplementary Figure 3D). An interesting result arose when comparing the frequency of T<sub>VM</sub> vs T<sub>MEM</sub>/T<sub>EFF</sub> cells between WT and the KO mice. In contrast to WT mice, we observed that the frequency of T<sub>MEM</sub>/T<sub>EFF</sub> cells in IL-4 KO mice is similar in control and 12 + 18-treated mice. Unexpectedly, in IFNAR KO mice, T<sub>MEM</sub>/T<sub>EFF</sub> cells were almost undetectable in control mice and even though the cells increased after IL-12+IL-18 treatment, they did not reach the proportion observed in WT mice (Supplementary Figures 3E, F).

These data demonstrate how the presence of these cytokines can regulate the normal proportions of T<sub>VM</sub> and T<sub>MEM</sub>/T<sub>EFF</sub>

cells in SLO in steady-state and also during systemic Th1 inflammatory situations. In spite of the changes observed in the frequency of these cell populations, the antitumor capacity in both IL-4 and IFNAR KO mice was high and similar to WT mice (Supplementary Figure 3G).

### 3.4 Enrichment of T<sub>VM</sub> cells by using OT-I mice

#### 3.4.1 The T<sub>VM</sub> cells vs T<sub>MEM</sub>/T<sub>EFF</sub> cells balance in SLO of WT and OT-I mice

It has been proposed that the chances of a CD5<sup>hi</sup>CD8<sup>+</sup> T cell that leaves the thymus to become a T<sub>VM</sub> cell in the periphery depends upon the accessibility of certain niches in SLO where the appropriate conditions for their differentiation are present (8, 34, 40). Then, the chances for a specific T cell to become a

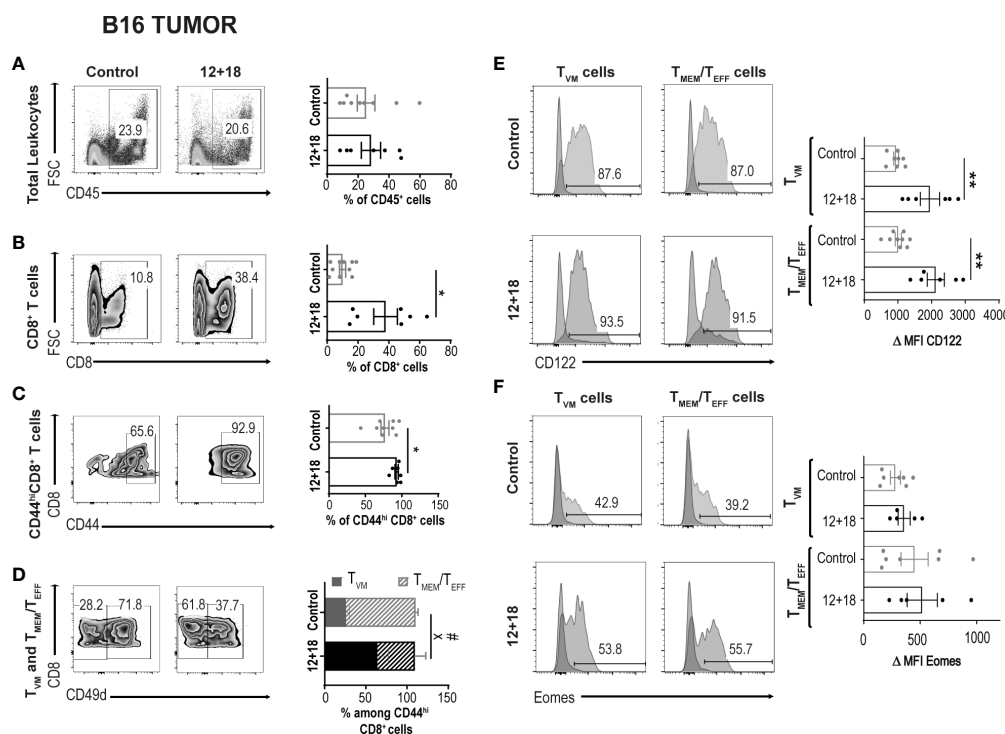


FIGURE 4

Effects of systemic co-expression of IL-12 plus IL-18 on leukocytes and CD8<sup>+</sup> T lymphocytes in tumors. B16-bearing C57BL/6 WT mice were hydrodynamically injected (HI) with IL-12 plus IL-18 cDNA (12 + 18) or empty cDNA as the control. After 7 days post-HI mice were euthanized, and tumors were harvested and processed for flow cytometry. (A–D) Dot plots and their respective bar graphs represent the frequencies of the specified subpopulations (total leukocytes, total CD8<sup>+</sup> T cells, CD44<sup>hi</sup>CD8<sup>+</sup> T cells and T<sub>MEM</sub>/T<sub>EFF</sub> and T<sub>VM</sub> cells among CD44<sup>hi</sup>CD8<sup>+</sup> T cells) from control (left dot plots) or 12 + 18 mice (right dot plots). (E, F) Histograms and their respective bar graphs represent CD122 (top) or Eomes (bottom) frequencies and Δ MFI on T<sub>VM</sub> (left histograms) and T<sub>MEM</sub>/T<sub>EFF</sub> cells (right histograms) from control (upper histograms) or 12+18 mice (lower histograms). Δ MFI was calculated as MFI of CD122 or Eomes minus MFI from their respective isotype control. Statistical analysis was performed with Student T test (A), with Welch correction (B–D) or with a One-Way (E) or Brown Forsythe and Welch (F) ANOVA test as appropriate. Values of \*p<0.05, \*\*p<0.01, were considered significant. # p<0.05 represent the statistical difference of the indicated T<sub>MEM</sub>/T<sub>EFF</sub> control vs 12 + 18 subpopulations while X p<0.05 represents the difference among control and 12 + 18 T<sub>VM</sub> cells.

$T_{VM}$  cell not only depends upon the type of selection that it received in the thymus but also on the competition for niches in SLO. Based on these data, we decided to evaluate a scenario where the proportion of  $T_{VM}$  cells over  $T_{MEM}/T_{EFF}$  is higher than in WT mice. We used non-RAG KO OT-I mice where most of the  $CD8^+$  T cells carry a TCR specific for OVA, a protein not expressed by B16 tumors. In these mice,  $T_{VM}$  and  $T_{MEM}/T_{EFF}$  cells still co-exist but with a larger proportion of  $T_{VM}$  cells (OVA specific) than in WT mice (Supplementary Figure 4). Interestingly, when using this experimental model we observed that while the number of  $CD8^+CD44^{hi}$  T cells is similar between WT and OT-I mice in the control groups, the frequency of these cell subsets increased in a larger proportion in OT-I compared to WT mice after IL-12+IL-18 *in vivo* stimulation in both SLO (Figures 5A, B). Furthermore, in OT-I mice the higher numbers of  $CD8^+CD44^{hi}$  T cells after IL-12+IL-18 treatment is mainly due to an increase in absolute cell numbers of  $T_{VM}$  cells over  $T_{MEM}/T_{EFF}$  cells in spleen (Figure 5C) and dLNs (Figure 5D). In addition, evaluation of CD122 and Eomes expression demonstrated similar results when comparing WT and OT-I mice with an up-regulation of CD122 in  $T_{MEM}/T_{EFF}$  cells after the 12 + 18 treatment, especially in dLNs (Figures 6A, B). Surprisingly, Eomes expression in both  $T_{VM}$  and  $T_{MEM}/T_{EFF}$  cells is lower in OT-I than in WT mice, especially in spleen (Figure 6C) and is not affected by the treatment (Figures 6C, D).

When we performed a non-supervised flow cytometry analysis (Trimap) of these cell subsets, we observed similar results to the supervised data (shown in Figures 5, 6).

Furthermore, as shown in Supplementary Figure 5,  $T_{MEM}/T_{EFF}$  cells predominate after IL-12+IL-18 treatment in WT mice while the opposite effect is seen in OT-I where  $T_{VM}$  cells are enriched after the cytokine treatment.

### 3.4.2 High and similar antitumor capacity of OT-I and WT mice after systemic expression of IL-12 and IL-18

When we compared the antitumor ability against B16 in OT-I and WT mice we observed that tumor growth is significantly lower in control OT-I than WT mice in the days post-treatment (Figures 7A, B). This effect is also confirmed by smaller tumors in OT-I control mice at day 7 post-treatment (Figure 7C). Although we observed a certain amount of  $CD4^+$  T cells in the non-RAG KO OT-I mice (Supplementary Figures 4, 7), we have not evaluated the proportion of conventional vs regulatory  $CD4^+$  T cells (Treg) cells and anti-tumor activity in control mice. However, the antitumor capacity is similar and highly efficient after IL-12+IL-18 systemic expression in both strains of mice (Figures 7A–C). Interestingly, we confirmed that a proportion of  $CD45^+$  cells infiltrating the B16 tumors from OT-I are OVAt<sup>+</sup> cells (~9-10% of total  $CD8^+$  cells) (Figure 7D). Moreover, IL-12+IL-18 stimulation increased the frequency of polyclonal  $T_{VM}$  cells (although OVAt<sup>+</sup> cells are in similar percentage compared to control mice) (Figure 7E). Importantly, OVAt<sup>+</sup> cells are  $CD49d^{lo}$  meaning that, at least in case of dual TCRs, they don't carry a TCR specific for tumor antigens or are activated by other antigens.

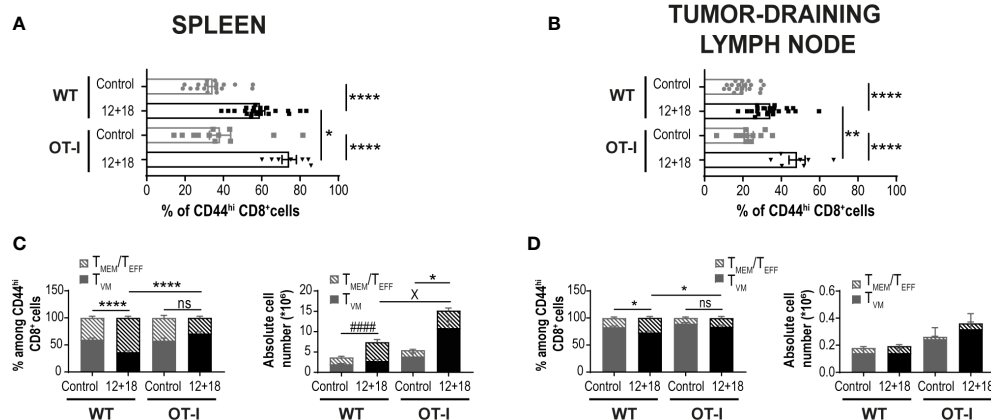


FIGURE 5

Effects of systemic co-expression of IL-12 plus IL-18 on  $CD8^+$  T lymphocytes in SLO from WT and OT-I mice. OVA<sup>neg</sup> B16-bearing C57BL/6 WT and OT-I mice were hydrodynamically injected (HI) with IL-12 plus IL-18 cDNA (12 + 18) or empty cDNA as the control. After 7 days post-HI mice were euthanized, and spleen and dLN were harvested and processed for flow cytometry. (A, B) Bar graphs represent frequencies of  $CD44^{hi}CD8^+$  T cells on (A) spleen or (B) dLN from control or 12 + 18 WT or OT-I mice. (C, D) Bar graphs show frequencies and absolute cell numbers of  $T_{MEM}/T_{EFF}$  and  $T_{VM}$  cells among  $CD44^{hi}CD8^+$  T cells from (C) spleen or (D) dLN from control or 12 + 18 WT or OT-I mice. Statistical analysis was performed with One-way ANOVA (A–D). Values of \* $p$ <0.05, \*\* $p$ <0.01, \*\*\* $p$ <0.0001 were considered significant. #####  $p$ <0.0001 represents the statistical difference of the indicated  $T_{MEM}/T_{EFF}$  control vs 12 + 18 subpopulations, while X  $p$ <0.01 represents the difference among the specified control and 12 + 18  $T_{VM}$  cells, \* indicates an statistical difference in both subpopulations of memory  $CD8^+$  T cells.

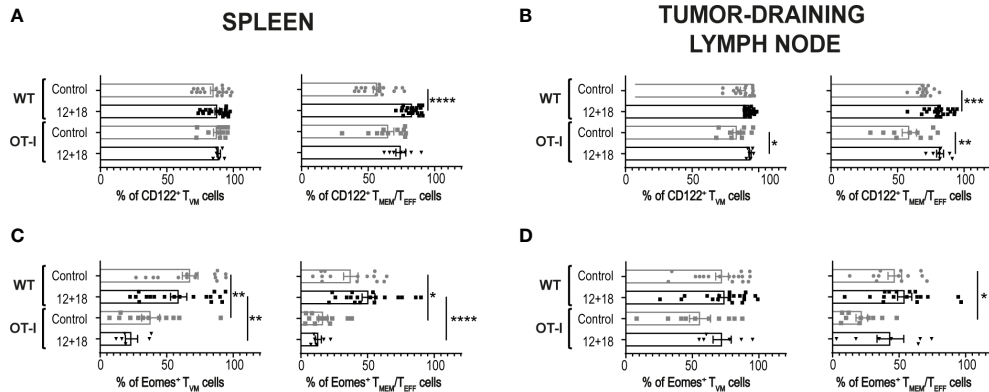


FIGURE 6

Effects of systemic co-expression of IL-12 plus IL-18 on  $T_{VM}$  and  $T_{MEM}/T_{EFF}$  cells in SLO from WT or OT-I mice. OVA<sup>neg</sup> B16-bearing C57BL/6 WT or OT-I mice were hydrodynamically injected (HI) with IL-12 plus IL-18 cDNA (12 + 18) or empty cDNA as the control. After 7 days post-HI mice were euthanized, and spleen and tumor-draining lymph nodes (dLN) were harvested and processed for flow cytometry. Bar graphs show the frequencies of (A, B) CD122<sup>+</sup> or (C, D) Eomes<sup>+</sup>  $T_{VM}$  or  $T_{MEM}/T_{EFF}$  cells (left and right graphs respectively) on (A, C) spleen and (B, D) dLN from each experimental group. Statistical analysis was performed with One-Way ANOVA (A, D, left B, and left C) or Brown-Forsthy and Welch ANOVA test (right B and right C). Values of \*p<0.05, \*\*p<0.01, \*\*\*p<0.001, \*\*\*\*p<0.0001 were considered significant.

We have previously demonstrated the potent antitumor capacity of IL-12+IL-18 cDNA (at higher doses) (27) or IL-12 cDNA systemic expression (25, 28) in B16 and other murine tumor models *in vivo* (3LL and EL4). In Figure 4 we show that there is a significant increment in total CD8<sup>+</sup> T cell infiltration in B16 tumors after systemic expression of IL-12+IL-18. Based on these results, we evaluated CD8<sup>+</sup> T cell infiltration in tumors that have poor leukocyte infiltration due to the development of mechanisms of T cell exclusion. We have chosen the OVA<sup>neg</sup> KPC cell line (pancreatic ductal adenocarcinoma) model because it demonstrates an inflammatory infiltrate with a scarcity of effector T cells (41). We asked if in this “cold” tumor model, systemic IL-12+IL-18 treatment was able to increase the capacity of CD8<sup>+</sup> T cells to infiltrate the tumors. Moreover, this cell line, by not undergoing the epithelial-mesenchymal transition process, is able to recapitulate the biology of human cancers in mice as characterized by islets of tumor cells surrounded by stroma (Supplementary Figure 6). This type of structure allows us to differentiate not only the location, but also the behavior and migratory pattern of the cells that infiltrate the tumors. We first evaluated tumor sizes in KPC-bearing OT-I mice and similar to the B16 tumor model, KPC tumors were significantly smaller in 12 + 18-treated mice than in control mice (Figure 8A).

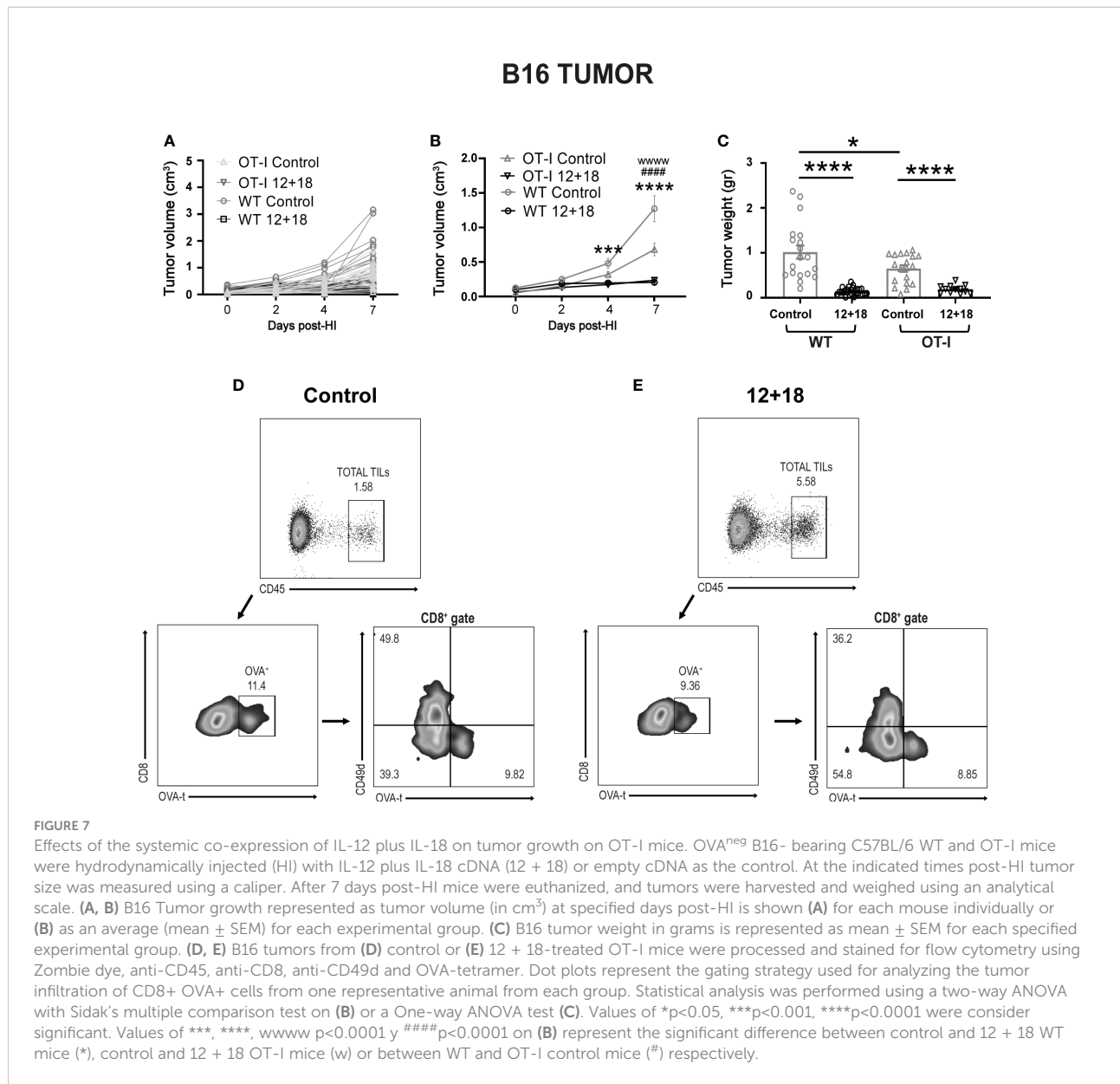
The results shown in Figure 5 (OT-I mice) demonstrate that when  $T_{VM}$  cells predominate over  $T_{MEM}/T_{EFF}$  cells, a higher antitumor capacity is observed. By using an OVA tetramer (OVAt), we evaluated the exclusive role of  $T_{VM}$  cells in KPC-bearing mice by selecting OT-I animals that carry 99-100% CD8<sup>+</sup>OVAt<sup>+</sup> T cells where CD8<sup>+</sup> T cells carry a TCR non-specific for tumor antigens (Supplementary Figure 7).

In this experimental setting, we observed that tumors from 12 + 18-treated mice were highly infiltrated by  $T_{VM}$  cells as compared to control mice (quantification in Figure 8B and representative images in Figures 8C, D). Magnification images (Figures 8E–H) show that in both groups of mice,  $T_{VM}$  cells are quite restricted to the stromal areas. However, in 12 + 18-treated mice,  $T_{VM}$  cells were able to infiltrate more efficiently into the tumor areas compared to tumors from control mice (Figures 8G, H).

To analyze the behavior of the lymphocytes inside the tumor, we performed *ex vivo* real-time imaging experiments in which we observed that  $T_{VM}$  cells from tumors of control animals showed a high mobility (Supplementary Video 1) as compared to those present in tumors from 12 + 18-treated mice, where the cells were visualized as considerably more static (Supplementary Video 2) (statistical analysis in Figure 9A). In selected images obtained from the videos, it can be clearly observed that  $T_{VM}$  cells in control animals are mostly restricted to stromal areas (green) (Figure 9B), while those of 12 + 18 animals are in close contact with the tumor islets (blue) (Figure 9C).

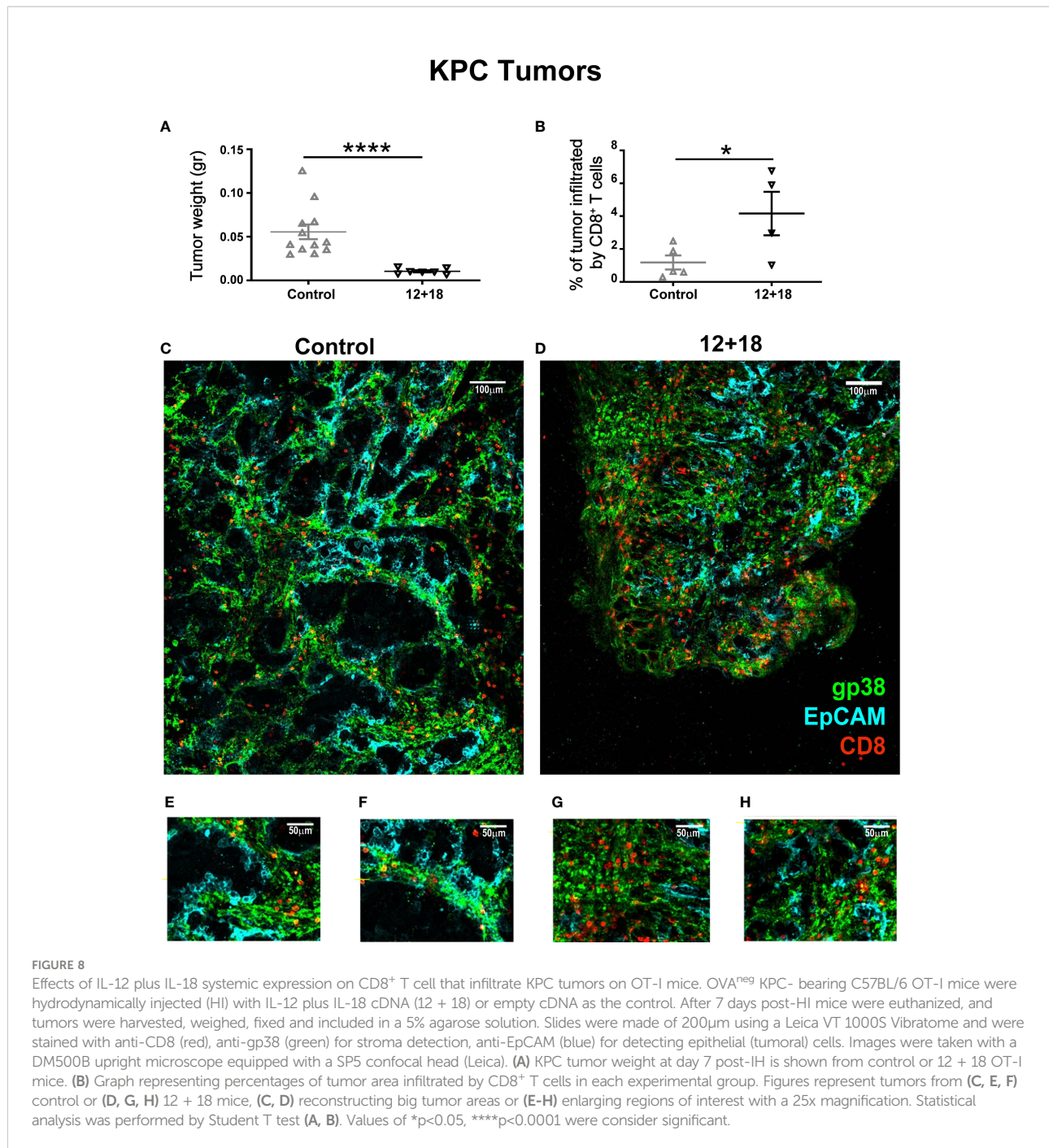
### 3.5 The antitumor effect of systemic IL-12+IL-18 is mainly mediated by IFN $\gamma$ production

Due to the results obtained from videos 1 and 2, it seems that high infiltration into tumor islets along with low motility of  $T_{VM}$  cells indicate that cell-cell interactions may be an important part of the antitumor mechanism after systemic IL-12+IL-18 expression.



The main candidate for this cell-cell interaction that has been previously described is NKG2D, a cell surface protein that is expressed in T<sub>VM</sub> cells. However, the fact that most of the cell lines that were used in our experiment do not express NKG2D ligands made this hypothesis unlikely (26). In contrast, IFN $\gamma$  production is synergistically produced in cells that simultaneously express IL-12R and IL-18R as in the case of T<sub>VM</sub> cells (3, 12–14). Moreover, IFN $\gamma$  has been demonstrated to induce a strong anti-angiogenic effect on tumor models (24). Based on these findings, we hypothesized that IFN $\gamma$  could be playing a main role in this system as an antitumor effector. Interestingly, T<sub>VM</sub> cells produce large amount of IFN $\gamma$  in response to IL-12+IL-18 as previously demonstrated in infectious disease murine models (3, 12–14).

To test this hypothesis, we first evaluated tumor growth and size after systemic expression of IL-12+IL-18 in B16-bearing WT or IFN $\gamma$ KO mice (GKO). As shown in Figure 10A, the potent antitumor capacity of IL-12+IL-18 is completely abolished in mice that lack IFN $\gamma$ . This effect is also visualized by similar tumor size when comparing control and 12 + 18-treated GKO mice (Figure 10B). When we evaluated the composition of TILs, we observed that even though the total leukocyte numbers were similar between WT and GKO mice in steady-state and Th1 inflammatory conditions (Figure 10C), the total number of infiltrating CD8<sup>+</sup> T cells is highly diminished in GKO mice (Figure 10D). More interestingly, the large proportion of T<sub>VM</sub> cells observed in WT mice after IL-12+IL-18 treatment is not



seen in GKO mice as they exhibited similar values to WT control mice (Figure 10E).

## 4 Discussion

In the field of cancer immunology, the role of CD8<sup>+</sup> T cells has been extensively addressed over the years. Solid tumors are

usually infiltrated by different types of leukocytes and during the last 20-30 years, accumulating evidence has suggested that there is a positive correlation between tumor CD8<sup>+</sup> T cells infiltration and a better prognosis for cancer patients. Moreover, this correlation is taken into account, both in the prognosis and in the choice of treatment for most cancers. For example, in colorectal cancer, Kirilovsky et al. have developed a prognostic score ('Immunoscore') in the classification system that takes into

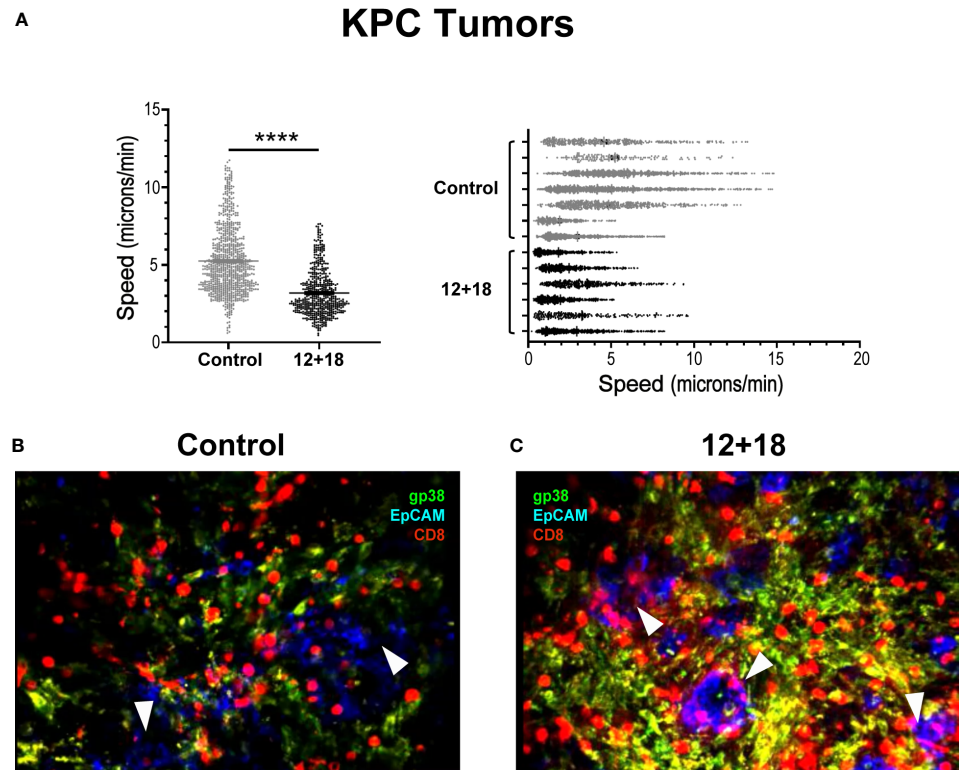


FIGURE 9

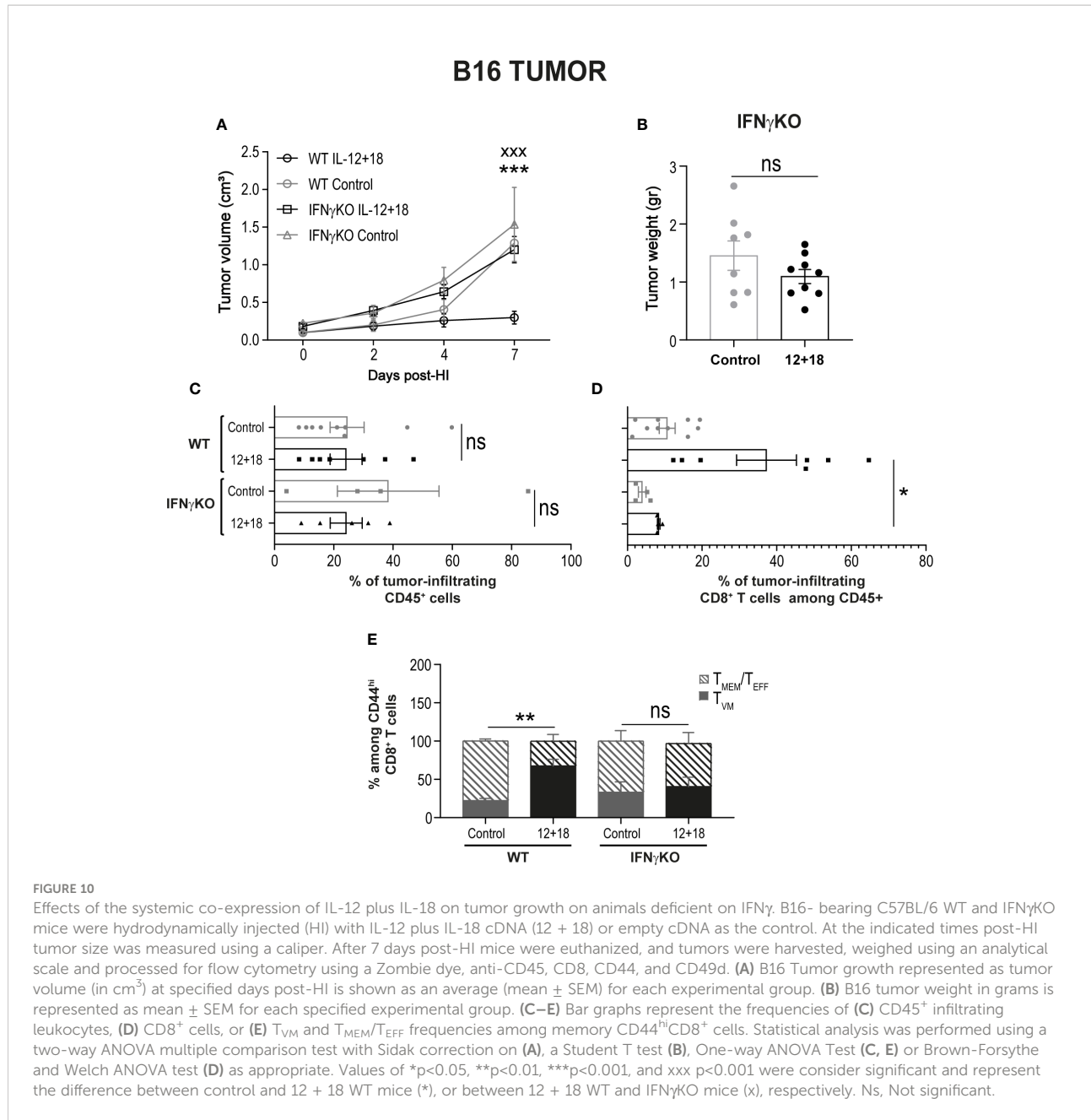
Effects of IL-12 plus IL-18 systemic expression on the behavior of tumor infiltrating CD8<sup>+</sup> T cells from OT-I mice. OVA<sup>neg</sup> KPC- bearing C57BL/6 OT-I mice were hydrodynamically injected (HI) with IL-12 plus IL-18 cDNA (12 + 18) or empty cDNA as controls. After 7 days post-HI mice were euthanized, and tumors were harvested. Tumors were immediately included in a 5% agarose solution. Slides were made of 200 $\mu$ m using a Leica VT 1000S Vibratome and were stained with anti-CD8 (red), anti-gp38 (green) for stroma detection, anti-EpCAM (blue) for detecting epithelial (tumoral) cells. Time lapse images were taken every 30 seconds for 20 minutes with a DM500B upright microscope equipped with a SP5 confocal head (Leica) and a 37°C thermostated chamber. (A) Graph shows the speed mean (microns/min) of each individual CD8<sup>+</sup> T cell across all the mice (left graph) or from each mouse individually (right graph) with the average speed corresponding to each experimental group (mean  $\pm$  SEM). (B, C) Images selected from two representative movies obtained from (B) control or (C) 12 + 18 KPC tumors show the infiltrate and distribution of CD8<sup>+</sup> T cells. Statistical analysis was performed by Student T test with Mann-Whitney correction (left C). Values of \*\*\*\*p<0.0001 were considered significant.

account the distribution of CD8<sup>+</sup> cytotoxic T cells both in the tumor core and in the invasive margins that include tumor, lymph nodes and metastases (TNM) (22, 23).

Despite the clinical importance of the characterization of leukocytes in human and mouse tumors, there is a lack of information on the subtype of CD8<sup>+</sup> T cells that infiltrate the tumors. For many years, it was assumed they are CD8<sup>+</sup> T cells specific for Ags expressed by cancer cells. However, several reports suggest that CD8<sup>+</sup> T cells with innate cell markers, not only infiltrate human and murine tumors, but also contribute to their eradication through mechanisms that are Ag-independent (11, 42, 43). Moreover, a recent review profoundly addresses the composition of tumor infiltrating CD8<sup>+</sup> T cells and presents evidence demonstrating that a large fraction of human and murine tumor-infiltrating T cells are cancer unrelated and are designated as “bystanders T cells” (2). For example, Mognol et al. showed that, transferred activated “cancer-ignorant CD8<sup>+</sup> cells”

infiltrated murine tumors at levels comparable to those of cancer-specific CD8<sup>+</sup> cells (44).

Comparative studies that simultaneously address T<sub>MEM</sub> and T<sub>VM</sub> cell differences and similarities in the cancer environment are rarely reported. Other than the work by Quinn et al. in humans (45), there is a complete absence of such reports in humans and the subject has only been approached by a few laboratories utilizing mouse models (4, 34, 46). However, it is important to note the work of Hussain et al. that presents a comprehensive comparative review of various aspects of the biology of both cell types (34). The appreciation of the role of T<sub>VM</sub> cells as a first wave of immune protection, especially in infectious diseases, has become more obvious over the years. Moreover, the fact that T<sub>VM</sub> cells can exhibit cytotoxicity more rapidly than naïve T cells, with similar kinetics and efficiencies of T<sub>MEM</sub> cells (4, 45, 46), makes the investigation of T<sub>VM</sub> cells very relevant in the cancer field.



Even though T<sub>VM</sub> cells carry a functional TCR, these cells exhibit particularly high responsiveness to cytokines including IL-12, IL-18 and IL-15 as compared to specific Ag stimulation. Moreover, both Ag-inexperienced (T<sub>VM</sub>) and Ag-experienced (T<sub>MEM</sub> and T<sub>EFF</sub>) cells proliferate in response to IL-15 and upon stimulation by IL-12 and IL-18 can elicit TCR independent proliferation, cytokine production and bystander cytotoxicity (4, 9, 34, 47, 48).

Based on these reports and the significant lack of information on the competitive role of T<sub>VM</sub> vs T<sub>MEM</sub>/T<sub>EFF</sub> cells in cancer, we aimed to investigate the prevalence of T<sub>VM</sub>

vs T<sub>MEM</sub>/T<sub>EFF</sub> cells in SLO from mice bearing early established tumors, both in steady-state conditions and after systemic expression of IL-12, IL-18 and IL-15.

In our models, mice bear either B16 or KPC tumors for no longer than 8 to 10 days before cytokine induction. Moreover, the rapid antitumor response observed as early as 4 days (and up to 7 days) post-IL-12+IL-18 treatment leads us to speculate that the composition of the CD44<sup>hi</sup>CD8<sup>+</sup> T cell subset is a mix of T<sub>VM</sub> cells (CD49d<sup>lo</sup>) and Ag-specific CD8<sup>+</sup> T effector cells and possibly early T<sub>MEM</sub> cells (CD49d<sup>hi</sup>). Thus, this provides us with a model where these memory/activated cells co-exist.

As previously reported, the constitutive high expression of IL-12R, IL-18R and CD122 situates  $T_{VM}$  cells in an advantagous position to rapidly respond to these cytokines (10, 49). Unexpectedly, our data demonstrate that systemic induction of IL-12+IL-18 (and IL-15) led to an enrichment of  $T_{MEM}/T_{EFF}$  cells with high expression of CD122 in SLO while  $T_{VM}$  cells remained at similar numbers and phenotype as compared to control mice. Even though we predicted the opposite results would be found, our data are similar to what is reported by Akue et al. The authors state that the frequency of pre-existing  $T_{VM}$  cells is stable in both steady-state conditions and after a greatly expanded Ag-driven memory CD8 $^{+}$  T cell immune response (47).

Another explanation for the prevalence of  $T_{MEM}$  cells after systemic IL-12+IL-18 expression could arise from the fact that  $T_{VM}$  cells in WT mice are a polyclonal population of memory-like CD8 $^{+}$  T cells. As such, after contacting their cognate Ag, these cells could convert to  $T_{EFF}$  and  $T_{MEM}$  cells as reported during influenza and listeria infections (4, 15). In our tumor models, the prevalence of  $T_{MEM}$  cells after Th1 systemic conditions could be the result of conversion of tumor-specific T naïve ( $T_N$ ) cells plus tumor-specific  $T_{VM}$  cells to a  $T_{EFF}/T_{MEM}$  phenotype. To test this hypothesis, we performed similar experiments utilizing non-RAG OT-I mice. In this model system (Supplementary Figure 4), we increased the number of  $T_{VM}$  cells (non-specific for tumor Ags) while a remnant number of polyclonal  $T_{MEM}/T_{EFF}$  are still present. Interestingly under these conditions, after IL-12+IL-18 expression we observed a significantly larger number of CD8 $^{+}$ CD44 $^{hi}$  T cells in OT-I mice than what was observed in WT mice. This population was mainly composed of  $T_{VM}$  rather than  $T_{MEM}/T_{EFF}$  cells, especially in the spleen. An interesting finding was that after IL-12+IL-18 treatment, the levels of Eomes do not change compared to the levels in control mice both in  $T_{VM}$  and in  $T_{MEM}/T_{EFF}$  cells. More surprisingly, in OT-I mice, Eomes levels are significantly lower in  $T_{VM}$  and  $T_{MEM}/T_{EFF}$  from spleen but not in LNs as compared to WT mice. This is an unexpected finding since it has been reported that Eomes is able to bind to the *il2rb* promoter leading to increases in CD122 expression, thus driving increased  $T_{VM}$  cell sensitivity to IL-15 (6). This result led us to assume that up-regulation of CD122 in  $T_{MEM}/T_{EFF}$  cells after the cytokine treatment correlated with higher Eomes expression in this population. However, other stimuli could be responsible for CD122 up-regulation in  $T_{MEM}$  cells as it is reported that TCR signaling augments IL-2R $\beta$  expression *via* both transcriptional and post-transcriptional regulation (50).

Interestingly, despite the higher proportion of  $T_{MEM}/T_{EFF}$  than  $T_{VM}$  cells in spleen and tumor-draining lymph nodes after IL-12+IL-18 expression, this is not what is observed on CD8 $^{+}$ CD44 $^{hi}$  T cells infiltrating the tumors. These cells show a predominant presence of  $T_{VM}$  cells after cytokine expression. We could not determine if this effect is due to a preferential migration of  $T_{VM}$  cells to tumors under Th1 conditions or if the

permanence/survival within tumors is favored by  $T_{VM}$  cells over  $T_{MEM}/T_{EFF}$ , similar to what has been reported by Miller et al. with  $T_N$  cells. Those authors demonstrated that when they co-transferred polyclonal CD8  $T_N$  cells and polyclonal CD8  $T_{VM}$  cells into TRAMP bearing mice, they found that donor  $T_{VM}$  cells constituted a substantial fraction of the tumor-infiltrating CD8 $^{+}$  T cells 4 months later (40).

The rapid antitumor immune response observed after systemic expression of IL-12+IL-18 points out to innate effector mechanisms rather than a TCR-mediated effect. The Ag-independent mechanisms achieved by bystander CD8 $^{+}$  T cells might rely on NKG2D-ligands recognition (10, 11), granzyme/perforin release (15, 16) and high IFN $\gamma$  production (3, 12–14). The fact that B16 cells do not express ligands for NKG2D (51) may indicate that this pathway is not involved in the control of B16 tumor growth. Instead, rapid production of IFN $\gamma$ , driven by IL-12+IL-18 could be responsible for the antitumor results observed in the experimental settings described here. Interestingly, we found that either IL-12 alone or IL-12+IL-18 systemic expression generated almost a complete disappearance of NK cells at 7–10 days post-treatment (25, 28) indicating that expression of IFN $\gamma$  can largely arise from T cells. In this context we speculated that IFN $\gamma$  produced by CD8 $^{+}$  T cells could be responsible for this early antitumor effect, especially since previous reports have demonstrated that IFN $\gamma$  participates in different stages of tumor growth control (24, 52, 53). In our laboratory, we have previously documented that high expression of IFN $\gamma$  is systemically induced after IL-12 or IL-12+IL-18 expression (27). Furthermore, there is a significantly higher number of IFN $\gamma$  $^{+}$ CD8 $^{+}$  T cells infiltrating B16 and EL-4 tumors after cytokine treatment compared to tumors from control mice (25). Data presented in this work demonstrates that in the absence of IFN $\gamma$ , the strong antitumor outcome observed after IL-12+IL-18 systemic expression is completely lost and this effect correlates with a significantly lower presence of  $T_{VM}$  cells in the tumors of IFN $\gamma$ KO mice compared to WT mice.

As mentioned earlier, IFN $\gamma$  is able to induce different antitumor mechanisms. For example, interferon-inducible protein 10 (IP-10)-induced by IFN $\gamma$  can exert a potent anti-angiogenic effect (53). Also, it is reported that IFN $\gamma$  produced within tumors suppresses VEGFR3 expression by acting directly on tumor vessel endothelial cells and on the tumor-infiltrating lymphocytes to indirectly alter endothelial cells' VEGFR3 expression (24). Consistent with this effect, previous work from our laboratory has demonstrated a significant reduction in the number of blood vessels present in B16 and EL-4 tumors after systemic expression of IL-12 (25). Additionally, Dangaj et al., using murine and human experimental systems, demonstrated that the initial recruitment of T cells to tumors is driven by tumor-derived CCL5 along with IFN $\gamma$ -inducible CXCR3 ligands secreted by myeloid cells present in the tumors (54). Interestingly, not only do we report here that IFN $\gamma$  KO mice show a reduced CD8 $^{+}$  T cell infiltration but we have also demonstrated that IFN $\gamma$  is produced mainly by infiltrating CD8 $^{+}$

T cells rather than by NK cells in B16 tumors after IL-12 systemic expression (25). Furthermore, our preliminary data indicates higher CCR5 expression on CD8<sup>+</sup> T cells infiltrating B16 tumors from 12 + 18-treated mice, as compared to control mice (unpublished data).

To further demonstrate the antitumor role of T<sub>VM</sub> cells, we developed a model utilizing the KPC tumor cell line that shows poor T cell infiltration. In this murine pancreatic tumor model, most T cells are excluded (41). Moreover, contrary to most murine tumor models, KPC tumors recapitulate the structure of human cancers, with the presence of tumor islets surrounded by stromal cells. By using OT-I mice, our study demonstrated that CD8<sup>+</sup> T cells (99-100% OVA-specific CD8<sup>+</sup> T cells) not only highly infiltrate KPC tumors but also preferentially localized in the tumor islet after IL-12+IL-18 expression, contrary to the control OT-I mice where most CD8<sup>+</sup> cells are found in the stromal areas. Consistent with our finding, Kantari-Mimoun et al. have reported that activated CAR T cells triggered the up-regulation of ICAM-1 on tumor cells in an IFN $\gamma$ -dependent pathway that enabled T cell entry into tumor islets (52).

Based on this evidence from our and other laboratories, we hypothesize that systemic IL-12+IL-18 is able to trigger, in turn, expression of IL-15 and IFN $\gamma$ . This pro-inflammatory environment could establish the perfect scenario for tumor eradication by different Ag-independent mechanisms mediated preferentially by IFN $\gamma$ -producing T<sub>VM</sub> cells. We speculate that in these conditions, CCR5<sup>+</sup>T<sub>VM</sub> cells can preferentially migrate or selectively persist in tumors and locally produce IFN $\gamma$ . The IFN $\gamma$  could then stimulate an anti-angiogenic effect along with the induction of adhesion molecules that permit the entry of T cells into the tumor islet. Even though we have presented solid evidence that tumor growth control is largely associated to the prevalence of T<sub>VM</sub> cells in the tumor environment, the limitation of this work is to exclusively point to T<sub>VM</sub> as the cells responsible for this effect. Currently experiments in our laboratory are focused on developing a more appropriate experimental strategy to substantiate this hypothesis.

The control of tumor growth through Ag-independent pathways is a topic of growing interest, especially considering that several tumors lose the expression of MHC type I as an immune evasion mechanism (55, 56). This loss of expression makes the tumor less susceptible to Ag-specific lysis, but more susceptible to innate control mechanisms such as the one exerted by T<sub>VM</sub> cells. Furthermore, as proposed by White et al. and Drobek et al., the T<sub>VM</sub> pool does not stochastically originate from the naïve T cell repertoire; instead, it is derived from a subset of naïve T cells that present a high affinity for self-ligands (visualized in mice as T cells with high levels of CD5) (40, 57). In this context, it is interesting to hypothesize that the continuous low level of homeostatic TCR signaling could result as an important signal for their anti-tumor responses. Accordingly, OT-I T cells are reported to be relatively highly self-reactive (40, 57). Even though systemic IL-12+IL-18 is normally triggered in

infectious diseases, their use as an antitumor treatment has been difficult to accomplish, largely due to toxicity. However, type I IFNs, IL-12, IL-15 and IL-18 are produced by activated antigen presenting cells and other cell types that are often present in the tumor microenvironment, thus suggesting that an innate immune response may be important in the host anti-tumor response (58, 59). Moreover, BATF3<sup>+</sup> dendritic cells are predominant producers of IL-15. Curiously, tumor-residing BATF3<sup>+</sup> dendritic cells have been shown to be required for T cell trafficking (60) that can ultimately participate in the recruitment of T<sub>VM</sub> cells to tumors due to high avidity of T<sub>VM</sub> cells for IL-15. Based on this evidence, it could be possible that alternative therapies, able to induce expression of these cytokine in the tumor microenvironment, may become quite promising for the direction of future therapeutic strategies.

## Data availability statement

The original contributions presented in the study are included in the article/[Supplementary Material](#). Further inquiries can be directed to the corresponding author.

## Ethics statement

The animal study was reviewed and approved by Comité Institucional de Cuidado y Uso de Animales de Laboratorio of the Facultad de Ciencias Químicas of Universidad Nacional de Córdoba (CICUAL-FCQ).

## Author contributions

CS-F: Methodology, validation, formal analysis, investigation. MV: Methodology, validation, formal analysis. NB: Methodology, investigation. NL: Methodology, validation. QF: Methodology, validation. HY: Conceptualization, original draft, review and editing. LV: Methodology, validation, formal analysis. ED: Conceptualization, investigation, funding acquisition. MR-G: Conceptualization, methodology, investigation, supervision, project administration, funding acquisition, writing. All authors contributed to the article and approved the submitted version.

## Funding

This work was supported by Secretaría de Ciencia y Tecnología from Universidad Nacional de Córdoba (SECyT); Agencia Nacional de Promoción Científica y Tecnológica (ANPCyT); Fondo para la Investigación Científica y Tecnológica (FONCyT); Fundación para el Progreso de la Medicina and P-UE 22920160100116CO - CONICET. This

work was supported in part by the Intramural Research Program of the Center for Cancer Research, National Cancer Institute (NCI), Cancer Innovation Laboratory (CIL) USA, under grant No. 1ZIABC009283-36. The views expressed in this article are those of the authors and do not necessarily reflect the official policy or position of the Department of Health and Human Services, nor does mention of trade names, commercial products, or organizations imply endorsement by the United States Government.

## Acknowledgments

The authors thank Diego Luti, Victoria Blanco, Cecilia Noriega, Dr. Soledad Miro, Sergio Oms and Dr. Ivanna Novotny, for animal care. Dr. Pilar Crespo and Dr. Paula Abadie for FACS technical support. Dr. Laura Gatica, Lic. Gabriela Furlan and Dr. Noelia Maldonado for cell culture support and Paula Icely for overall experimental technical assistance. We acknowledge the NIH Tetramer Core Facility for provision of the PE and APC-labeled SINFEKL/Kb tetramers.

## References

1. Freeman BE, Hammarlund E, Raue HP, Slifka MK. Regulation of innate CD8+ T-cell activation mediated by cytokines. *Proc Natl Acad Sci U.S.A.* (2012) 109(25):9971–6. doi: 10.1073/pnas.1203543109
2. Meier SL, Satpathy AT, Wells DK. Bystander T cells in cancer immunology and therapy. *Nat Cancer.* (2022) 3(2):143–55. doi: 10.1038/s43018-022-00335-8
3. Haluszczak C, Akue AD, Hamilton SE, Johnson LD, Pujanauski L, Teodorovic L, et al. The antigen-specific CD8+ T cell repertoire in unimmunized mice includes memory phenotype cells bearing markers of homeostatic expansion. *J Exp Med* (2009) 206(2):435–48. doi: 10.1084/jem.20081829
4. Lee JY, Hamilton SE, Akue AD, Hogquist KA, Jameson SC. Virtual memory CD8 T cells display unique functional properties. *Proc Natl Acad Sci U.S.A.* (2013) 110(33):13498–503. doi: 10.1073/pnas.1307572110
5. Quinn KM, Hussain T, Kraus F, Formosa LE, Lam WK, Dagley MJ, et al. Metabolic characteristics of CD8(+) T cell subsets in young and aged individuals are not predictive of functionality. *Nat Commun* (2020) 11(1):2857. doi: 10.1038/s41467-020-16633-7
6. Intlekofer AM, Takemoto N, Wherry EJ, Longworth SA, Northrup JT, Palanivel VR, et al. Effector and memory CD8+ T cell fate coupled by T-bet and eomesodermin. *Nat Immunol.* (2005) 6(12):1236–44. doi: 10.1038/ni1268
7. Pearce EL, Mullen AC, Martins GA, Krawczyk CM, Hutchins AS, Zediak VP, et al. Control of effector CD8+ T cell function by the transcription factor eomesodermin. *Science.* (2003) 302(5647):1041–3. doi: 10.1126/science.1090148
8. White JT, Cross EW, Kedl RM. Antigen-inexperienced memory CD8(+) T cells: where they come from and why we need them. *Nat Rev Immunol.* (2017) 17(6):391–400. doi: 10.1038/nri.2017.34
9. White JT, Cross EW, Burchill MA, Danhorn T, McCarter MD, Rosen HR, et al. Virtual memory T cells develop and mediate bystander protective immunity in an IL-15-dependent manner. *Nat Commun* (2016) 7:11291. doi: 10.1038/ncomms11291
10. Chu T, Tyznik AJ, Roepke S, Berkley AM, Woodward-Davis A, Paccagnini L, et al. Bystander-activated memory CD8 T cells control early pathogen load in an innate-like, NKG2D-dependent manner. *Cell Rep* (2013) 3(3):701–8. doi: 10.1016/j.celrep.2013.02.020
11. Tietze JK, Wilkins DE, Sckisel GD, Bouchlaka MN, Alderson KL, Weiss JM, et al. Delineation of antigen-specific and antigen-nonspecific CD8(+) memory T-
12. Moudra A, Niederlova V, Novotny J, Schmiedova L, Kubovciak J, Matejkova T, et al. Phenotypic and clonal stability of antigen-inexperienced memory-like T cells across the genetic background, hygienic status, and aging. *J Immunol* (2021) 206(9):2109–21. doi: 10.4049/jimmunol.2001028
13. Baez NS, Cerban F, Savid-Frontera C, Hodge DL, Tosello J, Acosta-Rodriguez E, et al. Thymic expression of IL-4 and IL-15 after systemic inflammatory or infectious Th1 disease processes induce the acquisition of “innate” characteristics during CD8+ T cell development. *PLoS Pathog* (2019) 15(1):e1007456. doi: 10.1371/journal.ppat.1007456
14. Berg RE, Cordes CJ, Forman J. Contribution of CD8+ T cells to innate immunity: IFN-gamma secretion induced by IL-12 and IL-18. *Eur J Immunol* (2002) 32(10):2807–16. doi: 10.1002/1521-4141(2002010)32:10<2807::AID-IMMU2807>3.0.CO;2-0
15. Lanzer KG, Cookenham T, Reiley WW, Blackman MA. Virtual memory cells make a major contribution to the response of aged influenza-naive mice to influenza virus infection. *Immun Ageing.* (2018) 15:17. doi: 10.1186/s12979-018-0122-y
16. Wang X, Waschke BC, Woolaver RA, Chen SMY, Chen Z, Wang JH. MHC class I-independent activation of virtual memory CD8 T cells induced by chemotherapeutic agent-treated cancer cells. *Cell Mol Immunol* (2021) 18(3):723–34. doi: 10.1038/s41423-020-0463-2
17. Trinchieri G. Interleukin-12 and the regulation of innate resistance and adaptive immunity. *Nat Rev Immunol.* (2003) 3(2):133–46. doi: 10.1038/nri1001
18. Berg RE, Crossley E, Murray S, Forman J. Memory CD8+ T cells provide innate immune protection against listeria monocytogenes in the absence of cognate antigen. *J Exp Med* (2003) 198(10):1583–93. doi: 10.1084/jem.20031051
19. Lertmemongkolchai G, Cai G, Hunter CA, Bancroft GJ. Bystander activation of CD8+ T cells contributes to the rapid production of IFN-gamma in response to bacterial pathogens. *J Immunol* (2001) 166(2):1097–105. doi: 10.4049/jimmunol.166.2.1097
20. Lee A, Park SP, Park CH, Kang BH, Park SH, Ha SJ, et al. IL-4 induced innate CD8+ T cells control persistent viral infection. *PLoS Pathog* (2015) 11(10):e1005193. doi: 10.1371/journal.ppat.1005193
21. Sckisel GD, Tietze JK, Zamora AE, Hsiao HH, Priest SO, Wilkins DE, et al. Influenza infection results in local expansion of memory CD8(+) T cells with

## Conflict of interest

The authors declare that the research was conducted in the absence of any commercial or financial relationships that could be construed as a potential conflict of interest.

## Publisher's note

All claims expressed in this article are solely those of the authors and do not necessarily represent those of their affiliated organizations, or those of the publisher, the editors and the reviewers. Any product that may be evaluated in this article, or claim that may be made by its manufacturer, is not guaranteed or endorsed by the publisher.

## Supplementary material

The Supplementary Material for this article can be found online at: <https://www.frontiersin.org/articles/10.3389/fimmu.2022.971001/full#supplementary-material>

antigen non-specific phenotype and function. *Clin Exp Immunol* (2014) 175(1):79–91. doi: 10.1111/cei.12186

22. Anitei MG, Zeitoun G, Mlecnik B, Marliot F, Haicheur N, Todosi AM, et al. Prognostic and predictive values of the immunoscore in patients with rectal cancer. *Clin Cancer Res* (2014) 20(7):1891–9. doi: 10.1158/1078-0432.CCR-13-2830

23. Kirilovsky A, Marliot F, El Sissy C, Haicheur N, Galon J, Pages F. Rational bases for the use of the immunoscore in routine clinical settings as a prognostic and predictive biomarker in cancer patients. *Int Immunopharmacol* (2016) 28(8):373–82. doi: 10.1093/intimm/dxw021

24. Sorensen EW, Gerber SA, Frelinger JG, Lord EM. IL-12 suppresses vascular endothelial growth factor receptor 3 expression on tumor vessels by two distinct IFN-gamma-dependent mechanisms. *J Immunol* (2010) 184(4):1858–66. doi: 10.4049/jimmunol.0903210

25. Savid-Frontera C, Viano ME, Baez NS, Reynolds D, Matellon M, AY H, et al. Safety levels of systemic IL-12 induced by cDNA expression as a cancer therapeutic. *Immunotherapy* (2022) 14(2):115–33. doi: 10.2217/int-2021-0080

26. Diefenbach A, Jamieson AM, Liu SD, Shastri N, Raulet DH. Ligands for the murine NKG2D receptor: expression by tumor cells and activation of NK cells and macrophages. *Nat Immunol* (2000) 1(2):119–26. doi: 10.1038/77793

27. Rodriguez-Galan MC, Reynolds D, Correa SG, Iribarren P, Watanabe M, Young HA. Coexpression of IL-18 strongly attenuates IL-12-induced systemic toxicity through a rapid induction of IL-10 without affecting its antitumor capacity. *J Immunol* (2009) 183(1):740–8. doi: 10.4049/jimmunol.0804166

28. Barrios B, Baez NS, Reynolds D, Iribarren P, Cejas H, Young HA, et al. Abrogation of TNFalpha production during cancer immunotherapy is crucial for suppressing side effects due to the systemic expression of IL-12. *PLoS One* (2014) 9(2):e90116. doi: 10.1371/journal.pone.0090116

29. Hodge DL, Reynolds D, Cerban FM, Correa SG, Baez NS, Young HA, et al. MCP-1/CCR2 interactions direct migration of peripheral b and T lymphocytes to the thymus during acute infectious/inflammatory processes. *Eur J Immunol* (2012) 42(10):2644–54. doi: 10.1002/eji.201242408

30. Rodriguez-Galan MC, Bream JH, Farr A, Young HA. Synergistic effect of IL-2, IL-12, and IL-18 on thymocyte apoptosis and Th1/Th2 cytokine expression. *J Immunol* (2005) 174(5):2796–804. doi: 10.4049/jimmunol.174.5.2796

31. Salmon H, Franciszkiewicz K, Damotte D, Dieu-Nosjean MC, Validire P, Trautmann A, et al. Matrix architecture defines the preferential localization and migration of T cells into the stroma of human lung tumors. *J Clin Invest.* (2012) 122(3):899–910. doi: 10.1172/JCI45817

32. Bougherara H, Mansuet-Lupo A, Alifano M, Ngo C, Damotte D, Le Frere-Belda MA, et al. Real-time imaging of resident T cells in human lung and ovarian carcinomas reveals how different tumor microenvironments control T lymphocyte migration. *Front Immunol* (2015) 6:500. doi: 10.3389/fimmu.2015.00500

33. Liu F, Song Y, Liu D. Hydrodynamics-based transfection in animals by systemic administration of plasmid DNA. *Gene Ther* (1999) 6(7):1258–66. doi: 10.1038/sj.gt.3300947

34. Hussain T, Quinn KM. Similar but different: virtual memory CD8 T cells as a memory-like cell population. *Immunol Cell Biol* (2019) 97(7):675–84. doi: 10.1111/imcb.12227

35. Ashman RB, Vijayan D, Wells CA. IL-12 and related cytokines: function and regulatory implications in candida albicans infection. *Clin Dev Immunol* (2011) 2011:686597. doi: 10.1155/2011/686597

36. Cardillo F, Postol E, Nihei J, Aroeira LS, Nomizo A, Mengel J. B cells modulate T cells so as to favour T helper type 1 and CD8+ T-cell responses in the acute phase of trypanosoma cruzi infection. *Immunology* (2007) 122(4):584–95. doi: 10.1111/j.1365-2567.2007.02677.x

37. Romani L, Puccetti P, Bistoni F. Interleukin-12 in infectious diseases. *Clin Microbiol Rev* (1997) 10(4):611–36. doi: 10.1128/CMR.10.4.611

38. Martinet V, Tonon S, Torres D, Azouz A, Nguyen M, Kohler A, et al. Type I interferons regulate comesodermin expression and the development of unconventional memory CD8(+) T cells. *Nat Commun* (2015) 6:7089. doi: 10.1038/ncomms8089

39. Kurzweil V, LaRoche A, Oliver PM. Increased peripheral IL-4 leads to an expanded virtual memory CD8+ population. *J Immunol* (2014) 192(12):5643–51. doi: 10.4049/jimmunol.1301755

40. Miller CH, Klawon DEJ, Zeng S, Lee V, Soccia ND, Savage PA. Eomes identifies thymic precursors of self-specific memory-phenotype CD8(+) T cells. *Nat Immunol* (2020) 21(5):567–77. doi: 10.1038/s41590-020-0653-1

41. Bayne LJ, Beatty GL, Jhala N, Clark CE, Rhim AD, Stanger BZ, et al. Tumor-derived granulocyte-macrophage colony-stimulating factor regulates myeloid inflammation and T cell immunity in pancreatic cancer. *Cancer Cell* (2012) 21(6):822–35. doi: 10.1016/j.ccr.2012.04.025

42. Hu J, Zhu S, Xia X, Zhang L, Kleinerman ES, Li S. CD8+T cell-specific induction of NKG2D receptor by doxorubicin plus interleukin-12 and its contribution to CD8+T cell accumulation in tumors. *Mol Cancer* (2014) 13:34. doi: 10.1186/1476-4598-13-34

43. Xu W, Jones M, Liu B, Zhu X, Johnson CB, Edwards AC, et al. Efficacy and mechanism-of-action of a novel superagonist interleukin-15: Interleukin-15 receptor alphaSu/Fc fusion complex in syngeneic murine models of multiple myeloma. *Cancer Res* (2013) 73(10):3075–86. doi: 10.1158/0008-5472.CAN-12-2357

44. Mognol GP, Spreafico R, Wong V, Scott-Browne JP, Togher S, Hoffmann A, et al. Exhaustion-associated regulatory regions in CD8(+) tumor-infiltrating T cells. *Proc Natl Acad Sci U S A.* (2017) 114(13):E2776–E85. doi: 10.1073/pnas.1620498114

45. Quinn KM, Fox A, Harland KL, Russ BE, Li J, Nguyen THO, et al. Age-related decline in primary CD8(+) T cell responses is associated with the development of senescence in virtual memory CD8(+) T cells. *Cell Rep* (2018) 23(12):3512–24. doi: 10.1016/j.celrep.2018.05.057

46. Renkema KR, Li G, Wu A, Smithey MJ, Nikolich-Zugich J. Two separate defects affecting true naive or virtual memory T cell precursors combine to reduce naive T cell responses with aging. *J Immunol* (2014) 192(1):151–9. doi: 10.4049/jimmunol.1301453

47. Akue AD, Lee JY, Jameson SC. Derivation and maintenance of virtual memory CD8 T cells. *J Immunol* (2012) 188(6):2516–23. doi: 10.4049/jimmunol.1102213

48. Yoshimoto T, Takeda K, Tanaka T, Ohkusu K, Kashiwamura S, Okamura H, et al. IL-12 up-regulates IL-18 receptor expression on T cells, Th1 cells, and b cells: synergism with IL-18 for IFN-gamma production. *J Immunol* (1998) 161(7):3400–7.

49. Tripathi P, Morris SC, Perkins C, Sholl A, Finkelman FD, Hildeman DA. IL-4 and IL-15 promotion of virtual memory CD8(+) T cells is determined by genetic background. *Eur J Immunol* (2016) 46(10):2333–9. doi: 10.1002/eji.201646404

50. Kim HP, Imbert J, Leonard WJ. Both integrated and differential regulation of components of the IL-2/IL-2 receptor system. *Cytokine Growth Factor Rev* (2006) 17(5):349–66. doi: 10.1016/j.cytogfr.2006.07.003

51. Diefenbach A, Jensen ER, Jamieson AM, Raulet DH. Rae1 and H60 ligands of the NKG2D receptor stimulate tumour immunity. *Nature* (2001) 413(6852):165–71. doi: 10.1038/35093109

52. Kantari-Mimoun C, Barrin S, Vimeux L, Haghiri S, Gervais C, Joaquina S, et al. CAR T-cell entry into tumor islets is a two-step process dependent on IFNgamma and ICAM-1. *Cancer Immunol Res* (2021) 9(12):1425–38. doi: 10.1158/2326-6066.CIR-20-0837

53. Sgadari C, Angiolillo AL, Tosato G. Inhibition of angiogenesis by interleukin-12 is mediated by the interferon-inducible protein 10. *Blood* (1996) 87(9):3877–82. doi: 10.1182/blood.V87.9.3877.bloodjournal8793877

54. Dangaj D, Bruand M, Grimm AJ, Ronet C, Barras D, Duttagupta PA, et al. Cooperation between constitutive and inducible chemokines enables T cell engraftment and immune attack in solid tumors. *Cancer Cell* (2019) 35(6):885–900 e10. doi: 10.1016/j.ccr.2019.05.004

55. Garrido F, Cabrera T, Aptsiauri N. "Hard" and "soft" lesions underlying the HLA class I alterations in cancer cells: implications for immunotherapy. *Int J Cancer* (2010) 127(2):249–56. doi: 10.1002/ijc.25270

56. Challa-Malladi M, Lieu YK, Califano O, Holmes AB, Bhagat G, Murty VV, et al. Combined genetic inactivation of beta2-microglobulin and CD58 reveals frequent escape from immune recognition in diffuse large b cell lymphoma. *Cancer Cell* (2011) 20(6):728–40. doi: 10.1016/j.ccr.2011.11.006

57. Drobek A, Moudra A, Mueller D, Huranova M, Horkova V, Pribikova M, et al. Strong homeostatic TCR signals induce formation of self-tolerant virtual memory CD8 T cells. *EMBO J* (2018) 37(14):e98518. doi: 10.15252/embj.201798518

58. Lippitz BE. Cytokine patterns in patients with cancer: a systematic review. *Lancet Oncol* (2013) 14(6):e218–28. doi: 10.1016/S1470-2045(12)70582-X

59. Zitvogel L, Galluzzi L, Kepp O, Smyth MJ, Kroemer G. Type I interferons in anticancer immunity. *Nat Rev Immunol* (2015) 15(7):405–14. doi: 10.1038/nri3845

60. Spranger S, Dai D, Horton B, Gajewski TF. Tumor-residing Batf3 dendritic cells are required for effector T cell trafficking and adoptive T cell therapy. *Cancer Cell* (2017) 31(5):711–23 e4. doi: 10.1016/j.ccr.2017.04.003



## OPEN ACCESS

## EDITED BY

Ana Carolina Monteiro,  
Fluminense Federal University, Brazil

## REVIEWED BY

Mai Chan Lau,  
Institute of Molecular and Cell Biology  
(A\*STAR), Singapore  
Zhengshi Wang,  
Tongji University, China

## \*CORRESPONDENCE

Bo Xu  
eyboxu@scut.edu.cn  
Qing-Zhi Liu  
liuqzh@scut.edu.cn

## †PRESENT ADDRESS

Meng-Li Guo,  
Xiangyang Central Hospital, Affiliated  
with Hubei University of Arts and  
Science, Xiangyang, Hubei, China

<sup>†</sup>These authors have contributed  
equally to this work and share  
first authorship

## SPECIALTY SECTION

This article was submitted to  
Cancer Immunity  
and Immunotherapy,  
a section of the journal  
Frontiers in Immunology

RECEIVED 12 March 2022  
ACCEPTED 19 October 2022  
PUBLISHED 07 November 2022

## CITATION

Chen Z, Guo M-L, Li Y-Y, Yan K, Li L, Shen F, Guan H, Liu Q-Z, Xu B and Lian Z-X (2022) Immune profiling identifies CD8<sup>+</sup> T-cell subset signatures as prognostic markers for recurrence in papillary thyroid cancer. *Front. Immunol.* 13:894919. doi: 10.3389/fimmu.2022.894919

## COPYRIGHT

© 2022 Chen, Guo, Li, Yan, Li, Shen, Guan, Liu, Xu and Lian. This is an open-access article distributed under the terms of the [Creative Commons Attribution License \(CC BY\)](#). The use, distribution or reproduction in other forums is permitted, provided the original author(s) and the copyright owner(s) are credited and that the original publication in this journal is cited, in accordance with accepted academic practice. No use, distribution or reproduction is permitted which does not comply with these terms.

# Immune profiling identifies CD8<sup>+</sup> T-cell subset signatures as prognostic markers for recurrence in papillary thyroid cancer

Zhen Chen<sup>1†</sup>, Meng-Li Guo<sup>2†</sup>, Ya-Yi Li<sup>1</sup>, Kai Yan<sup>3</sup>, Liang Li<sup>4</sup>, Fei Shen<sup>1</sup>, Haixia Guan<sup>5,6</sup>, Qing-Zhi Liu<sup>7\*</sup>, Bo Xu<sup>1\*</sup> and Zhe-Xiong Lian<sup>4</sup>

<sup>1</sup>Department of Thyroid Surgery, the Second Affiliated Hospital, School of Medicine, South China University of Technology, Guangzhou, China, <sup>2</sup>Department of Thyroid Surgery, Guangzhou First People's Hospital, Guangzhou Medical University, Guangzhou, China, <sup>3</sup>Department of Thoracic Surgery, Guangdong Provincial People's Hospital, Guangdong Academy of Medical Sciences, Guangzhou, Guangdong, China, <sup>4</sup>Guangdong Provincial People's Hospital, Guangdong Academy of Medical Sciences, Guangzhou, Guangdong, China, <sup>5</sup>Department of Endocrinology, Guangdong Provincial People's Hospital, Guangdong Academy of Medical Sciences, Guangzhou, Guangdong, China, <sup>6</sup>The Second School of Clinical Medicine, Southern Medical University, Guangzhou, Guangdong, China, <sup>7</sup>Chronic Disease Laboratory, School of Medicine, South China University of Technology, Guangzhou, Guangdong, China

**Background:** Thyroid tissue has a special immune microenvironment that is not well characterized. Whether immune cells have a prognostic value in the recurrence of papillary thyroid cancer (PTC) needs further investigation.

**Methods:** Multinodular non-toxic goiter (MNG) was taken as normal tissue for the difficulty in obtaining completely normal thyroid tissue (normal thyroid function, no thyroiditis, and no nodules). We compared the composition of mononuclear cells (MNCs) in peripheral blood and thyroid tissues from MNG and PTC patients by high-dimensional flow cytometry profiling and verified the results by multiplex immunohistochemistry. The recurrence rates of PTC patients with different CD8<sup>+</sup>T cell subset signatures were compared using TCGA database.

**Results:** We observed that the immune cell composition of MNG was different from that in peripheral blood. Thyroid tissue contains higher percentages of T cells and NK cells. Moreover, the percentages of memory T cells and Treg cells were higher in thyroid than in peripheral blood and increased in PTC tumors. We further focused on the antitumoral CD8<sup>+</sup>T cells and found that the expression patterns of PD-1, CD39, and CD103 on CD8<sup>+</sup>T cells were different between MNG and PTC. Importantly, we found higher percentages of PD-1<sup>+</sup>CD39<sup>+</sup>CD103<sup>+</sup>CD8<sup>+</sup>T and PD-1<sup>+</sup>CD39<sup>+</sup>CD103<sup>-</sup>CD8<sup>+</sup>T cells in PTC tumor tissues from recurrent patients than non-recurrent patients. By analyzing PTC data from TCGA database, we found that the expression

patterns of these molecules were associated with different pathologic types and genders among PTC patients. Moreover, patients with PD-1<sup>hi</sup>CD39<sup>lo</sup>CD103<sup>hi</sup>CD8<sup>hi</sup>, PD-1<sup>hi</sup>CD39<sup>hi</sup>CD103<sup>lo</sup>CD8<sup>hi</sup>, and PD-1<sup>lo</sup>CD39<sup>hi</sup>CD103<sup>hi</sup>CD8<sup>hi</sup> expression patterns have a higher 10-year recurrence-free survival.

**Conclusion:** The immune microenvironment in MNG tissue is distinct from that in peripheral blood and paratumor tissue. More memory CD8<sup>+</sup>T cells were detected in PTC, and expression patterns of PD-1, CD39, and CD103 on CD8<sup>+</sup>T cells were significantly different in physiology and gender and associated with the recurrence rate of PTC. These observations indicate that CD8<sup>+</sup>T cell signatures may be useful prognostic markers for PTC recurrence.

#### KEYWORDS

papillary thyroid cancer (PTC), recurrence, CD8<sup>+</sup>T cells, multiplex immunohistochemistry, PD-1, CD39, CD103

## Introduction

Papillary thyroid cancer (PTC), the most common endocrine malignancy, accounts for 90% of thyroid cancer which has the seventh increase in new cases of cancer in women (1). Although it has low mortality, PTC, in some cases, can develop into progressive invasive primary disease. Ten percent to 30% of patients experience tumor recurrence and even distant metastasis, especially 10 years after initial treatment (2, 3). Most recurrences require additional surgical intervention with increased psychological stress to patients and expense (4). Patients with aggressive PTC who are resistant to standard treatments may benefit from immunotherapy (5).

Immune responses against thyroid carcinoma have long been recognized (6, 7), evidenced by the frequent existence of lymphocytes within primary thyroid tumor and tumor surrounding areas (8). CD4<sup>+</sup>T, CD8<sup>+</sup>T, B, NK, and regulatory T (Treg) cells have been reported to be present in nodular goiter (NG) (9–11) and play different roles during thyroid tumor progression (12, 13). CD4<sup>+</sup>T and B cells are reported to be positively correlated with reduced tumor sizes in PTC (14). Increased tissue infiltration of Treg cells was positively correlated with advanced thyroid cancer stage, whereas NK-cell infiltration was negatively correlated, indicating that NK and Treg cells might be important regulators of PTC progression (10, 11, 15). High tumor-infiltrating CD8<sup>+</sup>T cell density was associated with a favorable prognosis in thyroid cancer patients (14, 16). On the other hand, a retrospective cohort study found that patients whose thyroid tumor samples were enriched in CD8<sup>+</sup>T cells present a poor outcome (17). Thus, the prognostic value of CD8<sup>+</sup>T cells in thyroid cancer is controversial, and the association of different CD8<sup>+</sup>T-cell subsets with PTC recurrence remains unclear. Moreover, in view of the differences in

experimental methods and samples, the proportions of lymphocytes from PTC and MNG patients varied in different studies (9, 11, 15, 16, 18, 19). It is of great importance to profile the immune cells in tissues and peripheral blood of MNG and PTC patients.

Here, we delineated the specific immune landscape of multinodular non-toxic goiter (MNG) tissue and PTC tumor tissue *via* flow cytometry and multiplex immunohistochemistry. Interestingly, we found significant differences in phenotypes of thyroid infiltrated CD8<sup>+</sup>T cells between MNG and PTC patients. Particularly, PD-1<sup>-</sup>CD39<sup>+</sup>CD103<sup>+</sup>CD8<sup>+</sup>T, PD-1<sup>-</sup>CD39<sup>-</sup>CD103<sup>+</sup>CD8<sup>+</sup>T, and PD-1<sup>+</sup>CD39<sup>+</sup>CD103<sup>-</sup>CD8<sup>+</sup>T cells were associated with the recurrence of PTC.

## Materials and methods

### Patients

This study was performed following the regulations of the ethics committee of the second affiliated hospital of South China University of Technology. Thirteen multinodular non-toxic goiter (MNG) samples paired with peripheral blood samples and 17 papillary thyroid cancer (PTC) samples paired with paratumor and peripheral blood samples were analyzed by flow cytometry (Table 1). Thirteen MNG, 23 non-recurrent PTC, and eight recurrent PTC samples were subjected to multiplex immunohistochemistry (Table 1). Paratumor tissue was defined as 2~3 cm away from lesions. Thyroid tissue was collected and placed in 1640 medium containing 10% fetal bovine serum. PTC and MNG patients were confirmed by surgery and pathology. Patients with the following conditions were excluded: treated with

TABLE 1 Demographics and clinicopathologic characteristics of PTC patients.

Characteristics	PTC (%)			MNG (%)	
	FCM	mIHC			
		Recurrence	Non-recurrence		
No. patients	17	8	23	13	
Gender					
Male	3 (17.65)	4 (50)	4 (17.39)	2 (15.38)	
Female	14 (82.35)	4 (50)	19 (82.61)	11 (84.62)	
Age (years)					
Mean ± SD	39.47 ± 11.09	49.5 ± 18.81	41.26 ± 12.34	48.92 ± 10.38	
<55	15 (88.24)	4 (50)	18 (78.26)	8 (61.54)	
≥55	2 (11.76)	4 (50)	5 (21.74)	5 (38.46)	
Tumor size (cm)					
<2	14 (82.35)	7 (87.5)	19 (82.61)		
≥2	3 (17.65)	1 (12.5)	4 (17.39)		
T stage					
T1					
T1a	11 (64.71)	1 (12.5)	16 (69.56)		
T1b	4 (23.53)	7 (87.5)	5 (21.74)		
T2	0	0	2 (8.70)		
T3	0	0	0		
T4					
T4a	1 (5.88)	0	0		
T4b	1 (5.88)	0	0		
N stage					
N0	10 (58.82)	0	11 (47.83)		
N1					
N1a	5 (29.41)	3 (37.5)	11 (47.83)		
N1b	2 (11.76)	5 (62.5)	1 (4.35)		
M stage					
M0	16 (94.12)	8 (100)	23 (100)		
M1	1 (5.88)	0	0		

SD, standard deviation.

chemoradiation therapy preoperatively; with hyperthyroidism, hypothyroidism, diabetes, hypertension and hyperlipidemia, or serum anti-thyroglobulin antibody (TGA<sub>b</sub>) or thyroid peroxidase antibody (TPO<sub>a</sub>b) levels higher than the reference range (TGA<sub>b</sub> >115 IU/ml, TPO<sub>a</sub>b >35 IU/ml); or with a background of thyroiditis. PTC recurrence was defined as recurrent or persistent disease based on authoritative histologic, cytologic, radiographic, or biochemical criteria (20). Patients with local, regional, and distant recurrences were all included.

## Data availability and calculation of microenvironment cell abundance

THCA RNA-seq expression profiles from TCGA database (<https://portal.gdc.cancer.gov/>) were downloaded using the

GDC Data Transfer Tool Client (<https://gdc.cancer.gov/access-data/gdc-data-transfer-tool>). Custom Perl scripts (Perl version 5.8.9) used for processing the FPKM expression data are available on request. Four sets of datasets GSE197852 (21), GSE3467 (22), GSE33630 (23), and GSE6004 (24) from the GEO database were used to analyze Treg-cell subpopulations. Marker genes for microenvironment cells were obtained from previous studies (25–30). The 470 genes representing 18 microenvironment cell types are listed in [Supplementary Table 3](#). We used single-sample gene set enrichment analysis (ssGSEA, “GSVA” function in R) to calculate the abundance of microenvironment cells in each sample. The CD8<sup>hi</sup> samples were selected based on the mean level of CD8<sup>+</sup>T-cell marker gene expression and were considered to be enriched in CD8<sup>+</sup>T cells. These patients were separated into eight clusters based on the expression levels of PDCD1, ENTPD1, and ITGAE genes. PD-

$1^{\text{hi}}$ , CD103 $^{\text{hi}}$ , and CD39 $^{\text{hi}}$  were defined as higher than the mean expression levels of PDCD1, ENTPD1, and ITGAE in the CD8 $^{\text{hi}}$  samples, respectively, whereas PD-1 $^{\text{lo}}$ , CD103 $^{\text{lo}}$ , and CD39 $^{\text{lo}}$  were the opposite.

## Mononuclear cell isolation

Tumor or paratumor tissues from PTC and control thyroid tissue from MNG were washed with precooled saline. Tissues were cut into small pieces in a tube containing RPMI-1640 medium and 10% FBS on ice. Cells were collected by washing the thyroid tissues and filtering cell suspension through a 100-mesh strainer. After centrifugation at 450g for 5 min, cells were collected and red blood cells were depleted by adding 1–2 ml red blood cell lysis buffer (Beyotime, China) and incubating at 4°C for 5 min. Lymphoprep (Axis Shield, Norway) was used to isolate peripheral blood mononuclear cells (PBMCs) according to the manufacturer's instructions. Peripheral blood was centrifuged to collect plasma and cells. The cells were diluted by addition of an equal volume of 0.9% saline. Diluted blood was layered over 3 ml Lymphoprep and centrifuged at 800g for 20 min at room temperature. Cells at the interface were collected and counted on a hemocytometer in the presence of trypan blue.

## Flow cytometry

For surface marker staining, mononuclear cells (MNCs) from tissue and blood were incubated with mouse serum for 15 min at 4°C, followed by fluorescent antibodies at 4°C for 20 min. BV421-conjugated anti-CD39 (A1), BV510-conjugated anti-CD3 (OKT3), BV605-conjugated anti-CD123 (6H6), BV650-conjugated anti-CD45RA (HI100), BV711-conjugated anti-CD14 (M5E2), BV785-conjugated anti-CD19 (HIB19), FITC-conjugated anti-CD45RO (UCHL1), PerCP-Cy5.5-conjugated anti-CD16 (3G8), PE-conjugated anti-CD25 (BC96), PE/Dazzle594-conjugated anti-PD-1 (EH12.2H7), PE/Cy5-conjugated anti-CD56 (5.1H11), Alexa700-conjugated anti-CD8a (HIT8a), PE/Cy7-conjugated anti-HLA-DR (LN3), APC-conjugated antibodies against CD103 (Ber-ACT8), and APC/Cy7-conjugated anti-CD45 (HI30) were purchased from BioLegend (San Diego, CA, USA). BUV563-conjugated anti-CD4 (SP3) and BUV737-conjugated anti-CD127 (HIL-7R-M21) were purchased from BD Biosciences (Franklin Lakes, New Jersey, USA). Dead cells were stained with DAPI (Beyotime, China). Live cells were gated as CD45 $^+$ DAPI $^-$ . Data were acquired using a FACS LSRFortessa flow cytometer (BD Biosciences) and analyzed with the FlowJo (Tree Star, Ashland, OR, USA). Gating strategies for the flow experiment are described in Figure S1.

## t-Distributed stochastic neighbor embedding analysis

Live MNCs were gated in FlowJo to perform t-distributed stochastic neighbor embedding (t-SNE) analysis. Data from 10,000 cells of PBMCs or tissue MNCs were randomly selected and merged into one matrix and normalized by a channel using the scale function in R (version 3.5.3). Then, we ran the t-SNE algorithm by the RunTSNE function in the Seurat package (version 3.0.1) to output the results. The parameters used for t-SNE analysis were CD3, CD56, CD19, CD4, CD8, CD45RA, CD45RO, and CD14.

## Multiplex immunohistochemistry

Formalin-fixed paraffin-embedded tissues were cut into 4- $\mu\text{m}$  slices and stained using the PANO 7-plex IHC kit (TSA-RM) (Panovue) according to the manufacturer's instructions. Slides were deparaffinized with xylene and rehydrated with an ethanol gradient. Heat-induced antigen retrieval was performed in sodium citrate buffer (0.01M, pH = 6.0) before each primary antibody incubation, and the slides were cooled to room temperature. After deactivating the endogenous peroxidase with 3% H<sub>2</sub>O<sub>2</sub> in methanol, the slices were blocked with 10% goat serum for 30 min followed by primary antibody staining. The primary antibodies and dilutions with PANO amplification diluent were applied in the following order: CD4 (ab133616, 1:500, Abcam) with Opal 620, CD20 (ab78237, 1:2,000, Abcam) with Opal 520, CD8 (C8/144B, 1:200, CST) with Opal 690, CD56 (123C3, 1:200, CST) with Opal 570, and CD45 (60287-1-Ig, 1:4,000, Proteintech) with Akoya 580. The CD8 $^+$ T-cell subsets were labeled by CD8 (C8/144B, 1:200, CST) with Opal 690, CD103 (ab224202, 1:200, Abcam) with Opal 620, PD-1 (EH33, 1:200, CST) with Opal 520, and CD39 (ab223842, 1:3000, Abcam) with Opal 540. All slides were incubated with PANO polymer HRP Ms+Rb for 15 min at room temperature. Nuclei were stained for 10 min with DAPI (Beyotime, China). All slides were scanned using the Vectra Automated Quantitative Pathology Imaging System (Vectra Polaris featuring MOTiF<sup>TM</sup>), and images were analyzed with the HALO (version 3.1.1076) Digital Pathology system (Indica Labs).

## Statistical analysis

All data were presented as mean  $\pm$  standard error of mean (SEM) and analyzed using GraphPad Prism 8.3 (San Diego, CA) and R (version 3.6.2). The comparison between two groups was performed with two-tailed Student's t test (paired or unpaired) if both data conformed normal distribution and equality of

variance in standard deviation. Otherwise, the non-parametric test (Wilcoxon signed-rank test or Mann–Whitney U test) was used. Recurrence-free survival (RFS) was analyzed with Kaplan–Meier estimates and log-rank tests. Cox proportional hazard regression models were constructed for clinicopathologic characteristics, CD8<sup>hi</sup>T-cell subsets, and RFS. Results were expressed as hazard ratio (HR) with 95% confidence interval (CI). Univariate logistic regression was used to estimate associations between clinical parameters and CD8<sup>+</sup>T subsets in tumor from flow cytometry and multiplex immunohistochemistry (mIHC) data, respectively. The relationships of PD-1<sup>lo</sup>CD39<sup>hi</sup>CD103<sup>hi</sup> CD8<sup>hi</sup>T, PD-1<sup>hi</sup>CD39<sup>hi</sup>CD103<sup>lo</sup> CD8<sup>hi</sup>T, and PD-1<sup>hi</sup>CD39<sup>lo</sup>CD103<sup>hi</sup> CD8<sup>hi</sup>T cells in tumor from TCGA data with clinical parameters and other immune cells were analyzed using multinomial logistic regression analyses. Pearson's chi-square test or Fisher's exact test were employed for the comparison of unordered categorical variables. \*p < 0.05; \*\*p < 0.01; \*\*\*p < 0.001.

## Results

### Landscape of the immune microenvironment in thyroid tissues and peripheral blood

To explore the immune microenvironment of thyroid, we collected thyroid tissues and peripheral blood from MNG and PTC patients and performed flow cytometry and mIHC, in combination with bioinformatics analysis (Figure 1A). First, we used t-SNE maps to present the immune landscape of the thyroid and peripheral blood from MNG patients. Specific immune lineages were recognized using a color-based representation of expression levels of a single parameter. We identified six major cell clusters: CD8<sup>+</sup>T, CD4<sup>+</sup>T, CD3<sup>+</sup>CD56<sup>+</sup>, NK, B cells, and monocytes (Figures 1B, S2A). We also used mIHC to detect the locations of these immune cell subsets in the thyroid. We found these immune cell subsets aggregated in the thyroid interfollicular space (Figure 1C). The frequencies and density of CD8<sup>+</sup>T, CD4<sup>+</sup>T, NK, and B cells of MNG tissues obtained by mIHC were displayed (Figures S2B, C). The percentages of T and NK cells from thyroid tissues were decreased compared with peripheral blood (p = 0.0068 for T cells, p = 0.0134 for NK cells, Figures 1D, E). However, the percentage of CD3<sup>+</sup>CD56<sup>+</sup> cells was significantly higher in thyroid tissues than in peripheral blood (p < 0.0001, Figure 1F). For T-cell subgroups in thyroid, the CD8<sup>+</sup>T/CD4<sup>+</sup>T-cell ratio (p = 0.0171, Figure 1G) and the percentage of Treg cells (CD127<sup>-</sup>CD25<sup>+</sup>CD4<sup>+</sup>T cells, p = 0.0044, Figure 1H) were increased when compared with peripheral blood. Moreover, T cells presented increased memory CD4<sup>+</sup>T cells (CD45RO<sup>+</sup>CD45RA<sup>-</sup>CD4<sup>+</sup>T cells, p = 0.0005, Figure 1I) and memory CD8<sup>+</sup>T cells (CD45RO<sup>+</sup>CD45RA<sup>-</sup>CD8<sup>+</sup>T cells, p =

0.0002, Figure 1J) in thyroid tissues. The percentages of B cells (Figure S2D) and monocytes (Figure S2E), between two groups did not show a statistically significant difference. These results show diverse immune landscapes across MNG tissues and paired peripheral blood, especially T-cell subsets.

### Higher percentage of memory T cells and Treg cells in PTC

There was no statistical difference in percentages of CD8<sup>+</sup>T, CD4<sup>+</sup>T, CD3<sup>+</sup>CD56<sup>+</sup>, NK, B cells, and monocytes between tumor, paratumor, and MNG tissues (Figure S3A), nor between the peripheral blood from PTC and MNG patients (Figure S3B). However, CD45RO was highly expressed on CD8<sup>+</sup>T and CD4<sup>+</sup>T cells in thyroid tissues (Figure 2A). Correspondingly, percentages of memory CD8<sup>+</sup>T cells were increased in tumor and paratumor as compared with MNG (p = 0.0216 for tumor vs. MNG, p = 0.0154 for paratumor vs. MNG), whereas a significant difference was not detected between tumor and paratumor (Figure 2B). Percentages of memory CD4<sup>+</sup>T cells were also significantly higher in tumor whether compared with MNG or paratumor, but there was no difference between paratumor and MNG (p = 0.0011 for tumor vs. MNG, p < 0.0001 for tumor vs. paratumor, Figure 2C). Furthermore, CD4<sup>+</sup>T cells from PTC and MNG patients exhibited different expression levels of CD25 (Figure 2D). The percentage of Treg cells was increased in tumor compared with MNG or paratumor but decreased in paratumor when compared with MNG (p = 0.0012 for tumor vs. MNG, p < 0.0001, for tumor vs. paratumor, p = 0.0284, for paratumor vs. MNG, Figure 2E). Furthermore, we found that the ssGSEA score of CD45RA<sup>+</sup>FoxP3<sup>lo</sup>CD25<sup>++</sup> cells in MNG was higher than that in paratumor (p = 0.0008) and tumor (p = 0.0102). The ssGSEA score of CD45RA<sup>+</sup>FoxP3<sup>lo</sup>CD25<sup>++</sup> cells was higher in MNG compared with paratumor (p = 0.0019). The ssGSEA scores of CD45RA<sup>+</sup>FoxP3<sup>lo</sup>CD25<sup>++</sup> cells (p = 0.0016), CD45RA<sup>-</sup>FoxP3<sup>hi</sup>CD25<sup>++</sup> cells (p < 0.0001), or CD45RA<sup>-</sup>FoxP3<sup>lo</sup>CD25<sup>+</sup> cells (p < 0.0001) in tumor were all higher than paratumor (Figure S4).

### Different expression patterns of PD-1, CD39, and CD103 on CD8<sup>+</sup>T cells in PTC

The controversial prognostic value of CD8<sup>+</sup>T cells in thyroid cancer may be due to the complexity and heterogeneity of the CD8<sup>+</sup>T-cell landscape. PD-1, CD103, and CD39 have been independently proposed as markers of tumor-reactive CD8<sup>+</sup>T cells in various cancers, possessing a distinct prognostic implication (31–33). Thus, we investigated the clinical relevance of these CD8<sup>+</sup>T-cell subsets in PTC. First, based on the expressions of PD-1 and CD39, CD8<sup>+</sup>T cells from PTC and

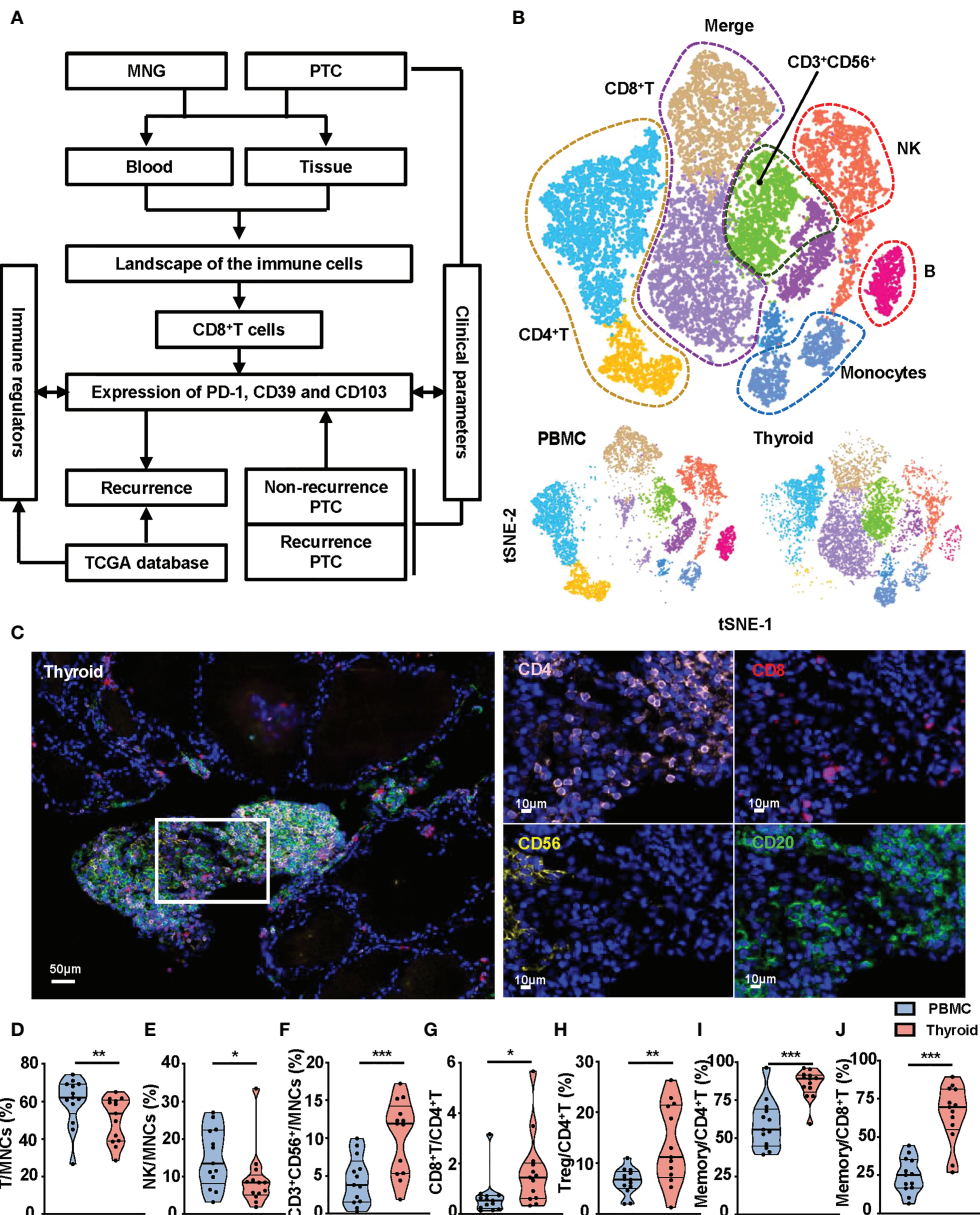


FIGURE 1

Composition of immune cell subsets in peripheral blood and thyroid tissues from MNG patients. (A) The flowchart of the work. (B) t-SNE islands for CD3<sup>+</sup>T cells, CD4<sup>+</sup>T cells, CD8<sup>+</sup>T cells, CD3<sup>+</sup>CD56<sup>+</sup> cells, CD56<sup>+</sup> NK cells, CD19<sup>+</sup> B cells, and CD14<sup>+</sup> monocytes of flow cytometry data. (C) Representative immunofluorescence staining of CD4 (pink), CD8 (red), CD56 (yellow), and CD20 (green) in an MNG. DAPI staining is shown in blue. Scale bar, 50  $\mu$ m (left), 10  $\mu$ m (right). Percentages of T cells (D), NK cells (E), and CD3<sup>+</sup>CD56<sup>+</sup> cells (F) in MNCs in peripheral blood and thyroid tissue. (G) Ratio of CD8<sup>+</sup>T to CD4<sup>+</sup>T cells in peripheral blood and thyroid tissue. (H) Percentage of Treg cells in total CD4<sup>+</sup>T cells. Percentages of memory T cells (CD45RO<sup>+</sup>CD45RA<sup>-</sup>) in CD4<sup>+</sup>T (I) and CD8<sup>+</sup>T (J) cells. (D–J) The individual dot represents a patient, and data are presented as mean  $\pm$  SEM. \*p < 0.05; \*\*p < 0.01; \*\*\*p < 0.001.

MNG tissues were divided into four subgroups (PD-1<sup>+</sup>: PD-1<sup>+</sup>CD39<sup>-</sup>, DN: PD-1<sup>-</sup>CD39<sup>-</sup>, CD39<sup>+</sup>: PD-1<sup>-</sup>CD39<sup>+</sup>, DP: PD-1<sup>+</sup>CD39<sup>+</sup>). These four subgroups were further divided into eight subsets according to the expression levels of CD103 (Figure 3A). Percentages of triple-positive subsets (p = 0.0067), PD-1<sup>-</sup>CD39<sup>+</sup>CD103<sup>+</sup>CD8<sup>+</sup>T (p = 0.0005), and PD-

1<sup>+</sup>CD39<sup>+</sup>CD103<sup>+</sup>CD8<sup>+</sup>T cells (p = 0.0106) were higher in tumor than in paratumor (Figures 3B–D). The percentages of PD-1<sup>-</sup>CD39<sup>+</sup>CD103<sup>+</sup>CD8<sup>+</sup>T cells (p = 0.0133) and PD-1<sup>+</sup>CD39<sup>+</sup>CD103<sup>+</sup>CD8<sup>+</sup>T cells (p = 0.0174) from paratumor were lower than from MNG (Figures 3C, D). The percentage of PD-1<sup>+</sup>CD39<sup>+</sup>CD103<sup>+</sup> cells in tumor was lower compared with

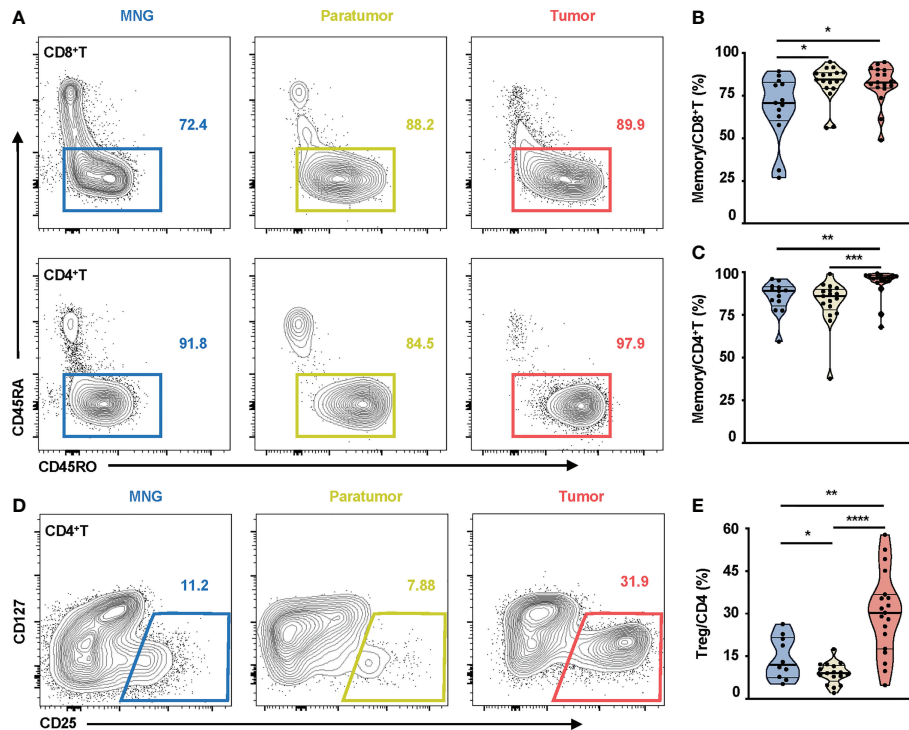


FIGURE 2

Memory T cells and Treg cells in thyroid tissues from MNG and PTC patients. **(A)** Representative FACS plots show CD45RO and CD45RA expressions on CD8<sup>+</sup>T and CD4<sup>+</sup>T cells. The values within solid line boxes indicate the proportions of memory T cells (CD45RO<sup>+</sup>CD45RA<sup>-</sup>) to CD8<sup>+</sup>T or CD4<sup>+</sup>T cells. **(B)** Frequencies of memory T cells relative to CD8<sup>+</sup>T cells are shown. **(C)** Frequencies of memory T cells relative to CD4<sup>+</sup>T cells are shown. **(D)** Representative FACS plots show CD25 and CD127 expressions on CD4<sup>+</sup>T cells. The values within solid line boxes indicate the proportions of Treg cells (CD25<sup>+</sup>CD127<sup>-</sup>) to CD4<sup>+</sup>T cells. **(E)** Frequencies of Treg cells relative to CD4<sup>+</sup>T cells are shown. Blue means MNG, yellow means paratumor, and red means tumor. **(B–E)** Data presented as mean  $\pm$  SEM. \*p < 0.05; \*\*p < 0.01; \*\*\*p < 0.001; \*\*\*\*p < 0.0001.

paratumor ( $p < 0.0001$ ) but higher than MNG ( $p = 0.0389$ , Figure 3E). In addition, the percentage of PD-1<sup>+</sup>CD39<sup>+</sup>CD103<sup>+</sup>CD8<sup>+</sup>T cells derived from paratumor was significantly increased compared with MNG ( $p = 0.0004$ , Figure 3E). Our univariate logistic regression analysis of CD8<sup>+</sup>T-cell subsets and clinical parameters indicated that big tumor size was a risk factor for high PD-1<sup>+</sup>CD39<sup>+</sup>CD103<sup>+</sup>CD8<sup>+</sup>T cells, but older age was a protective factor for high PD-1<sup>+</sup>CD39<sup>+</sup>CD103<sup>+</sup>CD8<sup>+</sup>T cells (Table S1). Together, these results revealed CD8<sup>+</sup>T-cell subsets may play different roles during PTC tumor development and progression.

### PD-1<sup>+</sup>CD39<sup>+</sup>CD103<sup>+</sup>CD8<sup>+</sup>T-cell and PD-1<sup>+</sup>CD39<sup>+</sup>CD103<sup>-</sup>CD8<sup>+</sup>T-cell frequencies are associated with recurrence of PTC patients

We further compared the percentages of these subsets in tumors from recurrent and non-recurrent PTC patients by miHIC. Immunofluorescence staining of CD8<sup>+</sup>T-cell subset

markers (PD-1, CD39, CD103, CD8) was used to calculate their number in the PTC (Figures 4A, B). The percentages ( $p = 0.0015$ ) and density ( $p = 0.0251$ ) of PD-1<sup>+</sup>CD39<sup>+</sup>CD8<sup>+</sup>T cells were both significantly higher in recurrence tumor than in non-recurrence tumor (Figure S5A). Furthermore, the percentages of PD-1<sup>+</sup>CD39<sup>+</sup>CD103<sup>+</sup>CD8<sup>+</sup>T ( $p = 0.0022$ ) and PD-1<sup>+</sup>CD39<sup>+</sup>CD103<sup>-</sup>CD8<sup>+</sup>T ( $p = 0.001$ ) cells were significantly higher in recurrence tumor than non-recurrence tumor, and this phenomenon was seen for the density of these two CD8<sup>+</sup>T-cell subsets ( $p = 0.0178$  for PD-1<sup>+</sup>CD39<sup>+</sup>CD103<sup>+</sup>CD8<sup>+</sup>T cells,  $p = 0.0332$ , for PD-1<sup>+</sup>CD39<sup>+</sup>CD103<sup>-</sup>CD8<sup>+</sup>T cells, Figures 4C, D). As for other CD8<sup>+</sup>T-cell subsets, there was no significant difference in the two groups of PTC patients (Figures S5B–G). It was notable that no difference between tumors with recurrence and without recurrence was observed in the number and density of CD8<sup>+</sup>T cells (data not shown). Logistic regression analysis also demonstrated that PD-1<sup>+</sup>CD39<sup>+</sup>CD103<sup>+</sup>CD8<sup>+</sup>T (OR = 13.125, 95% CI: 1.876–268.997,  $p = 0.026$ ) and PD-1<sup>+</sup>CD39<sup>+</sup>CD103<sup>-</sup>CD8<sup>+</sup>T (OR = 13.125, 95% CI: 1.876–268.997,  $p = 0.026$ ) cells in tumor were both associated with high risk of tumor recurrence, despite no association found between these

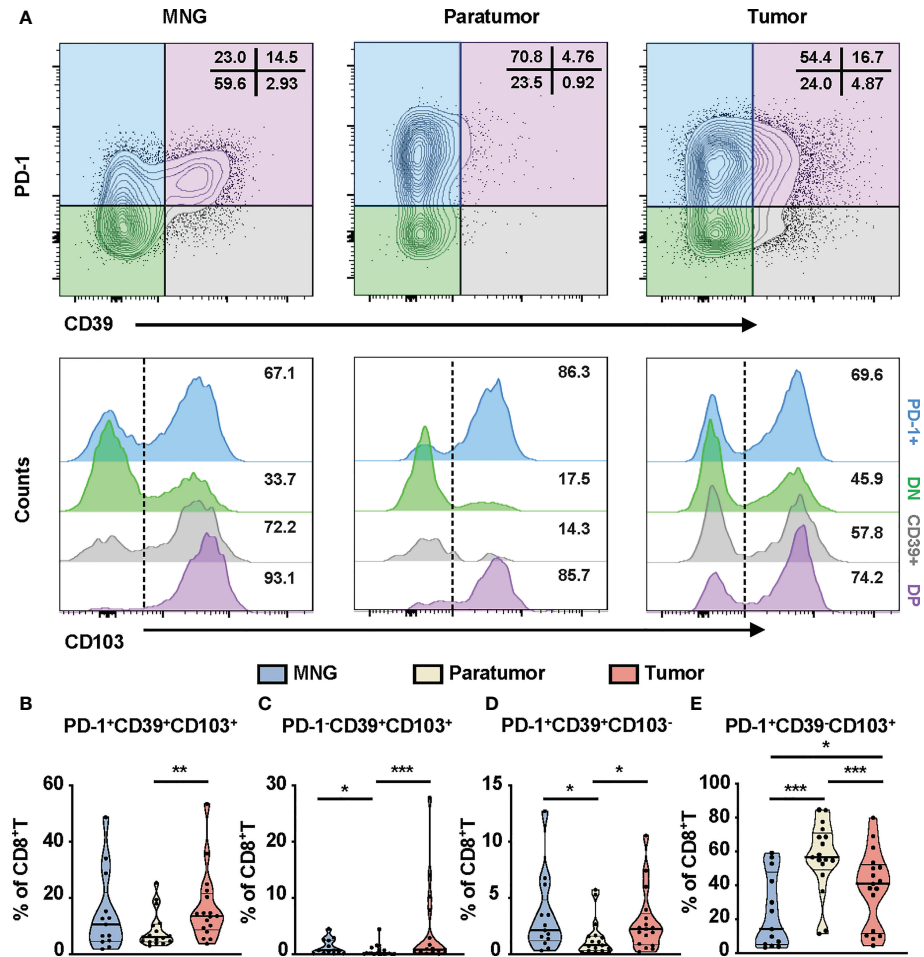


FIGURE 3

Phenotypic characteristics of CD8<sup>+</sup>T cells in thyroid tissues from MNG and PTC patients. (A) Flow cytometric analysis PD-1 and CD39 expression on CD8<sup>+</sup>T cells from thyroid tissues of MNG and PTC patients. Numbers in each quadrant indicate percent cells positive for PD-1 and/or CD39 on CD8<sup>+</sup>T cells. Below, histograms show the CD103 expression on PD-1<sup>+</sup>CD39<sup>+</sup> (PD-1<sup>+</sup>, blue), PD-1<sup>+</sup>CD39<sup>-</sup> (DN, green), PD-1<sup>-</sup>CD39<sup>+</sup> (CD39<sup>+</sup>, gray), and PD-1<sup>-</sup>CD39<sup>-</sup> (DP, purple) cells. Frequencies of PD-1<sup>+</sup>CD39<sup>+</sup>CD103<sup>+</sup>CD8<sup>+</sup>T (B), PD-1<sup>+</sup>CD39<sup>+</sup>CD103<sup>+</sup>CD8<sup>+</sup>T (C), PD-1<sup>+</sup>CD39<sup>+</sup>CD103<sup>+</sup>CD8<sup>+</sup>T (D), and PD-1<sup>+</sup>CD39<sup>+</sup>CD103<sup>+</sup>CD8<sup>+</sup>T (E) cells in thyroid tissues of MNG and PTC patients. Data presented as mean  $\pm$  SEM. \*p < 0.05; \*\*p < 0.01; \*\*\*p < 0.001.

two CD8<sup>+</sup>T subsets and clinical parameters (Table S2). These results confirmed that the prominent infiltration of PD-1<sup>+</sup>CD39<sup>+</sup>CD103<sup>+</sup>CD8<sup>+</sup>T and PD-1<sup>+</sup>CD39<sup>+</sup>CD103<sup>-</sup>CD8<sup>+</sup>T cells was associated with relapse of PTC.

### CD8<sup>+</sup>T-cell subset signatures are associated with clinical features and recurrence of PTC patients

We also investigated the clinical relevance and prognostic significance of these CD8<sup>+</sup>T-cell subsets by employing TCGA database. Although the PD-1<sup>hi</sup>CD39<sup>hi</sup>CD8<sup>hi</sup>T-cell subset was not associated with clinical features and recurrence of PTC (Figure S5H), significant differences in histology (p = 0.0406)

and sex (p = 0.0019) were observed among the eight clusters of CD8<sup>hi</sup> patients (Figures 5A, B). Male (OR = inf, 95% CI: 9.86E +32-1.52E+35, p < 0.001) was a significant risk factor for high PD-1<sup>lo</sup>CD39<sup>hi</sup>CD103<sup>hi</sup> CD8<sup>hi</sup>T cells, but no significant association was detected between the other two CD8<sup>hi</sup>T subsets and clinical parameters (Table 2). More importantly, the PD-1<sup>hi</sup>CD39<sup>lo</sup>CD103<sup>hi</sup> (p = 0.021), PD-1<sup>hi</sup>CD39<sup>hi</sup>CD103<sup>lo</sup> (p = 0.046), and PD-1<sup>lo</sup>CD39<sup>hi</sup>CD103<sup>hi</sup> (p = 0.021) clusters showed a higher recurrence risk in CD8<sup>hi</sup> samples as compared with the PD-1<sup>hi</sup>CD39<sup>hi</sup>CD103<sup>hi</sup> cluster (Figure 5C). When other five clusters as a whole were compared with these three clusters, only the PD-1<sup>hi</sup>CD39<sup>lo</sup>CD103<sup>hi</sup> cluster still had a greater recurrence risk (p = 0.011, Figure 5D). The multivariate Cox proportional hazard model also revealed that the PD-1<sup>hi</sup>CD39<sup>lo</sup>CD103<sup>hi</sup> cluster independently predicted worse

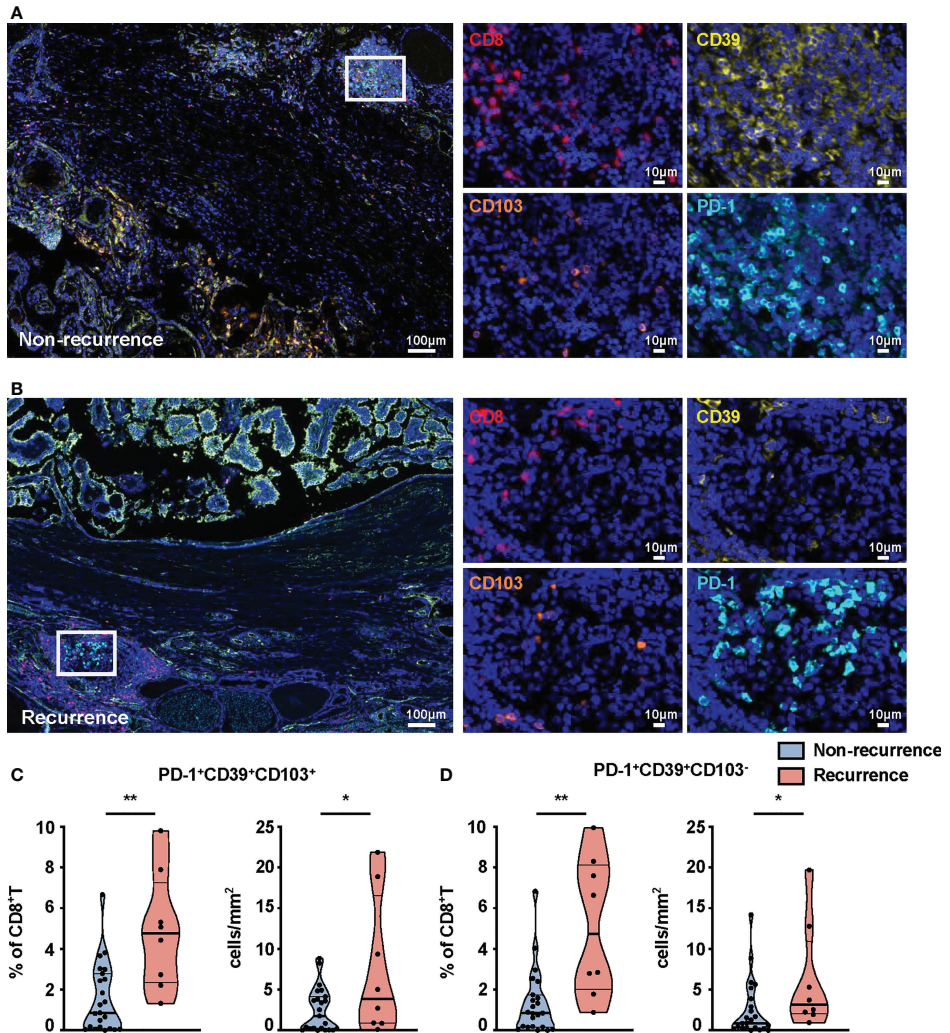


FIGURE 4

miHC-based quantification of CD8<sup>+</sup>T-cell subsets in tissues from non-recurrent and recurrent PTC patients. Representative immunofluorescence staining of CD8 (red), CD39 (yellow), CD103 (orange), and PD-1 (cyan) in non-recurrent (A) and recurrent PTC tissues (B). DAPI staining is shown in blue. Scale bar, 100  $\mu$ m, 10  $\mu$ m. Frequencies (C) and density (D) of PD-1<sup>+</sup>CD39<sup>+</sup>CD103<sup>+</sup>CD8<sup>+</sup>T cells and PD-1<sup>+</sup>CD39<sup>+</sup>CD103<sup>-</sup>CD8<sup>+</sup>T cells in non-recurrent PTC tissues ( $n = 23$ ) and recurrent PTC tissues ( $n = 8$ ). (Density: total PD-1<sup>+</sup>CD39<sup>+</sup>CD103<sup>-</sup>CD8<sup>+</sup>T- and PD-1<sup>+</sup>CD39<sup>+</sup>CD103<sup>-</sup>CD8<sup>+</sup>T-cell numbers divided by area of tissue per paraffin sections). Data presented as mean  $\pm$  SEM. \* $p < 0.05$ ; \*\* $p < 0.01$ .

recurrence-free survival (HR = 3.600, 95% CI: 1.070–12.110,  $p = 0.0385$ , Table 3).

### The immune environment of PTC patients with different CD8<sup>+</sup>T-cell subset signatures

We also analyzed the immune environment in the PD-1<sup>hi</sup>CD39<sup>lo</sup>CD103<sup>hi</sup>, PD-1<sup>hi</sup>CD39<sup>hi</sup>CD103<sup>lo</sup>, and PD-

1<sup>lo</sup>CD39<sup>hi</sup>CD103<sup>hi</sup> clusters and compared them with the other five clusters. We found that the PD-1<sup>hi</sup>CD39<sup>lo</sup>CD103<sup>hi</sup> subset was markedly enriched in the monocytic lineage ( $p < 0.0001$ ), myeloid-derived suppressor cells (MDSC,  $p < 0.0001$ ), macrophage ( $p < 0.0001$ ), fibroblasts ( $p < 0.0001$ ), B cells ( $p < 0.001$ ), regulatory T cells (Treg,  $p < 0.0001$ ), myeloid dendritic cells (mDC,  $p < 0.0001$ ), T follicular helper cells (Tfh,  $p < 0.0001$ ), T cells ( $p < 0.0001$ ), type 1 T helper cells (Th1,  $p < 0.0001$ ), and type 2 T helper cells (Th2,  $p < 0.0001$ ) (Figure 6A). Multinomial logistic regression analysis results also showed that the

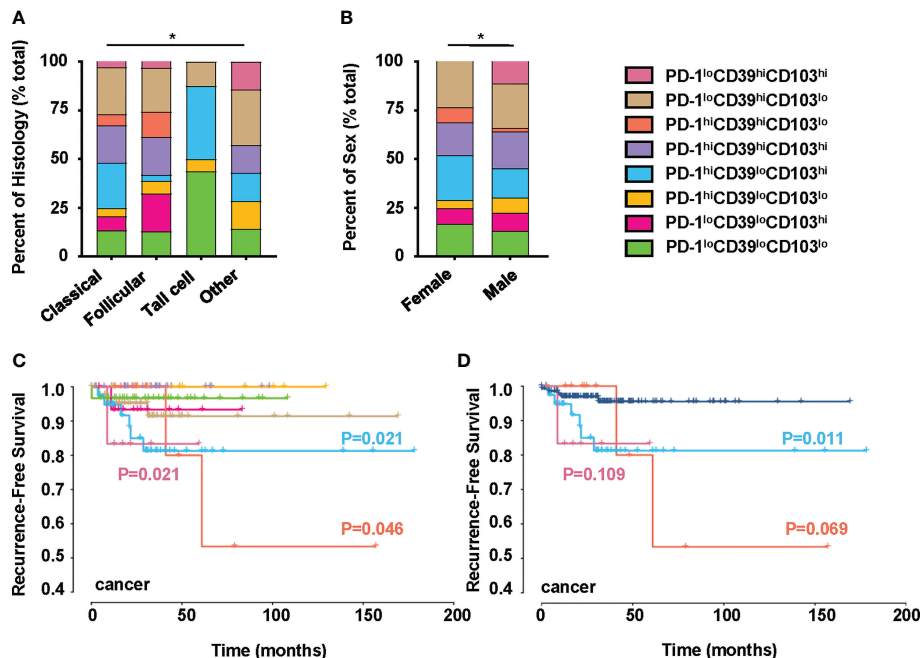


FIGURE 5

Clinical significance of PTC-infiltrating CD8<sup>hi</sup>T-cell subsets. This figure refers to TCGA THCA cohort ( $n = 195$ ). (A) Comparison of pathological subtypes with CD8<sup>hi</sup>T-cell subsets. (B) Comparison of gender with CD8<sup>hi</sup>T-cell subsets. (C) The recurrence-free survival compared among eight clusters in TCGA database, including the PD-1<sup>lo</sup>CD39<sup>lo</sup>CD103<sup>lo</sup> ( $n = 31$ ), PD-1<sup>lo</sup>CD39<sup>lo</sup>CD103<sup>hi</sup> ( $n = 16$ ), PD-1<sup>hi</sup>CD39<sup>lo</sup>CD103<sup>lo</sup> ( $n = 10$ ), PD-1<sup>hi</sup>CD39<sup>lo</sup>CD103<sup>hi</sup> ( $n = 41$ ), PD-1<sup>hi</sup>CD39<sup>hi</sup>CD103<sup>hi</sup> ( $n = 34$ ), PD-1<sup>hi</sup>CD39<sup>hi</sup>CD103<sup>lo</sup> ( $n = 12$ ), PD-1<sup>lo</sup>CD39<sup>hi</sup>CD103<sup>lo</sup> ( $n = 45$ ), and PD-1<sup>lo</sup>CD39<sup>hi</sup>CD103<sup>hi</sup> ( $n = 6$ ) clusters. (D) The recurrence-free survival compared between the PD-1<sup>hi</sup>CD39<sup>lo</sup>CD103<sup>hi</sup>, PD-1<sup>hi</sup>CD39<sup>lo</sup>CD103<sup>lo</sup>, and PD-1<sup>lo</sup>CD39<sup>hi</sup>CD103<sup>hi</sup> clusters and the other five clusters. Analyses were performed with Kaplan-Meier estimates and two-sided log-rank tests.  $p < 0.05$  was considered significant. \* $p < 0.05$ .

PD-1<sup>hi</sup>CD39<sup>lo</sup>CD103<sup>hi</sup> subset was associated with the monocytic lineage (OR = 202.519, 95% CI: 27.920–1469.000,  $p < 0.001$ ), MDSC (OR = 631.485, 95% CI: 65.345–6102.553,  $p < 0.001$ ), macrophage (OR = 133.061, 95% CI: 18.424–960.976,  $p < 0.001$ ), fibroblast (OR = 19.328, 95% CI: 3.085–121.090,  $p = 0.002$ ), B cells (OR = 319.830, 95% CI: 46.454–2201.962,  $p < 0.001$ ), Treg cells (OR = 123.978, 95% CI: 20.187–761.406,  $p < 0.001$ ), mDC (OR = 11.857, 95% CI: 2.552–55.092,  $p = 0.002$ ), Tfh cells (OR = 212.966, 95% CI: 28.659–1582.536,  $p < 0.001$ ), T cells (OR = 545.290, 95% CI: 69.589–4272.833,  $p < 0.001$ ), Th1 cells (OR = 413.319, 95% CI: 51.615–3309.738,  $p < 0.001$ ), and Th2 cells (OR = 32.775, 95% CI: 5.808–184.943,  $p < 0.001$ ) (Table 4). However, B cells ( $p < 0.001$ ), mDC ( $p = 0.044$ ), and T cells ( $p = 0.011$ ) were decreased in the PD-1<sup>lo</sup>CD39<sup>hi</sup>CD103<sup>hi</sup> cluster than in the other five clusters (Figure 6A). There was no statistical difference in the scores of neutrophil, NK cell, and type 17 T helper cell (Th17) among these four CD8<sup>hi</sup>T-cell subsets (Figure S6). There was a decreased trend of mDC ( $p = 0.068$ ) in the PD-1<sup>hi</sup>CD39<sup>hi</sup>CD103<sup>lo</sup> cluster than in the other five clusters, whereas the difference did not reach statistical significance (Figure 6A). Of note, compared with the other five clusters, the PD-1<sup>hi</sup>CD39<sup>lo</sup>CD103<sup>hi</sup> subset was highly enriched in immune checkpoint molecules (*LAG3*, *CTLA4*, *TIGIT*, *IDO1*,

$p < 0.001$  for all molecules), cytotoxic molecules (*GZMA*, *GZMB*, *PRF1*, *IFNG*,  $p < 0.001$  for all molecules), and chemokines (*CCL4*, *CCL5*, *CXCL9*, *CXCL10*,  $p < 0.001$  for molecules). However, these genes in the PD-1<sup>lo</sup>CD39<sup>hi</sup>CD103<sup>hi</sup> subset were in a low-expression state (Figure 6B). These results indicate that there are different mechanisms of CD8<sup>hi</sup>T-cell subsets in PTC recurrence.

## Discussion

In this study, multinodular non-toxic goiter (MNG), a benign disease with normal function of the thyroid gland, was taken as normal tissue to delineate the immune microenvironment, because completely normal thyroid tissue could not be obtained. We found that mononuclear cells distributed in clusters around the thyroid follicles and the percentages of mononuclear cells in MNG tissues were altered as compared with peripheral blood, especially the increase in memory T cells. During thyroid tumorigenesis, more memory T cells and Treg cells were detected in PTC tumor tissues. By delineating the immune microenvironment of MNG tissues, relatively normal thyroid tissues, and comparing them with

TABLE 2 Multinomial logistic regression analysis of clinical parameters associated with PD-1<sup>lo</sup>CD39<sup>hi</sup>CD103<sup>hi</sup> CD8<sup>hi</sup>T, PD-1<sup>hi</sup>CD39<sup>hi</sup>CD103<sup>lo</sup> CD8<sup>hi</sup>T, and PD-1<sup>hi</sup>CD39<sup>lo</sup>CD103<sup>hi</sup> CD8<sup>hi</sup>T cells in tumor from TCGA data.

PD-1 <sup>lo</sup> CD39 <sup>hi</sup> CD103 <sup>hi</sup> CD8 <sup>hi</sup> T cell	OR (95% CI)	P
Age	0.866 (0.733-1.023)	0.091
Sex male	inf (9.86E+32-1.52E+35)	<b>0.000</b>
N stage		
N1	0.289 (0.008-10.324)	0.496
N1a	0	NA
N1b	0.803 (0.030-21.511)	0.896
T stage		
T1a	0	NA
T1b	2.09E+09 (2.09E+09-2.09E+09)	<b>0.000</b>
T2	inf (4.97E+13-7.30E+15)	<b>0.000</b>
T3	inf (1.39E+13-8.03E+14)	<b>0.000</b>
T4	0	NA
Extrathyroidal extension	4.326 (0.088-212.915)	0.461
Recurrence	792.944 (1.438-437195.562)	<b>0.038</b>
PD-1 <sup>hi</sup> CD39 <sup>hi</sup> CD103 <sup>lo</sup> CD8 <sup>hi</sup> T cell	OR (95% CI)	P
Age	1.005 (0.095-1.057)	0.836
Sex male	0.339 (0.030-3.837)	0.382
N stage		
N1	0.525 (0.044-6.308)	0.611
N1a	4.139 (0.891-19.220)	0.070
N1b	0	NA
T stage		
T1a	0	NA
T1b	0.947 (0.102-8.810)	0.962
T2	0.834 (0.106-6.571)	0.863
T3	1.006 (0.085-11.960)	0.996
T4	0	NA
Extrathyroidal extension	1.617 (0.159-16.453)	0.685
Recurrence	20.924 (2.056-212.926)	<b>0.010</b>
PD-1 <sup>hi</sup> CD39 <sup>lo</sup> CD103 <sup>hi</sup> CD8 <sup>hi</sup> T cell	OR (95% CI)	P
Age	0.993 (0.966-1.022)	0.645
Sex male	0.816 (0.303-2.202)	0.689
N stage		
N1	0.404 (0.113-1.441)	0.162
N1a	1.010 (0.365-2.798)	0.985
N1b	0.154 (0.029-0.805)	<b>0.027</b>
T stage		
T1a	4.816 (0.675-34.373)	0.117
T1b	1.936 (0.408-9.181)	0.405
T2	1.322 (0.285-6.132)	0.721
T3	1.104 (0.180-6.768)	0.915
T4	1.678 (0.063-44.893)	0.758
Extrathyroidal extension	1.487 (0.385-5.751)	0.565
Recurrence	5.144 (1.259-21.015)	<b>0.023</b>

Bold values refers to the risk factors associated with clinical features and other immune cells for the three tumor patient subsets of PD-1<sup>lo</sup>CD39<sup>hi</sup>CD103<sup>hi</sup>CD8<sup>hi</sup>T, PD-1<sup>hi</sup>CD39<sup>hi</sup>CD103<sup>lo</sup>CD8<sup>hi</sup>T, PD-1<sup>hi</sup>CD39<sup>lo</sup>CD103<sup>hi</sup>CD8<sup>hi</sup>T cells, respectively.

TABLE 3 Univariate and multivariate Cox proportional hazard models for recurrence-free survival.

Variables	Univariate		Multivariate	
	HR (95% CI)	P	HR (95% CI)	P
<b>Age (years)</b>				
<55				Not included
≥55	1.1209 (0.3502-3.588)	0.848		
<b>Gender</b>				
Female				Not included
Male	1.6003 (0.5352-4.786)	0.400		
<b>Histology</b>				
Classical				
Follicular	0.4654 (0.0595-3.64)	0.446	0.6673 (0.082-5.461)	0.7061
Other	0.000 (0-Inf)	0.998	0.000 (0-Inf)	0.998
Tall cell	3.783 (1.0237-13.98)	<b>0.046</b>	4.549 (1.159-17.859)	<b>0.0299</b>
<b>Stage</b>				
I				not include
II	0.000 (0-Inf)	0.998		
III	1.783 (0.5830-5.456)	0.310		
IV+IVA	1.069 (0.1333-8.579)	0.95		
<b>CD8<sup>hi</sup>T cell subsets</b>				
other 5 clusters				
PD-1 <sup>hi</sup> CD39 <sup>hi</sup> CD103 <sup>lo</sup>	4.3422 (0.8408-22.42)	0.0796	4.998 (0.937-26.666)	0.0596
PD-1 <sup>hi</sup> CD39 <sup>lo</sup> CD103 <sup>hi</sup>	4.2236 (1.2880-13.85)	<b>0.0174</b>	3.600 (1.070-12.110)	<b>0.0385</b>
PD-1 <sup>lo</sup> CD39 <sup>hi</sup> CD103 <sup>hi</sup>	5.7237 (0.6632-49.40)	0.1126	8.909 (0.999-79.468)	0.0501

Bold values refers to the establishment of univariate and multivariate Cox proportional hazards models for recurrence-free survival. The P value less than 0.05 has a statistical difference.

PTC, we illustrated that CD8<sup>+</sup>T cells exhibited distinct activation patterns according to PD-1, CD39, and CD103 expression profiles in PTC, which were correlated with PTC relapse.

In line with the previous studies (11), we detected approximately 30.55% CD8<sup>+</sup>T (Figure S2F) and 62.32% CD4<sup>+</sup>T (Figure S2G) cells in PBMC of MNG. However, the percentages of several cell subsets in our observations differ markedly from those in a previous study (34), including 59.18% vs. 18.74% for memory CD4<sup>+</sup>T cells (Figure 1I), 23.16% vs. 42.8% for memory CD8<sup>+</sup>T cells (Figure 1J), and 9.61% vs. 12.7% for B cells (Figure S2D) in PBMC. We speculated that this may be due to differences in the method of peripheral blood immune cell preparation. Consistent with the results of Gogali et al. (11), we found the Treg cell and CD8<sup>+</sup>T/CD4<sup>+</sup>T cell ratio especially memory T cells in thyroid tissues significantly higher than peripheral blood of MNG patients, whereas that in NK cells was the opposite (Figures 1E–J), indicating the activation of antigen-specific naïve T cells in thyroid tissue and migration of memory T cells through blood and home to inflamed tissue (35). CD3<sup>+</sup>CD56<sup>+</sup> cells are a heterogeneous lymphoid population that recognizes the lipid antigens presented by CD1d and has both immune-enhancing and immunosuppressive roles (36). The proportion of CD3<sup>+</sup>CD56<sup>+</sup> cells was increased in thyroid tissues than in peripheral blood. NKT cells have not been characterized in thyroid tissues. In this study, we summarized

the percentage of immune cells from MNG, which was different from peripheral blood and mapped the lymphocyte cells in spatial positions.

Consistent with previous studies (9, 11), we found no significant differences in the percentages of CD8<sup>+</sup>T, CD4<sup>+</sup>T, and NK cells in PTC tissues compared with MNG tissues (Figure S3A) and in PTC peripheral blood compared with MNG peripheral blood (Figure S3B). The difference in the percentages of CD8<sup>+</sup>T and CD4<sup>+</sup>T cells between tumor and paratumor tissues also had no statistical significance (Figure S3A). However, in TCGA database, the proportion of CD8<sup>+</sup>T cells was significantly decreased (16), whereas the proportion of CD4<sup>+</sup>T cells from tumor tissues was increased as compared with that from paratumor (37). It is well known that memory T cells are antigen-specific T cells that typically express CD45RO and can rapidly differentiate into effector T cells to kill the target cells once encountering the same antigen again (38). Therefore, increased memory T cells in PTC reflect that the immune response has been fully activated. Paratumor had more memory CD8<sup>+</sup>T cells compared with MNG, suggesting that the immune microenvironment of the thyroid lobe with tumor involvement may have already altered. Our data displayed that there were differences in Treg cells between MNG, paratumor, and tumor, with the highest proportion of tumor, which was consistent with other PTC studies (11, 19). Notably, the proportion of Treg cells in

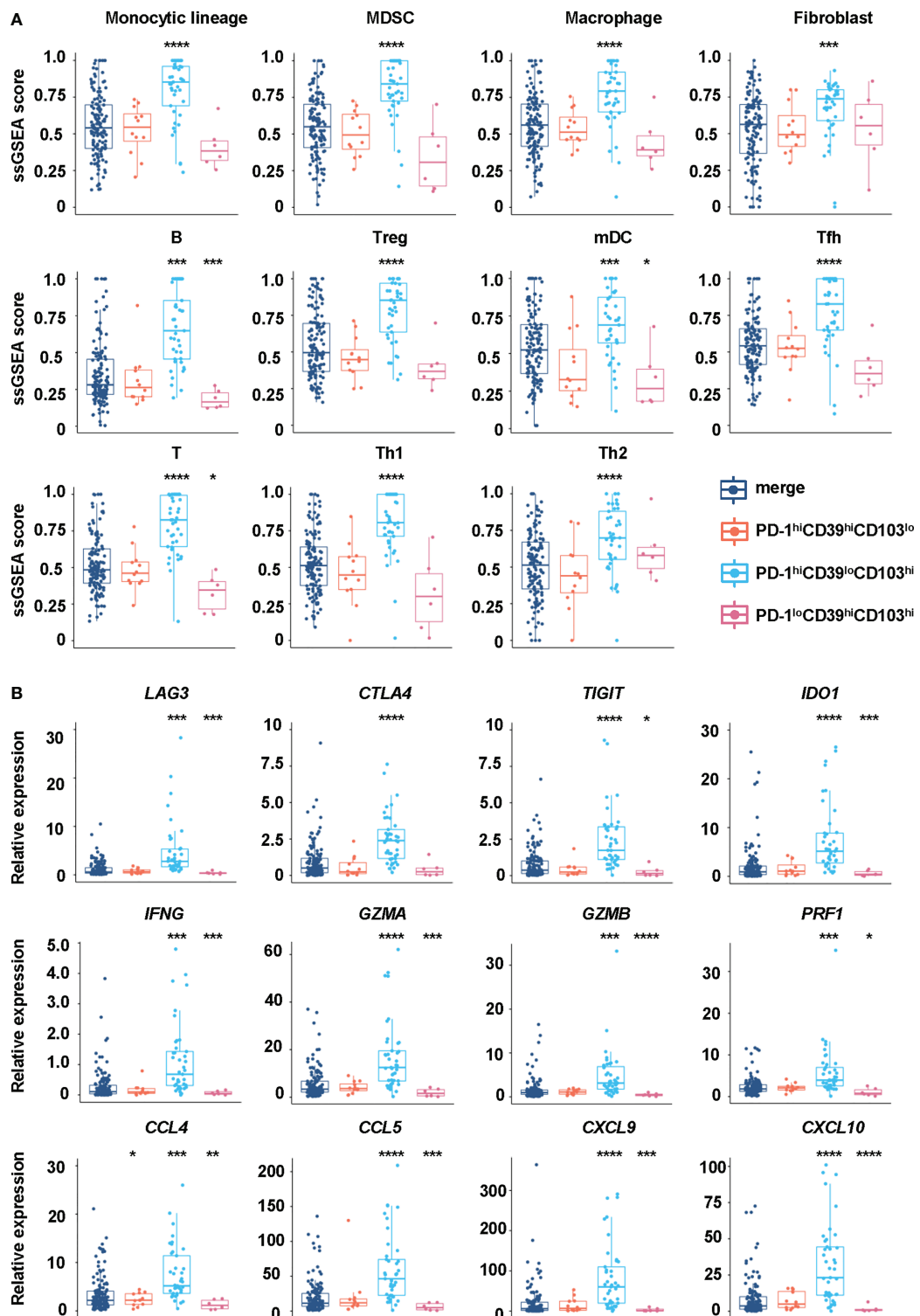


FIGURE 6

Differences in immune cells and regulatory factors in CD8<sup>hi</sup>-T-cell subsets. (A) GSVA enrichment scores of the classical gene signatures for immune cells among the PD-1<sup>hi</sup>CD39<sup>lo</sup>CD103<sup>hi</sup>, PD-1<sup>hi</sup>CD39<sup>hi</sup>CD103<sup>lo</sup>, and PD-1<sup>lo</sup>CD39<sup>hi</sup>CD103<sup>hi</sup> clusters and the other five clusters. (B) The mRNA expression of immune cell regulatory factors in the PD-1<sup>hi</sup>CD39<sup>lo</sup>CD103<sup>hi</sup>, PD-1<sup>hi</sup>CD39<sup>hi</sup>CD103<sup>lo</sup>, and PD-1<sup>lo</sup>CD39<sup>hi</sup>CD103<sup>hi</sup> clusters compared with the other five clusters. \*p < 0.05; \*\*p < 0.01; \*\*\*p < 0.001; \*\*\*\*p < 0.0001.

TABLE 4 Multinomial logistic regression analysis of immune cells associated with PD-1<sup>hi</sup>CD39<sup>hi</sup>CD103<sup>lo</sup> CD8<sup>hi</sup>T, PD-1<sup>hi</sup>CD39<sup>lo</sup>CD103<sup>hi</sup> CD8<sup>hi</sup>T, and PD-1<sup>lo</sup>CD39<sup>hi</sup>CD103<sup>hi</sup> CD8<sup>hi</sup>T cells in tumor from TCGA data.

PD-1 <sup>hi</sup> CD39 <sup>hi</sup> CD103 <sup>lo</sup> CD8 <sup>hi</sup> T cell	OR (95% CI)	P
Monocytic lineage	0.510 (0.033-8.014)	0.632
Myeloid dendritic cells	0.066 (0.004-1.120)	0.060
Neutrophil	0.557 (0.037-8.385)	0.673
B cells	0.260 (0.004-15.738)	0.520
Fibroblast	1.071 (0.089-12.892)	0.957
Macrophage	0.598 (0.035-10.305)	0.724
MDSC	0.399 (0.025-6.344)	0.515
NK cells	0.913 (0.055-15.033)	0.949
Regulatory T cells	0.156 (0.008-3.229)	0.230
T cells	0.356 (0.013-9.504)	0.538
T follicular helper cell	0.695 (0.036-13.567)	0.810
Type 1 T helper cell	0.204 (0.012-3.503)	0.273
Type 17 T helper cell	0.321 (0.020-5.261)	0.426
Type 2 T helper cell	0.283 (0.021-3.831)	0.343
PD-1 <sup>hi</sup> CD39 <sup>lo</sup> CD103 <sup>hi</sup> CD8 <sup>hi</sup> T cell	OR (95% CI)	P
Monocytic lineage	202.519 (27.920-1469.000)	0.000
Myeloid dendritic cells	11.857 (2.552-55.092)	0.002
Neutrophil	1.834 (0.355-9.479)	0.469
B cells	319.830 (46.454-2201.962)	0.000
Fibroblast	19.328 (3.085-121.090)	0.002
Macrophage	133.061 (18.424-960.976)	0.000
MDSC	631.485 (65.345-6102.553)	0.000
NK cells	0.911 (0.173-4.789)	0.913
Regulatory T cells	123.978 (20.187-761.406)	0.000
T cells	545.290 (69.589-4272.833)	0.000
T follicular helper cell	212.966 (28.659-1582.536)	0.000
Type 1 T helper cell	413.319 (51.615-3309.738)	0.000
Type 17 T helper cell	2.792 (0.527-14.795)	0.228
Type 2 T helper cell	32.775 (5.808-184.943)	0.000
PD-1 <sup>lo</sup> CD39 <sup>hi</sup> CD103 <sup>hi</sup> CD8 <sup>hi</sup> T cell	OR (95% CI)	P
Monocytic lineage	0.033 (0.000-2.575)	0.125
Myeloid dendritic cells	0.009 (0.000-0.839)	0.042
Neutrophil	0.085 (0.002-3.217)	0.184
B cells	0.000 (0.000-0.445)	0.035
Fibroblast	1.081 (0.034-34.036)	0.965
Macrophage	0.056 (0.001-3.689)	0.177
MDSC	0.008 (0.000-0.632)	0.030
NK cells	0.011 (0.000-0.386)	0.013
Regulatory T cells	0.025 (0.000-3.527)	0.144
T cells	0.000 (0.000-0.243)	0.017
T follicular helper cell	0.011 (0.000-1.130)	0.056
Type 1 T helper cell	0.007 (0.000-0.568)	0.027
Type 17 T helper cell	0.009 (0.000-0.541)	0.024
Type 2 T helper cell	6.731 (0.171-264.189)	0.309

Bold values refers to the risk factors associated with clinical features and other immune cells for the three tumor patient subsets of PD-1<sup>lo</sup>CD39<sup>hi</sup>CD103<sup>hi</sup>CD8<sup>hi</sup>T, PD-1<sup>hi</sup>CD39<sup>hi</sup>CD103<sup>lo</sup>CD8<sup>hi</sup>T, PD-1<sup>hi</sup>CD39<sup>lo</sup>CD103<sup>hi</sup>CD8<sup>hi</sup>T cells, respectively.

paratumor was the lowest and distinct from MNG in our results. Human CD4<sup>+</sup>CD25<sup>+</sup> Treg cells were composed of phenotypically and functionally distinct subpopulations, which could be separated by the combination of FoxP3 and CD45RA staining, including CD45RA<sup>+</sup>FoxP3<sup>lo</sup>CD25<sup>++</sup> resting Treg cells (rTreg cells) and CD45RA<sup>-</sup>FoxP3<sup>hi</sup>CD25<sup>+++</sup> activated Treg cells (aTreg cells), both of which were suppressive *in vitro*, and cytokine-secreting CD45RA FoxP3<sup>lo</sup>CD25<sup>++</sup> (non-suppressive Treg cells) (26). Our results showed that rTreg cells and non-suppressive Treg cells were dominant Treg-cell subsets in MNG (Figure S4). In addition, Treg cells can migrate into the tumor microenvironment *via* various chemokine–chemokine receptor pathways (39–43). Based on this, we speculated that Treg cells in paratumor migrated into tumor nests, resulting in lower Treg cells than MNG (Figure 2E). Altogether, once PTC had developed, T cells presented a more activated state, and the variations of paratumor and MNG were different.

Our results found that PD-1, CD39, and CD103 were expressed on the CD8<sup>+</sup>T-cell surface in MNG and PTC tissues and presented diverse phenotypes. PD-1 is primarily a marker of T-cell activation (44, 45), but the PD-1 pathway can also regulate T-cell responses during cancer, where persistent antigen stimulation can lead to T-cell exhaustion (46). PD-1 has also been reported to be highly expressed on the T-cell surface in PTC, which was related to the aggressiveness of the disease (47, 48). CD39 is an ectonucleotidase encoded by the ENTPD1 gene, which can catalyze the hydrolysis of eATP and ADP released due to inflammatory stimulation or cell damage into AMP, which is then used by CD73 to synthesize adenosine with immunosuppressive effects (49). CD103 is expressed on a population of T cells found among peripheral tissues, known as tissue-resident memory T cells (T<sub>RM</sub>) (50). CD8<sup>+</sup>T cells are important for PTC recurrence (17), but we found that only some PTC patients with a specific phenotype of CD8<sup>+</sup>T cells showed a high recurrence risk. In our study, not only did PD-1<sup>+</sup>CD39<sup>+</sup>CD103<sup>+</sup>CD8<sup>+</sup>T, PD-1<sup>+</sup>CD39<sup>+</sup>CD103<sup>+</sup>CD8<sup>+</sup>T, and PD-1<sup>-</sup>CD39<sup>+</sup>CD103<sup>+</sup>CD8<sup>+</sup>T cells increase in PTC (Figures 3, 4) but also the increase in these three CD8<sup>+</sup>T-cell subsets, especially PD-1<sup>+</sup>CD39<sup>+</sup>CD103<sup>+</sup>CD8<sup>+</sup>T cells, predicted a poor recurrence-free survival of PTC patients (Figure 5). In lung cancer with a more advanced stage, the fractions of PD-1<sup>+</sup>CD39<sup>+</sup>CD8<sup>+</sup>T cells tend to be higher (51). PTC patients with PD-1<sup>-</sup>CD39<sup>+</sup>CD103<sup>+</sup>CD8<sup>+</sup>T cells had decreased B cells and mDC (Figure 6A), which are essential for CD8<sup>+</sup>T-cell activation and antitumor response (52, 53). In addition, our research showed that CD8<sup>+</sup>T cells in these patients were also in a state of impaired function with low expressions of cytotoxic molecules and perforin, which is critical for antitumor immunity (46) (Figure 6B). Interestingly, PTC patients with PD-1<sup>+</sup>CD39<sup>+</sup>CD103<sup>+</sup>CD8<sup>+</sup>T cells were enriched in immune cells and had a high expression of inhibitory immune checkpoints and chemokines (Figure 6, Table 4), which is similar with the phenotype of anaplastic thyroid carcinoma-like PTC

(54). The anaplastic thyroid carcinoma-like tumors are hot and altered-immunosuppressed tumors, indicating that PD-1<sup>+</sup>CD39<sup>+</sup>CD103<sup>+</sup>CD8<sup>+</sup>T cells may be in a dysfunctional state and exert immune suppressive potential in PTC progression. Although BRAF<sup>V600E</sup> mutation is related to CD8<sup>+</sup>T cells in PTC (16), our data showed that CD8<sup>+</sup>T-cell subsets were not correlated with BRAF<sup>V600E</sup> mutation (data not shown), only with histology and sex (Figures 5A, B). Herein, these specific CD8<sup>+</sup>T cells in PTC were detected to have an association with age, tumor size, or sex (Tables 2, S1), which are reported as risk factors for PTC recurrence (55–57).

In summary, we described the differences in immune cell composition between thyroid tissues and peripheral blood of MNG patients. More importantly, we compared the changes of immune cells in the process of MNG to PTC and discovered the changes in the active status of T cells after the occurrence of malignancy. We also revealed the heterogeneity for PTC based on the expressions of PD1, CD39, and CD103 on CD8<sup>+</sup>T cells. Although the detailed mechanisms need to be further elucidated in future studies, our findings have shown an important role of CD8<sup>+</sup>T-cell subsets in PTC rapid progression or recurrence, which might provide new ideas for the treatment of patients who dedifferentiate from differentiated thyroid cancer to anaplastic thyroid carcinoma.

## Data availability statement

The raw data supporting the conclusions of this article will be made available by the authors, without undue reservation.

## Ethics statement

The research was approved by Medical Ethics Committee of the second affiliated hospital of South China University of Technology (K-2019-185). The patients/participants provided their written informed consent to participate in this study. Written informed consent was obtained from the individual(s) for the publication of any potentially identifiable images or data included in this article.

## Author contributions

ZC, M-LG, and Y-YL performed the experiments. ZC and M-LG analyzed the data. KY and LL helped to analyze the miHIC results. FS and HG collected samples for the experiments. Q-ZL, BX, and Z-XL designed and provided the funding of the project. ZC wrote the manuscript. Q-ZL, LL, HG, BX, and Z-XL revised the manuscript. All authors contributed to the article and approved the submitted version.

## Funding

This work was supported by the Guangzhou Science and Technology Plan Project (202102080170).

## Acknowledgments

We would like to thank The Cancer Genome Atlas (TCGA) database for providing great help to our research.

## Conflict of interest

The authors declare that the research was conducted in the absence of any commercial or financial relationships that could be construed as a potential conflict of interest.

## Publisher's note

All claims expressed in this article are solely those of the authors and do not necessarily represent those of their affiliated organizations, or those of the publisher, the editors and the reviewers. Any product that may be evaluated in this article, or claim that may be made by its manufacturer, is not guaranteed or endorsed by the publisher.

## Supplementary material

The Supplementary Material for this article can be found online at: <https://www.frontiersin.org/articles/10.3389/fimmu.2022.894919/full#supplementary-material>

### SUPPLEMENTARY FIGURE 1

Gating strategies for flow cytometry of peripheral blood (A) and tissue (B). Mononuclear cells (MNCs, DAPI<sup>+</sup>CD45<sup>+</sup>CD16<sup>-</sup>) were gated from live leukocytes without doublets. T cells (CD3<sup>+</sup>CD56<sup>-</sup>), NK cells (CD3<sup>-</sup>

## References

1. Siegel RL, Miller KD, Fuchs HE, Jemal A. Cancer statistics, 2021. *CA Cancer J Clin* (2021) 71(1):7–33. doi: 10.3322/caac.21654
2. Sipos JA, Mazzafferi EL. Thyroid cancer epidemiology and prognostic variables. *Clin Oncol (R Coll Radiol)* (2010) 22(6):395–404. doi: 10.1016/j.clon.2010.05.004
3. Dong W, Horiuchi K, Tokumitsu H, Sakamoto A, Noguchi E, Ueda Y, et al. Time-varying patterns of mortality and recurrence from papillary thyroid cancer: Lessons from a long-term follow-up. *Thyroid* (2019) 29(6):802–8. doi: 10.1089/thy.2018.0128
4. Young S, Harari A, Smoode-Praw S, Ituarte PH, Yeh MW. Effect of reoperation on outcomes in papillary thyroid cancer. *Surgery* (2013) 154(6):1354–61. doi: 10.1016/j.surg.2013.06.043
5. French JD. Immunotherapy for advanced thyroid cancers - rationale, current advances and future strategies. *Nat Rev Endocrinol* (2020) 16(11):629–41. doi: 10.1038/s41574-020-0398-9
6. Matsubayashi S, Kawai K, Matsumoto Y, Mukuta T, Morita T, Hirai K, et al. The correlation between papillary thyroid carcinoma and lymphocytic infiltration in the thyroid gland. *J Clin Endocrinol Metab* (1995) 80(12):3421–4. doi: 10.1210/jcem.80.12.8530576
7. Modi J, Patel A, Terrell R, Tuttle RM, Francis GL. Papillary thyroid carcinomas from young adults and children contain a mixture of lymphocytes. *J Clin Endocrinol Metab* (2003) 88(9):4418–25. doi: 10.1210/jc.2003-030342
8. Yin H, Tang Y, Guo Y, Wen S. Immune microenvironment of thyroid cancer. *J Cancer* (2020) 11(16):4884–96. doi: 10.7150/jca.44506
9. Yu H, Huang X, Liu X, Jin H, Zhang G, Zhang Q, et al. Regulatory T cells and plasmacytoid dendritic cells contribute to the immune escape of papillary thyroid cancer coexisting with multinodular non-toxic goiter. *Endocrine* (2013) 44(1):172–81. doi: 10.1007/s12020-012-9853-2
10. Gogali F, Paterakis G, Rassidakis GZ, Liakou CI, Liapi C. CD3(-)CD16(-)CD56(bright) immunoregulatory NK cells are increased in the tumor microenvironment and inversely correlate with advanced stages in patients with papillary thyroid cancer. *Thyroid* (2013) 23(12):1561–8. doi: 10.1089/thy.2012.0560

11. Gogal F, Paterakis G, Rassidakis GZ, Kaltsas G, Liakou CI, Gousis P, et al. Phenotypical analysis of lymphocytes with suppressive and regulatory properties (Tregs) and NK cells in the papillary carcinoma of thyroid. *J Clin Endocrinol Metab* (2012) 97(5):1474–82. doi: 10.1210/jc.2011-1838
12. Wang X, Li J, Lu C, Wang G, Wang Z, Liu X, et al. IL-10-producing b cells in differentiated thyroid cancer suppress the effector function of T cells but improve their survival upon activation. *Exp Cell Res* (2019) 376(2):192–7. doi: 10.1016/j.yexcr.2019.01.021
13. Varricchi G, Loffredo S, Marone G, Modestino L, Fallahi P, Ferrari SM, et al. The immune landscape of thyroid cancer in the context of immune checkpoint inhibition. *Int J Mol Sci* (2019) 20(16):3934. doi: 10.3390/ijms20163934
14. Cunha LL, Morari EC, Guihen AC, Razolli D, Gerhard R, Nonogaki S, et al. Infiltration of a mixture of immune cells may be related to good prognosis in patients with differentiated thyroid carcinoma. *Clin Endocrinol (Oxf)* (2012) 77(6):918–25. doi: 10.1111/j.1365-2265.2012.04482.x
15. French JD, Weber ZJ, Fretwell DL, Said S, Kloppen JP, Haugen BR. Tumor-associated lymphocytes and increased FoxP3+ regulatory T cell frequency correlate with more aggressive papillary thyroid cancer. *J Clin Endocrinol Metab* (2010) 95(5):2325–33. doi: 10.1210/jc.2009-2564
16. Yang Z, Wei X, Pan Y, Xu J, Si Y, Min Z, et al. A new risk factor indicator for papillary thyroid cancer based on immune infiltration. *Cell Death Dis* (2021) 12(1):51. doi: 10.1038/s41419-020-03294-z
17. Cunha LL, Marcello MA, Nonogaki S, Morari EC, Soares FA, Vassallo J, et al. CD8+ tumour-infiltrating lymphocytes and COX2 expression may predict relapse in differentiated thyroid cancer. *Clin Endocrinol (Oxf)* (2015) 83(2):246–53. doi: 10.1111/cen.12586
18. Imam S, Paparodis R, Sharma D, Jaume JC. Lymphocytic profiling in thyroid cancer provides clues for failure of tumor immunity. *Endocr Relat Cancer* (2014) 21(3):505–16. doi: 10.1530/erc-13-0436
19. Liu Y, Yun X, Gao M, Yu Y, Li X. Analysis of regulatory T cells frequency in peripheral blood and tumor tissues in papillary thyroid carcinoma with and without hashimoto's thyroiditis. *Clin Transl Oncol* (2015) 17(4):274–80. doi: 10.1007/s12094-014-1222-6
20. Luster M, Aktolun C, Amendoeira I, Barczyński M, Bible KC, Duntas LH, et al. European Perspective on 2015 American thyroid association management guidelines for adult patients with thyroid nodules and differentiated thyroid cancer: Proceedings of an interactive international symposium. *Thyroid* (2019) 29(1):7–26. doi: 10.1089/thy.2017.0129
21. Yao Y, Xu P, Ying T, Wang Y, Wang X, Shu L, et al. Integrative analysis of DNA methylation and gene expression identified follicular thyroid cancer-specific diagnostic biomarkers. *Front Endocrinol (Lausanne)* (2021) 12:736068. doi: 10.3389/fendo.2021.736068
22. He H, Jazdzewski K, Li W, Liyanarachchi S, Nagy R, Volinia S, et al. The role of microRNA genes in papillary thyroid carcinoma. *Proc Natl Acad Sci U.S.A.* (2005) 102(52):19075–80. doi: 10.1073/pnas.0509603102
23. Dom G, Tarabichi M, Unger K, Thomas G, Oczko-Wojciechowska M, Bogdanova T, et al. A gene expression signature distinguishes normal tissues of sporadic and radiation-induced papillary thyroid carcinomas. *Br J Cancer* (2012) 107(6):994–1000. doi: 10.1038/bjc.2012.302
24. Vasko V, Espinosa AV, Scouten W, He H, Auer H, Liyanarachchi S, et al. Gene expression and functional evidence of epithelial-to-mesenchymal transition in papillary thyroid carcinoma invasion. *Proc Natl Acad Sci U.S.A.* (2007) 104(8):2803–8. doi: 10.1073/pnas.0610733104
25. Bindea G, Mlecnik B, Tosolini M, Kirilovsky A, Waldner M, Obenauf AC, et al. Spatiotemporal dynamics of intratumoral immune cells reveal the immune landscape in human cancer. *Immunity* (2013) 39(4):782–95. doi: 10.1016/j.immuni.2013.10.003
26. Miyara M, Yoshioka Y, Kitoh A, Shima T, Wing K, Niwa A, et al. Functional delineation and differentiation dynamics of human CD4+ T cells expressing the FoxP3 transcription factor. *Immunity* (2009) 30(6):899–911. doi: 10.1016/j.immuni.2009.03.019
27. Sharma A, Rudra D. Emerging functions of regulatory T cells in tissue homeostasis. *Front Immunol* (2018) 9:883. doi: 10.3389/fimmu.2018.00883
28. Mohr A, Malhotra R, Mayer G, Gorochov G, Miyara M. Human FOXP3(+) T regulatory cell heterogeneity. *Clin Transl Immunol* (2018) 7(1):e1005. doi: 10.1002/cti2.1005
29. Zemmour D, Zilionis R, Kiner E, Klein AM, Mathis D, Benoist C. Single-cell gene expression reveals a landscape of regulatory T cell phenotypes shaped by the TCR. *Nat Immunol* (2018) 19(3):291–301. doi: 10.1038/s41590-018-0051-0
30. Charoentong P, Finotello F, Angelova M, Mayer C, Efremova M, Rieder D, et al. Pan-cancer immunogenomic analyses reveal genotype-immunophenotype relationships and predictors of response to checkpoint blockade. *Cell Rep* (2017) 18(1):248–62. doi: 10.1016/j.celrep.2016.12.019
31. Kansy BA, Concha-Benavente F, Srivastava RM, Jie HB, Shayan G, Lei Y, et al. PD-1 status in CD8(+) T cells associates with survival and anti-PD-1 therapeutic outcomes in head and neck cancer. *Cancer Res* (2017) 77(22):6353–64. doi: 10.1158/0008-5472.CAN-16-3167
32. Xiao Y, Li H, Mao L, Yang QC, Fu LQ, Wu CC, et al. CD103(+) T and dendritic cells indicate a favorable prognosis in oral cancer. *J Dent Res* (2019) 98(13):1480–7. doi: 10.1177/0022034519882618
33. Qi Y, Xia Y, Lin Z, Qu Y, Qi Y, Chen Y, et al. Tumor-infiltrating CD39(+) CD8(+) T cells determine poor prognosis and immune evasion in clear cell renal cell carcinoma patients. *Cancer Immunol Immunother* (2020) 69(8):1565–76. doi: 10.1007/s00262-020-02563-2
34. Bossowski A, Urban M, Stasiak-Barmuta A. Analysis of changes in the percentage of b (CD19) and T (CD3) lymphocytes, subsets CD4, CD8 and their memory (CD45RO), and naive (CD45RA) T cells in children with immune and non-immune thyroid diseases. *J Pediatr Endocrinol Metab* (2003) 16(1):63–70. doi: 10.1515/jpem.2003.16.1.63
35. Masopust D, Schenkel JM. The integration of T cell migration, differentiation and function. *Nat Rev Immunol* (2013) 13(5):309–20. doi: 10.1038/nri3442
36. Crosby CM, Kronenberg M. Tissue-specific functions of invariant natural killer T cells. *Nat Rev Immunol* (2018) 18(9):559–74. doi: 10.1038/s41577-018-0034-2
37. Xie Z, Li X, He Y, Wu S, Wang S, Sun J, et al. Immune cell confrontation in the papillary thyroid carcinoma microenvironment. *Front Endocrinol (Lausanne)* (2020) 11:570604. doi: 10.3389/fendo.2020.570604
38. Han J, Khatwani N, Seales TG, Turk MJ, Angeles CV. Memory CD8(+) T cell responses to cancer. *Semin Immunol* (2020) 49:101435. doi: 10.1016/j.smim.2020.101435
39. Sugiyama D, Nishikawa H, Maeda Y, Nishioka M, Tanemura A, Katayama I, et al. Anti-CCR4 mAb selectively depletes effector-type FoxP3+CD4+ regulatory T cells, evoking antitumor immune responses in humans. *Proc Natl Acad Sci U.S.A.* (2013) 110(44):17945–50. doi: 10.1073/pnas.1316796110
40. Tan MC, Goedegbuure PS, Belt BA, Flaherty B, Sankpal N, Gillanders WE, et al. Disruption of CCR5-dependent homing of regulatory T cells inhibits tumor growth in a murine model of pancreatic cancer. *J Immunol* (2009) 182(3):1746–55. doi: 10.4049/jimmunol.182.3.1746
41. De Simone M, Arrigoni A, Rossetti G, Gruarin P, Ranzani V, Politano C, et al. Transcriptional landscape of human tissue lymphocytes unveils uniqueness of tumor-infiltrating T regulatory cells. *Immunity* (2016) 45(5):1135–47. doi: 10.1016/j.immuni.2016.10.021
42. Nishikawa H, Koyama S. Mechanisms of regulatory T cell infiltration in tumors: implications for innovative immune precision therapies. *J Immunother Cancer* (2021) 9(7):e002591. doi: 10.1136/jitc-2021-002591
43. Facciabene A, Peng X, Hagemann IS, Balint K, Barchetti A, Wang LP, et al. Tumour hypoxia promotes tolerance and angiogenesis via CCL28 and t(reg) cells. *Nature* (2011) 475(7355):226–30. doi: 10.1038/nature10169
44. Gros A, Robbins PF, Yao X, Li YF, Turcotte S, Tran E, et al. PD-1 identifies the patient-specific CD8+ tumor-reactive repertoire infiltrating human tumors. *J Clin Invest* (2014) 124(5):2246–59. doi: 10.1172/jci73639
45. Gros A, Parkhurst MR, Tran E, Pasetto A, Robbins PF, Ilyas S, et al. Prospective identification of neoantigen-specific lymphocytes in the peripheral blood of melanoma patients. *Nat Med* (2016) 22(4):433–8. doi: 10.1038/nm.4051
46. van der Leun AM, Thommen DS, Schumacher TN. CD8(+) T cell states in human cancer: insights from single-cell analysis. *Nat Rev Cancer* (2020) 20(4):218–32. doi: 10.1038/s41568-019-0235-4
47. Bastman JJ, Serracino HS, Zhu Y, Koenig MR, Mateescu V, Sams SB, et al. Tumor-infiltrating T cells and the PD-1 checkpoint pathway in advanced differentiated and anaplastic thyroid cancer. *J Clin Endocrinol Metab* (2016) 101(7):2863–73. doi: 10.1210/jc.2015-4227
48. Severson JJ, Serracino HS, Mateescu V, Raeburn CD, McIntyre RC Jr, Sams SB, et al. PD-1+Tim-3+ CD8+ T lymphocytes display varied degrees of functional exhaustion in patients with regionally metastatic differentiated thyroid cancer. *Cancer Immunol Res* (2015) 3(6):620–30. doi: 10.1158/2326-6066.CIR-14-0201
49. Moesta AK, Li XY, Smyth MJ. Targeting CD39 in cancer. *Nat Rev Immunol* (2020) 20(12):739–55. doi: 10.1038/s41577-020-0376-4
50. Yang K, Kallies A. Tissue-specific differentiation of CD8(+) resident memory T cells. *Trends Immunol* (2021) 42(10):876–90. doi: 10.1016/j.it.2021.08.002
51. Tøndell A, Wahl SG, Sponaas AM, Sørhaug S, Børset M, Haug M. Ectonucleotidase CD39 and checkpoint signalling receptor programmed death 1 are highly elevated in intratumoral immune cells in non-small-cell lung cancer. *Transl Oncol* (2020) 13(1):17–24. doi: 10.1016/j.tranon.2019.09.003
52. Smith AS, Knochelmann HM, Wyatt MM, Rangel Rivera GO, Rivera-Reyes AM, Dwyer CJ, et al. B cells imprint adoptively transferred CD8(+) T cells with enhanced tumor immunity. *J Immunother Cancer* (2022) 10(1):e003078. doi: 10.1136/jitc-2021-003078
53. Kuhn S, Hyde EJ, Yang J, Rich FJ, Harper JL, Kirman JR, et al. Increased numbers of monocyte-derived dendritic cells during successful tumor

immunotherapy with immune-activating agents. *J Immunol* (2013) 191(4):1984–92. doi: 10.4049/jimmunol.1301135

54. Giannini R, Moretti S, Ugolini C, Macerola E, Menicali E, Nucci N, et al. Immune profiling of thyroid carcinomas suggests the existence of two major phenotypes: An ATC-like and a PDTC-like. *J Clin Endocrinol Metab* (2019) 104(8):3557–75. doi: 10.1210/jc.2018-01167

55. Hwangbo Y, Kim JM, Park YJ, Lee EK, Lee YJ, Park DJ, et al. Long-term recurrence of small papillary thyroid cancer and its risk factors in a Korean multicenter study. *J Clin Endocrinol Metab* (2017) 102(2):625–33. doi: 10.1210/jc.2016-2287

56. Zahedi A, Bondaz L, Rajaraman M, Leslie WD, Jefford C, Young JE, et al. Risk for thyroid cancer recurrence is higher in men than in women independent of disease stage at presentation. *Thyroid* (2020) 30(6):871–7. doi: 10.1089/thy.2018.0775

57. Hollenbeck CS, Boltz MM, Schaefer EW, Saunders BD, Goldenberg D. Recurrence of differentiated thyroid cancer in the elderly. *Eur J Endocrinol* (2013) 168(4):549–56. doi: 10.1530/eje-12-0848

# Frontiers in Immunology

Explores novel approaches and diagnoses to treat immune disorders.

The official journal of the International Union of Immunological Societies (IUIS) and the most cited in its field, leading the way for research across basic, translational and clinical immunology.

## Discover the latest Research Topics

See more →

Frontiers

Avenue du Tribunal-Fédéral 34  
1005 Lausanne, Switzerland  
[frontiersin.org](http://frontiersin.org)

Contact us

+41 (0)21 510 17 00  
[frontiersin.org/about/contact](http://frontiersin.org/about/contact)



Frontiers in  
Immunology

